

INVESTIGATING THE LOSS OF SODIUM/PROTON EXCHANGER ISOFORM 6 (NHE6) FUNCTION IN CHRISTIANSON SYNDROME



By

Andy Yuan Lee Gao, B. Sc.

Integrated Program in Neuroscience

McGill University

Montréal, Québec, Canada

December 2020

A thesis submitted to McGill University in partial fulfillment of the requirements of the degree
of Doctor of Philosophy

© Andy Gao, 2020

TABLE OF CONTENTS

ABSTRACT	3
RÉSUMÉ.....	6
ACKNOWLEDGEMENTS.....	10
ABBREVIATIONS	12
PREFACE	17
CONTRIBUTIONS TO ORIGINAL SCIENCE	19
CHAPTER 1. INTRODUCTION	22
1.1 OVERVIEW OF CHRISTIANSON SYNDROME	22
1.2 PHYSIOLOGY OF CENTRAL SYNAPSES.....	25
1.2.1 The hippocampus	25
1.2.2 Dendritic spines and synaptic plasticity	29
1.2.3 Dendritic spines in neurological disorders	34
1.3 ENDOMEMBRANE TRAFFICKING	35
1.3.1 Overview of the endolysosomal system.....	35
1.3.2 Membrane trafficking in excitatory synaptic plasticity	37
1.3.3 Membrane trafficking in inhibitory synaptic plasticity.....	42
1.3.4 pH regulation in the endolysosomal system	45
1.4 Na⁺/H⁺ EXCHANGERS	47
1.4.1 Overview of NHEs	47
1.4.2 NHEs in nervous system function	49
1.4.3 NHE6 function in cellular physiology	53
1.4.4 Insights from <i>Nhe6</i> KO mice	55
1.4.5 Insights from patient-derived NHE6 mutations	59
1.4.6 Involvement of NHE6 in other neurological disorders	62
1.5 RATIONALE AND OBJECTIVES	64
CHAPTER 2. A CHRISTIANSON SYNDROME-LINKED DELETION MUTATION (Δ(287)ES(288)) IN <i>SLC9A6</i> IMPAIRS HIPPOCAMPAL NEURONAL PLASTICITY	66
FOREWARD.....	66
2.1 ABSTRACT	68
2.2 INTRODUCTION	69
2.3 METHODS	71
2.4 RESULTS	78
2.4.1 NHE6 ΔES reduces excitatory synaptic density.....	78
2.4.2 Differential intracellular localization of NHE6 WT and ΔES	81
2.4.3 NHE6 ΔES disrupts AMPA receptor trafficking	84
2.4.4 NHE6 ΔES impairs the response to glycine-mediated chemical LTP.....	86
2.4.5 Restoring spine density and remodeling in NHE6 ΔES-expressing neurons	91
2.5 DISCUSSION	96
2.6 REFERENCES	102
2.7 SUPPLEMENTAL DATA	107

CHAPTER 3. IMPAIRED HIPPOCAMPAL EXCITATORY NEUROTRANSMISSION AND PLASTICITY ASSOCIATED WITH LOSS OF THE CHRISTIANSON SYNDROME PROTEIN <i>SLC9A6/NHE6</i> IS AMELIORATED BY 7,8-DIHYDROXYFLAVONE	109
FOREWARD.....	109
3.1 ABSTRACT.....	111
3.2 INTRODUCTION	112
3.3 METHODS.....	115
3.4 RESULTS	127
3.4.1 Assessing excitatory synaptic number and function in <i>Nhe6</i> KO	127
3.4.2 Investigating potential changes in NMDAR-dependent LTP in <i>Nhe6</i> KO.....	133
3.4.3 Evaluating <i>Nhe6</i> KO animals in behavioural paradigms	139
3.4.4 Restoring losses in <i>Nhe6</i> KO synaptic density and plasticity using a TrkB agonist	141
3.5 DISCUSSION.....	145
3.6 REFERENCES	155
CHAPTER 4. DYSREGULATION OF INHIBITORY NEUROTRANSMISSION PROMOTES HYPEREXCITABILITY OF HIPPOCAMPAL CIRCUITRY IN THE <i>SLC9A6/NHE6</i> KNOCK-OUT MODEL OF CHRISTIANSON SYNDROME.....	164
FOREWARD.....	164
4.1 ABSTRACT.....	166
4.2 INTRODUCTION	167
4.3 METHODS.....	171
4.4 RESULTS	179
4.4.1 Verifying hippocampal circuitry hyperexcitability in <i>Nhe6</i> KO	179
4.4.2 Evaluating inhibitory synaptic regulation in <i>Nhe6</i> KO area CA1	182
4.4.3 Examining GABAergic transmission on to <i>Nhe6</i> KO CA1 principal cells	186
4.4.4 Recapitulating inhibitory synaptic changes in a clinical NHE6 mutant <i>in vitro</i>	192
4.5 DISCUSSION.....	196
4.6 REFERENCES	205
CHAPTER 5. DISCUSSION AND CONCLUSIONS.....	213
5.1 SUMMARY	213
5.2 DISCUSSION.....	214
5.2.1 Prospective concerns over comparing <i>SLC9A6</i> KO and variants	214
5.2.2 Activity-dependent NHE6 trafficking in structural LTP	218
5.2.3 Potential for epileptogenesis via enhancement of TrkB activation.....	221
5.2.4 Additional considerations of cation-Cl ⁻ cotransporter dysregulation in <i>Nhe6</i> KO	224
5.2.5 Possible crosstalk between cellular excitability and excitatory synaptic density	228
5.2.6 Divergent and compensatory mechanisms from NHE9.....	230
5.3 FUTURE DIRECTIONS.....	234
5.4 CONCLUSIONS	238
REFERENCES	240
APPENDIX	274

ABSTRACT

The formation, maintenance, and plasticity of synaptic connections between neurons are critical to allow for the processing and retention of new information in the brain. Perturbations in these tightly regulated yet dynamic mechanisms can impair neural transmission and remodeling in response to environmental stimuli, eventually resulting in neurological deficits. An example of this occurs in Christianson syndrome (CS), a neurodevelopmental/neurodegenerative disorder that commonly presents with moderate to severe intellectual disability, epileptic seizures, truncal ataxia, and autistic traits. CS is an X-linked monogenic disorder resulting from deleterious mutations in the *SLC9A6* gene that encodes (Na⁺ or K⁺)/H⁺ exchanger isoform 6 (NHE6), a regulator of endosomal alkalinisation. Widely expressed throughout the body, NHE6 is enriched in the brain and primarily localizes to early and recycling endosomes to regulate cargo transport to and from the cell surface. In particular, NHE6 has recently been shown to be critical for the trafficking of ionotropic glutamatergic AMPA receptors, which mediate the majority of fast excitatory neurotransmission in the central nervous system, as well as tyrosine receptor kinase B (TrkB), the high-affinity receptor for brain-derived neurotrophic factor (BDNF). Although these data underscore the importance of NHE6 in synaptic transmission and plasticity, its function within the brain is only beginning to be elucidated. As such, the consequences of ablating NHE6 function are also unclear, and clinical interventions for individuals suffering from CS are currently lacking.

In my thesis, I hypothesized that the lack of NHE6 function could (1) disrupt AMPA receptor trafficking to and from synapses, (2) impair synaptic remodeling in response to cellular learning paradigms, and (3) disrupt the balance of excitatory/inhibitory neurotransmission that could favour the development of epileptiform activity. In order to evaluate my hypotheses, I used a wide variety of techniques, including molecular biology, immunofluorescence, confocal

microscopy, electrophysiology, and behavioural paradigms, upon *in vivo*, *ex vivo*, and *in vitro* murine models incorporating either a whole gene *Slc9a6/Nhe6* knock-out (KO) or a patient-derived loss-of-function variant of *SLC9A6* (p.Glu287_Ser288del; Δ ES). To address these questions, I focused on the hippocampus given its well-defined trisynaptic circuitry and inherent involvement in learning and memory in the brain.

A major aspect of my research focused upon excitatory synaptic function and plasticity. Initially, I found that both *Nhe6* KO and Δ ES NHE6-transfected hippocampal neurons exhibited a reduction in the number of mature dendritic spines, or excitatory postsynaptic sites. AMPA receptor protein levels and localization in dendrites were also downregulated when compared to wild-type (WT) neurons. In primary hippocampal neurons expressing Δ ES NHE6, AMPA receptors were mistargeted to late endosomes and lysosomes for presumptive degradation. Consequently, Δ ES-transfected neurons subjected to chemical long-term potentiation (LTP) stimulation were unable to recruit AMPA receptors to postsynaptic sites and undergo both functional and structural potentiation. However, I was able to rescue receptor trafficking and synaptic remodeling by treating Δ ES-positive cells with a lysosomal inhibitor.

In light of these results, I then investigated how LTP could be impacted at the level of the whole hippocampal circuit in *Nhe6* KO animals. Upon LTP induction, KO hippocampal slices showed significantly less potentiation when compared to WT animals. Similar to my findings on the Δ ES mutant, primary KO neurons were unable to properly traffic AMPA receptors and consequently showed impairments in spine motility and remodeling. Interestingly, application of a TrkB agonist, 7,8-dihydroxyflavone (7,8-DHF), ameliorated synaptic density and plasticity. Taken together, these data indicate that removing NHE6 function disrupts the trafficking of AMPA

receptors through the endosomal system, and excitatory synapses were thus unable to be properly strengthen and mature in response to LTP induction.

Finally, I sought to uncover how hyperexcitability could develop within *Nhe6* KO circuitry by focusing on transmission through the inhibitory neurotransmitter γ -aminobutyric acid (GABA). I first found that *Nhe6* KO hippocampi were prone to displaying hyperexcitable firing, even in response to minor elevations in activity. Subpopulations of inhibitory interneurons and molecules involved in GABAergic function, including ionotropic GABA_A receptors and K⁺/Cl⁻ cotransporter 2 (KCC2), were also decreased in KO tissue. As such, I then uncovered evidence from adult *Nhe6* KO hippocampi suggesting that the polarity of GABAergic transmission itself may be dysregulated, possibly attenuating the inhibitory function of GABA. Interestingly, these findings in GABA_A receptor trafficking could be recapitulated in primary hippocampal neurons transfected with Δ ES NHE6 as well. These results suggest that the loss of NHE6 function disrupts the trafficking of molecules involved in inhibitory GABAergic transmission, which could lead to the development of hyperexcitability in *Nhe6* KO.

In summary, my results comprise some of the first to investigate the role of NHE6 in excitatory LTP mechanisms and GABAergic inhibition. Importantly, I also uncovered novel therapeutic avenues that could be taken to potentially address cognitive deficits and epilepsy in CS. With my thesis work, I hope to have furthered our understanding of NHE6 within the brain, and how the consequences of removing NHE6 function could be targeted to improve patient outcomes in CS and other neurological disorders involving endosomal dysfunction.

RÉSUMÉ

La formation, le maintien et la plasticité des connexions synaptiques entre les neurones sont essentiels pour permettre le traitement et la rétention de nouvelles informations dans le cerveau. Dans ces mécanismes dynamiques mais étroitement régulés, les perturbations peuvent altérer la transmission et le remodelage neuronaux en réponse à des stimulations environnementales, ce qui peut entraîner à terme des déficits neurologiques. C'est le cas du syndrome de Christianson (SC), une maladie neurodéveloppementale/neurodégénérative qui se présente généralement sous la forme d'une déficience intellectuelle modérée à sévère, de crises d'épilepsie, d'ataxie troncale et de traits autistiques. Le SC est un trouble monogénique lié à l'X résultant de mutations délétères dans le gène *SLC9A6* qui code l'isoforme 6 de l'échangeur (Na^+ ou K^+)/ H^+ (NHE6), un régulateur de l'alcalinisation endosomale. Largement exprimé dans tout l'organisme, NHE6 est enrichi dans le cerveau et se localise principalement dans les endosomes précoces et de recyclage pour réguler le transport protéique vers et depuis la surface cellulaire. En particulier, il a récemment été démontré que NHE6 est essentiel pour le trafic des récepteurs au glutamate ionotropiques AMPA, qui assurent la majorité de la neurotransmission excitatrice rapide dans le système nerveux central, ainsi que pour le récepteur à la tyrosine kinase B (TrkB), le récepteur à haute affinité pour le facteur neurotrophique dérivé du cerveau (BDNF). Bien que ces données soulignent l'importance de NHE6 dans la transmission synaptique et la plasticité, sa fonction dans le cerveau commence seulement à être élucidée. Ainsi, les conséquences de la perte de NHE6 ne sont pas claires, et les interventions cliniques pour les personnes souffrant de SC sont actuellement inexistantes. Dans le cadre de ma thèse, j'ai émis l'hypothèse que l'absence de fonction NHE6 pourrait (1) perturber le trafic des récepteurs AMPA vers et depuis les synapses, (2) entraver le remodelage synaptique en réponse aux modèles d'apprentissage cellulaire, et (3) perturber l'équilibre de la neurotransmission

excitatrice/inhibitrice au sein des circuits neuronaux, ce qui pourrait favoriser le développement de l'activité épileptique convulsive ou épileptiforme. Afin d'évaluer mes hypothèses, j'ai utilisé une grande variété de techniques, notamment la biologie moléculaire, l'immunofluorescence, la microscopie confocale, l'électrophysiologie et les paradigmes comportementaux, sur des modèles murins *in vivo*, *ex vivo* et *in vitro* incorporant soit un gène entier *Slc9a6/Nhe6 knock-out* (KO), soit une variante de perte de fonction de *SLC9A6* dérivée du patient (p.Glu287_Ser288del ; Δ ES). Pour répondre à ces questions, je me suis concentré sur l'hippocampe, étant donné son circuit tri-synaptique bien défini et son implication fondamentale dans l'apprentissage et la mémoire dans le cerveau.

Un aspect majeur de mes recherches a porté sur la fonction synaptique excitatrice et la plasticité. Au départ, j'ai constaté que les neurones de l'hippocampe *Nhe6* KO et Δ ES NHE6-transfectés présentaient une réduction du nombre d'épines dendritiques matures, ou sites postsynaptiques excitateurs. Les niveaux de protéines des récepteurs AMPA et la localisation dans les dendrites ont également été sous-régulés par rapport aux neurones de type sauvage (WT). Dans les neurones primaires de l'hippocampe exprimant Δ ES NHE6, les récepteurs AMPA ont été mal ciblés vers les endosomes et lysosomes tardifs pour une dégradation supposée. Par conséquent, les neurones transfectés Δ ES soumis à une potentialisation à long terme (PLT) chimique n'ont pas pu recruter de récepteurs AMPA sur les sites postsynaptiques et donc réaliser une potentialisation à la fois fonctionnelle et structurelle. Cependant, j'ai pu rétablir le trafic de récepteurs et le remodelage synaptique en traitant les cellules Δ ES-positives avec un inhibiteur lysosomal. À la lumière de ces résultats, j'ai ensuite étudié comment la PLT pouvait être affecté au niveau de l'ensemble du circuit hippocampique chez les animaux *Nhe6* KO. Lors de l'induction de la PLT, les tranches d'hippocampe KO ont montré une potentialisation significativement moindre par rapport aux

animaux WT. Tout comme mes conclusions sur le mutant Δ ES, les neurones KO primaires étaient incapables de faire circuler correctement les récepteurs AMPA et ont donc montré des déficiences dans la motilité et le remodelage des épines. Il est intéressant de noter que l'application d'un agoniste TrkB, la 7,8-dihydroxyflavone (7,8-DHF), a amélioré la densité synaptique et la plasticité. Ensemble, ces données indiquent que l'élimination de la fonction NHE6 perturbe le trafic des récepteurs AMPA à travers le système endosomal, et que les synapses excitatrices n'ont donc pas pu être correctement renforcées et maturées en réponse à l'induction du PLT.

Enfin, j'ai cherché à découvrir comment l'hyperexcitabilité pouvait se développer dans le circuit *Nhe6* KO en me concentrant sur la transmission par le neurotransmetteur inhibiteur GABA ou acide γ -aminobutyrique. J'ai d'abord découvert que les hippocampes NHE6-KO étaient enclins à afficher une hyperexcitabilité, même en réponse à une légère augmentation de l'activité. Des sous-populations d'interneurones inhibiteurs et de molécules impliquées dans la fonction GABAergique, y compris les récepteurs ionotropiques GABA_A et le co-transporteur 2 de K⁺/Cl⁻ (KCC2), ont également été diminuées dans le tissu KO. À ce titre, j'ai ensuite découvert des preuves provenant d'hippocampes *Nhe6* KO adultes suggérant que la polarité de la transmission GABAergique elle-même pourrait être dérégulée, ce qui pourrait atténuer la fonction inhibitrice du GABA. Il est intéressant de noter que ces découvertes sur le trafic des récepteurs GABA_A pourraient être réitérées dans les neurones primaires des hippocampes transfectés avec Δ ES NHE6 également. Ces résultats suggèrent que la perte de la fonction NHE6 perturbe le trafic des molécules impliquées dans la transmission inhibitrice du GABA_A, ce qui pourrait conduire au développement d'une hyperexcitabilité dans le modèle animal *Nhe6* KO.

En résumé, mes résultats sont parmi les premiers à étudier le rôle de NHE6 dans la LTP des neurones excitations et dans l'inhibition GABAergique. Il est également important de noter

que j'ai découvert de nouvelles voies thérapeutiques qui pourraient être utilisées pour traiter les déficits cognitifs et l'épilepsie dans le SC. Avec mon travail de thèse, j'espère avoir fait progresser notre compréhension de NHE6 dans le cerveau, ainsi ouvert de nouvelles pistes thérapeutiques pour les patients atteints du SC et d'autres troubles neurologiques impliquant un dysfonctionnement endosomal.

ACKNOWLEDGEMENTS

To preface, I'd like to acknowledge that McGill University is situated on the traditional territory of the Kanien'kehà:ka, a place which has long served as a site of meeting and exchange amongst nations. I recognize and respect the Kanien'kehà:ka as the traditional custodians of the lands and waters on which I carried out the majority of the work presented in this thesis.

If you're reading this, that means I'm nearing the end of my graduate school experience! Who thought this day would ever finally come? First and foremost, I'd like to thank my supervisor, Dr. Anne McKinney, for accepting me as a graduate student and for all of the ongoing support over the years. Even when the proverbial ship of scientific research felt like it was going to capsize, she was always there to steer us back in the right direction. Thanks for helping me grow both as a scientist and as a person. I'd also like to thank the members of my committee, Drs. John Orłowski, Ed Ruthazer, and Tim Kennedy for all of the insightful feedback and suggestions over the years, as well as my IPN mentor Dr. Alanna Watt for the helpful discussions and advice. A big thanks to the various funding agencies for supporting my studies over the years, including NSERC, the McGill Faculty of Medicine, Healthy Brains Healthy Lives, and the IPN.

Furthermore, I'd like to thank the past and present members of the McKinney lab with whom I've had the chance to work, including Fiorella Guido, Melanie Chan, Jennifer Boateng, Louis-Charles Masson, Pei You Wu, Jonathan Reid, Roy Shi, Albert Le, Lingxiao Chen, and Drs. Phil Chang, Raminder Gill, Talia James, and Yanis Inglebert. Thanks for all of the support, helpful discussions, and laughs, and thanks to Yanis for translating my abstract into français. A special shout-out to Phil for all of his infinite wine and wisdom, as well as for spending his evenings and weekends watching me as I struggled to locate my pipette under the objective at the electrophysiology rig. "Un gros merci" to François Charron for the extensive technical assistance,

ordering our countless supply of reagents, showing me how to remove wee hippocampi, culture prep, mouse coordination, and casual French practice.

Outside of the immediate lab, I'd also like to express my utmost gratitude for Tanya Koch and the members of the CMARC for helping us deal with the trickiest of critters and for trying to meet my constant requests for mice. I'd like to thank the members of the Orlowski lab, including Dr. Alina Ilie, Mark Jacunski, and Annie Boucher for all of the molecular biology and cell culture support; the members of the Watt lab, including Kim Gruver, Anna Cook, Eviatar Fields, and Dr. Brenda Toscano Marquez for the mice, friendship, and perfusion pump and vibratome usage; and our close collaborators from the Sonenberg lab, including Anmol Nagpal, Shane Wiebe, and Dr. Jelena Popic, for carrying out the work in mouse behaviour and tissue collection. I'd also like to thank Drs. Stephen Glasgow, Gary Huang, Hugues Petitjean, and Chris Salmon for coming to my talks and for all of the undeniably helpful advice and support for the work presented in this thesis. An additional thanks to the members of the Cell Information Systems group, the ABIF, and my fellow worker bees on the Bellini first floor as well.

Of course, I'd like to extend my deepest gratitude to the many friends and acquaintances I've made along the way. Thank you all for keeping me grounded, level-headed, and entertained outside of the lab over the past few years. Finally, I'd also like to thank my parents and the rest of my family for all of their support over the years. Without you all, I wouldn't have been able to accomplish so much and make it this far.

ABBREVIATIONS

4-AP: 4-aminopyridine

7,8-DHF: 7,8-dihydroxyflavone

A9S: missense mutation in NHE6 in which alanine 9 is replaced with serine

(n)ACSF: (normal) artificial cerebrospinal fluid

AD: Alzheimer's disease

ADHD: attention deficit hyperactive disorder

ADNP: activity-dependent neuroprotective protein

AMPA: α -amino-3-hydroxy-5-methyl-4-isoxazolepropionic acid receptor

AMPK: adenosine monophosphate (AMP)-activated protein kinase

ANOVA: analysis of variance

AP: action potential

AP-1: Chinese hamster ovary (CHO) cells deficient in the Na^+/H^+ antiporter 1 isoform

AP2: adaptor protein 2

ApoE4: Apolipoprotein E

APP: amyloid precursor protein

Arc: activity-regulated cytoskeleton-associated protein

Arp2/3: actin-related protein 2/3

AS: Angelman syndrome

ASD: autism spectrum disorder

AT2: angiotensin II receptor subtype 2

ATP: adenosine triphosphate

A β : amyloid beta

BACE1: β -secretase 1

BDNF: brain-derived neurotrophic factor

BSA: bovine serum albumin

CA: *cornu ammonis*

CaM: calmodulin

CaMKII: Ca^{2+} /calmodulin-dependent protein kinase 2

CFC: contextual fear conditioning

CLC: $2\text{Cl}^-/1\text{H}^+$ exchanger

CME: clathrin/AP2-mediated endocytosis

CNS: central nervous system

CP-AMPA: Ca^{2+} -permeable AMPAR

(RS)-CPP: (RS)-3-(2-carboxypiperazin-4-yl)-propyl-1-phosphonic acid

CR: calretinin

CS: Christianson syndrome

DG: dentate gyrus

DIV: day(s) *in vitro*

DMEM: Dulbecco's Modified Eagle's Medium
DMSO: dimethyl sulfoxide
DNA: deoxyribonucleic acid
E(D): embryonic day
E/I: excitatory/inhibitory
EAAT1: excitatory amino acid transporter 1
EDTA: ethylenediaminetetraacetic acid
EE: early endosome
EEA1: early endosomal antigen-1
EEG: electroencephalogram
EGF: epidermal growth factor
EGFP: enhanced green fluorescent protein
EGTA: ethylene glycol-bis(β -aminoethyl ether)-N,N,N',N'-tetraacetic acid
EHD: Eps15 homology domain-containing proteins
EIPA: 5'-(N-ethyl-N-isopropyl)-amiloride
EL: extracellular loop
eNHE: endosomal NHE
Eps8: epidermal growth factor receptor kinase substrate 8
ER: endoplasmic reticulum
ERAD: ER-associated protein degradation
ESES: electrical *status epilepticus* during slow-wave sleep
ESCRT: endosomal sorting complexes required for transport
EZ: endocytic zone
 E_{GABA} : membrane reversal potential of GABA
FBS: fetal bovine serum
fEPSP: field excitatory postsynaptic potential
FGF1: fibroblast growth factor receptor 1
FXS: Fragile X syndrome
G218R: missense mutation in NHE6 in which glycine 218 is replaced with arginine
GABA: γ -aminobutyric acid
GAD: glutamic acid decarboxylase
GAPDH: glyceraldehyde 3-phosphate dehydrogenase
GFP: green fluorescent protein
gly-ChemLTP: glycine-mediated chemical long-term potentiation
GM: ganglioside monosialiac
HA: influenza virus hemagglutinin epitope
HAP1: Huntingtin-associated protein 1
HBSS: Hank's Balanced Salt Solution
HDAC: histone deacetylase
HEK-293: human embryonic kidney 293 cells

HeLa: immortalized cancer cell line derived from Henrietta Lacks
HEPES: 4-(2-hydroxyethyl)-1-piperazineethanesulfonic acid
HepG2: liver hepatocellular carcinoma cells
HIHS: heat-inactivated horse serum
HPC: hippocampus
HRP: horseradish peroxidase
IEI: interevent interval
iLTP: inhibitory LTP
KCC2: K^+ - $2Cl^-$ co-transporter 2
KD: knock-down
KIF5: kinesin family 5
KO: knock-out
LAMP1: lysosomal-associated membrane protein 1
LE: late endosome
leu: leupeptin
LIMK1: Lin11/Isl-1/Mec-3 (LIM) domain kinase 1
LRP1: lipoprotein-related receptor protein 1
LSD: lysosomal storage disease
LTD: long-term depression
(E/L)-LTP: (early/late)-long-term potentiation of excitatory synapses
Lys: lysosome
mCh: mCherry fluorescent protein
mEPSC: miniature excitatory postsynaptic current
MES: 2-(4-morpholino) ethanesulfonic acid
mGFP: membrane-tagged enhanced green fluorescent protein
mIPSC: miniature inhibitory postsynaptic current
NBQX: 2,3-dioxo-6-nitro-7-sulfamoyl-benzo[f]quinoxaline
Nedd: neural precursor cell expressed developmentally down-regulated protein
NHA: mammalian Na^+/H^+ antiporters
NhaA: bacterial Na^+/H^+ antiporter
NHE: mammalian alkali cation (Na^+ or K^+)/ H^+ exchanger
NKCC1: Na^+ - K^+ - $2Cl^-$ co-transporter 1
NMDAR: N-methyl D-aspartate receptor
NOL: novel object location
NOR: novel object recognition
pGluA: phosphorylated GluA AMPAR subunit
P(D): post-natal day
PB: phosphate buffer
PBS(-T): phosphate-buffered saline (with 0.1% Tween-20)
PCR: polymerase chain reaction

PD: Parkinson's disease
PFA: paraformaldehyde
PTP: post-tetanic potentiation
pTrkB: phosphorylated TrkB receptor
pH_i: cytosolic/intracellular pH
pH_o: outside/extracellular pH
PIP2: phosphatidylinositol 4,5-bisphosphate
PKA: protein kinase A
PKC: protein kinase C
PP1: protein phosphatase 1
PPR: paired-pulse ratio
PSD: post-synaptic density
PV: parvalbumin
PVDF: polyvinylidene fluoride
R568Q: missense mutation in NHE6 in which arginine 568 is replaced with glutamine
RACK1: receptor of activated C kinase 1
RE: recycling endosome
RIPA: radioimmunoprecipitation assay
RNA: ribonucleic acid
RRP: readily releasable pool
RS: Rett's syndrome
SC: Schaffer collateral
SDS: sodium dodecyl sulfate
SE: signaling endosome
SEP: superecliptic pHluorin
sGluA: surface GluA AMPAR subunit
SHV: spine head volume
sIPSC: spontaneous inhibitory postsynaptic current
SNARE: soluble N-ethylmaleimide sensitive factor (NSF) attachment protein (SNAP) receptor
SLC: solute carrier family
SOM: somatostatin
Stx-13: syntaxin-12/13
NHS: N-hydroxysuccinyl
SV2: synaptic vesicle 2
SUDEP: sudden unexplained death due to epilepsy
SUMO: small ubiquitin-like modifier
TARP: transmembrane AMPA receptor regulatory protein
TBS(-T): Tris-buffered saline (with 0.5% Tween-20)
TBS: theta burst stimulation
tdT: tdTomato fluorescent protein

TLE: temporal lobe epilepsy

TM: transmembrane

(AF-)Tfn: (AlexaFluor-tagged) transferrin

TrkB: tropomyosin receptor kinase B

TTX: tetrodotoxin

UBE3A: ubiquitin-protein ligase E3A

V-ATPase: vacuolar H⁺-ATPase

VIP: vasoactive intestinal peptide

WT: wild-type

XLID: X-linked intellectual disability

ΔES: in-frame deletion mutation of amino acid residues glutamic acid 277 and serine 278 in NHE6

ΔWST: in-frame deletion mutation of tryptophan 370, serine 371, and threonine 372 in NHE6

PREFACE

This thesis is written in manuscript form in compliance with thesis preparation guidelines issued by Graduate and Postdoctoral Studies of McGill University and contains three manuscripts. Chapters 2, 3, and 4 of my dissertation are modified versions of the following manuscripts:

1. **Gao AYL**, Ilie A, Chang PKY, Orlowski J, McKinney RA (2019). A Christianson syndrome-linked deletion mutation ($\Delta 287\text{ES}288$) in *SLC9A6* impairs hippocampal neuronal plasticity. *Neurobiol Dis.* 130:104490. DOI: [10.1016/j.nbd.2019.104490](https://doi.org/10.1016/j.nbd.2019.104490)
 - AYLG generated and analyzed all of the data in the present study and prepared the figures in the manuscript. AI designed, generated, and helped to transfect DNA constructs. PKYC helped to collect electrophysiological data. JO and RAM contributed to study design, supervision, and coordination. AYLG and RAM wrote the manuscript with contributions from all authors.
2. **Gao AYL**, Inglebert Y, Nagpal A, Wiebe S, Shi R, Popic J, Sonenberg N, Orlowski J, McKinney RA (2020). Impaired hippocampal excitatory neurotransmission and plasticity associated with loss of the Christianson syndrome protein *Slc9a6/Nhe6* is ameliorated by 7,8-dihydroxyflavone. *In preparation*.
 - AYLG and RAM designed experiments. AYLG collected and analyzed all of the data except for electrophysiological field recordings (performed by YI), mouse behaviour experiments (performed by AN and SW), and synaptic density drug treatments (performed by RS). JP also contributed to sample preparation. AYLG prepared all figures and wrote the manuscript with RAM.

3. **Gao AYL**, Masson LC, James TF, Glasgow SD, Orlowski J, McKinney RA (2020). Dysregulation of inhibitory neurotransmission promotes hyperexcitability of hippocampal circuitry in the *Slc9a6/Nhe6* knock-out model of Christianson syndrome. *In preparation*.
 - AYL and RAM designed experiments. AYL collected and analyzed all of the data except for electrophysiological action potential recordings (performed by TFJ and SDG). LCM contributed to immunohistochemistry data collection and analysis. AYL prepared all figures and wrote the manuscript with RAM.

Over the course of my doctoral work, I have also co-authored other publications pertaining to *SLC9A6* mutations using similar methods as those presented here. However, I have not included them in the main body of my thesis because they do not directly relate to my research focusing on synaptic function and plasticity. The following manuscripts appear in my Appendix:

1. Ilie A, **Gao AY**, Reid J, Boucher A, McEwan C, Barrière H, Lukacs GL, McKinney RA, Orlowski J (2016). A Christianson syndrome-linked deletion mutation ($\Delta(287)ES(288)$) in *SLC9A6* disrupts recycling endosomal function and elicits neurodegeneration and cell death. *Mol Neurodegener.* 11(1):63. DOI: [10.1186/s13024-016-0129-9](https://doi.org/10.1186/s13024-016-0129-9)
2. Ilie A, **Gao AYL**, Boucher A, Park J, Berghuis AM, Hoffer MJV, Hilhorst-Hofstee Y, McKinney RA, Orlowski J (2019). A potential gain-of-function variant of *SLC9A6* leads to endosomal alkalinization and neuronal atrophy associated with Christianson Syndrome. *Neurobiol Dis.* 121:187-204. DOI: [10.1016/j.nbd.2018.10.002](https://doi.org/10.1016/j.nbd.2018.10.002)

CONTRIBUTIONS TO ORIGINAL SCIENCE

My findings reveal novel ways in which ablating or mutating NHE6 impairs synaptic function within murine hippocampal circuitry, which may parallel molecular mechanisms in individuals with Christianson syndrome.

Although not included in the main body of my thesis, I initially contributed to a manuscript entitled “A Christianson syndrome-linked deletion mutation ($\Delta(287)ES(288)$) in *SLC9A6* disrupts recycling endosomal function and elicits neurodegeneration and cell death” published in the journal *Molecular Neurodegeneration*. For this manuscript, I prepared primary hippocampal neuron cultures and transfected a patient-derived *SLC9A6* variant (p.E287_S288del, or ΔES) to demonstrate the ensuing neurodegeneration. This publication primarily focused on the effects of this particular mutation upon its biochemical characteristics and impacts upon cellular physiology, as elucidated by members of Dr. J. Orłowski’s laboratory. Using a plasmid constructed by Dr. A. Ilie, I collected and analyzed data on changes in neuronal branching, endocytosis, and apoptosis induced by the ΔES variant. I also prepared representative images and quantifications for Dr. J. Orłowski for Figures 11, 12, and 13 of this paper. Readers seeking to gain a background understanding of this mutation are first directed to this manuscript in my Appendix.

Extending this initial publication on ΔES NHE6, I then studied the effects of the mutation specifically upon neuronal function and plasticity. These data are presented in Chapter 2 of my thesis and published in a manuscript entitled “A Christianson syndrome-linked deletion mutation ($\Delta(287)ES(288)$) in *SLC9A6* impairs hippocampal neuronal plasticity” published in *Neurobiology of Disease*. For this study, I found additional impairments in neuronal dendritic spine density, AMPA receptor trafficking, and long-term potentiation (LTP) mechanisms upon transfection of the ΔES variant. However, I was able to restore these deficits in synaptic number and plasticity by applying

leupeptin, an inhibitor of lysosomal proteases. For this publication, Dr. P. K.-Y. Chang helped to collect the electrophysiological data. I collected and analyzed all of the data and prepared all of the figures and wrote the published manuscript with Dr. R. A. McKinney.

In a similar vein, I have also contributed to another manuscript entitled “A potential gain-of-function variant of *SLC9A6* leads to endosomal alkalinization and neuronal atrophy associated with Christianson Syndrome,” which was also published in *Neurobiology of Disease* and can be found in my Appendix. For this study, I assessed the impact of another patient-derived NHE6 mutation (p.Gly218Arg; G218R) upon neuronal function. I again prepared primary hippocampal neurons and expressed G218R NHE6 into them. I then collected and analyzed data from transfected cells to study dendritic branching, spine density, and vesicular pH measurements with Dr. A. Ilie. I then provided representative images and data values for Dr. J. Orlowski for Figures 7 and 8 of the manuscript.

In Chapter 3, I subsequently investigated how the complete ablation of NHE6 impacts excitatory synaptic function and plasticity in the murine hippocampus. For these experiments, I purchased *Slc9a6/Nhe6* knock-out (KO) mice from Jackson laboratories and crossbred them with Thy1-mGFP (L15 mice) (generously provided by Dr. P. Caroni, FMI, Basel) to generate a line of NHE6 deficient mice expressing mGFP in a subset of hippocampal pyramidal neurons. I then found that dendritic spine density, excitatory neurotransmission, AMPA receptor trafficking, and functional and structural plasticity were disrupted in these KO animals. However, by applying a tyrosine receptor kinase B (TrkB) agonist, 7,8-dihydroxyflavone (7,8-DHF), I was able to rescue the deficits in spine density and remodeling. Surprisingly, A. Nagpal and S. Wiebe from Dr. N. Sonenberg’s laboratory found that adult KO male mice did not show deficits in hippocampal-dependent learning paradigms, although they showed strong locomotor impairments while

performing in these tasks. For this manuscript, Dr. Y. Inglebert collected and analyzed the field LTP data, Dr. J. Popic provided brain tissue and assistance with immunoblotting experiments, and R. Shi helped with imaging and analyzing spine counts for the 7,8-DHF rescue experiments. I generated and analyzed the remainder of data and prepared all of the figures for the manuscript.

In Chapter 4, I sought to elucidate mechanisms that could underlie seizure generation in *Nhe6* KO mice. Together with Drs. T. F. James and S. D. Glasgow, we found that acute hippocampal slice preparations from KO animals were more susceptible to showing burst discharges in response to subthreshold concentrations of the convulsant 4-aminopyridine, confirming that the hippocampal circuitry of these mice was indeed hyperexcitable. With L. C. Masson, we then uncovered reduced counts of parvalbumin-expressing interneurons across time points in KO hippocampi. Accordingly, I then found that the trafficking of inhibitory synaptic molecules, including GABA_A receptors and gephyrin, were reduced, which also lead to alterations in inhibitory neurotransmission in CA1 pyramidal neurons. Interestingly, I was able to recapitulate similar findings from primary hippocampal neurons transfected with the Δ ES NHE6 mutant. Furthermore, I noted a significant increase in NKCC1 protein with a concomitant decrease in KCC2 protein in adult KO hippocampi, which was suggestive of a dysregulation in Cl⁻ homeostasis and a possible change in the polarity of GABA. I collected and analyzed all of the data for these experiments (except where noted) and prepared all of the figures for this chapter.

CHAPTER 1. INTRODUCTION

1.1 OVERVIEW OF CHRISTIANSON SYNDROME

Neurodevelopmental disorders comprise a heterogeneous group of conditions that result from disturbances in early brain development. One such condition is the recently characterized Christianson syndrome (CS) (OMIM 300243). CS was first described in 1999 as a form of severe X-linked intellectual disability (XLID) syndrome in a cohort of South African patients with non-verbalism, truncal ataxia, musculoskeletal malformations, and cerebellar atrophy [1]. Initially localized to a gene locus within chromosomal region Xq24-q27, mutations in the *SLC9A6* gene encoding (Na⁺ or K⁺)/H⁺ exchanger (NHE) isoform 6 (NHE6) were later identified as the underlying cause of CS [2]. As I will elaborate upon later, NHE6 is a mediator of endosomal pH and cargo trafficking in various cell types, including brain cells. Over the past decade, additional insights into a greater cohort of patients revealed numerous other clinical findings, including developmental delay, hyperkinesia, epilepsy, and postnatal microcephaly. Some patients additionally present with abnormal eye movements (such as strabismus), gastrointestinal issues, and low height and/or weight gain (for further details on existing clinical findings, see [3,4]). Altered somatosensory processing, including reduced sensitivity to pain, has also been reported recently [5]. In spite of the severity of CS, insights into the molecular mechanisms that lead to its broad phenotypic spectrum are only beginning to be elucidated.

To date, over 80 mutations in the human *SLC9A6* gene have been identified worldwide, including in-frame deletions, missense mutations, splice variants, single nucleotide variations, microduplications, and others [2,5–18] (see also ClinVar (<https://www.ncbi.nlm.nih.gov/clinvar/>) and DECIPHER (<https://decipher.sanger.ac.uk/>) (Fig. 1). Although it is typically considered a “rare” disease, CS may actually comprise 1-2% of all forms of XLID, with a frequency between

10% to 50% that of Fragile X Syndrome (FXS), the most common form XLID. As such, it is presently estimated to affect between 1 in 16,000 to 1 in 100,000 people worldwide [5,12]. In fact, *SLC9A6* is one of the six most commonly mutated loci in patients with XLID, autistic traits, and seizures [12]. While both inherited and *de novo* *SLC9A6* mutations have been characterized in hemizygous males with CS, females heterozygous for mutant *SLC9A6* alleles show a more intermediate phenotype ranging from being asymptomatic to having mild cognitive impairments that may only be evident with standardized neuropsychological testing [1,5,9,14]. Consequently, recent reports have suggested a diverse range of impairments in female carriers that are reminiscent of male CS patients, including developmental delays, mood disorders, and deficits in attention, visuospatial processing, and executive function [19,20]. These findings underscore the impact of *SLC9A6* mutations upon proper nervous system function, even in heterozygous carriers.

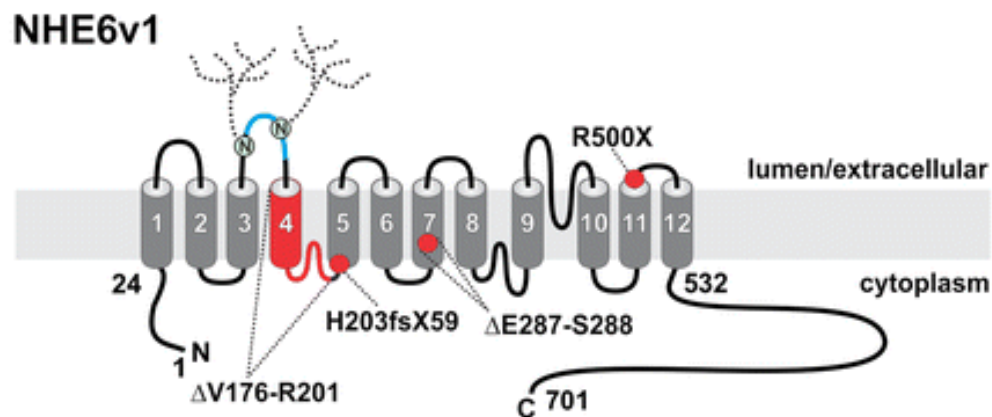


Figure 1: Schematic of the predicted membrane topology of the longest mammalian splice variant of NHE6 (NHE6v1) as extrapolated from the structure of NHE1, with predicted N-linked glycosylation sites on extracellular loop 2 (EL2) shown. Locations of some Christianson syndrome mutations, as identified by [2], are indicated by red points. The blue shading in EL2 indicates the location of the 32 extra amino acids (residues 145-176) present in the NHE6v1 variant that are absent in NHE6v0. This figure is a modified version from [83], published in *Molecular Neurodegeneration*, © Springer Nature and distributed under the terms of the Creative Commons Attribution 4.0 International License (<http://creativecommons.org/licenses/by/4.0/>).

Although life expectancy data is currently limited, CS patients have been reported to pass away within the second to fifth decades of life [2]. Anecdotal evidence suggests that epileptic seizures, including sudden unexplained death due to epilepsy (SUDEP), are often a root cause of death [14]. Post-mortem data from adult CS patients have shown substantial neurodegeneration and gliosis accompanied by tau depositions in the cerebellum, brain stem, and additional subcortical brain areas [13]. Brain transcriptome analyses have additionally revealed a correlation between decreased *SLC9A6* expression and the density of tau tangles [20]. Furthermore, at least a third of male CS patients also show regression in their symptoms between 15 months and 16 years of age, including the loss of previously acquired skills such as motor abilities, use of basic words or sounds, and facial recognition [5,13,14,16,17]. Interestingly, neuroimaging data from older female carriers have likewise demonstrated signs of neurodegeneration, including atrophy of the frontoparietal lobe and cerebellum [20]. Accordingly, heterozygous females have also shown signs of atypical Parkinsonism and corticobasal degeneration [7,15,20]. These results indicate that alterations in NHE6 function may also contribute to the pathogenesis of neurodegenerative disorders, such as Alzheimer's disease (AD) and Parkinson's diseases (PD).

It should be noted that many patients with *SLC9A6* mutations were initially misdiagnosed as having Angelman syndrome (AS) or cerebral palsy. These conditions share several aspects in their clinical presentation with CS, including intellectual disability, ataxia, epilepsy, and autistic traits [14,21,22]. However, patients that initially presented with CS were not found to have mutations in the *UBE3A* gene that give rise to AS [2,21], leading to the conclusion that CS was a monogenic disorder specifically arising from mutations in the *SLC9A6* gene. CS also presents with some key differences from AS. For instance, although developmental regression and cerebellar atrophy are common symptoms of CS patients after the first decade of life [5], these are not

commonly seen in AS [23]. Obesity is also often observed in AS by young adulthood [23], while CS patients remain lean [2,5]. Genetic screening to specifically identify *SLC9A6* mutations is thus required to confirm diagnosis of CS versus other similar disorders. To date, interventions employed to improve the quality of life for CS patients have primarily focused on alleviating gastrointestinal symptoms and seizures [3,4]. Indeed, CS patients have been reported to display a wide range of seizure types, including tonic-clonic, tonic, myoclonic, atonic, and absence seizures, with some patients experiencing up to 15 seizures each day (reviewed further in [24]). Electrical *status epilepticus* during slow-wave sleep (ESES) has also been reported in many CS patient case studies [7,25]. Currently, the precise cause of seizure generation in CS is virtually unknown, and CS patients frequently become resistant to standard antiepileptic drug treatment and consequently develop refractory seizures [24]. Therefore, there is a clear necessity to gain a greater understanding of the role that NHE6 plays at both excitatory and inhibitory synapses, and how the absence of NHE6 function may underlie the pathogenesis of CS as well as other neurodegenerative disorders, including AD and PD.

1.2 PHYSIOLOGY OF CENTRAL SYNAPSES

1.2.1 The hippocampus

To gain insights into the function of NHE6 in the central nervous system (CNS), I opted to study its function within the hippocampus, a medial temporal lobe structure that has long been implicated in learning and memory [26]. It has long been recognized that patients with lesions or damage to the hippocampus display a profound anterograde amnesia, or an inability to form new memories [27]. Evidence from freely moving animals has also implicated the hippocampus in navigation and the formation of spatial memory [28,29]. Additionally, the hippocampus is particularly vulnerable

to epileptic seizures [30], and the temporal lobe is often a focal point for epileptic seizures and other psychiatric disorders [31]. The hippocampus is thus an ideal system in which to study learning and memory deficits, as well as epileptogenesis, in CS.

Furthermore, the hippocampus offers numerous advantages as an experimental model. For instance, its well-ordered morphology and layered anatomy remains relatively consistent between animals of the same species and developmental stage. Moreover, the unidirectional trisynaptic excitatory circuitry of the hippocampus has been well-characterized after decades of scientific advancements. The perforant pathway from the entorhinal cortex sends projections to granule cells in the dentate gyrus, which then send mossy fibres to pyramidal neurons in area *cornu ammonis* (CA) 3. Next, these neurons project Schaffer collaterals (SCs) onto pyramidal neurons in area CA1 (**Fig. 2**) [32]. These synapses utilize the neurotransmitter glutamate to mediate fast excitatory neurotransmission from one region to the next. Additional information between the hippocampus and other cortical and subcortical brain areas flows reciprocally through the subiculum and entorhinal cortex [33]. Area CA1 pyramidal cells thus serve as a key output from the hippocampus, and the synapses between CA3 and CA1 pyramidal neurons are some of the most studied CNS synapses [34–36]. Interestingly, a case study of two deceased CS patients reported that CA1 pyramidal neurons were preferentially lost over other cells in the hippocampus [13], giving me further reason to focus on neurons and connections within this specific hippocampal area.

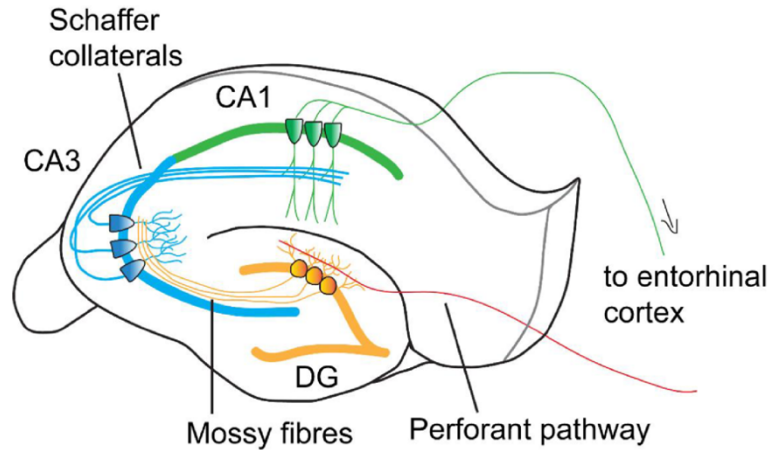


Figure 2: Illustration of the hippocampal formation, highlighting some of the major pathways within. Mossy fibres emanating from granule cells in the dentate gyrus (DG, orange) synapse upon pyramidal neurons in area CA3 (blue), which then send Schaffer collateral (SC) axons to area CA1 (green) pyramidal neurons that then project (arrow) to the entorhinal cortex. Figure adapted from [32] published in *Nature Reviews Neuroscience* © Springer Nature, license #4896610683445.

Area CA1 pyramidal cells are orderly arranged in *stratum pyramidale* and can be compartmentalized into a soma or cell body (~20 μm in mice), dendritic branches, and a single axon. The soma contains the nucleus and other organelles carrying out metabolic processes, such as protein synthesis and degradation, that allow the neuron to maintain basic cellular homeostasis and function. From the soma, one primary dendritic branch emanates apically into the *stratum radiatum*, while two primary dendritic branches project basally into the *stratum oriens*; these branches segregate into higher order secondary and tertiary dendrites as well [37,38]. SCs typically target proximal dendritic segments, while distal sections of dendrite in the *stratum lacunosum-moleculare* receive perforant path inputs from the entorhinal cortex and thalamus [39,40]. In addition to excitatory connections, pyramidal cell activity is regulated by the action of inhibitory interneurons, a heterogeneous group of cells that synthesize and release the inhibitory neurotransmitter γ -amino-butyric acid (GABA). GABAergic interneurons differ from one another in terms of their morphology, molecular expression, axonal projections, and firing patterns [41].

In the hippocampus, interneurons expressing the Ca^{2+} buffering protein parvalbumin (PV) usually form axoaxonic and axosomatic connections, whereas those containing the neuropeptide somatostatin (SOM) synapse upon the distal sections of dendrites [42–44]. The activity of these cells is further gated by the action of additional upstream GABAergic interneurons that express other markers, such as vasoactive intestinal peptide (VIP) or calretinin (CR) [45,46]. In spite of their importance, GABAergic regulation is much less well understood, although they are believed to play important roles in tampering the excitability of neuronal circuitry as a whole [29,47].

Inhibitory interneurons are also responsible for generating patterns of activity that allow for proper circuit function and memory formation. Throughout the cortex and hippocampus, extracellular field potential recordings typically show oscillations of neuronal activity at different frequencies that allow for efficient information encoding and processing of spiking neurons [48–50]. For instance, the coupling of theta (4–12 Hz) and gamma (35–85 Hz) oscillations are thought to underlie cognition during memory tasks, spatial navigation, and paradoxical rapid eye movement sleep [51–57]. Interestingly, the hippocampus can generate its own theta rhythms when isolated *in vitro*. This occurs, in part, through the action of GABAergic interneurons, which regulate the spiking activity of postsynaptic neurons to generate these synchronous activity patterns [58,59]. Two major populations of interneurons are hypothesized to be key players in theta wave generation. These include axodendritic SOM+ cells in the *stratum oriens* and *stratum lacunosum-moleculare*, as well as axosomatic and axoaxonic PV+ basket cells in *stratum pyramidale* [58,60–62]. Indeed, a recent study using optogenetic stimulation to activate PV+ cells has definitively proven their role in synchronizing principal cell firing and theta rhythm generation [63]. PV+ interneurons also reciprocally regulate each other and can be further gated by inhibitory afferents from the medial septum as well as other interneuron populations (such as CR- and VIP-

positive cells), lending further complexity to their function [64–66]. Thus, in addition to modulating the activation of individual neurons, GABAergic interneurons are also critical for the synchronization of circuit oscillations that can underlie cognitive processing and memory formation through the hippocampus.

1.2.2 Dendritic spines and synaptic plasticity

Along the dendrites of area CA1 pyramidal neurons, the axon boutons of SCs impinge upon dendritic spines, small (1 μm) protrusions that emanate from the dendritic shaft [67,68]. First observed in the avian cerebellar cortex by Santiago Ramón y Cajal during the 19th century, Cajal hypothesized that these spines maximized the dendritic surface area to accommodate the number and complexity of connections that could be made upon one neuron [69,70]. Indeed, the dendritic arbor of a single neuron can be populated by more than 100,000 spines [71]. With the development of high-resolution microscopy techniques, these microscopic structures have become a fascinating field of research in the study of excitatory synaptic function in both health and disease.

In general, spines contain a “head” structure joined to the dendritic shaft by a thinner “neck” apparatus [72]. Observations from electron micrographs have revealed that the heads of dendritic spines contain an electron-dense region known as the postsynaptic density (PSD) in direct apposition to the presynaptic active zone [73,74]. The PSD contains hundreds of proteins involved in excitatory postsynaptic signaling, including ionotropic glutamatergic α -amino-3-hydroxy-5-methyl-4-isoxazolepropionic acid (AMPA) and *N*-methyl-D-aspartate (NMDA) receptors. While AMPA receptors (AMPA receptors) are non-specific cation channels that propagate fast excitatory neurotransmission, NMDA receptors (NMDARs) are also permeable to Ca^{2+} , and their activation can go on to trigger downstream signaling cascades that alter synaptic strength [67]. Because

bigger spines typically contain a larger PSD and presumably more AMPARs, it is widely believed that spine size correlates with the strength of the corresponding synapse [75]. PSDs additionally contain metabotropic glutamate receptors, scaffolding proteins such as PSD-95, and downstream effectors such as Ca^{2+} /calmodulin kinase II (CaMKII). Functionally, spines serve as a means of biochemical and electrical compartmentalization to concentrate ions, signaling molecules, and gene expression within the spine head. This allows the cell to fine-tune the activity and efficacy of specific synapses, thus lending greater computational capacity to the neuron [71,76].

During development, spines mostly appear as long ($>2\ \mu\text{m}$) filopodia-like structures that lack a discernible head. As filopodia have limited synaptic functionality, they are generally regarded as transient or immature. However, these structures are highly labile and can become more stable dendritic spines in response to activity. In rodents, synaptogenesis begins during the first postnatal week, with spines and synaptic specificities becoming apparent by the following week [77,78]. Heterogeneous in shape, spines can be broadly sorted into stubby, thin, and mushroom subtypes (**Fig. 3**) [72,79]. Short ($<0.5\ \mu\text{m}$) stubby spines lack a discernable separation between their head and neck regions and, in conjunction with immature filopodia-like structures, comprise $\sim 10\%$ of all spines [72,77,80]. Larger mushroom-type spines, which account for $\sim 25\%$ of all spines in the adult hippocampus and neocortex, are believed to be “memory” spines that can persist for months and even years *in vivo* [81]. Accordingly, they contain larger PSDs with more AMPARs that allow for stronger functional synapses. Mushroom spines are also more likely to possess a spine apparatus, a modified section of smooth endoplasmic reticulum (ER) that can regulate $[\text{Ca}^{2+}]$ in the spine, as well as polyribosomes and monosomes for local protein synthesis [68,82,83]. In contrast, long ($>1\ \mu\text{m}$) thin spines, which make up $\sim 65\%$ of all spines, have a smaller PSD and thus contain fewer AMPARs. Although these synapses are functionally weaker, they

contain a greater proportion of NMDARs and are thus considered as “hot spots” for activity-dependent synaptic plasticity [68,84,85].

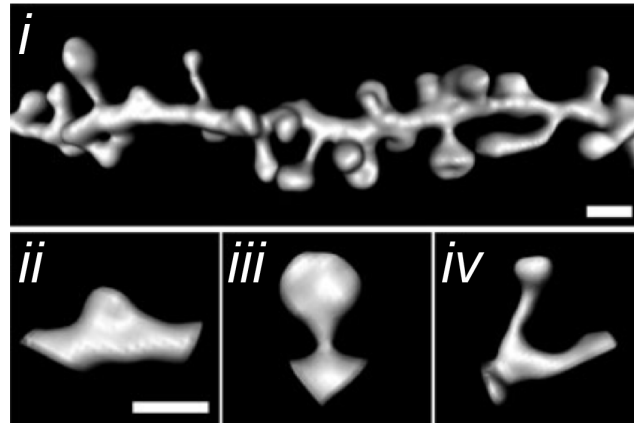


Figure 3: Three-dimensional reconstruction of the tertiary dendrite of a CA1 pyramidal cell (*i*), showing a diverse distribution of different spine subtypes. The three major subtypes of dendritic spines include short, stubby spines (*ii*), mushroom-type spines with short necks and a large head (*iii*), and long, thin spines, with long necks and a small head (*iv*). Scale bar: 1 μm . Figure adapted from [44] published in *Journal of Physiology*, © John Wiley & Sons, license #4896610479624.

Indeed, dendritic spines are not static structures but are highly dynamic and can rapidly remodel in response to activity or experience. Unlike the dendritic shaft, which is primarily made up of microtubules, spines possess a rich underlying actin cytoskeleton that lends itself well to rapid structural modifications [86,87]. The actin cytoskeleton of naïve spines is generally in an equilibrium of filamentous (F)-actin polymerization and depolymerization from globular (G)-actin (known as F-actin treadmilling). Changes in the rates of F-actin treadmilling thus allow for spine head remodeling, as well as the delivery of polyribosomes and plasticity-related proteins into the spine [82]. To study synaptic plasticity, long-term potentiation (LTP) and long-term depression (LTD), or the strengthening and weakening of synaptic strength, respectively, have long been used as cellular correlates of learning and memory in the hippocampus and other brain areas. *In vitro* measurements of cultured hippocampal neurons initially revealed bidirectional changes in spine

morphology, with spine growth in response to LTP and spine shrinkage following LTD [88–90]. Changes in spine volume and morphology are thus regarded as structural correlates of plasticity.

In response to the onset of LTP, F-actin treadmilling within the core of the spine is stabilized while polymerization mostly occurs in peripheral regions, thus allowing spine head enlargement [91,92]. To mediate these changes in actin dynamics, activated forms of numerous molecules involved in actin depolymerization, branching, and stabilization, such as cofilin, actin-related protein 2/3 (Arp2/3), and epidermal growth factor receptor kinase substrate 8 (Eps8), respectively, undergo precise spatiotemporal trafficking into spines following LTP induction [93,94]. The translocation and regulation of these actin-associated proteins into spines is thus critical for their volumetric enhancements. Consistent LTP induction further leads to the formation of new spines within close proximity with one another while enhancing the elimination of inactive spines [95]. LTP induction of the CA3-CA1 synapse in the hippocampi of postnatal day (PD) 15 rats lead to a similar increase in spine number, suggesting that these patterns apply *in vivo* as well [96]. In the opposite direction, LTD induction leads to spine shrinkage or retraction due to actin depolymerization [82,90,97]. Given these lines of evidence, it is hypothesized that short-term memory relies predominantly upon changes in spine size and synaptic strength [32,98], whereas longer forms of memory may depend upon the formation of new spines or the loss of existing synapses [81]. As I will discuss later, rapid spine remodeling is known to be highly dependent upon the function of the endosomal system, of which NHE6 is implicated.

While classical LTP and LTD paradigms employ exaggerated forms of neuronal activity, more contemporary reports on *in vivo* imaging experiments of fluorescently-labeled cortical neurons from awake, behaving mice has confirmed that spines consistently remodel in response to physiological stimuli [99–101]. For instance, spines in the motor and somatosensory barrel cortices

can dynamically remodel in mice subjected to novel motor learning tasks or sensory experiences, respectively. Specifically, spines were formed within hours of exposure, and a small fraction of these *de novo* spines were found to persist for months thereafter [102,103]. Like *in vitro* experiments performed on hippocampal slices, persistent training also lead to the elimination of unutilized spines as well [102,103]. These studies suggest that changes in spine morphology reflect the fine-tuning of synaptic connections during learning paradigms that allow for memory formation. Interestingly, a recent study has shown that destabilizing the actin cytoskeleton within newly formed motor cortical spines can eliminate learned motor behaviours [104], suggesting that spine dynamics themselves may actually be important for learning. Taken together, it is evident that changes in spine shape and number are not only an anatomical correlate for cognitive function but are intrinsically involved in the acquisition and retention of new memories as well.

Due to the technical challenges of imaging the hippocampus *in vivo*, the majority of these insights have come from studies of the neocortex. More recent advances in two-photon imaging have allowed longitudinal *in vivo* imaging of hippocampal cells, which has revealed that spines along the dendrites of CA1 hippocampal neurons also undergo a high degree of structural plasticity [105]. Additional studies on freely moving mice have shown that spines along area CA1 hippocampal neurons turnover at a much faster rate than what has previously been reported for cortical spines [106,107], with a recent report estimating that ~40% of CA1 spines may turnover every 4 days [107]. Interestingly, thin and mushroom spines were found to be replaced at about the same rate, in contrast to the idea that larger spines are “memory” spines [108]. As methodologies for imaging subcortical structures continue to evolve, we will undoubtedly gain further insights into how hippocampal spine dynamics can directly influence learning and behaviour.

1.2.3 Dendritic spines in neurological disorders

Notably, alterations in the density and relative proportion of spine subtypes are considered to be hallmarks of neuropsychiatric conditions. It is typically assumed that the dysgenesis of spines is indicative of the perturbances in excitatory neurotransmission and cellular learning, which may underlie the cognitive deficits observed in such disorders. For instance, hippocampal dendritic spines are both shorter and fewer in number in patients and mouse models of AS [109,110]. Similarly, post-mortem tissue from individuals with Rett's syndrome (RS), another neurodevelopmental disorder involving intellectual disability and epilepsy that primarily affects females heterozygous for mutations in the *MECP2* gene, show decreases in spine density with notable reductions in the proportion of larger, mushroom-type spines [111–113]. Spine morphology is also dysregulated in FXS: while younger FXS patients appear to exhibit an increase in spine density, these spines have a “torturous” appearance that more greatly resemble filopodia and are suggestive of an impairment in spine maturation [114–116]. However, these excess spines may be properly pruned upon adulthood, although they still appear long and thin [86]. Moreover, in neurodegenerative diseases such as AD, the loss of dendritic spines is believed to be one of first morphological changes to occur in the neurons of AD patients [117,118].

Therefore, it is evident that quantifying changes in different dendritic spine subtypes, as well as their overall density, can serve as a reliable measure of cognitive impairments in various neurological disorders. While there are currently no reports of hippocampal spine density taken from human CS patients, it is more than likely that such neuropathological findings will eventually show similar changes in dendritic spine density and subtype distribution in the cortex and hippocampus.

1.3 ENDOMEMBRANE TRAFFICKING

1.3.1 Overview of the endolysosomal system

Although studies of spines dynamics often focus on actin remodeling, the endolysosomal system is equally as important for the development, maturation, and remodeling of synapses [119,120]. Aside from basic mechanisms of protein turnover common to all cells, endocytic mechanisms are important in regulating a number of neuron-specific functions, including neurotrophin signaling, presynaptic vesicle recycling, axonal growth cone migration, and synaptic plasticity [121–123]. However, the distinctive morphology of neurons establishes a remarkable complexity in the compartmentalization and regulation of protein transport and degradation [124]. As NHE6 is a regulator of endosomal pH and thus endosomal trafficking in neurons, I will briefly overview this system and its strong involvement in synaptic plasticity.

Cells of all types internalize molecules from the extracellular space by endocytosis, including ligand-bound membrane receptors localized at their surface. This can occur through clathrin/adaptor protein 2 (AP2)-mediated endocytosis (CME). This process is usually initiated by membrane receptor complexes that bind and recruit AP2 and clathrin to invaginate a portion of the cell membrane to form a clathrin-coated pit, which is cleaved by the GTPase fission protein dynamin to form an endocytic vesicle [125]. Following clathrin uncoating, these carrier vesicles then transport cargos to early endosomes (EEs) for sorting. From the EE, the majority of internalized cargos may undergo “fast” recycling back to the plasmalemma, shuttled into a “slow” recycling cycle to recycling endosomes (REs), or sent for degradation through late endosomes (LEs) and degradative lysosomes [119] (**Fig. 4**). In neurons and other cell types, resident proteins specific to each endolysosomal structure are typically used to distinguish between them. These include the small GTPase Rab5, as well as early endosomal antigen 1 (EEA1), for EEs; Rab8,

Rab11, and syntaxin-13 (stx-13) for REs; Rab7 for LEs; and lysosomal-associated membrane protein 1 (LAMP1) for lysosomes [119,126,127].

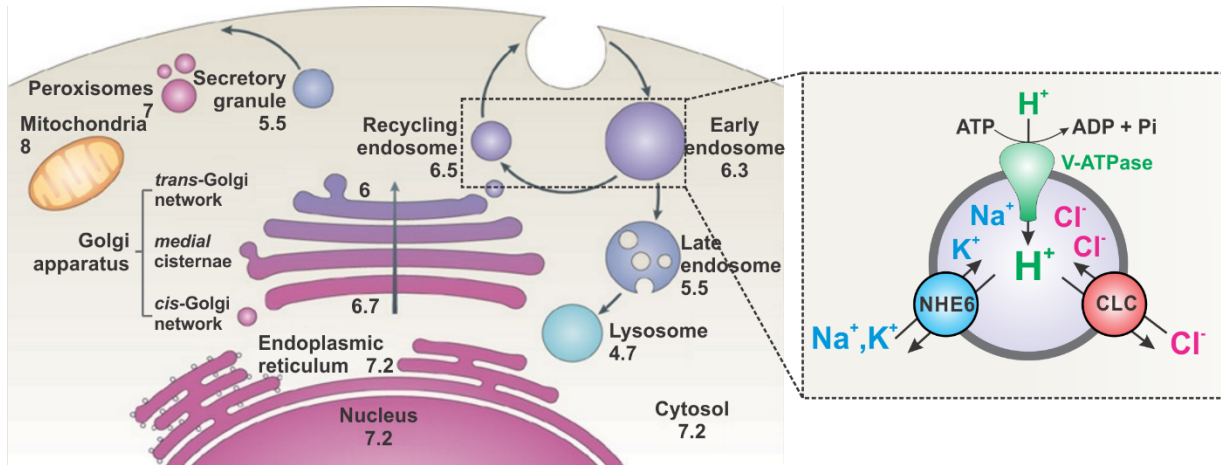


Figure 4: Schematic of endomembrane compartments of mammalian cells, with luminal pH values given. Inset shows a schematic of early and recycling endosomes with directionality of ion flow mediated by NHE6, the vacuolar H^+ -ATPase pump (V-ATPase) and the $2Cl^-/1H^+$ exchanger (CLC). Figure adapted from [241] published in *Journal of Physiology* © Springer Nature, license #4896601351984.

The recycling of proteins back to the cell surface can be mediated by specific endosomal proteins, such as Rab11 and Eps15 homology domain-containing proteins (EHDs) in canonical “slow” recycling [119] and sorting nexins and the retromer complex in “fast” recycling [128–130]. Cargos targeted by degradation are instead ubiquitinated by E1-3 enzymes. These ubiquitin tags are then recognized by endosomal sorting complexes required for transport (ESCRT), which mediate the delivery of targeted substrates to LEs [131]. Finally, LEs either directly receive hydrolase content from a lysosomal compartment via a transient “kiss-and-run” mechanism or undergo complete fusion with lysosomes, thereby forming either endolysosomes or autolysosomes, respectively [132]. Lysosomes are responsible for degrading a variety of

macromolecules, including nucleic acids, proteins, lipids, and carbohydrates, as well as in the clearance of protein aggregates and damaged organelles in a process known as macroautophagy (or cellular “self-eating”) [133–136]. The products of these degradative processes can then be recycled to form new biosynthetic reactions [124]. In neurons, autolysosomal degradation is primarily responsible for the degradation of synaptic proteins and vesicles as well as pathogenic protein aggregates [124,137–139]. It follows that disturbances in proteolysis are associated with neurodevelopmental irregularities and neurodegeneration [140,141].

Being complex, polarized cells, the spatial organization of the endolysosomal system is particularly noteworthy. For instance, while lysosomal membrane proteins may be detected in more distal neurites using immunofluorescence, hydrolase-containing lysosomes with degradative capacity are mostly found in perisomatic regions [133,142]. Conversely, REs are found throughout the axon, soma, and dendrites of the neuron [143–145]. In hippocampal CA1 pyramidal neurons, ~70% of dendritic endosomes are found at the base of a spine, while approximately a third are found within the spine itself [146]. Thus, cargos targeted for degradation must undergo retrograde transport back to the cell soma with the use of molecular motor proteins [133,142]. However, recent ultrastructural analyses have also suggested the presence of lysosomes and local degradation directly at synapses [147]. While still understudied, local protein degradation may thus also be a prominent mediator in the rapid regulation of synaptic function.

1.3.2 Membrane trafficking in excitatory synaptic plasticity

In neurons, endosomal trafficking is particularly important during synaptic plasticity, including during excitatory LTP. At SC-CA1 synapses, LTP is dependent upon NMDAR opening following postsynaptic depolarization and relief of the Mg^{2+} block upon these receptors, which then allows

Ca²⁺ influx into postsynaptic cell and the activation of various downstream mediators, such as CaMKII and protein kinase A (PKA) [148,149]. In the early stages of LTP, these mechanisms enable excitatory synaptic strengthening through an enhancement of AMPAR function, which may arise from changes in AMPAR channel conductance, open probability, and synaptic density [150–157]. AMPARs usually assemble as tetramers made up of two homodimers of two out of four possible subunits (GluA1-4). In CA1 pyramidal neurons, the majority of AMPARs are GluA1/GluA2 and GluA2/GluA3 heteromers, with a small amount of GluA1 homomers as well [158]. It is generally believed that GluA1/GluA2 heteromers are the principal population of receptors that initially traffic to excitatory synaptic sites during LTP, whereas GluA2/GluA3 heteromers are more involved in constitutive AMPAR recycling to maintain synaptic strength [159–161]. Following the induction of LTP, biochemical and immunofluorescent microscopy techniques have revealed a rapid increase in GluA1-containing AMPAR clustering at postsynaptic sites, which is believed to underlie the immediate potentiation in synaptic strength during the earlier stages of LTP (E-LTP) [155,162–164]. To mediate AMPAR clustering, two major pools of extrasynaptic AMPARs exist: those that undergo lateral diffusion throughout the cell membrane, or those that are added to the cell surface from intracellular stores (**Fig. 5**). Determining which of these two sources is predominant during LTP has long been a source of controversy.

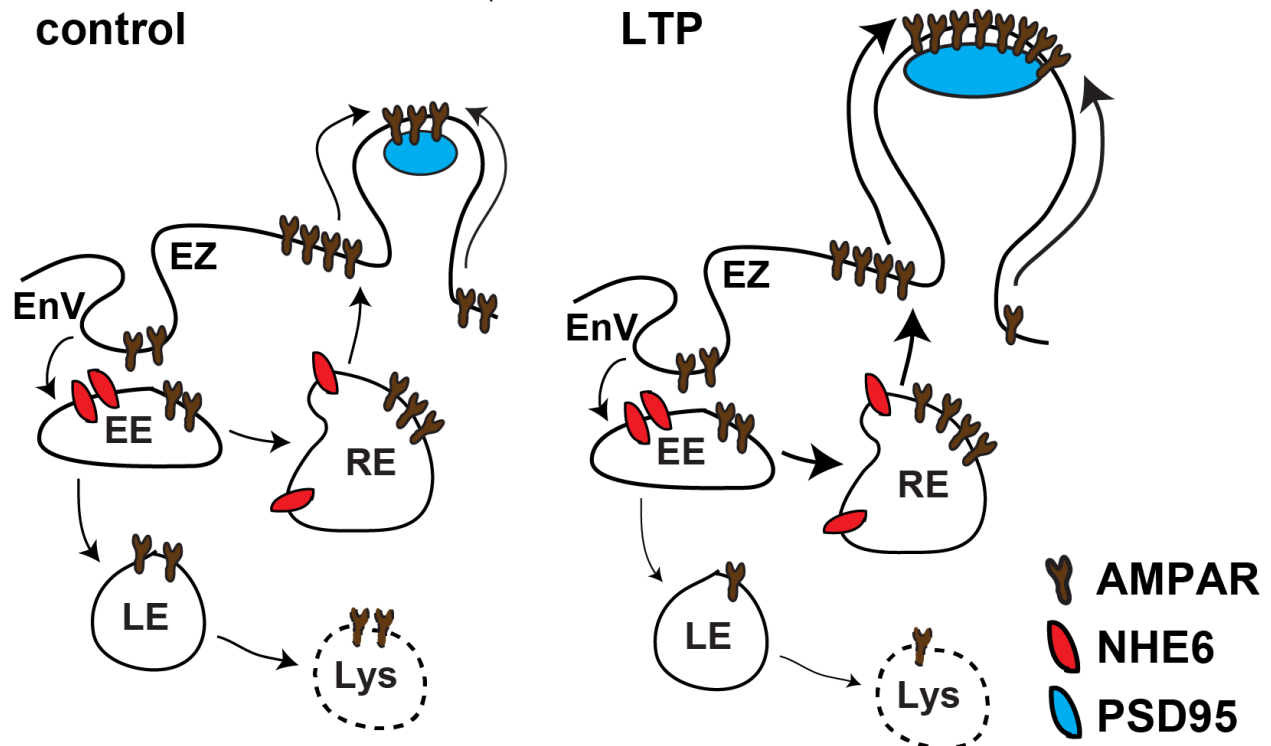


Figure 5: Basic schematic of AMPA receptor (AMPA) trafficking around excitatory sites under control conditions (left) and during long-term potentiation (LTP, right). AMPARs (brown) at the cell surface laterally diffuse via Brownian motion through the plasma membrane and can become trapped at the heads of dendritic spines by postsynaptic density 95 (PSD95) scaffolds (blue). AMPARs at endocytic zones (EZs) are internalized through endocytic vesicles (EnV) into the early endosome (EE), where they may then be reinserted into the membrane through the recycling endosome (RE) or subjected to degradation through the late endosome (LE) and lysosome (lys). NHE6 (red) is also localized at the same EEs and REs. Upon LTP induction, RE exocytosis near dendritic spines contributes additional AMPARs and expands spine head volume. Arrowheads indicate direction of movement; arrow widths indicate relative extent of movement.

Early studies demonstrated that exposing neurons to toxins interfering with soluble N-ethylmaleimide sensitive factor attachment protein receptor (SNARE) family protein interactions, such as N-ethylmaleimide and botulinum neurotoxin B, blocked membrane fusion and disrupted LTP expression [165] as well as surface AMPAR upregulation [144,164,166,167]. These findings support the hypothesis that LTP primarily relies upon the exocytosis of AMPAR-containing vesicles to the cell surface. To mediate these exocytic events, dendritic REs mobilize to spines and undergo stx13-dependent plasmalemmal fusion in response to LTP induction, suggesting that REs

are responsible for supplying additional AMPARs during LTP [168–173]. Whether these fusion events occur directly within the activated spine or along the dendrite remains uncertain, although disparate yet complementary studies have suggested that RE exocytosis at both sites can occur [172,174]. However, more recent evidence has implicated that the lateral diffusion of surface AMPARs that are localized extrasynaptically may play a greater role in the immediate phase of LTP. Normally, AMPARs mobilize throughout the cell membrane via Brownian diffusion (*i.e.*, random movements due to thermodynamic energy) [175,176]. Freely diffusing AMPARs frequently encounter synaptic sites, and they are capable of becoming reversibly immobilized to PSDs in response to activity induction [176–180]. Intriguingly, the initial phase of potentiation was still intact when SNARE function and exocytic events were disrupted [165], suggesting that “diffusion trapping” of AMPARs at PSDs is more prevalent immediately after LTP onset. More recent insights have confirmed that AMPARs indeed become trapped by their binding to PSD95 at rapid time scales (< 1 min) following LTP induction, which coincided with the rapid functional potentiation of synapses [178,181–183]. CaMKII- and PKA-mediated phosphorylation of laterally diffusing AMPARs promotes their anchoring to PSD95 as well as their interactions with auxiliary transmembrane AMPA receptor regulatory proteins (TARPs), which further assist in their stabilization and function at postsynaptic sites [183–186]. In all, while the trapping of laterally diffusing membrane AMPARs mediates the initial increase in synaptic strength after LTP stimulation, the delivery of AMPARs from intracellular stores are nonetheless critical for sustained LTP expression [181].

As I have mentioned before, dendritic spines also expand significantly in volume following LTP (**Fig. 5**). Indeed, smaller thin-type spines can double their volume in response to LTP induction, thus serving as a morphological correlate for synaptic strengthening [68,82]. In addition

to actin cytoskeletal remodeling, the mobilization of large amorphous vesicular clumps acts as a source of supplementary lipid membrane to enhance spine head volume, which is maintained by the exocytosis of additional REs [144,166,168,187]. Disrupting RE fusion by expressing dominant-negative Rab11 or stx13 constructs or pharmacologically blocking SNARE fusion can thus impair spine growth as well [144,166,167]. The transport of REs by molecular motors, such as the actin motor protein myosin Vb, is also critical for RE fusion, as manipulating RE placement can adversely affect synaptic remodeling [188,189]. In summary, RE fusion following LTP is required for both the functional and strengthening of excitatory synapses [68,160].

AMPA receptors also continually cycle between membrane and intracellular domains through endocytic mechanisms (**Fig. 5**) [190–192]. Surface AMPARs are internalized via CME from specialized endocytic zones (EZs) [190,193,194], regions of membrane adjacent to the PSD that are enriched in endocytic machinery, such as clathrin and AP2 [193,195]. AP2 and the clathrin-adaptor complex are capable of directly interacting with AMPARs, NMDARs, and other PSD proteins to mediate CME [196–198]. Functionally, AMPAR internalization through EZs allows freely diffusing extrasynaptic AMPARs to be maintained within close proximity to the synapse such that they can be rapidly inserted following LTP induction [178,193]. Within the endosome, this sorting decision can be partially mediated by the post-translational states of AMPAR subunits; for instance, GluA1 phosphorylations at the CaMKII S831 and PKA S845 sites promote AMPAR recycling back to the cell membrane and can also alter numerous single-channel properties [191,199,200]. Reinsertion usually occurs in an exocytic site away from the PSD itself, to which AMPARs can then travel through lateral diffusion [178,193].

Conversely, during NMDAR-dependent LTD at hippocampal CA3-CA1 synapses, AMPARs are dispersed from synaptic sites to result in synaptic weakening [201]. Following low

Ca²⁺ entry from weak NMDAR activation, dephosphorylation of the GluA1 subunit by protein phosphatase 1 (PP1) [202] triggers AMPAR dissociation from PSD-95, allowing its diffusion to and subsequent internalization from EZs via CME [193,203,204]. As lysosomes are also recruited to spines following NMDAR activation [205], these dephosphorylation events may also promote their degradation through the lysosome [191]. The GluA1 subunit can additionally be ubiquitinated by the E3 ligase neural precursor cell expressed developmentally down-regulated protein (Nedd)4-1, which leads to its endocytosis and degradation through lysosomes [206,207]. More recent evidence has indicated that ubiquitination of all four major AMPARs, GluA1-4, can also promote their trafficking to late endosomes and lysosomes for putative degradation [208]. Therefore, both the endolysosomal system is critical for the bidirectional remodeling of excitatory synapses, highlighting the necessity of this system in neuronal plasticity.

1.3.3 Membrane trafficking in inhibitory synaptic plasticity

It is worth noting that although these mechanisms have been extensively studied with regards to glutamate receptors in excitatory plasticity, ionotropic GABA_A receptors (GABA_ARs) also show similar patterns of behaviour during inhibitory plasticity mechanisms, including inhibitory LTP (iLTP). GABA_ARs are Cys-loop ligand-gated Cl⁻/HCO₃⁻ channels that mediate the majority of inhibitory neurotransmission in the mature CNS. In mammals, GABA_ARs are composed of five out of 19 possible subunits (α 1– α 6, β 1– β 3, γ 1– γ 3, δ , ϵ , π , τ , ρ 1– ρ 3), with the most common synaptic variants involving two α (of α 1-3), two β , and one γ 2 subunit [209]. Because of this heterogeneity, GABA_AR complexes vary widely in their membrane localization, channel and gating properties, sensitivity to drugs, and implications in development, plasticity, and disease (reviewed further in [209–212]).

Like AMPARs, GABA_ARs also undergo lateral diffusion throughout the plasma membrane and can become reversibly stabilized at postsynaptic sites in an activity-dependent manner [213–216]. This is contingent upon the synaptic trapping of GABA_ARs by gephyrin, the major inhibitory postsynaptic scaffolding molecule [217–220]. The $\alpha 2$, β , and $\gamma 2$ subunits interact directly with gephyrin while other subunits (such as $\alpha 1$) do not, suggesting the existence of both gephyrin dependent and independent clustering mechanisms [212]. Post-translational modifications of various residues on GABA_AR subunits act as an important regulator in their recruitment and retention at postsynaptic sites, as well as in their gating and kinetic properties [210–212]. For instance, the palmitoylation of the $\gamma 2$ subunit can regulate GABA_AR membrane anchoring [221]. Moreover, phosphorylation of the $\beta 3$ subunit following chemical NMDAR-dependent iLTP can upregulate surface GABA_AR expression [219]. Intriguingly, gephyrin is also subject to numerous post-translational modifications, including phosphorylation, acetylation, and SUMOylation [222], and activity-induced Ca²⁺ influx can also lead to gephyrin dispersal as well [215]. The dynamic regulation of the gephyrin scaffold itself thus lends even greater complexity to the regulation of GABAergic transmission (reviewed further in [222]). Like excitatory synapses, GABA_AR insertion into and removal from the cell surface also occur at extrasynaptic membrane domains before migrating to synaptic sites [213]. This allows the accumulation of an extrasynaptic pool of surface GABA_ARs, which can be rapidly inserted into synapses during iLTP [223]. GABA_ARs localized in perisynaptic EZs also undergo CME in a process that is regulated by phosphorylation of the $\beta 3$ and $\gamma 2$ subunits, which interact with AP2 [211,224]. Accordingly, interference with phosphorylation sites in these subunits reduced GABA_AR docking at these EZs and impaired their endocytosis, leading to enhanced inhibitory neurotransmission [225,226]. Similar to other cargos, internalized GABA_ARs may then be recycled back to the cell surface or be targeted for lysosomal

degradation. This endosomal sorting decision is regulated by Huntingtin-associated protein 1 (HAP1), which interacts directly with the $\beta 1$ subunit [227,228]. Specifically, HAP1 inhibits receptor degradation and, in conjunction with the kinesin family 5 (KIF5) microtubule motor, facilitates its reinsertion into the cell surface [228,229]. In all, it is clear that like AMPARs, GABA_AR trafficking through the endosomal system is similarly critical in regulating the strength of inhibitory synaptic transmission.

In the mature CNS, the opening of GABA_ARs allows for the influx of Cl⁻, which can either hyperpolarize or depolarize but shunt the membrane potential below the threshold for action potential (AP) generation. To allow for an outward-inward gradient of Cl⁻, intracellular [Cl⁻] is kept low through the Cl⁻ exporter K⁺-2Cl⁻ co-transporter 2 (KCC2) in mature neurons [230]. However, in immature developing neurons, GABAergic signaling is initially excitatory due to the relatively high expression of Na⁺-K⁺-2Cl⁻ co-transporter 1 (NKCC1), which instead maintains a high intracellular [Cl⁻]; as such, activation of GABA_ARs results in the efflux of Cl⁻ and membrane depolarization [231]. During development, NKCC1 is downregulated but KCC2 is upregulated, decreasing intracellular [Cl⁻] to eventually switch the polarity of GABAergic transmission from excitatory to inhibitory [232]. As these transporters are also membrane-bound proteins, it is reasonable to expect that their localization and transport may be similarly reliant upon the endolysosomal system. However, details on their trafficking through the endosome remain relatively scarce in comparison to the aforementioned findings on neurotransmitter receptors. However, disturbances in this developmental switch are often observed in different forms of epilepsy [233–235] as well as in neurodevelopmental disorders, including RS [236], Down syndrome [237], and ASDs [238]. In such disorders, the dysregulation of these transporters significantly elevates intracellular [Cl⁻] that could lead to a depolarizing shift of E_{GABA} . As a result,

GABA_AR activation may no longer be inhibitory, but it may raise the membrane potential past the threshold of AP firing to instead enhance cellular excitability [239,240]. Therefore, GABAergic transmission may not always be synonymous with inhibition.

In summary, it is evident that the endolysosomal system is critical in allowing the development and plasticity of both excitatory and inhibitory synapses. As NHE6 is intimately involved in endosomal function, it is reasonable to expect that a deficiency in its function may have a profound effect upon neurotransmission and cellular excitability.

1.3.4 pH regulation in the endolysosomal system

In addition to their resident membrane proteins and enzymes, the pH of each component of the endolysosomal system is also critical for their function. This is because the luminal pH of each structure can mediate (1) cargo sorting, (2) receptor-ligand dissociation and processing, (3) the maturation and transport of endolysosomal vesicles, (4) membrane protein and receptor recycling, and (5) the activity of luminal enzymes [241–243]. Degradation through the lysosome is particularly reliant upon proper vesicular acidification, as proteolytic hydrolases only become active in acidified, low pH environments [244,245]. Consequently, to mediate trafficking and degradation in the lysosome, cargos targeted for degradation are subjected to a gradient of acidification from the EE (pH ~ 6.3) to the LE (pH ~5.5) and lysosome (pH ~4.7). In contrast, REs that contain cargos that are meant to be recycled back to the cell surface instead show an alkalinisation (pH ~ 6.5) of their internal pH [241] (**Fig. 4**). The internal acidity of these compartments is established by a combination of active cation transport and anion counter-conductances, thus balancing the electrochemical gradient of ions across the vesicular membrane

[241] (**Fig. 4**). While pH regulation in the secretory and endosomal systems share the same basic principles [241], I will primarily focus upon the latter given the involvement of NHE6.

Vesicular acidification in both the endocytic and secretory pathways is primarily achieved by the vacuolar H⁺-ATPase (V-ATPase), an evolutionarily proton pump that utilizes the chemical energy present in adenosine triphosphate (ATP) to transport H⁺ from the cytosol into the endosomal lumen (**Fig. 4**). V-ATPases are multi-subunit complexes composed of two domains: the integral membrane complex V₀, which is made up of six subunits and mediates proton translocation, and the peripheral V₁ complex, which is responsible for ATP hydrolysis [246]. To maintain the pH of each structure within a certain range, V-ATPase activity may be regulated by various mechanisms, such as differential V-ATPase isoforms, redox state, assembly of the V₀ and V₁ domains, and changes in V-ATPase membrane density [241,247,248]. Indeed, it has been hypothesized that the membranes of more acidic structures may simply contain a higher degree of V-ATPase molecules and less H⁺ leak mechanisms [249]. However, other ion currents are nonetheless critical for the proper establishment of endolysosomal pH.

As V-ATPase-mediated activity imports only H⁺ independently of other ions, this results in the generation of an inside-positive voltage gradient across organellar membranes. As this could prohibit additional H⁺ influx, it is offset by compensatory counterion conductances, such as the influx of anions (**Fig. 4**) [241,250]. This is mediated by members of the 2Cl⁻/1H⁺ exchanger (CLC) family - namely the protein products of the *CLCN3-7* genes - that localize to the membranes of the endolysosomal system and allow for Cl⁻ entry into the vesicular lumen. These CLC exchangers are gated by the luminal pH of their resident compartments such that an accumulation of luminal H⁺ promotes vesicular Cl⁻ influx to offset H⁺-induced voltage gradients and enable further acidification if necessary [243,251]. Interestingly, CLC3-7 also act as electrogenic exchangers to

import Cl^- and export H^+ [252], thereby serving as mechanisms of both compensatory anion flux into the organelle as well as luminal alkalization. The importance of these counter-conductances is highlighted by studies showing that disruptions to CLCs in the nervous system impairs organellar H^+ loading and thus proper proteolysis, which has been associated with the accumulation of tau tangles in neurodegenerative diseases such as AD and PD [253,254].

While these mechanisms are mostly responsible for organellar acidification, H^+ extrusion from endomembrane compartments is carried out by members of the NHE family, including NHE6 (Fig. 4). I will now provide an overview of these NHEs, with a particular emphasis on their burgeoning roles in the brain.

1.4 Na^+/H^+ EXCHANGERS

1.4.1 Overview of NHEs

NHE6 is a member of a larger family of evolutionarily conserved eukaryotic NHEs that couple the countertransport of monovalent alkali cations (such as Na^+ , K^+ , or Li^+) for H^+ across biological membranes. To date, 13 mammalian genes from five phylogenetically distinct categories have been reported, including NHE/solute carrier family 9 (SLC) isoforms 1 through 9 (SLC9A1-SLC9A9), Na^+/H^+ antiporters 1 and 2 (NHA1-2/SLC9B1-2), and the recently characterized SLC9C1 and SLC9C2 isoforms [255,256]. NHE proteins differ in their drug sensitivity, cation selectivity, and tissue and subcellular localization, with some being predominantly localized to specific subdomains of the cell surface and others to intracellular organelles [241,255,256]. Together, these exchangers regulate cellular and organellar pH, vesicular trafficking and recycling, cell volume and osmolality, growth and migration, ion homeostasis, and signaling mechanisms [255,256].

Five NHE isoforms (NHE1-5/SLC9A1-5) predominantly localize to the cell surface and are important for ion resorption in certain organ systems, such as the intestinal and renal epithelia (for more extensive description of plasmalemmal NHE function outside of the nervous system, see [255–257]). The four remaining SLC9A isoforms (NHE6/SLC9A6 through NHE9/SLC9A9) are instead found within intracellular compartments [256,258]. The functions of the SLC9B and SLC9C isoforms are much less well characterized, with the current literature primarily implicating them in sperm motility [257,259,260]. Here, I will provide an overview of what is currently known about NHE isoforms that are expressed in the brain, with a particular focus on NHE6.

The molecular structures of the orthologous bacterial Na^+/H^+ antiporter (NhaA) and mammalian NHE1 have been extensively studied, and these insights have been extrapolated to other NHEs (**Fig. 1**). Upon protein translation and biochemical maturation through glycosylation, NHEs typically assemble and function as homodimers through interactions between the transmembrane and cytosolic domains of their monomers [261,262]. NHE1 (and other NHE isoforms) are predicted to contain 12 hydrophobic transmembrane (TM) domains at its N-terminus that span 400-500 amino acids and are involved in ion exchange and drug sensitivity. In NhaA and NHE1, TM domains TM4 and TM11 are within close proximity to one another and form a loop from the middle of their membrane-spanning segments that allows for ion passage [256,263–265]. Accordingly, mutations in residues within these TM domains alter the ion sensitivity of NHE1 [266–268].

While the N-terminal domains are relatively conserved between NHE family members, the intracellular hydrophilic C-terminus tail, which ranges in length from 50-450 amino acids, are believed be much more variable [256]. Importantly, the C-terminal contains various residues for post-translational modifications that are responsible for regulating kinase activity in response to

external stimuli [256,269]. Additionally, the C-terminal tail of NHE1 has binding sites for a number of interacting partners, including receptor of activated C kinase 1 (RACK1), phosphatidylinositol 4,5-bisphosphate (PIP2), and calmodulin (CaM), [269]. As C-terminal tails drastically vary between NHE isoforms, there is still a need to elucidate which proteins interact with which NHE family members, as well as the effects and relevance of such interactions.

1.4.2 NHEs in nervous system function

Of the plasmalemmal NHEs, two isoforms, NHE1 and NHE5, can be found within the hippocampus [256]. pH regulation of brain cells is particularly important because severe fluctuations in intracellular (pH_i , or cytosolic pH) and extracellular pH (pH_o , or pH outside of the cell) can greatly alter neuronal function and transmission [270,271]. Under physiological conditions, pH_o is slightly alkaline ($\text{pH} \sim 7.3\text{-}7.4$), whereas pH_i is slightly more acidic ($\text{pH} \sim 7.2$) (**Fig. 4**) [241]. In general, increases or decreases in pH_o can enhance or repress neuronal activity, respectively [272]. However, strong electrical stimulation or synchronized neural activity may give way to prolonged acidosis and thus inhibit synaptic transmission, eventually leading to coma [273,274]. Conversely, alkalinisation of pH_o may instead result in hyperexcitability and seizure induction [275]. The pH of synaptic domains is thus a critical determinant of their efficacy.

The ubiquitously expressed NHE1 isoform has been broadly implicated in cytosolic pH homeostasis as well as in the regulation of cellular volume, cytoskeletal components, and cell migration [256,276]. At the cell membrane, NHE1 mediates the electroneutral secondary active transport of Na^+ into the cell in exchange for cytosolic H^+ with a stoichiometry of 1:1 or 2:2 [277,278]. As NHE1 is also highly expressed in the brain [256,276], alterations in NHE1 are associated with a number of neurological deficits in humans and mice. For instance, mutations in

NHE1 have been implicated in Lichtenstein-Knorr syndrome, an autosomal recessive disorder characterized by hearing loss and cerebellar ataxia [279]. Alterations in NHE1 function are further associated with other forms of ataxia, spastic paraplegia, intellectual disability, and epilepsy [280–282]. Accordingly, deletion of the *Slc9a1/Nhe1* gene in mice results in locomotor impairments, epileptic seizures, neurodegeneration, and reductions in lifespan [283,284].

Because NHE1 acts as a means of H^+ extrusion, neurons deficient in NHE1 show a significantly lower steady-state pH_i [285]. At the cellular level, loss of NHE1 results in a complex phenotype involving cellular hyperexcitability, increased Na^+ channel density [286,287], and enhanced cell death [283], although the mechanisms behind these phenotypes remain unclear. Although characterizing its precise localization has been challenging, NHE1 appears to be primarily expressed at GABAergic presynaptic terminals [288–290]. As such, specific removal of NHE1 from PV+ GABAergic interneurons impairs quantal GABA release, demonstrating that NHE1 can modulate network excitability through regulation of GABAergic transmission [291]. Interestingly, NHE blockade using the broad-spectrum inhibitor 5'-(N-ethyl-N-isopropyl)-amiloride (EIPA) was found to significantly improve LTP maintenance [292]. Whether this is the result of a reduction in inhibitory regulation due to NHE1 inhibition, or a direct modulation of an as-of-yet unidentified role of NHE1 at excitatory synapses, remains to be further examined. Nonetheless, this further underscores the fact that NHE1-specific pH regulation can dramatically impact network activity by acting as a regulator of neuronal excitability.

Another NHE isoform, NHE5, is also enriched in multiple brain areas, including the hippocampus [293]. Although often categorized as a plasmalemmal NHE, a substantial proportion of NHE5 is also internalized via CME and localizes within somatodendritic REs [294,295]. Interestingly, the transient insertion of NHE5 to the neuronal cell surface can regulate both pH_o

and pH_i in a stimulus-dependent fashion. For instance, under conditions of metabolic stress and an acidification of pH_i , NHE5 is recruited to the neuronal cell surface through activation of AMP-activated protein kinase (AMPK) to counter heightened acidification of pH_i [296]. Furthermore, in response to NMDAR-dependent chemical LTP, REs containing NHE5s are recruited to spines and undergo fusion with the perisynaptic membrane. These newly inserted exchangers then transport cytosolic H^+ into the synaptic cleft, which negatively regulates NMDAR activation and thus delimits excessive spine expansion [297]. Indeed, mice deficient in NHE5 display improvements in their performances in behavioural learning tasks accompanied by enhanced neurotrophin signaling and an increase in hippocampal dendritic spine density [298]. These results suggest that through its role in regulating neuronal pH, NHE5 acts as a negative regulator of synaptic plasticity to allow the fine-tuning of excitatory synaptic development in the hippocampus.

In contrast to plasmalemmal NHEs, endomembrane NHEs mediate the electroneutral secondary active transport of luminal H^+ for a cytosolic cation (likely K^+ , given its high intracellular concentration) at a stoichiometry of 1:1, thereby acting as a means of H^+ extrusion from organelles to alkalinize their internal pH [241,256] (**Fig. 4**). In the secretory pathway, NHE7 and NHE8 regulate the luminal pH of the trans-Golgi network and post-Golgi vesicles [258,299,300]. NHE7 is widely expressed throughout the body and is also enriched in the brain, skeletal muscle, and various secretory tissues. Consequently, genetic variants in the *SLC9A7* gene encoding NHE7 have been discovered in some forms of non-syndromic intellectual disability accompanied by muscular dystrophy and hypotonia [301], highlighting the role of organellar pH regulation in the secretory system for neural function as well as in neuromuscular physiology.

In a similar fashion, two phylogenetically-related intracellular NHE isoforms, NHE6 and NHE9 primarily localize to endosomes (**Figs. 4, 5**) [241,256,302]. I will primarily focus on NHE6

given its involvement in CS, although I will later discuss potential overlaps and differences between NHE6 and NHE9 function. Endosomal NHEs (eNHEs) primarily localize to EEs and REs in a partially overlapping manner, with some reports showing their presence in LEs as well [258,300,303–305]. As eNHEs act as a means of H⁺ leak from endosomes, overexpression of eNHEs results in an elevation of endosomal pH [258,306], whereas knock-down (KD) or ablation of eNHEs tends to result in an acidification of vesicular pH [307–309]. Thus, it is unsurprising that eNHEs play a pivotal role in the endocytosis and trafficking of cell surface receptors [258,276]. In particular, NHE6 KD in HeLa cells disrupted the CME of transferrin, a carrier of iron often used to study the integrity of CME and REs, through its cognate transferrin receptor [308,310]. Given that AMPARs, GABA_ARs, and other cell surface receptors also heavily rely upon CME to be internalized into the cell [201,224], disruptions in CME due to the loss of NHE6 function may thus also have a strong impact upon synaptic transmission.

The expression of eNHEs is ubiquitous throughout the body but is enriched in more metabolically active tissues, including the brain (for detailed RNA sequencing data in human tissues, see also <https://www.ncbi.nlm.nih.gov/gene/10479>) [258,311]. As such, the dysregulation of eNHEs are directly associated with a number of neurodevelopmental and neurodegenerative conditions. As discussed prior, mutations in the *SLC9A6* gene encoding NHE6 give rise to CS [2]. Furthermore, variants in the *SLC9A9* gene have been associated with epilepsy, autism spectrum disorders (ASDs), and attention deficit hyperactive disorder (ADHD) [3,257,302,312]. Moreover, both eNHEs have recently been implicated in neurodegenerative disorders, including AD. Indeed, NHE6 transcript and protein are both reduced in post-mortem AD tissue [313], and variants of *SLC9A9* have also been linked to AD in genome-wide association studies [314,315]. I will now

summarize the existing literature on NHE6 in neurons and non-neuronal cells, with particular attention to its role in neurons and the pathogenesis of CS while touching on recent data from AD.

1.4.3 NHE6 function in cellular physiology

The *SLC9A6* gene encoding NHE6 is present at chromosomal position Xq26.3 [256]. In humans, protein exists as two alternate splice forms, NHE6v0 and NHE6v1, with the latter containing an additional 32 amino acid insertion within its second extracellular loop (**Fig. 1**). The significance of this is unclear, as the two variants appear to be functionally identical [311,316]. Like NHE1, both eNHEs interact with the cytoplasmic scaffold protein RACK1 through their C-terminal domains [317]. This interaction appears to regulate the plasmalemmal expression of NHE6, as KD of RACK1 decreased surface NHE6 localization [317]. NHE6 activity can also be regulated through its direct interaction with angiotensin II receptor subtype 2 (AT2), a regulator of body fluid and Na⁺ homeostasis, in a ligand-dependent fashion [318]. Interestingly, AT2 is also expressed in the hippocampus and can regulate neuronal excitability by downregulating Ca²⁺ influx while stimulating K⁺ transients, thereby dampening excitation [319–321]. AT2 activation can also regulate neurite outgrowth and migration as well [320]. Notably, some human mutations in AT2 appear to cause a similar phenotype to CS, including intellectual disability and epilepsy [318]. However, the functional implications of this interaction between NHE6 and AT2, and whether not it is potentially involved in disease pathogenesis, is presently unclear.

Curiously, eNHEs primarily localize to the plasma membrane of some cell types to extrude excess levels of H⁺ generated during periods of high metabolic activity. Both NHE6 and NHE9 are present at the surface of vestibular hair cells [322], while NHE6 was also found to act in concert with NHE1 at the cell membrane of developing osteoclasts [323]. Unlike neurons and most other

organs, these cells are exposed to a relatively high extracellular $[K^+]$ and presumably require the action of eNHEs, which are more specific for K^+ , to aid in H^+ extrusion. Interestingly, these plasmalemmal roles of NHE6 in other organs could underlie some of the non-neurological symptoms of CS. For instance, skeletal malformations are commonly reported in CS patients [1,2,5,14], which may be the result of improper bone mineralization from a paucity of NHE6-mediated H^+ extrusion. A recent study has also reported that NHE6 is highly expressed in hair cells of the murine cochlea, and mice deficient in NHE6 were more prone to developing hearing loss symptoms over time [324]. Although hearing loss was not reported from the initial cohort of CS patients [1], strabismus is a commonly reported finding in patients [2], and inner ear impairments may thus comprise a significant fraction of the diagnostic criteria of CS.

Over the past decade, there has been a greater focus on determining the expression patterns and functions of NHE6 within the brain. During murine embryogenesis, NHE6 is highly expressed in developing fiber tracts across multiple brain areas, including the cortex, striatum, thalamus, and hippocampus, by embryonic day (ED) 15 [309]. NHE6 expression is then persistent throughout the post-natal brain [325]. Interestingly, its expression appears to peak at PD 50, during a period of intense synaptic pruning and refinement, before being downregulated by PD 120 [326]. In hippocampal pyramidal neurons, NHE6 is broadly present throughout the axons, soma, and dendrites and colocalizes substantially with markers of EEs and REs at the base and head subregions of dendritic spines [309,326]. Moreover, NHE6 strongly colocalizes with synaptic vesicle 2 (SV2) and PSD95, which serve as markers of pre- and postsynaptic sites, respectively [309]. This suggests that not only is NHE6 involved in transcytotic trafficking across neuronal compartments, but it may play a direct role in synaptic transmission as well.

Which cargos are trafficked by NHE6? As REs are critical for AMPAR exocytosis and spine enlargement during LTP [144,166], it is reasonable to hypothesize that NHE6, a regulator of RE function, is involved in the response to LTP. In hippocampal pyramidal neurons, NHE6 colocalizes strongly with the AMPAR subunit GluA1 and is upregulated at spines and spine heads following NMDAR-mediated chemical LTP [326]. Presumably, NHE6 mediates the trafficking of AMPARs and other proteins that are necessary for postsynaptic strengthening. NHE6 also overlaps strongly with tropomyosin receptor kinase B (TrkB) [309], the high affinity receptor for the neurotrophin brain-derived neurotrophic factor (BDNF). During development, signaling through BDNF/TrkB promotes neuronal outgrowth, differentiation, and survival [327,328] and can further regulate synaptic dynamics during plasticity induction [329,330]. Importantly, this system is heavily reliant upon endosomal machinery, as the binding of BDNF to TrkB results in the dimerization, autophosphorylation, and internalization of the receptor into signaling endosomes (SEs) [331–334]. They are then capable of activating downstream signaling cascades either locally near the site of endocytosis, or as they undergo long-range, dynein-dependent retrograde transport back to the cell soma [335]. Because NHE6 is presumed to regulate the luminal pH and thus the trafficking of SEs containing activated, phosphorylated TrkB (pTrkB), it is likely that the absence of NHE6 may perturb signaling downstream of the BDNF/TrkB complex.

1.4.4 Insights from *Nhe6* KO mice

Recent work has employed homozygous *Slc9a6*^{-/-} mice to gain a better understanding of NHE6 function in the brain. Initial studies into these KO mice reported that they show a number of neurological abnormalities that mirror neurodegeneration in CS as well as lysosomal storage diseases (LSDs). LSDs generally arise from improper lipid clearance, thus resulting in the

accumulation of glycosphingolipids, such as GM2 and GM3 gangliosides, within endolysosomal compartments [336]. Indeed, *Nhe6* KO mice exemplify unesterified cholesterol and GM2 gangliosides across multiple brain areas alongside the absence of β -hexosaminidase, the enzyme responsible for degrading GM2 ganglioside [337]. These findings mirror the reports of tau disposition found in post-mortem CS tissue [13,15] and imply some degree of lysosomal dysfunction. The cerebella of these mice also display a patterned loss of Zebrin II-negative Purkinje cells within anterior regions of the vermis, with surviving Purkinje cells showing spheroid swellings along their axons [337]. These findings are further characteristic of LSDs [338] and are also in line with the progressive cerebellar atrophy commonly seen in CS [1,2,5]. Moreover, measurements of gross brain volumes of *Nhe6* KO mice found a pronounced overall undergrowth in addition to progressive volume loss in the cortex, striatum, hippocampus, and cerebellum with age [339]. Again, this is in accordance with the prevalence of postnatal microcephaly in CS [5], which was highly suggestive of reduced brain size in human patients. Consequently, behavioural data collected from homozygous male *Slc9a6*^{-/-} mice are similarly reflective of phenotypic findings from individuals with CS. Perhaps the most robust of these data is the severe locomotor deficits exhibited by these KO mice, as evidenced by their relatively poor performance in rotarod and balance beam tasks [337]. These animals further exhibit hyperactivity and anxiety-like behaviours in open field paradigms [337,340], as well as a reduced sensitivity to pain and pressure stimuli [341,342]. Interestingly, female heterozygous *Slc9a6*^{+/-} mice show an intermediate phenotype in these paradigms when compared to homozygous *Slc9a6*^{-/-} males and controls [340], alluding to the possibility of a gene dosage effect of NHE6 in controlling these behaviours. Taken together, it is evident that both neuropathological and behavioural findings from *Nhe6* KO mice are indeed reflective of clinical observations made from human CS patients.

Given these neurological abnormalities, the loss of NHE6 evidently has a profound impact upon the development and function of individual neurons. Membrane trafficking is particularly crucial for the establishment of polarity in all cells, including neurons [343]. As such, NHE6-associated trafficking was first implicated in the development of cellular polarity, even in non-neuronal cells. In polarized liver hepatoma HepG2 cells, which show distinct apical and basolateral surface domains, NHE6 KD acidified endosomal pH and disrupted the transcytotic recycling of cargo necessary for the establishment of the apical domain [306]. In a similar vein, CA1 pyramidal neurons deficient in NHE6 show prominent reductions in axodendritic branching and mature dendritic spine density [309]. In this study, the researchers attributed these morphological deficits to impairments in BDNF/TrkB signaling, as they observed an attenuation in pTrkB protein in hippocampal neurons derived from *Nhe6* KO mice. However, application of exogenous BDNF in conjunction with lysosomal hydrolase impairment was sufficient to restore pTrkB levels and neurite branching in cultured hippocampal KO neurons [309]. These results suggest that SEs become overacidified due to a lack of NHE6-mediated endosomal pH regulation, causing activated pTrkB complexes in these SEs to be aberrantly degraded through the lysosome. This raises the question of which other proteins could undergo such a fate in the absence of NHE6 function.

As I alluded to earlier, NHE6 may be involved in the trafficking of proteins that mediate synaptic function. Interestingly, NHE6 colocalizes with the presynaptic marker SV2 to a significantly greater extent than PSD95 [309], suggesting that NHE6 may be in fact be more involved in presynaptic rather than postsynaptic function. Despite this distinction, there has yet to be evidence to suggest that presynaptic function is impacted by a loss of NHE6. Fiber volleys, which are reflective of presynaptic firing and activation, obtained from *Nhe6* KO hippocampal slices were significantly reduced in amplitude when compared to WT, implying a loss in the overall

number of functional synapses that correlated with the reductions in spine density [309]. However, WT and *Nhe6* KO hippocampi did not significantly differ in paired pulse ratio (PPR) recordings [309], suggesting that presynaptic function were mostly intact. Conversely, the closely related NHE9 may play a clearer role in presynaptic function. Insights from *Nhe9* KO mice demonstrated that although fiber volley amplitudes were comparable between WT and KO, the latter showed an increase in PPR that was suggestive of a decrease in presynaptic release probability at glutamatergic synapses [304]. This supposition was confirmed in the same study, in which the authors demonstrated that in the absence of NHE9, presynaptic Ca^{2+} influx was reduced, and synaptic vesicle exocytosis was subsequently impaired [304]. Interestingly, the authors also demonstrated that transient organellar alkalinisation using the V-ATPase inhibitor bafilomycin in *Nhe9* KO neurons was sufficient to restore presynaptic Ca^{2+} entry, suggesting that an aberrant decrease in endosomal pH hindered presynaptic release [304]. These results underscore the importance of regulating endosomal pH within the axonal bouton to maintain Ca^{2+} dynamics and quantal release, although further work into the potential involvement of NHE6 is needed.

Aside from neurons, NHE6 is also present in protoplasmic astrocytes within hippocampal area CA1 [326]. Additional findings have further shown a higher number of activated microglia in the cerebella of *Nhe6* KO mice [339,340], which is indicative of gliosis and has also been observed in CS patients [13]. However, further insights into the function of NHE6 in astrocytes and other glia are lacking. One report on NHE9 has shown that astrocytes lacking NHE9 or expressing ASD-associated variants in *SLC9A9* exhibited a significant acidification in endosomal pH [344]. Astrocytes transfected with these ASD-associated *SLC9A9* variants also failed to upregulate the surface expression of excitatory amino acid transporter 1 (EAAT1), resulting in a decrease in glutamate uptake when compared to WT NHE9 overexpression [344]. These findings suggest that

NHE9-mediated trafficking is important for the surface expression of EAAT1 and other glutamate re-uptake transporters in astrocytes, though whether NHE6 plays a similar role is presently unknown. If this were the case, then excess glutamate in the synaptic cleft could underlie the development of epileptic seizures in CS patients, especially because magnetic resonance spectroscopy data from patients with *SLC9A6* mutations have shown an increase in glutamate concentration in the brain [2,14]. Further work on the function of NHE6 in the transport of glutamate transporters and glutamate clearance remains to be performed.

1.4.5 Insights from patient-derived NHE6 mutations

It is evident that a lack of NHE6 can disrupt neuronal structure and trafficking. However, human CS patients do not possess complete gene KOs and instead express genetic variants of *SLC9A6* (**Fig. 1**). Although many patients possess nonsense mutations that introduce a premature stop codon and prohibit protein production, some mutations can result in the production of a full-length protein product [2,5]. The expression of such variants in non-neuronal cells and cultured neurons *in vitro* have provided a number of insights into their biochemical characteristics and impact upon cellular function [305,307,345–347].

In Chinese hamster ovary AP-1 cells, which do not natively express NHE6, most transfected NHE6 variants display impairments in post-translational maturation (as indicated by a lack of glycosylation states) and reduced biochemical stability [305,345–347]. These mutant exchangers are highly ubiquitinated and primarily undergo endoplasmic reticulum (ER)-associated protein degradation (ERAD) through the proteasome, a mechanism of protein quality control that eliminates misfolded or unassembled proteins from the ER [348]. The fraction of mutant NHE6 that escapes ERAD is targeted by the ESCRT system and degraded in the lysosome

[305,307,345,347]. Moreover, vesicles containing some of these NHE6 variants failed to alkalinize compared to those expressing WT [345,347]. This suggests a loss of ion exchange function and endosomal pH regulation, which could impair endocytic mechanisms. Indeed, expression of these mutant exchangers in HeLa cells and primary hippocampal neurons disrupted transferrin uptake [305,345–347]. Intriguingly, these deficits may be selective for certain cargos, as uptake of epidermal growth factor (EGF) was not disrupted in HeLa cells expressing an in-frame deletion NHE6 mutant (p.Glu287_Ser288del; Δ ES, see **Fig. 1** and Appendix 1) [345]. In primary hippocampal neurons, the transient expression of Δ ES NHE6 or another in-frame deletion mutant (p.Trp370_Ser_Thr372del; Δ WST) also disrupted neuronal branching [305,345], akin to findings in *Nhe6* KO neurons [309]. Notably, transfection of exchanger-deficient NHE6 variants into neurons deficient in NHE6 failed to rescue neuronal branching [309], indicating that the ion exchange function of NHE6 is indeed necessary for neuronal morphogenesis. In Chapter 2, I will discuss my work on the effect of the Δ ES mutant upon synaptic density and plasticity.

Furthermore, transfecting some of these mutations into AP-1 cells also induced apoptosis [345,347], as did expression of Δ ES NHE6 into primary hippocampal neurons [345]. This indicates that a lack of NHE6 function indeed gives way to the pronounced neurodegeneration observed in *Nhe6* KO mice [337,339]. However, it is also possible that the overexpression of mutant NHE6 constructs itself may result in the accumulation of misfolded proteins in the ER, which could initiate the unfolded protein response and ERAD in an attempt to restore cellular homeostasis [349–351]. However, continued ER stress may additionally activate various downstream pathways leading to the induction of apoptosis over time [349,351–354]. Post-mitotic neurons are particularly sensitive to ER stress, as they cannot dilute toxic protein accumulations through cell division [355,356]. Thus, combined with a possible dissolution of cellular trafficking

mechanisms, ER stress may also contribute to the pronounced apoptosis observed in neurons transfected with Δ ES NHE6. Taken together, these *in vitro* data corroborate the findings in *Nhe6* KO mice and underscore the idea that NHE6-mediated endosomal pH regulation regulates endocytic trafficking necessary for neurite outgrowth and survival.

Nevertheless, not all genetic *SLC9A6* mutations identified from CS patients result in a LOF phenotype and aberrant lysosomal degradation. During my thesis work, I contributed to a manuscript that focused on the impact of a *de novo* missense *SLC9A6* variant (p.Gly218Arg; G218R) (see Appendix 2). Upon transfection into AP-1 cells and primary hippocampal neurons, we surprisingly observed a significant elevation in the pH of G218R NHE6-containing vesicles when compared to WT NHE6. Unlike Δ ES NHE6 and other LOF variants, which exhibited endosomal overacidification when expressed, this was instead suggestive of a gain-of-function (GOF) effect. Moreover, while most other LOF variants were found to be degraded through the proteasome or lysosome [305,345,347], a significant fraction of the G218R NHE6 that escaped ERAD was trafficked to LEs and instead secreted out of the cell through exosomes [346]. In spite of these key differences, I found that neurons expressing G218R NHE6 showed similar morphological impairments to those expressing deletion mutations or complete gene KO [309], including reduced dendritic arborization and spine density [346]. These insights underscore the importance of tightly maintaining endosomal pH, as significant deviations in either direction may severely impact cellular function [241].

Notably, it is possible that not all human *SLC9A6* variants impact exchanger function to potentially give rise to a disease phenotype. Indeed, recent evidence has shown that two missense mutations - one in the extreme N-terminal cytoplasmic segment (pAla9Ser; A9S) and another in the regulatory C-terminal cytoplasmic domain (Arg568Gln; R568Q) - appear to have comparable

biochemical characteristics to that of WT NHE6 when expressed in AP-1 cells, including their stability and functionality [347]. Engineering of the equivalent A9S mutation in mice revealed effectively normal brain development, neuronal arborization, and endosomal pH regulation [357], confirming that this mutation alone does not lead to neurological impairments [11]. Conversely, while the biochemical attributes of the R568Q mutation also appeared to be benign, it is possible that this mutation may alter the interactions between the C-terminal tail of NHE6 with its interacting proteins and perturb other cellular mechanisms independently from its pH regulatory function. Additional analyses expressing this particular variant into neurons are required to better understand the impact, if any, of this mutation upon cellular physiology. Further insights into these particular mutations in human patients from which they were identified will also be required to gain a better understanding of the genetic factors underlying their cognitive deficits.

1.4.6 Involvement of NHE6 in other neurological disorders

Fascinatingly, NHE6 may not only be implicated in CS but could also be implicated in the pathogenesis of other forms of cognitive impairment as well. Accordingly, neurodegenerative disorders, such as AD and PD, are also characterized by the dissolution of endolysosomal mechanisms, hinting at a possible role for NHE6-mediated pH regulation. Indeed, insoluble protein deposits, such as tangles of the microtubule-associated protein tau, are a neuropathological hallmark of such disorders [358]. Notably, post-mortem samples from CS patients have revealed striking tau depositions [13,15], and female carriers of *SLC9A6* mutations have also been reported to exhibit symptoms of PD later in life [15,20]. These findings suggest that a lack of NHE6 function may further be involved in more common neurodegenerative disorders as well. Thus far, recent evidence has highlighted a potential role for NHE6 in the pathogenesis of AD.

AD is the most common neurodegenerative disorder and commonly presents with severe cognitive decline and dementia. Histologically, AD is characterized by the presence of extracellular A β plaques and intracellular hyperphosphorylated tau tangles, which are believed to underlie synaptic impairments and neuronal cell death [359,360]. A β is generated by the sequential cleavage of amyloid precursor protein (APP) by β -secretase 1 (BACE1) and γ -secretase, which occurs in the endosome [361–363]. In fact, the rate-limiting step of A β generation is the physical convergence between membrane-bound APP and BACE1 in endosomes [364–367]. BACE1 activity is further reliant upon an acidic vesicular environment [365]. As endosomes are hyperacidified in the absence of eNHEs [307,309], it is logical to assume that changes in NHE6 activity could also impact APP processing. Accordingly, elevated levels of hyperphosphorylated tau and A β have also been found in *Slc9a6* KO mice [337].

Indeed, a recent study has shown that in APP-expressing human embryonic kidney 293 (HEK293) cells, which reliably secrete substantial levels of A β , raising endosomal pH - either by co-expression of NHE6 or through application of the endosomal alkalisation agent monensin - was sufficient to prevent pathological APP cleavage and A β secretion [313]. The same group has further shown that in astrocytes carrying the ϵ 4 allele of Apolipoprotein E (ApoE4), the strongest genetic risk factor for AD, endosomes are also overacidified due to a transcriptional downregulation of NHE6. This results in the intracellular retention of lipoprotein receptor-related protein 1 (LRP1), which normally functions to extrude A β , and these ApoE4 astrocytes were thus unable to properly clear pathological A β aggregates. However, by applying histone deacetylase (HDAC) inhibitors to increase NHE6 transcription, the researchers were able to elevate endosomal pH, restore LRP1 trafficking, and allow for proper A β clearance [368]. These findings show multiple ways in which the loss of NHE6 may promote pathological APP processing and prohibit

proper clearance of protein aggregates to result in an AD-like pathology. As such, manipulating vesicular pH by altering NHE6 expression or applying endosomal alkalization agents may hold promise as a novel therapeutic option for AD patients.

1.5 RATIONALE AND OBJECTIVES

Although the prevalence of CS continues to rise, treatment options are extremely limited for patients afflicted by this disorder due to a naivety behind our present understanding of its underlying etiology at the cellular and molecular levels. Clearly, there is an urgent need to gain a greater understanding into the cellular mechanisms behind how the loss of NHE6 function may perturb neural function to result in the severe impairments in CS and potentially in other more common disorders, including AD. Nevertheless, study into the role of NHE6 in the brain is still comparatively nascent. As I have discussed, NHE6 is a critical regulator of membrane trafficking in neurons, which rely upon the endosomal system to regulate the surface expression and recycling of receptors for neurotransmitters and neurotrophins. Hence, one can imagine that perturbations in the precise trafficking of certain membrane-bound receptors and other cargos may have a devastating impact upon basic cellular physiology, as well as synaptic formation, transmission, and remodeling. However, the identity of affected cargos and the consequences of their mistrafficking upon neural physiology, are still unclear.

In my thesis, I sought to untangle the ways in which the loss of NHE6 function perturbs neural function at the level of individual proteins, synapse, and cells, as well as in the hippocampal circuit and cognitive processing of the whole animal. As CS is a monogenic disorder arising from mutations in the human *SLC9A6/NHE6* gene, commercially available KO mice deficient in the *Slc9a6/Nhe6* gene have been used in the past to study how the complete absence of NHE6 can

impact neural function *in vivo*. Importantly, these mice appear to replicate numerous neuropathological and behavioural phenotypes of CS, including cerebellar atrophy, ataxia, hyperactivity, and impaired somatosensory processing [309,337,339–342]. Thus, they can serve as a suitable model for patients with nonsense *SLC9A6* mutations that presumably result in a loss of NHE6 function. However, some mutations are still capable of producing a full-length protein product. As such, I also extensively studied the effects of one patient-derived variant in *SLC9A6* upon cultured mouse hippocampal neurons to gain a better understanding of whether these mutations in NHE6 have a cell-autonomous effect upon neuronal function.

In addressing the severe intellectual disability in CS, I will first describe my findings on the impact of mutating or removing NHE6 upon excitatory synaptic function and plasticity. Moreover, as anecdotal evidence suggests that epilepsy is perhaps the most devastating symptom affecting the quality of life of CS patients, I will also describe my work on how hyperexcitability may develop in the absence of NHE6 function. It is my hope that the data and conclusions presented in my thesis will lay the foundation for additional research to gain a better understanding of the cellular mechanisms behind CS with the overall intention of providing novel treatment options for individuals afflicted by this devastating disorder.

CHAPTER 2. A CHRISTIANSON SYNDROME-LINKED DELETION MUTATION ($\Delta(287)ES(288)$) IN *SLC9A6* IMPAIRS HIPPOCAMPAL NEURONAL PLASTICITY

FOREWARD

Background and Rationale

In neurons and other cell types, NHE6 primarily localizes to early and recycling endosomes to regulate their luminal pH. Previously, we have reported that NHE6 (1) is strongly expressed in the murine hippocampus, (2) colocalizes significantly with the GluA1 subunit of AMPARs, and (3) is recruited to excitatory synapses following LTP induction. However, genetic *SLC9A6* variants have not yet been thoroughly investigated, particularly in neurons. To this end, members of Dr. J. Orłowski's laboratory investigated the biochemical properties of one such mutation (p.E287-S288del, or ΔES ; see Appendix 1). They first noted that the ΔES mutant showed disturbances in its post-translational maturation and biochemical stability, being preferentially degraded by both the proteasome and lysosome. Vesicles containing the ΔES NHE6 mutant were also significantly more acidic than those with WT NHE6, suggesting that the ΔES mutation indeed ablates the ion transport and pH regulatory functions of the exchanger. When I transfected ΔES NHE6 into primary hippocampal neurons, I observed that this similarly disrupted neurite outgrowth and transferrin uptake and also induced apoptosis. By extension, I also wished to verify whether this mutation could elicit changes in dendritic spine density and plasticity in hippocampal neurons.

Hypothesis

I hypothesized that ΔES NHE6 expression will reduce dendritic spine density and be mislocalized in neurons. The presence of the ΔES mutant in hippocampal neurons will also impair the

trafficking of GluA1 AMPARs and favour its localization to lysosomes for putative degradation. As a result, this will perturb both functional and structural potentiation in response to LTP induction.

Experimental Outline

The work detailed in this chapter has been presented in an article entitled “A Christianson syndrome-linked deletion mutation (Δ 287ES288) in *SLC9A6* impairs hippocampal neuronal plasticity,” published in the journal *Neurobiology of Disease* in 2019. In brief, I prepared primary hippocampal neurons from early postnatal WT mice and sparsely transfected plasmids encoding a fluorescently tagged Δ ES NHE6 construct and a cytosolic marker to visualize cell structure. I then studied the impacts of this mutation upon endolysosomal trafficking and excitatory synaptic density and remodeling using a combination of immunofluorescence, confocal microscopy, and electrophysiology. Finally, to verify whether these changes are due to an excessive degree of lysosomal degradation, I applied inhibitors of lysosomal acidification or protease function to restore these deficits in spine number and plasticity.

2.1 ABSTRACT

Christianson Syndrome is a rare but increasingly diagnosed X-linked intellectual disability that arises from mutations in SLC9A6/NHE6, a pH-regulating transporter that localizes to early and recycling endosomes. We have recently reported that one of the originally identified disease-causing mutations in NHE6 (p.E287-S288del, or Δ ES) resulted in a loss of its pH homeostasis function. However, the impact of this mutation upon neuronal synapse formation and plasticity is unknown. Here, we investigate the consequences of the Δ ES mutant upon mouse hippocampal pyramidal neurons by expressing a fluorescently labeled Δ ES NHE6 construct into primary hippocampal neurons. Neurons expressing the Δ ES mutant showed significant reductions in mature dendritic spine density with a concurrent increase in immature filopodia. Furthermore, compared to wild-type (WT), Δ ES-containing endosomes are redirected away from early and recycling endosomes toward lysosomes. In parallel, the Δ ES mutant reduced the trafficking of glutamatergic AMPA receptors to excitatory synapses and increased their accumulation within lysosomes for potential degradation. Upon long-term potentiation (LTP), neurons expressing Δ ES failed to undergo significant structural and functional changes as observed in controls and WT transfectants. Interestingly, synapse density and LTP-induced synaptic remodeling in Δ ES-expressing neurons were partially restored by bafilomycin, a vesicular alkalisation agent, or by leupeptin, an inhibitor of lysosomal proteolytic degradation. Overall, our results demonstrate that the Δ ES mutation attenuates synapse density and structural and functional plasticity in hippocampal neurons. These deficits may be partially due to the mistargeting of AMPA receptors and other cargos to lysosomes, thereby preventing their trafficking during synaptic remodeling. This mechanism may contribute to the cognitive learning deficits observed in patients with Christianson syndrome and suggests a potential therapeutic strategy for treatment.

2.2 INTRODUCTION

Genetic or environmental mediated disturbances in early brain growth and maturation result in a heterogeneous group of neurodevelopmental disorders that can manifest as deficits in learning ability and memory, language and communication skills, emotion or motor coordination, amongst other behaviours. A recent addition to this spectrum of disorders is Christianson Syndrome (CS), an X-linked condition that becomes apparent in infancy and is characterized by moderate to severe intellectual disability, epilepsy, non-verbalism, ataxia, and autism-like behaviours [1–3]. These patients also exemplify further deterioration in their symptoms, namely in cerebellar atrophy and Purkinje cell loss associated with a progressive loss of mobility after the first decade of life [1,3,4]. SLC9A6 knock-out (KO) mice have also been reported to exhibit reductions in cortical and hippocampal volume with age, suggestive of further degeneration in these brain areas as well [5]. The frequency of CS is estimated at 1 in 16,000 to 1 in 100,000 people worldwide, which ranks it among the more common forms of X-linked intellectual disability [6]. At present, however, the molecular mechanisms underlying CS are poorly understood, and effective interventions are lacking. CS results from mutations in the solute carrier gene *SLC9A6* located at chromosome position Xq26.3, which encodes the electroneutral alkali cation (Na⁺, K⁺)/proton (H⁺) exchanger isoform 6 (commonly referred to as NHE6) [7]. The *NHE6* gene is transcribed in most tissues but is especially abundant in brain [8], which likely accounts for the pronounced neuropathological appearance of CS. In neurons and other cell types, NHE6 localizes primarily to the membranes of early and recycling endosomes [8,9] and acts as a H⁺ extrusion mechanism to moderate luminal acidification driven by the electrogenic vacuolar H⁺-ATPase pump [10]. This is an important regulatory process, as endosomes carrying cargo intended for either recycling to the plasma membrane or degradation in lysosomes experience an increase or decrease in luminal pH,

respectively. Indeed, graded acidification of endomembrane compartments along the recycling and degradative pathways is an important determinant of their biogenesis, trafficking and function [11–14]. While the significance of this phenomenon has long been appreciated in non-neuronal cells, its impact on neuronal function is less well studied. Endosomal transport of lipids and membrane receptors, such as the neurotrophin tropomyosin receptor kinase B (TrkB) and glutamatergic α -amino-3-hydroxy-5-methyl-4-isoxazolepropionic acid receptors (AMPA), is essential for axonal and dendritic development, synaptogenesis, and plasticity mechanisms [15–17]. Thus, further investigation into the role of endosomal pH—and NHE6 in particular—in the optimal function and maintenance of neurons is warranted.

Our current understanding of how mutations in *SLC9A6* alter neuronal function in the pathophysiology of CS is limited. To date, over 50 *de novo* and inherited mutations in *SLC9A6* have been reported in CS patients [1,4,18,19] (also see the databases ClinVar (<https://www.ncbi.nlm.nih.gov/clinvar/>) and DECIPHER (<https://decipher.sanger.ac.uk/>)). Many of these mutations truncate the protein in the transmembrane ion translocation domain, leading to a complete loss of function [1]. Previous experimental studies have focused mainly on an *SLC9A6* knock-out (KO) mouse, in which endosomal-lysosomal function is impaired in neurons across various brain regions [20]. In hippocampal neurons prepared from NHE6 KO mice, axodendritic branching and the density of mature excitatory synapses is reduced compared to wild-type (WT) neurons [21]. While these experiments provide valuable insight into the consequences of the complete loss of NHE6 protein, it is unclear if these changes are mirrored in neurons expressing other disease-causing NHE6 mutants that generate an intact protein. Importantly, how disease-causing mutants may affect receptor trafficking and plasticity mechanisms, which could underlie the severe learning deficits observed in CS patients, is currently unknown.

We recently reported that an in-frame deletion mutant of NHE6 (NM_001042537.1:c.860_865delAAAGTG:p.E287_S288del, referred to as Δ ES) resulted in excess acidification of NHE6-containing endosomes and elicited significant reductions in dendritic arborization of primary cultures of transfected mouse hippocampal neurons [22]. In this report, we further investigate the effects of the Δ ES mutant on excitatory synaptic density, AMPA receptor trafficking and synaptic plasticity. Specifically, expression of the Δ ES mutant in primary hippocampal neurons results in a reduction of dendritic spine density and in impaired functional and structural spine remodeling in response to glycine-mediated chemically-induced long-term potentiation (i.e., gly-ChemLTP stimulation). We also show that the Δ ES mutant is mislocalized within cells when compared to WT and disrupts the trafficking of glutamatergic AMPARS. Interestingly, treating Δ ES-expressing neurons with either a lysosomal inhibitor or a vesicular alkalization agent partially rescues neuronal structure and plasticity. Our results highlight a critical role for NHE6 in synaptic morphology, remodeling and excitatory synaptic potentiation in hippocampal neurons, providing new mechanistic insight into some of the cognitive impairments associated with CS. In addition, NHE6 dysfunction has been implicated in the progression of other neurodegenerative disorders [23–26]. Hence, our findings may be relevant to a broader number of neuropathological conditions than previously realized.

2.3 METHODS

Recombinant DNA constructs and mutagenesis. The long transcript splice-variant of human NHE6 (NHE6v1; NCBI refseq NM_001042537) was cloned from a human brain Matchmaker™ cDNA library (Clontech) using PCR methodology and was engineered to contain the influenza virus hemagglutinin (HA) (YPYDVPDYAS) epitope at its extreme C-terminal end.

This construct was termed wild-type NHE6-HA (NHE6_{WT}-HA) and inserted into the HindIII and XbaI sites of the mammalian expression vector pcDNA3 (Invitrogen), as described previously [27]. NHE6-HA was then used as a template to engineer the double deletion mutation of amino acids E287 and S288 (Δ E287/S288, Δ ES) by PCR mutagenesis. mCherry fluorescent protein (mCh) C-terminal-tagged forms of NHE6 WT and Δ ES mutant were constructed by insertion between the XhoI and HindIII restriction sites of the pAcGFP1-N1 vector (BD Biosciences Clontech, Palo Alto, CA). Insertion of the different epitope tags in the various positions did not alter the biochemical properties or cellular distribution of exogenous NHE6 compared to the endogenous protein [22,27]. All constructs were sequenced to ensure that no additional mutations were introduced during PCR.

Mouse primary hippocampal cultures. *In vitro* experiments were performed on primary hippocampal cultures prepared from early postnatal C57BL/6 mice, prepared as previously described [8,28]. In brief, post-natal day (PD) 0-1 mice pups were decapitated, their brains removed, and the hippocampi dissected out. These hippocampi were maintained in chilled HBSS supplemented with 0.1 M HEPES buffer and 0.6% glucose, then digested with 165 U papain for 20 min in a shaking water bath at 37°C. Neurons and glia were dissociated by trituration and suspended in DMEM supplemented with 1% penicillin-streptomycin, 10% FBS, and 0.6% glucose. Cells were then plated onto poly-D-lysine-coated 10 mm coverslips at an approximate density of 12,000 cells/cm² and placed in an incubator at 37°C. 24 h later, plating media was replaced with Neurobasal-A growth media supplemented with 2% B-27 supplement, 1% GlutaMAX, and 1% penicillin-streptomycin. Cultures were then fed every 3 – 4 d and allowed to mature until 14+ days *in vitro* (DIV) at 37°C in a humidified environment of 5% CO₂. Over the

course of this time period, these cells develop and form a functional neuronal network in a controlled manner [29].

Calcium phosphate transfection. Primary neurons were transfected via calcium phosphate transfection as previously described [30]. In summary, at 11-12 DIV, coverslips were transferred into a 35 mm dish filled with warmed preconditioned growth media. 4 μ g of DNA plasmids were mixed with 50 μ l 250 mM CaCl_2 solution, which was next added to 50 μ l 2x HEPES-buffered phosphate solution to form DNA-tagged calcium phosphate precipitate. This was then added dropwise to each dish of coverslips and incubated at 37°C in a humidified environment of 3% CO_2 for 90 min. Prior to returning them to their original plates, 80 μ l of sterile 0.3 M 2-(4-morpholino) ethanesulfonic acid (MES) acid buffer (pH 5.5) were added to each dish, which acidified the media to dissolve any remaining precipitate. The cultures were then maintained at 37°C, 5% CO_2 for \geq 48 h before being further processed. In these experiments, we will mostly focus on the longest splice variant of NHE6, NHE6v1 (i.e., p.E287_S288del in NHE6v1, or NHE6 Δ ES). Cultures were generally co-transfected with plasmids encoding enhanced green fluorescent protein (EGFP) or tdTomato (to mark neuronal structure) and mCherry alone (as a transfection control) or either WT or Δ ES NHE6 tagged to mCherry or influenza virus hemagglutinin epitope (HA). In surface GluA1 experiments, a construct encoding the AMPAR subunit GluA1 with N-terminally fused pH-sensitive superecliptic pHluorin (SEP-GluA1, gift from Dr. Edward Ruthazer) is utilized.

Glycine-mediated chemical LTP. Glycine-mediated chemical long-term potentiation (gly-ChemLTP) was performed on primary hippocampal cultures as previously described [8,31]. To summarize, transfected neurons at 14+ DIV were placed into a heated (30°C) recording chamber of an upright microscope (DM LFSA, Leica Microsystems, Heidelberg, Germany). Cultures were first perfused continuously for 15 min with normal artificial CSF (nASCF) containing the

following (in mM): 125 NaCl, 2.5 KCl, 2 CaCl₂, 1 MgCl₂·6H₂O, 5 HEPES, and 33 D(+)-glucose, pH 7.3, osmolarity 290 mOsmol/L, and gassed with 95% O₂/5% CO₂. The nACSF was then replaced with a stimulating solution of Mg²⁺-deficient ACSF with the following (in mM): 125 NaCl, 2.5 KCl, 2 CaCl₂·2H₂O, 5 HEPES, 33 D(+)-glucose, 0.2 glycine, 0.02 (-)-bicuculline methochloride, and 0.003 strychnine hydrochloride. After 10 min, neurons were be reperfused with nACSF for 20 min. To confirm that this phenomenon is NMDA receptor-dependent, this protocol was repeated in NHE6 WT-transfected cultures pretreated with (*RS*)-3-(2-carboxypiperazin-4-yl)-propyl-1-phosphonic acid ((*RS*)-CPP; 50 μ M), a competitive antagonist of the NMDA receptor, for 15 min prior to gly-ChemLTP stimulation. This antagonist was also included in the stimulation solution (gly-ChemLTP + CPP).

Immunofluorescence. Primary cultures were fixed with 4% PFA/0.1 M PB, pH 7.4 (Sigma Aldrich) for 15 min at room temperature and washed with 0.1 M PB. Immunoprocessed cultures were first permeabilized for 1 min in 0.2% Triton X-100/0.1 M PB and blocked for 1 h at room temperature in 0.2% Triton X-100/1% HIHS/0.1 M PB, before being incubated with primary antibodies (GFP 1:1000, Stx-13 1:500, EEA1 1:1000, Rab7: 1:500, LAMP1: 1:500, GluA1 1:200) diluted in blocking solution overnight at 4°C. After subsequent washing, cells were incubated with secondary antibody (Alexa Fluor 488, Alexa Fluor 594, Alexa Fluor 647, Dylight649 1:1000) for 45 min at room temperature and washed again. For analysis of NHE6 colocalization with soluble transferrin, live primary neurons were incubated with AF-Tfn (100 μ g/ml) for 1 h at 37°C and then fixed. For the analysis of surface SEP-GluA1 (sGluA1), transfected coverslips were subjected to the previously described gly-ChemLTP solution for 10 min in their native plate in a bead bath warmed to 37°C and gassed with 95% O₂/5% CO₂. Afterwards, the stimulation solution was replaced with nACSF for a further 20 min before being incubated live with mouse GFP primary

antibody diluted in nASCF (1:1000) for 1 h at 4°C to prevent receptor internalization. Treated cultures were then fixed, washed, blocked, and stained with goat anti-mouse Dylight 649 secondary antibody under non-permeabilizing conditions (to stain the surface fraction of SEP-GluA1 only) before permeabilization and further immunoprocessing as previously described. This procedure was repeated with neurons pre-treated with CPP and subjected to gly-ChemLTP + CPP solution. All fixed coverslips were mounted onto SuperFrost (Menzel-Glaser) microscope slides using UltraMount fluorescence mounting medium (Dako) and left to dry overnight at room temperature in the dark.

Electrophysiology. 48 h following transfection, cultures were placed into the recording chamber of an upright microscope (BX51WI, Olympus, XLUMPlanF1 20x 0.95 NA water immersion objective) and placed in consistent perfusion of nACSF (as described previously) supplemented with (in μM): 1 TTX, 25 CPP, 50 picrotoxin, and 5 CGP 55845 to isolate AMPAR-mediated mEPSCs. Whole-cell voltage clamp recordings were then performed upon transfected neurons (found upon visual observation with fluorescence) held at -60 mV with an Axopatch 400 amplifier (Molecular Devices, Sunnyvale, CA, USA) at room temperature (23-25 °C). Borosilicate patch pipettes (4-7 M Ω) were filled with (in mM): 120 K-gluconate, 1 EGTA, 10 HEPES, 5 MgATP, 0.5 Na₂GTP, 5 NaCl, 5 KCl, and 10 phosphocreatine K₂ (pH 7.2-7.3 with KOH and 285-295 mOsm). To monitor access resistance, transient test pulses were applied consistently every 2 min throughout the duration of the recording. Access resistance typically fell within the range of 7-10 G Ω , and data was discarded if the access resistance deviated > 20% during the recording. After holding current was stabilized, data was acquired at a sampling frequency of 20 kHz and filtered at 2 kHz for 10 min. All AMPAR-mEPSCs were identified offline through use of Mini Analysis Software (Synaptosoft, Decature, GA, USA). Thresholding for mEPSC amplitude

detection was set at eight times the root-mean-square value of a visually-determined event-free recording span, and 300-450 events per cell were analyzed and utilized to determine mean values.

Pharmacological treatments. To assess the effects of leupeptin, bafilomycin, and MG132 treatment upon spine density and NHE6 levels in transfected primary hippocampal neurons, leupeptin (100 µg/ml), bafilomycin A1 (100 nM), or MG132 (40 µM) were added to the culture media 24h post-transfection, and cultures were left for an additional 24 h prior to fixation. In evaluating the effects of leupeptin upon the response to gly-ChemLTP, transfected neurons were pre-treated with either of these inhibitors in for ≥ 30 min prior to gly-ChemLTP stimulation and further processing.

Confocal microscopy. Fixed and mounted primary neuron cultures were examined using a Leica SP2 confocal microscope with images acquired using 40x and 63x HCXPL APO oil-immersion objectives (NAs 1.25 and 1.4, respectively). GFP was imaged using a 488 nm Ar laser line, mCherry and PI were imaged using a 543 nm HeNe laser line, and Alexa Fluor 633 and 647 and Dylight 649 were imaged using a 633 nm HeNe laser line. Channels were acquired sequentially to prevent spectral overlap of fluorophores. Optical sections of 300-500 nm were taken and frame averaged 3x at low resolution or line-averaged 2x at high resolution to improve the signal-to-noise ratio. Live imaging of spine dynamics was performed using the same Leica SP2 confocal microscope with a 63x water immersion long working distance lens (HXC APO L U-V-I; NA 0.9).

Measurements and quantifications. All image stacks were first deconvolved using Huygens Essential software by using a full maximum likelihood extrapolation algorithm (Scientific Volume Imaging, Hilversum, The Netherlands), and 3D images and 4D time-lapse stacks were compiled as maximum intensity projections using the Surpass function on Imaris software (Bitplane AG, Zurich, Switzerland). Spines were then quantified using a

detection/classification program that automatically detected the length of the spine head and neck. From the ratio of the diameter and length of the head and neck of spines, it was possible to visually distinguish between stubby, mushroom, and long thin spines, as well as filopodia, based off of previously distinguished criteria [32,33]. In brief, if the spine had no visible distinction between its head and neck subregions, it was classified as stubby. If the spine was short had a larger head ($> 1 \mu\text{m}$ in diameter) and neck subregions, it was identified as mushroom. If it had a small head ($< 1 \mu\text{m}$ in diameter) and was longer in length, it was counted as a long thin-type spine. Filopodia, precursors of either new dendrites or spines, were typically identified if they had 1) no distinguishable spine head and 2) a length of longer than $3 \mu\text{m}$ and were quantified separately. Colocalization analyses between transfected mCherry-tagged NHE6 WT and ΔES and EEA1, Stx-13, AF-Tfn, Rab7, LAMP1, and GluA1 were determined using the ImarisColoc algorithm, which generated a new channel (coloc) containing voxels representing channel overlap based off of a threshold of colocalization. Thresholds were applied consistently between images in order to remove subjectivity during the analysis. During these colocalization steps, the stacks were masked according to the dendritic EGFP signal to ensure that the puncta in question were indeed in the neuron itself. A puncta of individual or colocalized markers was counted as being localized to a dendritic spine if it was within $\leq 0.5 \mu\text{m}$ of the spine. The proportion of spines containing single or colocalized markers in each image was then quantified. Next, protein localization within the spine was localized to its base (a), neck (b), or head (c), as previously described [8]. The fraction of puncta in each spine subregion relative to the total number of puncta localized to spines was then determined.

For live imaging experiments, changes in the localization of mCherry-tagged NHE6 puncta were quantified in a similar fashion. Changes in spine head volume were also assessed as averages

of spine head volume before and after gly-ChemLTP, as previously described [34]. Briefly, the time-lapse confocal image stacks were four-dimensionally rendered using the Surpass function of Imaris. The spines of interest were then isolated at each time point, and the volume was automatically calculated. In this case, volume changes in all thin and mushroom spines in response to gly-ChemLTP were measured relative to their baseline values. However, stubby spines were excluded because the resolution limit of light microscopy prevents their proper volume analysis. The distribution and number of spine subtypes were also quantified before and after gly-ChemLTP, and the changes in their number were calculated relative to baseline values.

Statistical analyses. The data represent the mean \pm the standard error of the mean (S.E.M.) and statistical analyses were performed using the Student's t-test, Dunn's multiple comparison test, or a one-way analysis of variance (ANOVA) followed by a Bonferroni post-hoc test. A minimum *p*-value of < 0.05 was considered significant.

2.4 RESULTS

2.4.1 NHE6 Δ ES reduces excitatory synaptic density

To assess the impact of the Δ ES mutant on neuronal morphology and function *in vitro*, we used primary hippocampal neuron cultures prepared from early postnatal C57BL/6 mice as previously described [28]. At 10-12 days *in vitro* (DIV), the cultures were co-transfected with DNA plasmids encoding enhanced green fluorescent protein (EGFP) to demarcate neuronal morphology and either mCherry fluorescent protein (mCh) (as a transfection control), mCh-tagged WT NHE6 (NHE6_{WT}-mCh) or the Δ ES mutant (NHE6 _{Δ ES}-mCh). Although neurons express endogenous WT NHE6, we posit that the Δ ES mutant exerts a dominant-negative effect in this culture system based on the following observations. Firstly, we showed previously that the transfected Δ ES mutant can

physically interact with WT NHE6, as observed through co-immunoprecipitation experiments performed on HeLa cells. Secondly, we also demonstrated that fluorescently-tagged NHE6 WT and Δ ES constructs strongly colocalize with WT NHE6 when expressed in AP-1 cells, further suggesting that the Δ ES mutant is capable of forming heterodimers with WT NHE6. [22]. Thirdly, in the present study, we found that NHE6 $_{\Delta$ ES-mCh transfection attenuated the trafficking of total NHE6 (i.e., endogenous WT plus exogenous Δ ES, as measured by immunostaining with a rabbit polyclonal NHE6 antibody capable of recognizing both WT and Δ ES NHE6) into spines located on the distal dendrites of primary hippocampal neurons (**Fig. S1**). Overall, the data imply that exogenous Δ ES NHE6 heterodimerizes with endogenous WT NHE6 and impairs its trafficking into dendrites, presumably diminishing overall NHE6 function at excitatory postsynaptic sites in transfected cells as a result.

In the current study, we extend our analysis of the Δ ES mutant by examining whether changes in dendritic arbor are accompanied by changes in excitatory synaptic structure. As shown in **Fig. 1A-B**, secondary and tertiary dendrites of primary hippocampal neurons transfected with NHE6 $_{\Delta$ ES-mCh showed a significant decrease in overall spine density, with significant reductions in both mushroom- and thin-type dendritic spines when compared to the mCh control or NHE6 $_{WT}$ -mCh. Concurrent with this decrease in spines, we also observed a reciprocal increase in the density of filopodia, immature structures that may develop into either new spines or dendritic branches [35], in NHE6 $_{\Delta$ ES-mCh transfected cells (**Fig. 1A, C**). Overall, these data indicate that introducing NHE6 $_{\Delta$ ES-mCh into primary hippocampal neurons has a deleterious effect on the maintenance of spine density and morphology.

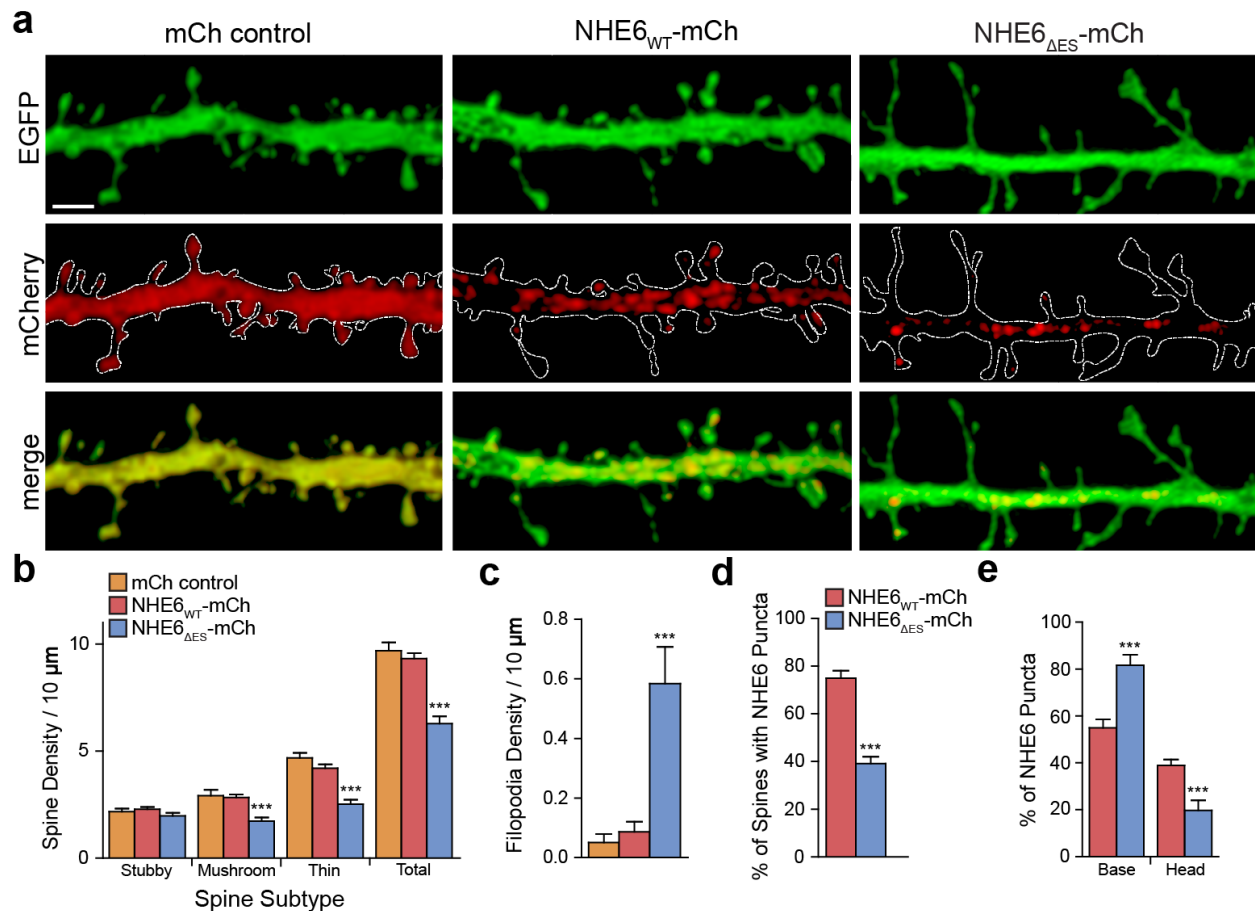


Figure 1: NHE6 Δ ES overexpression reduces the density of mature dendritic spines in hippocampal pyramidal neurons. **A:** Representative confocal images of primary hippocampal neurons transfected with EGFP and mCh alone (as a transfection control), NHE6_{WT}-mCh, or NHE6 _{Δ ES}-mCh. EGFP and mCh channels are shown individually and merged; white outlines denote location of EGFP-positive dendrite. Scale bar: 2 μ m. **B-C:** Mean \pm S.E.M. density of all and each major spine subtype, *i.e.* stubby, mushroom, and thin (**B**), as well as filopodia (**C**). **D:** Mean \pm S.E.M. fraction of spines containing puncta of transfected, overexpressed NHE6 WT or Δ ES puncta of all spines analyzed for each transfection condition. **E:** Mean \pm S.E.M. proportion of spine-localized puncta of overexpressed NHE6 WT and Δ ES in the base and head subregions of spines. mCh control: n = 543 spines and 3 filopodia along 560.636 μ m of dendrite from 20 cells; NHE6 WT: n = 549 spines and 4 filopodia along 591.383 μ m of dendrite from 20 cells; NHE6 Δ ES: n = 360 spines and 34 filopodia along 577.992 μ m of dendrite from 20 cells, 6 separate experiments. For NHE6 puncta counts, NHE6 WT: n = 1940 spines along 2615.825 μ m of dendrite from 90 cells; NHE6 Δ ES: n = 1292 spines and 2600.605 μ m of dendrite from 90 cells, 29 separate experiments. **: $p < 0.01$; ***: $p < 0.0001$; Dunnett's Multiple Comparison Test (**B-C**); independent Student's t-test, two-tailed (**D-E**).

2.4.2 Differential intracellular localization of NHE6 WT and Δ ES

Next, we investigated if there was a difference in the neuronal subcellular localization of NHE6 Δ ES-mCh compared to NHE6_{WT}-mCh. We found that in dendrites, NHE6_{WT}-mCh localized to approximately 75% of dendritic spines, with the majority present in the base and head subregions. In contrast, NHE6 Δ ES-mCh was present in only 40% of spines and localized mainly to the spine base, with significantly less present in the spine head (**Fig. 1A, D-E**). This suggests that the trafficking of NHE6 Δ ES-mCh to excitatory synaptic sites may be compromised.

In most cell types, internalized plasma membrane cargo is initially sorted to early endosomes, where it may be trafficked either back to the cell surface via recycling endosomes for reuse or redirected to lysosomes for degradation (*illustrated in Fig. 2D*) [36,37]. In a previous study in neurons [8], we reported that endogenous NHE6 colocalizes with early endosomal antigen-1 (EEA1), an early endosome marker [38], as well as syntaxin-12/13 (stx-13) and AlexaFluor 633-Transferrin (AF-Tfn), both markers for recycling endosomes [39,40]. We assessed whether the localization of the Δ ES mutant with these endosomal markers is altered in spines and further calculated the degree of colocalization using thresholded Mander's coefficients. We found that NHE6 Δ ES-mCh showed a significant reduction in colocalization with EEA1, stx-13, and AF-Tfn in comparison to NHE6_{WT}-mCh (**Fig. 2**). Interestingly, levels of AF-Tfn, which is internalized in a clathrin/adaptor protein 2 (AP2)-dependent process, were downregulated in the dendrites of Δ ES-positive cells (**Fig. 2C, E**), corroborating our previous observations in HeLa cells and neuronal soma [22]. Together, these results suggest the Δ ES mutant is mislocalized and alters trafficking of at least some endocytosed cargo.

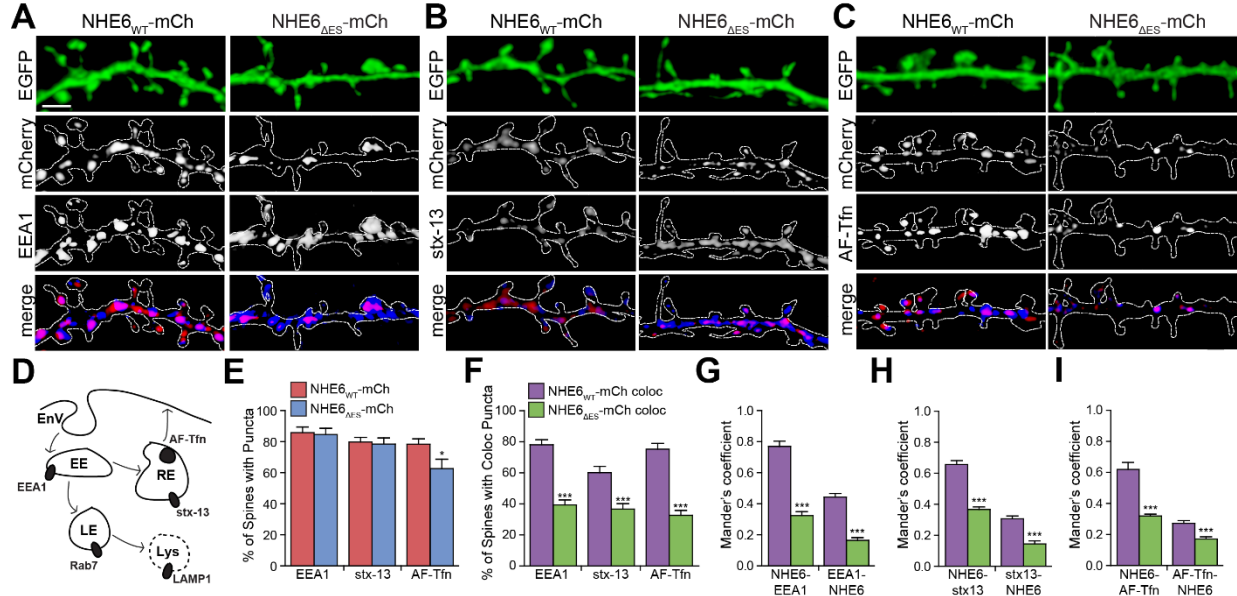


Figure 2: NHE6 Δ ES shows reduced colocalization with markers for early and recycling endosomes in comparison to NHE6 WT. **A-D:** Representative confocal images showing a section of secondary or tertiary dendrite of a primary hippocampal neuron co-transfected with EGFP and NHE6_{WT}-mCh or NHE6 _{Δ ES}-mCh and immunolabelled with an early endosomal marker, early endosomal antigen 1 (EEA1, **A**) or recycling endosomal markers syntaxin 12/13 (stx-13, **B**) and AlexaFluor633-Transferrin (AF-Tfn, **C**). Channels are shown separately and merged; white outlines denote location of EGFP-positive dendrite. Scale bar: 2 μ m. **D:** Representative schematic of different endolysosomal compartments within the cell, with the utilized markers for each major compartment. EnV: endocytic vesicle; EE: early endosome; RE: recycling endosome; LE: late endosome, Lys: lysosome. **E:** Mean \pm S.E.M. fraction of spines containing puncta of EEA1, stx-13, and AF-Tfn of all spines analyzed for each transfection condition. **F:** Quantification of the mean \pm S.E.M. fraction of spines containing colocalized puncta of overexpressed NHE6 WT or Δ ES and each vesicular marker of all spines analyzed. **G-I:** Mean \pm S.E.M. thresholded Mander's coefficient values between NHE6 WT or Δ ES and EEA1 (**G**), stx-13 (**H**), and AF-Tfn (**I**). For EEA1, NHE6 WT: $n = 242$ spines along 293.30 μ m of dendrite from 10 cells; NHE6 Δ ES: $n = 135$ spines along 296.81 μ m of dendrite from 10 cells, 3 separate experiments. For stx-13, NHE6 WT: $n = 229$ spines along 293.94 μ m of dendrite from 10 cells; NHE6 Δ ES: $n = 132$ spines from 283.06 μ m of dendrite from 10 cells, 3 separate experiments. For AF-Trf, NHE6 WT: $n = 148$ spines along 295.97 μ m of dendrite from 10 cells; NHE6 Δ ES: $n = 116$ spines from 309.07 μ m of dendrite from 10 cells, 4 separate experiments. *: $p < 0.05$; **: $p < 0.01$; ***: $p < 0.0001$; independent Student's t-test, two-tailed.

We have previously demonstrated in live non-neuronal AP-1 cells that NHE6 Δ ES-containing endosomes are more acidic than those containing NHE6 WT [22]. Hence, we further

probed the subcellular localization of the Δ ES mutant using markers of acidic organellar compartments of the degradative pathway [41]. To this end, we performed immunostaining for Rab7, a marker for late endosomes/multivesicular bodies [42], as well as lysosomal-associated membrane protein 1 (LAMP1), a lysosomal marker [43]. As shown visually (**Fig. 3A, B**) and quantitatively (**Fig. 3D-F**), colocalization with Rab7 and LAMP1 was greater in NHE6 $_{\Delta$ ES-mCh compared to WT. In addition, we found a significant increase in LAMP1 puncta at spines in NHE6 $_{\Delta$ ES-mCh-transfected cells (**Fig. 3B-C**), indicating an increase of lysosomal bodies in these neurons. Overall, the data suggest that Δ ES mutant vesicles are directed away from early and recycling endosomes toward late endosomes and lysosomes.

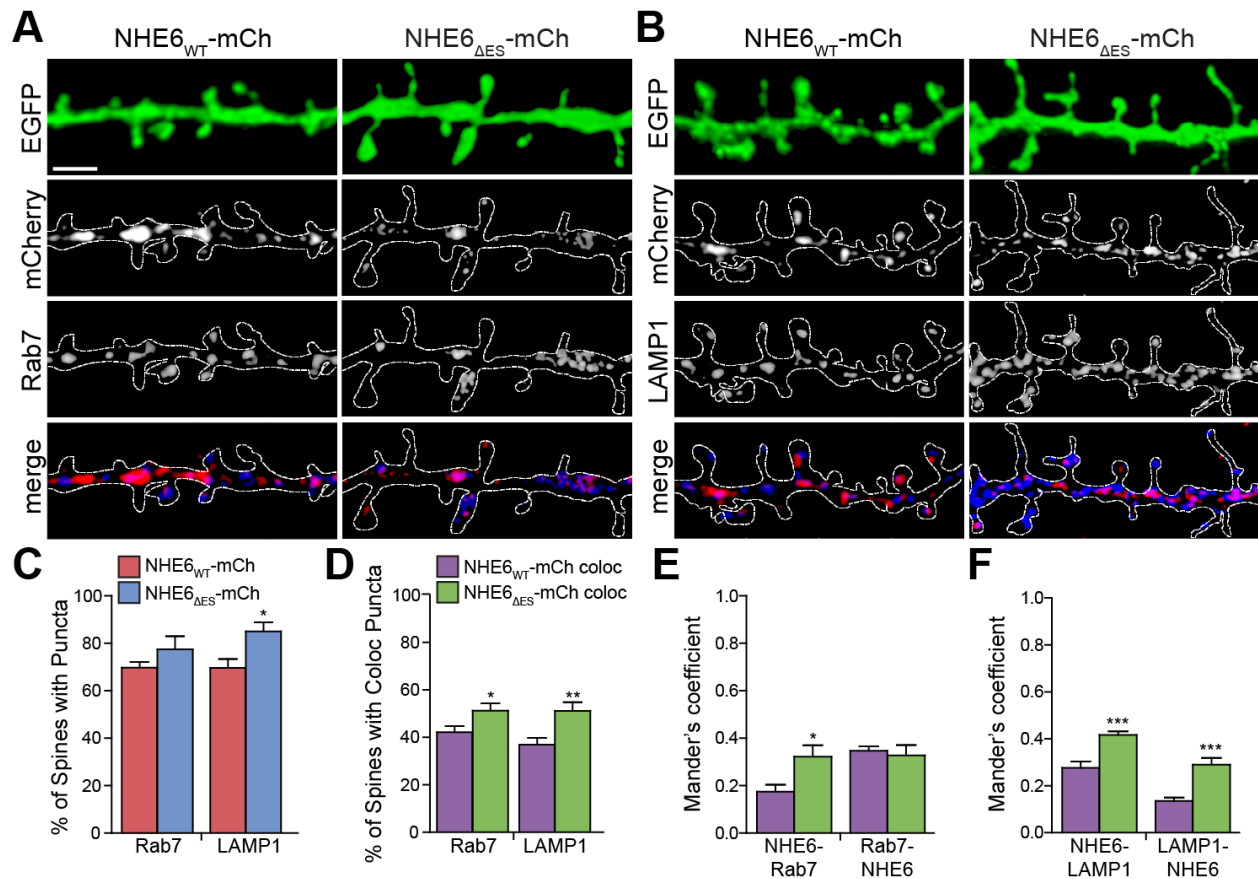


Figure 3: In contrast to NHE6 WT, NHE6 Δ ES shows increased colocalization with markers for late endosomes and lysosomes, more acidic compartments. A-B: Representative confocal images showing a section of secondary or tertiary dendrite of a primary hippocampal neuron co-

transfected with EGFP and NHE6_{WT}-mCh or NHE6_{ΔES}-mCh and immunolabelled with the late endosomal marker Ras-related protein Rab7 (**A**) or the lysosomal marker lysosomal associated membrane protein 1 LAMP1 (**B**). Channels are shown separately and merged; white outlines denote location of EGFP-positive dendrites. Scale bar: 2 μm. **C**: Quantification of the mean ± S.E.M. fraction of spines containing puncta of Rab7 or LAMP1 of all spines analyzed under each transfection condition. **D**: Quantification of the mean ± S.E.M. fraction of spines containing colocalized puncta of overexpressed NHE6 WT or ΔES and Rab7 or LAMP1 of all spines analyzed. **E-F**: Quantified mean ± S.E.M. thresholded Mander's coefficient values between NHE6 WT or ΔES and Rab7 (**E**) or LAMP1 (**F**). For Rab7, NHE6 WT: n = 210 spines along 232.69 μm of dendrite from 8 cells; NHE6 ΔES: n = 176 spines from 235.88 μm of dendrite from 8 cells, 3 separate experiments. For LAMP1, NHE6 WT: n = 212 spines along 289.24 μm of dendrite from 10 cells; NHE6 ΔES: n = 132 spines from 269.44 μm of dendrite from 10 cells, 4 separate experiments. *: $p < 0.05$; **: $p < 0.01$, ***: $p < 0.0001$, independent Student's t-test, two-tailed for all other comparisons.

2.4.3 NHE6 ΔES disrupts AMPA receptor trafficking

Next, we looked for signs of dysregulation of synaptic cargo in NHE6_{ΔES}-mCh cells by assessing the localization of glutamatergic AMPARs, which mediate most fast excitatory neurotransmission in the central nervous system [44]. We have already shown that endogenous WT NHE6 colocalizes strongly with the GluA1 subunit of AMPARs [8], and we have recapitulated that finding in transfected NHE6_{WT}-mCh neurons (**Fig. 4A-C**). However, this overlap was significantly attenuated in neurons expressing NHE6_{ΔES}-mCh and was accompanied by a significant decrease in GluA1 puncta at spines (**Fig. 4A-C**), indicating that the ΔES mutant also deters the trafficking of GluA1 to excitatory synapses. To investigate if this decrease in GluA1 levels was due to enhanced trafficking of these receptors to lysosomes in the presence of the ΔES mutant, we co-transfected neurons with EGFP and influenza virus hemagglutinin (HA)-tagged constructs of NHE6 WT or ΔES to allow for double immunolabeling of the lysosomal marker LAMP1 and GluA1. Interestingly, in NHE6_{ΔES}-HA-expressing cells, there was greater colocalization between LAMP1 and GluA1 compared to neurons expressing NHE6_{WT}-HA (**Fig. 4D-F**). This finding

implies that in the presence of the Δ ES mutant, GluA1 is preferentially targeted to lysosomal compartments rather than recycling endosomes, which may result in their enhanced degradation.

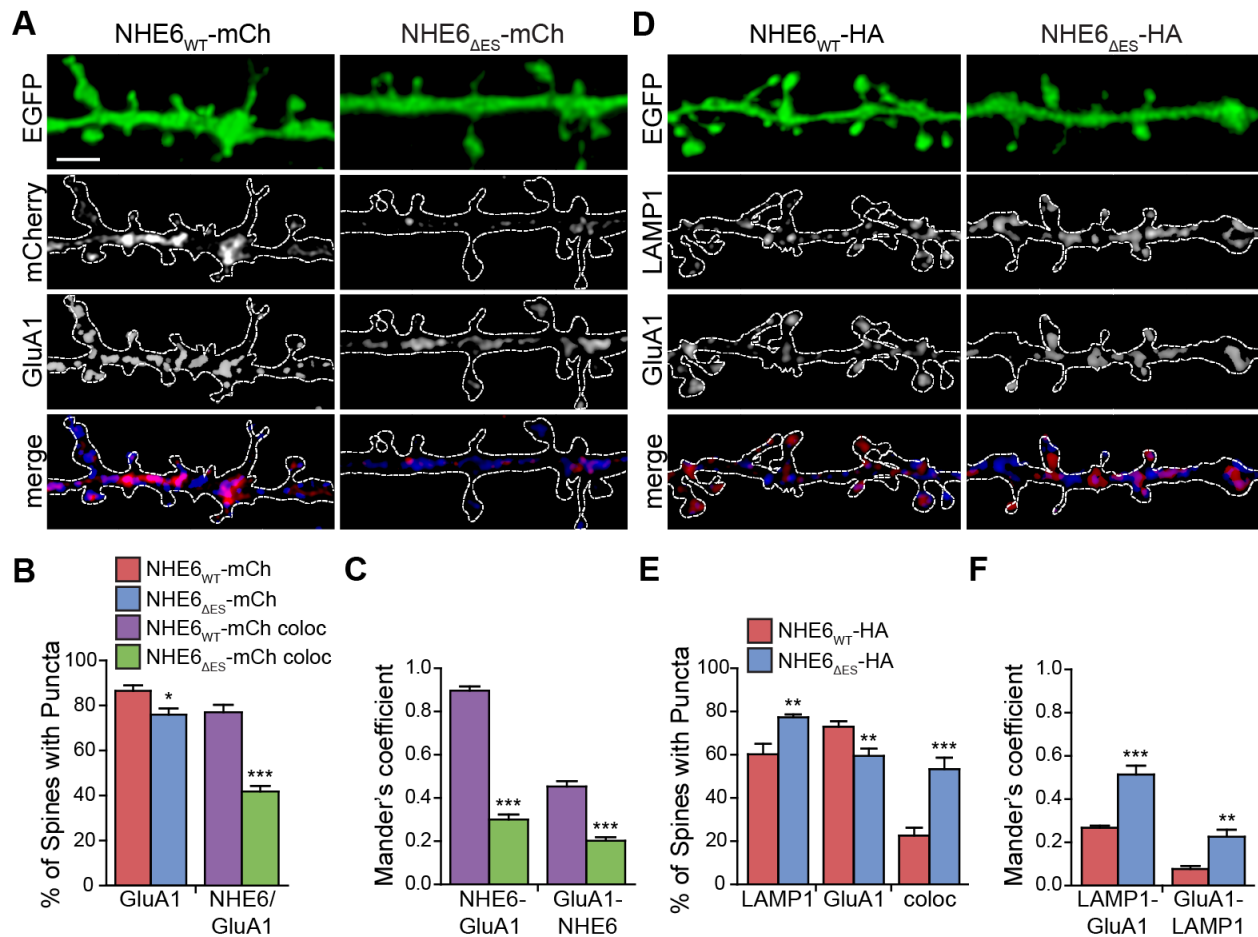


Figure 4: NHE6 Δ ES transfection attenuates the trafficking of GluA1-containing AMPA receptors to spines and enhances their localization to lysosomes. **A:** Representative confocal images showing a section of the secondary or tertiary dendrite of a primary hippocampal neuron co-transfected with EGFP and NHE6_{WT}-mCh or NHE6 _{Δ ES}-mCh and immunolabeled for the AMPA receptor subunit GluA1. Channels are shown separately and merged; white outlines denote location of EGFP-positive dendrite. Scale bar: 2 μ m. **B:** Mean \pm S.E.M. fraction of spines containing puncta of GluA1 (left) or colocalized puncta of NHE6 and GluA1 (right) of all spines analyzed under each transfection condition. **C:** Mean \pm S.E.M. thresholded Mander's coefficient values between NHE6 WT or Δ ES and GluA1. **D:** Representative confocal images showing a section of the secondary or tertiary dendrite of a primary hippocampal neuron co-transfected with EGFP and NHE6_{WT}-HA or NHE6 _{Δ ES}-HA and double immunolabeled for GluA1 and LAMP1. **E:** Quantification of the mean \pm S.E.M. fraction of spines containing puncta of LAMP1 (left), GluA1 (center), and colocalized puncta of LAMP1 and GluA1 (right) of all spines analyzed under each transfection condition. **F:** Quantified mean \pm S.E.M. thresholded Mander's coefficient values between LAMP1 and GluA1 under each transfection condition. For GluA1, NHE6 WT: n = 190

spines along 288.93 μm of dendrite from 10 cells; NHE6 ΔES : $n = 129$ spines along 281.50 μm of dendrite from 10 cells, 4 separate experiments. For GluA1 and LAMP1 colocalization analyses NHE6 WT: $n = 182$ spines along 152.725 μm of dendrite from 6 cells; NHE6 ΔES : $n = 116$ spines along 151.752 μm of dendrite from 6 cells, 3 separate experiments. *: $p < 0.05$, **: $p < 0.01$, ***: $p < 0.0001$; independent Student's t-test, two-tailed.

2.4.4 NHE6 ΔES impairs the response to glycine-mediated chemical LTP

Enhanced delivery of AMPARs to the post-synaptic compartment is an important contributing factor for generating long-term potentiation (LTP), a cellular model of learning and memory [45–48]. Given that NHE6 is implicated in the trafficking of AMPARs, we assessed whether the ΔES mutation also impairs the response to LTP in hippocampal neurons. Initially, to investigate the insertion of GluA1-containing AMPARs into synaptic sites following LTP [49], we co-transfected neurons with tdTomato (tdT) and N-terminal fused pH-sensitive superecliptic pHluorin (SEP)-GluA1 (sGluA1) alone, or with HA-tagged NHE6 WT or ΔES . We then subjected live transfected cells to a glycine-mediated chemical LTP (gly-ChemLTP) protocol to emulate NMDA receptor (NMDAR)-dependent LTP induction at Schaffer collateral-CA1 synapses in the hippocampus [8,31]. If LTP is functioning properly, we would expect to see an increase in sGluA1 fluorescence in spine heads. Twenty min following gly-ChemLTP induction in tdT control- and NHE6_{WT}-HA-transfected neurons, we observed a significant increase in the number of spines containing sGluA1 and an upregulation of their puncta in the heads of these spines compared to unstimulated sister control cultures. In contrast, gly-ChemLTP stimulation in NHE6 _{ΔES} -HA-expressing neurons did not show an increase in sGluA1 localization at spines or within the spine head compared to unstimulated controls (**Fig. 5A-C**). To verify the NMDAR dependency of this protocol, additional sister NHE6_{WT}-HA-expressing cultures were subjected to gly-ChemLTP supplemented with (*RS*)-3-(2-carboxypiperazin-4-yl)-propyl-1-phosphonic acid ((*RS*)-CPP), a potent NMDAR antagonist

[50]. As expected, these cells did not show an upregulation of sGluA1 puncta at spines or in spine heads (**Fig. S2A-C**). Hence, in addition to preventing GluA1 trafficking to spines, NHE6 Δ ES-HA impairs the insertion of AMPARs at the cell surface following NMDAR-dependent LTP.

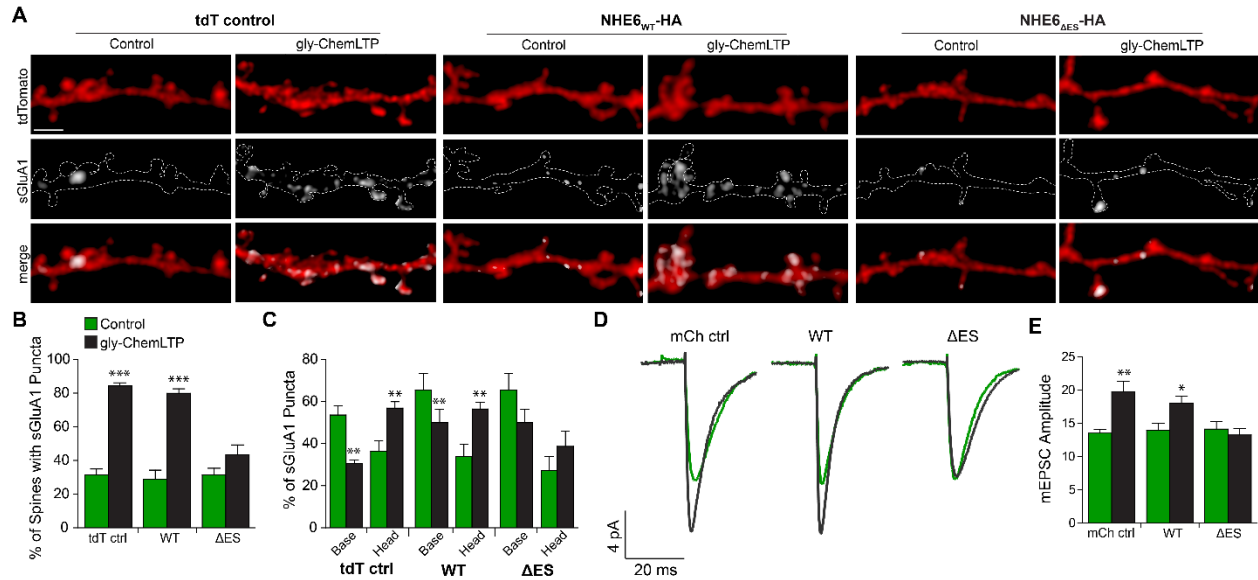


Figure 5: NHE6 Δ ES-expressing cells fail to show insertion of GluA1-positive AMPA receptors at spines and potentiation of miniature excitatory postsynaptic current (mEPSC) amplitude following glycine-mediated chemical LTP. **A:** Representative confocal micrographs of secondary or tertiary dendrites from transfected primary hippocampal neurons for sister unstimulated control and gly-ChemLTP-stimulated cultures for each transfection condition. Channels are shown separately and merged; white outlines denote location of tdTomato-positive dendrite. Scale bar: 2 μ m. **B:** Mean \pm S.E.M. percentage of spines containing surface SEP-GluA1 (sGluA1) puncta for control and glyChemLTP conditions for each transfection condition. **C:** Mean \pm S.E.M. proportion of sGluA1 puncta in each spine subregion for control, gly-ChemLTP-stimulated, and CPP-treated, gly-ChemLTP-stimulated cultures. For tdT control, control: n = 125 spines along 188.156 μ m of dendrite from 8 cells; gly-ChemLTP: n = 150 spines along 197.145 μ m of dendrite from 8 cells; for NHE6 WT, control: n = 100 spines along 156.529 μ m of dendrite from 8 cells, gly-ChemLTP: n = 116 spines along 191.817 μ m of dendrite from 8 cells; for NHE6 Δ ES, control: 102 spines along 184.925 μ m of dendrite from 8 cells, gly-ChemLTP: 113 spines along 193.374 μ m of dendrite from 8 cells. **D:** Average AMPAR-mEPSC event trace of an unstimulated control and gly-ChemLTP-stimulated cell for each transfection condition. **E:** Mean \pm S.E.M. mEPSC amplitude of all cells analyzed under each stimulation and transfection condition. For all conditions, n = 14 cells, 5 separate experiments. *: $p < 0.05$, **: $p < 0.01$, ***: $p < 0.0001$; independent Student's t-test, two-tailed.

Does this impairment in AMPAR trafficking lead to functional changes in synaptic strengthening? To address this, we acquired whole-cell voltage clamp recordings of AMPAR-mediated miniature excitatory postsynaptic currents (mEPSCs) from transfected hippocampal cells 20 min after gly-ChemLTP induction. Normally, cells subjected to LTP stimulation show an increase in mEPSC amplitude compared to unstimulated sister cultures due to the addition of AMPARs at the cell surface [15]. Accordingly, we found that gly-ChemLTP-stimulated mCh- and NHE6_{WT}-mCh-expressing cells showed an increase in overall mEPSC amplitude compared to untreated sister cultures. In contrast, stimulated NHE6_{ΔES}-mCh-expressing cells failed to show a significant increase in mEPSC amplitude (**Fig. 5D-E**). Again, this increase in mEPSC amplitude in NHE6_{WT}-mCh-expressing cells was NMDAR-dependent, as we observed no change in mEPSC amplitude in additional NHE6_{WT}-mCh-transfected cultures subjected to gly-ChemLTP in the presence of (*RS*)-CPP (**Fig. S2D-E**). Given the large variation in inter-event intervals between dissociated culture preparations, we did not assess mEPSC frequency using this method. Significant differences were not observed in other mEPSC parameters (*e.g.* rise and decay times) across conditions. Overall, these findings demonstrate that the Δ ES mutant impairs excitatory synaptic potentiation in response to gly-ChemLTP.

Functional potentiation is normally accompanied by structural changes at the synapse, including an increase in spine head volume (SHV) as well as the potential formation of new spines [31,33,51,52]. We previously reported that endogenous NHE6 is recruited to the heads of dendritic spines following gly-ChemLTP stimulation [8]. Now, we investigated whether the recruitment of exogenous NHE6 also occurs in response to gly-ChemLTP in transfected neurons. We performed time-lapse confocal imaging on a section of dendrite for 15 min to establish a structural baseline, stimulated for 10 min, and then continued to image for an additional 20 min (**Fig. 6B**). Following

gly-ChemLTP stimulation, NHE6_{WT}-mCh-expressing neurons exhibited a significantly greater increase in the percentage of NHE6-containing spines, with NHE6 puncta being redistributed from the base to the heads of these spines. In contrast, NHE6_{ΔES}-mCh puncta did not traffic to spines. Moreover, mushroom- and thin-type spines on NHE6_{ΔES}-mCh-transfected neurons failed to show significant enlargements of SHV compared to controls in response to gly-ChemLTP (**Fig. 6A, C-H**). As such, mCh- and NHE6_{WT}-mCh-expressing neurons showed a much more significant change from baseline in SHV across spine subtypes when compared to NHE6_{ΔES}-mCh-transfected neurons (**Fig. 6I**). These changes in NHE6 recruitment and SHV in NHE6_{WT}-mCh-transfected neurons were also blocked by (*RS*)-CPP included in the gly-ChemLTP stimulation solution, again demonstrating NMDAR dependency (**Fig. S2F-I**). Together, the data demonstrate that the ΔES mutant disrupts both the functional and morphological response to gly-ChemLTP induction by impairing recycling endosomal trafficking within the dendrites of hippocampal neurons.

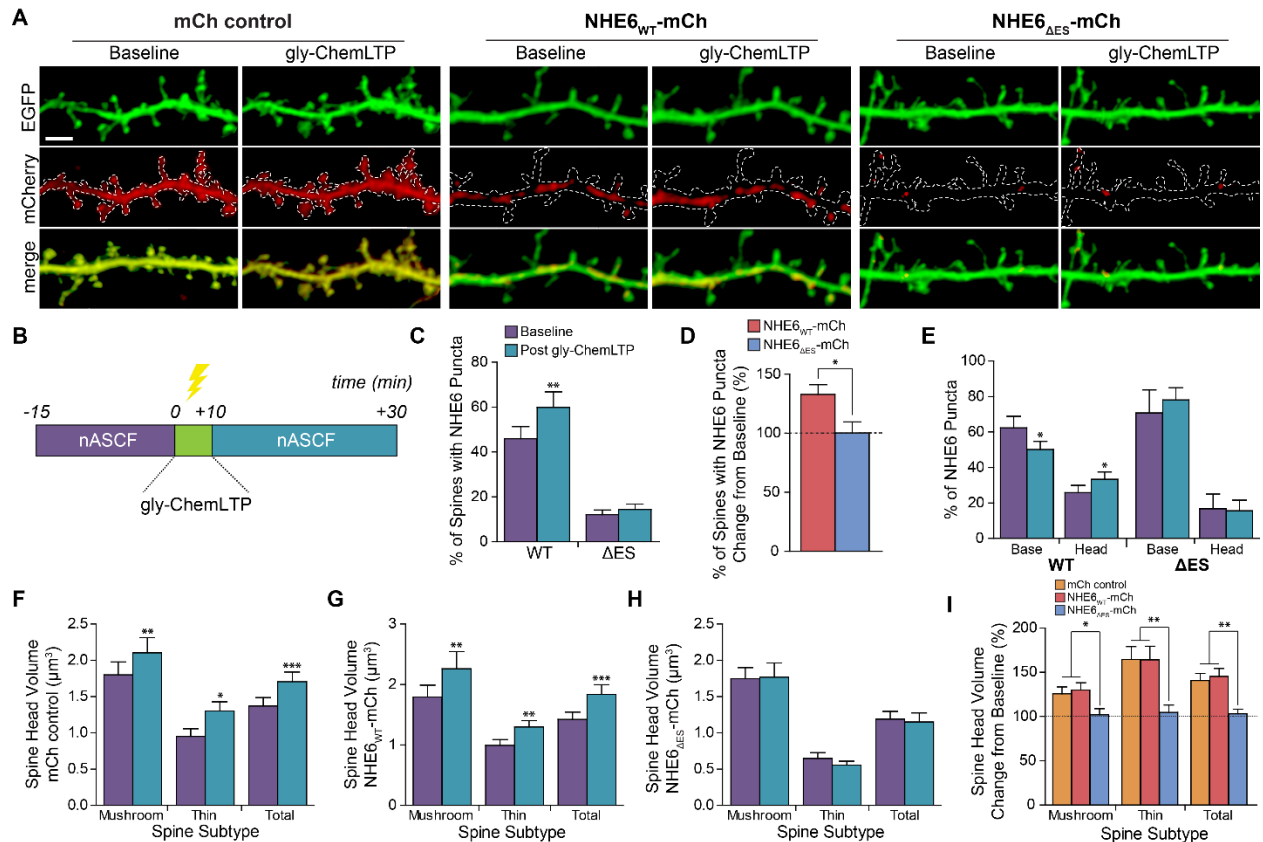


Figure 6: NHE6 Δ ES inhibits the structural response to gly-ChemLTP. **A:** Representative confocal micrographs of secondary or tertiary dendrites from transfected neurons at baseline and post gly-ChemLTP for each transfection condition. Channels are shown separately and merged; white outlines denote location of EGFP-positive dendrite. Scale bar: 3 μ m. **B:** Schematic showing the time course of the gly-ChemLTP protocol. **C:** Mean \pm S.E.M. percentage of spines containing NHE6 WT or Δ ES puncta at baseline and 20 min post gly-ChemLTP. **D:** Following gly-ChemLTP, the mean \pm S.E.M. percent change of NHE6 WT or Δ ES-positive spines. **E:** Mean \pm S.E.M. proportion of NHE6 WT or Δ ES puncta in each spine subregion at baseline and following gly-ChemLTP. **F-H:** Mean \pm S.E.M. spine head volume measurements for mushroom, thin, and total spines in mCh control- (**F**), NHE6 WT- (**G**), and NHE6 Δ ES- (**H**)-transfected neurons at baseline and 20 min following gly-ChemLTP. **I:** Mean \pm S.E.M. percent change in spine head volume from baseline (100%) following gly-ChemLTP for each spine subtype under each transfection condition. mCh control: $n = 173$ spines along 206.597 μ m of dendrite from 8 cells; NHE6 WT: $n = 155$ spines along 210.906 μ m of dendrite from 4 cells, NHE6 Δ ES: 142 spines along 210.201 μ m of dendrite from 8 cells; 3 separate experiments. *: $p < 0.05$, **: $p < 0.01$, ***: $p < 0.0001$; paired Student's t -test, two-tailed (**C-H**), one-way ANOVA with Berforroni post-hoc test (**I**).

2.4.5 Restoring spine density and remodeling in NHE6 Δ ES-expressing neurons

Next, we explored whether it was possible to restore these deficits in neuronal morphology, receptor trafficking, and plasticity in Δ ES-expressing neurons. As noted previously, the Δ ES mutant induces excess acidification [22] and an increase in spine-localized endolysosomal vesicles (**Fig. 3**). Considering these results, we sought to prevent potential endolysosomal degradation by treating cultures (24 h post-transfection) overnight with leupeptin (100 μ g/ml), a reversible, competitive antagonist of endolysosomal proteases, or bafilomycin A1 (100 nM), a vacuolar H⁺-ATPase inhibitor. Compared to untreated NHE6 Δ ES-mCh-expressing neurons, we found that leupeptin treatment restored the densities of all three spine types (stubby, thin and mushroom) to levels comparable with the spine densities of untreated mCh- or NHE6_{WT}-mCh-transfected neurons (**Fig. 7A-E**). By comparison, bafilomycin appeared to partially restore only the density of thin spines compared to untreated NHE6 Δ ES-mCh-expressing neurons cultures. On the other hand, mCh- and NHE6_{WT}-mCh-expressing neurons were not profoundly affected by treatment with leupeptin. Moreover, bafilomycin administration significantly reduced the density of each spine subtype as well as total spine density (**Fig. 7A-E**). When we quantified NHE6 levels following these treatments, we found overall levels of NHE6_{WT}-mCh were not significantly changed relative to control (**Fig. 7A, F**). However, leupeptin and bafilomycin significantly increased the fraction of spines containing NHE6 Δ ES-mCh puncta compared to untreated controls (**Fig. 7A, F**). As we previously reported that the Δ ES mutant is also subjected to partial degradation by the proteasome [22], we investigated whether inhibition of the proteasome could restore spine density. However, application of the general proteasomal inhibitor MG132 (40 μ M) did not increase spine density in NHE6 Δ ES-mCh-expressing neurons, nor did it significantly increase NHE6 Δ ES-mCh trafficking to

spines (**Fig. 7**). Collectively, these data show that specifically preventing lysosomal degradation mitigates some of the morphological deficits induced by expression of the Δ ES mutant.

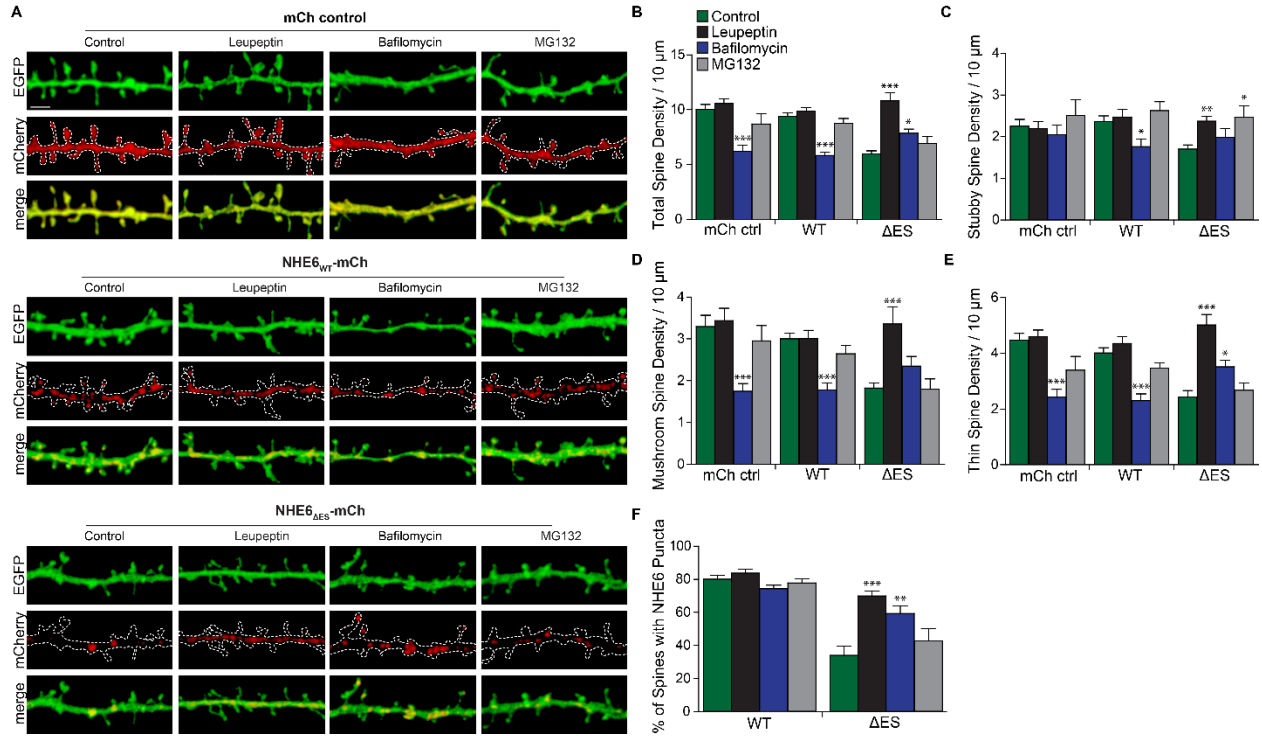


Figure 7: Inhibitors of lysosomal function, but not proteasomal function, are beneficial for spine density in NHE6 Δ ES-transfected neurons. **A:** Representative confocal micrographs of secondary or tertiary dendrites from transfected primary hippocampal neuron co-transfected with EGFP and mCh alone, NHE6_{WT}-mCh or NHE6 _{Δ ES}-mCh and untreated (control) or treated overnight with leupeptin, bafilomycin, or MG132. Channels are shown separately and merged; white outlines denote location of EGFP-positive dendrite. Scale bar: 2 μ m. **B-E:** Quantification of mean \pm S.E.M. density of stubby (**B**), mushroom (**C**), thin (**D**), and total (**E**) spines following each treatment for each transfection condition. **F:** Quantification of mean \pm S.E.M. fraction of spines containing puncta of transfected, overexpressed NHE6 WT or Δ ES puncta of all spines analyzed for NHE6 WT-mCh and NHE6 Δ ES-mCh cells for each treatment condition. For mCh control, control: n = 461 spines along 450.302 μ m of dendrite from 16 cells, leupeptin: n = 431 spines along 411.083 μ m of dendrite from 14 cells; bafilomycin: n = 199 spines along 316.209 μ m of dendrite from 12 cells; MG132: n = 193 spines along 223.232 μ m of dendrite from 8 cells. For NHE6 WT, control: n = 440 spines along 469.836 μ m of dendrite from 16 cells; leupeptin: n = 377 spines along 385.183 μ m of dendrite from 12 cells; bafilomycin: n = 178 spines along 308.887 μ m of dendrite from 12 cells; MG132: n = 207 spines along 238.938 μ m of dendrite from 8 cells. For NHE6 Δ ES, control: n = 275 spines along 459.203 μ m of dendrite from 16 cells; leupeptin: n = 460 spines along 434.558 μ m of dendrite from 14 cells; bafilomycin: n = 236 spines along 298.703 μ m of dendrite from 12 cells; MG132: n = 159 spines along 234.028 μ m of dendrite from 8 cells, 10 separate experiments. *: $p < 0.05$, **: $p < 0.01$, ***: $p < 0.0001$; Dunnett's Multiple Comparison Test.

Based on the above findings, we next examined whether the defective functional and structural response to LTP in NHE6 $_{\Delta ES}$ -mCh-transfected cells could be restored by acutely pre-treating transfected cultures with leupeptin (100 μ g/ml) for 30 min prior to the gly-ChemLTP protocol. It has previously been shown that 30 min of leupeptin treatment can enhance activated levels of the neurotrophic TrkB receptor in NHE6 KO neurons [21], indicating that this time frame is sufficient to prohibit aberrant endolysosomal degradation and restore receptor trafficking. Twenty min post-stimulation, we again probed for the subcellular distribution of sGluA1 and found significant insertion of GluA1 into the cell surface in ΔES -expressing cells, similar to controls (**Fig. 8A-C**). Whole-cell voltage clamp recordings revealed that pre-treatment with leupeptin did not significantly alter mEPSC amplitude in mCh- and NHE6 $_{WT}$ -mCh-transfected cells or their ability to potentiate beyond the stimulatory effects observed in the absence of leupeptin (see **Fig. 5E**). In contrast, leupeptin-treated NHE6 $_{\Delta ES}$ -mCh-transfected neurons restored the increases in mEPSC amplitude following gly-ChemLTP stimulation comparable to levels in mCh- and NHE6 $_{WT}$ -mCh-transfected cells (compare **Fig. 8D-E** and **Fig. 5E**).

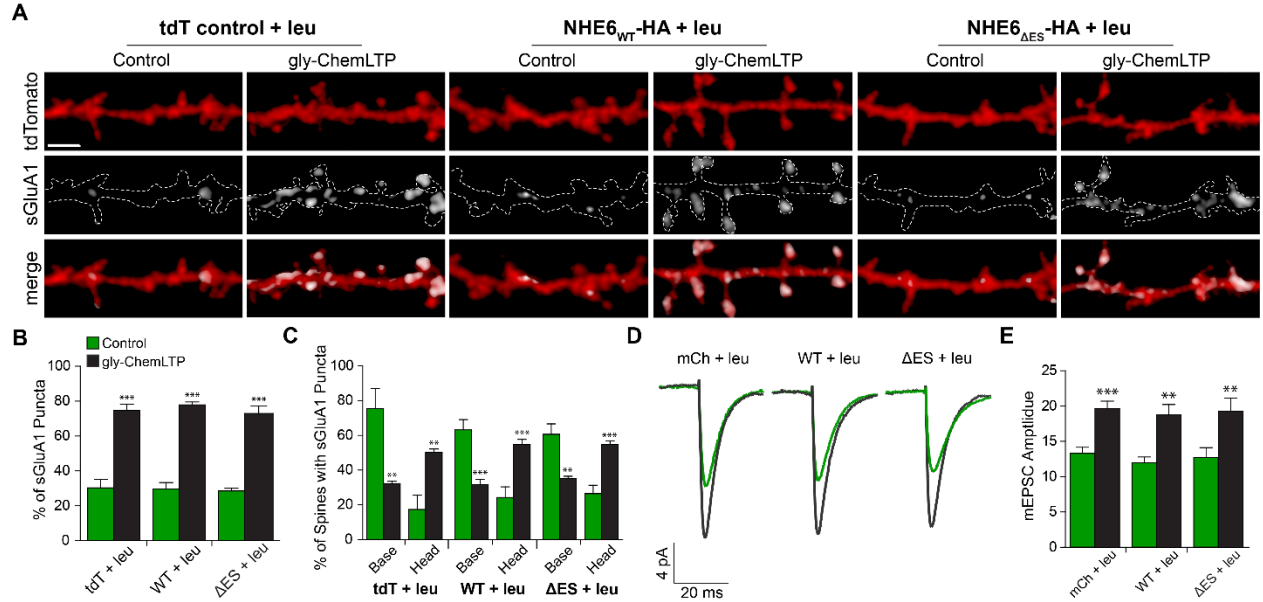


Figure 8: Leupeptin, a lysosomal protease inhibitor, restores the functional response to gly-ChemLTP in NHE6 Δ ES-transfected neurons. **A:** Representative confocal micrographs of secondary or tertiary dendrites from leupeptin-treated primary hippocampal neurons that were either unstimulated (control) or stimulated (gly-ChemLTP) for each transfection condition and stained for surface SEP-GluA1 (sGluA1) under non-permeabilizing conditions. Channels are shown separately and merged; white outlines denote location of tdTomato-positive dendrite. Scale bar: 2 μ m. **B:** Mean \pm S.E.M. percentage of spines containing sGluA1 puncta for control and gly-ChemLTP conditions for each transfection condition. **C:** Mean \pm S.E.M. proportion of sGluA1 puncta in each spine subregion for control and gly-ChemLTP-stimulated, leupeptin-treated cultures. For mCh + leu, control: n = 155 spines along 189.456 μ m of dendrite from 7 cells; gly-ChemLTP: n = 131 spines along 178.699 μ m of dendrite from 7 cells; for NHE6 WT + leu, control: n = 120 spines along 166.109 μ m of dendrite from 7 cells, gly-ChemLTP: n = 150 spines along 179.799 μ m of dendrite from 7 cells; for NHE6 Δ ES + leu, control: 104 spines along 174.24 μ m of dendrite from 7 cells; gly-ChemLTP: n = 101 spines along 164.519 μ m of dendrite from 7 cells, 3 separate experiments. **D:** Average AMPAR-mEPSC event trace of an unstimulated control and gly-ChemLTP-stimulated cell for each transfection condition with leupeptin pre-treatment. **E:** Mean \pm S.E.M. mEPSC amplitude of all cells analyzed under each stimulation and transfection condition with leupeptin pre-treatment. n = 13 cells for each transfection and stimulation condition, 5 separate experiments. **: $p < 0.01$, ***: $p < 0.0001$; independent Student's t-test, two-tailed.

Given that inhibiting excessive endolysosomal proteolysis helped restore the functional response to LTP, we performed additional time-lapse confocal imaging experiments to assess the impact of leupeptin on spine structural remodeling after LTP. Following 30 min pre-treatment with

leupeptin, NHE6 $_{\Delta ES}$ -mCh-expressing cells showed both enhanced recruitment of NHE6 $_{\Delta ES}$ -mCh puncta to spines, as well as an enlargement in thin-type spines comparable to controls in response to gly-Chem LTP stimulation (**Fig. 9A-H**). Interestingly, leupeptin-treated mCh- and NHE6 $_{WT}$ -mCh-positive neurons did not show a significant increase in mushroom-type spines, though their relative increase in spine head volume was still greater than that of NHE6 $_{\Delta ES}$ -mCh transfectants (**Fig. 9E-F, H**). Overall, these data strongly indicate an elevated accumulation of endolysosomal vesicles in the vicinity of spines in NHE6 $_{\Delta ES}$ -mCh transfectants. They also demonstrate that inhibiting endolysosomal mediated proteolysis restores the ability of ΔES -expressing neurons to structurally remodel and recruit AMPARs to the cell surface in response to gly-ChemLTP.

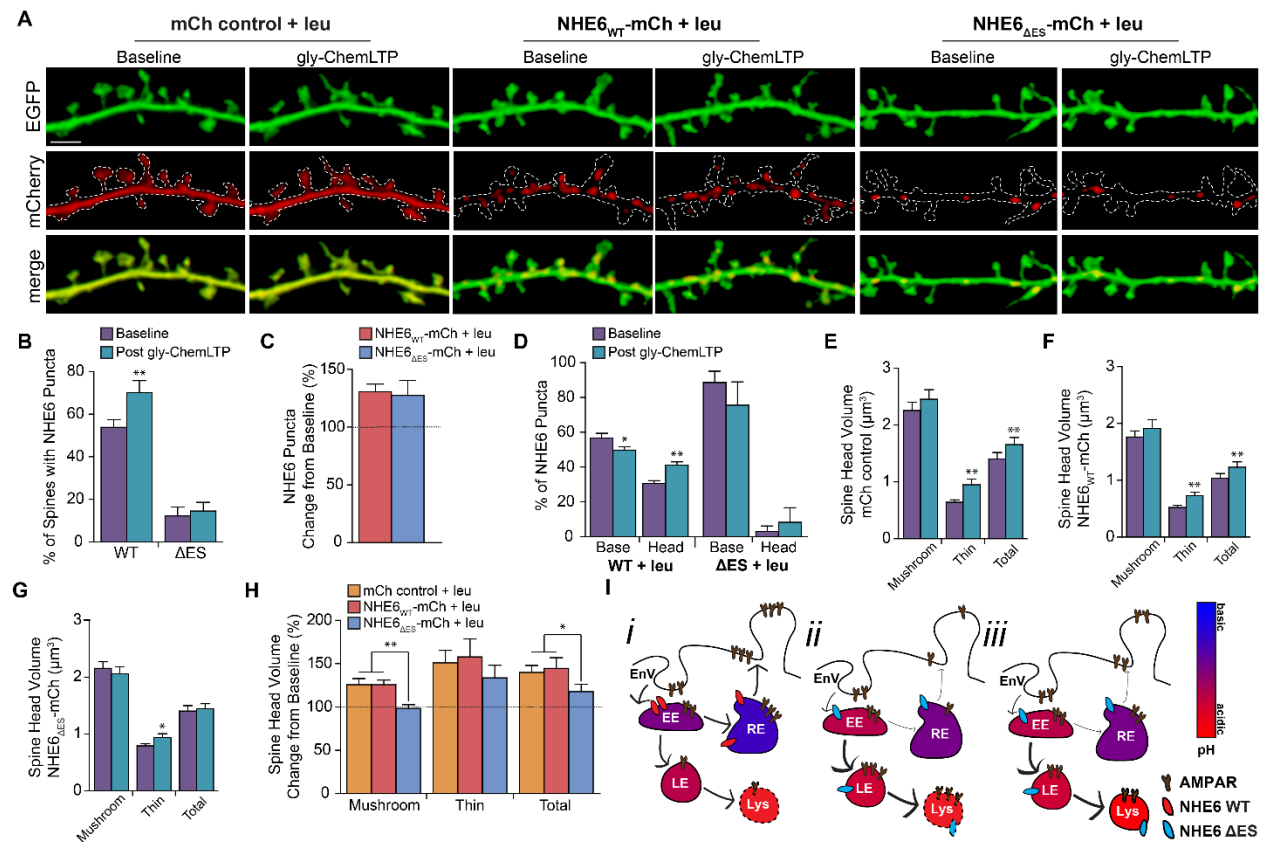


Figure 9: Leupeptin partially restores the structural response to gly-ChemLTP. **A:** Representative confocal micrographs of secondary or tertiary dendrites from transfected, leupeptin-treated primary hippocampal neurons at baseline and post gly-ChemLTP for each transfection condition. Channels are shown separately and merged; white outlines denote location of EGFP-positive dendrite. Scale bar: 3 μm . **B:** Mean \pm S.E.M. percentage of spines containing

NHE6 WT or Δ ES puncta at baseline and 20 min post gly-ChemLTP following leupeptin pre-treatment. **C**: Following gly-ChemLTP, the mean \pm S.E.M. percent change of NHE6 WT or Δ ES-positive spines. **D**: Mean \pm S.E.M. proportion of NHE6 WT or Δ ES puncta in each spine subregion at baseline and following gly-ChemLTP with leupeptin pre-treatment. **E-G**: Mean \pm S.E.M. spine head volume measurements for mushroom, thin, and total spines in mCh control- (**E**), NHE6 WT- (**F**), and NHE6 Δ ES- (**G**)-transfected neurons at baseline and following gly-ChemLTP with leupeptin pre-treatment. **H**: Following leupeptin pre-treatment and gly-ChemLTP stimulation, the mean \pm S.E.M. percent change from baseline in spine head volume. For mCh control + leu: 168 spines along 202.54 μ m of dendrite from 8 cells; NHE6 WT + leu: 225 spines along 231.468 μ m of dendrite from 8 cells; NHE6 Δ ES + leu: 185 spines along 227.988 μ m of dendrite from 8 cells, 5 separate experiments. *: $p < 0.05$, **: $p < 0.01$; paired Student's t-test, two-tailed (**B-D**), Wilcoxon signed rank test (**E-G**), Kruskal-Wallis test with Dunn's Multiple Comparison test (**H**). **I**: Representative schematic. Under normal conditions with NHE6 WT (*i*), internalized cargo, such as AMPARs, are preferentially recycled back to perisynaptic zones. However, with NHE6 Δ ES (*ii*), AMPARs are instead targeted to the late endosome and lysosome and subsequently degraded, decreasing their availability at synaptic sites. With leupeptin treatment (*iii*), this aberrant lysosomal degradation is prevented, thereby allowing for these AMPARs to be trafficked to the membrane instead.

2.5 DISCUSSION

In recent years, studies on CS have expanded the genetic and phenotypic heterogeneity of this disorder [1,4,18,19], yet the impact of these genetic alterations on cellular trafficking and learning mechanisms in neurons remains to be fully elucidated. In the present study, we initially chose to focus on the Δ ES (p.E287_S288del) mutation because this was one of the first SLC9A6 mutations to be reported [4]. In this particular study, the authors reported that all affected individuals included in the study showed profound developmental delay and learning problems. Importantly, this mutation was one of the first discovered that still results in the production of a full-length protein product (as opposed to other mutations that introduce a premature stop codon into the gene). Furthermore, deletions of the analogous glutamate residues in NHE1 and NHE8, a other NHE family members, has previously been shown to ablate the ion transport function of these

exchangers [53,54], and we have also reported that the Δ ES mutation ablated the ability of NHE6 to regulate vesicular pH as well [22]. Thus, this mutation identified from a patient provided us with an advantageous loss-of-function, full-length protein product of which to study the impact on neuronal structure and function.

Using primary hippocampal neurons, we now report that NHE6 $_{\Delta$ ES-mCh puncta localize less to early and recycling endosomes and more to acidic late endosomes and lysosomes when compared to NHE6 $_{WT}$ -mCh. Also, NHE6 $_{\Delta$ ES-mCh transfection significantly decreased dendritic spine density compared to controls, paralleling previous observations of hippocampal neurons from NHE6 KO mice [21]. Spine morphology is typically correlated with AMPAR density and post-synaptic density (PSD) size, and thus spine size is a common measure of synaptic strength and stability [55]. As such, the observed reduction in the density of larger mushroom-type spines in neurons expressing NHE6 $_{\Delta$ ES-mCh is indicative of a reduction in excitatory synaptic neurotransmission and proper neuronal circuit connectivity, as even minimal shifts in spine size are associated with significant changes in synaptic function at both the cellular and circuit levels [52]. Indeed, disruptions in spine density, size, and stability are common to a number of neurodevelopmental disorders that present with cognitive impairment, including Angelman, Rett, Fragile X, and Down syndromes [55]. Interestingly, in Fragile X syndrome and other such disorders involving intellectual disability, post-mortem examinations have revealed a “torturous” spine morphology resulting from an increase in immature filopodia density, similar to our observations [52,55]. Together, these findings reveal that NHE6 mutants induce deficits in the formation and maintenance of excitatory synapses, which could underlie the learning deficits observed in individuals with CS.

We also observed that NHE6 $_{\Delta ES}$ -mCh-expressing neurons fail to undergo significant structural and functional remodeling in response to gly-ChemLTP stimulation. Increases in spine head volume are a common response to LTP in the hippocampus and cortex and are reflective of a recruitment of excitatory postsynaptic machinery to the spine and an increase in synaptic strength [55]. This is seen predominantly in smaller spines, which are thought to be more labile and plastic than larger, more stable spines. Importantly, it has been shown that recycling endosomes, the pH and function of which are mediated in part by NHE6, provides additional AMPARs and lipid membranes to dendritic spines following LTP induction, thus accounting for the associated changes in synaptic structure and function [47,48]. We thus postulate that the inability of smaller, thin-type spines to enlarge in ΔES -transfected cells results from impaired trafficking mechanisms that normally regulate structural plasticity mechanisms. Likewise, NHE6 $_{\Delta ES}$ -mCh-transfected neurons also had significantly fewer spine-localized GluA1 puncta and failed to recruit additional AMPARs to these spines following gly-ChemLTP stimulation. This resulted in a functional change at the synapse: specifically, ΔES -expressing cells failed to show the expected increase in mEPSC amplitude in response to gly-ChemLTP-stimulation, as seen in controls. Given that NHE6 normally traffics into spine heads alongside GluA1 following gly-ChemLTP [8], this suggests that NHE6 plays an essential role in AMPAR trafficking mechanisms at the synapse. It should be noted that NHE6 is found extensively within excitatory postsynaptic compartments, with significant trafficking to the base and head regions of spines. We and others have also shown that the endocytosis of certain integral plasma membrane proteins is regulated by NHE6 function [22,27,56]. Therefore, we hypothesize that NHE6 specifically participates in the maintenance of endocytic zones, which are located adjacent to PSDs and contain machinery necessary to internalize AMPARs into endosomes and maintain them close to the synapse. In response to LTP

induction, this pool of recycling endosomes is then important for the addition of both AMPARs and additional lipid membrane to spine heads to mediate their enlargement and functional potentiation [51,57,58]. As such, Petrini and colleagues reported that impairing AMPAR recycling through endocytic zones by interfering with endocytic machinery diminishes the number of PSD-localized AMPARs [48]. Likewise, we postulated that synaptic AMPAR recycling in Δ ES-transfected neurons is impaired by the overacidification of endosomes containing GluA1-positive AMPARs, which increases the likelihood the receptors will be erroneously targeted to and degraded within lysosomes (**Fig. 9I**). Overall, it follows that impairments in structural and functional changes at synaptic sites could arise from Δ ES-induced deficiencies in endosomal trafficking mechanisms at the synapse.

Given that the localization of AMPARs is heavily dependent on endosomal trafficking mechanisms, we hypothesized that NHE6 Δ ES may lead to an excessive endolysosomal degradation of these receptors. We verified this hypothesis using leupeptin, an inhibitor of cysteine, serine and threonine proteases in the endolysosomal pathway [59], and found that in Δ ES-expressing neurons, leupeptin restored spine density to levels comparable to controls. Moreover, in Δ ES-expressing cells that were pre-treated with leupeptin before being subjected to LTP induction, the spines were enlarged and were able to recruit GluA1-containing AMPARs; these cells underwent functional potentiation as well. Thus, the loss of NHE6 function may indeed favour both enhanced endolysosomal trafficking and degradation of AMPARs and other such cargo in hippocampal neurons, subsequently disrupting their signaling. By preventing excessive degradation of GluA1 in Δ ES mutants, we were then able to replenish the pool of AMPARs available for insertion into synaptic sites following LTP induction (illustrated in **Fig. 9I**). Parenthetically, it has been shown that in dorsal root ganglion neurons, 24 h leupeptin treatment

prevented the ligand-induced degradation of fibroblast growth factor (FGF) receptor 1, enhancing its recycling and thereby promoting axon elongation in these cells [60,61]. This finding emphasizes the potential benefit of regulating lysosomal function in neurons to promote changes in their morphology and function. To verify that excessive lysosomal degradation was the result of endosomal overacidification, we rendered endosomes more alkaline by applying bafilomycin, an H⁺-ATPase inhibitor. Surprisingly, this treatment was detrimental to spine density in both mCh- and NHE6_{WT}-mCh-transfected neurons. Since bafilomycin blocks acidification of all endomembrane compartments of the secretory and degradative pathways, this detrimental effect may be the result of an overalkalinization of most secretory and endocytic compartments, which then broadly disrupts endomembrane trafficking mechanisms and cellular function. Thus, bafilomycin treatment likely had a more pervasive suppressive effect on organellar dynamics in healthy cells. This observation underpins the importance of regulating organellar pH within a tight range, as both drastic increases and decreases in this parameter can disrupt trafficking mechanisms and cell function [11,12]. Conversely, bafilomycin treatment partially restored spine density in NHE6_{ΔES}-mCh-expressing neurons, presumably by limiting excessive acidification and degradation of endosomal cargo under these conditions. Indeed, previous work has demonstrated that bafilomycin treatment can prevent the degradation of internalized receptors in cultured heterologous cells [62]. Interestingly, while we have shown that NHE6_{ΔES}-mCh also partially undergoes degradation through proteasomes [22], proteasomal inhibition with MG132 did not rescue spine density in ΔES-expressing neurons. This suggests that specifically limiting excessive endosomal acidification and mistrafficking and degradation of cargo within the lysosome may be a potential strategy to ameliorate some of the deleterious effects induced by the ΔES mutation.

Overall, our results suggest that mutations in NHE6 can lead to dysregulation of endosomal trafficking and disruption of neuronal morphology and synaptic function. These findings could have important implications for understanding the pathogenesis of other neurological disorders as well. For instance, NHE6 levels have been found to be downregulated in the brains of patients with AD, Parkinson's disease, and autism spectrum disorders [25,26,63]. This suggests that similar mechanisms of endosomal mistrafficking may occur in these pathological states as well. As such, additional studies of NHE6 function and regulation will prove valuable in the development of novel therapeutic strategies for treating cognitive deficits observed in rare disorders such as CS, as well as other common neurodegenerative disorders that affect a more significant proportion of the global population.

2.6 REFERENCES

1. Pescosolido MF, Stein DM, Schmidt M, Moufawad El Achkar C, Sabbagh M, Rogg JM, et al. Genetic and phenotypic diversity of NHE6 mutations in Christianson syndrome. *Ann Neurol*. 2014;581–93.
2. Schroer RJ, Holden KR, Tarpey PS, Matheus MG, Griesemer D a, Friez MJ, et al. Natural history of Christianson syndrome. *Am J Med Genet A*. 2010 Nov;152A(11):2775–83.
3. Christianson AL, Stevenson RE, van der Meyden CH, Pelser J, Theron FW, van Rensburg PL, et al. X linked severe mental retardation, craniofacial dysmorphology, epilepsy, ophthalmoplegia, and cerebellar atrophy in a large South African kindred is localised to Xq24-q27. *J Med Genet*. 1999 Oct;36(10):759–66.
4. Gilfillan GD, Selmer KK, Roxrud I, Smith R, Kyllerman M, Eiklid K, et al. SLC9A6 mutations cause X-linked mental retardation, microcephaly, epilepsy, and ataxia, a phenotype mimicking Angelman syndrome. *Am J Hum Genet*. 2008 Apr;82(4):1003–10.
5. Xu M, Ouyang Q, Gong J, Pescosolido MF, Pruett BS, Mishra S, et al. Mixed Neurodevelopmental and Neurodegenerative Pathology in Nhe6 -Null Mouse Model of Christianson Syndrome. *eNeuro*. 2017 Nov;4(6):ENEURO.0388-17.2017.
6. Tarpey PS, Smith R, Pleasance E, Whibley A, Edkins S, Hardy C, et al. A systematic, large-scale resequencing screen of X-chromosome coding exons in mental retardation. *Nat Genet*. 2009;41(5):535–43.
7. Orlowski J, Grinstein S. Na⁺/H⁺ exchangers. *Compr Physiol*. 2011 Oct;1(4):2083–100.
8. Deane EC, Ilie AE, Sizdahkhani S, Das Gupta M, Orlowski J, McKinney RA. Enhanced recruitment of endosomal Na⁺/H⁺ exchanger NHE6 into Dendritic spines of hippocampal pyramidal neurons during NMDA receptor-dependent long-term potentiation. *J Neurosci*. 2013 Jan 9;33(2):595–610.
9. Brett CL, Wei Y, Donowitz M, Rao R. Human Na⁽⁺⁾/H⁽⁺⁾ exchanger isoform 6 is found in recycling endosomes of cells, not in mitochondria. *Am J Physiol Cell Physiol*. 2002 May;282(5):C1031-41.
10. Xinhan L, Matsushita M, Numaza M, Taguchi A, Mitsui K, Kanazawa H. Na⁺/H⁺ exchanger isoform 6 (NHE6/SLC9A6) is involved in clathrin-dependent endocytosis of transferrin. *Am J Physiol Cell Physiol*. 2011 Dec;301(6):C1431-44.
11. Casey JR, Grinstein S, Orlowski J. Sensors and regulators of intracellular pH. *Nat Rev Mol Cell Biol*. 2010;11(1):50–61.
12. Paroutis P, Touret N, Grinstein S. The pH of the secretory pathway: measurement, determinants, and regulation. *Physiology (Bethesda)*. 2004 Aug;19:207–15.
13. Yamashiro DJ, Maxfield FR. Acidification of endocytic compartments and the intracellular pathways of ligands and receptors. *J Cell Biochem*. 1984;26(4):231–46.
14. Weisz OA. Acidification and Protein Traffic. In: *International Review of Cytology*. 2003. p. 259–319.
15. Chater TE, Goda Y. The role of AMPA receptors in postsynaptic mechanisms of synaptic plasticity. *Front Cell Neurosci*. 2014;8(November):1–14.

16. Overly CC, Hollenbeck PJ. Dynamic organization of endocytic pathways in axons of cultured sympathetic neurons. *J Neurosci*. 1996;16(19):6056–64.
17. Numakawa T, Suzuki S, Kumamaru E, Adachi N, Richards M, Kunugi H. BDNF function and intracellular signaling in neurons. *Histol Histopathol*. 2010;25(2):237–58.
18. Garbern JY, Neumann M, Trojanowski JQ, Lee VM-Y, Feldman G, Norris JW, et al. A mutation affecting the sodium/proton exchanger, SLC9A6, causes mental retardation with tau deposition. *Brain*. 2010 May;133(5):1391–402.
19. Takahashi Y, Hosoki K, Matsushita M, Funatsuka M, Saito K, Kanazawa H, et al. A loss-of-function mutation in the SLC9A6 gene causes X-linked mental retardation resembling Angelman syndrome. *Am J Med Genet B Neuropsychiatr Genet*. 2011 Dec;156B(7):799–807.
20. Strømme P, Dobrenis K, Sillitoe R V, Gulinello M, Ali NF, Davidson C, et al. X-linked Angelman-like syndrome caused by Slc9a6 knockout in mice exhibits evidence of endosomal-lysosomal dysfunction. *Brain a J Neurol*. 2011 Nov;134(Pt 11):3369–83.
21. Ouyang Q, Lizarraga SB, Schmidt M, Yang U, Gong J, Ellisor D, et al. Christianson Syndrome Protein NHE6 Modulates TrkB Endosomal Signaling Required for Neuronal Circuit Development. *Neuron*. 2013 Oct 2;80(1):97–112.
22. Ilie A, Gao AYL, Reid J, Boucher A, Barriere H, McEwan C, et al. A Christianson Syndrome-linked deletion mutation (Δ 287ES288) in SLC9A6 disrupts recycling endosomal function and induces neurodegeneration and cell death. *Mol Neurodegener*. 2016;1–28.
23. Verma V, Bali A, Singh N, Jaggi AS. Implications of sodium hydrogen exchangers in various brain diseases. *J Basic Clin Physiol Pharmacol*. 2015;26(5):417–26.
24. Zhao H, Carney KE, Falgoust L, Pan JW, Sun D, Zhang Z. Emerging roles of Na⁺ / H⁺ exchangers in epilepsy and developmental brain disorders. *Prog Neurobiol*. 2016;
25. Prasad H, Rao R. The Na⁺ / H⁺ Exchanger NHE6 Modulates Endosomal pH to Control Processing of Amyloid Precursor Protein in a Cell Culture Model of Alzheimer Disease. *J Biol Chem*. 2015 Feb 27;290(9):5311–27.
26. Schwede M, Garbett K, Mirnics K, Geschwind DH, Morrow EM. Genes for endosomal NHE6 and NHE9 are misregulated in autism brains. *Mol Psychiatry*. 2013 Mar;19(3):1–3.
27. Ilie A, Weinstein E, Boucher A, McKinney RA, Orlowski J. Impaired posttranslational processing and trafficking of an endosomal Na⁺/H⁺ exchanger NHE6 mutant (Δ (370)WST(372)) associated with X-linked intellectual disability and autism. *Neurochem Int*. 2014 Jul;73:192–203.
28. Brewer GJ, Torricelli JR. Isolation and culture of adult neurons and neurospheres. *Nat Protoc*. 2007 Jan;2(6):1490–8.
29. Potter SM, DeMarse TB. A new approach to neural cell culture for long-term studies. *J Neurosci Methods*. 2001;110(1–2):17–24.
30. Jiang M, Chen G. High Ca²⁺-phosphate transfection efficiency in low-density neuronal cultures. *Nat Protoc*. 2006;1(2):695–700.
31. Fortin D a, Davare M a, Srivastava T, Brady JD, Nygaard S, Derkach V a, et al. Long-term

- potentiation-dependent spine enlargement requires synaptic Ca^{2+} -permeable AMPA receptors recruited by CaM-kinase I. *J Neurosci*. 2010 Sep 1;30(35):11565–75.
32. Harris KM, Jensen FE, Tsao B. Three-dimensional structure of dendritic spines and synapses in rat hippocampus (CA1) at postnatal day 15 and adult ages: implications for the maturation of synaptic physiology and long-term potentiation. *J Neurosci*. 1992;12(7):2685–705.
 33. Sorra KE, Harris KM. Overview on the structure, composition, function, development, and plasticity of hippocampal dendritic spines. *Hippocampus*. 2000;10(5):501–11.
 34. Chang PKY, Prenosil GA, Verbich D, Gill R, McKinney RA. Prolonged ampakine exposure prunes dendritic spines and increases presynaptic release probability for enhanced long-term potentiation in the hippocampus. *Eur J Neurosci*. 2014;40(5):2766–76.
 35. Koleske AJ. Molecular mechanisms of dendrite stability. *Nat Rev Neurosci*. 2013;14(8):536–50.
 36. Maxfield FR, McGraw TE. Endocytic recycling. *Nat Rev Mol Cell Biol*. 2004;5(2):121–32.
 37. Grant BD, Donaldson JG. Pathways and mechanisms of endocytic recycling. *Nat Rev Mol Cell Biol*. 2009;10(9):597–608.
 38. Mu F-T, Callaghan JM, Steele-Mortimer O, Stenmark H, Parton RG, Campbell PL, et al. EEA1, an Early Endosome-Associated Protein. *J Biol Chem*. 1995;13503–11.
 39. Willingham MC, Hanover JA, Dickson RB, Pastan I. Morphologic characterization of the pathway of transferrin endocytosis and recycling in human KB cells. *Proc Natl Acad Sci*. 1984 Jan 1;81(1):175–9.
 40. Prekeris R, Klumperman J, Chen YA, Scheller RH. Syntaxin 13 mediates cycling of plasma membrane proteins via tubulovesicular recycling endosomes. *J Cell Biol*. 1998;143(4):957–71.
 41. Mellman I, Fuchs R, Helenius A. Acidification of the Endocytotic and Exocytic Pathways. *Ann Rev Biochem*. 1986;55:663–700.
 42. Vanlandingham PA, Ceresa BP. Rab7 regulates late endocytic trafficking downstream of multivesicular body biogenesis and cargo sequestration. *J Biol Chem*. 2009;284(18):12110–24.
 43. Carlsson SR, Fukuda M. Structure of human lysosomal membrane glycoprotein 1. Assignment of disulfide bonds and visualization of its domain arrangement. *J Biol Chem*. 1989;264(34):20526–31.
 44. McKinney RA. Excitatory amino acid involvement in dendritic spine formation, maintenance and remodelling. *J Physiol*. 2010 Jan 1;588(Pt 1):107–16.
 45. Lynch MA. Long-Term Potentiation and Memory. *Physiol Rev*. 2004;84(1):87–136.
 46. Malenka RC, Nicoll RA. Long-term potentiation -- A decade of progress ? *Science* (80-). 1999;285:1870–4.
 47. Park M, Penick EC, Edwards JG, Kauer J a, Ehlers MD. Recycling endosomes supply AMPA receptors for LTP. *Science*. 2004;305(5692):1972–5.

48. Petrini EM, Lu J, Cognet L, Lounis B, Ehlers MD, Choquet D. Endocytic trafficking and recycling maintain a pool of mobile surface AMPA receptors required for synaptic potentiation. *Neuron*. 2009;63(1):92–105.
49. Selcher JC, Xu W, Hanson JE, Malenka RC, Madison D V. Glutamate receptor subunit GluA1 is necessary for long-term potentiation and synapse unsilencing, but not long-term depression in mouse hippocampus. *Brain Res*. 2012;1435:8–14.
50. Davies J, Evans RH, Herrling PL, Jones AW, Olverman HJ, Pook P, et al. CPP, a new potent and selective NMDA antagonist. Depression of central neuron responses, affinity for [3H]d-AP5 binding sites on brain membranes and anticonvulsant activity. *Brain Res*. 1986;382(1):169–73.
51. Park M, Salgado JM, Ostroff L, Helton TD, Camenzind G, Harris KM, et al. Plasticity-induced growth of dendritic spines by exocytic trafficking from recycling endosomes. *Neuron*. 2006;52(5):817–30.
52. Forrest MP, Parnell E, Penzes P. Dendritic structural plasticity and neuropsychiatric disease. *Nat Rev Neurosci*. 2018;19(4):215–34.
53. Ding J, Rainey JK, Xu C, Sykes BD, Fliegel L. Structural and functional characterization of transmembrane segment VII of the Na⁺/H⁺ exchanger isoform 1. *J Biol Chem*. 2006;281(40):29817–29.
54. Nakamura N, Tanaka S, Teko Y, Mitsui K, Kanazawa H. Four Na⁺/H⁺ exchanger isoforms are distributed to Golgi and post-Golgi compartments and are involved in organelle pH regulation. *J Biol Chem*. 2005 Jan 14;280(2):1561–72.
55. Phillips M, Pozzo-Miller L. Dendritic spine dysgenesis in autism related disorders. *Neurosci Lett*. 2015;1–11.
56. Ohgaki R, Matsushita M, Kanazawa H, Ogihara S, Hoekstra D, van Ijzendoorn SCD. The Na⁺/H⁺ exchanger NHE6 in the endosomal recycling system is involved in the development of apical bile canalicular surface domains in HepG2 cells. *Mol Biol Cell*. 2010 Apr 1;21(7):1293–304.
57. Rácz B, Blanpied T a, Ehlers MD, Weinberg RJ. Lateral organization of endocytic machinery in dendritic spines. *Nat Neurosci*. 2004;7(9):917–8.
58. Yudowski G a., Puthenveedu M a., Leonoudakis D, Panicker S, Thorn KS, Beattie EC, et al. Real-Time Imaging of Discrete Exocytic Events Mediating Surface Delivery of AMPA Receptors. *J Neurosci*. 2007;27(41):11112–21.
59. Monti B, Sparapani M, Contestabile a. Differential toxicity of protease inhibitors in cultures of cerebellar granule neurons. *Exp Neurol*. 1998;153(2):335–41.
60. Hausott B, Schlick B, Vallant N, Dorn R, Klimaschewski L. Promotion of neurite outgrowth by fibroblast growth factor receptor 1 overexpression and lysosomal inhibition of receptor degradation in pheochromocytoma cells and adult sensory neurons. *Neuroscience*. 2008;153(2):461–73.
61. Hausott B, Vallant N, Hochfilzer M, Mangger S, Irschick R, Haugsten EM, et al. Leupeptin enhances cell surface localization of fibroblast growth factor receptor 1 in adult sensory

- neurons by increased recycling. *Eur J Cell Biol.* 2012;91(2):129–38.
62. Yoshimori T, Yamamoto a, Moriyama Y, Futai M, Tashiro Y. Bafilomycin-a1, a Specific Inhibitor of Vacuolar-Type H⁺-Atpase, Inhibits Acidification and Protein-Degradation in Lysosomes of Cultured-Cells. *J Biol Chem.* 1991;266(26):17707–12.
63. Kondapalli KC, Prasad H, Rao R. An inside job: how endosomal Na⁽⁺⁾/H⁽⁺⁾ exchangers link to autism and neurological disease. *Front Cell Neurosci.* 2014 Jan;8(June):172.

2.7 SUPPLEMENTAL DATA

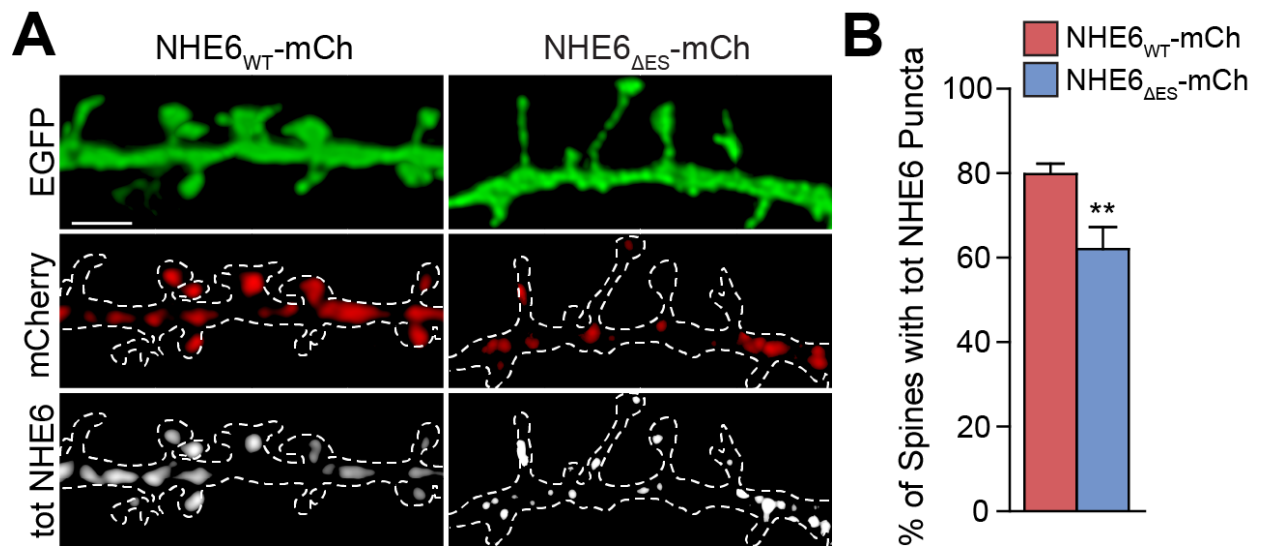


Fig. S1: NHE6 Δ ES expression impairs total NHE6 trafficking in the dendrites of hippocampal neurons. **A:** Representative confocal micrographs of secondary or tertiary dendrites from transfected primary hippocampal neurons and immunolabelled with a rabbit polyclonal antibody targeting total NHE6. Scale bar: 2 μ m. **B:** Mean \pm S.E.M. fraction of spines containing immunolabeled puncta of NHE6 of all spines analyzed under each transfection condition. NHE6 WT: n = 194 spines along 288.671 μ m of dendrite from 10 cells; NHE6 Δ ES: n = 123 spines along 295.049 μ m of dendrite from 10 cells, 3 separate experiments. **: $p < 0.01$, independent Student's t-test, two-tailed.

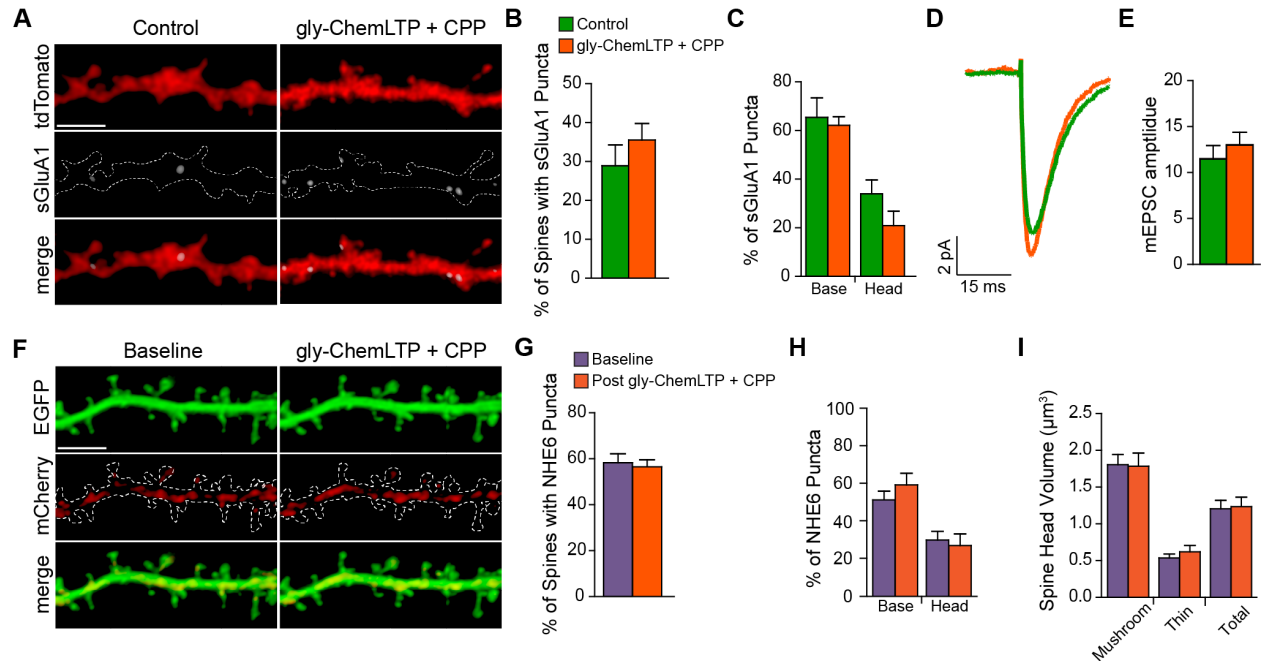


Fig. S2: The response to gly-ChemLTP is NMDA receptor-dependent. **A:** Representative confocal micrographs of secondary or tertiary dendrites from NHE6 WT-transfected primary hippocampal neurons that were either unstimulated (control) or stimulated (gly-ChemLTP) for each transfection condition and stained for surface SEP-GluA1 (sGluA1) under non-permeabilizing conditions. Channels are shown separately and merged; white outlines denote location of tdTomato-positive dendrite. Scale bar: 2 μ m. **B:** Mean \pm S.E.M. percentage of spines containing sGluA1 puncta for control and gly-ChemLTP + CPP-treated cells. **C:** Mean \pm S.E.M. proportion of sGluA1 puncta in each subregion for control and gly-ChemLTP + CPP-treated cells. For control, $n = 100$ spines along 156.529 μ m of dendrite from 8 cells; gly-ChemLTP + CPP: $n = 94$ spines along 157.616 μ m of dendrite from 7 cells. **D:** Average AMPAR-mEPSC event trace of an unstimulated control and gly-ChemLTP + CPP-treated NHE6 WT-positive neuron. **E:** Mean \pm S.E.M. mEPSC amplitude of all cells analyzed under each stimulation condition. For control, $n = 8$ cells; gly-ChemLTP + CPP: $n = 11$ cells. **F:** Representative confocal micrographs of secondary or tertiary dendrites from NHE6 WT-transfected neurons at baseline and post gly-ChemLTP + CPP. Channels are shown separately and merged; white outlines denote location of EGFP-positive dendrite. Scale bar: 3 μ m. **G:** Mean \pm S.E.M. percentage of spines containing NHE6 puncta at baseline and following gly-ChemLTP + CPP. **H:** Mean \pm S.E.M. proportion of NHE6 puncta in each spine subregion at baseline and following gly-ChemLTP + CPP. **I:** Mean \pm S.E.M. spine head volume of mushroom, thin, and total spines at baseline and following gly-ChemLTP + CPP. $n = 123$ spines along 158.058 μ m of dendrite from 6 cells.

CHAPTER 3. IMPAIRED HIPPOCAMPAL EXCITATORY NEUROTRANSMISSION AND PLASTICITY ASSOCIATED WITH LOSS OF THE CHRISTIANSON SYNDROME PROTEIN *SLC9A6/NHE6* IS AMELIORATED BY 7,8-DIHYDROXYFLAVONE

FOREWARD

Background and Rationale

In Chapter 2, I demonstrated that transfection of the patient-derived Δ ES mutant in NHE6 reduced mature dendritic spine density and disrupted endosomal AMPAR trafficking. Consequently, Δ ES-expressing neurons were unable to upregulate surface GluA1-containing AMPARs and did not show volumetric spine head enlargements following NMDAR-dependent ChemLTP. However, application of a lysosomal protease inhibitor was sufficient to restore the deficiencies in spine density and structural remodeling. These findings indicated that disrupting NHE6 function through the dominant negative overexpression of a LOF variant *in vitro* could induce a profound cell-autonomous impact upon excitatory postsynaptic function and plasticity. The question then arose of whether these findings applied to mice genetically deficient in NHE6. Previous work on neurons from these *Nhe6* KO mice demonstrated endosomal overacidification and disruptions in neurite outgrowth. Notably, *Nhe6* KO hippocampal neurons also showed significant reductions in activated levels of the activated, phosphorylated TrkB. In light of these conclusions, I next sought to investigate if *Nhe6* KO mice showed impairments in excitatory synaptic function, AMPAR trafficking, and the response to NMDAR-dependent LTP at the circuit level.

Hypothesis

I hypothesize that the loss of NHE6 impairs dendritic spine density and excitatory neurotransmission owing to a mistrafficking of AMPARs. As a result, both functional and

structural LTP will be impaired in *Nhe6* KO hippocampi. *Nhe6* KO mice will also demonstrate impairments in behavioural learning. However, targeting downregulated levels of phosphorylated TrkB could rescue some of these deficits in synaptic density and remodeling.

Experimental Outline

To test my hypotheses, I will crossbreed *Slc9a6/Nhe6* KO mice with our line of mGFP-expressing mice to label a subset of hippocampal pyramidal neurons with a membrane-tagged fluorescent marker to readily visualize neuronal structure. Using hippocampal slice preparations these mice, I will first quantify dendritic spine densities and assess both protein levels and dendritic trafficking of ionotropic glutamate receptor subunits. I will also use whole-cell patch clamp electrophysiology to assess excitatory neurotransmission from area CA1 pyramidal neurons. Next, electrophysiological field potential recordings will be used to verify if *Nhe6* KO hippocampi show deficiencies in CA3-CA1 LTP. If so, I will again use primary hippocampal neuron cultures to investigate if changes in the surface levels or post-translational modifications of AMPARs may underlie these deficiencies in functional LTP. I will also perform time-lapse confocal imaging on mGFP-labeled primary hippocampal neurons stimulated with the same NMDAR-dependent ChemLTP protocol from Chapter 2 to verify if KO cells similarly show deficiencies in structural LTP. In collaboration with members of Dr. N. Sonenberg's lab, we will also subject KO mice to a battery of behavioural learning tasks to see if these cellular and molecular changes translate to changes in memory acquisition. Finally, I will attempt to rescue these deficits in dendritic spine density and LTP by employing a competitive TrkB agonist, 7,8-dihydroxyflavone, to pharmacologically enhance TrkB activation.

3.1 ABSTRACT

Mutations in the *SLC9A6* gene encoding Na⁺/H⁺ exchanger isoform 6 (NHE6), a regulator of endosomal pH and function, result in Christianson syndrome (CS), an increasingly prevalent form of X-linked intellectual disability. Unfortunately, little is presently known of how ablation of NHE6 function perturbs excitatory synaptic plasticity, such as long-term potentiation (LTP), to potentially result in the severe cognitive impairments associated with CS. To address this, we generated a novel line of *Nhe6* KO expressing fluorescent labeling within hippocampal neurons to assess synaptic structure, function, and learning mechanisms. In *Nhe6* KO mice, we uncovered a significant reduction in mature dendritic spines along CA1 pyramidal neuronal dendrites, which was accompanied by reduced levels of the AMPA receptor (AMPA) subunit GluA2 and dampened AMPAR-mediated neurotransmission. Moreover, when compared to wild-type (WT) hippocampi, *Nhe6* KO hippocampi showed abnormal LTP expression in response to theta burst stimulation. Upon induction of glycine-mediated chemical LTP (ChemLTP), KO neurons also failed to show increases in surface GluA2 and phosphorylation of the AMPAR subunit GluA1 at the S845 site, indicating deficiencies in AMPAR surface insertion and post-translational modifications. In addition, spines along the dendrites of *Nhe6* KO neurons were excessively motile, and larger KO spines failed to enlarge after LTP, as typically seen in WT. Interestingly, young adult *Nhe6* KO male mice exhibited comparable performance to age- and sex-matched WT animals in behavioural learning paradigms. Finally, we sought to restore these deficits by enhancing activation of the tropomyosin receptor kinase B (TrkB) using the agonist 7,8-dihydroxyflavone (7,8-DHF). Acute application of 7,8-DHF restored spine density and structural remodeling after ChemLTP in *Nhe6* KO neurons. Taken together, the results suggest that NHE6 ablation disrupts AMPA receptor trafficking and consequently impairs hippocampal excitatory

synaptic density and remodeling, which may impair learning and memory in CS patients. However, targeting TrkB activation may hold potential as a clinical intervention to ameliorate these severe deficits.

3.2 INTRODUCTION

In neurons, precise intracellular trafficking is necessary for the development and plasticity of synapses and neuronal circuitry [1–3]. Perturbations in this process can result in severe neurological deficits [4–7], which occurs in the recently characterized neurodevelopmental genetic disorder Christianson syndrome (CS). Individuals with CS are primarily male and present with X-linked intellectual disability (XLID), epilepsy, truncal ataxia, non-verbalism, altered sensory processing, and autistic behaviours [8–11]. Many patients also show a progressive phenotype after the first decade of life, with severe cerebellar atrophy and loss of locomotor control being the most apparent [8,12]. Although CS is considered to be a rare disorder, it has been estimated to affect between 1 in 16,000 to 100,000 individuals worldwide and is possibly one of the more common forms of XLID [8,13]. Despite this relatively high frequency, little is currently known about the underlying etiology behind CS, and therapeutic options remain scarce. CS is the result of mutations in the *SLC9A6* gene, which is mapped to chromosome position Xq26.3 and encodes the electroneutral alkali cation (Na^+ or K^+)/proton (H^+) exchanger isoform 6 (NHE6) [14]. To date, over 80 unique inherited *and de novo* mutations have been discovered at this gene locus (for further information, see ClinVar ([https:// www.ncbi.nlm.nih.gov/clinvar/](https://www.ncbi.nlm.nih.gov/clinvar/)) and DECIPHER (<https://decipher.sanger.ac.uk/>) databases). However, the functional consequences of these mutations upon NHE6 function and cellular trafficking are only beginning to be uncovered [15–18].

NHE6 shows a broad distribution throughout the body, with enrichment in the brain [19]. In neurons and other cell types, NHE6 predominantly localizes to the membranes of early and recycling endosomes [20,21], where it acts as a means of H⁺ extrusion to counteract luminal acidification facilitated by the electrogenic vacuolar H⁺-ATPase (V-ATPase) transporter [22]. The precise regulation of luminal pH is necessary for endosomal trafficking, as minute increases or decreases in pH can impact whether certain cargo are recycled back to the cell surface or degraded through acidic lysosomes, respectively [22–24]. As such, cultured neurons deficient in NHE6 display an overacidification of endosomal pH when compared to wild-type (WT) neurons [25]. In neurons, proper endosomal dynamics are essential for the trafficking of cargos such as neurotrophin and neurotransmitter receptors, which enables morphological development as well as synaptic formation and plasticity. For instance, signaling through tyrosine receptor kinase B (TrkB), the high-affinity receptor for the mature form of the neurotrophin brain-derived neurotrophic factor (BDNF), mediates several downstream signaling pathways that are crucial for neurite outgrowth, cell survival, and synaptic refinement [26,27]. Importantly, BDNF binding to two TrkB molecules induces their dimerization, autophosphorylation, and internalization of phosphorylated TrkB (pTrkB) into intracellular signaling endosomes for either local or retrograde signaling [28,29]. As such, disruptions in signaling endosome maintenance can impair BDNF/TrkB signaling, resulting in the dysregulation of synaptic development and plasticity [30,31].

In addition, long-term potentiation (LTP) of neurotransmission at Schaffer collateral (SC)-CA1 synapses in the hippocampus is dependent upon the postsynaptic insertion of ionotropic glutamatergic α -amino-3-hydroxy-5-methyl-4-isoxazolepropionic acid (AMPA) receptors (AMPA receptors), which mediate the majority of fast excitatory neurotransmission in the central nervous

system [32,33]. AMPARs are usually heterotetrameric complexes consisting of two out of four possible subunits, GluA1-4, which regulate the properties and trafficking of the receptor: GluA1-positive AMPARs are thought to be inserted into synapses initially before being replaced with GluA2- and GluA3-containing AMPARs [33–35]. Dendritic spines, small protrusions that comprise the majority of excitatory postsynaptic sites on pyramidal cell dendrites, typically expand in size to accommodate the insertion of AMPARs and other scaffolding proteins during LTP [36,37]. Importantly, dendritic recycling endosomes have been shown to be essential for providing both additional lipid membrane and AMPARs to allow LTP expression [38–40]. As such, we have previously shown that NHE6 colocalizes strongly with GluA1 in dendrites, and both are recruited to spines following N-methyl-D-aspartate (NMDA) receptor (NMDAR)-dependent LTP [21]. While these findings implicate NHE6 in the functional response to LTP, the consequences of NHE6 ablation upon hippocampal plasticity remains unknown.

To investigate this further, we have recently reported that transfecting prevalent CS-associated *SLC9A6* mutants into murine hippocampal neurons disrupted axodendritic branching, spine number, and the functional and structural responses to NMDAR-dependent LTP in a cell autonomous manner [41,42]. Similar morphological deficits were previously reported in hippocampal area CA1 pyramidal neurons in male hemizygous *Slc9a6/Nhe6* knock-out (KO) mice [25]. *Nhe6* KO hippocampal neurons were also found to contain significantly less pTrkB protein when compared to WT [25]. This was indeed suggestive of an impairment in endosomal function in the absence of NHE6, which likely dampened endosomal BDNF/TrkB signaling and disrupted the proper development of hippocampal circuitry. Accordingly, *Nhe6* KO mice have also been reported to recapitulate a number of phenotypes associated with human CS patients, including neurodegeneration in the cerebellum and other brain areas as well as significant impairments in

locomotion and sensory processing [43–46]. Nonetheless, the manner in which the complete ablation of NHE6 impairs AMPAR trafficking and learning at the circuit and behavioural levels remains to be explored. In the present study, we sought to address these questions by uncovering deficits in hippocampal plasticity that could alter learning and memory in rodents. In light of these disturbances in cellular function, we then ameliorated them by targeting BDNF/TrkB signaling in the hopes of finding a potential avenue for therapeutic inventions in CS.

3.3 METHODS

Transgenic animals. As wild-type (WT) controls, either C57BL/6 or L15 mice, which express sparse but consistent levels of membrane-tagged enhanced GFP (mGFP) in a subset of hippocampal pyramidal neurons under the Thy1.2 promoter [126], were utilized. The mGFP tag is not known to effect neural development or function. To generate mGFP-labeled *Nhe6* knock-out (KO) mice, *Slc9a6^{tm1Dgen}* mice, bred on a C57/BL6 background and deficient in the *Nhe6* gene, were purchased from Jackson laboratories (<https://www.jax.org/strain/005843>) and crossed with the L15 line to generate heterozygous *Slc9a6^{+/-}* females, which were then crossed with L15 males to generate homozygous *Slc9a6^{-/-}* females and hemizygous *Slc9a6^{-Y}* males. For structural and immunohistochemical experiments, only mGFP-positive animals were utilized. For molecular biology and behavioural experiments, both mGFP-expressing and mGFP-negative mice were used. For the majority of *in* and *ex vivo* experiments described herein, hemizygous *Nhe6* KO males were used at the indicated time points. However, litters of homozygous females and hemizygous *Nhe6* KO males were pooled together during *in vitro* culture preparations, as we did not believe sex-dependent differences to have a significant impact at these early postnatal stages. All animal handling procedures were carried out according to the guidelines of the Canadian Council on

Animal Care and the McGill University Comparative Medicine and Animal Resources animal handling protocols 5057 and 5205.

Cell culture. Immunoblotting and live spine imaging experiments were performed on primary hippocampal cultures prepared from early postnatal WT or *Nhe6* KO mice, prepared as previously described [21,127]. In brief, postnatal day (PD) 0-1 mice pups were decapitated, and the hippocampi were dissected out of their brains. These hippocampi were held in ice-cold HBSS supplemented with 0.1 M HEPES buffer and 0.6% glucose until all tissue was collected, then digested with 165 U papain for 20-30 min in a shaking water bath heated to 37°C. Neurons and glia were dissociated by mechanical trituration and suspended in DMEM supplemented with 1% penicillin-streptomycin, 10% FBS, and 0.6% glucose. Cells were then plated onto poly-D-lysine-coated 10 mm glass coverslips (for imaging experiments) or 60 mm plastic Petri dishes (for immunoblotting experiments) at an approximate density of 12,000-24,000 cells/cm² and placed in a sterile humidified environment of 5% CO₂ at 37°C. 24 h later, plating media was replaced with Neurobasal-A growth media supplemented with 2% B-27 supplement, 1% GlutaMAX, and 1% penicillin-streptomycin and fed every 3 – 4 d until 14+ days *in vitro* (DIV) to allow development of a functional neuronal network [128].

To assess acute spine changes in response to *ex vivo* pharmacological treatment, organotypic hippocampal slice cultures were generated using the roller-tube method, as previously described [54]. Briefly, P6-8 mouse pups of either sex were decapitated, their brains removed, and their hippocampi isolated in an aseptic environment. Transverse hippocampal slices (400 µm thick) were cut with a McIlwain tissue chopper (Lafayette Instrument) and adhered to coverslips with a chicken plasma (Cocalico Biologicals; Reamstown, PA, USA) clot. Coverslips were then transferred to flat bottom tubes with medium (50% (v/v) Eagle's basal medium (Gibco), 25%

HBSS (Gibco), and 25% New Zealand horse serum) and placed in a roller-drum dry-air incubator at 36°C at approximately 10 revolutions per hour to enable oxygen-nutrient interchange in the cultures. Media was replenished until slices matured to 21+ DIV to allow for spine innervation and maturation before experimentation [129,130].

Pharmacological treatments. Glycine-mediated chemical long-term potentiation (ChemLTP) was performed on some primary hippocampal cultures for imaging or immunoblotting as previously described [21,41,49]. To summarize, the media of +14 DIV neurons was replaced with normal Tyrode's solution containing the following (in mM): 125 NaCl, 2.5 KCl, 2 CaCl₂, 1 MgCl₂·6H₂O, 5 HEPES, and 33 D(+)-glucose, pH 7.3, osmolarity 290 mOsmol/L, and gassed with 95% O₂/5% CO₂ at 32-37°C. The normal Tyrode's was then replaced with a stimulating solution of modified Mg²⁺-deficient Tyrode's solution with the following (in mM): 125 NaCl, 2.5 KCl, 2 CaCl₂·2H₂O, 5 HEPES, 33 D(+)-glucose, 0.2 glycine, 0.02 (-)-bicuculline methochloride, and 0.003 strychnine hydrochloride, for 10 min. Neurons were then perfused with normal Tyrode's for 20 min. We have previously confirmed that this phenomenon is NMDAR-dependent [21,41], as addition of (*RS*)-3-(2-carboxypiperazin-4-yl)-propyl-1-phosphonic acid ((*RS*)-CPP; 50 μM), a competitive antagonist of the NMDAR, prior to and during ChemLTP stimulation prevented structural and functional LTP response in WT cells. For immunoblotting experiments, one additional dish from each culture preparation was concurrently treated only with normal Tyrode's solution as a control.

For TrkB rescue experiments, 7,8-dihydroxyflavone (7,8-DHF, Tocris, 1 μM) was added to culture media (for static experiments) or Tyrode's solution (for live experiments) at the indicated time points. As 7,8-DHF was diluted in dimethyl sulfoxide (DMSO), stock solutions were prepared

at high concentrations to minimize the potential cytotoxic effects of DMSO. For controls *in vitro*, equivalent volumes of vehicle (DMSO) were added to sister cultures from the same preparation.

Immunoblotting. For whole adult hippocampal immunoblotting, animals were deeply anesthetized, decapitated, their brains removed, and their hippocampi rapidly isolated and transferred into tubes on dry ice. Approximately every 40 µg of whole adult hippocampal tissue was homogenized in 300 µl ice-cold radioimmunoprecipitation assay (RIPA) buffer consisting of 1% Nonidet P-40, 0.5% sodium deoxycholate, 0.1% sodium dodecyl sulfate (SDS), 50 mM Tris-HCl (pH 8.0), 150 mM NaCl, 10 mM NaF, 1 mM sodium orthovanadate, 1 mM beta-glycerophosphate, and completeMINI protease inhibitors (Roche). Lysates were then sonicated and centrifuged at 12,000 revolutions per min for 10 min at 4°C, and supernatant was removed from pellet.

For protein phosphorylation experiments, cells were lysed in 1X Western blot lysis buffer (PhosphoSolutions; 10% (w/v) SDS, 100 mM Tris, 10 mM EDTA, pH 8.0; diluted to 1X with ddH₂O) following manufacturer protocols. Briefly, cells grown in 60 mm dishes were washed with 0.1 M PB or normal Tyrode's solution, and 350 µl lysis buffer heated to 95°C was added. After gentle swirling and scraping, lysate was transferred to microcentrifuge tubes and sonicated in 20 s intervals until lysate turned clear before being heated at 95 °C for 10 min and centrifuged at 1800 x g for 5 min. Supernatant was then removed from pellet cell debris and transferred into new tubes. Supernatant protein concentrations were then measured using a bicinchoninic acid dye-binding assay (Thermo Scientific) and compared against bovine serum albumin (BSA) as a standard.

For surface expression assays, cell-surface biotinylation was performed following a modified protocol [131]. In summary, following ChemLTP stimulation, 60 mm dishes were washed and incubated in ice-cold Tyrode's solution with sulfo-N-hydroxysuccinyl-SS-biotin

(sulfo-NHS-SS-biotin, Pierce, 1.0 mg/ml) with gentle agitation for 45 min. Dishes were then washed, incubated in ice-cold Tyrode's solution for 10 min, and free-floating biotin was washed off and quenched in Tyrode's solution supplemented with 200 mM glycine. After subsequent washing in Tyrode's solution, approximately 350 μ l ice-cold RIPA buffer was added to each dish, and cells were removed using a cell scraper into microcentrifuge tubes. Lysates were sonicated and then rotated 4 °C for 2 h before being spun down at 13,200 x g for 30 min to pellet cellular debris. Supernatant was then removed, and protein concentrations were subsequently acquired as described above. To isolate biotinylated membrane proteins, neuronal lysate containing 150-250 μ g protein was incubated with streptavidin-agarose beads (Pierce), washed with Tyrode's solution, overnight at 4 °C with gentle agitation to ensure mixing. Beads were then pelleted, washed several times with ice-cold Tyrode's solution, and biotinylated proteins were subsequently eluted by incubation with 50 μ l 2X sodium dodecyl sulfate (SDS)-sample buffer (BioRad) supplemented with 50 mM dithiothreitol for 30 min with rotations. Beads were then pelleted again before loading.

To separate proteins for immunoblotting, 15-25 μ g protein from tissue and cellular lysates were loaded and subjected to 8-9% SDS-polyacrylamide gel electrophoresis (SDS-PAGE), then transferred to methanol-activated polyvinylidene fluoride (PVDF) membranes (Millipore, Nepean, Ontario, Canada) overnight at 4°C. Membranes were blocked with 5% non-fat skim milk/0.01% Tween-20 in phosphate-buffered saline (PBS-T) or 5% BSA/0.05% Tween-20 in Tris-buffered saline (TBS-T) for 1 h, then incubated for 2 h at room temperature or overnight at 4°C with the specified primary antibodies (NHE6 (in-house): 1:3,000; GluA1 (Abcam): 1:1,000; GluA2 (Abcam): 1:1,000; GluN2B: 1:1,000 (Abcam); pGluA1-S831 (PhosphoSolutions): 1:1,000; pGluA1-S845 (PhosphoSolutions): 1:1000; pTrkB-Y816 (Millipore): 1:2,000; TrkB (Abcam): 1:1,000; β -actin (Sigma-Aldrich): 1:10,000; β -III tubulin (R&D Systems): 1:5,000;

glyceraldehyde 3-phosphate dehydrogenase (GAPDH) (Sigma-Aldrich): 1:10,000) diluted in blocking buffer. Membranes were then washed and incubated with mouse (1:5,000) or rabbit (1:2,000) horseradish peroxidase (HRP)-conjugated secondary antibodies (Jackson) diluted in blocking buffer for 1 h at room temperature with rotation. After extensive washing, immunoreactive signals were detected by exposing membranes to Western Lightning™ Plus-ECL blotting detection reagents (Perkin Elmer Inc, Waltham, MA) in an Amersham™ Imager 6000 (GE Life Sciences, Buckinghamshire, UK). To strip blots during phosphorylation assays to quantify total protein levels, previously exposed membranes were incubated with 0.5 M NaOH for 15 min at room temperature before subsequent washing with ddH₂O and PBS-T/TBS-T and repetition of the immunoblotting procedure described above. Quantification of immunoreactive bands were determined by analysis of digital image files using ImageJ software.

Immunohistochemistry. Intracardiac perfusions and coronal sectioning were performed as previously described [132]. Briefly, adult mice (P60) were deeply anesthetized and perfused intracardially with 0.1 M PBS followed by 4% PFA/0.1 M PBS (Sigma Aldrich). The brain was extracted and stored in PFA at 4°C for 24-48 h, then transferred to 30% sucrose solution until saturation. Cortices were then sliced into 100 µm thick coronal sections on a Leica Vibratome 3000 Plus sectioning system (Concord, ON, Canada) and stored in 0.5% sodium azide/0.1 M PB. Organotypic slice cultures were fixed with 4% PFA/0.1 M PB, pH 7.4 (Sigma Aldrich) for 1 h at room temperature and washed with 0.1 M PB. Coronal sections and slice cultures were immunostained, as described previously. Cultures or slice sections were then permeabilized and blocked overnight at 4°C in 0.4% Triton X-100/1.5% HIHS/0.1 M PB, and primary antibodies were then diluted (GFP (Invitrogen) or GluA2 (Abcam): 1:250) in this solution for five days at 4°C with gentle agitation. After subsequent washing, secondary antibodies were diluted (Alexa

Fluor 488, Alexa Fluor 594, Invitrogen, 1:250) in 1.5% HHS/0.1 M PB and applied overnight at 4°C. Slices were then washed again and mounted onto charged SuperFrost (Menzel-Glaser) microscopy slides using UltraMount fluorescent mounting medium (Dako) and left to dry overnight at room temperature in the dark.

Confocal microscopy. Fixed and mounted sections were imaged using a Leica TCS SP2 confocal microscope with data acquired using 40x (NA 1.25) and 63x (NA 1.4) HCXPL APO oil-immersion objectives. mGFP and Alexa Fluor 488 were imaged using a 488 nm Ar laser line, and Alexa Fluor 594 was imaged using a 543 nm HeNe laser line. Channels were acquired sequentially to prevent spectral overlap of fluorophores. Optical sections of 300-500 nm were taken and line-averaged 2x to improve the signal-to-noise ratio. Live imaging of spine dynamics during the previously described ChemLTP protocol was performed by placing mature primary hippocampal neurons into a perfusion chamber of an upright Leica TCS SP8 confocal microscope with a 40x water immersion dipping lens (HXC APO L 40x/0.80 W U-V-I). In each coverslip, a section of spiny dendrite from a neuron with a strong mGFP signal was visually identified, and a z -stack of 300 nm optical sections was then rapidly acquired every min using a 488 nm Ar laser line, set at minimal power to prevent photobleaching, for the duration of the experiment. Additional optical sections were taken above and below each dendrite to allow for changes in the structure over time.

Image analysis. All image stacks were first deconvolved using Huygens Essential software by using a full maximum likelihood extrapolation algorithm (Scientific Volume Imaging, Hilversum, The Netherlands), and 3D images and 4D time-lapse stacks were compiled as maximum intensity projections using the Surpass function on Imaris software (Bitplane AG, Zurich, Switzerland). The Imaris Filament Tracer function was used to manually trace and quantify spines. From the ratio of the diameter and length of the head and neck of spines, it was possible to

visually distinguish between different spine subtypes (stubby, mushroom, and long thin spines) based off of previously distinguished criteria [133,134]. In brief, stubby spines had no visible distinction between its head and neck subregions, mushroom spines were short had a larger head (> 1 μm in diameter) and neck regions, and long thin spines were longer in length but had smaller heads (< 1 μm in diameter). To quantify puncta density, the channel containing the protein of interest was masked based off of the dendritic mGFP signal to ensure that the puncta in question were localized within the neuron. Once masked, puncta for each stack were then determined automatically using the Imaris Spots function, with a minimum puncta diameter of 0.3 μm . Spine and puncta counts were divided by the length of the analyzed dendrite to calculate densities.

For time-lapse confocal imaging experiments, spine head volume (SHV) was measured at every minute of the experiment and pooled into five min intervals, as previously described [135]. Briefly, the time-lapse confocal image stacks were four-dimensionally rendered using the Surpass function of Imaris, and a drift correction was performed automatically using the Spots function. The spines of interest were then isolated at each time point, and the volume was automatically calculated based off of the mGFP signal using the Surfaces function. Volume changes in all thin- and mushroom-type spines in response to ChemLTP were measured relative to their average baseline values. However, stubby spines were excluded because the resolution limit of light microscopy prevents their proper volume analysis. The motility index of each spine was calculated as an average, between 0 and 1, in the time periods before and after ChemLTP stimulation using a modified version of a previously established formula [51]:

$$\text{Motility index} = \frac{(\text{largest measured volume} - \text{smallest measured volume})}{\text{average measured volume}}$$

The average motility index was then pooled together for each time period and genotype.

Electrophysiology. Acute transverse hippocampal brain slices were prepared from male *Nhe6* KO mice (P30-P49), with age- and sex-matched WT as controls. After mice were deeply anaesthetized and decapitated, their brains were quickly removed and sectioned into 250 or 400 μm thick brain slices using a vibrating microtome (VT1000S, Leica), the chamber of which was filled with ice-cold sucrose-based artificial cerebrospinal fluid (ACSF). Slices were then allowed to recover in regular ACSF containing (in mM): 24 NaCl, 5 KCl, 1.25 NaH_2PO_4 , 2 MgSO_4 , 26 NaHCO_3 , 2 CaCl_2 , and 10 glucose saturated with 95% O_2 /5% CO_2 (pH 7.3, 300 mOsm) at 32 °C for 1 h before being maintained at room temperature prior to experimentation. Sections were bubbled constantly with 95% O_2 /5% CO_2 in all of the described preparation, recovery, and recording solutions.

To isolate AMPAR-mediated miniature excitatory postsynaptic currents (mEPSCs), 250 μm thick acute slices were placed into the recording chamber of an upright microscope (BX51WI, Olympus, XLUMPlanF1 20x 0.95 NA water immersion objective) and perfused continuously with ACSF (as described above) supplemented with (in μM): 1 TTX, 25 CPP, 50 picrotoxin, and 5 CGP 55845. Patch clamp recordings were then performed under whole-cell conditions from visually identified hippocampal CA1 pyramidal neurons held at -60 mV with an Axopatch 400 amplifier (Molecular Devices, Sunnyvale, CA, USA) at room temperature (23-25 °C) using borosilicate patch pipettes (4-8 M Ω) filled with (in mM): 120 K-gluconate, 1 EGTA, 10 HEPES, 5 MgATP, 0.5 Na_2GTP , 5 NaCl, 5 KCl, and 10 phosphocreatine K_2 (pH 7.2-7.3 with KOH and 285-295 mOsm). To monitor access resistance, transient test pulses were applied consistently every 2 min throughout the duration of the recording. Access resistance typically fell within the range of 7-10 G Ω , and data was discarded if the access resistance deviated > 20% during the recording. After holding current was stabilized, data was acquired at a sampling frequency of 20 kHz and filtered

at 2 kHz for 15 min. All AMPAR-mEPSCs were identified offline through use of Mini Analysis Software (Synaptosoft, Decature, GA). Thresholding for mEPSC amplitude detection was set at eight time the root-mean-square value of a visually-determined event-free recording span, and 450 events per cell were analyzed and utilized to determine mean values for each cell. A maximum of two cells was obtained from each slice before being discarded.

To assess functional LTP response, 400 μ m thick acute slices were placed into a heated (31-32 °C) recording chamber of an upright microscope (DM LFSA Microsystems, Heidelberg, Germany) and perfused continuously with regular ACSF (as described above). To assess functional LTP response, 400 μ m thick acute slices were placed into a heated (31-32 °C) recording chamber of an upright microscope (DM LFSA Microsystems, Heidelberg, Germany) and perfused continuously with regular ACSF (as described above). Field excitatory postsynaptic potentials (fEPSPs) were recorded in the *stratum radiatum* of the CA1 region using glass microelectrodes filled with 3 M NaCl. Glass stimulating electrodes filled with extracellular saline were placed in the *stratum radiatum*. After obtaining a stable fEPSP baseline for a period of 15 min, long-term synaptic modification was induced with theta burst stimulation (TBS; 5 stimuli at 100 Hz repeated at 5Hz). fEPSP slopes were monitored at least for 40 min after each stimulation. In control and test conditions, fEPSPs were elicited at 0.1 Hz by a digital stimulator that fed a stimulation isolator unit. All data analyses were performed with custom written software in Igor Pro 6 (Wavemetrics). fEPSP slope was measured as an index of synaptic strength. Pooled data are presented as mean \pm SEM.

Behaviour. For all behavioural tasks, male WT and *Nhe6* KO mice aged eight to 12 weeks during the time course of the experiments were utilized. For the T-maze spontaneous alternation task, a mouse was first placed in one arm of a T-shaped maze and allowed to explore the maze

with access to only two of the three arms for 10 min. Next, the mouse was introduced to the maze 1 h later and allowed to explore it for 10 min with access to all three arms. The time spent in the familiar versus the novel arm was then quantified against the total time spent exploring (to normalize for possible locomotor impairments in KO animals), and memory was represented as a mouse spending more time in the novel arm than the familiar arm. For contextual fear conditioning (CFC) tasks, mice were placed in a context with an electric grid floor. The mice were first habituated for 2 min (naïve) before receiving a 0.7 mA footshock for 2 s, and freezing was recorded for 1 min following the footshock. After 1 h, mice were placed into the same context for 4 min where freezing was again recorded to assess short-term memory.

For novel object location (NOL) tasks, on day 1, male mice (aged 8–12 weeks) were habituated for 10 min in a white square testing arena (40 cm × 40 cm × 40 cm) and subsequently returned to their home cages. Habituation occurred 2x with a 4 h interval between habituations. On days 2, 3 and 4, mice were presented with 2 identical objects each placed 20 cm apart aligned at the center axis of the arena. Mice were allowed to explore the arena and objects for 10 min 2x each day, with a 4-hour interval between same-day training trials. During all 4 h intervals and end of habituation/testing days mice were returned to their home cages. On day 5, one of the objects was moved to a new location in the arena and 24 h following the final training trial, mice were allowed to explore the arena and objects for 10 min. The moved object was chosen from the right or left side of the arena equally. Further, the moved object was counterbalanced for object location within the arena. Time spent exploring each object was measured, defined as the mouse sniffing and touching the object within a 2 cm radius around the object. Total exploration time was the time spent interacting with both objects. To determine any preferential attention towards an object in a new location over an unmoved object, we calculated a percent discrimination index as

$(t_{\text{moved}} - t_{\text{unmoved}})/(t_{\text{total}})$, where t represents time exploring. A positive percent index (above 0%) represents a preference for exploring the moved object.

For novel object recognition (NOR) tasks, on day 1, male mice (aged 8–12 weeks) were habituated for 10 min in a white square testing arena (40 cm × 40 cm × 40 cm) and subsequently returned to their home cages. On days 2 and 3, mice were put back in the arena for 10 min and presented with two identical objects (familiar) located within specific areas of the arena. The test was counterbalanced for object location within the arena. Mice were allowed to freely explore the arena and objects for this time and then returned to their home cages. On day 4, one of the objects (used for days 2 and 3) was replaced with a third object (novel object), and the mice were allowed to explore the arena and objects for 10 min. Time spent exploring each object was measured, defined as the mouse sniffing and touching the object within a 2 cm radius around the object. Total exploration time was the time spent interacting with both objects. To determine preferential attention towards one object over another, we calculated a percent discrimination index as $(t_{\text{novel}} - t_{\text{familiar}})/(t_{\text{total}})$, where t represents time exploring. A positive percent index (above 0%) represents a preference for exploring the novel object.

Statistical analysis. The data represent the mean ± the standard error of the mean (S.E.M.). Statistical analyses were generally performed using the Student's t-test (for two groups) or a one-way analysis of variance (ANOVA) followed by a Bonferroni post-hoc test (for three or more groups), including non-parametric equivalents when appropriate. Interactions between genotype and time or treatment were measured using a repeated-measures ANOVA. For LTP data, statistical comparisons were made using Wilcoxon or Mann-Whitney test as appropriate. For dynamic spine imaging experiments, spine motility changes were assessed using a paired Student's t-test. A minimum p -value of < 0.05 was considered significant.

3.4 RESULTS

3.4.1 Assessing excitatory synaptic number and function in *Nhe6* KO

To elucidate differences in neuronal CA1 pyramidal cell cytoarchitecture between WT and *Nhe6* KO brains, we crossed the commercially available *Nhe6* KO mice with a mouse line (L15) expressing membrane-tagged GFP (mGFP) reporter protein under a Thy1 promoter in a subset of CA1 hippocampal pyramidal neurons. We first verified that NHE6 protein was indeed absent in the hippocampi of KO mice, and that hippocampal area CA1 principal neurons were indeed sparsely labeled (**Fig. 1A-B**). These transgenic mice enabled us to perform high-resolution analyses of neuronal morphology of CA1 pyramidal cells using a membrane-tagged genetic fluorescent marker. It has previously been reported that *Nhe6* KO neurons show a decrease in mature spine density with a concomitant increase in immature filopodia-like structures [25]. In light of this, we initially performed a detailed analysis of dendritic spines by separating these structures into their three major subtypes (*i.e.* stubby, mushroom, and thin) to better exemplify the differences in synaptic density and maturation [47]. In brain sections taken from P60 male animals, we discovered significant decreases in thin- and mushroom-type spine density on tertiary dendrites of KO hippocampal CA1 pyramidal neurons when compared to WT that resulted in a significant decrease in total spine density; stubby spine density was not significantly affected (**Fig. 1C-D**).

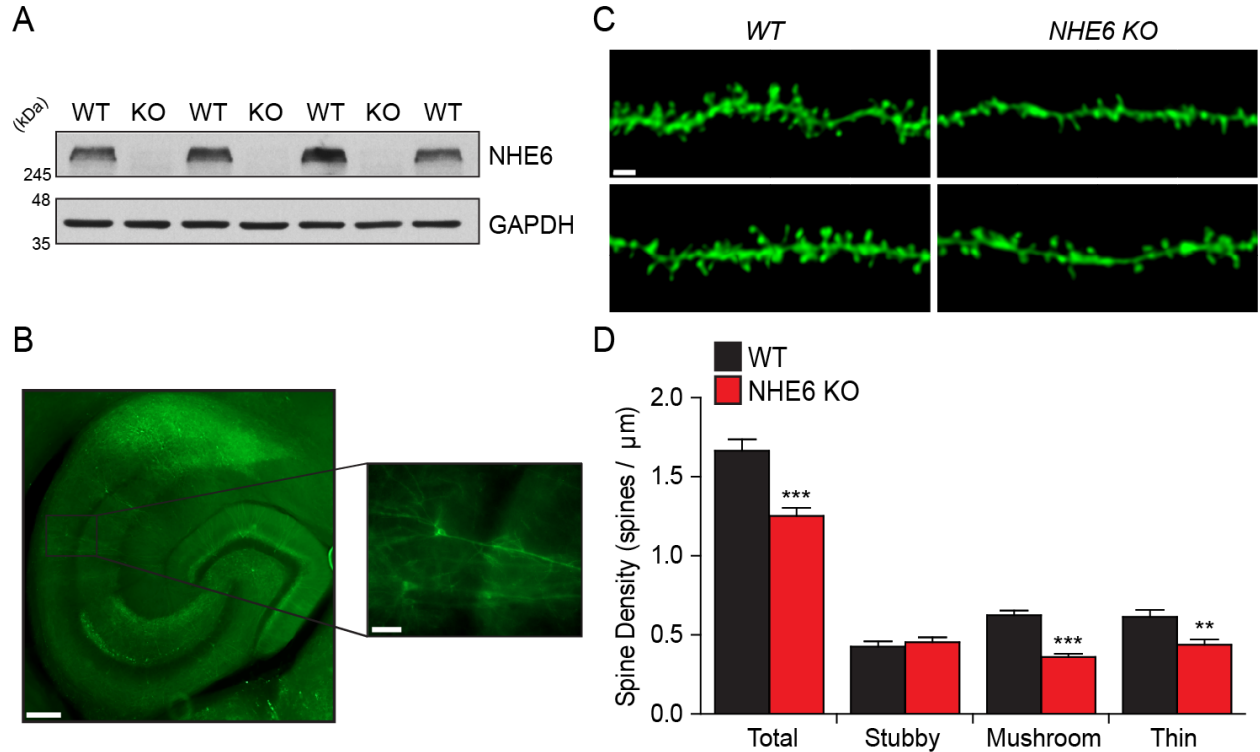


Figure 1: Characterizing reductions in hippocampal CA1 excitatory synapse morphology using a novel mGFP-expressing *Nhe6* KO mouse line. **A:** Representative immunoblot of NHE6 adult WT and *Nhe6* KO hippocampi showing the absence of fully glycosylated and dimerized mature form of NHE6 in KO tissue, with glyceraldehyde 3-phosphate dehydrogenase (GAPDH) included as loading control. **B:** Representative immunofluorescent micrograph of a transverse slice of hippocampus taken from adult *Nhe6* KO mouse expressing mGFP in a subset of hippocampal neurons (scale bar: 200 μm); inset shows magnified view of area CA1 *stratum pyramidale* showing a hippocampal pyramidal neuron (scale bar: 40 μm). **C:** Example confocal micrographs of two mGFP-labeled sections of tertiary dendrite taken from a coronal hippocampal section from an adult WT (left) or *Nhe6* KO (right) male mouse (scale bar: 2 μm). **D:** Mean ± SEM values for total, stubby, mushroom, and thin spines per genotype. WT: n = 743 spines from 449.59 μm of dendrite taken from 17 different cells; KO: n = 678 spines from 543.21 μm of dendrite taken from 20 different cells, 3-4 mice per genotype. **: $p < 0.01$, ***: $p < 0.0001$, unpaired Student's t-test.

As spine size is often correlated with synaptic strength, we next recorded AMPAR-mediated miniature excitatory post-synaptic currents (mEPSCs) under voltage clamp conditions from whole CA1 pyramidal cells in acute brain slices from young adult (P30-P49) WT and KO animals. These recordings revealed a decrease in mEPSC amplitude and an increase in inter-event interval (**Fig. 2A-B, E-J**). The latter finding was indicative of a concomitant reduction in mEPSC frequency, which suggests a loss in the number of functional synapses or a reduction in presynaptic release probability. Intriguingly, we also observed significant increases in rise and decay times of *Nhe6* KO events compared to WT (**Fig. 2C-D**), possibly alluding to a change in the subunit composition of synaptic AMPARs in KO neurons. Thus, adult *Nhe6* KO CA1 principal neurons exemplify a significant reduction in the number and strength of functional excitatory synapses under basal conditions.

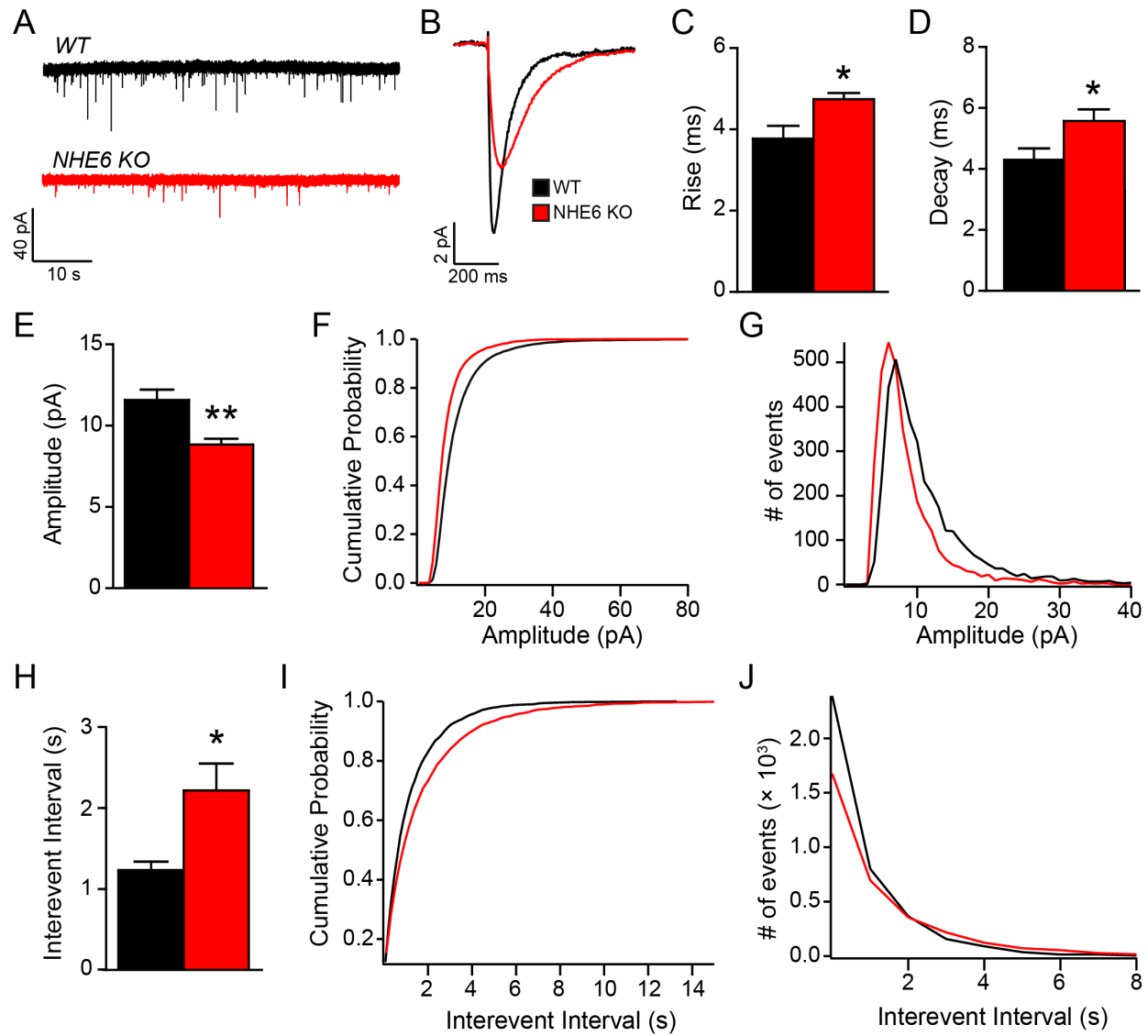


Figure 2: *Nhe6* KO hippocampal pyramidal neurons show alterations in AMPA receptor-mediated excitatory neurotransmission. **A-B:** Example mEPSC current recordings (**A**) and average mEPSC trace (**B**) from a CA1 pyramidal neuron taken from a young adult WT (black) or *Nhe6* KO (red) mouse. **C-D:** Mean \pm SEM rise (**C**) and decay (**D**) times compiled from mean mEPSC kinetic values of each neuron recorded per genotype. **E, H:** Mean \pm S.E.M. values of average mEPSC amplitude (**E**) and interevent interval (**H**) compiled from mean values of each neuron recorded per genotype. **F-G, I-J:** Cumulative probability plots of amplitude (**F**) and interevent interval (**I**), and frequency histogram plots of amplitude (**G**) and interevent interval (**J**), of all mEPSCs recorded from WT and *Nhe6* KO CA1 pyramidal neurons. WT: $n = 17$, KO: $n = 15$ neurons from 3-5 mice per genotype. *: $p < 0.05$, **: $p < 0.01$, unpaired Student's t-test.

These alterations in mEPSC parameters led us to consider possible alterations in both the number and subunit composition of synaptic AMPARs in *Nhe6* KO. To investigate this, we performed immunoblots probing protein levels of AMPAR subunits GluA1 and GluA2. While GluA1 protein levels were comparable between adult WT and *Nhe6* KO hippocampi, we interestingly observed a significant downregulation of GluA2 protein in *Nhe6* KO (**Fig. 3A-B**). Accordingly, additional immunohistochemical experiments showed a significant reduction in GluA2 puncta localized within adult *Nhe6* KO CA1 pyramidal cell dendrites when compared to WT (**Fig. 3C-D**). Overall, the data imply a reduction in overall AMPAR content in dendrites and synapses, which could account for the observed changes in mEPSC amplitude and kinetics. Tangentially, we did not observe any substantial changes in NMDA receptor (NMDAR) subunit GluN2B levels (**Fig. 3A-B**), suggesting that specific subunits of AMPARs are selectively affected as opposed to those of NMDARs in *Nhe6* KO hippocampi.

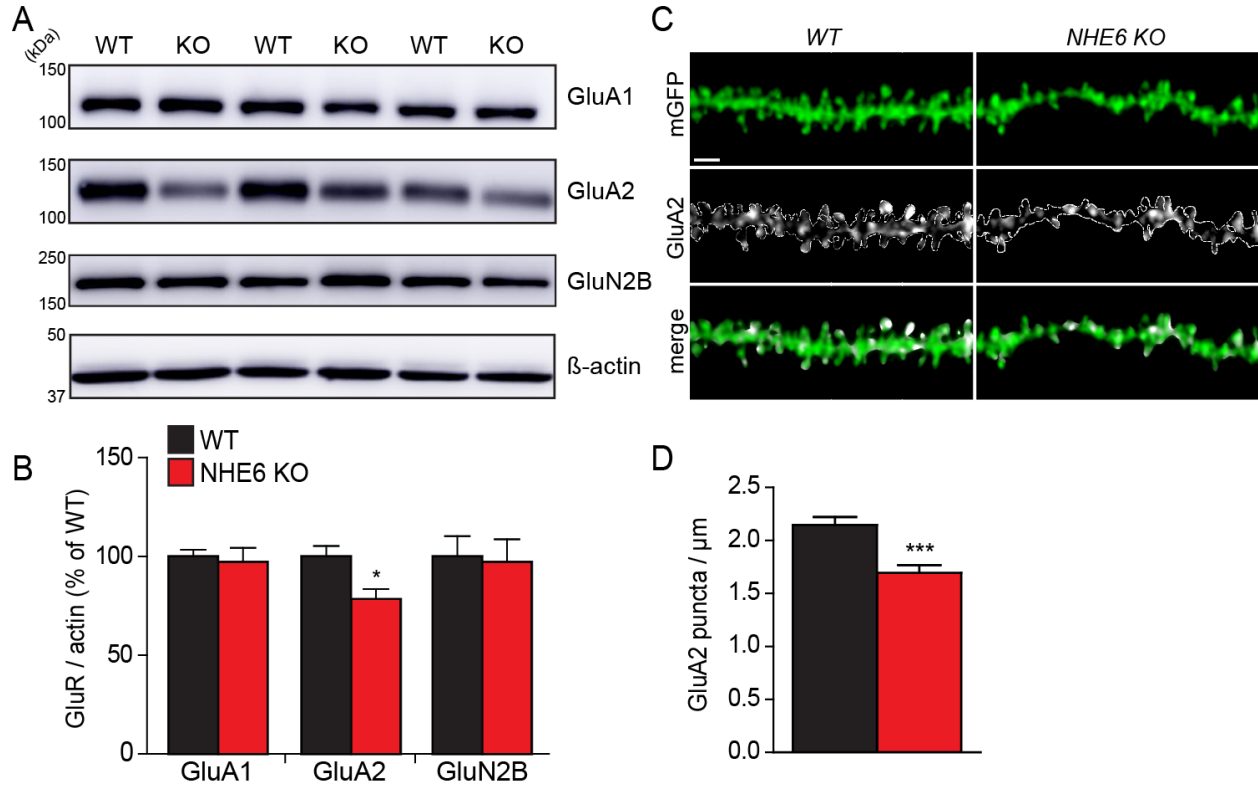


Figure 3: Reduced AMPA receptor protein expression and trafficking in *Nhe6* KO neurons. **A:** Representative immunoblots of GluA1, GluA2, and GluN2B protein levels from adult WT and *Nhe6* KO whole hippocampal lysates, with β-actin shown as loading control. **B:** Mean ± SEM quantification of glutamate receptor protein levels relative to β-actin signal and normalized to WT for each protein of interest in WT and KO tissue. n = 7 animals per genotype. **C:** Example confocal micrographs of a mGFP-labeled section of tertiary dendrite taken from a coronal hippocampal section immunostained with GluA2 from an adult WT (left) or *Nhe6* KO (right) male mouse. Channels are shown separately and merged; dotted line in GluA2 channel indicates mGFP-positive signal (scale bar: 2 μm). **D:** Mean ± SEM quantification of GluA2 puncta density from WT and KO dendrites. n = 18 cells from 4 animals per genotype, *: $p < 0.05$, ***: $p < 0.0001$, unpaired Student's t-test.

3.4.2 Investigating potential changes in NMDAR-dependent LTP in *Nhe6* KO

After uncovering basal changes in synaptic number and function in *Nhe6* KO, we next assessed possible changes in synaptic plasticity within *Nhe6* KO hippocampal circuitry. To this end, we again prepared acute hippocampal slices from young adult (P30-49) male animals, subjected Schaffer collaterals (SCs) to theta-burst stimulation (TBS), and recorded field excitatory postsynaptic potential (fEPSP) responses from hippocampal area CA1. We found that upon TBS, WT slices were able to show a significant post-tetanic potentiation (PTP), with fEPSP amplitude initially peaking at ~165% of baseline before diminishing somewhat to ~135% and then gradually increasing to ~180% 40 min post-TBS (**Fig. 4**); this response matches standard TBS-LTP expression [48]. In contrast, *Nhe6* KO slices surprisingly underwent a transient synaptic depression after TBS, with relative fEPSP amplitude dropping to ~75% of baseline before steadily increasing to ~135% over the course of the recording (**Fig. 4**). Therefore, KO hippocampal slices show a clear significant deficit in PTP immediately following TBS before potentiating thereafter, albeit to a significantly smaller degree than WT slices. These results suggest clear deficits in post-tetanic mechanisms as well as protein synthesis-independent functional potentiation at SC-CA1 synapses in *Nhe6* KO.

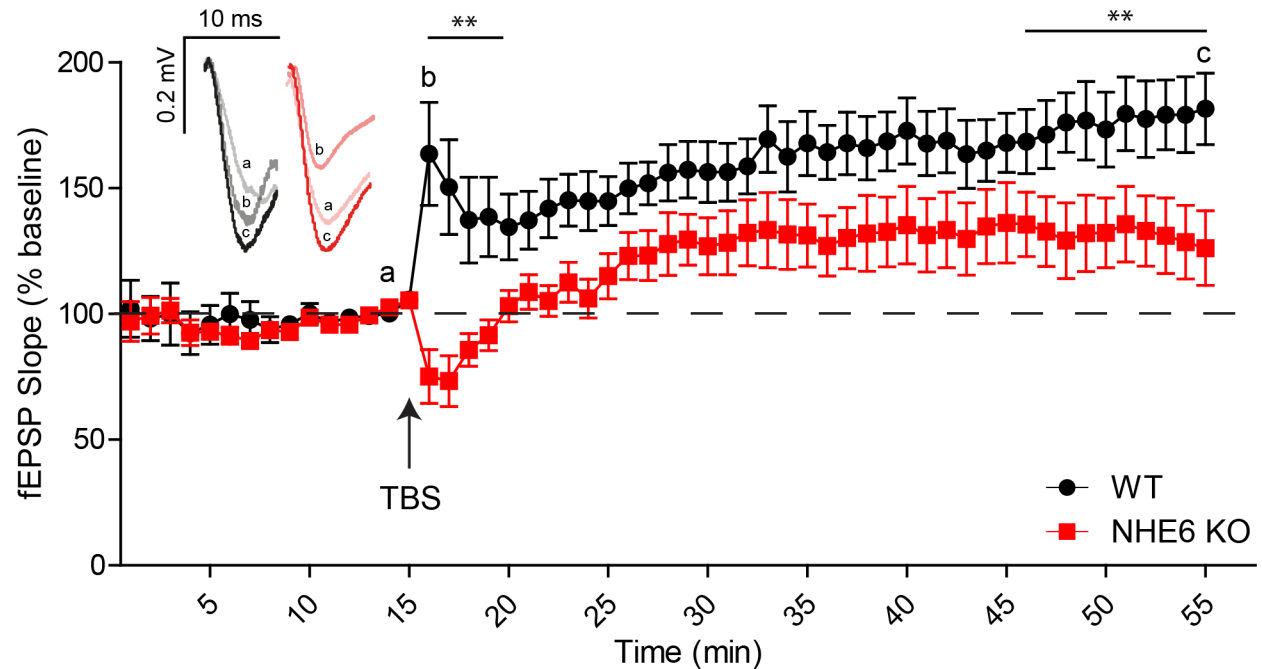


Figure 4: Reduced Schaffer collateral-CA1 TBS-LTP in *Nhe6* KO hippocampi when compared to WT. Quantification shows mean \pm S.E.M. of field EPSP (fEPSP) amplitudes (% relative to baseline) from 15 min pre-TBS until 40 min post-TBS. Inset shows representative traces selected 1 min pre-TBS (a), 1 min post-TBS (b), and 40 min post-TBS (c) from WT (left, black) and KO (right, red); WT: $n = 12$, KO: $n = 11$ slices from 4-6 animals per genotype. **: $p < 0.01$, Mann-Whitney U test.

We next sought to address whether impairments in the trafficking and post-translational modifications of AMPARs could explain the occlusion of LTP in *Nhe6* KO. To properly assess this experimentally, we prepared primary hippocampal neurons from either WT or KO pups and subjected mature (≥ 14 DIV) cultures to glycine-mediated chemical LTP (ChemLTP) to activate all synapses, with unstimulated sister WT and KO cultures as controls. This protocol has previously been shown to mimic NMDAR-dependent LTP at SC-CA1 synapses *in vivo* [21,41,49] and allowed us to extract sufficient amounts of protein for immunoblotting experiments. We first performed cell-surface biotinylation experiments to assess the plasmalemmal insertion of AMPARs following stimulation. As expected, stimulated WT cultures showed significant

upregulations of both surface GluA1 and GluA2 by 20 min post-ChemLTP relative to controls. In contrast, while *Nhe6* KO cultures demonstrated increases in surface GluA1, they did not show the same change in surface GluA2 20 min following ChemLTP (**Fig. 5A, C**). Thus, KO neurons show a deficiency in GluA2 exocytosis following LTP, mimicking the subunit-specific decreases in GluA2 protein levels and dendritic trafficking previously observed *in vivo*. While we did not observe changes in overall GluA1 protein levels *in vivo* or in its insertion of into the cell membrane following LTP in KO, phosphorylation of GluA1 at specific serine residues is also known to play a prominent role in regulating activity-dependent AMPAR trafficking and channel properties. Hence, we then investigated two prominent phosphorylated GluA1 (pGluA1) states: the Ca^{2+} /calmodulin-dependent kinase II (CaMKII)/protein kinase C (PKC) site S831, and the protein kinase A (PKA) site S845, as these are two of the most well-defined post-translational modifications that occur following the induction of NMDAR-dependent LTP [32,33,50]. Although we saw a significant increase in pGluA1-S831 in both WT and *Nhe6* KO cultures subjected to ChemLTP stimulation, we did not observe a similar upregulation of pGluA1-S845 levels in *Nhe6* KO neurons 20 min post-ChemLTP when compared to WT (**Fig. 5B, D**), suggesting that there may be some deficit in the phosphorylation of GluA1 by PKA that normally mediates the functional response to LTP in *Nhe6* KO. Neither total GluA1 or GluA2 protein levels differed significantly between WT and KO whole cell lysates at this developmental time point *in vitro* (**Fig. 5E-F**), indicating that changes in total protein levels do not account for the lack of AMPAR modifications in KO neurons following ChemLTP.

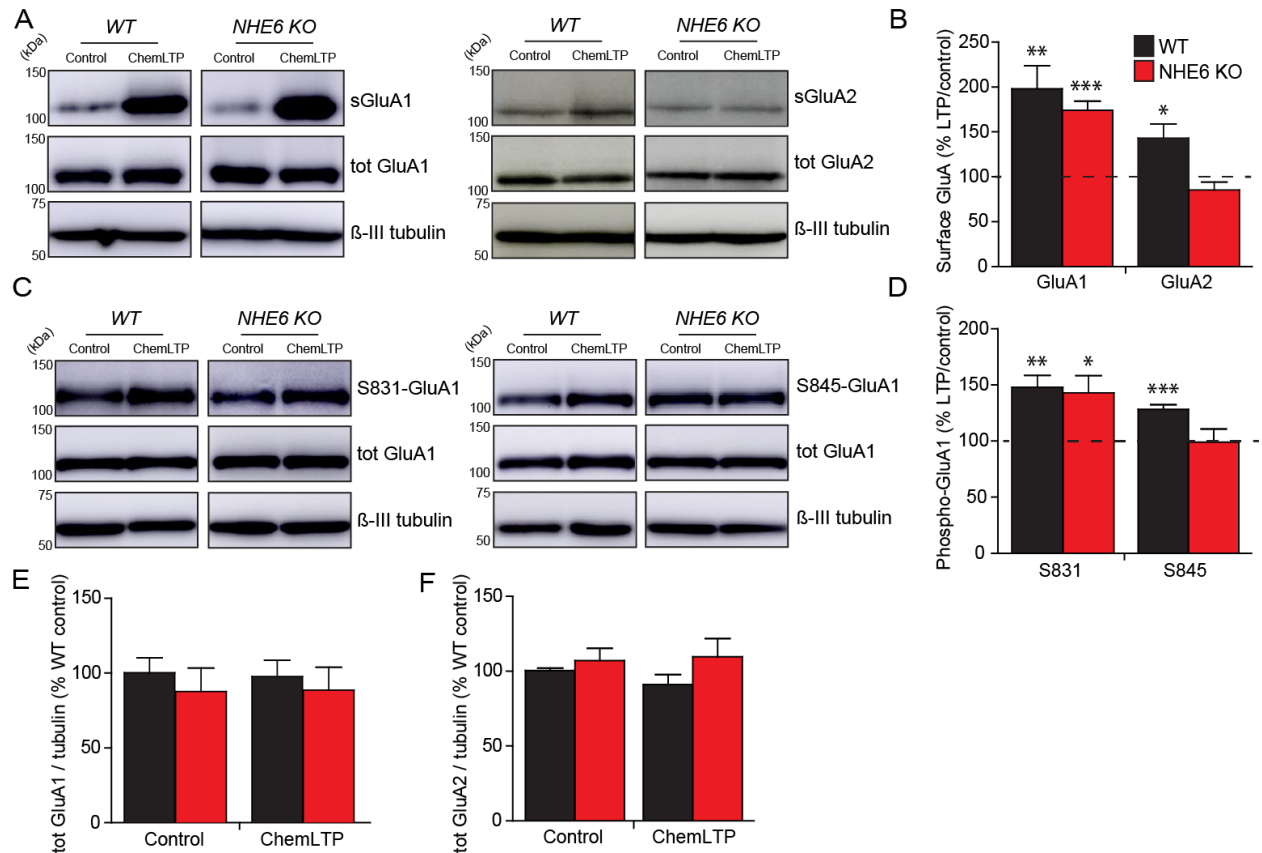


Figure 5: *Nhe6* KO hippocampal neurons show reductions in AMPA receptor membrane insertion and post-translational modifications following glycine-mediated ChemLTP. A, C: Representative immunoblots of cell surface biotinylation experiments analyzing AMPA receptor subunits GluA1 (left) and GluA2 (right) (A), as well as immunoblots of GluA1 phosphorylated at S831 (left) and S845 (right) sites (C), performed on lysates taken from unstimulated control or ChemLTP-stimulated primary hippocampal neuron cultures prepared from WT and *Nhe6* KO tissue. Surface GluA (sGluA, A) or phospho-GluA1 (C) (top) and total GluA (tot GluA, middle) fractions are shown, with β -III tubulin (bottom) as loading control. **B, D:** Mean \pm S.E.M. change of surface GluA (B) and phospho-GluA1 (D) signal intensity, relative to total GluA fraction and normalized to control (indicated by dotted line at 100%), for WT and *Nhe6* KO cultures. **E-F:** Mean \pm S.E.M. fluorescence intensity of total GluA1 (E) and GluA2 (F) fractions of control and ChemLTP-stimulated WT and *Nhe6* KO cultures relative to β -III tubulin and normalized to WT control. sGluA1: A-B: WT: n = 6, KO: n = 4; sGluA2: WT: n = 4, KO: n = 3 culture preparations; C-D: S831-GluA1: n = 4, S845-GluA1: n = 8 culture preparations per genotype. *: $p < 0.05$, **: $p < 0.01$, ***: $p < 0.0001$, unpaired Student's t-test.

After uncovering electrophysiological and protein trafficking disturbances in the response to LTP from *Nhe6* KO hippocampi, we next evaluated whether the spines of *Nhe6* KO pyramidal neurons would also show structural impairments after LTP. To this end, we performed volumetric time-lapse confocal analyses on mGFP-labeled primary hippocampal neurons subjected to ChemLTP stimulation. As anticipated, WT neurons showed significant increases in the spine head volume (SHV) of mushroom- and thin-type spines relative to baseline, which continued steadily over a 20 min period following ChemLTP stimulation. Conversely, KO neurons only demonstrated significant increases in the SHV of thin spines, while larger mushroom-type spines failed to enlarge after stimulation relative to baseline (**Fig. 6A-C**). Pooling together total analyzed spines within each genotype, we noted that WT SHV was significantly greater than that of KO at five min after ChemLTP (**Fig. 6D**), which also suggested an overall delay in spine remodeling. Mirroring our functional recordings, these volumetric findings again exemplify some degree of impairment in structural LTP in *Nhe6* KO. Remarkably, when we assessed spine motility using previously established parameters [51], KO spines of all types showed a significantly higher spine motility index values than WT spines. Even prior to ChemLTP stimulation, KO spines showed a high degree of protractions and retractions that was significantly accentuated upon activity induction, which did not occur in WT (**Fig. 6E-G**). Taken together, *Nhe6* KO hippocampi show significantly less functional and structural LTP expression than that seen in WT.

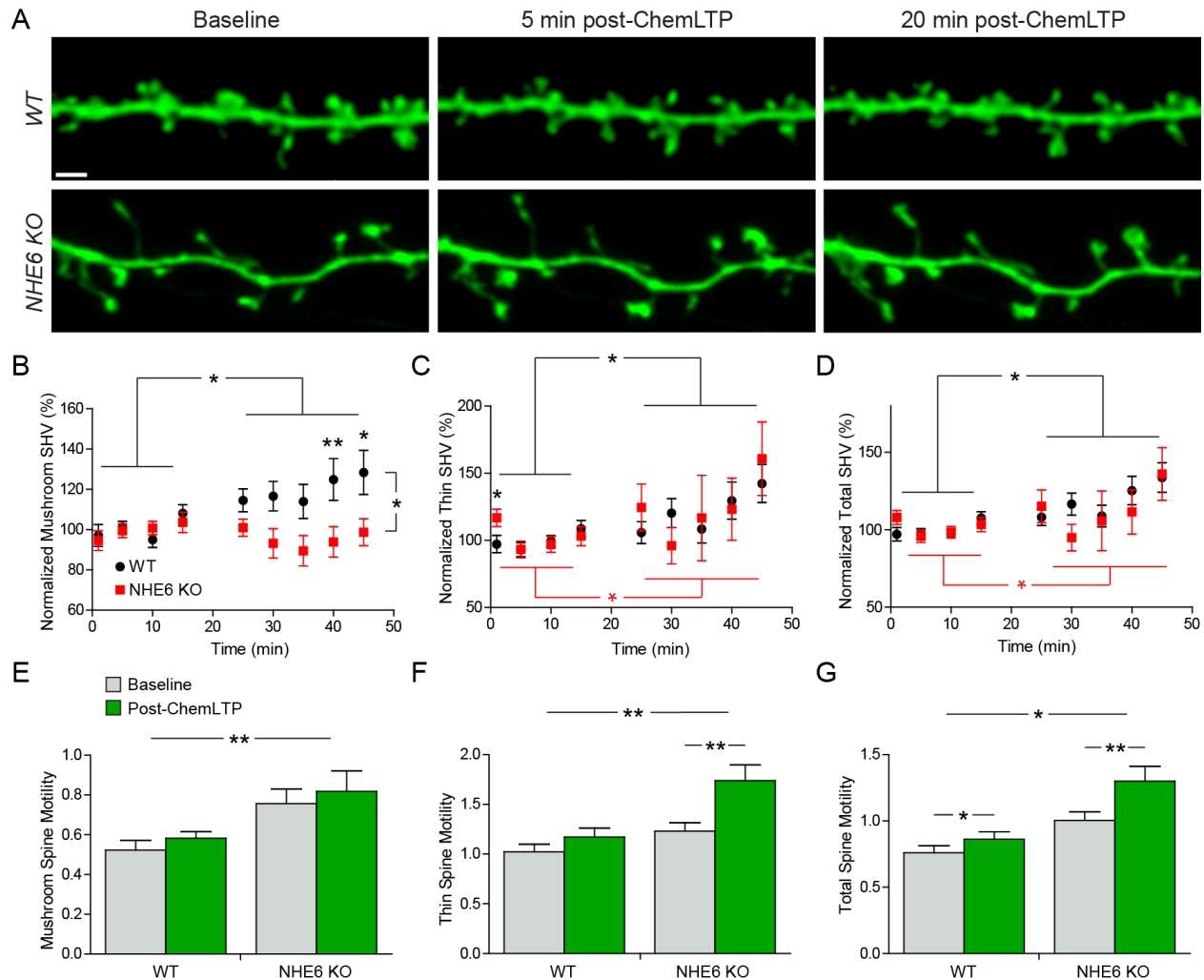


Figure 6: *Nhe6* KO hippocampal neuron spines show impairments in structural remodeling and enhanced motility following glycine-mediated ChemLTP. **A:** Representative confocal micrographs of a section of mGFP-labeled dendrite taken from a WT (top) or *Nhe6* KO (bottom) primary hippocampal neuron imaged 15 min before (left), and 5 min (middle) and 20 min (right) following ChemLTP stimulation (right). Scale bar: 2 μ m. **B-D:** Mean \pm SEM quantification of spine head volume (normalized to mean baseline measurements) for mushroom (**B**), thin (**C**), and total (**D**) spines for all cells analyzed of each genotype. **E-G:** Mean \pm SEM spine motility indices at all time points before and post-ChemLTP for mushroom (**E**), thin (**F**), and total spines (**G**) for each genotype. WT: $n = 60$ spines from 12 cells, KO: $n = 60$ spines from 12 cells, 3 separate experiments. *: $p < 0.05$, **: $p < 0.01$, ***: $p < 0.0001$, Repeated Measures ANOVA with Bonferroni post-hoc test (**B-G**), paired Student's t-test (**E-G**).

3.4.3 Evaluating *Nhe6* KO animals in behavioural paradigms

Taking into account these deficits in neuronal circuit formation and plasticity within the KO hippocampus, we next assessed if such changes would impair the performance of adult (P60-P90) *Nhe6* KO mice in hippocampal-dependent learning and memory tasks. Given that our electrophysiological experiments primarily focused on deficits in the earlier phases of LTP, we first tested the mice in tasks with shorter latency periods. Employing a T-maze spontaneous alternation task, we found that both WT and KO mice spent a significantly greater time spent in the novel arm of the maze upon being granted access, with no difference in total exploration time (**Fig. 7A-B**). Moreover, when we subjected the mice to a short-term contextual fear conditioning (CFC) task, we found that both WT and *Nhe6* KO mice showed a substantial and comparable freezing response one hour after the initial foot-shock (**Fig. 7C**). These results indicated that *Nhe6* KO mice were able to learn comparably well to WT mice in these short-term memory paradigms.

We then investigated if P60-P90 *Nhe6* KO mice showed possible differences in novel object location (NOL) and novel object recognition (NOR) tasks, which assess longer-term forms of memory. In both tasks, WT and *Nhe6* KO animals showed no difference in their ability to distinguish between familiar objects and novel objects or object locations (**Fig. 7D, F**). However, the KO animals spent significantly less time exploring the objects overall when compared to WT (**Fig. 7E, G**), which was primarily indicative of locomotor impairments in NHE6 deficient animals. Taken together, these results suggest that between two to three months of age, *Nhe6* KO males are indeed able to demonstrate learning in short- and long-term memory tasks similarly to age- and sex-matched WT. In spite of the indications that KO mice at this age already show significant deficits in locomotor ability when compared to WT, these deficiencies did not appear to impact their performance in these tasks.

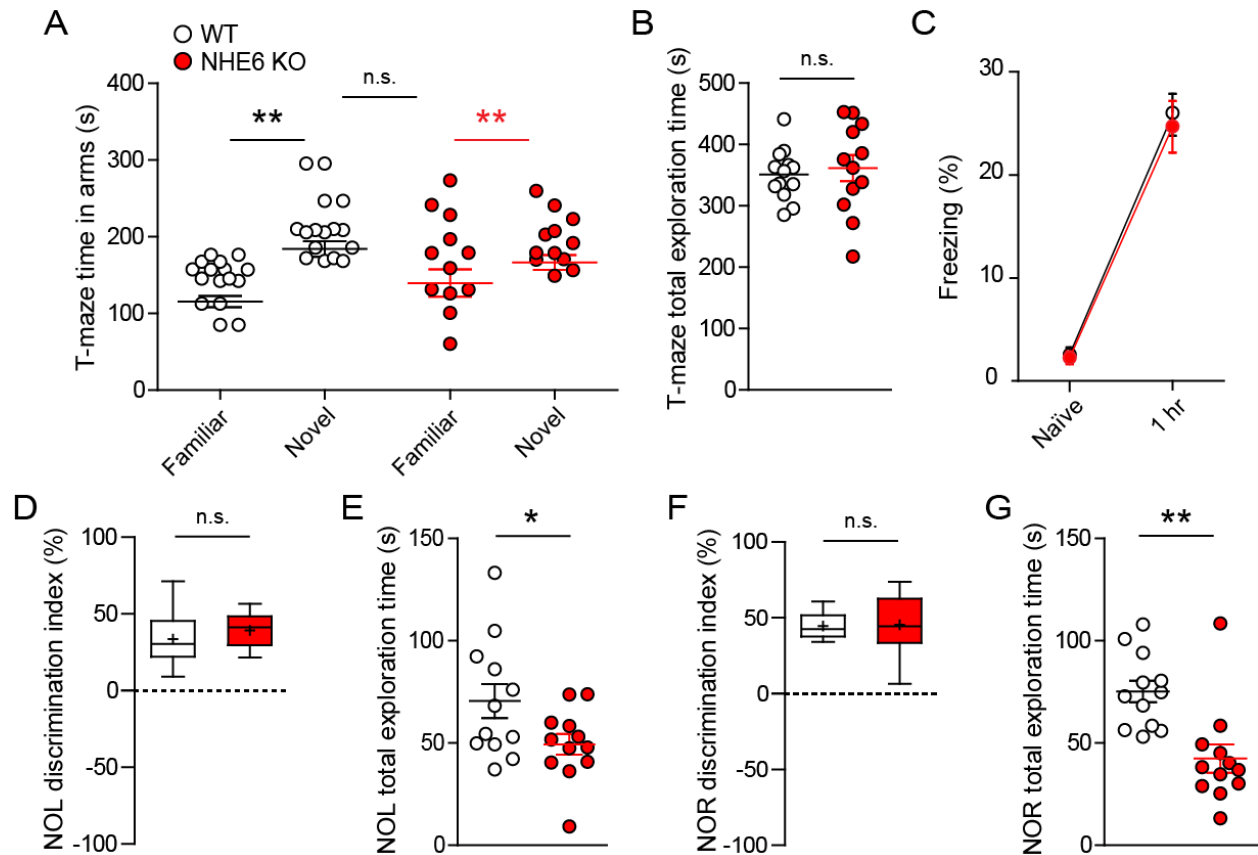


Figure 7: Adult *Nhe6* KO mice do not show apparent deficits in learning tasks when compared to age- and sex-matched WT mice. **A-B:** Summary of results from spontaneous T-maze alternation tasks. **A:** Mean \pm SEM of time spent in familiar and novel arms for WT and KO mice. **B:** Mean \pm SEM total time spent exploring in T-maze for WT and KO mice. WT: $n = 13$, KO: $n = 12$ mice. **C:** Mean \pm SEM freezing response in a contextual fear conditioning task (1 shock, 0.7 mA, 2 sec) before pairing with shock (naïve) and 1 h later. **WT:** $n = 20$, KO: $n = 18$ mice. **D-E:** Summary of results from novel object location (NOL) task. **D:** Box plot of discrimination indices in NOL task for WT and KO mice; median indicated by midline, mean indicated by + symbol. **E:** Mean \pm SEM total time spent exploring in NOL task for WT and KO mice. **F-G:** Summary of results from novel object recognition (NOR) task. **F:** Box plot of discrimination indices in NOL task for WT and KO mice; median indicated by midline, mean indicated by + symbol. **G:** Mean \pm SEM total time spent exploring in NOR task for WT and KO mice. For NOL and NOR tasks, WT: $n = 12$, KO: $n = 12$ mice. *: $p < 0.05$; **: $p < 0.01$; paired Student's t-test (**A**, **C**); Repeated Measures ANOVA (**A**, **C**); unpaired Student's t-test (**B**, **D-E**, **G**); Welch's t-test (**F**).

3.4.4 Restoring losses in *Nhe6* KO synaptic density and plasticity using a TrkB agonist

Previous reports have shown decreases in activated levels of pTrkB in *Nhe6* KO neurons [25,52], which was associated with deficits in circuit development. In light of this, we attempted to enhance TrkB activation directly using the small-molecule BDNF mimetic 7,8-dihydroxyflavone (7,8-DHF) to examine whether this prodrug could restore spine density and plasticity in *Nhe6* KO neurons. To first verify if 7,8-DHF augmented TrkB activation in our model by applying 7,8-DHF (1 μ M) for 30 min to WT and KO primary hippocampal neurons. As expected, we observed elevated levels of TrkB phosphorylated at the Y816 site, which undergoes extensive phosphorylation in response to both BDNF and 7,8-DHF [53], in treated cultures from both genotypes when compared to sister cultures treated with an equivalent volume of vehicle (dimethyl sulfoxide, DMSO) (**Fig. 8A-B**). Intriguingly, 7,8-DHF treatment also significantly increased levels of total TrkB protein in *Nhe6* KO cells (**Fig. 8A-B**), which implied that TrkB was rapidly synthesized in response to the compound. To assess if 7,8-DHF could then modulate spine density, we instead employed organotypic hippocampal slice cultures, which better preserve the *in vivo* neuronal cytoarchitecture of the hippocampus upon maturity (≥ 21 DIV) [54]. Akin to our observations in adult mice, mature *Nhe6* KO cultures treated only with vehicle exhibited similar attenuations in mushroom, thin, and total spine densities when compared to WT cultures (**Fig. 8D-E**). 24 h after supplementation of culture media with 7,8-DHF (1 μ M), *Nhe6* KO organotypic cultures experienced a significant upregulation of thin- and total-spine densities when compared to vehicle-treated KO sister cultures (**Fig. 8D-E**). Conversely, 24 h 7,8-DHF treatment resulted in a small yet significant decrease of WT mushroom spine density, although it did not significantly impact overall spine density (**Fig. 8D-E**). These results suggest that in the absence of external stimuli, 7,8-DHF treatment could induce the formation or stabilization of synapses in KO neurons.

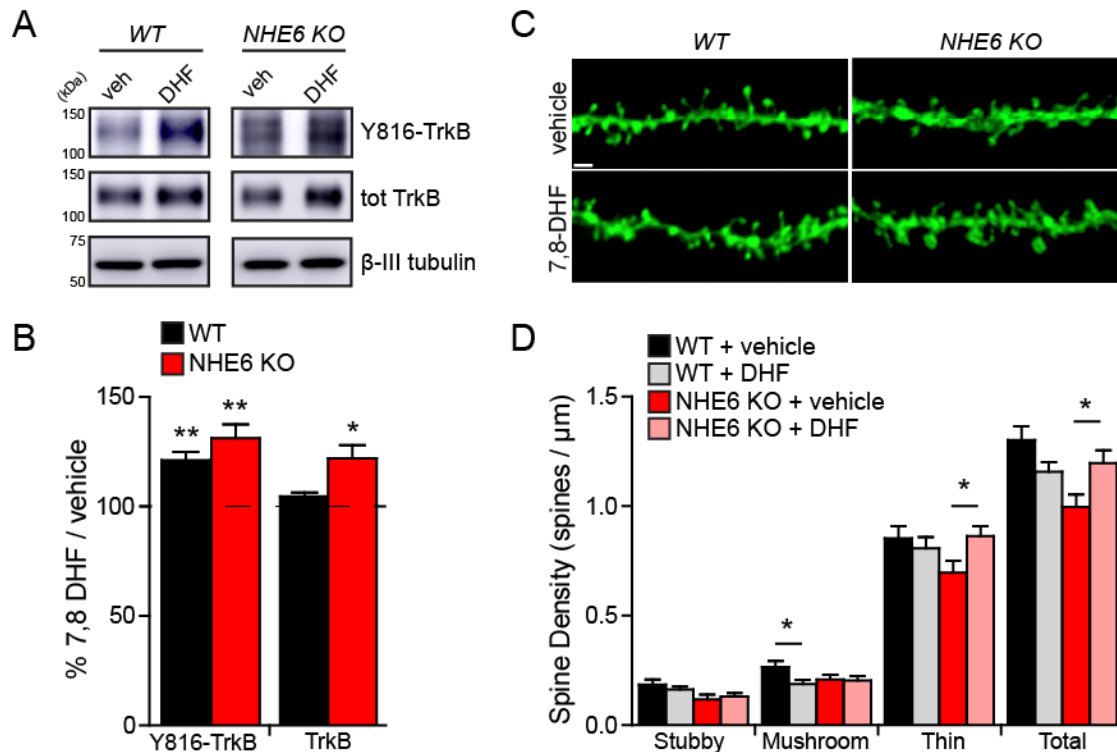


Figure 8: Treatment of TrkB agonist 7,8-DHF restores dendritic spine density in *Nhe6* KO hippocampal neurons. **A:** Representative immunoblot of phosphorylated TrkB at the Y816 site (Y816-TrkB, top) and total TrkB protein (tot TrkB, middle) of whole cell lysates taken from primary hippocampal neurons treated with vehicle (DMSO) or 7,8-dihydroxyflavone (7,8-DHF), with β -III tubulin (bottom) as loading control. **B:** Mean \pm SEM quantification of fluorescent band intensities of Y816-TrkB (left) and TrkB (right) relative to vehicle treatment for each culture preparation. $n = 3$ separate culture experiments per genotype. **C:** Example confocal micrographs of a mGFP-labeled section of tertiary dendrite taken from a > 21 DIV organotypic hippocampal slice culture prepared from WT (left) or *Nhe6* KO (right) tissue and treated with vehicle (top) or 7,8-DHF (1 μ m for 24 h, bottom). Scale bar: 2 μ m. **D:** Mean \pm SEM values for total, stubby, mushroom, and thin spines per genotype and treatment condition. WT + vehicle: $n = 689$ spines along 537.71 μ m of dendrite taken from 22 different cells from 7 cultures; WT + DHF: $n = 659$ spines along 566.63 μ m of dendrite taken from 24 different cells from 7 cultures; KO + vehicle: $n = 436$ spines along 441.96 μ m of dendrite taken from 18 different cells from 6 cultures; KO + DHF: 376 spines along 322.34 μ m of dendrite taken from 14 different cells from 4 cultures. *: $p < 0.05$, unpaired Student's t-test.

We then tested if 7,8-DHF application could also rescue the structural synaptic deficits in *Nhe6* KO. To this end, we repeated time-lapse confocal imaging experiments with WT and *Nhe6* KO primary hippocampal neurons pre-treated with 7,8-DHF (1 μ M) for 30 min prior to ChemLTP stimulation. In KO neurons, 7,8-DHF application enabled significant SHV enlargements of both mushroom- and thin-type spines following ChemLTP, signifying a restoration of structural LTP in these cells (**Fig. 9A-D**). In contrast, 7,8-DHF pre-treatment dampened morphological remodeling in WT spines, with average SHV showing only a modest increase following ChemLTP before returning to baseline values by the end of the experiment (**Fig. 9A-D**). Moreover, 7,8-DHF pre-treatment dampened KO mushroom spine motility to levels comparable to that recorded in WT (**Fig. 9E**). While the mean motility of thin and total spines remained significantly elevated in *Nhe6* KO spines when compared to WT, 7,8-DHF-treated spines no longer showed a significant increase in spine motility following ChemLTP stimulation (**Fig. 9E-G**). Thus, 7,8-DHF treatment appears to exert a genotype-specific effect with regards to activity-dependent spine remodeling: while 7,8-DHF partially improves spine stability and volumetric augmentations to allow for structural potentiation in *Nhe6* KO spines, the drug conversely has a restrictive effect in WT by blocking the development and maintenance of larger, mushroom-type spines. It is possible that this trend may also apply to functional LTP expression as well, although this remains to be verified with future fEPSP recordings from WT and KO hippocampi.

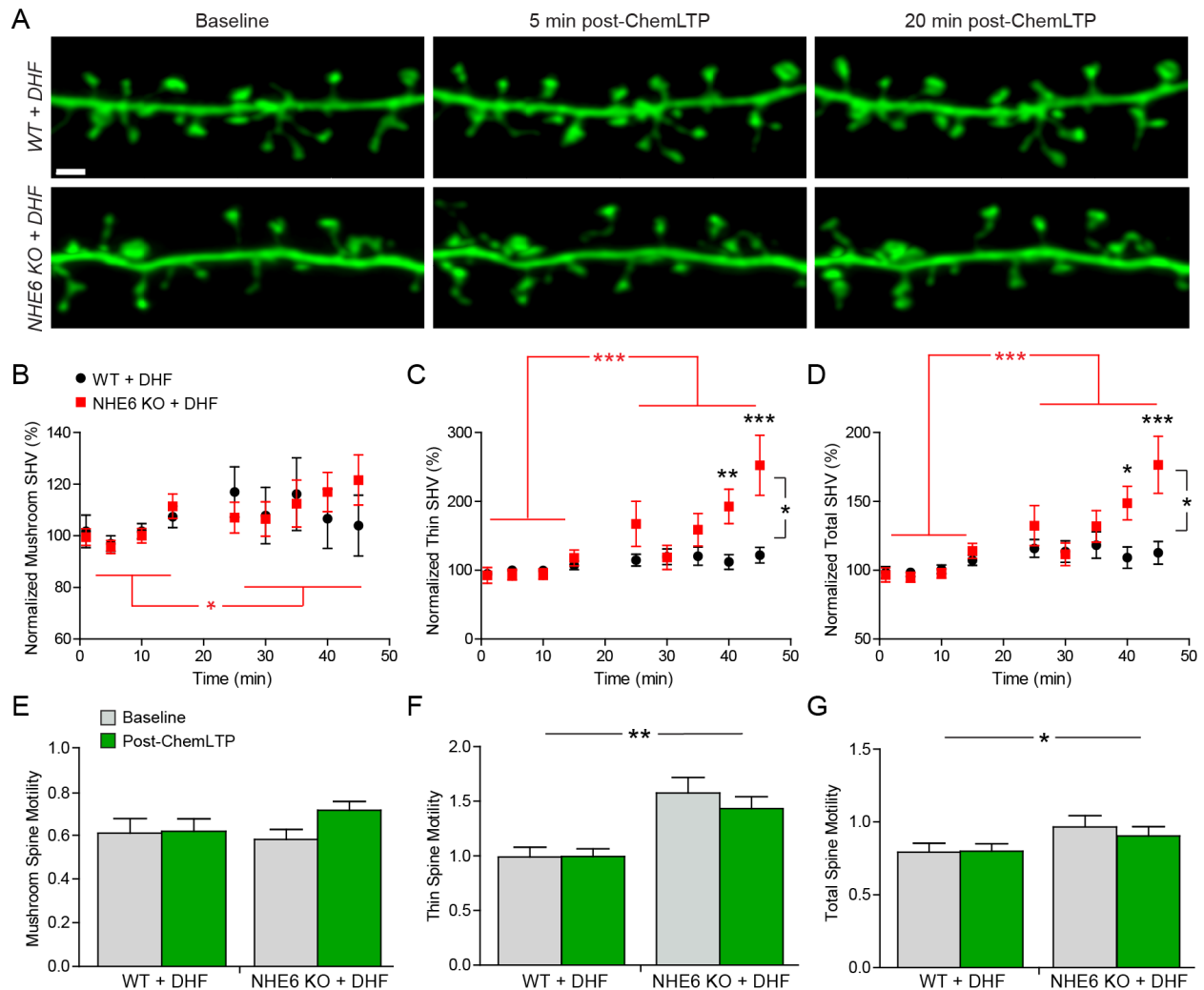


Figure 9: 7,8-DHF ameliorates structural remodeling in *Nhe6* KO spines following glycine-mediated ChemLTP. **A:** Representative confocal micrographs of a section of mGFP-labeled dendrite taken from a WT (top) or *Nhe6* KO (bottom) primary hippocampal neuron pre-treated with 7,8-DHF for 30 min, and imaged 15 min before (left), and 5 min (middle) and 20 min (right) following ChemLTP stimulation (right). Scale bar: 2 μ m. **B-D:** Mean \pm SEM quantification of spine head volume (normalized to mean baseline measurements) for mushroom (**B**), thin (**C**), and total (**D**) spines for all cells analyzed of each genotype. **E-G:** Mean \pm SEM spine motility indices at all time points before and post-ChemLTP for mushroom (**E**), thin (**F**), and total spines (**G**) for each genotype. WT: n = 58 spines from 10 cells, KO: n = 62 spines from 12 cells, 3 separate experiments. *: $p < 0.05$, **: $p < 0.01$, ***: $p < 0.0001$, Repeated Measures ANOVA with Bonferroni post-hoc test (**B-G**), paired Student's t-test (**E-G**).

3.5 DISCUSSION

Although patients diagnosed with CS present with moderate to severe intellectual disability that likely arises from dysfunctional neural circuitry, in-depth analyses of the potential mechanisms underlying these deficits have been lacking. In the present study, we addressed this by investigating how the absence of NHE6 perturbs the trafficking of membrane-bound receptors to disrupt excitatory synaptic number, transmission, and plasticity in the hippocampus.

We were first intrigued by possible changes in excitatory synaptic morphology in *Nhe6* KO pyramidal neurons. Initially, we noted a significant decrease in mature dendritic spine density along mGFP-labeled CA1 hippocampal pyramidal neurons within adult *Nhe6* KO hippocampi. This finding was reflective of previously reported observations in more juvenile (P21) KO tissue [25], as well as our previous *in vitro* data on clinical *SLC9A6* mutations [16,41]. Patch clamp recordings also revealed that AMPAR-mediated mEPSC frequency was reduced in *Nhe6* KO CA1 pyramidal neurons, which further corroborated the significant reduction of excitatory synaptic connections on to CA1 principal cells. This finding builds upon previous fiber volley data showing reduced membrane responses in *Nhe6* KO hippocampi, which was also implicative of a decrease in the number of functional synapses [25]. As *in vivo* spine densities can vary greatly depending on experience and time of sacrifice, we later assessed spine remodeling by performing time-lapse confocal imaging data on primary hippocampal neurons subjected to glycine-mediated ChemLTP stimulation. From these live-imaging experiments, we found that *Nhe6* KO spines were significantly more motile when compared to WT both prior to and following ChemLTP. Larger mushroom KO spines were thus unable to significantly show a significant increase in SHV following ChemLTP, presumably due to this impairment in spine stabilization. Although smaller thin spines along *Nhe6* KO dendrites were able to enlarge upon stimulation, these treated spines

were also significantly more motile when compared to their baseline motility and to that of WT spines overall, resulting in their SHV changes being quite variable after ChemLTP. Whether these enlarged thin spines in *Nhe6* KO are able to persist beyond the time frame measured in the present study remains to be investigated with longer term evaluations.

As spine motility generally dampens over development [51], the enhanced spine dynamics seen in *Nhe6* KO suggest a lack of proper spine maturation and stabilization. From this structural data, we speculate that cytoskeletal dynamics, which normally allow for spine formation, plasticity, and maintenance, are disrupted in *Nhe6* KO neurons. The morphogenesis and remodeling of dendritic spines are dependent upon the trafficking and regulation of numerous actin-associated proteins, synaptic scaffolds, and cell surface molecules, which could be impaired due to endosomal trafficking deficits in *Nhe6* KO. Elucidating of these numerous regulators are impaired in *Nhe6* KO is a topic warranting further study. Spine motility can also be influenced by Ca^{2+} activity within the spine. While the influence of Ca^{2+} has been controversial, it has previously been hypothesized that high or low levels of intracellular $[\text{Ca}^{2+}]$ may cause spine retractions, while intermediate levels can enhance spine growth [55]. Given the role of NHE6 in mediating activity-dependent endosomal trafficking into spines [21,41], it is conceivable that one or more of these mechanisms that regulate actin or Ca^{2+} dynamics are dependent upon NHE6 and impaired in its absence, thereby prohibiting spine formation and expansion following LTP induction.

Disturbances in spine density are frequently observed in human patients and murine models of neurodevelopmental disorders, and changes in spine motility have been reported in the latter [56–59]. For instance, reduced spine density is commonly observed in Angelman syndrome (AS), another rare genetic disorder characterized by intellectual disability and autistic behaviours akin to CS [45,60–62]. The motility changes reported here are also comparable to those seen in mice

lacking the *Fmr1* gene encoding fragile X mental retardation protein (FMRP), which serve as a model for Fragile X syndrome (FXS), the most prevalent form of X-linked intellectual disability [63,64]. Interestingly, *Fmr1* KO cortical pyramidal neurons show an increase in the proportion of thin, filopodia-like structures, which are indicative of defective synaptic maturation [65–67]. Accordingly, *in vivo* live imaging of *Fmr1* KO cortical pyramidal cells revealed augmented spine turnover similar to those reported here in *Nhe6* KO neurons [68–70]. These aberrations in *Fmr1* KO neurons have been found to be due, in part, to altered signaling through Rho-family GTPase Rac1 [71]. As Rac1 is involved in cytoskeletal reorganization and is thus necessary for spine growth and stabilization [72], it is possible that similar mechanisms may also play a role in *Nhe6* KO neurons. Additional investigations into the levels, activation, and trafficking of actin remodeling proteins may provide further insights into the abnormal spine dynamics reported here.

In accordance with the reduced mushroom spine density observed along *Nhe6* KO dendrites, we subsequently discovered attenuations in synaptic strength and AMPAR content, all of which are typically correlated with one another [56]. Specifically, we saw a dampening of mEPSC amplitude that was accompanied by decreased GluA2 protein levels and dendritic AMPAR trafficking in KO hippocampi. While these deficits could arise from impairments in GluA2 transcription and translation, we believe that this reduction in GluA2 is primarily the result of endosomes being hyperacidified in *Nhe6* KO neurons [25], which could result in GluA2 being mistargeted to and degraded within acidic lysosomal compartments. Indeed, we and others have recently reported that the loss of proper endosomal pH homeostasis in the absence of NHE6 can lead to the aberrant lysosomal degradation of various membrane-bound cargo, including endosomal AMPARs and pTrkB receptors [25,41,73]. As such, these trafficking deficits may impair the localization of GluA2-positive AMPARs at synapses in *Nhe6* KO circuitry. Notably,

the specific loss of GluA2 can indeed pose a profound effect on excitatory synaptic function. This is because the short-tailed GluA2 subunit is found in the majority of AMPAR complexes and confers Ca^{2+} impermeability due to Q/R editing of the mRNA encoding the subunit [74,75]. Moreover, the GluA2 C-terminal region is important for the proper trafficking and stability of synaptic AMPARs, though it is not absolutely essential [76,77]. Removal of GluA2 has been shown to diminish AMPAR localization at hippocampal synapses and induce the assembly of GluA1 and GluA3 homomers that are not typically present *in vivo* [78–80]. Thus, a mistrafficking of GluA2 in *Nhe6* KO raises the possibility of a global disturbance in AMPAR composition and synaptic stabilization, and whether issues in AMPAR gene expression and protein synthesis are also prevalent in *Nhe6* KO remains to be determined. Indeed, the *GRIA2* gene encoding GluA2 has recently been put forward as a commonly mutated locus in patients with intellectual disability and neurodevelopmental deficits [81], highlighting the importance of this subunit in mediating excitatory neurotransmission and cognitive function. Parenthetically, a selective decrease in GluA2 may also result in an aberrant increase in the assembly of Ca^{2+} -permeable (CP)-AMPARs that lack the edited form of the GluA2 subunit. Although CP-AMPARs are important during development and plasticity, upregulations in CP-AMPARs has been found to contribute to excitotoxic neuronal death in other chronic neurodegenerative disorders [82–85]. However, we did not observe a change in GluA1 protein content or mEPSC amplitude in *Nhe6* KO principal neurons, suggesting that a pathological increase of CP-AMPARs in *Nhe6* KO unlikely.

Taking into account these changes in AMPAR trafficking, we also assessed LTP expression at hippocampal SC-CA1 synapses. Disruptions in synaptic plasticity are typically regarded as cellular correlates for cognitive impairments and have been reported in murine models of disorders involving intellectual disability, such as AS, FXS, Down's syndrome, and Rett's

syndrome, as well as neurodegenerative disorders such as Alzheimer's and Parkinson's diseases [86–89]. Accordingly, we observed that while *Nhe6* KO hippocampi eventually showed some degree of potentiation compared to control 40 min following TBS, they potentiated to a significantly less extent than WT. At SC-CA1 synapses, the earlier stages of protein synthesis-independent LTP primarily rely upon the enhanced trafficking of AMPARs to postsynaptic sites. These additional AMPARs may come from the trapping of laterally diffusing extrasynaptic surface AMPARs (or “diffusion trapping”) at postsynaptic sites as well as the exocytosis of intracellular AMPARs from vesicular pools [90–93]. In view of our data indicating reductions in GluA2 protein and trafficking into dendrites, we hypothesize that this functional LTP deficit arises from a reduction in the pool of dendritic AMPAR-containing endosomes that can undergo activity-dependent exocytosis into perisynaptic membrane domains to provide additional surface AMPARs [34,94,95]. In concordance with this supposition, cell-surface biotinylation experiments revealed that ChemLTP-stimulated *Nhe6* KO primary failed to upregulate surface GluA2 above control levels, as observed in stimulated WT cultures. Interestingly, the upregulation of surface GluA1 in ChemLTP-treated *Nhe6* KO neurons was comparable to that of WT, showing that some fraction of AMPARs can still undergo exocytosis after stimulation. The exocytosis of a reduced population of GluA2-lacking receptors likely accounts for the dampened potentiation still observed in KO hippocampi, although they are evidently not sufficient to allow for the full expression of LTP seen in WT.

In addition to plasmalemmal expression, we also investigated GluA1 phosphorylation at the S831 and S845 sites, which are the most well-studied modifications because of their roles in stabilizing AMPARs at synaptic sites and accentuating their single-channel properties to allow for LTP expression [33]. While S831 phosphorylation was upregulated in stimulated *Nhe6* KO

cultures, we noted a lack of enhanced S845 phosphorylation following ChemLTP. Importantly, phosphorylation at the S845 site can regulate single-channel open probability and cell surface insertion and retention of the resident AMPAR during LTP [96,97]. Interestingly, it has previously been reported that eliminating S845 phosphorylation alone did not occlude LTP at SC-CA1 synapses, while prohibiting phosphorylation at both the S831 and the S845 sites did [50]. Taken together, we postulate that although the increase in pGluA1-S831 may be sufficient to allow GluA1 exocytosis and some degree of LTP in *Nhe6* KO, a lack of upregulated surface GluA2 and pGluA1-S845 may impair the full expression of LTP in *Nhe6* KO [98]. Further live-imaging experiments directly assessing AMPAR exocytosis following LTP could further demonstrate how the temporospatial dynamics of this process may be perturbed in *Nhe6* KO. In addition to AMPAR exocytosis, the pool of extrasynaptic surface AMPARs that laterally diffuse to postsynaptic sites should also be considered, as these translocations mediate the rapid increase in synaptic strength in the first few minutes following LTP induction [40,99–101]. Although we see a significant decrease in the immediate response to TBS in KO hippocampi, it is presently unknown if AMPAR diffusion or trapping at synapses is affected. In the future, this question could be addressed by employing novel tools that manipulate AMPAR diffusion and trapping [100,102] and assessing the impact upon LTP in *Nhe6* KO.

Aside from considerations pertaining to postsynaptic AMPAR trafficking, the distinctive difference between WT and *Nhe6* KO within the first five min following TBS suggests that presynaptic changes should also be considered. At SC-CA1 synapses, a period of high-frequency stimulation usually results in an immediate PTP of membrane response that lasts for tens of seconds to minutes, which we observe here in WT slices. PTP at hippocampal synapses arises from a build-up of residual Ca^{2+} in axonal terminals, which can activate PKC and other mediators

upstream of intracellular signaling cascades. Eventually, these pathways enhance the Ca^{2+} sensitivity of presynaptic release machinery such that more vesicles from the readily-releasable pool (RRP) are released upon subsequent stimulations [103–107]. However, KO slices surprisingly showed a robust depression following TBS. This may occur through (1) a depletion of the RRP, (2) an inactivation of vesicular release sites, or (3) perturbations in presynaptic Ca^{2+} entry [104]. While NHE6 is known to be present within some axonal boutons and presumptive presynaptic terminals [21,25], its role in synaptic vesicular release has yet to be elucidated. To date, the only experiments directly assessing presynaptic function in *Nhe6* KO has shown no change in paired-pulse ratio (PPR) at hippocampal synapses [25], suggesting that baseline presynaptic release probabilities are unchanged. Interestingly, insights from the closely-related NHE isoform 9 (NHE9), which also localizes primarily to early and recycling endosomes, have shown that the loss of NHE9 decreases presynaptic release probability as a result of impaired presynaptic Ca^{2+} entry [108]. It is thus possible that a similar mechanism may underlie the short-term depression observed following TBS in *Nhe6* KO, although whether PPR at *Nhe6* KO synapses is altered by activity or other forms of stimulation remains to be determined. In all, it is clear that additional research into the presynaptic function of NHE6 will be required to elucidate whether deficiencies in Ca^{2+} entry, synaptic vesicle cycling, or biochemical signaling pertaining to PTP might act synergistically with the aforementioned changes in postsynaptic AMPAR transport to alter LTP expression in *Nhe6* KO.

In light of these deficits in cellular plasticity, we evaluated whether they also led to changes in behavior. To date, much of the work done in *Nhe6* KO mice has primarily focused on assessing sensorimotor impairments [43–45], while insights into memory paradigms have been relatively limited. In the present study, we found that P60-P90 *Nhe6* KO male mice did not show significant

differences in tasks measuring short- and long-term learning and memory tasks when compared with age- and sex-matched WT animals. We were surprised by the learning capacity of these KO mice, as severe intellectual disability is a hallmark of CS [8,9,11]. However, because we observed that hippocampal LTP mechanisms were persistent - albeit dampened - in young adult *Nhe6* KO hippocampal slices, this potentiation may still be sufficient to allow the animals to demonstrate some degree of learning at this age. Intriguingly, a recent study has reported that older 20- to 22-week-old *Nhe6* KO males did show impairments in a novel object location task compared to age-matched WT animals [44]. This finding is suggestive of a possible age-dependence in memory deficiencies, a possibility made more likely given the neurodegenerative phenotypes seen in both *Nhe6* KO mice as well as CS patients [8,12,46]. Therefore, additional paradigms to correlate behaviour and plasticity at later time points may be necessary to reveal deficits in learning and memory. However, it should be noted that KO mice spent significantly less time exploring novel objects or locations than WT, which is likely indicative of the reduced locomotor ability of these mice [109,110]. Indeed, this phenotype has consistently been shown to gradually worsen over time in *Nhe6* KO animals [44,45]. As such, when repeating behavioural experiments in aged KO animals, it will be even more essential to take into account the appropriate controls and analyses to compensate for the progressive deterioration in their locomotor abilities.

Upon having uncovered a multitude of impairments in synaptic density and plasticity in *Nhe6* KO, we sought to reverse them with a compound with potential clinical applications. To this end, we targeted BDNF/TrkB signaling, which is critical for neural development and plasticity yet is impaired in both the hippocampi and cochlea of *Nhe6* KO mice [25,52]. However, BDNF itself is unsuitable for *in vivo* oral administration because of its relatively short half-life, low blood-brain barrier penetrance, and rapid degradation by digestive enzymes [111,112]. To circumvent these

obstacles, we employed the flavonoid prodrug 7,8-DHF, a competitive TrkB agonist that exemplifies stronger blood-brain barrier penetrance and higher bioavailability when compared with BDNF [113,114]. Recent studies have shown that 7,8-DHF improved reduced synaptogenesis, learning deficits, and synaptic plasticity in murine models of FXS and other inherited forms of intellectual disability [115–118], as well as in aging- and Alzheimer's disease-associated deficits in cognition [119–123]. In *Nhe6* KO neurons, we found that acute treatment with 7,8-DHF alone was sufficient to enhance attenuated pTrkB levels and accentuate spine density and remodeling. Presumably, enhancing TrkB activation also activated intracellular signaling cascades downstream of the receptor and, in longer-term treatments, potentially allowed for the synthesis of proteins involved in spine formation and maturation. Specifically, 7,8-DHF increased thin spine density and enabled SHV enlargement in *Nhe6* KO neurons subjected to ChemLTP stimulation, which suggests that 7,8-DHF is capable of inducing the formation of nascent synapses that can also undergo activity-dependent remodeling. Further experiments investigating the potential of 7,8-DHF in restoring impairments in TrkB-dependent downstream signaling pathways, AMPAR dynamics, and electrophysiological potentiation in *Nhe6* KO remain to be performed. These data could further validate the use of this drug as a potential therapeutic intervention for the severe learning impairments associated with CS. Accordingly, increased emphasis is now being placed upon developing 7,8-DHF derivatives with better oral bioavailability and pharmacokinetic profile to administer clinically in human patients [124,125].

In conclusion, it is clear that young adult *Nhe6* KO mice show a myriad of deficits in terms of excitatory synaptic development and plasticity, which may progress to more significant impairments in behavioural learning over time. We hypothesize that these impairments arise from the dissolution of endosomal trafficking of cargos, such as AMPARs and TrkB, induced by a loss

of NHE6-mediated pH regulation. Nevertheless, the use of 7,8-DHF or other compounds that enhance TrkB activation could prove to be a novel option to ameliorate some of these deficits and, ideally, improve clinical outcomes in CS patients.

3.6 REFERENCES

1. Yap CC, Winckler B. Harnessing the Power of the Endosome to Regulate Neural Development. *Neuron*. 2012;74(3):440–51.
2. Cajigas IJ, Will T, Schuman EM. Protein homeostasis and synaptic plasticity. *EMBO J*. 2010;29(16):2746–52.
3. Wang YC, Lauwers E, Verstreken P. Presynaptic protein homeostasis and neuronal function. *Curr Opin Genet Dev*. 2017;44:38–46.
4. Maxfield FR. Role of Endosomes and Lysosomes in Human Disease. *Cold Spring Harb Perspect Biol*. 2014 May 1;6(5):a016931–a016931.
5. Winckler B, Faundez V, Maday S, Cai Q, Guimas Almeida C, Zhang H. The Endolysosomal System and Proteostasis: From Development to Degeneration. *J Neurosci*. 2018;38(44):9364–74.
6. Hu YB, Dammer EB, Ren RJ, Wang G. The endosomal-lysosomal system: From acidification and cargo sorting to neurodegeneration. *Transl Neurodegener*. 2015;4(1).
7. Schreijf AMA, Fon EA, McPherson PS. Endocytic membrane trafficking and neurodegenerative disease. *Cell Mol Life Sci*. 2016;73(8):1529–45.
8. Pescosolido MF, Stein DM, Schmidt M, Moufawad El Achkar C, Sabbagh M, Rogg JM, et al. Genetic and phenotypic diversity of NHE6 mutations in Christianson syndrome. *Ann Neurol*. 2014;581–93.
9. Gilfillan GD, Selmer KK, Roxrud I, Smith R, Kyllerman M, Eiklid K, et al. SLC9A6 mutations cause X-linked mental retardation, microcephaly, epilepsy, and ataxia, a phenotype mimicking Angelman syndrome. *Am J Hum Genet*. 2008 Apr;82(4):1003–10.
10. Christianson AL, Stevenson RE, van der Meyden CH, Pelsers J, Theron FW, van Rensburg PL, et al. X linked severe mental retardation, craniofacial dysmorphism, epilepsy, ophthalmoplegia, and cerebellar atrophy in a large South African kindred is localised to Xq24-q27. *J Med Genet*. 1999 Oct;36(10):759–66.
11. Schroer RJ, Holden KR, Tarpey PS, Matheus MG, Griesemer D a, Friez MJ, et al. Natural history of Christianson syndrome. *Am J Med Genet A*. 2010 Nov;152A(11):2775–83.
12. Garbern JY, Neumann M, Trojanowski JQ, Lee VM-Y, Feldman G, Norris JW, et al. A mutation affecting the sodium/proton exchanger, SLC9A6, causes mental retardation with tau deposition. *Brain*. 2010 May;133(5):1391–402.
13. Tarpey PS, Smith R, Pleasance E, Whibley A, Edkins S, Hardy C, et al. A systematic, large-scale resequencing screen of X-chromosome coding exons in mental retardation. *Nat Genet*. 2009;41(5):535–43.
14. Orłowski J, Grinstein S. Na⁺/H⁺ exchangers. *Compr Physiol*. 2011 Oct;1(4):2083–100.
15. Ilie A, Weinstein E, Boucher A, McKinney RA, Orłowski J. Impaired posttranslational processing and trafficking of an endosomal Na⁺/H⁺ exchanger NHE6 mutant ($\Delta(370)$ WST(372)) associated with X-linked intellectual disability and autism. *Neurochem Int*. 2014 Jul;73:192–203.
16. Ilie A, Gao AYL, Boucher A, Park J, Berghuis AM, Hoffer MJV, et al. A potential gain-of-

- function variant of SLC9A6 leads to endosomal alkalization and neuronal atrophy associated with Christianson Syndrome. *Neurobiol Dis.* 2019;121.
17. Ilie A, Boucher A, Park J, Berghuis AM, McKinney RA, Orlowski J. Assorted dysfunctions of endosomal alkali cation/proton exchanger SLC9A6 variants linked to Christianson syndrome. *J Biol Chem.* 2020 May 15;295(20):7075–95.
 18. Ouyang Q, Lena J-C, Mishra S, Riaz HA, Schmidt M, Morrow EM. Functional Assessment In Vivo of the Mouse Homologue of the Human Ala-9-Ser NHE6 Variant. *eNeuro.* 2019;6(December):1–15.
 19. Numata M, Petrecca K, Lake N, Orlowski J. Identification of a Mitochondrial Na/H Exchanger. *J Biol Chem.* 1998;273(12):6951–9.
 20. Brett CL, Wei Y, Donowitz M, Rao R. Human Na(+)/H(+) exchanger isoform 6 is found in recycling endosomes of cells, not in mitochondria. *Am J Physiol Cell Physiol.* 2002 May;282(5):C1031–41.
 21. Deane EC, Ilie AE, Sizdahkhani S, Das Gupta M, Orlowski J, McKinney RA. Enhanced recruitment of endosomal Na⁺/H⁺ exchanger NHE6 into Dendritic spines of hippocampal pyramidal neurons during NMDA receptor-dependent long-term potentiation. *J Neurosci.* 2013 Jan 9;33(2):595–610.
 22. Casey JR, Grinstein S, Orlowski J. Sensors and regulators of intracellular pH. *Nat Rev Mol Cell Biol.* 2010;11(1):50–61.
 23. Yamashiro DJ, Maxfield FR. Acidification of endocytic compartments and the intracellular pathways of ligands and receptors. *J Cell Biochem.* 1984;26(4):231–46.
 24. Weisz OA. Acidification and Protein Traffic. In: *International Review of Cytology.* 2003. p. 259–319.
 25. Ouyang Q, Lizarraga SB, Schmidt M, Yang U, Gong J, Ellisor D, et al. Christianson Syndrome Protein NHE6 Modulates TrkB Endosomal Signaling Required for Neuronal Circuit Development. *Neuron.* 2013 Oct 2;80(1):97–112.
 26. Zheng J, Shen WH, Lu TJ, Zhou Y, Chen Q, Wang Z, et al. Clathrin-dependent endocytosis is required for TrkB-dependent Akt-mediated neuronal protection and dendritic growth. *J Biol Chem.* 2008;283(19):13280–8.
 27. Gonzalez A, Moya-Alvarado G, Gonzalez-Billaut C, Bronfman FC. Cellular and molecular mechanisms regulating neuronal growth by brain-derived neurotrophic factor. Cytoskeleton. 2016;73(10):612–28.
 28. Mitchell DJ, Blasier KR, Jeffery ED, Ross MW, Pullikuth AK, Suo D, et al. Trk Activation of the ERK1/2 Kinase Pathway Stimulates Intermediate Chain Phosphorylation and Recruits Cytoplasmic Dynein to Signaling Endosomes for Retrograde Axonal Transport. *J Neurosci.* 2012 Oct 31;32(44):15495–510.
 29. Cosker KE, Segal RA. Neuronal signaling through endocytosis. *Cold Spring Harb Perspect Biol.* 2014;6(2):1–15.
 30. Lazo OM, Gonzalez A, Ascaño M, Kuruvilla R, Couve A, Bronfman FC. BDNF regulates Rab11-mediated recycling endosome dynamics to induce dendritic branching. *J Neurosci.*

- 2013;33(14):6112–22.
31. Pang PT, Teng HK, Zaitsev E, Woo NT, Sakata K, Zhen S, et al. Cleavage of proBDNF by tPA/plasmin is essential for long-term hippocampal plasticity. *Science* (80-). 2004 Oct 15;306(5695):487–91.
 32. Huganir RL, Nicoll R a. AMPARs and synaptic plasticity: The last 25 years. *Neuron*. 2013;80(3):704–17.
 33. Diering GH, Huganir RL. The AMPA Receptor Code of Synaptic Plasticity. *Neuron*. 2018;100(2):314–29.
 34. Chater TE, Goda Y. The role of AMPA receptors in postsynaptic mechanisms of synaptic plasticity. *Front Cell Neurosci*. 2014;8(November):1–14.
 35. Shi S-H, Hayashi Y, Esteban J a., Malinow R. Subunit-Specific Rules Governing AMPA Receptor Trafficking to Synapses in Hippocampal Pyramidal Neurons. *Cell*. 2001 May;105(3):331–43.
 36. Matsuzaki M, Honkura N, Ellis-Davies GCR, Kasai H. Structural basis of long-term potentiation in single dendritic spines. *Nature*. 2004;429(June):761–6.
 37. Okamoto KI, Nagai T, Miyawaki A, Hayashi Y. Rapid and persistent modulation of actin dynamics regulates postsynaptic reorganization underlying bidirectional plasticity. *Nat Neurosci*. 2004;7(10):1104–12.
 38. Park M, Salgado JM, Ostroff L, Helton TD, Camenzind G, Harris KM, et al. Plasticity-induced growth of dendritic spines by exocytic trafficking from recycling endosomes. *Neuron*. 2006;52(5):817–30.
 39. Park M, Penick EC, Edwards JG, Kauer J a, Ehlers MD. Recycling endosomes supply AMPA receptors for LTP. *Science*. 2004;305(5692):1972–5.
 40. Petrini EM, Lu J, Cognet L, Lounis B, Ehlers MD, Choquet D. Endocytic trafficking and recycling maintain a pool of mobile surface AMPA receptors required for synaptic potentiation. *Neuron*. 2009;63(1):92–105.
 41. Gao AYL, Ilie A, Chang PKY, Orlowski J, McKinney RA. A Christianson syndrome-linked deletion mutation (Δ 287ES288) in SLC9A6 impairs hippocampal neuronal plasticity. *Neurobiol Dis*. 2019;130(April):104490.
 42. Ilie A, Gao AYL, Reid J, Boucher A, McEwan C, Barrière H, et al. A Christianson syndrome-linked deletion mutation (Δ 287ES288) in SLC9A6 disrupts recycling endosomal function and elicits neurodegeneration and cell death. *Mol Neurodegener*. 2016;11(1).
 43. Kerner-Rossi M, Gulinello M, Walkley S, Dobrenis K. Pathobiology of Christianson syndrome: Linking disrupted endosomal-lysosomal function with intellectual disability and sensory impairments. *Neurobiol Learn Mem*. 2018;(December 2017):0–1.
 44. Sikora J, Leddy J, Gulinello M, Walkley SU. X-linked Christianson syndrome: heterozygous female Slc9a6 knockout mice develop mosaic neuropathological changes and related behavioral abnormalities. *Dis Model Mech*. 2015;(October).
 45. Strømme P, Dobrenis K, Sillitoe R V, Gulinello M, Ali NF, Davidson C, et al. X-linked Angelman-like syndrome caused by Slc9a6 knockout in mice exhibits evidence of

- endosomal-lysosomal dysfunction. *Brain a J Neurol*. 2011 Nov;134(Pt 11):3369–83.
46. Xu M, Ouyang Q, Gong J, Pescosolido MF, Pruett BS, Mishra S, et al. Mixed Neurodevelopmental and Neurodegenerative Pathology in Nhe6 -Null Mouse Model of Christianson Syndrome. *eNeuro*. 2017 Nov;4(6):ENEURO.0388-17.2017.
 47. De Paola V, Arber S, Caroni P. AMPA receptors regulate dynamic equilibrium of presynaptic terminals in mature hippocampal networks. *Nat Neurosci*. 2003;6(5):491–500.
 48. Brewer GJ, Torricelli JR. Isolation and culture of adult neurons and neurospheres. *Nat Protoc*. 2007 Jan;2(6):1490–8.
 49. Potter SM, DeMarse TB. A new approach to neural cell culture for long-term studies. *J Neurosci Methods*. 2001;110(1–2):17–24.
 50. Gähwiler BH, Capogna M, Debanne D, McKinney RA, Thompson SM. Organotypic slice cultures: a technique has come of age. *Trends Neurosci*. 1997;20(10):471–7.
 51. Mateos JM, Lüthi A, Savic N, Stierli B, Streit P, Gähwiler BH, et al. Synaptic modifications at the CA3-CA1 synapse after chronic AMPA receptor blockade in rat hippocampal slices. *J Physiol*. 2007;581(Pt 1):129–38.
 52. Verbich D, Prenosil G a, Chang PK-Y, Murai KK, McKinney RA. Glial glutamate transport modulates dendritic spine head protrusions in the hippocampus. *Glia*. 2012 Jul;60(7):1067–77.
 53. Fortin D a, Davare M a, Srivastava T, Brady JD, Nygaard S, Derkach V a, et al. Long-term potentiation-dependent spine enlargement requires synaptic Ca²⁺-permeable AMPA receptors recruited by CaM-kinase I. *J Neurosci*. 2010 Sep 1;30(35):11565–75.
 54. Gabriel LR, Wu S, Melikian HE. Brain slice biotinylation: An ex vivo approach to measure region-specific plasma membrane protein trafficking in adult neurons. *J Vis Exp*. 2014;(86):2–8.
 55. Jayabal S, Ljungberg L, Erwes T, Cormier A, Quilez S, El Jaouhari S, et al. Rapid onset of motor deficits in a mouse model of spinocerebellar ataxia type 6 precedes late cerebellar degeneration. *eNeuro*. 2015;2(6).
 56. Harris KM, Jensen FE, Tsao B. Three-dimensional structure of dendritic spines and synapses in rat hippocampus (CA1) at postnatal day 15 and adult ages: implications for the maturation of synaptic physiology and long-term potentiation. *J Neurosci*. 1992;12(7):2685–705.
 57. Sorra KE, Harris KM. Overview on the structure, composition, function, development, and plasticity of hippocampal dendritic spines. *Hippocampus*. 2000;10(5):501–11.
 58. Chang PKY, Prenosil GA, Verbich D, Gill R, McKinney RA. Prolonged ampakine exposure prunes dendritic spines and increases presynaptic release probability for enhanced long-term potentiation in the hippocampus. *Eur J Neurosci*. 2014;40(5):2766–76.
 59. Dunaevsky A, Tashiro A, Majewska A, Mason C, Yuste R. Developmental regulation of spine motility in the mammalian central nervous system. *Proc Natl Acad Sci U S A*. 1999;96(23):13438–43.
 60. Bourne JN, Harris KM. Balancing Structure and Function at Hippocampal Dendritic Spines.

- Annu Rev Neurosci. 2008 Jul;31(1):47–67.
61. Larson J, Munkácsy E. Theta-burst LTP. *Brain Res.* 2015;1621:38–50.
 62. Lee HK, Takamiya K, He K, Song L, Huganir RL. Specific roles of AMPA receptor subunit GluR1 (GluA1) phosphorylation sites in regulating synaptic plasticity in the CA1 region of hippocampus. *J Neurophysiol.* 2010;103(1):479–89.
 63. Kucharava K, Brand Y, Albano G, Sekulic-Jablanovic M, Glutz A, Xian X, et al. Sodium-hydrogen exchanger 6 (NHE6) deficiency leads to hearing loss, via reduced endosomal signalling through the BDNF/Trk pathway. *Sci Rep.* 2020;10(1):1–14.
 64. Liu X, Obiany O, Chan CB, Huang J, Xue S, Yang JJ, et al. Biochemical and biophysical investigation of the brain-derived neurotrophic factor mimetic 7,8-dihydroxyflavone in the binding and activation of the trkb receptor. *J Biol Chem.* 2014;289(40):27571–84.
 65. Bonhoeffer T, Yuste R. Spine Motility. *Neuron.* 2002;35(6):1019–27.
 66. Phillips M, Pozzo-Miller L. Dendritic spine dysgenesis in autism related disorders. *Neurosci Lett.* 2015;1–11.
 67. Forrest MP, Parnell E, Penzes P. Dendritic structural plasticity and neuropsychiatric disease. *Nat Rev Neurosci.* 2018;19(4):215–34.
 68. Nishiyama J. Plasticity of dendritic spines: Molecular function and dysfunction in neurodevelopmental disorders. *Psychiatry Clin Neurosci.* 2019;73(9):541–50.
 69. Bernardinelli Y, Nikonenko I, Muller D. Structural plasticity: mechanisms and contribution to developmental psychiatric disorders. *Front Neuroanat.* 2014 Jan;8(November):123.
 70. Jay V, Becker LE, Chan F-W, Perry TL. Puppet-like syndrome of Angelman: A pathologic and neurochemical study. *Neurology.* 1991 Mar 1;41(3):416–416.
 71. Yashiro K, Riday TT, Condon KH, Roberts AC, Bernardo DR, Prakash R, et al. Ube3a is required for experience-dependent maturation of the neocortex. *Nat Neurosci.* 2009;12(6):777–83.
 72. Dindot S V., Antalffy BA, Bhattacharjee MB, Beaudet AL. The Angelman syndrome ubiquitin ligase localizes to the synapse and nucleus, and maternal deficiency results in abnormal dendritic spine morphology. *Hum Mol Genet.* 2008;17(1):111–8.
 73. Irwin SA, Patel B, Idupulapati M, Harris JB, Crisostomo RA, Larsen BP, et al. Abnormal dendritic spine characteristics in the temporal and visual cortices of patients with fragile-X syndrome: A quantitative examination. *Am J Med Genet.* 2001 Jan 15;98(2):161–7.
 74. Rudelli RD, Brown WT, Wisniewski K, Jenkins EC, Laure-Kamionowska M, Connell F, et al. Adult fragile X syndrome. *Acta Neuropathol.* 1985;67(3–4):289–95.
 75. Comery TA, Harris JB, Willems PJ, Oostra BA, Irwin SA, Weiler IJ, et al. Abnormal dendritic spines in fragile X knockout mice: Maturation and pruning deficits. *Proc Natl Acad Sci.* 1997 May 13;94(10):5401–4.
 76. Irwin SA, Idupulapati M, Gilbert ME, Harris JB, Chakravarti AB, Rogers EJ, et al. Dendritic spine and dendritic field characteristics of layer V pyramidal neurons in the visual cortex of fragile-X knockout mice. *Am J Med Genet.* 2002 Aug 1;111(2):140–6.
 77. Nimchinsky EA, Oberlander AM, Svoboda K. Abnormal development of dendritic spines

- in FMR1 knock-out mice. *J Neurosci*. 2001;
78. Cruz-Martín A, Crespo M, Portera-Cailliau C. Delayed stabilization of dendritic spines in fragile X mice. *J Neurosci*. 2010;30(23):7793–803.
 79. Nagaoka A, Takehara H, Hayashi-Takagi A, Noguchi J, Ishii K, Shirai F, et al. Abnormal intrinsic dynamics of dendritic spines in a fragile X syndrome mouse model in vivo. *Sci Rep*. 2016;6(May):26651.
 80. Padmashri R, Reiner BC, Suresh A, Spartz E, Dunaevsky A. Altered structural and functional synaptic plasticity with motor skill learning in a mouse model of fragile X syndrome. *J Neurosci*. 2013;33(50):19715–23.
 81. Pyronneau A, He Q, Hwang JY, Porch M, Contractor A, Zukin RS. Aberrant Rac1-cofilin signaling mediates defects in dendritic spines, synaptic function, and sensory perception in fragile X syndrome. *Sci Signal*. 2017;10(504):1–16.
 82. Spence EF, Soderling SH. Actin out: Regulation of the synaptic cytoskeleton. *J Biol Chem*. 2015;290(48):28613–22.
 83. Ilie A, Gao AYL, Reid J, Boucher A, Barriere H, McEwan C, et al. A Christianson Syndrome-linked deletion mutation (Δ 287ES288) in SLC9A6 disrupts recycling endosomal function and induces neurodegeneration and cell death. *Mol Neurodegener*. 2016;1–28.
 84. Isaac JTR, Ashby M, McBain CJ. The Role of the GluR2 Subunit in AMPA Receptor Function and Synaptic Plasticity. *Neuron*. 2007;54(6):859–71.
 85. Liu SJ, Zukin RS. Ca²⁺-permeable AMPA receptors in synaptic plasticity and neuronal death. *Trends Neurosci*. 2007;30(3):126–34.
 86. Wright A, Vissel B. The essential role of AMPA receptor GluA2 subunit RNA editing in the normal and diseased brain. *Front Mol Neurosci*. 2012;5(APRIL):1–13.
 87. Bassani S, Valnegri P, Beretta F, Passafaro M. The GLUR2 subunit of AMPA receptors: Synaptic role. *Neuroscience*. 2009;158(1):55–61.
 88. Tanaka H, Grooms SY, Bennett MVL, Zukin RS. The AMPAR subunit GluR2: still front and center-stage. *Brain Res*. 2000 Dec;886(1–2):190–207.
 89. Sans N, Vissel B, Petralia RS, Wang YX, Chang K, Royle GA, et al. Aberrant Formation of Glutamate Receptor Complexes in Hippocampal Neurons of Mice Lacking the GluR2 AMPA Receptor Subunit. *J Neurosci*. 2003;23(28):9367–73.
 90. Wenthold R, Petralia R, Blahos J I, Niedzielski A. Evidence for multiple AMPA receptor complexes in hippocampal CA1/CA2 neurons. *J Neurosci*. 1996 Mar 15;16(6):1982–9.
 91. Salpietro V, Dixon CL, Guo H, Bello OD, Vandrovicova J, Efthymiou S, et al. AMPA receptor GluA2 subunit defects are a cause of neurodevelopmental disorders. *Nat Commun*. 2019;10(1).
 92. Akbarian S, Smith MA, Jones EG. Editing for an AMPA receptor subunit RNA in prefrontal cortex and striatum in Alzheimer's disease, Huntington's disease and schizophrenia. *Brain Res*. 1995 Nov;699(2):297–304.
 93. Takuma H, Kwak S, Yoshizawa T, Kanazawa I. Reduction of GluR2 RNA editing, a molecular change that increases calcium influx through AMPA receptors, selective in the

- spinal ventral gray of patients with amyotrophic lateral sclerosis. *Ann Neurol*. 1999 Dec;46(6):806–15.
94. Kwak S, Kawahara Y. Deficient RNA editing of GluR2 and neuronal death in amyotrophic lateral sclerosis. *J Mol Med*. 2005 Feb;83(2):110–20.
 95. Rajasekaran K, Todorovic M, Kapur J. Calcium-permeable AMPA receptors are expressed in a rodent model of status epilepticus. *Ann Neurol*. 2012;72(1):91–102.
 96. Hu H, Qin Y, Bochorishvili G, Zhu Y, Van Aelst L, Zhu JJ. Ras signaling mechanisms underlying impaired GluR1-dependent plasticity associated with fragile X syndrome. *J Neurosci*. 2008;28(31):7847–62.
 97. Jiang Y hui, Armstrong D, Albrecht U, Atkins CM, Noebels JL, Eichele G, et al. Mutation of the Angelman ubiquitin ligase in mice causes increased cytoplasmic p53 and deficits of contextual learning and long-term potentiation. *Neuron*. 1998;21(4):799–811.
 98. Lauterborn JC, Rex CS, Kramár E, Chen LY, Pandeyarajan V, Lynch G, et al. Brain-derived neurotrophic factor rescues synaptic plasticity in a mouse model of fragile X syndrome. *J Neurosci*. 2007;27(40):10685–94.
 99. Kumar A. Long-term potentiation at CA3-CA1 hippocampal synapses with special emphasis on aging, disease, and stress. *Front Aging Neurosci*. 2011;3(MAY):1–20.
 100. Shi SH, Hayashi Y, Petralia RS, Zaman SH, Wenthold RJ, Svoboda K, et al. Rapid spine delivery and redistribution of AMPA receptors after synaptic NMDA receptor activation. *Science*. 1999 Jun 11;284(5421):1811–6.
 101. Heynen AJ, Quinlan EM, Bae DC, Bear MF. Bidirectional, Activity-Dependent Regulation of Glutamate Receptors in the Adult Hippocampus In Vivo. *Neuron*. 2000 Nov;28(2):527–36.
 102. Broutman G, Baudry M. Involvement of the Secretory Pathway for AMPA Receptors in NMDA-Induced Potentiation in Hippocampus. *J Neurosci*. 2001 Jan 1;21(1):27–34.
 103. Lu W-Y, Man H-Y, Ju W, Trimble WS, MacDonald JF, Wang YT. Activation of Synaptic NMDA Receptors Induces Membrane Insertion of New AMPA Receptors and LTP in Cultured Hippocampal Neurons. *Neuron*. 2001 Jan;29(1):243–54.
 104. Rácz B, Blanpied T a, Ehlers MD, Weinberg RJ. Lateral organization of endocytic machinery in dendritic spines. *Nat Neurosci*. 2004;7(9):917–8.
 105. Yudowski G a., Puthenveedu M a., Leonoudakis D, Panicker S, Thorn KS, Beattie EC, et al. Real-Time Imaging of Discrete Exocytic Events Mediating Surface Delivery of AMPA Receptors. *J Neurosci*. 2007;27(41):11112–21.
 106. Man H-Y, Sekine-Aizawa Y, Hugarir RL. Regulation of α -amino-3-hydroxy-5-methyl-4-isoxazolepropionic acid receptor trafficking through PKA phosphorylation of the Glu receptor 1 subunit. *Proc Natl Acad Sci*. 2007 Feb 27;104(9):3579–84.
 107. Banke TG, Bowie D, Lee H-K, Hugarir RL, Schousboe A, Traynelis SF. Control of GluR1 AMPA Receptor Function by cAMP-Dependent Protein Kinase. *J Neurosci*. 2000 Jan 1;20(1):89–102.
 108. Oh MC, Derkach VA, Guire ES, Soderling TR. Extrasynaptic membrane trafficking

- regulated by GluR1 serine 845 phosphorylation primes AMPA receptors for long-term potentiation. *J Biol Chem*. 2006;281(2):752–8.
109. Penn AC, Zhang CL, Georges F, Royer L, Breillat C, Hosy E, et al. Hippocampal LTP and contextual learning require surface diffusion of AMPA receptors. *Nature*. 2017;549(7672):384–8.
 110. Choquet D. Linking Nanoscale Dynamics of AMPA Receptor Organization to Plasticity of Excitatory Synapses and Learning. *J Neurosci*. 2018;38(44):9318–29.
 111. Opazo P, Labrecque S, Tigaret CM, Frouin A, Wiseman PW, De Koninck P, et al. CaMKII Triggers the Diffusional Trapping of Surface AMPARs through Phosphorylation of Stargazin. *Neuron*. 2010 Jul;67(2):239–52.
 112. Groc L, Choquet D. Linking glutamate receptor movements and synapse function. *Science*. 2020;368(6496).
 113. Lou X, Korogod N, Brose N, Schneggenburger R. Phorbol Esters Modulate Spontaneous and Ca²⁺-Evoked Transmitter Release via Acting on Both Munc13 and Protein Kinase C. *J Neurosci*. 2008 Aug 13;28(33):8257–67.
 114. Fioravante D, Regehr WG. Short-term forms of presynaptic plasticity. *Curr Opin Neurobiol*. 2011;21(2):269–74.
 115. Zucker RS, Regehr WG. Short-Term Synaptic Plasticity. *Annu Rev Physiol*. 2002 Mar;64(1):355–405.
 116. Korogod N, Lou X, Schneggenburger R. Posttetanic potentiation critically depends on an enhanced Ca²⁺ sensitivity of vesicle fusion mediated by presynaptic PKC. *Proc Natl Acad Sci*. 2007 Oct 2;104(40):15923–8.
 117. Brager DH, Cai X, Thompson SM. Activity-dependent activation of presynaptic protein kinase C mediates post-tetanic potentiation. *Nat Neurosci*. 2003 Jun 18;6(6):551–2.
 118. Ullman JC, Yang J, Sullivan M, Bendor J, Levy J, Pham E, et al. A mouse model of autism implicates endosome pH in the regulation of presynaptic calcium entry. 2018;
 119. Moy SS, Nadler JJ, Perez A, P BR, M JJ, R MT, et al. Sociability and preference for social novelty in five inbred strains: an approach to assess autistic-like behavior in mice. *Genes, Brain Behav*. 2004;287–302.
 120. Antunes M, Biala G. The novel object recognition memory: neurobiology, test procedure, and its modifications. *Cogn Process*. 2012 May 9;13(2):93–110.
 121. Poduslo JF, Curran GL. Permeability at the blood-brain and blood-nerve barriers of the neurotrophic factors: NGF, CNTF, NT-3, BDNF. *Mol Brain Res*. 1996 Mar;36(2):280–6.
 122. Du X, Hill RA. 7,8-Dihydroxyflavone as a pro-neurotrophic treatment for neurodevelopmental disorders. *Neurochem Int*. 2015;89:170–80.
 123. Jang S-W, Liu X, Yepes M, Shepherd KR, Miller GW, Liu Y, et al. A selective TrkB agonist with potent neurotrophic activities by 7,8-dihydroxyflavone. *Proc Natl Acad Sci*. 2010 Feb 9;107(6):2687–92.
 124. Liu X, Chan CB, Jang SW, Pradoldej S, Huang J, He K, et al. A synthetic 7,8-dihydroxyflavone derivative promotes neurogenesis and exhibits potent antidepressant

- effect. *J Med Chem.* 2010;53(23):8274–86.
125. Seese RR, Le AA, Wang K, Cox CD, Lynch G, Gall CM. A TrkB agonist and ampakine rescue synaptic plasticity and multiple forms of memory in a mouse model of intellectual disability. *Neurobiol Dis.* 2020;134(July 2019):104604.
 126. Ren E, Roncagé V, Trazzi S, Fuchs C, Medici G, Gennaccaro L, et al. Functional and structural impairments in the perirhinal cortex of a mouse model of CDKL5 deficiency disorder are rescued by a TrkB agonist. *Front Cell Neurosci.* 2019;13(April):1–15.
 127. Stagni F, Giacomini A, Guidi S, Emili M, Uguagliati B, Salvalai ME, et al. A flavonoid agonist of the TrkB receptor for BDNF improves hippocampal neurogenesis and hippocampus-dependent memory in the Ts65Dn mouse model of DS. *Exp Neurol.* 2017;298(September):79–96.
 128. Tian M, Zeng Y, Hu Y, Yuan X, Liu S, Li J, et al. 7, 8-Dihydroxyflavone induces synapse expression of AMPA GluA1 and ameliorates cognitive and spine abnormalities in a mouse model of fragile X syndrome. *Neuropharmacology.* 2015;89:43–53.
 129. Gao L, Tian M, Zhao HY, Xu QQ, Huang YM, Si QC, et al. TrkB activation by 7, 8-dihydroxyflavone increases synapse AMPA subunits and ameliorates spatial memory deficits in a mouse model of Alzheimer's disease. *J Neurochem.* 2016;136(3):620–36.
 130. Zeng Y, Lv F, Li L, Yu H, Dong M, Fu Q. 7,8-Dihydroxyflavone Rescues Spatial Memory and Synaptic Plasticity in Cognitively Impaired Aged Rats. *J Neurochem.* 2012;122(4):800–11.
 131. Castello NA, Nguyen MH, Tran JD, Cheng D, Green KN, LaFerla FM. 7,8-dihydroxyflavone, a small molecule TrkB agonist, improves spatial memory and increases thin spine density in a mouse model of alzheimer disease-like neuronal loss. *PLoS One.* 2014;9(3):17–9.
 132. Zhang Z, Liu X, Schroeder JP, Chan CB, Song M, Yu SP, et al. 7,8-dihydroxyflavone prevents synaptic loss and memory deficits in a mouse model of Alzheimer's disease. *Neuropsychopharmacology.* 2014;39(3):638–50.
 133. Devi L, Ohno M. 7,8-dihydroxyflavone, a small-molecule TrkB agonist, reverses memory deficits and BACE1 elevation in a mouse model of alzheimer's disease. *Neuropsychopharmacology.* 2012;37(2):434–44.
 134. Liu C, Chan CB, Ye K. 7,8-dihydroxyflavone, a small molecular TrkB agonist, is useful for treating various BDNF-implicated human disorders. *Transl Neurodegener.* 2016;5(1):1–9.
 135. Chen C, Wang Z, Zhang Z, Liu X, Kang SS, Zhang Y, et al. The prodrug of 7,8-dihydroxyflavone development and therapeutic efficacy for treating Alzheimer's disease. *Proc Natl Acad Sci U S A.* 2018;115(3):578–83.

CHAPTER 4. DYSREGULATION OF INHIBITORY NEUROTRANSMISSION PROMOTES HYPEREXCITABILITY OF HIPPOCAMPAL CIRCUITRY IN THE *SLC9A6/NHE6* KNOCK-OUT MODEL OF CHRISTIASON SYNDROME

FOREWARD

Background and Rationale

In Chapters 2 and 3, I have primarily focused on changes in excitatory synaptic density and plasticity in murine NHE6 Δ ES and KO models. My findings suggest that deficits in receptor trafficking and synaptic function may indeed account for the pronounced intellectual disability that is a hallmark of CS. However, these results do not explain the epileptic seizures that are also frequently observed in CS patients. In contrast to other neurodevelopmental disorders, epileptic seizures of varying types have been reported in almost every patient diagnosed with CS thus far. Data from single cell RNA sequencing has also recently revealed that *SLC9A6* is strongly expressed in hippocampal interneurons. In spite of these findings, little is presently known about the role of NHE6 in mediating inhibitory synaptic function. Furthermore, anecdotal evidence suggests that seizures are among the most prominent deterrents against the quality of life of individuals with CS and their families and caretakers. There is thus a pronounced and urgent need to better understand how the loss of NHE6 function leads to the development of hyperexcitability in neural circuitry. Such knowledge will ideally advance the discovery of novel therapeutic targets that can reduce the severity and frequency of epileptic seizures in these patients.

Hypothesis

I hypothesize that the ablation of NHE6 function will give way to the development of hyperexcitability in neural circuitry. Specifically, I hypothesize that *Nhe6* KO hippocampi will

show a reduction in inhibitory interneurons, as well as inhibitory synaptic sites and ionotropic GABA_AR trafficking within CA1 pyramidal neurons. *Nhe6* KO neurons may also show a dysregulation of GABAergic neurotransmission owing to a lack of proper Cl⁻ regulation. Some of these findings in inhibitory postsynaptic trafficking may also pertain to cultured hippocampal neurons expressing Δ ES NHE6.

Experimental Outline

To address these hypotheses, I will again employ mGFP-labeled *Nhe6* KO mice developed in Chapter 3. First, I will confirm that the hippocampal circuitry is indeed hyperexcitable in *Nhe6* KO by preparing acute slice preparations, subjecting them to subthreshold concentrations of the epileptic drug 4-aminopyridine, and obtaining extracellular field recordings from area CA1. I will then perform whole-cell current clamp recordings from CA1 pyramidal neurons to assess their intrinsic membrane properties and excitability. Next, I will use immunoblotting and immunofluorescence to assess the relative density of GABAergic interneurons in the hippocampus, specifically those expressing parvalbumin given their fundamental role in regulating pyramidal cell excitability. I will also employ immunohistochemical methods to probe for pre- and postsynaptic inhibitory molecules to assess the number of inhibitory synaptic sites and GABA_AR trafficking in CA1 pyramidal neurons. Furthermore, I will perform additional immunoblots to obtain a time-course of the protein levels of NKCC1 and KCC2 in KO hippocampal tissue. After, I will verify the integrity of inhibitory regulation on to CA1 pyramidal neurons by recording GABA_AR-mediated currents from CA1 pyramidal neurons under whole-cell voltage clamp conditions. Finally, I will assess some of these inhibitory synaptic markers and GABA_AR-mediated neurotransmission in primary hippocampal neurons expressing the Δ ES NHE6 mutant *in vitro*.

4.1 ABSTRACT

Christianson syndrome (CS) is an X-linked form of intellectual disability arising from mutations in the *SLC9A6* gene encoding Na⁺/H⁺ exchanger isoform 6 (NHE6), a regulator of endosomal pH. Importantly, almost all patients diagnosed with CS thus far have also presented with severe epilepsy beginning in infancy, with individuals having been reported to develop a range of different seizure types (*e.g.* tonic, tonic-clonic, myoclonic) as early as three months of age. However, little is presently known of how the loss of NHE6 function leads to the development of epilepsy in CS. To this end, we sought to uncover potential mechanisms that may imbalance the ratio of excitatory/inhibitory (E/I) neurotransmission within the hippocampus of adult *Nhe6* knock-out (KO) male mice. We first found that *ex vivo* hippocampal slice preparations from KO animals developed hyperexcitable discharges in response to a subthreshold concentration of the convulsant 4-aminopyridine (4-AP) that was insufficient to enhance firing in wild-type (WT) tissue. Nevertheless, KO hippocampal pyramidal neurons did not show significant differences in active or passive membrane properties when compared to WT. We thus focused primarily on possible disturbances in inhibitory γ -aminobutyric acid (GABA)-mediated transmission. At two months of age, we first noted a loss of parvalbumin-expressing GABAergic interneurons in area CA1 of *Nhe6* KO hippocampi that progressed to reductions throughout the whole hippocampus in six-month-old mice. This coincided with the loss of inhibitory synaptic markers and ionotropic GABA_A receptor subunit $\alpha 2$ within CA1 pyramidal neurons, which also exhibited alterations in functional inhibitory neurotransmission. We further noted a reciprocal increase and decrease in the cation-Cl⁻ transporters Na⁺-K⁺-Cl⁻ cotransporter isoform 1 (NKCC1) and K⁺-Cl⁻ cotransporter isoform 2 (KCC2), respectively, in adult KO hippocampi when compared to age-matched WT samples, which suggested a possible dysregulation in Cl⁻ homeostasis and GABAergic polarity.

Interestingly, primary hippocampal neurons expressing a patient-derived *SLC9A6* variant (p.Glu287_Ser288del) recapitulated the deficits in postsynaptic inhibitory trafficking seen in *Nhe6* KO mice. In all, the present study reveals that the loss of NHE6 may lessen or reverse the impact of GABA release on to hippocampal pyramidal neurons, thus leading to the development of hyperexcitability in NHE6-deficient hippocampi. These data will ideally lead to the development of novel therapeutic approaches to ameliorate epileptic seizures and overall clinical outcomes in individuals suffering from CS.

4.2 INTRODUCTION

Due to the pH dependence of channels and receptors involved in neuronal excitability and synaptic transmission, the excitability of neuronal circuitry is particularly sensitive to changes in the acidity of intracellular and extracellular compartments [1–4]. Accordingly, dramatic shifts in brain pH have been associated with network hyperexcitability and seizure generation [5–7]. Epileptic seizures are associated with a number of neurodevelopmental conditions, including the recently characterized Christianson syndrome (CS), a rare, X-linked form of intellectual disability that also presents with non-verbalism, truncal ataxia, hyperkinesia, postnatal microcephaly, and cerebellar atrophy [8–10]. Importantly, epilepsy has been reported in all patients diagnosed with CS to date, with most individuals beginning to experience generalized tonic-clonic or clonic seizures within the first two years of life [8,11]. Despite the use of antiepileptic medications, patients with CS often develop resistance to standard drugs and can experience up to 15 seizures a day. As such, many patients unfortunately die in childhood or as young adults due to sudden unexplained death due to epilepsy (SUDEP) [12]. Although further investigation into how epilepsy develops in these patients is urgently needed, this topic has yet to be addressed.

CS arises from loss-of-function mutations (>80 reported thus far) in the X-chromosome *SLC9A6* gene encoding (Na⁺, K⁺)/H⁺ exchanger isoform 6 (NHE6) [9,13]. In neurons and other cell types, NHE6 primarily localizes to the membranes of early and recycling endosomes [14,15]. There, it functions to offset endosomal acidification established by the electrogenic vacuolar H⁺-ATPase by transporting H⁺ out of the organellar lumen in exchange for cytosolic Na⁺ or K⁺ [16,17]. Thus, NHE6 is a critical regulator of endosomal pH, which is a critical determinant of their function in cargo trafficking and recycling and is normally regulated within a precise range [18–20]. These mechanisms are especially important in neurons, which rely on endosomes to appropriately deliver various membrane-bound cargos (*e.g.* ionotropic neurotransmitter and neurotrophic receptors, ion channels, and transporters) to allow for rapid changes in the strength and morphology of excitatory and inhibitory synaptic connections between neurons [21–23]. As such, neurons lacking NHE6 function demonstrate a significant reduction in endosomal pH [24]. Importantly, disturbances in endosomal pH regulation and cargo trafficking have been shown to underlie functional deficits observed in various neurological disorders [7,25–27]. Although recent work has focused on how the loss of NHE6 function can disrupt the trafficking of receptors involved in excitatory neurotransmission [24,28,29], little is presently known of how inhibitory regulation and circuit-level excitability may also be dysregulated. As *SLC9A6* is highly expressed in the hippocampus (<https://www.gtexportal.org/home/gene/SLC9A6>) [15,24], and especially within inhibitory interneurons (http://dropviz.org/?state_id=9887ffac31b2fa28), it is highly possible that ablation of its function could disrupt inhibitory drive in the hippocampal circuit.

For the most part, excitatory inputs in neuronal circuitry are offset by inhibitory signals that prevent runaway excitation to maintain a balance of excitatory/inhibitory (E/I) neurotransmission. The majority of inhibitory regulation in the central nervous system (CNS) is

mediated by γ -aminobutyric acid (GABA)-releasing interneurons, a heterogeneous group of cells that differ in their morphology and functional properties and play a fundamental role in controlling the excitability and synchronicity of neural circuitry [30,31]. As such, disruptions in their number or activity have been associated with imbalances in excitatory/inhibitory transmission in epilepsy and other disorders [32–35]. In the mature central nervous system, postsynaptic ionotropic GABA_A receptors (GABA_ARs) allow for the entry of Cl⁻ anions into the cell to hyperpolarize or shunt the membrane potential below action potential (AP) threshold, thus mediating fast inhibitory neurotransmission [36,37]. GABA_ARs are Cys-loop, ligand gated pentameric channels composed from 19 possible subunits, different combinations of which display variable localization and functional properties. For example, synaptic GABA_ARs usually contain α 1-3 subunits and mediate phasic inhibition following quantal GABA release, while extrasynaptic GABA_ARs generally possess α 4-6 subunits and allow for tonic inhibition in response to ambient extracellular GABA [36,37]. Synaptic GABA_ARs are clustered and retained at synapses by the inhibitory scaffolding molecule gephyrin, which cross-links these receptors to the cytoskeleton [38,39]. GABA_AR trafficking and retention to postsynaptic inhibitory sites are vital for maintaining the integrity of inhibitory regulation, as even minor reductions in GABA_ARs surface expression or function can impose epilepsy, memory impairments, and other significant consequences in rodents [40,41].

GABAergic inhibition further relies on the electrochemical gradient of Cl⁻ established by cation-Cl⁻ transporters Na⁺-K⁺-Cl⁻ cotransporter isoform 1 (NKCC1) and K⁺-Cl⁻ cotransporter isoform 2 (KCC2), which transport Cl⁻ into and out of neurons, respectively [42,43]. In the mature CNS, KCC2 expression is upregulated to keep [Cl⁻]_i low, resulting in Cl⁻ efflux and thus hyperpolarization when GABA_ARs open. During development, however, the predominant expression of NKCC1 results in a relatively high [Cl⁻]_i, depolarizing the GABA reversal potential

(E_{GABA}) and causing GABAergic transmission to be depolarizing as well. This typically persists until the second post-natal week in mice, when KCC2 expression is upregulated and $[Cl^-]_i$ is subsequently reduced to hyperpolarize E_{GABA} and reverse the polarity of GABA from excitatory to inhibitory [42,43]. Although depolarizing GABA is nonetheless important during development for interneuron migration and proper neuronal wiring, a reversion of GABAergic polarity to this state in developmentally mature neurons can underlie neuronal dysfunction and hyperexcitability that may give rise to epileptic seizures [44–47].

Thus far, whether disturbances in GABAergic transmission occur in CS are unknown. A previous DeltaGen phenotypic assessment in *Slc9a6/Nhe6* knock-out (KO) mice, a rodent model used to study CS [24,48–50], stated that while these mice are not spontaneously epileptic, they required significantly lower doses of the convulsant metrazol to reach various seizure states when compared with age- and sex-matched wild-type (WT) animals (Jackson laboratories, http://www.informatics.jax.org/knockout_mice/deltagen/1688.html). In the present study, we wished to investigate if the genetic disturbance of NHE6 engenders the development of network seizure activity in hippocampal circuitry. We then sought to elucidate changes in the composition and function of inhibitory synapses on to area CA1 principal neurons that could underlie such changes in excitability, including potential changes in inhibitory interneurons and the trafficking of postsynaptic inhibitory molecules. Finally, we then wished to verify if such alterations in animals with a full-gene *Nhe6* KO could also be found in primary hippocampal neurons expressing a patient-derived loss-of-function (LOF) *Slc9a6* variant to verify the translational capacity of these data to human CS patients who possess such mutations.

4.3 METHODS

Transgenic animals. To study the effects of a full gene NHE6 knock-out (KO), *Slc9a6^{tm1Dgen}* mice, bred on a C57/BL6 background and deficient in the *Nhe6* gene, were purchased from Jackson laboratories (<https://www.jax.org/strain/005843>). In experiments in which visualization of cellular structure was necessary, we crossed these mice with a line of mice expressing sparse but consistent levels of membrane-tagged EGFP (mGFP) in a subset of hippocampal pyramidal neurons under the Thy1.2 promoter (L15 mice). This GFP tag is not known to cause changes in cellular function. These initial crosses produced heterozygous *Slc9a6^{+/-}* females, which were then crossed with L15 males to generate homozygous *Slc9a6^{-/-}* females, which were crossed again with L15 males to create homozygous *Slc9a6^{-/-}* females and hemizygous *Slc9a6^{-Y}* males. These hemizygous *Nhe6* KO/L15 males were used in the experiments described in the present study, with age-matched C57/BL6 or L15 males used as controls. All animal handling procedures were carried out according to the guidelines of the Canadian Council on Animal Care and the McGill University Comparative Medicine and Animal Resources animal handling protocol 5057.

Recombinant DNA constructs. The long transcript splice-variant of human NHE6 (NHE6v1; NCBI refseq NM_001042537) was cloned from a human brain Matchmaker™ cDNA library (Clontech) with PCR methodology and engineered to contain the influenza virus hemagglutinin (HA) (YPYDVDPYAS) epitope at the extreme C-terminal end. This wild-type NHE6-HA construct was inserted into the *HindIII* and *XbaI* sites of the mammalian expression vector pcDNA3 (Invitrogen). NHE6-HA was then used as a template to create the double deletion mutation of amino acids E287 and S288 (Δ E287/S288, Δ ES) by PCR mutagenesis. NHE6 WT and Δ ES mutant constructs with mCherry fluorescent protein (mCh) tagged to their C-terminals were then created by insertion between the *XhoI* and *HindIII* restriction sites of the pAcGFP1-N1

vector (BD Biosciences Clontech, Palo Alto, CA). Insertion of the different epitope tags in the various positions did not alter the biochemical properties or cellular distribution of exogenous NHE6 compared to the endogenous protein [29]. All constructs were sequenced to ensure that no additional mutations were introduced during PCR.

Primary cell culture. Dissociated hippocampal cultures of mixed neuron and glia populations were prepared, maintained, and transfected as previously described [15,28]. In brief, postnatal day (PD) 0-1 litters from WT or homozygous *Nhe6* KO females were decapitated, their brains removed, and their hippocampi isolated and placed in ice-cold HBSS supplemented with 0.1 M HEPES buffer and 0.6% glucose. We did not separate pups based on sex because all pups were homozygous or hemizygous for the *Slc9a6/Nhe6* gene, and we did not believe sex would significantly impact *in vitro* results at this early stage of development. After all tissue was collected, they were digested with 165 U papain for 20 min in a shaking water bath heated to 37 °C. Cells were then dissociated by mechanical trituration and suspended in DMEM supplemented with 1% penicillin-streptomycin, 10% FBS, and 0.6% glucose. Cells were then plated onto poly-D-lysine coated 10 mm glass coverslips at an approximate density of 12,000 cells/cm² and transferred into a sterile humidified environment of 5% CO₂, 37°C. 24 h later, initial plating media was removed and replaced with Neurobasal-A growth media supplemented with 2% B-27 supplement, 1% GlutaMAX, and 1% penicillin-streptomycin. Media was replenished every 3 – 4 d until 14+ days *in vitro* (DIV) to allow for development of a functional neuronal network [119].

Primary neurons were then transfected with DNA constructs via calcium phosphate transfection as previously described [15,28,120]. At 11-12 DIV, coverslips with viable cell cultures (by visual inspection) were transferred into a 35 mm dish filled with warmed preconditioned growth media collected from previous feedings. Four µg of DNA plasmids were

mixed with 50 μ l 250 mM CaCl_2 solution and added to 50 μ l 2 \times HEPES-buffered phosphate solution, forming DNA-tagged calcium phosphate precipitate that was then pipetted dropwise to coverslips and incubated at 37 $^\circ\text{C}$ in a humidified environment of 3% CO_2 for 90 min. Prior to the coverslips being returned to their original plates, 80 μ l of sterile 0.3 M 2-(4-morpholino) ethanesulfonic acid (MES) acid buffer (pH 5.5) were added to each dish to rapidly acidify media and dissolve remaining precipitate. Cultures were then maintained in their home environment for 48 h before being processed to allow for expression of DNA plasmids. In the present study, neurons were transfected with a mutant NHE6v1 construct (*i.e.* p.E287_S288del in NHE6v1, or NHE6 Δ ES), with WT NHE6v1 as controls. Cells were also co-transfected with plasmids encoding enhanced green fluorescent protein (GFP) to allow visualization of cell structure. We have previously shown that expression of the Δ ES construct exerts a dominant negative overexpression effect upon expression of the endogenous WT form of the exchanger [28], thus allowing us to study the impact of the Δ ES mutation upon neuronal function *in vitro*.

Electrophysiology. Acute transverse hippocampal brain slices were prepared from male *Nhe6* KO mice (P28-35 for firing experiments, P30-P49 for inhibitory current measurements) with age- and sex-matched WT as controls. After mice were deeply anesthetized and rapidly decapitated, their brains were extracted and sectioned into 250 or 400 μm thick brain slices in ice-cold sucrose-based artificial cerebrospinal fluid (ACSF) using a vibrating microtome (VT1000S, Leica). Slices recovered for 1 h at 32 $^\circ\text{C}$ in regular ACSF containing (in mM): 24 NaCl, 5 KCl, 1.25 NaH_2PO_4 , 2 MgSO_4 , 26 NaHCO_3 , 2 CaCl_2 , and 10 glucose saturated with 95% O_2 /5% CO_2 (pH 7.3, 300 mOsm). Slices were then maintained at room temperature and bubbled constantly with 95% O_2 /5% CO_2 for the duration of the experiments.

To assess network excitability, 400 μm thick acute brain sections were placed into the recording chamber of an upright microscope (DM LFSA Microsystems, Heidelberg, Germany) and perfused continuously with regular ACSF (as described above). Low resistance borosilicate patch pipettes were back-filled with ACSF and placed around hippocampal area CA1 stratum radiatum, and extracellular responses were measured in I_o mode using an AxoPatch 400B Amplifier (Molecular Devices, San Jose, USA). After a 15 min stable baseline response was achieved, the external solution was replaced with ACSF supplemented with 10 μM 4-aminopyridine (4-AP) to measure the effect of subthreshold application of 4-AP on network excitability. Additional positive controls were performed upon WT slices using ACSF supplemented with 100 μM 4-AP to ensure experimental set-up was adequate.

To perform whole-cell patch clamp electrophysiology, 250 μm slices or transfected 14+ DIV cultures were placed into the recording chamber of an upright microscope (BX51WI, Olympus, XLUMPlanF1 20x 0.95 NA water immersion objective) and perfused continuously in regular ACSF (for intrinsic firing) or ACSF supplemented with (in μM): 25 CPP, 5 CGP 55845, 20 2,3-dioxo-6-nitro-7-sulfamoyl-benzo[f]quinoxaline (NBQX), and 0.3 strychnine (for GABA_AR-mediated sIPSC recordings). To isolate GABA_AR-mediated mIPSCs, 1 μM TTX was also included in the external solution. Whole-patch-clamp recordings were performed on visually identified hippocampal CA1 pyramidal neurons or fluorescent transfected primary neurons held at -60 mV with an Axopatch 400 amplifier (Molecular Devices, Sunnyvale, CA, USA) at room temperature (23-25 °C) using borosilicate patch pipettes (4-8 M Ω) filled with (in mM): 120 K-gluconate, 1 EGTA, 10 HEPES, 5 MgATP, 0.5 Na₂GTP, 5 NaCl, 5 KCl, and 10 phosphocreatine K₂ (pH 7.2-7.3 adjusted with KOH and 285-295 mOsm) (for intrinsic firing) or 140 CsCl, 4 NaCl,

0.5 CaCl₂, 10 HEPES, 5 EGTA, 2 qX-314, 2 Mg-ATP, 0.5 Na-GTP (pH 7.36 adjusted with CsOH and 290 mOsm).

Intrinsic firing was measured by injecting 1 s-long current of increasing intensities, from 0 to 400 pA, in 10 pA increments. sIPSCs and mIPSCs were acquired by constantly holding cells at -60 mV for a 10 (*in vitro*) or 15 min (*ex vivo*) period after a stable holding current was achieved, with a sampling frequency of 20 kHz and filtered at 2 kHz. To monitor access resistance, transient test pulses were applied consistently every 2-3 min throughout the recording. Access resistance typically fell within a range of 7-10 GΩ, and data was discarded if this deviated > 20% over the course of the recording.

For each cell analyzed in property scatterplots, passive parameters were recorded from pClamp software automatically five min after whole cell mode was achieved. Action potential firing and parameters were quantified offline using ClampFit 10.3 Software. All sIPSCs and mIPSCs were detected offline using the Mini Analysis Software (Synaptosoft, Decatur, USA). The amplitude threshold for sIPSC and mIPSC detection was set at four times the root-mean-square value of a visually event-free recording period. From every experiment, 3 min of stabling recording was randomly selected for blinded analysis of amplitude, inter-event interval, and kinetics. Amplitude analysis was conducted only on single events that did not have additional events superimposed upon their rising and decaying phases. All selected events were considered for frequency analysis. All data obtained was then used to plot cumulative histogram with equal contributions from every cell per genotype. For statistical analysis, data were instead averaged for every cell acquired.

Immunoblotting. To extract whole hippocampi from developmentally mature mice for immunoblotting experiments, animals were deeply anesthetized and decapitated prior to extraction

of their brains and hippocampi, which were transferred on to dry ice. For every 40 µl of tissue, approximately 300 µl of ice-cold radioimmunoprecipitation assay (RIPA) buffer (consisting of 1% Nonidet P-40, 0.5% sodium deoxycholate, 0.1% sodium dodecyl sulfate (SDS), 50 mM Tris-HCl (pH 8.0), 1.50 mM NaCl, 10 mM NaF, 1 mM sodium orthovanadate, 1 mM beta-glycerophosphate, and completeMINI protease inhibitors (Roche)) added to homogenize hippocampi. Lysates were then sonicated and centrifuged at 12,000 revolutions per min for 10 min at 4°C, and supernatant was removed from pellet. Protein concentrations in the supernatant were then measured using a bicinchoninic acid dye-binding assay (Thermo Scientific) and compared against a standard concentration of bovine serum albumin (BSA).

To separate proteins, 15 µg protein from lysates were loaded and subjected to 8-9% SDS-polyacrylamide gel electrophoresis (SDS-PAGE), then transferred to methanol-activated polyvinylidene fluoride (PVDF) membranes (Millipore, Nepean, Ontario, Canada) overnight at 4°C. Membranes were subsequently blocked with 5% non-fat skim milk/0.01% Tween-20 in phosphate-buffered saline (PBS-T) for 1 h, then incubated overnight at 4°C with primary antibodies diluted in blocking buffer, as specified: GAD67 (Millipore): 1:5,000; NKCC1 (Millipore): 1:1,000; KCC2 (Millipore): 1:1,000; β-actin (Sigma-Aldrich): 1:10,000; β-III tubulin (R&D Systems): 1:5,000. Membranes were then washed and incubated with mouse (1:5,000) or rabbit (1:2,000) horseradish peroxidase (HRP)-conjugated secondary antibodies (Jackson) diluted in blocking buffer for 1 h at room temperature with agitation. After extensive washing, immunoreactive signals were detected by exposing membranes to Western Lightning™ Plus-ECL blotting detection reagents (Perkin Elmer Inc, Waltham, MA) in an Amersham™ Imager 6000 (GE Life Sciences, Buckinghamshire, UK). Immunoreactive bands were then quantified by analysis of digital image files using ImageJ software.

Immunohistochemistry. Whole coronal sections of adult mouse brains were prepared to analyze *in vivo* protein expression using intracardiac perfusions and coronal sectioning, performed as previously described [121]. In summary, adult mice (P60) were deeply anesthetized and perfused intracardially with 0.1 M PBS followed by 4% PFA/0.1 M PBS, pH 7.4 (Sigma Aldrich). After perfusion, the brain was extracted and stored in PFA at 4°C for 24-48 h, then transferred into a 30% sucrose solution until completely saturated. Cortices were then sliced into 100 µm thick coronal sections on a Leica Vibratome 3000 Plus sectioning system (Concord, ON, Canada) and stored in 0.5% sodium azide/0.1 M PB. Mature primary neuron cultures at > 14 DIV were washed briefly with 0.1 M PB and fixed for 15 min in 4% PFA/0.1 M PB, followed by extensive washing.

Fixed brain sections and primary cultures were stored at 4°C until subsequent immunolabeling. Fixed slice sections were permeabilized and blocked overnight at 4°C in 0.4% Triton X-100/1.5% HIHS/0.1 M PB. Primary antibodies were then diluted (parvalbumin (Swant): 1:500; GFP (Invitrogen): 1:250; gephyrin (Synaptic Signaling): 1:500; GAD65 (Abcam): 1:500; GABA_AR α1 and α2 (gifts from Dr. Jean-Marc Fritschy): 1:3,000) in this solution for five days at 4°C with gentle shaking. After incubation and washing, secondary antibodies were diluted (Alexa Fluor 488/594 or DyLight 649, 1:250) in 1.5% HIHS/0.1 M PB and applied overnight at 4°C. Primary cultures were instead permeabilized for 1 min in 0.2% Triton X-100/0.1 M PB and blocked for 1 h at room temperature in 0.2% Triton X-100/1% HIHS/0.1 M PB, before being incubated overnight at 4° C with primary antibodies (same as above, except GFP (Invitrogen): 1:1000) diluted in blocking solution with gentle agitation. After subsequent washing, cells were incubated with secondary antibody (same as above, except with 1:1,000 dilution) diluted in 1% HIHS/0.1M PB for 45 min at room temperature and washed again. All slices and coverslips were

mounted onto SuperFrost (Menzel-Glaser) microscope slides using UltraMount fluorescence mounting medium (Dako) and left to dry overnight at room temperature in the dark.

Microscopy. To capture high-resolution images of the structure of individual neurons, mounted slides were imaged using a Leica TCS SP2 confocal microscope with data acquired using a 63x (NA 1.4) HCXPL APO oil-immersion objective. mGFP and Alexa Fluor 488 were imaged using a 488 nm Ar laser line, Alexa Fluor 594 was imaged using a 543 nm HeNe laser line, and DyLight 649 was imaged with a 633 nm HeNe laser line. Channels were acquired sequentially to prevent spectral overlap of fluorophores. Optical sections of 300-500 nm were taken and line-averaged 2x at high resolution to improve the signal-to-noise ratio.

To acquire wide-field images of whole brain sections, mounted slides were imaged on a Zeiss Axiovert 200M Fully Automated Inverted Microscope using a 10X PLAN NEOFLUAR (NA = 0.30, Ph 1) objective equipped with a X-Cite 120 LED and FS10 (eGFP) and FS15 (TRITC) fluorescence cubes. Tiling parameters were set to capture regions of interest, determined visually, and set points were placed to counter minor shifts in z -position. Scan times were determined automatically based off of fluorescence intensity and minimized to prevent photobleaching. After acquisition, tiles were then stitched together automatically into a composite image using ZEN software.

Image analysis. High-resolution confocal stacks were first deconvolved using Huygen Essentials software using a full maximum likelihood extrapolation algorithm (Scientific Volume Imaging, Hilversum, The Netherlands). 3D images were then compiled as maximum intensity projections using the Surpass function on Imaris software (Bitplane AG, Zurich, Switzerland). To quantify puncta density, the channel containing signal for the protein of interest was masked based off of the dendritic mGFP signal using the Imaris Surfaces function to ensure puncta were localized

within neurons. For presynaptic terminal markers, the threshold for Surface creation was lowered such that the Surface was oversaturated relative to the mGFP signal in order capture puncta in direct apposition to the neuron of interest. The number of puncta localized in or around the soma or dendrite for each stack were then determined automatically using the Imaris Spots function, with a minimum puncta diameter of 0.3 μm . Puncta counts were divided by the length of the analyzed dendrite (determined using the Imaris Filament Tracer function) or volume of the analyzed soma (determined using the Surface function) to calculate densities. Widefield images of whole brain sections were directly opened in Imaris software. The Imaris Surface function was used to isolate individual brain areas to determine the area (in μm^2) and to create a mask of the channel to allow automatic detection of cell bodies using the Imaris Spots function, based off of an approximate average diameter of all cell bodies. A density was then calculated by dividing the number of spots by the area calculated from the Surface function.

Statistical analysis. The data throughout the present study represent the mean \pm the standard error of the mean (S.E.M.). Statistical analyses were generally performed using the Student's t-test (parametric data) or Mann-Whitney test (non-parametric data), as indicated. A minimum *p*-value of < 0.05 was considered significant.

4.4 RESULTS

4.4.1 Verifying hippocampal circuitry hyperexcitability in *Nhe6* KO

We first assessed the excitability of hippocampal circuitry in the absence of NHE6 by exposing acute hippocampal slices prepared from juvenile (P28-35) WT and *Nhe6* KO male mice to the convulsant 4-aminopyridine (4-AP), a blocker of voltage-gated K^+ channels that depolarizes membrane potentials. To properly determine if KO neurons were more prone to developing

hyperexcitability, we employed a subthreshold concentration (10 μ M) standard concentration that is five to ten times less than that which is normally used to elicit epileptiform discharges in WT mouse brain slices [51,52]. Recording extracellular potentials from hippocampal area CA1, we found that 30 min after bath application of 4-AP, KO slices began to show drastic bursts of discharges that were absent in WT slices (**Fig. 1A**). This suggests that *Nhe6* KO hippocampal neurons are indeed more sensitive to relatively small elevations in neuronal activity, which cause aberrant epileptiform discharges that are not observed in WT.

We then examined if this increase in network excitability could be due to changes in the intrinsic excitability of *Nhe6* KO principal neurons. To this end, we performed current clamp recordings on CA1 pyramidal cells in *Nhe6* KO acute brain slice preparations. After achieving whole cell patch clamp conditions, we noted that *Nhe6* KO cells did not show significant differences in resting membrane potential, input resistance, or membrane capacitance when compared to WT cells, suggesting that passive membrane properties of KO neurons were unchanged (**Fig. 1E**). We then performed currents injections ranging from 0 to 400 pA for a duration of 1 s and quantified the number of AP spikes to measure their intrinsic firing in the absence of synaptic inputs. However, we did not find that *Nhe6* KO cells produced significantly more APs than WT cells at any current amplitude (**Fig. 1B-C**), nor did they show any significant differences in AP parameters such as magnitude, half-width, kinetics, or adaptation (**Fig. 1D-E**). From our observations, we conclude that excitatory pyramidal cells in area CA1 are not intrinsically more excitable in *Nhe6* KO neurons than WT at this time point.

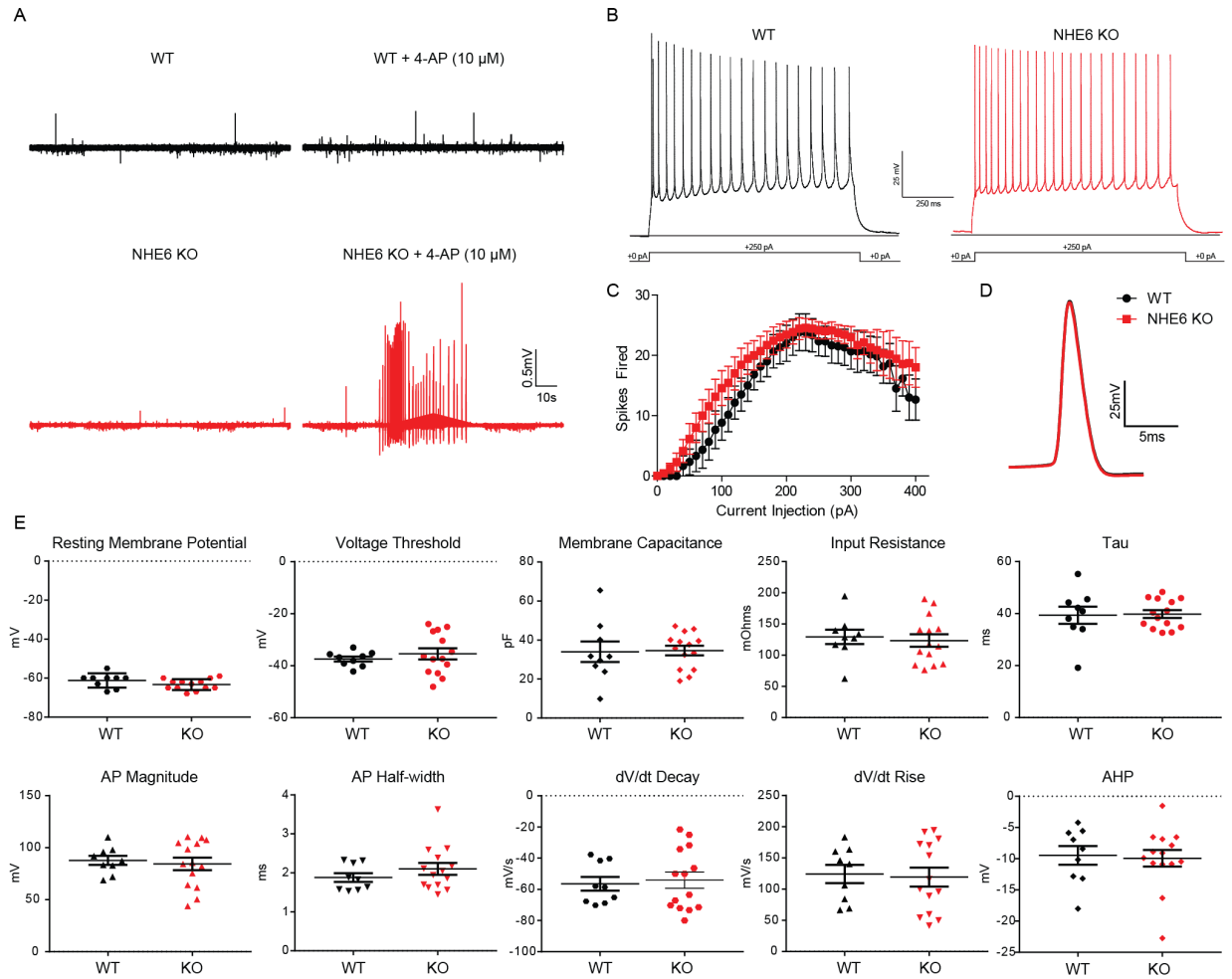


Figure 1: *Nhe6* KO hippocampal circuitry is hyperexcitable when compared to WT in response to 4-AP challenge, yet WT and *Nhe6* KO CA1 pyramidal neurons do not differ in active or passive membrane properties. **A:** Example extracellular potential recordings from area CA1 of WT (top) and *Nhe6* KO (bottom) acute hippocampal slices at baseline (left) and 30 min following application of 4-AP (10 μ M, right). **B:** Example membrane potential responses from WT (left) and *Nhe6* KO (right) CA1 pyramidal cells following a current injection of +250 pA, 1 sec. **C:** Mean \pm SEM number of APs fired at current injections ranging from 0 to 400 pA in WT (black) and KO (red) CA1 cells. **D:** Average AP trace from WT and KO cells. WT: n = 6 cells from 2 animals; KO: n = 6 cells from 2 animals. **E:** Scatterplots of intrinsic and action potential properties from each genotype; each point corresponds to an individual cell, horizontal line with error bars indicate mean \pm SEM. WT: n = 9 cells from 6 animals; KO: n = 14 cells from 9 animals. Results in C and E were not significant ($p > 0.05$), unpaired Student's t-test.

4.4.2 Evaluating inhibitory synaptic regulation in *Nhe6* KO area CA1

Given that NHE6 is highly expressed in GABAergic cells of the hippocampus, we next assessed possible alterations in inhibitory interneurons. To this end, we first performed immunoblotting experiments probing glutamic acid decarboxylase 67 (GAD67), a key enzyme in the synthesis of GABA that is expressed diffusely throughout GABAergic interneurons [53,54], at two and six months of age. While GAD67 levels were comparable between WT and *Nhe6* KO hippocampi at P60, KO tissue expressed significantly less GAD67 than WT by P180 (**Fig. 2A-B**). This suggests an age-dependent loss of GAD67, and hence GABAergic interneurons, in *Nhe6* KO hippocampi. To better validate this theory, we performed immunohistochemistry experiments to directly visualize cells expressing parvalbumin (PV), a Ca²⁺-buffering protein used as a marker for fast-spiking basket cells that form perisomatic connections onto pyramidal neurons [55,56]. In accordance with our GAD67 immunoblotting data, PV+ cell counts throughout the entire hippocampus were similar between WT and *Nhe6* KO at P60, yet significantly decreased in KO at P180 (**Fig. 2C-F**). However, when we divided these cells into their respective hippocampal areas, PV+ cell density was elevated in area CA3, but significantly lower in area CA1, in *Nhe6* KO P60 tissue when compared to age-matched WT samples (**Fig. 2C-D**). Nevertheless, by P180, PV+ cells were significantly decreased in both areas CA3 and CA1 in KO hippocampi relative to WT (**Fig. 2E-F**). Thus, while the data demonstrate a time-dependent loss of PV+ interneurons throughout the hippocampus in *Nhe6* KO, these mice already show region-specific changes at younger stages of adulthood that suggest possible alterations in inhibitory regulation of area CA1 cells at two months of age. However, by six months of age, GABAergic interneurons, particularly those expressing PV, appear to be lost throughout the KO hippocampus when compared to control mice.

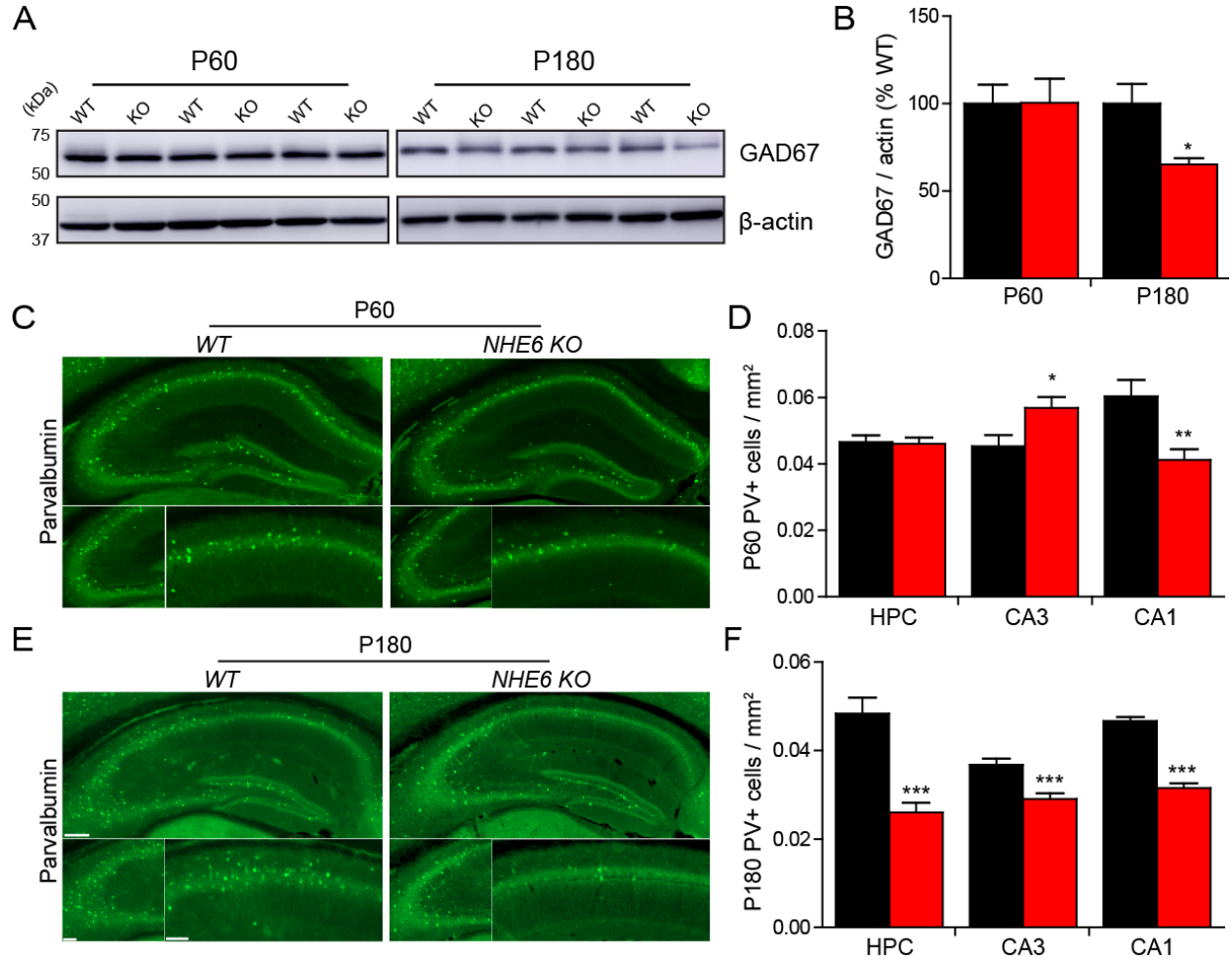


Figure 2: Age-dependent loss of GAD protein and PV+ interneuron density in *Nhe6* KO hippocampi. **A:** Representative immunoblots of glutamic acid decarboxylase 67 (GAD67) in whole adult hippocampal lysates from P60 and P180 WT and *Nhe6* KO mice, with β -actin as loading control. **B:** Mean \pm SEM quantification of GAD67 signal intensity relative to actin loading control and normalized to WT for each time point. For P60, WT: $n = 4$, KO: $n = 4$; for P180, WT: $n = 5$, KO: $n = 4$. **C, E:** Example immunofluorescent images of coronal brain sections taken from P60 (**C**) and P180 (**E**) WT and *Nhe6* KO male mice and immunoprocessed for parvalbumin (PV). For each set of images, top image shows whole hippocampus (scale bar: 200 μ m), bottom-left image shows zoom-in of area CA3 (scale bar: 100 μ m), and bottom-right image shows zoom-in of area CA1 (scale bar: 100 μ m). Image sets in **C** and **E** are of equal magnification. **D, F:** Mean \pm SEM quantification of PV+ cell density within areas CA3 and CA1, as well as whole hippocampus (HPC) at P60 (**D**) and P180 (**F**), for each genotype. For P60, WT: $n = 17$ hippocampi in 10 sections from 5 animals; KO: $n = 19$ hippocampi in 10 sections from 6 animals. For P180: $n = 32$ hippocampi in 16 sections from 4 animals of each genotype. *: $p < 0.05$, **: $p < 0.01$, ***: $p < 0.0001$, unpaired Student's t-test.

Taking into account the reduced density of PV+ interneurons in area CA1 in young adult *Nhe6* KO animals, we performed further immunohistochemical experiments to directly assess inhibitory synapses onto CA1 pyramidal cells. For this purpose, we collected tissue from P60 WT and *Nhe6* KO mice in which subsets of hippocampal pyramidal neurons express a membrane-tagged EGFP (mGFP), allowing us to easily visualize neuronal structures. We first examined expression of glutamic acid decarboxylase 65 (GAD65), another GAD isoform that primarily localizes to GABAergic presynaptic terminals, as well as the inhibitory postsynaptic scaffolding molecule gephyrin. In accordance with the aforementioned reduction in perisomatic-targeting PV+ interneurons, we found that GAD65 puncta apposing and gephyrin puncta within CA1 pyramidal cell somata were both reduced in P60 tissue (**Fig. 3A-B**). This loss of both pre- and postsynaptic inhibitory markers suggested a loss of somatic inhibitory synapses on to CA1 principal cells. We also observed a reduction of gephyrin puncta in the dendrites of KO CA1 pyramidal neurons, indicating a decrease in dendritic inhibitory postsynaptic sites as well (**Fig. 3C-D**). Interestingly, upon assessing the dendritic localization of the synaptic GABA_AR subunits $\alpha 1$ and $\alpha 2$, we found a reduction in the trafficking of $\alpha 2$, but not $\alpha 1$, in *Nhe6* KO when compared to WT (**Fig. 3C-D**). In all, these findings suggest a subunit-specific loss of GABA_ARs and inhibitory postsynaptic sites, leading us to speculate that inhibitory transmission on to pyramidal neurons may be dampened.

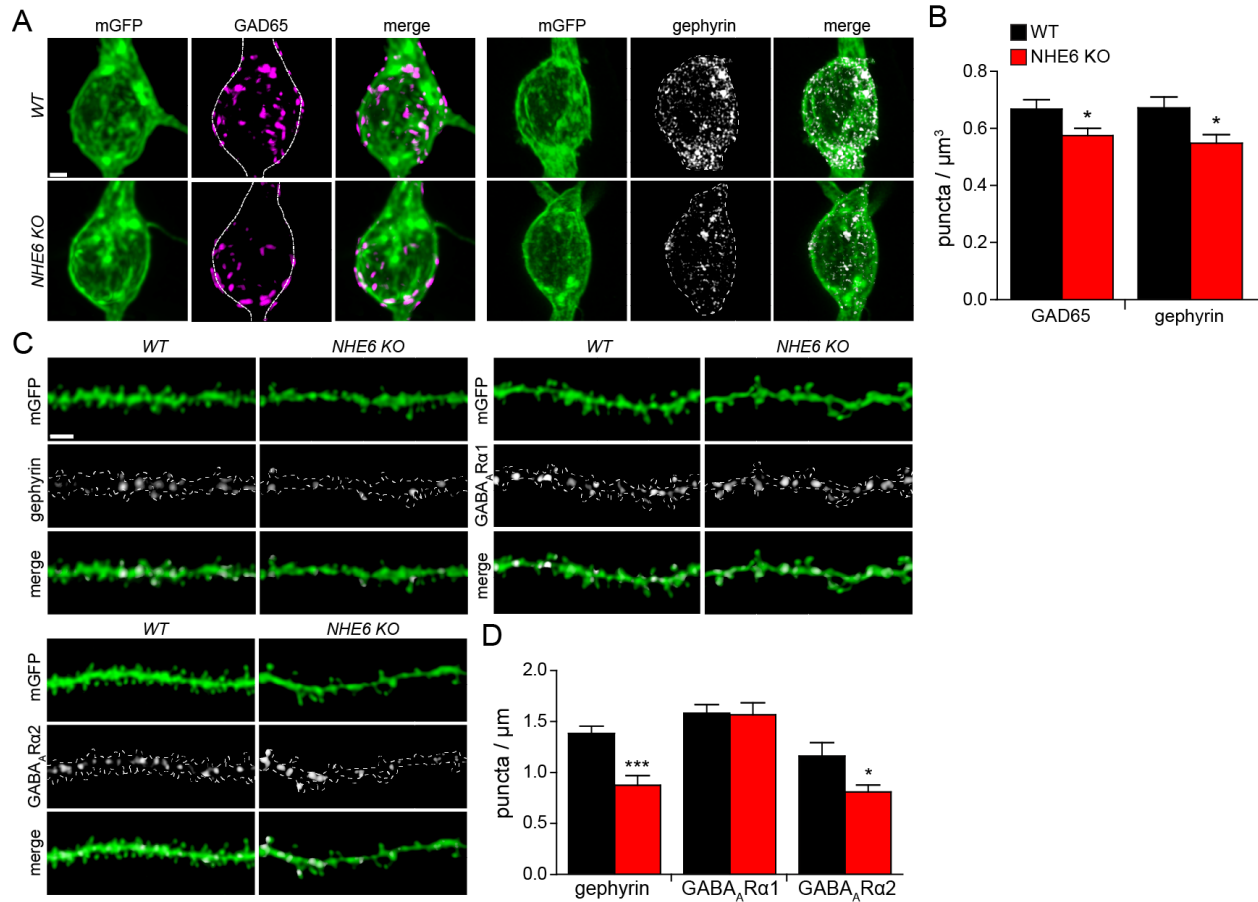


Figure 3: Reduced inhibitory markers in the soma and dendrites of *Nhe6* KO CA1 pyramidal neurons. **A:** Example confocal micrographs of mGFP-labeled WT and *Nhe6* KO CA1 pyramidal neuron somata stained for glutamic acid decarboxylase 65 (left) and gephyrin (right). Channels are shown separate and merged; dotted lines in middle channels show outline of the cell body denoted by the mGFP signal. Scale bar: 4 μm . **B:** Mean \pm SEM quantification of GAD65 puncta in apposition to (left), and gephyrin puncta within (right), CA1 pyramidal neuron somata. For GAD65, WT: $n = 18$ cells, KO: $n = 17$ cells from 4 animals per genotype. For gephyrin, WT: $n = 19$ cells from 4 animals; KO: $n = 16$ cells from 3 animals. **C:** Example confocal micrographs of mGFP-labeled WT and *Nhe6* KO CA1 pyramidal neuron dendrites stained for gephyrin (top left) and GABA_AR subunits α 1 (top right) and α 2 (bottom). Channels are shown separate and merged; dotted lines in middle channel show outline of the dendrite denoted by the mGFP signal. Scale bar: 2 μm . **D:** Mean \pm SEM quantification of gephyrin, GABA_AR α 1, and GABA_AR α 2 dendritic puncta density in WT and *Nhe6* KO CA1 pyramidal neurons. For gephyrin, $n = 19$ cells from 3 animals for both genotypes. For GABA_AR α 1, WT: $n = 17$ cells, KO: $n = 15$ cells from 3 animals per genotype. For GABA_AR α 2, $n = 12$ cells from 3 animals per genotype. *: $p < 0.05$, ***: $p < 0.0001$, unpaired Student's t-test.

4.4.3 Examining GABAergic transmission on to *Nhe6* KO CA1 principal cells

Taking into account the decreases in both PV cell density and perisomatic GABAergic synapses, we hypothesized that we would observe changes in GABAergic transmission as well. To verify this, we recorded GABA_AR-mediated miniature inhibitory postsynaptic currents (mIPSCs) from CA1 pyramidal neurons in the presence of tetrodotoxin (TTX) to block phasic transmission owing to interneuron firing. As expected, we found a significant reduction in mIPSC amplitude in *Nhe6* KO relative to WT, confirming an attenuation of synaptic GABA_ARs in KO cells (**Fig. 4A-B, E-G**). The rise time of mIPSCs recorded from KO cells were also significantly longer when compared to WT, although decay times were not significantly altered (**Fig. 4B-D**). These changes in kinetics suggest a corresponding alteration in synaptic GABA_AR subunit composition [57,58] and are thus in line with the selective downregulation of the $\alpha 2$ in *Nhe6* KO principal cells. In spite of this loss, we did not observe a significant change in mIPSC interevent interval (IEI), an inverse measure of event frequency (**Fig. 4A, H-J**). This may be indicative of an increase in release probability from presynaptic GABAergic terminals. When taken together, our immunohistochemistry and physiological data suggest deficits in the function and composition of postsynaptic GABAergic sites onto CA1 pyramidal cells.

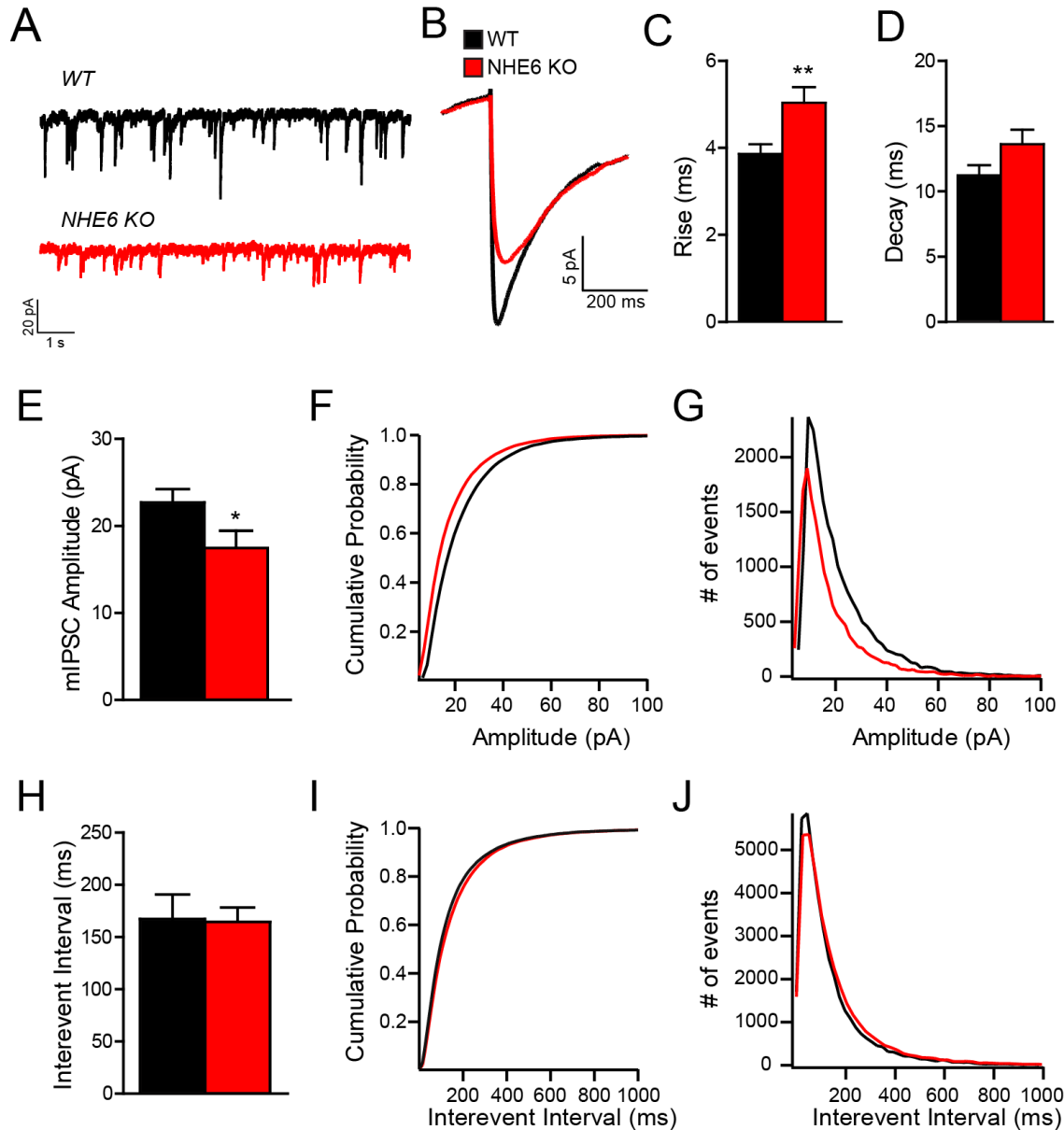


Figure 4: Reduced GABA_AR-mediated inhibitory neurotransmission on to *Nhe6* KO CA1 pyramidal neurons. **A-B:** Example recordings (**A**) and average event traces (**B**) of GABA_AR-mediated miniature inhibitory postsynaptic currents (mIPSCs) recorded from WT (black) and *Nhe6* KO (red) CA1 pyramidal neurons within acute hippocampal slice preparations. **C-D:** Mean \pm SEM mIPSC rise (**C**) and decay (**D**) times. **E-G:** Mean \pm SEM (**E**), cumulative probability (**F**) and frequency histogram (**G**) plots of mIPSC amplitudes. **H-J:** Mean \pm SEM (**H**), cumulative probability (**I**) and frequency histogram (**J**) plots of mIPSC interevent intervals. WT: $n = 18$ cells from 3 animals; *Nhe6* KO: $n = 15$ cells from 2 animals. *: $p < 0.05$; **: $p < 0.01$, unpaired Student's t-test.

We next sought to investigate GABAergic transmission on to postsynaptic pyramidal neurons in the presence of interneuron activity by recording GABA_AR-mediated spontaneous inhibitory postsynaptic currents (sIPSCs) from CA1 pyramidal neurons in the absence of TTX. We found a similar change in sIPSC kinetics as observed from our mIPSC data, with a significant increase in rise time and no change in decay in *Nhe6* KO when compared to WT (**Fig. 5B-D**). Again, the data suggest a possible change in GABA_AR subunit composition, but it may also represent a dispersal of inhibitory sites away from the pyramidal cell body in favour of more distal sites. Indeed, studies assessing interneurons synapsing on to axosomatic and dendritic regions of pyramidal cells have shown a delay in the kinetics of the IPSC recorded upon activation of the later [59], thereby insinuating that axosomatic-targeting PV+ interneurons may have a reduced impact on downstream GABAergic transmission on to *Nhe6* KO CA1 cells. Interestingly, despite the attenuation in somatic inhibitory synapses, IEI was again unchanged between WT and KO neurons (**Fig. 5A, H-J**), which more strongly implies an increase in the firing or release probability of surviving PV+ cell axon terminals. Moreover, although the trafficking of some GABA_ARs (**Fig. 3**) and mIPSC amplitude (**Fig. 4**) were both found to be reduced in *Nhe6* KO, we found that KO neurons showed a significantly greater mean sIPSC amplitude than WT cells (**Fig. 5A-B, E-G**). This surprising observation suggested a severe dysregulation in inhibitory signaling within area CA1 circuitry in *Nhe6* KO. Overall, relative to WT, we hypothesize that *Nhe6* KO CA1 pyramidal neurons receive an enhanced degree of phasic GABAergic synaptic transmission from a reduced but potentially hyperactive population of surviving PV+ cells.

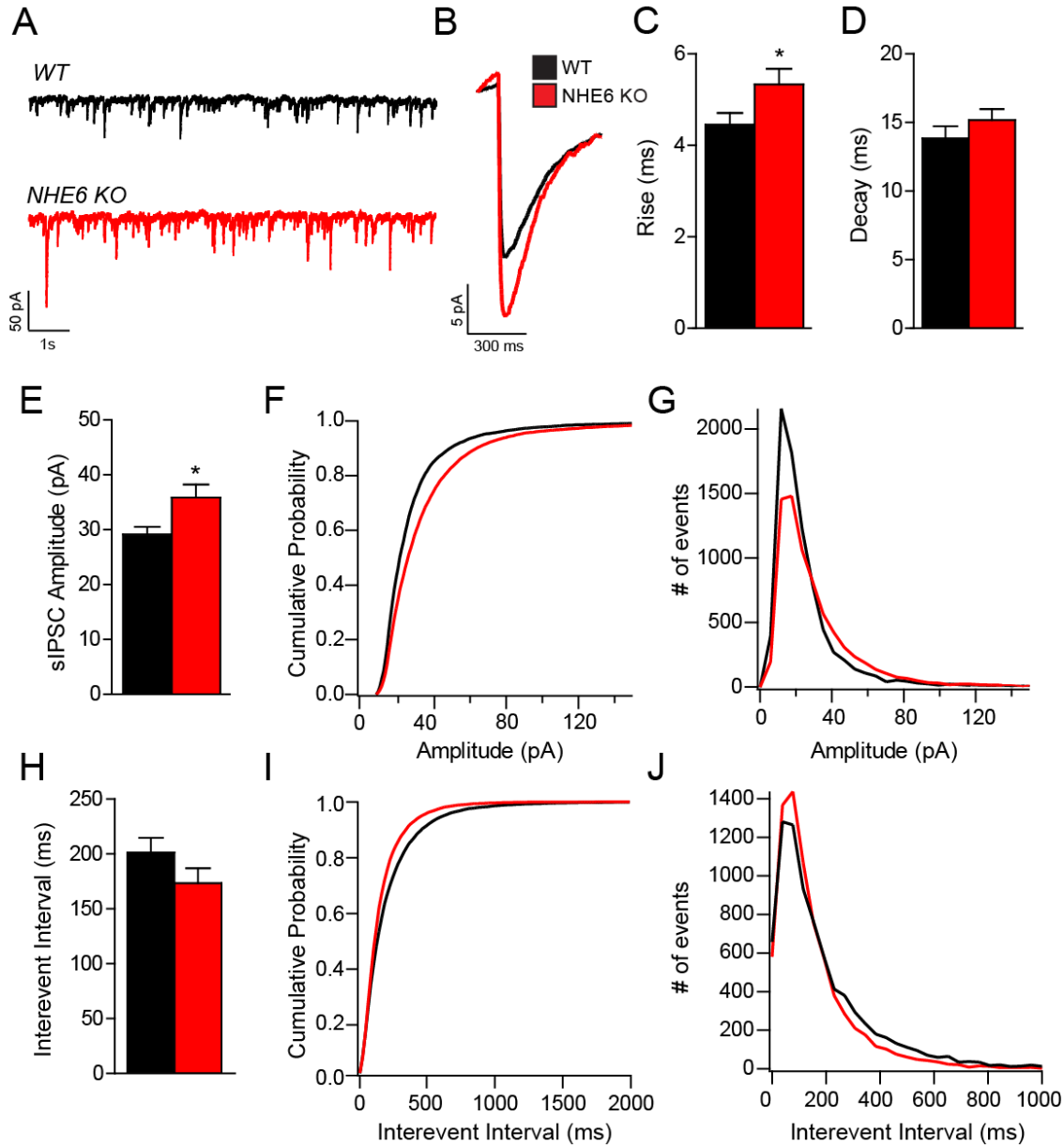


Figure 5: Altered GABAergic network inhibitory neurotransmission on to *Nhe6* KO CA1 pyramidal neurons. **A-B:** Example recordings (**A**) and average event traces (**B**) of GABA_AR-mediated spontaneous inhibitory postsynaptic currents (sIPSCs) recorded from WT (black) and *Nhe6* KO (red) CA1 pyramidal neurons within acute hippocampal slice preparations. **C-D:** Mean \pm SEM sIPSC rise (**C**) and decay (**D**) times. **E-G:** Mean \pm SEM (**E**), cumulative probability (**F**) and frequency histogram (**G**) plots of sIPSC amplitudes. **H-J:** Mean \pm SEM (**H**), cumulative probability (**I**) and frequency histogram (**J**) plots of sIPSC interevent intervals. For both WT and KO, $n = 19$ cells from 3 animals per genotype. *: $p < 0.05$, unpaired Student's t-test.

Could this change in sIPSC amplitude result from a dysregulation of Cl^- homeostasis and thus E_{GABA} in CA1 pyramidal neurons? To address this possibility, we measured protein levels of the two primary neuron cation- Cl^- cotransporters NKCC1 and KCC2 at multiple time points. At P21, an age by which the NKCC1/KCC2 switch should have occurred in mice [43], *Nhe6* KO hippocampal tissue showed significantly reduced KCC2 levels when compared to WT; this pattern persisted over time, as KCC2 levels were consistently significantly decreased in *Nhe6* KO lysates compared to age-matched WT samples at P60 and P180 (**Fig. 6B, D**). Interestingly, at these later time points, we found that NKCC1 levels were also significantly elevated in KO tissue relative to WT (**Fig. 6A, C**). These findings suggest a disturbance in the molecular mechanisms regulating the expression of these cotransporters and allude to the possibility of $[\text{Cl}^-]_i$ being significantly elevated in adult *Nhe6* KO neurons. As a result, E_{GABA} may be significantly depolarized in KO hippocampi relative to WT, resulting in GABA becoming less inhibitory or potentially excitatory, which could account for the elevation in sIPSC amplitude seen in KO (**Fig. 5**). In the future, additional perforated patch-clamp experiments will be required to verify potential changes in E_{GABA} between WT and *Nhe6* KO CA1 pyramidal neurons.

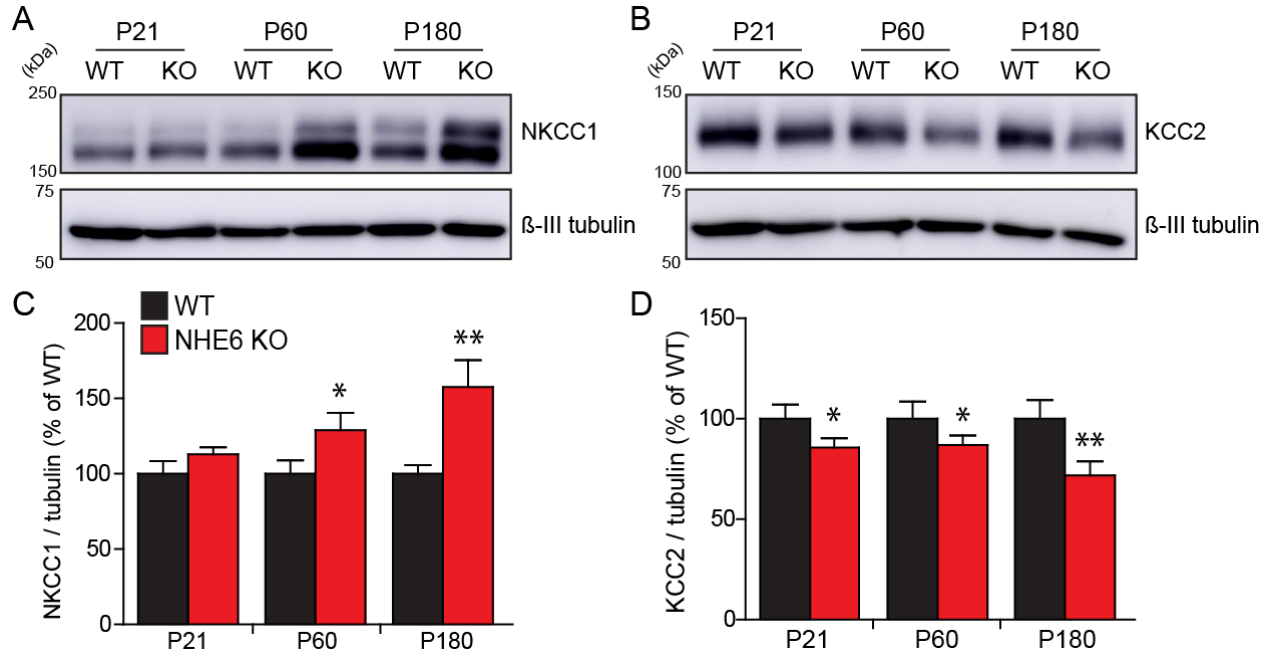


Figure 6: Upregulation of NKCC1 and downregulation of KCC2 in adult *Nhe6* KO hippocampi. **A-B:** Example immunoblots of NKCC1 (**A**) and KCC2 (**B**) from P21, P60, and P180 WT and *Nhe6* KO whole hippocampal lysates, with β -III tubulin as loading control. **B-C:** Mean \pm SEM quantification of NKCC1 (**C**) and KCC2 (**D**) relative to tubulin loading control and normalized to WT for each time point. For NKCC1: P21, WT: n = 4, KO: n = 4; P60, WT: n = 7, KO: n = 8; P180: WT: n = 5, KO: n = 4. For KCC2: P21, WT: n = 6, KO: n = 6; P60, WT: n = 7, KO: n = 8; P180, WT: n = 5, KO: n = 4. *: $p < 0.05$, **: $p < 0.01$, unpaired Student's t-test.

4.4.4 Recapitulating inhibitory synaptic changes in a clinical NHE6 mutant *in vitro*

Our inferences to this point have been taken from *Nhe6* KO mice, in which the *Slc9a6* gene is completely ablated. However, human CS patient genomes typically contain mutations in *SLC9A6* as opposed to a full gene KO. While many of these variants introduce a premature stop codon that results in a truncation of the NHE6 protein upon translation, some mutations can still produce a full-length protein product [8,10]. We have recently investigated the effect of one of these mutations, an in-frame LOF deletion variant of NHE6 (p.Glu287_Ser288del, or Δ ES), upon neuronal structure, plasticity and behaviour [28,29], but we wished to expand upon the findings of the current study by investigating whether the Δ ES mutation could also impact inhibitory postsynaptic sites. To this end, we transfected an mCherry fluorescent protein (mCh)-tagged NHE6 Δ ES construct into mouse primary hippocampal neurons, which we have previously shown to have a dominant negative effect over the endogenous WT form of the exchanger [28]. Primary neurons overexpressing mCh-tagged NHE6 WT were used as controls. Similar to our observations in *Nhe6* KO mice, we saw a significant decrease in somatic gephyrin puncta density (**Fig. 7A-B**) as well as the dendritic localization of gephyrin and GABA_AR subunit α 2, but not α 1, in NHE6 Δ ES-expressing cells in comparison to control (**Fig. 7E-H**). Notably, we also found a higher degree of colocalization between punctae of NHE6 WT and these inhibitory markers than that with NHE6 Δ ES, with GABA_AR α 2 showing the most colocalization with NHE6 WT of the molecules investigated (**Fig. 7C-D, I-J**). This observation brought forth the possibility that NHE6 may be more commonly found in GABA_AR α 2-positive vesicles compared to those containing α 1 to regulate the trafficking of the former, hence the selective decrease in the α 2 subunit in Δ ES-expressing cells.

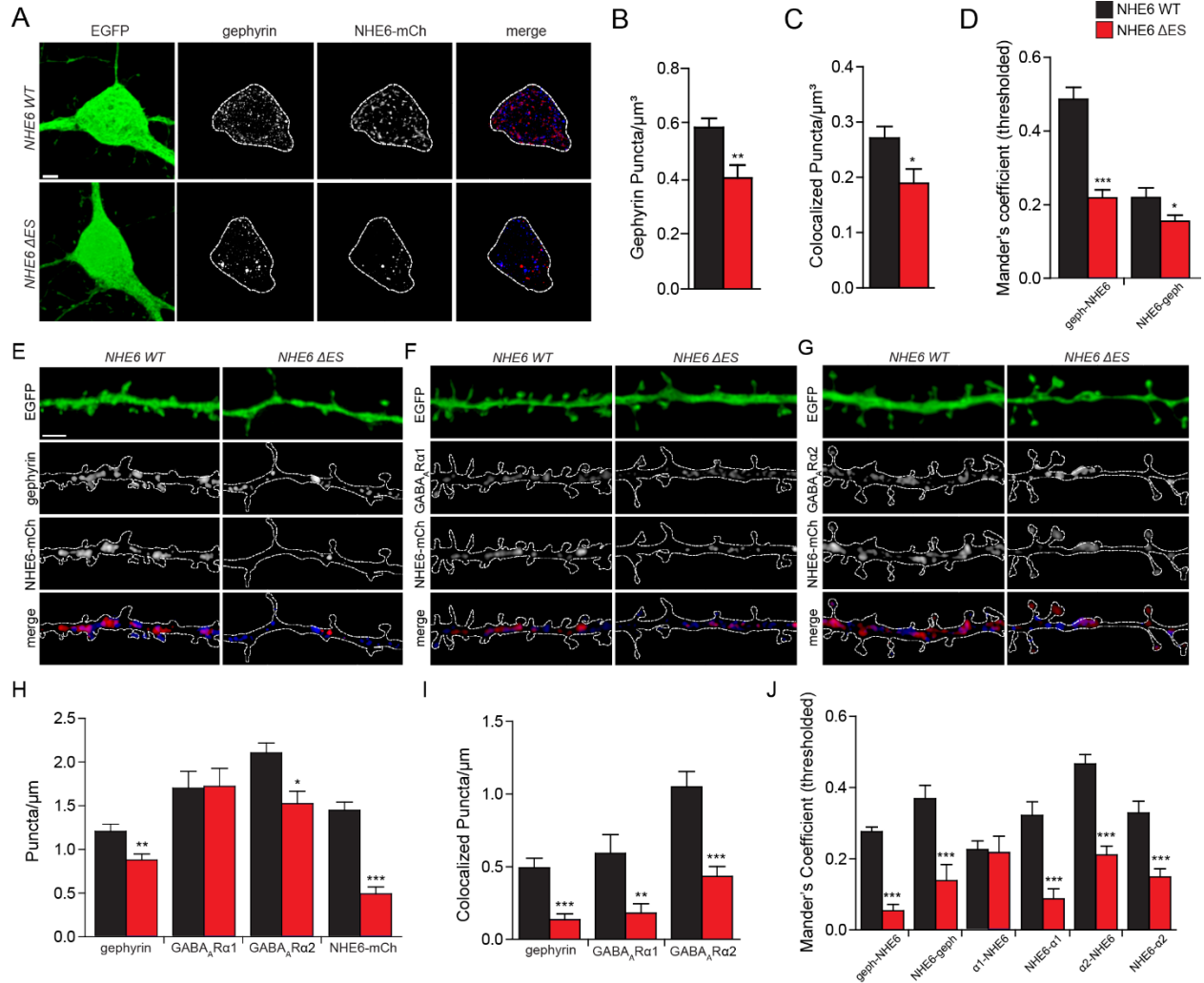


Figure 7: Similar downregulations of inhibitory postsynaptic proteins in primary hippocampal neurons expressing loss-of-function NHE6 Δ ES mutant. A, E-G: Example confocal images of 14 DIV EGFP-positive primary hippocampal neuron soma (A) or dendrites (E-G) co-transfected with mCherry-tagged NHE6 WT or Δ ES and immunostained with gephyrin (A, E), GABA_AR α 1 (F) and GABA_AR α 2 (G). Channels are shown separately and merged; dotted line in white channel denotes EGFP signal. Scale bar: 4 μ m (A), 2 μ m (E). B, H; Mean \pm SEM puncta density for each marker in the soma (B) and dendrites (H). C, I: Mean \pm SEM density of colocalized puncta between NHE6 and each marker in the soma (C) and dendrites (I). D, J: Mean \pm SEM thresholded Mander's coefficients between each marker and NHE6 in the soma (D) and dendrites (J). For somatic gephyrin, n = 13 cells per condition, 3 separate experiments. For dendritic gephyrin, n = 14 cells per condition. For GABA_AR α 1, n = 15 cells per condition; for GABA_AR α 2, n = 13 cells per condition, 3 separate experiments. *: $p < 0.05$; **: $p < 0.01$, ***: $p < 0.0001$, unpaired Student's t-test.

These *in vitro* data suggest a mistrafficking of inhibitory postsynaptic molecules mutant-transfected cells, which we hypothesized could also disturb GABA_AR-mediated neurotransmission. Accordingly, when we measured mIPSCs from Δ ES-expressing dissociated neurons, we noted a significant increase in IEI compared to NHE6 WT transfectants (**Fig. 8A, H-J**). This was suggestive of a cell-autonomous loss of functional inhibitory synapses, in line with our immunohistochemical findings (**Fig. 7**). In contrast to our observations in *Nhe6* KO pyramidal neurons, we did not observe a change in mIPSC amplitude or kinetics (**Fig. 8A-G**), thus representing a possible divergence between these *in vivo* KO and *in vitro* mutant models. Nonetheless, these results suggest that the expression of a clinically relevant *SLC9A6* variant disrupts the trafficking of inhibitory postsynaptic molecules and GABA_AR-mediated currents in a similar fashion to NHE6 deficient neurons. Therefore, these findings strongly suggest that our findings from *Nhe6* KO mice may indeed be reflective of molecular changes in the neural circuitry of CS patients possessing this NHE6 mutation, and possibly other such LOF variants, as well.

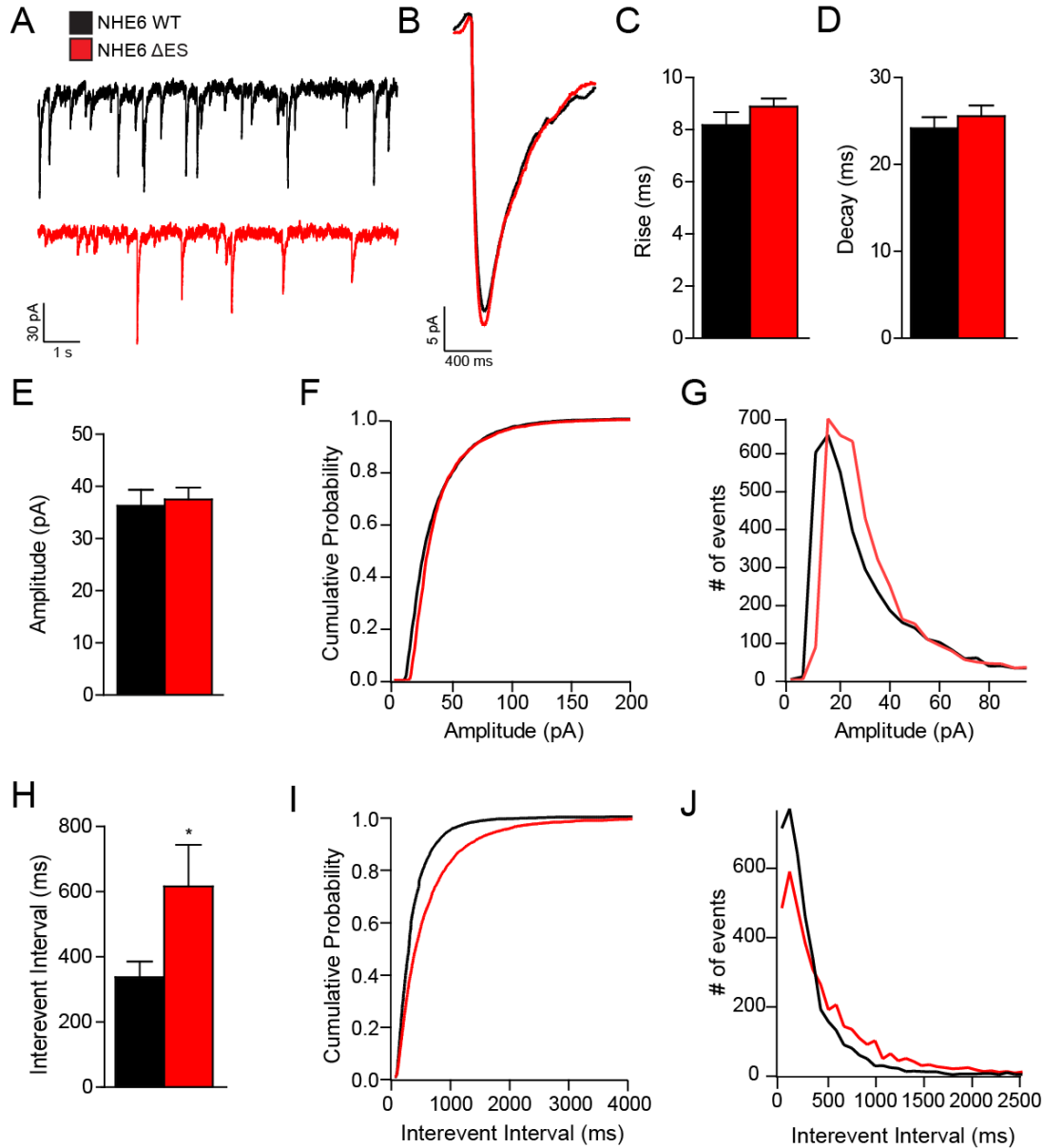


Figure 8: Primary hippocampal neurons expressing NHE6 Δ ES receive reduced GABAergic neurotransmission. A-B: Example recordings (A) and average event traces (B) of GABA_AR-mediated miniature inhibitory postsynaptic currents (mIPSCs) recorded from 14 DIV primary hippocampal neurons expressed with mCherry-tagged NHE6 WT (black) or NHE6 Δ ES (red). C-D: Mean \pm SEM mIPSC rise (C) and decay (D) times. E-G: Mean \pm SEM (E), cumulative probability (F) and frequency histogram (G) plots of mIPSC amplitudes. H-J: Mean \pm SEM (H), cumulative probability (I) and frequency histogram (J) plots of mIPSC interevent intervals. For NHE6 WT, $n = 11$ cells, NHE6 Δ ES, $n = 10$ cells from 3 separate experiments. *: $p < 0.05$, Mann-Whitney test.

4.5 DISCUSSION

In recent years, emerging work on the pathophysiology of CS has primarily focused on changes in excitatory neuronal structure and plasticity. While the growing interest in CS has been encouraging, little is currently known of the cellular changes in hippocampal circuitry that could underlie the development of hyperexcitability. Given the numerous case reports of CS patients developing epileptic seizures early in life (reviewed in [11]), this area of research is especially critical to further explore. In the present study, we have uncovered multiple ways in which inhibitory regulation in *Nhe6* KO may be perturbed, ranging from changes in interneuron density, postsynaptic GABA_AR composition, and Cl⁻ homeostasis. We strongly believe that these changes may act together in synergy to disrupt E/I balance and give way to seizure generation in human patients with CS, thus providing various potential targets to ameliorate epilepsy in this disorder.

Initially, we recorded extracellular potentials from hippocampal area CA1 in acute slice preparations from juvenile animals to assess network excitability in this region. While baseline activity did not appear to differ between genotypes, *Nhe6* KO slices exhibited epileptiform discharges in response to a subthreshold concentration of the K⁺-channel antagonist 4-AP. As expected, this treatment was insufficient to cause drastic activity increases in WT. Incidentally, these data fall in line with a phenotypic report stating that male *Nhe6* KO mice show a lower threshold for chemically induced seizures (DeltaGen). The present study thus confirms that hippocampal circuitry deficient in NHE6 is indeed more susceptible to epileptiform activity, which may give way to ictogenesis in human individuals with CS. To investigate the molecular basis underlying the development of hyperexcitability, we assessed AP firing from *Nhe6* KO CA1 pyramidal neurons under whole-cell current clamp conditions. However, we did not find that KO cells showed significant deviations in passive or active properties when compared to WT neurons,

suggesting that they are not intrinsically more excitable. We instead hypothesized that this effect arose from changes in the circuitry in area CA1, as 4-AP can result in the depolarization of both excitatory and inhibitory inputs [60–62]. Previous work has shown that hippocampal pyramidal neurons lacking NHE6 function experience a reduction in excitatory synapse density and function [24,28], suggesting that enhanced glutamatergic activity does not explain increased excitability in CA1 neurons in *Nhe6* KO. Conversely, it has also been shown that a persistent depolarization of inhibitory GABAergic inputs – either through direct stimulation or application of 4-AP – can paradoxically result in a long-lasting depolarizing shift in GABAergic transmission due to a build-up of postsynaptic $[Cl^-]_i$ [63–66]. This possibility further underscores the importance of KCC2 function in rapidly extruding Cl^- from the cell to prevent prolonged changes in E_{GABA} .

However, *Nhe6* KO hippocampi showed decreased KCC2 protein expression in line with increased NKCC1 levels. This likely results in a pathological elevation of $[Cl^-]_i$ and a depolarizing shift of E_{GABA} in *Nhe6* KO neurons compared to age-matched WT, which may be additionally aggravated by even a subthreshold concentration of 4-AP to further depolarize GABAergic inputs. Upon further stimulation, the polarity of GABAergic signaling may reverse from inhibitory to excitatory to give way to the hyperexcitability observed in *Nhe6* KO slices that are absent in WT slices. The dysregulation of NKCC1 and KCC2 protein levels in developmentally mature *Nhe6* KO hippocampi may thus be a central factor underlying the E/I imbalance observed in KO tissue. Importantly, alterations in the levels and activities of these cation- Cl^- cotransporters are commonly found in a number of human epilepsy conditions, many of which arise from genetic deficiencies in the *SLC12A5* gene encoding KCC2 [43,47,67–69]. For instance, induction of seizures in adult mice by lithium-pilocarpine resulted in a persistent increase and decrease in NKCC1 and KCC2 mRNA and protein levels, respectively, in hippocampal area CA1 for weeks following kindling

[70]. Data from post-mortem tissue taken from human patients with chronic temporal lobe epilepsy have further revealed a dysregulation in the expression of these transporters, which functionally resulted in a reversal in GABA polarity to excitatory [71–73]. Thus, the mechanisms underlying these changes in transporter expression in *Nhe6* KO warrants further investigation. For KCC2, it is possible that endosomal mistrafficking in the absence of NHE6-mediated pH regulation may result in the mislocalization and degradation of KCC2 through the lysosome, as similar disruptions have been observed in the trafficking of neurotrophin [24] and glutamate receptors [28]. Conversely, the concomitant upregulation of NKCC1 suggests a change in gene expression, although how NKCC1 expression is increased in multiple forms of epilepsy is still unclear.

Beyond broad changes in NKCC1 and KCC2 protein levels, there are numerous questions with regards to these cotransporters that remain to be addressed. For one, the post-translational modifications of these cation-Cl⁻ cotransporters are arguably more important than their global protein levels and therefore should also be analyzed in *Nhe6* KO. In particular, the intracellular C-terminal tail of KCC2 has recently come under greater scrutiny, as it contains various residues that can be modified to impact its membrane stabilization and ion transport activity [74–76]. In fact, the phosphorylation and dephosphorylation of some tyrosine and threonine residues mediate the developmental upregulation of KCC2 at the cell surface and can become dysregulated in response to seizure generation [77–84]. Furthermore, the subcellular localization of these transporters must be further characterized, as even minute changes in the plasmalemmal fractions of these transporters can substantially impact Cl⁻ homeostasis [47,85]. Finally, their relative expression in different cellular identities remains to be seen. While KCC2 is specifically expressed by neurons, NKCC1 is also found within glia and other non-neuronal cell types, and hence uncertainty arises in which cell types produce these elevated levels of NKCC1 [85]. Interestingly, inhibitory

interneurons usually express relatively more NKCC1 than excitatory pyramidal cells in the mature CNS under WT conditions [86]. If NKCC1 expression is indeed increased selectively in *Nhe6* KO interneurons, this could contribute to the proposed hyperexcitability of PV+ interneurons (as discussed later), either intrinsically or from upstream “gatekeeping” GABAergic interneurons [31,87]. In all, it will be critical to address the phosphorylation and expression patterns of these cation-Cl⁻ cotransporters to gain further insights into their activity, regulation, and ultimate impact on hippocampal circuit function.

Aside from downstream postsynaptic changes in inhibitory transmission, we also wished to study upstream GABAergic interneurons. Single cell RNA sequencing data from adult murine hippocampi has revealed that interneurons express the highest degree of *Slc9a6* when compared to other hippocampal cell types (http://dropviz.org/?state_id=9887ffac31b2fa28). This finding alludes to the importance of NHE6 in interneurons, yet its potential roles in mediating interneuron function and viability remain unclear. To this end, we first used immunoblotting to probe for GAD67 to obtain a general measure of the number of GABA-producing cells within adult *Nhe6* KO hippocampi. Notably, we found a reduction in GAD67 protein in six-month-old KO tissue relative to age-matched WT samples. We then assessed if specific subpopulations of interneurons were lost by performing immunohistochemical analyses of PV, as axosomatic PV+ interneurons are known to play crucial roles in regulating pyramidal cell excitability and in synchronizing oscillatory patterns of activity in the hippocampus [56,88–90]. Mirroring our biochemical data, KO slices showed significantly less PV+ cell densities than WT across hippocampal regions. Our observed reductions in interneuron number over time aligned with previous volumetric analyses showing a progressive reduction in hippocampal volume in *Nhe6* KO [50]. Interestingly, we have previously demonstrated that transient expression of some genetic variants of *SLC9A6* into

cultured cells, including hippocampal neurons, induced cell death via apoptosis [29,94]. As the loss of NHE6 function clearly results in a neurodegenerative phenotype, we hypothesize that the viability of certain interneuron subtypes - namely fast-spiking PV+ cells with relatively high energy requirements [55,56] - may be especially impacted by the loss of NHE6. Notably, NHE6 has also been implicated in regulating cellular metabolism under conditions of stress [95,96]. Thus, if NHE6 deficient PV+ interneurons are indeed hyperactive, they may become more sensitive to energetic challenges and subsequently die over time. Importantly, the loss or dysfunction of PV+ interneurons has been associated with cognitive impairments in other psychiatric disorders, including schizophrenia [91] and Alzheimer's disease [92,93], and could impair hippocampal function in CS as well. Future work reintroducing NHE6 specifically within PV+ neurons during development could validate whether the presence of NHE6 is sufficient to prevent cell loss and prevent kindling in KO mice. It should be noted that these results primarily indicate a decrease in PV translation, and it is possible that PV cells may indeed persist but show deficits in protein synthesis. Future work analyzing levels of PV mRNA will thus be required to determine whether PV downregulation also occurs at the transcriptional level. Furthermore, whether similar fates befall other interneuron populations, including somatostatin-expressing dendritic-targeting cells and upstream regulatory interneurons, are similarly impacted in *Nhe6* KO remains to be elucidated.

Remarkably, the loss of PV+ interneurons appears to be age-dependent in KO tissue, as whole hippocampal GAD67 protein and PV+ cell densities were comparable in younger two-month-old WT and *Nhe6* KO tissue. Nevertheless, areas CA3 and CA1 showed reciprocal increases and decreases, respectively, in PV+ cell counts in *Nhe6* KO hippocampi when compared to WT. Accordingly, *Nhe6* KO CA1 pyramidal neuron somata displayed reductions in inhibitory synaptic markers and prolongations of GABA_AR-mediated current kinetics when compared to WT.

Although these data imply a decrease in somatic inhibitory synapse number, the frequency of currents recorded from KO CA1 pyramidal neurons were unchanged when compared to WT. This suggests a possible increase in the release probability and firing activity of surviving PV+ cells that masks the apparent decrease in GABAergic synapses. In combination with the proposed dysregulation of Cl^- homeostasis and possible depolarization of E_{GABA} , persistent PV+ activation in response to relatively minor membrane depolarizations (such as those induced by subthreshold 4-AP challenge) could therefore drive seizure generation rather than attenuate it. Indeed, numerous reports have implicated the action of somatic-targeting, fast-spiking PV+ interneurons in synchronizing rhythmic network activity to allow seizures to spread across cortical territories [90]. Accordingly, recent work has shown that optogenetically enhancing PV+ interneuron function during an epileptiform discharge can facilitate and prolong the seizure [71,97]. Additional investigations of PV+ interneuron firing and presynaptic release properties in *Nhe6* KO could verify their hyperactivity, as well as whether they play a pro- or anti-seizure effect in maintaining E/I balance. The relative increase in area CA3 PV+ cells in P60 *Nhe6* KO hippocampi further suggests an enhancement in the function of these interneurons, which may directly or indirectly contribute to the hyperexcitability seen in area CA1. The striking observation that area CA3 PV+ cells are initially spared in *Nhe6* KO nonetheless warrants further investigation.

While the increase in sIPSC amplitude may indicate enhanced phasic GABAergic transmission, our examination of quantal transmission through additional mIPSC recordings showed a significant reduction of their amplitude in *Nhe6* KO cells in comparison to WT. In combination with immunohistochemical data demonstrating decreased puncta of inhibitory synaptic marker, this strongly suggests that GABAergic synapses on CA1 principal cells are weaker and fewer in *Nhe6* KOs. Interestingly, we saw a similar pattern of downregulation in these

inhibitory postsynaptic molecules in cultured hippocampal neurons expressing the deletion LOF mutant NHE6 Δ ES. Like other membrane-bound receptors, GABA_ARs undergo constitutive and activity-dependent trafficking to and from the cell surface [37,99–101], which may critically depend on NHE6-mediated pH regulation. Thus, as we hypothesize to be the case for KCC2 trafficking, the overacidification of endosomes in the absence of NHE6 function may also result in the mislocalization and subsequent lysosomal degradation of GABA_ARs as well. Colocalization analyses between KCC2 or GABA_AR with lysosomal markers could verify if these molecules are indeed mistrafficked for putative proteolysis within these degradative compartments.

Strikingly, only GABA_AR α 2 trafficking was downregulated while levels of GABA_AR α 1 were comparable to WT in both KO and Δ ES neurons. Accordingly, we observed a stronger degree of colocalization between transfected WT NHE6 and the α 2 subunit than that with α 1 in primary hippocampal neurons. This suggests that while NHE6 is broadly involved in GABA_AR trafficking, there may also be some degree of selectivity in which GABA_AR subunits are trafficked by NHE6. As of yet, the contents of NHE6-containing endosomes still remain unclear, but these findings imply that α 2-containing GABA_ARs may be one such cargo. Notably, we have reported similar trends in the specificity of NHE6-mediated trafficking of other membrane-bound proteins, such as glutamate and transferrin receptors [28,29]. Alternatively, the selective downregulation in the α 2 subunit of GABA_ARs could be coupled to the reduction of gephyrin in *Nhe6* KO CA1 pyramidal cells. Decreasing gephyrin expression has previously been shown to interfere with the localization and clustering of synaptic GABA_AR [102,103]. Conversely, other reports have suggested that GABA_AR clustering can also influence that of gephyrin [37,39,103,104]; specifically, deletion of α 2 subunit inhibits the clustering of gephyrin, but not that of α 1 or other inhibitory postsynaptic proteins [105]. Thus, it is possible that the mistrafficking of the α 2 subunit may be upstream of

disturbances in gephyrin clustering in *Nhe6* KO, which further highlights the importance of NHE6 trafficking in maintaining inhibitory postsynaptic integrity. This postulation is additionally substantiated by our *in vitro* findings showing that transfection of Δ ES NHE6 similarly attenuated gephyrin and GABA_AR α 2 in hippocampal neurons, which strongly suggested that functional NHE6 deficiency exerts a cell-autonomous effect in prohibiting the trafficking of these molecules. Further evaluation into the fate of other GABA_AR subtypes and inhibitory postsynaptic scaffolding molecules in *Nhe6* KO may reveal additional mechanisms underlying these pathological changes in cargo trafficking and whether they can be targeted to modulate circuit excitability.

It should be noted that while IPSCs recorded from *Nhe6* KO neurons did not show differences in IEI, Δ ES-expressing neurons instead showed a significant increase in IEI relative to controls. This was primarily indicative of a loss of functional inhibitory synapses. The discrepancies in event frequency observed between *Nhe6* KO and mutant may arise from the inherent differences in these two models, as *ex vivo* acute slice preparations preserve more of the intact *in vivo* network, whereas *in vitro* cell culture preparations disperse native interneuron connectivity on to downstream principal cells. Thus, because compensatory presynaptic changes are likely absent *in vitro* when compared to genetically deficient *Nhe6* KO hippocampi, the decrease in mIPSC frequency seen specifically in Δ ES transfectants further supports a cell-autonomous role for NHE6 in establishing and/or maintaining postsynaptic GABAergic synapse number. Parenthetically, the lack of significant changes in other mIPSC parameters in Δ ES-expressing cells may be reflective of the transient nature of the experimental paradigm. Given the wide variety of GABA_AR subunits, which lends both complexity and redundancy to the assembly of these receptors, it is possible that expressing the mutant construct for longer periods of time may be required to fully replicate the changes in amplitude and kinetics seen in *Nhe6* KO neurons.

Taken together, the current study presents multiple mechanisms that could dysregulate Cl⁻ homeostasis and perturb GABAergic transmission to give way to runaway excitation in the hippocampus and lead to epileptogenesis in CS. However, as has been alluded to before with PV+ cell firing, whether these alterations in inhibitory regulation promote or counteract epileptiform activity remains to be fully delineated. For instance, seizure induction itself can induce a rapid downregulation of surface KCC2 and GABA_ARs [77,106–108], leading to a transient reduction of inhibitory neurotransmission and, over time, the development of resistance to anticonvulsant drugs that work through GABA_AR activation [42,109,110]. However, if the polarity of GABA is indeed reversed in *Nhe6* KO, it is also possible that the aforementioned reductions in GABAergic function in KO may actually be beneficial in dampening hyperexcitability. As such, the reduction in interneuron density in older *Nhe6* KO hippocampi could counterintuitively serve to offset a potentially pro-ictal effect of pathological GABAergic transmission during seizure activity [97,111]. Likewise, persistent GABAergic transmission or KCC2 activity in pyramidal cells can substantially elevate [Cl⁻]_i or [K⁺]_o, respectively, which instead excessively depolarizes pyramidal cells [74]. Moreover, past results have also shown that depolarizing GABA can contribute to the initiation and maintenance of seizures [72,112–114], and inhibiting GABA_ARs can thus block ictal activity [115–118]. Determining whether these “deficits” in GABAergic function may in fact be homeostatic mechanisms that actually serve to deter hyperexcitability will likely require longitudinal analyses of how these changes coincide with kindling models to induce seizures in *Nhe6* KO mice *in vivo*. In the future, such work will be essential to ensure that appropriate therapeutic measures are taken to treat epilepsy in CS without inadvertently exacerbating the underlying mechanisms that promote seizure generation in these patients.

4.6 REFERENCES

1. Iijima T, Ciani S, Hagiwara S. Effects of the external pH on Ca channels: experimental studies and theoretical considerations using a two-site, two-ion model. *Proc Natl Acad Sci.* 1986 Feb 1;83(3):654–8.
2. Tang CM, Dichter M, Morad M. Modulation of the N-methyl-D-aspartate channel by extracellular H⁺. *Proc Natl Acad Sci.* 1990 Aug 1;87(16):6445–9.
3. McDonald JW, Bhattacharyya T, Sensi SL, Lobner D, Ying HS, Canzoniero LMT, et al. Extracellular Acidity Potentiates AMPA Receptor-Mediated Cortical Neuronal Death. *J Neurosci.* 1998 Aug 15;18(16):6290–9.
4. Kaila K. Ionic basis of GABAA receptor channel function in the nervous system. *Prog Neurobiol.* 1994 Mar;42(4):489–537.
5. Pavlov I, Kaila K, Kullmann DM, Miles R. Cortical inhibition, pH and cell excitability in epilepsy: what are optimal targets for antiepileptic interventions? *J Physiol.* 2013;591(4):765–74.
6. Tolner EA, Hochman DW, Hassinen P, Otáhal J, Gaily E, Haglund MM, et al. Five percent CO₂ is a potent, fast-acting inhalation anticonvulsant. *Epilepsia.* 2011;52(1):104–14.
7. Zhao H, Carney KE, Falgoust L, Pan JW, Sun D, Zhang Z. Emerging roles of Na⁺ / H⁺ exchangers in epilepsy and developmental brain disorders. *Prog Neurobiol.* 2016;
8. Pescosolido MF, Stein DM, Schmidt M, Moufawad El Achkar C, Sabbagh M, Rogg JM, et al. Genetic and phenotypic diversity of NHE6 mutations in Christianson syndrome. *Ann Neurol.* 2014;581–93.
9. Christianson AL, Stevenson RE, van der Meyden CH, Pelser J, Theron FW, van Rensburg PL, et al. X linked severe mental retardation, craniofacial dysmorphology, epilepsy, ophthalmoplegia, and cerebellar atrophy in a large South African kindred is localised to Xq24–q27. *J Med Genet.* 1999 Oct;36(10):759–66.
10. Gilfillan GD, Selmer KK, Roxrud I, Smith R, Kyllerman M, Eiklid K, et al. SLC9A6 mutations cause X-linked mental retardation, microcephaly, epilepsy, and ataxia, a phenotype mimicking Angelman syndrome. *Am J Hum Genet.* 2008 Apr;82(4):1003–10.
11. Ikeda A, Yamamoto A, Ichikawa K, Tsuyusaki Y, Tsuji M, Iai M, et al. Epilepsy in Christianson syndrome: Two cases of Lennox–Gastaut syndrome and a review of literature. *Epilepsy Behav Reports.* 2020;13:100349.
12. Pescosolido MF, Kavanaugh BC, Pochet N, Schmidt M, Jerskey BA, Rogg JM, et al. Complex Neurological Phenotype in Female Carriers of *NHE6* Mutations. *Mol Neuropsychiatry.* 2019;5(2):98–108.
13. Schroer RJ, Holden KR, Tarpey PS, Matheus MG, Griesemer D a, Friez MJ, et al. Natural history of Christianson syndrome. *Am J Med Genet A.* 2010 Nov;152A(11):2775–83.
14. Brett CL, Wei Y, Donowitz M, Rao R. Human Na⁽⁺⁾/H⁽⁺⁾ exchanger isoform 6 is found in recycling endosomes of cells, not in mitochondria. *Am J Physiol Cell Physiol.* 2002 May;282(5):C1031–41.
15. Deane EC, Ilie AE, Sizdahkhani S, Das Gupta M, Orlowski J, McKinney RA. Enhanced

- recruitment of endosomal Na⁺/H⁺ exchanger NHE6 into Dendritic spines of hippocampal pyramidal neurons during NMDA receptor-dependent long-term potentiation. *J Neurosci*. 2013 Jan 9;33(2):595–610.
16. Orlowski J, Grinstein S. Na⁺/H⁺ exchangers. *Compr Physiol*. 2011 Oct;1(4):2083–100.
 17. Casey JR, Grinstein S, Orlowski J. Sensors and regulators of intracellular pH. *Nat Rev Mol Cell Biol*. 2010;11(1):50–61.
 18. Yamashiro DJ, Maxfield FR. Acidification of endocytic compartments and the intracellular pathways of ligands and receptors. *J Cell Biochem*. 1984;26(4):231–46.
 19. Mellman I, Fuchs R, Helenius A. Acidification of the Endocytotic and Exocytic Pathways. *Ann Rev Biochem*. 1986;55:663–700.
 20. Weisz OA. Acidification and Protein Traffic. In: *International Review of Cytology*. 2003. p. 259–319.
 21. Yap CC, Winckler B. Harnessing the Power of the Endosome to Regulate Neural Development. *Neuron*. 2012;74(3):440–51.
 22. Ehlers MD. Dendritic trafficking for neuronal growth and plasticity. *Biochem Soc Trans*. 2013;41(6):1365–82.
 23. Gu Y, Chiu S-L, Liu B, Wu P-H, Delannoy M, Lin D-T, et al. Differential vesicular sorting of AMPA and GABAA receptors. *Proc Natl Acad Sci U S A*. 2016;201525726.
 24. Ouyang Q, Lizarraga SB, Schmidt M, Yang U, Gong J, Ellisor D, et al. Christianson Syndrome Protein NHE6 Modulates TrkB Endosomal Signaling Required for Neuronal Circuit Development. *Neuron*. 2013 Oct 2;80(1):97–112.
 25. Yap CC, Winckler B. Acid Indigestion in the Endosome: Linking Signaling Dysregulation to Neurodevelopmental Disorders. *Neuron*. 2013 Oct;80(1):4–6.
 26. Kondapalli KC, Prasad H, Rao R. An inside job: how endosomal Na⁽⁺⁾/H⁽⁺⁾ exchangers link to autism and neurological disease. *Front Cell Neurosci*. 2014 Jan;8(June):172.
 27. Schreijf AMA, Fon EA, McPherson PS. Endocytic membrane trafficking and neurodegenerative disease. *Cell Mol Life Sci*. 2016;73(8):1529–45.
 28. Gao AYL, Ilie A, Chang PKY, Orlowski J, McKinney RA. A Christianson syndrome-linked deletion mutation (Δ 287ES288) in SLC9A6 impairs hippocampal neuronal plasticity. *Neurobiol Dis*. 2019;130(April):104490.
 29. Ilie A, Gao AYL, Reid J, Boucher A, McEwan C, Barrière H, et al. A Christianson syndrome-linked deletion mutation (Δ 287ES288) in SLC9A6 disrupts recycling endosomal function and elicits neurodegeneration and cell death. *Mol Neurodegener*. 2016;11(1).
 30. Freund TF, Buzsáki G. Interneurons of the hippocampus. *Hippocampus*. 1996;6(4):347–470.
 31. Kepecs A, Fishell G. Interneuron cell types are fit to function. *Nature*. 2014;505(7483):318–26.
 32. Hu H, Gan J, Jonas P. Fast-spiking, parvalbumin+ GABAergic interneurons: From cellular design to microcircuit function. *Science* (80-). 2014 Aug 1;345(6196):1255263–1255263.
 33. Pelkey KA, Chittajallu R, Craig MT, Tricoire L, Wester JC, McBain CJ. Hippocampal

- GABAergic Inhibitory Interneurons. *Physiol Rev*. 2017;97(4):1619–747.
34. Favero M, Sotuyo NP, Lopez E, Kearney JA, Goldberg EM. A transient developmental window of fast-spiking interneuron dysfunction in a mouse model of Dravet syndrome. *J Neurosci*. 2018;38(36):0193–18.
 35. Goldberg EM, Coulter DA. Mechanisms of epileptogenesis: A convergence on neural circuit dysfunction. *Nat Rev Neurosci*. 2013;14(5):337–49.
 36. Fritschy JM, Panzanelli P. GABAA receptors and plasticity of inhibitory neurotransmission in the central nervous system. *Eur J Neurosci*. 2014;39(11):1845–65.
 37. Luscher B, Fuchs T, Kilpatrick CL. GABAA Receptor Trafficking-Mediated Plasticity of Inhibitory Synapses. *Neuron*. 2011;70(3):385–409.
 38. Fritschy JM, Panzanelli P, Tyagarajan SK. Molecular and functional heterogeneity of GABAergic synapses. *Cell Mol Life Sci*. 2012;69(15):2485–99.
 39. Tyagarajan SK, Fritschy J-M. Gephyrin: a master regulator of neuronal function? *Nat Rev Neurosci*. 2014;15(3):141–56.
 40. Shen Q, Lal R, Luellen BA, Earnheart JC, Andrews AM, Luscher B. γ -Aminobutyric Acid-Type A Receptor Deficits Cause Hypothalamic-Pituitary-Adrenal Axis Hyperactivity and Antidepressant Drug Sensitivity Reminiscent of Melancholic Forms of Depression. *Biol Psychiatry*. 2010 Sep;68(6):512–20.
 41. Crestani F, Lorez M, Baer K, Essrich C, Benke D, Laurent JP, et al. Decreased GABAA-receptor clustering results in enhanced anxiety and a bias for threat cues. *Nat Neurosci*. 1999 Sep;2(9):833–9.
 42. Kaila K, Ruusuvuori E, Seja P, Voipio J, Puskarjov M. GABA actions and ionic plasticity in epilepsy. *Curr Opin Neurobiol*. 2014;26(Figure 1):34–41.
 43. Kaila K, Price TJ, Payne JA, Puskarjov M, Voipio J. Cation-chloride cotransporters in neuronal development, plasticity and disease. *Nat Rev Neurosci*. 2014;15(10):637–54.
 44. Ben-Ari Y, Gaiarsa JL, Tyzio R, Khazipov R. GABA: A pioneer transmitter that excites immature neurons and generates primitive oscillations. *Physiol Rev*. 2007;87(4):1215–84.
 45. Cellot G, Cherubini E. Functional role of ambient GABA in refining neuronal circuits early in postnatal development. *Front Neural Circuits*. 2013;7.
 46. Bortone D, Polleux F. KCC2 Expression Promotes the Termination of Cortical Interneuron Migration in a Voltage-Sensitive Calcium-Dependent Manner. *Neuron*. 2009 Apr;62(1):53–71.
 47. Di Cristo G, Awad PN, Hamidi S, Avoli M. KCC2, epileptiform synchronization, and epileptic disorders. *Prog Neurobiol*. 2018;162:1–16.
 48. Strømme P, Dobrenis K, Sillitoe R V, Gulinello M, Ali NF, Davidson C, et al. X-linked Angelman-like syndrome caused by *Slc9a6* knockout in mice exhibits evidence of endosomal-lysosomal dysfunction. *Brain a J Neurol*. 2011 Nov;134(Pt 11):3369–83.
 49. Kerner-Rossi M, Gulinello M, Walkley S, Dobrenis K. Pathobiology of Christianson syndrome: Linking disrupted endosomal-lysosomal function with intellectual disability and sensory impairments. *Neurobiol Learn Mem*. 2018;(December 2017):0–1.

50. Xu M, Ouyang Q, Gong J, Pescosolido MF, Pruett BS, Mishra S, et al. Mixed Neurodevelopmental and Neurodegenerative Pathology in Nhe6⁻Null Mouse Model of Christianson Syndrome. *eNeuro*. 2017 Nov;4(6):ENEURO.0388-17.2017.
51. Potter SM, DeMarse TB. A new approach to neural cell culture for long-term studies. *J Neurosci Methods*. 2001;110(1–2):17–24.
52. Jiang M, Chen G. High Ca²⁺-phosphate transfection efficiency in low-density neuronal cultures. *Nat Protoc*. 2006;1(2):695–700.
53. Jayabal S, Ljungberg L, Erwes T, Cormier A, Quilez S, El Jaouhari S, et al. Rapid onset of motor deficits in a mouse model of spinocerebellar ataxia type 6 precedes late cerebellar degeneration. *eNeuro*. 2015;2(6).
54. Hamidi S, Avoli M. KCC2 function modulates in vitro ictogenesis. *Neurobiol Dis*. 2015;79:51–8.
55. González OC, Shiri Z, Krishnan GP, Myers TL, Williams S, Avoli M, et al. Role of KCC2-dependent potassium efflux in 4-Aminopyridine-induced Epileptiform synchronization. *Neurobiol Dis*. 2018;109(August 2017):137–47.
56. Bu DF, Erlander MG, Hitz BC, Tillakaratne NJ, Kaufman DL, Wagner-McPherson CB, et al. Two human glutamate decarboxylases, 65-kDa GAD and 67-kDa GAD, are each encoded by a single gene. *Proc Natl Acad Sci U S A*. 1992;89(6):2115–9.
57. Erlander MG, Tillakaratne NJK, Feldblum S, Patel N, Tobin AJ. Two genes encode distinct glutamate decarboxylases. *Neuron*. 1991 Jul;7(1):91–100.
58. Klausberger T. GABAergic interneurons targeting dendrites of pyramidal cells in the CA1 area of the hippocampus. *Eur J Neurosci*. 2009 Sep;30(6):947–57.
59. Rudy B, Fishell G, Lee S, Hjerling-Leffler J. Three groups of interneurons account for nearly 100% of neocortical GABAergic neurons. *Dev Neurobiol*. 2011;71(1):45–61.
60. Eyre MD, Renzi M, Farrant M, Nusser Z. Setting the Time Course of Inhibitory Synaptic Currents by Mixing Multiple GABAA Receptor Subunit Isoforms. *J Neurosci*. 2012;32(17):5853–67.
61. Labrakakis C, Rudolph U, De Koninck Y. The heterogeneity in GABAA receptor-mediated IPSC kinetics reflects heterogeneity of subunit composition among inhibitory and excitatory interneurons in spinal lamina II. *Front Cell Neurosci*. 2014 Dec 11;8.
62. Safari MS, Mirnajafi-Zadeh J, Hioki H, Tsumoto T. Parvalbumin-expressing interneurons can act solo while somatostatin-expressing interneurons act in chorus in most cases on cortical pyramidal cells. *Sci Rep*. 2017;7(1):1–14.
63. Avoli M, Perreault P. A GABAergic depolarizing potential in the hippocampus disclosed by the convulsant 4-aminopyridine. *Brain Res*. 1987 Jan;400(1):191–5.
64. Buckle PJ, Haas HL. Enhancement of synaptic transmission by 4-aminopyridine in hippocampal slices of the rat. *J Physiol*. 1982 May 1;326(1):109–22.
65. Perreault P, Avoli M. Effects of low concentrations of 4-aminopyridine on CA1 pyramidal cells of the hippocampus. *J Neurophysiol*. 1989 May 1;61(5):953–70.
66. Perreault P, Avoli M. Physiology and pharmacology of epileptiform activity induced by 4-

- aminopyridine in rat hippocampal slices. *J Neurophysiol.* 1991 Apr 1;65(4):771–85.
67. Perreault P, Avoli M. 4-aminopyridine-induced epileptiform activity and a GABA-mediated long- lasting depolarization in the rat hippocampus. *J Neurosci.* 1992 Jan 1;12(1):104–15.
 68. Staley K, Soldo B, Proctor W. Ionic mechanisms of neuronal excitation by inhibitory GABAA receptors. *Science* (80-). 1995 Aug 18;269(5226):977–81.
 69. Lamsa K, Kaila K. Ionic Mechanisms of Spontaneous GABAergic Events in Rat Hippocampal Slices Exposed to 4-Aminopyridine. *J Neurophysiol.* 1997 Nov 1;78(5):2582–91.
 70. Kahle KT, Khanna AR, Duan J, Staley KJ, Delpire E, Poduri A. The KCC2 Cotransporter and Human Epilepsy: Getting Excited About Inhibition. *Neurosci.* 2016;1073858416645087.
 71. Campbell SL, Robel S, Cuddapah VA, Robert S, Buckingham SC, Kahle KT, et al. GABAergic disinhibition and impaired KCC2 cotransporter activity underlie tumor-associated epilepsy. *Glia.* 2015 Jan;63(1):23–36.
 72. Duy PQ, David WB, Kahle KT. Identification of KCC2 Mutations in Human Epilepsy Suggests Strategies for Therapeutic Transporter Modulation. *Front Cell Neurosci.* 2019;13(November):1–6.
 73. Li X, Zhou J, Chen Z, Chen S, Zhu F, Zhou L. Long-term expressional changes of Na⁺-K⁺-Cl⁻ co-transporter 1 (NKCC1) and K⁺-Cl⁻ co-transporter 2 (KCC2) in CA1 region of hippocampus following lithium-pilocarpine induced status epilepticus (PISE). *Brain Res.* 2008;1221:141–6.
 74. Ye H, Kaszuba S. Inhibitory or excitatory? Optogenetic interrogation of the functional roles of GABAergic interneurons in epileptogenesis. *J Biomed Sci.* 2017;24(1):93.
 75. Cohen I, Navarro V, Clemenceau S, Baulac M, Miles R. On the Origin of Interictal Activity in Human Temporal Lobe Epilepsy in Vitro. *Science* (80-). 2002 Nov 15;298(5597):1418–21.
 76. Huberfeld G, Wittner L, Clemenceau S, Baulac M, Kaila K, Miles R, et al. Perturbed chloride homeostasis and GABAergic signaling in human temporal lobe epilepsy. *J Neurosci.* 2007;27(37):9866–73.
 77. Kahle KT, Deeb TZ, Puskarjov M, Silayeva L, Liang B, Kaila K, et al. Modulation of neuronal activity by phosphorylation of the K-Cl cotransporter KCC2. *Trends Neurosci.* 2013;36(12):726–37.
 78. Lee HHC, Walker JA, Williams JR, Goodier RJ, Payne JA, Moss SJ. Direct Protein Kinase C-dependent Phosphorylation Regulates the Cell Surface Stability and Activity of the Potassium Chloride Cotransporter KCC2. *J Biol Chem.* 2007 Oct 12;282(41):29777–84.
 79. Wake H, Watanabe M, Moorhouse AJ, Kanematsu T, Horibe S, Matsukawa N, et al. Early changes in KCC2 phosphorylation in response to neuronal stress result in functional downregulation. *J Neurosci.* 2007;27(7):1642–50.
 80. Lee HHC, Jurd R, Moss SJ. Tyrosine phosphorylation regulates the membrane trafficking

- of the potassium chloride co-transporter KCC2. *Mol Cell Neurosci*. 2010;45(2):173–9.
81. Kelsch W, Hormuzdi S, Straube E, Lewen A, Monyer H, Misgeld U. Insulin-Like Growth Factor 1 and a Cytosolic Tyrosine Kinase Activate Chloride Outward Transport during Maturation of Hippocampal Neurons. *J Neurosci*. 2001 Nov 1;21(21):8339–47.
 82. Watanabe M, Wake H, Moorhouse AJ, Nabekura J. Clustering of Neuronal K⁺ -Cl⁻ Cotransporters in Lipid Rafts by Tyrosine Phosphorylation. *J Biol Chem*. 2009 Oct 9;284(41):27980–8.
 83. Pisella LI, Gaiarsa JL, Diabira D, Zhang J, Khalilov I, Duan JJ, et al. Impaired regulation of KCC2 phosphorylation leads to neuronal network dysfunction and neurodevelopmental pathology. *Sci Signal*. 2019;12(603).
 84. Friedel P, Kahle KT, Zhang J, Hertz N, Pisella LI, Buhler E, et al. WNK1-regulated inhibitory phosphorylation of the KCC2 cotransporter maintains the depolarizing action of GABA in immature neurons. *Sci Signal*. 2015 Jun 30;8(383):ra65–ra65.
 85. Rinehart J, Maksimova YD, Tanis JE, Stone KL, Hodson CA, Zhang J, et al. Sites of Regulated Phosphorylation that Control K-Cl Cotransporter Activity. *Cell*. 2009 Aug;138(3):525–36.
 86. Watanabe M, Zhang J, Mansuri MS, Duan J, Karimy JK, Delpire E, et al. Developmentally regulated KCC2 phosphorylation is essential for dynamic GABA-mediated inhibition and survival. *Sci Signal*. 2019 Oct 15;12(603):eaaw9315.
 87. Moore YE, Deeb TZ, Chadchankar H, Brandon NJ, Moss SJ. Potentiating KCC2 activity is sufficient to limit the onset and severity of seizures. *Proc Natl Acad Sci U S A*. 2018;115(40):10166–71.
 88. Löscher W, Puskarjov M, Kaila K. Cation-chloride cotransporters NKCC1 and KCC2 as potential targets for novel antiepileptic and antiepileptogenic treatments. *Neuropharmacology*. 2013;69:62–74.
 89. Martina M, Royer S, Paré D. Cell-type-specific GABA responses and chloride homeostasis in the cortex and amygdala. *J Neurophysiol*. 2001;86(6):2887–95.
 90. Gulyás A I, Hájos N, Freund TF. Interneurons containing calretinin are specialized to control other interneurons in the rat hippocampus. *J Neurosci*. 1996;16(10):3397–411.
 91. Amilhon B, Huh CYL, Manseau F, Ducharme G, Nichol H, Adamantidis A, et al. Parvalbumin Interneurons of Hippocampus Tune Population Activity at Theta Frequency. *Neuron*. 2015 Jun;86(5):1277–89.
 92. Wulff P, Ponomarenko AA, Bartos M, Korotkova TM, Fuchs EC, Bähner F, et al. Hippocampal theta rhythm and its coupling with gamma oscillations require fast inhibition onto parvalbumin-positive interneurons. *Proc Natl Acad Sci U S A*. 2009;106(9):3561–6.
 93. Freund TF, Katona I. Perisomatic Inhibition. *Neuron*. 2007;56(1):33–42.
 94. Lodge DJ, Behrens MM, Grace AA. A Loss of Parvalbumin-Containing Interneurons Is Associated with Diminished Oscillatory Activity in an Animal Model of Schizophrenia. *J Neurosci*. 2009 Feb 25;29(8):2344–54.
 95. Yang X, Yao C, Tian T, Li X, Yan H, Wu J, et al. A novel mechanism of memory loss in

- Alzheimer's disease mice via the degeneration of entorhinal–CA1 synapses. *Mol Psychiatry*. 2018 Feb 27;23(2):199–210.
96. Verret L, Mann EO, Hang GB, Barth AMI, Cobos I, Ho K, et al. Inhibitory Interneuron Deficit Links Altered Network Activity and Cognitive Dysfunction in Alzheimer Model. *Cell*. 2012 Apr;149(3):708–21.
 97. Ilie A, Boucher A, Park J, Berghuis AM, McKinney RA, Orlowski J. Assorted dysfunctions of endosomal alkali cation/proton exchanger SLC9A6 variants linked to Christianson syndrome. *J Biol Chem*. 2020 May 15;295(20):7075–95.
 98. Lucien F, Pelletier P-P, Lavoie RR, Lacroix J-M, Roy S, Parent J-L, et al. Hypoxia-induced mobilization of NHE6 to the plasma membrane triggers endosome hyperacidification and chemoresistance. *Nat Commun*. 2017 Aug 21;8(1):15884.
 99. Prasad H, Rao R. Histone deacetylase-mediated regulation of endolysosomal pH. *J Biol Chem*. 2018;293(18):6721–35.
 100. Magloire V, Cornford J, Lieb A, Kullmann DM, Pavlov I. KCC2 overexpression prevents the paradoxical seizure-promoting action of somatic inhibition. *Nat Commun*. 2019;10(1):1–13.
 101. González MI. The possible role of GABAA receptors and gephyrin in epileptogenesis. *Front Cell Neurosci*. 2013;7(July):113.
 102. Lorenz-Guertin JM, Jacob TC. GABA type a receptor trafficking and the architecture of synaptic inhibition. *Dev Neurobiol*. 2018;78(3):238–70.
 103. Kittler JT, Thomas P, Tretter V, Bogdanov YD, Haucke V, Smart TG, et al. Huntingtin-associated protein 1 regulates inhibitory synaptic transmission by modulating γ -aminobutyric acid type A receptor membrane trafficking. *Proc Natl Acad Sci*. 2004 Aug 24;101(34):12736–41.
 104. Kneussel M, Brandstätter JH, Laube B, Stahl S, Müller U, Betz H. Loss of Postsynaptic GABA A Receptor Clustering in Gephyrin-Deficient Mice. *J Neurosci*. 1999 Nov 1;19(21):9289–97.
 105. Essrich C, Lorez M, Benson JA, Fritschy J-M, Lüscher B. Postsynaptic clustering of major GABAA receptor subtypes requires the $\gamma 2$ subunit and gephyrin. *Nat Neurosci*. 1998 Nov;1(7):563–71.
 106. Niwa F, Bannai H, Arizono M, Fukatsu K, Triller A, Mikoshiba K. Gephyrin-independent GABAAR mobility and clustering during plasticity. *PLoS One*. 2012;7(4).
 107. Panzanelli P, Gunn BG, Schlatter MC, Benke D, Tyagarajan SK, Scheiffele P, et al. Distinct mechanisms regulate GABA A receptor and gephyrin clustering at perisomatic and axo-axonic synapses on CA1 pyramidal cells. *J Physiol*. 2011;589(20):4959–80.
 108. Naylor DE, Liu H, Wasterlain CG. Trafficking of GABAA receptors, loss of inhibition, and a mechanism for pharmacoresistance in status epilepticus. *J Neurosci*. 2005;25(34):7724–33.
 109. Rivera C, Li H, Thomas-Crusells J, Lahtinen H, Viitanen T, Nanobashvili A, et al. BDNF-induced TrkB activation down-regulates the K⁺-Cl⁻ cotransporter KCC2 and impairs

- neuronal Cl⁻ extrusion. *J Cell Biol.* 2002;159(5):747–52.
110. Goodkin HP, Yeh JL, Kapur J. Status epilepticus increases the intracellular accumulation of GABA A receptors. *J Neurosci.* 2005;25(23):5511–20.
 111. Wasterlain CG, Liu H, Naylor DE, Thompson KW, Suchomelova L, Niquet J, et al. Molecular basis of self-sustaining seizures and pharmacoresistance during status epilepticus: The receptor trafficking hypothesis revisited. *Epilepsia.* 2009 Dec;50:16–8.
 112. Terunuma M, Xu J, Vithlani M, Sieghart W, Kittler J, Pangalos M, et al. Deficits in Phosphorylation of GABAA Receptors by Intimately Associated Protein Kinase C Activity Underlie Compromised Synaptic Inhibition during Status Epilepticus. *J Neurosci.* 2008 Jan 9;28(2):376–84.
 113. Ellender TJ, Raimondo J V., Irkle A, Lamsa KP, Akerman CJ. Excitatory Effects of Parvalbumin-Expressing Interneurons Maintain Hippocampal Epileptiform Activity via Synchronous Afterdischarges. *J Neurosci.* 2014 Nov 12;34(46):15208–22.
 114. Derchansky M, Jahromi SS, Mamani M, Shin DS, Sik A, Carlen PL. Transition to seizures in the isolated immature mouse hippocampus: a switch from dominant phasic inhibition to dominant phasic excitation. *J Physiol.* 2008 Jan 15;586(2):477–94.
 115. Huberfeld G, Menendez de la Prida L, Pallud J, Cohen I, Le Van Quyen M, Adam C, et al. Glutamatergic pre-ictal discharges emerge at the transition to seizure in human epilepsy. *Nat Neurosci.* 2011 May 3;14(5):627–34.
 116. Ziburkus J, Cressman JR, Barreto E, Schiff SJ. Interneuron and Pyramidal Cell Interplay During In Vitro Seizure-Like Events. *J Neurophysiol.* 2006 Jun;95(6):3948–54.
 117. Higashima M, Kinoshita H, Yamaguchi N, Koshino Y. Activation of GABAergic function necessary for afterdischarge generation in rat hippocampal slices. *Neurosci Lett.* 1996 Mar;207(2):101–4.
 118. Fujiwara-Tsukamoto Y, Isomura Y, Takada M. Comparable GABAergic Mechanisms of Hippocampal Seizurelike Activity in Posttetanic and Low-Mg²⁺ Conditions. *J Neurophysiol.* 2006 Mar;95(3):2013–9.
 119. Avoli M, Psarropoulou C, Tancredi V, Fueta Y. On the synchronous activity induced by 4-aminopyridine in the CA3 subfield of juvenile rat hippocampus. *J Neurophysiol.* 1993 Sep 1;70(3):1018–29.
 120. Avoli M, Barbarosie M, Lücke A, Nagao T, Lopantsev V, Köhling R. Synchronous GABA-Mediated Potentials and Epileptiform Discharges in the Rat Limbic System In Vitro. *J Neurosci.* 1996 Jun 15;16(12):3912–24.

CHAPTER 5. DISCUSSION AND CONCLUSIONS

5.1 SUMMARY

Although the worldwide incidence of CS has risen substantially over the past decade, very little is presently known of the cellular and molecular mechanisms that underlie the myriad of symptoms associated with this disorder. Consequently, viable therapeutic inventions are lacking, which likely stems from the fact that there are relatively few studies researching the physiological function of NHE6 itself in the brain. Previous work in our lab had implicated NHE6 in AMPAR localization and in mediating cargo trafficking during hippocampal synaptic plasticity [326]. In my thesis work, I elaborated upon these initial findings by expressing a patient-derived loss-of-function (LOF) *SLC9A6* mutation into cultured hippocampal neurons and by studying NHE6 deficient mice.

In brief, I found that Δ ES mutant-transfected or KO hippocampal neurons showed impairments in AMPAR trafficking, excitatory synaptic density, and functional and structural remodeling following NMDAR-dependent LTP. However, I also uncovered potential ways to correct these deficits in functional and structural plasticity within hippocampal neurons by inhibiting excessive lysosomal degradation or by applying a TrkB agonist. In addition, I described various mechanisms by which GABAergic dysregulation may be impaired in *Nhe6* KO hippocampi such that GABA could be less inhibitory and potentially excitatory. Moreover, GABAergic interneurons and inhibitory synaptic sites on area CA1 pyramidal neurons were both found to be downregulated in *Nhe6* KO hippocampi. Consequently, these changes may favour the development of hyperexcitability in NHE6 deficient circuitry that could underlie the generation of epileptic seizures in human patients with CS. In summary, I have reported novel roles for NHE6 in both excitatory and inhibitory neurotransmission and how these systems may become impaired to result in the learning impairments and epilepsy commonly seen in CS.

5.2 DISCUSSION

5.2.1 Prospective concerns over comparing *SLC9A6* KO and variants

By and large, NHE6 null mice have been found to be representative of human patients with LOF nonsense mutations in CS and are thus a suitable experimental model to study this disorder. However, many patients with CS also possess genetic mutations in the *SLC9A6* gene that are still capable of producing a full-length protein. As such, I initially elected to study the effects of one particular in-frame deletion mutation (p.Glu277_Ser278del; Δ ES), as this was one of the first identified variants that did not prohibit production of a protein [2]. I transfected a DNA plasmid encoding this variant into cultured murine hippocampal neurons in a dominant-negative fashion and studied the impact upon trafficking and LTP (see Chapter 2). I later turned to the KO mouse to better understand the circuit-level impacts of removing NHE6 function upon plasticity (see Chapter 3). I then used both models to assess GABAergic inhibitory function (see Chapter 4).

Although *Nhe6* KO and Δ ES show a number of similarities in terms of their spine density and remodeling, the most notable discrepancy between data from these models is: which AMPAR subunit is impacted by a lack of NHE6 function? As the long-tailed GluA1 and short-tailed GluA2 subunits differ in their trafficking, kinetics, and Ca^{2+} permeability [156,161,369], a reduction in either subunit could differentially impact excitatory neurotransmission and plasticity. In Chapter 2, I confirmed that NHE6 colocalized strongly with GluA1 [326], and I also found that GluA1 puncta density and activity-dependent insertion were both reduced in Δ ES-transfected neurons *in vitro*. Hence, we also expected GluA1 to be downregulated in *Nhe6* KO hippocampi *in vivo*. However, my data in Chapter 3 instead indicated that while GluA1 protein levels and surface expression after ChemLTP were comparable to that of WT, both GluA2 protein and ChemLTP-dependent surface insertion were impaired in *Nhe6* KO. Parenthetically, I also found differences

between KO and Δ ES when comparing mIPSC parameters between the two in Chapter 4, although I have addressed this already in the Discussion section of this chapter (see Chapter 4.4).

I hypothesize that the inconsistency in AMPAR subunit disruption between *in vivo* KO and *in vitro* mutant studies is likely due to differences in experimental models utilized, particularly with regards to the latter. As I discussed with greater detail in Chapter 2, glycosylated NHE6 monomers must dimerize to traffic properly, and the expression of the NHE6 variant into neurons results in a mosaic of endogenous WT and exogenous Δ ES NHE6 homodimers as well as heterodimers. This induces a dominant-negative overexpression phenotype over the WT form of the exchanger, as indicated by a significant decrease in NHE6 trafficking into dendrites (see Chapter 2). However, transfecting the Δ ES NHE6 mutant transiently in mature (12 DIV) cultured neurons *in vitro* is clearly in stark contrast to *Nhe6* KO mice, which do not express any NHE6 throughout the course of neural development. Thus, these findings from Δ ES-transfected neurons may primarily reflect an immediate, cell-autonomous disruption in cellular trafficking as induced by the introduction of the NHE6 mutant. It should also be noted that in Chapter 2, we did not directly study GluA2 because the sparse transfection efficacy of primary neuron cultures did not allow us to properly visualize GluA2 trafficking or levels using standard molecular biology or microscopy techniques. As GluA1 and GluA2 readily heteromerize together [156], distinguishing between the two using immunocytochemistry alone would not have been feasible. Therefore, it is possible that both subunits may indeed be perturbed in NHE6 Δ ES-expressing cells. In the future, using gene-editing technology to develop a knock-in Δ ES NHE6 mouse model would allow for the resolution of this and other possible disparities between *Nhe6* KO and Δ ES knock-in models. Nevertheless, it remains clear that even transient ablations in NHE6 function can strongly impact the trafficking of neurotransmitter receptors and activity-dependent remodeling.

An additional area of consideration is the impact upon proteolysis. *Nhe6* KO mice show signs of lysosomal dysfunction that mirror both tau pathology in CS patients [13,337,368] as well as lysosomal storage diseases (LSDs). Indeed, post-mortem examinations of neural tissue from these mice reveal the accumulation of undegraded GM2 gangliosides within lysosomes that are a distinct hallmark of LSDs [336,370]. However, the direct mechanism behind how the loss of NHE6 impairs lysosomal function remains to be elucidated. Notably, this is somewhat in discordance with hypotheses from us and other groups, as we have paradoxically suggested an enhancement of lysosomal function following NHE6 disruption [309,344]. Likewise, we postulate that endosomal overacidification, mistrafficking, and subsequent degradation of AMPARs, GABA_ARs, and other membrane-bound proteins in lysosomes are the root cause for the downregulation of these cargos in both *Nhe6* KO and Δ ES. Moreover, in Chapter 2, I show that blocking lysosomal function in Δ ES transfectants can prevent the aberrant degradation of GluA1 and restore its trafficking to synapses during LTP, in support of our theory of excessive lysosomal activity. These data raise the question of how lysosomal processing may be both impaired for some cargos yet enhanced for others in NHE6-deficient neurons. This will be an important distinction to clarify in future studies, especially because I postulate that lysosomal inhibition could be novel therapeutic strategy in CS.

However, the potential role of NHE6 in lysosomal function is still unclear. In Chapter 2, I reported some degree of colocalization between WT NHE6 and markers for LEs and lysosomes, suggesting that NHE6 could be active in regulating the internal pH of these compartments as well. However, observations from astrocytes found that overexpressing NHE6 did not alter lysosomal pH [368], strongly suggesting that NHE6 is not directly involved in maintaining the pH of these compartments. Assessing lysosomal pH in neurons deficient in NHE6 could nonetheless be performed to verify this supposition. It should be noted that autophagy through the lysosome is

also dependent upon the integrity of endocytic mechanisms to deliver proteases and lysosomal membrane proteins (such as ion channels and transporters) from the trans-Golgi network [133,371–374]. Thus, the trafficking of specific lysosomal enzymes, such as β -hexosaminidase, and other resident lysosomal proteins may depend upon NHE6 and are mistrafficked in its absence. Colocalization studies between NHE6 and β -hexosaminidase, as well as other factors involved in lysosomal function, could reveal which of these proteins may be trafficked in NHE6-positive vesicles and thus verify whether disturbances in their localization occur in the absence of NHE6. Indeed, future research on NHE6 should seek to systematically characterize which cargos are trafficked in NHE6-containing endosomes to assess those that may be mistrafficked its absence. Incidentally, other NHE isoforms are known to play indirect roles in cellular autophagy through mediating signaling cascades and endosomal function [375,376]. Indeed, such mechanisms have been proposed for the other endosomal NHE (eNHE), NHE9, which colocalizes with autophagy factors and is implicated in autophagic signaling cascades [258,377–379]. Whether NHE6 is similarly involved in the regulation of autophagy remains to be determined.

Thus, I postulate that the absence of NHE6 function promotes the aberrant targeting of endosomal cargos to the lysosome for degradation. In tandem, the lysosomal clearance of other substrates, including gangliosides and other macromolecule aggregates, is impaired downstream of an as-of-yet unidentified role of NHE6 in endolysosomal processing and cellular autophagy. Reintroducing NHE6 expression within KO neurons and assessing whether GM2 gangliosides and other substrates still accumulate in lysosomes of these cells could validate the role of NHE6 in proteolytic function. The divergence in lysosomal integrity may also be reflective of the differences in using the Δ ES and KO models, further underscoring the need for developing Δ ES knock-in mice to better understand the impact of this mutation upon neuronal circuitry as a whole.

5.2.2 Activity-dependent NHE6 trafficking in structural LTP

In spite of the potential disparities between comparing experimental models, time-lapse imaging experiments on both KO and Δ ES primary hippocampal neurons revealed deficits in spine enlargement following ChemLTP induction (see Chapters 2 and 3). *Nhe6* KO neurons further demonstrated a marked increase in spine motility, which was significantly exacerbated by NMDAR activation. Moreover, static observations of KO and Δ ES dendrites revealed a decrease in larger mature spines with an increase in smaller, more immature structures [309], the latter of which usually show a higher rate of motility while the former are thought to be more stable [82,380]. As I have alluded to throughout my thesis, NHE6 regulates endosomal trafficking to spines during LTP, which is crucial for mediating both their functional and volumetric augmentations [120,124,381]. Therefore, it is likely that the absence of NHE6 disrupts vesicular exocytotic events leading to impairments in spine head enlargement following LTP induction, corroborating findings from past studies showing that disrupting RE exocytosis could prevent the structural plasticity of dendritic spines [144]. However, modifications in the underlying spine actin cytoskeleton should also be considered, particularly in light of the excess spine motility observed in *Nhe6* KO neurons (see Chapter 3).

Like I mentioned in the Introduction, the regulation of the internal actin cytoskeleton by Rho family GTPases and other actin-associated proteins can impact the shape and volume of the spine [97,382]. As such, the absence of NHE6 may lead to the dysregulation or mistrafficking of such factors, thus enhancing spine motility while impairing stable spine enlargements. Previous work has shown that interference with the regulatory phosphorylation of the actin depolymerization factor cofilin still allows for spine enlargement but disrupts stabilization of the spine cytoskeleton, thereby occluding structural LTP [93,383]. As these findings mirror my

observations in *Nhe6* KO neurons, it is possible that cofilin phosphorylation by upstream kinases, such as LIM domain kinase 1 (LIMK1) [384], may be disrupted in *Nhe6* KO, thus leading to cofilin hyperactivity and excessive actin remodeling. Tangentially, LIMK1 activation is downstream of PKA activity [384], which I speculate to be decreased because of the lack of enhanced phosphorylation of GluA1 at the PKA site S845 following LTP induction (see Chapter 3). If PKA and, by extension, LIMK1 are indeed hypoactive in *Nhe6* KO, this might relieve the negative regulation of cofilin by LIMK1, thus resulting in cofilin hyperactivity and spine hypermotility. In addition, the synthesis or localization of actin stabilization proteins, such as capping protein CapZ or Eps8 [73], may also be perturbed, which could prevent spine maintenance following LTP. Presently, it is unknown whether the absence of NHE6 changes the integrity or regulation of the actin cytoskeleton. While plasmalemmal NHE isoforms are known to interact directly with cytoskeletal components and other actin regulatory proteins in some cell types through their C-terminal domains [255,385–387], such a role has not yet been defined for eNHEs in neurons. Direct investigations into whether alterations in the synthesis, trafficking, and regulation of these actin-associated proteins may further explain the aberrant spine motility in *Nhe6* KO. In addition, proteomic assays to identify whether such factors directly interact with NHE6 would be further suggestive of their dysregulation in the absence of NHE6 function.

Another possible cause for these structural impairments could be in the downregulation of signaling and trafficking through the BDNF/TrkB pathway. Although BDNF/TrkB signaling is commonly associated with protein synthesis-dependent late-LTP (L-LTP) [330,388,389], BDNF/TrkB signaling can also regulate immediate changes in spine volume following LTP stimulation. For instance, exogenous BDNF application alone can induce LTP expression by promoting the phosphorylation and subsequent inhibition of cofilin to enhance actin

polymerization [331]. Accordingly, LTP at hippocampal CA3-CA1 synapses is impaired in transgenic mice heterozygous for BDNF (*BDNF^{F+/+}*) [390]. Moreover, application of a function-blocking TrkB antibody inhibits actin polymerization and LTP maintenance. Sustained TrkB-dependent local synthesis of some of the factors involved in cytoskeletal remodeling, including RhoA and LIMK1, is also necessary for actin remodeling and F-actin stabilization during BDNF-LTP [391]. Importantly, TrkB is recruited to the postsynaptic membrane following NMDAR-dependent LTP to mediate these effects [392,393]. Because previous evidence has suggested that TrkB activation is impaired in *Nhe6* KO neurons, suggestive of an involvement of NHE6 in TrkB trafficking [309], NHE6 disruption may also disrupt activity-dependent TrkB recruitment to spines as well as signaling through the activated receptor. Thus, it is likely that impaired BDNF/TrkB activation in *Nhe6* KO may contribute to the previously shown deficits in neurite formation [309] as well as in the changes in structural, actin-dependent remodeling (see Chapter 3). As such, enhancement of TrkB activation through the application of the BDNF mimetic 7,8-DHF to KO cells was sufficient to ameliorate spine stability and enlargement following ChemLTP induction. The precise signaling cascades downstream of TrkB that are presumably impaired and subsequently restored through 7,8-DHF application in *Nhe6* KO remains to be properly determined. Such molecular determinants would provide better insights into which downstream signaling pathways are actually perturbed in the absence of NHE6-mediated TrkB trafficking.

It should also be noted that in my thesis, I have only focused on protein synthesis-independent early-LTP (E-LTP) that occurs during the first hour after TBS. This is because activity-dependent AMPAR trafficking, of which NHE6 evidently plays a strong role [326], is believed to be more critical in mediating E-LTP [120,381]. Nevertheless, extending these recordings to further assess protein synthesis-dependent L-LTP, which is more reliant upon

BDNF/TrkB signaling [389,394], could reveal if multiple stages of LTP are perturbed in *Nhe6* KO. Tangentially, recent evidence has shown that NHE6 expression is upregulated in response to the activation of cAMP-response element-binding protein (CREB), a prominent activity-dependent transcription factor in metabolic stress as well as in L-LTP [395]. This suggests that NHE6 transcription and translation may also be upregulated following prolonged activity stimulation, further implicating NHE6 in L-LTP consolidation. In tandem with the aforementioned decrease in TrkB activation and the substantial deficit already observed in E-LTP expression, these data strongly suggest that L-LTP will also be occluded in *Nhe6* KO hippocampi.

5.2.3 Potential for epileptogenesis via enhancement of TrkB activation

As I mentioned in Chapter 3, numerous recent studies have sought to employ 7,8-DHF to enhance TrkB signaling with the purpose of ameliorating behavioural and physiological deficits in mouse models of neuropsychiatric conditions [396–404]. While I have discussed the importance of TrkB activation in excitatory synaptic formation and plasticity, it is also vital to consider the potential consequences of enhancing this pathway upon epileptogenesis, as there is a strong association between the two. However, epileptic seizures are a prominent symptom of CS, thus raising the question of whether enhancing TrkB activation through 7,8-DHF is appropriate for these patients.

Hippocampal BDNF expression in area CA1 can increase substantially following prolonged seizure induction [405], as does TrkB protein expression and phosphorylation [406,407]. BDNF is also upregulated in the hippocampi of human epilepsy patients [408,409], and transgenic mice overexpressing BDNF in the hippocampus and forebrain develop spontaneous seizures by six months of age [410,411]. Curiously, findings from *BDNF^{+/-}* mice revealed an augmentation in GABAergic transmission [412–414], which was accompanied by reduced seizure

susceptibility following kindling [415]. Similarly, conditional deletion of TrkB from a subset of CNS neurons completely eliminated kindling in mice [416]. Taken together, these results led to the hypothesis that BDNF/TrkB signaling in the hippocampus exerts a pro-ictal effect upon epileptogenesis. As such, reduced TrkB activation in *Nhe6* KO [309,324] should be protective against seizure development. Nevertheless, it is still possible that applying an agonist of TrkB may paradoxically exacerbate these mechanisms to further impair inhibitory transmission and instead promote seizure generation [417,418].

In Chapter 4, I present multiple lines of evidence to demonstrably show the dysregulation of inhibitory function upon *Nhe6* KO CA1 pyramidal neurons. Unfortunately, the effects of BDNF/TrkB signaling upon inhibitory signaling are quite complex and can depend on the timing and extent of BDNF exposure. In younger hippocampal neurons, BDNF/TrkB signaling has been shown to be critical for the establishment of inhibitory synapses through the regulation of GABA_AR surface expression and synaptic clustering of both GABA_ARs and gephyrin [419,420]. Chronic exposure of exogenous BDNF also appears to increase the number of functional GABAergic synapses formed in cultures of dissociated hippocampal neurons, mostly through enhancing presynaptic function [421–423]. However, pulsed or bath BDNF application on mature hippocampal neurons transiently potentiates mIPSC amplitude, while continued exposure results in a prolonged depression through modulating the phosphorylation state of the GABA_AR $\beta 3$ subunit [424]. Complicating the situation further, the acute application of BDNF at older developmental stages has also been shown to enhance GABA_AR internalization and reduce GABAergic neurotransmission in primary hippocampal neurons [425] as well as in CA1 pyramidal neurons of acute hippocampal slices [426,427]. A study on isolated rat hippocampal CA1 neurons found that BDNF application at younger (PD 6) time points increased GABAergic function,

whereas the same treatment at older (PD 14) stages instead had an inhibitory effect upon GABAergic neurotransmission [428]. The impacts of BDNF/TrkB signaling upon the function of GABAergic synapses can thus be highly dependent upon age.

In addition to postsynaptic GABA_AR and gephyrin clustering, BDNF/TrkB signaling can also impact KCC2 expression. As I discussed in Chapter 4, the significant decrease in KCC2 protein in *Nhe6* KO hippocampi may substantially increase intracellular [Cl⁻] and subsequently lead to a depolarization of E_{GABA} , which could underlie the hyperexcitability observed in area CA1. In mature neurons, this could reverse the polarity of GABA to be excitatory and contribute to the development of hyperexcitability following subthreshold 4-AP challenge. Indeed, this trend has been observed frequently in human and animal models of epilepsy [429–434]. Importantly, BDNF contributes to the developmental upregulation of KCC2 transcription in immature neurons [435–437], and KCC2 expression is accordingly decreased in the hippocampi of TrkB-deficient mice [438]. However, exogenous BDNF exposure in adult neurons *in vitro* can promote KCC2 internalization and downregulate both mRNA and protein levels of KCC2 downstream of TrkB signaling [436,439–441]. In addition, short-term degradation of KCC2 protein may occur as a result of BDNF-triggered activation of the cellular protease calpain, while long-term changes are likely mediated by changes in gene expression [442,443]. Therefore, akin to the effects on GABAergic synapse formation, TrkB signaling may also differentially regulate KCC2 depending on the maturation state of the system.

Overall, these data suggest that BDNF/TrkB signaling plays a dual, developmentally regulated role in mediating inhibitory function: while BDNF supplements the establishment of inhibitory GABAergic signaling earlier in development, BDNF exposure at later time points has the opposite effect [444]. Thus, 7,8-DHF administration at younger time points may ameliorate

these inhibitory deficits in *Nhe6* KO, while the same treatment in adult animals may further aggravate these phenotypes by further downregulating KCC2 and GABA_ARs, which are already decreased in KO. It is even possible that a persistent decrease of TrkB activation well into adulthood may actually serve to counter its negative impact upon inhibitory function. However, some uncertainties remain with regards to the BDNF/TrkB pathway in *Nhe6* KO. The downregulation of pTrkB levels has only been observed in relatively young cultured hippocampal neurons *in vitro* [309], suggesting that defective TrkB signaling is prominent from an early developmental stage. Moreover, it is unknown if the expression or release of BDNF are similarly affected in the KO hippocampus *in vivo*. A recent report has revealed a similar downregulation of pTrkB in the cochlea of adult *Nhe6* KO mice with no change in BDNF protein when compared to WT mice [324]. As such, BDNF release may indeed be intact within KO brain cells as well, although this stipulation should be confirmed. Thus, direct investigations of the interplay between TrkB signaling and inhibitory neurotransmission in *Nhe6* KO will be necessary to properly resolve whether this pathway is causative or preventative in terms of seizure generation. Furthermore, obtaining time-courses of BDNF and activated TrkB levels in *Nhe6* KO hippocampal tissue could aid in determining appropriate start times and durations of 7,8-DHF administration to best alleviate the learning and memory deficits without aggravating kindling mechanisms. Ultimately, these studies will be necessary to validate its suitability for future clinical trials in human CS patients.

5.2.4 Additional considerations of cation-Cl⁻ cotransporter dysregulation in *Nhe6* KO

In Chapter 4, I found that two- and six-month-old *Nhe6* KO hippocampi contained significantly less KCC2 and greater NKCC1 protein when compared to WT samples. Importantly, the question still remains of how exactly the dysregulation of these cation-Cl⁻ cotransporters comes about in

adult *Nhe6* KO hippocampi. While the upregulation of NKCC1 in many forms of epilepsy is presently unclear, the majority of studies tend to focus on changes in KCC2 levels. I have just described how a lack of proper BDNF/TrkB signaling may in fact play a role in the lack of developmental KCC2 upregulation. Moreover, as I alluded to in Chapter 4, the “simplest” explanation for a decrease in KCC2 protein could be as follows: in the absence of NHE6-mediated regulation of endosomal pH, internalized cargos like KCC2 are not recycled properly to the cell membrane but misdirected to lysosomes for degradation. We and others have reported a similar fate for AMPARs and TrkB due to endosomal overacidification and mistrafficking to the lysosome, leading to their downregulation (see Chapter 2 and [309]). In support of this, I have previously found preliminary evidence to show that NHE6 and KCC2 punctae substantially overlap in mature primary hippocampal neurons (**Fig. 6**). This suggests that NHE6 is indeed involved in the intracellular trafficking of KCC2 through the endosomal system. Thus, akin to the experiments assessing GluA1 trafficking in Chapter 2, applying lysosomal hydrolase inhibitors to cultured KO hippocampal neurons and assessing KCC2 levels can determine whether KCC2 is similarly aberrantly degraded through the lysosome.

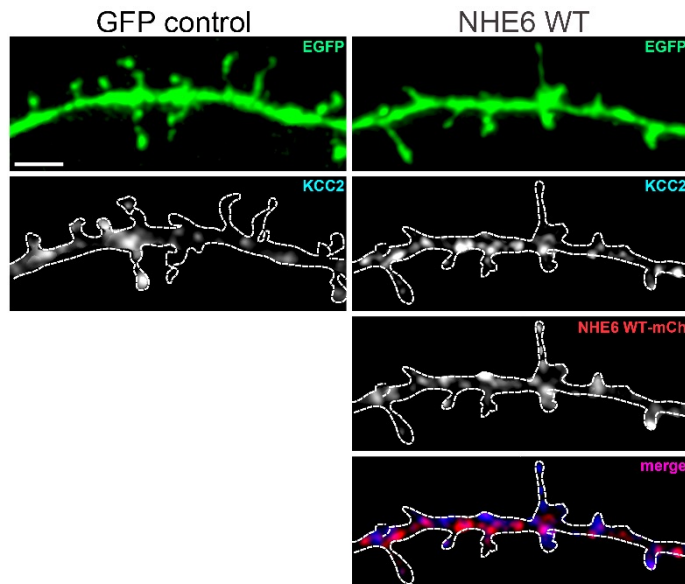


Figure 6: Colocalization of NHE6 and KCC2 in the spines and dendrites of hippocampal neurons. Representative confocal micrographs of 14 DIV primary murine hippocampal neurons transfected with EGFP alone (as transfection control, left) or EGFP and mCherry-tagged NHE6 WT (right). Channels are shown separately and merged; white dotted line denotes dendritic structure based off of EGFP signal. Scale bar: 2 μ m.

Interestingly, KCC2 can also be downregulated in response to enhancements in neuronal activity, such as during LTP [445] or epileptiform activity itself [429,434,436,446]. For instance, elevations in network activity can lead to the dispersal of KCC2 clusters and promote its internalization and degradation downstream of NMDAR-dependent Ca^{2+} influx, thereby reducing neuronal Cl^- efflux [442,447–449]. These findings imply that elevations in membrane potential could underlie the observed decrease in KCC2 within *Nhe6* KO hippocampi, especially because I hypothesize that the KO circuitry itself is already more prone to periods of heightened excitability. However, the deficiency in CA3-CA1 LTP in *Nhe6* KO refutes the idea that the potentiation of excitatory neurotransmission downregulates KCC2. Nevertheless, it is possible that a reversal of GABAergic polarity in *Nhe6* KO may cause elevations in membrane depolarization that could further decrease KCC2 levels. As I mention in Chapter 4, it is also unknown if the KCC2 downregulation is a cause or a response to enhanced circuit activity. Surprisingly, conflicting data from both human and animal models has suggested that KCC2 can sometimes be elevated in comparison to control, non-epileptic tissue [450]. Indeed, overactivation of KCC2 during a seizure may cause a build-up of extracellular $[\text{K}^+]$ that heightens membrane depolarization, thus resulting in a paradoxical pro-ictal effect [451,452]. It is important to note that these findings can depend on the brain area, cell type, and phase (*i.e.* before or during a seizure) studied [443]. As such, it is possible that the downregulation of KCC2 may in fact be a homeostatic mechanism to counter further membrane excitability during prolonged periods of hyperexcitability.

The potential dysregulation of Cl^- homeostasis in adult *Nhe6* KO mice raises the possibility of targeting cation- Cl^- cotransporters as a novel therapeutic area to treat epilepsy in CS without interfering with TrkB activation, the potential risks of which I have already discussed. As many CS patients develop neonatal seizures and often become resistant to conventional anticonvulsant

drugs [5,24], there is a particularly urgent need to identify novel compounds to reduce seizure severity and frequency. As potentiating KCC2 activity has remained challenging, inhibition of the presumed elevation in NKCC1 activity presently holds the most promise in this regard. The general NKCC inhibitor bumetanide, which can target both the widely expressed NKCC1 and the kidney-specific NKCC2 [453], has long been used as a loop diuretic in the treatment of systemic edema due to heart, liver, and kidney failure [454–456], as well as in ischemia or traumatic injury in the brain [457–461]. Because bumetanide also inhibits neural NKCC1 function and thus decreases Cl⁻ influx, bumetanide has been frequently used as an anticonvulsant to ameliorate kindling in experimental models and prevent neurobehavioural deficits induced by early-life seizures [462–464]. Moreover, bumetanide has been shown to improve deficits associated with aberrant GABAergic signaling in mouse models of other genetic intellectual disabilities, such as 22q11.2 deletion and Down syndromes [465,466]. Interestingly, this drug can also dampen epileptogenesis in mice lacking developmental KCC2 upregulation [467], highlighting the possibility of inhibiting elevated levels of NKCC1 to compensate for the loss of KCC2 activity.

As such, bumetanide is gaining traction for its off-label uses in the treatment of human brain disorders [468]. *In vitro* experiments initially reported that bath application of bumetanide blocked the development of epileptiform activity in resected tissue from recently deceased temporal lobe epilepsy (TLE) patients [432]. Recent clinical trials assessing the viability of administering bumetanide to human patients with ASD [469–474] and TLE [475] have also begun to show promise in improving symptoms associated with such disorders. However, because bumetanide can additionally inhibit the renal NKCC2 isoform [476,477], complications relating to its intense diuretic effects, such as polyuria and hypokalemia, have also been reported [470,472]. Moreover, bumetanide has a relatively poor blood-brain barrier penetrance, which is further

exacerbated by its active efflux via organic anion transporters [478–480]. Extremely high doses of bumetanide can also impair KCC2 function [481,482]. The development of more specific inhibitors of NKCC1 with improved brain bioavailability is thus required to overcome these caveats, research for which is currently ongoing [483]. Nevertheless, if E_{GABA} is indeed aberrantly depolarized in adult *Nhe6* KO hippocampi due to KCC2 downregulation, then bumetanide could first be tested experimentally in an effort to rescue the hyperexcitability observed in KO hippocampal circuitry. These data could establish the framework for employing novel NKCC1 inhibitors as a treatment option for epilepsy in CS.

5.2.5 Possible crosstalk between cellular excitability and excitatory synaptic density

Throughout my thesis, I have primarily attributed the decreases in dendritic spine density to disturbances in endosomal trafficking induced by the loss of NHE6. Although I propose that these deficits underlie the impairments in learning and memory, the interplay between spine loss and epileptic seizures in CS should also be considered. Dendritic spine pathologies are commonly seen in childhood genetic disorders involving epilepsy, such as Rett's and Fragile X syndromes [111–116]. Similarly, spine dysregulation and dendritic damage have also been observed following the induction of epilepsy *in vivo*, such as kainate induced *status epilepticus* [406,484,485] and lithium-pilocarpine kindling models [486–488], as well as in *in vitro* systems subjected to epileptiform burst discharges [489–491]. Seizure activity in CS patients could thus further exacerbate the loss of dendritic spines and the cognitive impairments associated with the disorder, as has been described for other forms of childhood and adult epilepsies [492,493].

Despite the fact that *Nhe6* KO pyramidal neurons are not intrinsically more excitable, nor do they develop obvious seizures spontaneously, I did note that *Nhe6* KO hippocampi have a

higher propensity to develop hyperexcitable firing in response to subthreshold 4-AP challenge (see Chapter 4). Likewise, spontaneous elevations in activity may also occur in *Nhe6* KO brains *in vivo* to induce sustained increases in neuronal firing, as bursts of ictal discharges are also routinely seen in electroencephalograms (EEGs) taken from CS patients [1,2,7,14,20,24]. Normally, prolonged elevations in circuit activity lead to reductions in the strength and number of excitatory synapses to maintain proper E/I balance [494,495]. Thus, I speculate that the constant increases in neuronal activity within KO hippocampi may promote the homeostatic downscaling of excitatory synapses to temper runaway excitation, as reflected by the reductions in spine density and AMPAR-mediated neurotransmission observed in *Nhe6* KO CA1 pyramidal neurons (see Chapter 3). Presently, it is unknown if homeostatic plasticity mechanisms are affected in a similar fashion as Hebbian plasticity in *Nhe6* KO. This could be addressed in the future by chronically applying GABA_AR blockers to cultured *Nhe6* KO neurons *in vitro* to verify if synaptic downscaling mechanisms are intact [495,496]. These findings will provide further insights into whether non-Hebbian forms of plasticity contribute to the changes in excitatory synaptic density and function.

In addition to network activity, KCC2 has also been shown to play an unexpected role in regulating spine dynamics independently of its ion transport function. Despite the fact that KCC2 is primarily studied in the context of GABAergic inhibition, KCC2 signal has also been observed at glutamatergic synapses [497]. Consequently, recent evidence has suggested that KCC2 plays additional roles in modulating dendritic spine dynamics. For example, the regulatory C-terminal tail of KCC2 interacts with the cytoskeletal protein 4.1N to mediate spine development, which did not require its ion transport domains [498,499]. As such, KCC2 KD in cortical and hippocampal pyramidal neurons resulted in an increase in long, filopodia-like dendritic protrusions concomitant with a reduction in the number of functional excitatory synapses [498,500]. Interestingly, KCC2

KD can also prevent GluA1 AMPA receptor clustering at spine heads, thereby implicating KCC2 in the regulation of excitatory postsynaptic signaling as well [500]. Thus, the loss of KCC2 in adult *Nhe6* KO hippocampi could also account for the relative decreases in large mature dendritic spines and AMPAR-mediated neurotransmission at CA1 pyramidal neurons (see Chapter 3 and [309]). In fact, the downregulation of KCC2 in the absence of NHE6 function may, in fact, be a shared link between the compromised establishment and function of both excitatory and inhibitory synapses [501]. This supposition further underscores the importance of identifying the mechanisms behind the decrease of KCC2 in *Nhe6* KO to uncover potential associations between the maintenance of functional excitatory synapses with the dysregulation of inhibitory signaling. An initial step to address this question could be to overexpress KCC2 in a NHE6 null background and assess the impact upon spine formation and glutamatergic neurotransmission. In such experiments, the precise timing of KCC2 expression must be considered carefully, as premature expression of KCC2 can actually delimit the role of excitatory GABA in synaptogenesis [502,503].

5.2.6 Divergent and compensatory mechanisms from NHE9

One additional point of consideration is the possibility of the other eNHE, NHE9, playing a compensatory role when NHE6 is mutated or ablated. Although both eNHEs localize to early and recycling endosomes to regulate their luminal pH [304,309,326], it has been proposed that NHE9 expression may be upregulated when NHE6 is downregulated. For instance, findings from post-mortem tissue of ASD patients revealed a downregulation of NHE6 expression with a concomitant increase in that of NHE9 [504]. Outside of the CNS, NHE6 dysfunction [505,506] and NHE9 overexpression [378,379,507] have also been reported in various forms of cancer. These data suggest a possible reciprocity in the function of these eNHEs in both health and disease.

Indeed, a recent report studying *Nhe9* KO mice has revealed a number of differences from NHE6 null animals. For instance, *Nhe9* KO mice do not show obvious changes in gross hippocampal morphology or impairments in locomotion, anxiety, or pain sensitivity [304], whereas *Nhe6* KO mice have exemplified deficits in all of these phenotypes [337,339–342]. However, *Nhe9* KO do exhibit characteristics of ASDs, including repetitive behaviours and impaired social and olfactory function [304]. In contrast, preliminary experiments from two-month-old male *Nhe6* KO mice assessing ASD-type behaviours did not reveal significant differences in grooming or social learning from age- and sex-matched WT animals, though KO mice again showed locomotor impairments during these experiments (**Fig. 7**). These findings were somewhat surprising given the autistic behaviours observed in some CS patients [5], though they imply a stronger association between ASDs and mutations in NHE9 as opposed to those in NHE6. As I stipulate with regards to the learning paradigms examined Chapter 3, it is possible that the performance of *Nhe6* KO animals in these tasks may be age-dependent due to their progressive neurodegeneration, and older *Nhe6* KO mice may begin to show ASD-like behaviours.

Moreover, the developmental profiles of these NHEs also vary in mice: while NHE6 is strongly expressed during embryonic development, NHE9 expression is relatively low until postnatal life [344] and peaks at around PD 50 [304]. Adult NHE9 expression is then primarily restricted to the olfactory bulb, superficial cortical layers, and the hippocampus [325]. Conversely, adult NHE6 expression remains consistent throughout the whole brain [325]. These differences in their expression patterns imply that NHE6 may be critical for neurite outgrowth, synaptogenesis, and neuronal plasticity in the developing brain, while NHE9 may play a greater role in postnatal circuit refinement. Importantly, disturbances in the latter are believed to underlie the development of ASDs [140,508], further suggesting a specific role for NHE9 dysfunction in ASDs.

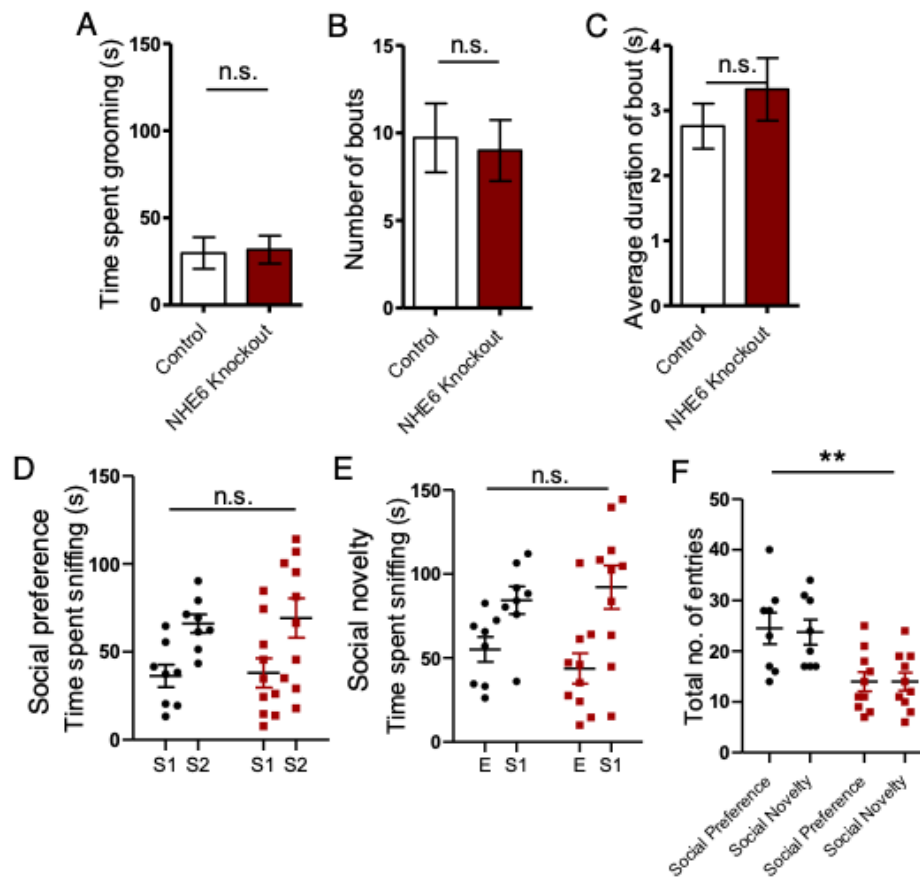


Figure 7: Adult *Nhe6* KO male mice do not show indications of autistic phenotypes. A-C: Mean \pm SEM time spent grooming (A), number of bouts (B), and average duration of bouts (C) of grooming behaviours between control WT and *Nhe6* KO mice. D-E: Mean \pm SEM quantification of performance of WT (black) and *Nhe6* KO (red) mice in social preference (D) and social novelty (E) tasks; E: empty chamber, S1: familiar mouse; S2: novel mouse. F: Mean \pm SEM quantification of total number of entries in three-chamber tasks in D and E. WT: $n = 8$; *Nhe6* KO: $n = 10$ animals. n.s. (not significant): $p > 0.05$, **: $p < 0.01$; Welch's t-test (A-C), two-way repeated measures ANOVA (D-E), one-way ANOVA (F).

At the cellular level, the overall morphology and dendritic spine density of *Nhe9* KO hippocampal neurons are comparable to WT, and basic electrophysiology recordings from *Nhe9* KO CA1 pyramidal neurons also revealed a cell-autonomous impairment in excitatory neurotransmission [304]. However, NHE9 did not colocalize strongly with the GluA2 AMPAR subunit, and loss of NHE9 did not impact total or surface levels of AMPARs or NMDARs [304].

Again, these data differ from my findings in *Nhe6* KO and Δ ES, which demonstrated reduced spine number and impaired AMPAR trafficking (see Chapters 2 and 3). Ultimately, the strongest deficit reported by the authors of this study was that the loss of NHE9 led to reductions in presynaptic Ca^{2+} entry and attenuated quantal release [304]. These data imply that NHE9 predominantly plays a presynaptic role in the axon terminal as opposed to the postsynaptic compartment. Unpublished work from our lab, however, has also demonstrated an activity-dependent role for postsynaptic NHE9-mediated dendritic trafficking during LTP and LTD. The importance of NHE9 in regulating postsynaptic plasticity mechanisms remains to be further elucidated.

Thus, although NHE6 and NHE9 are considered to be related eNHE isoforms, it is evident that the loss of either exchanger can have discernible yet divergent effects upon synaptic function, plasticity mechanisms, circuit development, and behaviour. As such, I do not believe that NHE9 is elevated in the absence of NHE6. For instance, the deficits in endosomal trafficking and alkalization observed in *Nhe6* KO neurons [309] strongly suggest that NHE9 does not experience a compensatory upregulation in expression when NHE6 is absent. Similarly, preliminary evidence from my work on Δ ES NHE6-transfected hippocampal neurons did not reveal a concomitant increase in NHE9 trafficking into dendrites (*data not shown*), although it is unknown whether this holds true for *Nhe6* KO hippocampi. Future studies directly comparing the two eNHEs and assessing whether there is indeed any redundancy in their function or respective cargos will better resolve this question. For instance, using immunofluorescent methods to compare the degree of colocalization between NHE6 and NHE9 with AMPARs, GABA_A Rs, or Trk receptors could readily reveal which cargos are localized in which eNHE-containing vesicle, and to what extent the two eNHEs show commonalities in their overlap with these receptor subtypes. Furthermore, overexpressing NHE9 into NHE6 null neurons and studying whether this is sufficient to restore

excitatory synaptic density and plasticity could also determine whether these two eNHEs are redundant in function. Moreover, if it is possible to generate a viable double KO mouse line lacking both NHE6 and NHE9, then these animals would provide a prime model with which to fully demonstrate the necessity of these eNHEs in neurophysiological function and behaviour.

5.3 FUTURE DIRECTIONS

Although I have provided a number of mechanisms that could underlie the learning deficits and generation of epileptic seizures in CS, it should be acknowledged that the majority of my work was performed *in vitro* or *ex vivo*. Consequently, future work should primarily focus on gathering *in vivo* evidence or manipulating NHE6 expression to better elaborate upon the pathogenesis of CS. While I have alluded to various future experiments throughout my thesis, I will now describe additional approaches that I believe should be taken from the *Nhe6* KO hippocampus to better understand the pathophysiology of this disorder, some of which are currently (or will soon be) ongoing as collaborative projects with other research groups.

Thus far, we and others have primarily employed the full-animal *Nhe6* KO mouse to extract evidence on the importance of NHE6 function in neural function. While these findings are undoubtedly important, the advent of modern genetic engineering techniques can allow us to determine if the maladapted circuitry within these KO mice can be returned to that of WT by restoring NHE6 expression within certain cell types. To this end, *Nhe6* KO/Cre-Lox mouse lines could be developed with drug-inducible Cre recombinase expression downstream of specific gene promoters that allows for the *Slc9a6* gene to be reintroduced in specific subsets of neurons. This system will also allow us to restore NHE6 at different developmental time points to assess the temporal dynamics of NHE6 reintroduction in rescuing the aforementioned deficits. Similar

conditional gene repair approaches have recently been used to ameliorate deficits in rodent models of other genetic disorders, such as Huntington's disease [509] and Gaucher disease [510]. Thus, employing this strategy in *Nhe6* KO mice will allow us to answer the important question of which cell types are most impacted by the ablation of NHE6. For instance, upon reintroducing NHE6 specifically in CA1 pyramidal neurons [511], we could repeat the LTP experiments at CA3-CA1 synapses to determine if the deficit in LTP predominantly lies within postsynaptic CA1 cells, as I postulate in Chapters 2 and 3. This could also allow us to determine if the downregulation of various membrane-bound cargos, including AMPAR subunits, GABA_AR subunits, and KCC2, are due to a cell-autonomous mistrafficking effect within *Nhe6* KO principal neurons. In addition, we can also verify if restoring NHE6 expression globally within all interneurons or within specific interneuron types - like those expressing PV or SOM - is sufficient to dampen the hyperexcitability observed in *Nhe6* KO hippocampi. In all, the data generated from these genetic repair experiments could provide valuable insights into the differential role of NHE6 within excitatory and inhibitory neurons. Moreover, they could also provide us with a means to guide targeted genetic therapeutic interventions in human CS patients to correct these deficits.

Throughout my thesis, I have discussed at length the consequences of losing NHE6 function primarily at level of the single cell, cell subtype, or brain area. However, the manner in which these various deficits coalesce together to impact neural circuitry as a whole remains to be investigated. Irregularities in EEG examinations are one of the most distinguishing diagnostic features observed in the majority of young children diagnosed with CS, with epileptiform discharges being commonly reported [1,2,7,14,20,24]. These findings suggest that oscillatory patterns of neural activity are dysregulated in the brains of CS patients, which may underlie the severe impairments in cognitive function and promote seizure generation. In light of these

distinctive electrophysiological findings, future work should also focus on longitudinally recording EEGs and other such patterns of neurobehavioural activity from *Nhe6* KO mice *in vivo*. This includes the future analysis of theta, gamma, and other activity patterns that mediate memory formation and spatial learning in the hippocampus [51–57]. Notably, theta rhythms are established through the regulatory action of interneurons, particularly those expressing PV [63]. As I reported in Chapter 4, PV+ GABAergic interneurons may become dysregulated and degenerate over time in KO hippocampi. Therefore, I strongly believe that the generation of theta rhythms will also be disturbed in *Nhe6* KO when compared to WT. Indeed, previous work has shown that disruption of PV+ cell function attenuated theta rhythms in area CA1 [512], thus highlighting the importance of these interneurons in the generation and maintenance of these frequencies. Interestingly, dampening PV+ cell hyperexcitability has recently been shown to improve learning mechanisms in a mouse model of Alzheimer’s disease [513], suggesting that paradoxical elevations in PV+ cell activity, which I describe in Chapter 4, may indeed be detrimental to memory acquisition in CS as well. Taken together, it is possible that PV+ cell loss and/or dysfunction may disrupt theta rhythm generation in *Nhe6* KO, which could further contribute to the deficits in LTP and learning mechanisms described in Chapter 3. These findings may also reflect the complex irregularities of EEGs obtained from CS patients and could indeed underlie their severe cognitive impairments.

In addition, *in vivo* recordings from KO mice will allow us to glean possible disruptions in their circadian rhythms and sleep/wake cycles, which are commonly reported by the families and caretakers of CS patients. Preliminary data obtained thus far has suggested a dysregulation in the circadian activity of *Nhe6* KO mice, which also show alterations in their sensitivity to light. Specifically, these mice have exemplified reductions and increases in their night- and daytime activity, respectively, when compared to age- and sex-matched WT mice (*data not shown*). This

fell in accordance with a recent study involving a small cohort of CS patients, in which sleep initiation and maintenance and sleep/wake transitions were the most common problems reported [514]. Additional case studies have also frequently reported electrical *status epilepticus* during slow-wave sleep (ESES) in individuals with CS [7,24,25,515], further exemplifying sleep disruptions in these patients. Accordingly, disturbances in circadian rhythms are frequently observed in various neuropsychiatric disorders, including schizophrenia and bipolar disorder [516–518]. There is thus a pressing need to gain a better understanding of how sleep/wake cycles and circadian rhythms are disrupted in *Nhe6* KO with the intention of potentially correcting them to improve the quality of life for CS patients and their caretakers.

Finally, an important phenotype of the *Nhe6* KO mouse model that has yet to be thoroughly addressed is the development of epileptic seizures. To my knowledge, the only available data that exists regarding epilepsy in these mice is from a DeltaGen phenotypic assessment (http://www.informatics.jax.org/knockout_mice/deltagen/1688.html), which indicated that these mice are not spontaneously epileptic but possess a lower threshold for metrazol-induced seizures when compared to age- and sex-matched WT mice. This corresponds with my findings in Chapter 4, where I report that the firing of *Nhe6* KO hippocampal area CA1 circuitry can readily transition into a hyperexcitable state in response to subthreshold concentrations of 4-AP. Given the robust epilepsy observed in CS patients, the lack of spontaneous seizures in *Nhe6* KO mice was somewhat surprising. However, proper kindling experiments in these animals have yet to be executed. Future *in vivo* observations of WT and KO mice exposed to low concentrations of metrazol and monitored using the adapted Racine scale (to measure seizure onset and severity [519]) would thus be a logical future direction to address this. It should also be noted that the first study on hemizygous *Nhe6* KO male mice stated that some, but not all, die spontaneously at around 3 weeks of age

[337]. Anecdotally, we have also observed the spontaneous death of adult KO mice across different ages, though this phenotype has not yet been formally quantified. Nonetheless, we hypothesize that the heightened propensity of the KO neural circuitry to reach hyperexcitable states may eventually lead to spontaneous seizure onset and result in the sudden unexplained death due to epilepsy (SUDEP) in these mice. This phenomenon has previously been described in mouse models of Dravet syndrome, another genetic form of infantile-onset epilepsy and SUDEP [520,521]. Although post-mortem necroscopy reports on these animals have yet to be performed, ongoing video monitoring that will be obtained during these aforementioned EEG recordings could provide a definitive answer into the unexplained deaths of these *Nhe6* KO mice and whether they indeed succumb to SUDEP.

Therefore, future *in vivo* studies on *Nhe6* KO mice will allow us to further our understanding of how CS progresses and develops in human patients, and how these mechanisms could be targeted to treat the various phenotypes of this disorder. Importantly, this information could also be extended to other neurological disorders in which NHE6 is affected, including ASDs and AD. In all, delving into these unexplored territories of NHE6 function within the brain will be a highly fascinating research area in the study of CS as well as other neurological disorders.

5.4 CONCLUSIONS

In conclusion, I have provided novel mechanisms through which intellectual disability and epilepsy may develop in patients with CS. By developing and investigating models in which NHE6 is either mutated or ablated entirely, I have demonstrated various deficiencies in neuronal protein trafficking and synaptic transmission that could result disrupt both excitatory and inhibitory neurotransmission that could result in these severe phenotypes in human patients. In particular:

1. *The loss of NHE6 disrupts excitatory synapse function and plasticity:* In neurons deficient in NHE6 or expressing a LOF mutant, neuronal structure and endosomal AMPAR trafficking were both impaired. Consequently, excitatory synapses of these neurons were unable to undergo both functional and structural potentiation following the induction of LTP. However, I was able to partially rescue these deficits in synaptic remodeling by inhibiting lysosomal hydrolase function or by applying 7,8-DHF, a TrkB agonist.
2. *Neuronal circuitry lacking NHE6 develops hyperexcitability due to impairments in GABAergic inhibition:* The loss of NHE6 renders the hippocampal circuitry more susceptible to the development of hyperexcitable burst discharges and also promotes the loss of GABAergic interneurons over time. As a result, area CA1 pyramidal neurons showed a loss of inhibitory synaptic molecules and GABA_AR trafficking. Notably, adult *Nhe6* KO tissue contained reciprocal increases and decreases in NKCC1 and KCC2 protein levels, respectively, which strongly suggested a dysregulation in Cl⁻ homeostasis and GABAergic neurotransmission. Notably, these deficits in GABA_AR localization and inhibitory neurotransmission carried over to cultured neurons expressing Δ ES NHE6, confirming the clinical relevance of these data.

Taken together, my findings are some of the first investigations into the role of NHE6 in the function and plasticity of both excitatory and inhibitory synapses, as well as in the excitability of individual pyramidal neurons and the hippocampal circuitry overall. In light of these findings, it is my hope that some of the pathways that are detrimentally impacted by the absence of NHE6 function can eventually be targeted clinically with novel therapeutic agents. Such treatments could address these cellular deficits and improve clinical outcomes for individuals afflicted by CS.

REFERENCES

1. Christianson AL, Stevenson RE, van der Meyden CH, Pelser J, Theron FW, van Rensburg PL, et al. X linked severe mental retardation, craniofacial dysmorphism, epilepsy, ophthalmoplegia, and cerebellar atrophy in a large South African kindred is localised to Xq24-q27. *J Med Genet*. 1999 Oct;36(10):759–66.
2. Gilfillan GD, Selmer KK, Roxrud I, Smith R, Kyllerman M, Eiklid K, et al. SLC9A6 mutations cause X-linked mental retardation, microcephaly, epilepsy, and ataxia, a phenotype mimicking Angelman syndrome. *Am J Hum Genet*. 2008 Apr;82(4):1003–10.
3. Kondapalli KC, Prasad H, Rao R. An inside job: how endosomal Na(+)/H(+) exchangers link to autism and neurological disease. *Front Cell Neurosci*. 2014 Jan;8(June):172.
4. Morrow EM, Pescosolido MF. Christianson Syndrome. In: Adam MP, Ardinger HH, Pagon RA, Wallace SE, Bean LJH, Stephens K, et al., editors. *GeneReviews*. Seattle (WA); 2018.
5. Pescosolido MF, Stein DM, Schmidt M, Moufawad El Achkar C, Sabbagh M, Rogg JM, et al. Genetic and phenotypic diversity of NHE6 mutations in Christianson syndrome. *Ann Neurol*. 2014;581–93.
6. Bosemani T, Zanni G, Hartman AL, Cohen R, Huisman TAGM, Bertini E, et al. Christianson syndrome: Spectrum of neuroimaging findings. *Neuropediatrics*. 2014;45(4):247–51.
7. Zanni G, Barresi S, Cohen R, Specchio N, Basel-Vanagaite L, Valente EM, et al. A novel mutation in the endosomal Na⁺/H⁺ exchanger NHE6 (SLC9A6) causes Christianson syndrome with electrical status epilepticus during slow-wave sleep (ESES). *Epilepsy Res*. 2014 May;108(4):811–5.
8. Trump N, McTague A, Brittain H, Papandreou A, Meyer E, Ngoh A, et al. Improving diagnosis and broadening the phenotypes in early-onset seizure and severe developmental delay disorders through gene panel analysis. *J Med Genet*. 2016;53(5):310–7.
9. Masurel-Paulet A, Piton A, Chancenotte S, Redin C, Thauvin-Robinet C, Henrenger Y, et al. A new family with an SLC9A6 mutation expanding the phenotypic spectrum of Christianson syndrome. *Am J Med Genet Part A*. 2016;170(8):2103–10.
10. Padmanabha H, Saini AG, Sahu JK, Singhi P. Syndrome of X linked intellectual disability, epilepsy, progressive brain atrophy and large head associated with SLC9A6 mutation. *BMJ Case Rep*. 2017;
11. Fichou Y, Bahi-Buisson N, Nectoux J, Chelly J, Héron D, Cuisset L, et al. Mutation in the SLC9A6 gene is not a frequent cause of sporadic Angelman-like syndrome. *Eur J Hum Genet*. 2009 Nov 27;17(11):1378–80.
12. Tarpey PS, Smith R, Pleasance E, Whibley A, Edkins S, Hardy C, et al. A systematic, large-scale resequencing screen of X-chromosome coding exons in mental retardation. *Nat Genet*. 2009;41(5):535–43.
13. Garbern JY, Neumann M, Trojanowski JQ, Lee VM-Y, Feldman G, Norris JW, et al. A mutation affecting the sodium/proton exchanger, SLC9A6, causes mental retardation with tau deposition. *Brain*. 2010 May;133(5):1391–402.

14. Schroer RJ, Holden KR, Tarpey PS, Matheus MG, Griesemer D a, Friez MJ, et al. Natural history of Christianson syndrome. *Am J Med Genet A*. 2010 Nov;152A(11):2775–83.
15. Mignot C, Héron D, Burszty J, Momtchilova M, Mayer M, Whalen S, et al. Novel mutation in SLC9A6 gene in a patient with Christianson syndrome and retinitis pigmentosum. *Brain Dev*. 2013 Feb;35(2):172–6.
16. Takahashi Y, Hosoki K, Matsushita M, Funatsuka M, Saito K, Kanazawa H, et al. A loss-of-function mutation in the SLC9A6 gene causes X-linked mental retardation resembling Angelman syndrome. *Am J Med Genet B Neuropsychiatr Genet*. 2011 Dec;156B(7):799–807.
17. Mignot C, Héron D, Burszty J, Momtchilova M, Mayer M, Whalen S, et al. Novel mutation in SLC9A6 gene in a patient with Christianson syndrome and retinitis pigmentosum. *Brain Dev*. 2013 Feb;35(2):172–6.
18. Schuurs-Hoeijmakers JHM, Vulto-van Silfhout AT, Vissers LELM, van de Vondervoort IIGM, van Bon BWM, de Ligt J, et al. Identification of pathogenic gene variants in small families with intellectually disabled siblings by exome sequencing. *J Med Genet*. 2013 Dec;50(12):802–11.
19. Sinajon P, Verbaan D, So J. The expanding phenotypic spectrum of female SLC9A6 mutation carriers: a case series and review of the literature. *Hum Genet*. 2016 Aug 3;135(8):841–50.
20. Pescosolido MF, Kavanaugh BC, Pochet N, Schmidt M, Jerskey BA, Rogg JM, et al. Complex Neurological Phenotype in Female Carriers of *NHE6* Mutations. *Mol Neuropsychiatry*. 2019;5(2):98–108.
21. Tan W-H, Bird LM, Thibert RL, Williams C a. If not Angelman, what is it? a review of Angelman-like syndromes. *Am J Med Genet Part A*. 2014 Apr 29;164(4):975–92.
22. Seltzer LE, Paciorkowski AR. Genetic disorders associated with postnatal microcephaly. *Am J Med Genet C Semin Med Genet*. 2014 Jun;166C(2):140–55.
23. Smith JC. Angelman syndrome: evolution of the phenotype in adolescents and adults. *Dev Med Child Neurol*. 2001 Jul;43(7):476–80.
24. Ikeda A, Yamamoto A, Ichikawa K, Tsuyusaki Y, Tsuji M, Iai M, et al. Epilepsy in Christianson syndrome: Two cases of Lennox–Gastaut syndrome and a review of literature. *Epilepsy Behav Reports*. 2020;13:100349.
25. Coorg R, Weisenberg JLZ. Successful Treatment of Electrographic Status Epilepticus of Sleep With Felbamate in a Patient With SLC9A6 Mutation. *Pediatr Neurol*. 2015 Dec;53(6):527–31.
26. Stuchlik A. Dynamic learning and memory, synaptic plasticity and neurogenesis: an update. *Front Behav Neurosci*. 2014;8(April):106.
27. Scoville WB, Milner B. LOSS OF RECENT MEMORY AFTER BILATERAL HIPPOCAMPAL LESIONS. *J Neurol Neurosurg Psychiatry*. 1957 Feb 1;20(1):11–21.
28. Burgess N, Maguire EA, O'Keefe J. The Human Hippocampus and Spatial and Episodic Memory. *Neuron*. 2002 Aug;35(4):625–41.

29. Buzsáki G, Moser EI. Memory, navigation and theta rhythm in the hippocampal-entorhinal system. *Nat Neurosci*. 2013 Feb 28;16(2):130–8.
30. Sommer W. Erkrankung des Ammonshorns als aetiologisches Moment der Epilepsie. *Arch Psychiatr Nervenkr*. 1880 Oct;10(3):631–75.
31. Nakahara S, Adachi M, Ito H, Matsumoto M, Tajinda K, Erp TGM van. Hippocampal Pathophysiology: Commonality Shared by Temporal Lobe Epilepsy and Psychiatric Disorders. *Neurosci J*. 2018;2018:1–9.
32. Neves G, Cooke SF, Bliss TVP. Synaptic plasticity, memory and the hippocampus: A neural network approach to causality. *Nat Rev Neurosci*. 2008;9:65–75.
33. Bentivoglio M, Swanson LW. On the fine structure of the pes Hippocampi major (with plates XIII-XXIII). Vol. 54, *Brain Research Bulletin*. 2001. p. 461–83.
34. Lisman JE, Harris KM. Quantal analysis and synaptic anatomy — integrating two views of hippocampal plasticity. *Trends Neurosci*. 1993 Apr;16(4):141–7.
35. Lisman JE, Raghavachari S, Tsien RW. The sequence of events that underlie quantal transmission at central glutamatergic synapses. *Nature Reviews Neuroscience*. 2007.
36. Kerchner GA, Nicoll RA. Silent synapses and the emergence of a postsynaptic mechanism for LTP. *Nat Rev Neurosci*. 2008;9(11):813–25.
37. Harris K, Stevens J. Dendritic spines of CA 1 pyramidal cells in the rat hippocampus: serial electron microscopy with reference to their biophysical characteristics. *J Neurosci*. 1989 Aug 1;9(8):2982–97.
38. Shepherd GMG, Harris KM. Three-Dimensional Structure and Composition of CA3→CA1 Axons in Rat Hippocampal Slices: Implications for Presynaptic Connectivity and Compartmentalization. *J Neurosci*. 1998 Oct 15;18(20):8300–10.
39. Hjorth-Simonsen A, Jeune B. Origin and termination of the hippocampal perforant path in the rat studied by silver impregnation. *J Comp Neurol*. 1972 Feb;144(2):215–31.
40. Steward O, Scoville SA. Cells of origin of entorhinal cortical afferents to the hippocampus and fascia dentata of the rat. *J Comp Neurol*. 1976 Oct 1;169(3):347–70.
41. Liu Y-Q, Yu F, Liu W-H, He X-H, Peng B-W. Dysfunction of hippocampal interneurons in epilepsy. *Neurosci Bull*. 2014;30(6):985–98.
42. Klausberger T. GABAergic interneurons targeting dendrites of pyramidal cells in the CA1 area of the hippocampus. *Eur J Neurosci*. 2009;30(6):947–57.
43. Pelkey KA, Chittajallu R, Craig MT, Tricoire L, Wester JC, McBain CJ. Hippocampal GABAergic Inhibitory Interneurons. *Physiol Rev*. 2017;97(4):1619–747.
44. Freund TF, Buzsáki G. Interneurons of the hippocampus. *Hippocampus*. 1996;6(4):347–470.
45. Gulyás a I, Hájos N, Freund TF. Interneurons containing calretinin are specialized to control other interneurons in the rat hippocampus. *J Neurosci*. 1996;16(10):3397–411.
46. Rudy B, Fishell G, Lee S, Hjerling-Leffler J. Three groups of interneurons account for nearly 100% of neocortical GABAergic neurons. *Dev Neurobiol*. 2011;71(1):45–61.
47. Roux L, Buzsáki G. Tasks for inhibitory interneurons in intact brain circuits.

- Neuropharmacology. 2015;88:10–23.
48. Klausberger T, Somogyi P. Neuronal Diversity and Temporal Dynamics: The Unity of Hippocampal Circuit Operations. *Science* (80-). 2008 Jul 4;321(5885):53–7.
 49. Engel AK, Fries P, Singer W. Dynamic predictions: Oscillations and synchrony in top–down processing. *Nat Rev Neurosci*. 2001 Oct;2(10):704–16.
 50. Buzsaki G. Neuronal Oscillations in Cortical Networks. *Science* (80-). 2004 Jun 25;304(5679):1926–9.
 51. Bragin A, Jando G, Nadasdy Z, Hetke J, Wise K, Buzsaki G. Gamma (40–100 Hz) oscillation in the hippocampus of the behaving rat. *J Neurosci*. 1995 Jan 1;15(1):47–60.
 52. Buzsáki G, Buhl DL, Harris KD, Csicsvari J, Czéh B, Morozov A. Hippocampal network patterns of activity in the mouse. *Neuroscience*. 2003 Jan;116(1):201–11.
 53. Canolty RT, Edwards E, Dalal SS, Soltani M, Nagarajan SS, Kirsch HE, et al. High Gamma Power Is Phase-Locked to Theta Oscillations in Human Neocortex. *Science* (80-). 2006 Sep 15;313(5793):1626–8.
 54. Lisman J, Buzsaki G. A Neural Coding Scheme Formed by the Combined Function of Gamma and Theta Oscillations. *Schizophr Bull*. 2008 Jul 21;34(5):974–80.
 55. Sirota A, Montgomery S, Fujisawa S, Isomura Y, Zugaro M, Buzsáki G. Entrainment of Neocortical Neurons and Gamma Oscillations by the Hippocampal Theta Rhythm. *Neuron*. 2008 Nov;60(4):683–97.
 56. Jones MW, Wilson MA. Theta Rhythms Coordinate Hippocampal–Prefrontal Interactions in a Spatial Memory Task. *Morris R, editor. PLoS Biol*. 2005 Nov 15;3(12):e402.
 57. Gyorgy B. Theta oscillations in the hippocampus. *Neuron*. 2002;33(3):325–40.
 58. Gloveli T, Dugladze T, Rotstein HG, Traub RD, Monyer H, Heinemann U, et al. Orthogonal arrangement of rhythm-generating microcircuits in the hippocampus. *Proc Natl Acad Sci U S A*. 2005 Sep;102(37):13295–300.
 59. Goutagny R, Jackson J, Williams S. Self-generated theta oscillations in the hippocampus. *Nat Neurosci*. 2009 Dec;12(12):1491–3.
 60. Rotstein HG, Pervouchine DD, Acker CD, Gillies MJ, White JA, Buhl EH, et al. Slow and Fast Inhibition and an H-Current Interact to Create a Theta Rhythm in a Model of CA1 Interneuron Network. *J Neurophysiol*. 2005 Aug 1;94(2):1509–18.
 61. Cobb SR, Buhl EH, Halasy K, Paulsen O, Somogyi P. Synchronization of neuronal activity in hippocampus by individual GABAergic interneurons. *Lett to Nat*. 1995;387:75–8.
 62. Stark E, Eichler R, Roux L, Fujisawa S, Rotstein HG, Buzsáki G. Inhibition-Induced Theta Resonance in Cortical Circuits. *Neuron*. 2013 Dec;80(5):1263–76.
 63. Amilhon B, Huh CYL, Manseau F, Ducharme G, Nichol H, Adamantidis A, et al. Parvalbumin Interneurons of Hippocampus Tune Population Activity at Theta Frequency. *Neuron*. 2015 Jun;86(5):1277–89.
 64. Bartos M, Vida I, Frotscher M, Meyer A, Monyer H, Geiger JRP, et al. Fast synaptic inhibition promotes synchronized gamma oscillations in hippocampal interneuron networks. *Proc Natl Acad Sci U S A*. 2002 Oct;99(20):13222–7.

65. Katona I, Acsády L, Freund TF. Postsynaptic targets of somatostatin-immunoreactive interneurons in the rat hippocampus. *Neuroscience*. 1999 Jan;88(1):37–55.
66. Tóth K, Freund TF, Miles R. Disinhibition of rat hippocampal pyramidal cells by GABAergic afferents from the septum. *J Physiol*. 1997 Apr 15;500(2):463–74.
67. McKinney RA. Excitatory amino acid involvement in dendritic spine formation, maintenance and remodelling. *J Physiol*. 2010 Jan 1;588(Pt 1):107–16.
68. Bourne JN, Harris KM. Balancing Structure and Function at Hippocampal Dendritic Spines. *Annu Rev Neurosci*. 2008 Jul;31(1):47–67.
69. Gray EG. Electron Microscopy of Synaptic Contacts on Dendrite Spines of the Cerebral Cortex. *Nature*. 1959 Jun;183(4675):1592–3.
70. Yuste R. The discovery of dendritic spines by Cajal. *Front Neuroanat*. 2015 Apr 21;9.
71. Gipson C, Olive M. Structural and functional plasticity of dendritic spines – root or result of behavior? *Physiol Behav*. 2017;176(12):139–48.
72. Harris KM, Jensen FE, Tsao B. Three-dimensional structure of dendritic spines and synapses in rat hippocampus (CA1) at postnatal day 15 and adult ages: implications for the maturation of synaptic physiology and long-term potentiation. *J Neurosci*. 1992;12(7):2685–705.
73. Lei W, Omotade OF, Myers KR, Zheng JQ. Actin cytoskeleton in dendritic spine development and plasticity. *Curr Opin Neurobiol*. 2016;39:86–92.
74. Borovac J, Bosch M, Okamoto K. Regulation of actin dynamics during structural plasticity of dendritic spines: Signaling messengers and actin-binding proteins. *Mol Cell Neurosci*. 2018;91(January):122–30.
75. Arellano JJ, Benavides-Piccione R, Defelipe J, Yuste R. Ultrastructure of dendritic spines: correlation between synaptic and spine morphologies. *Front Neurosci*. 2007;1(1):131–43.
76. Okabe S. Molecular anatomy of the postsynaptic density. *Mol Cell Neurosci*. 2007 Apr;34(4):503–18.
77. Harris KM. Structure, development, and plasticity of dendritic spines. *Curr Opin Neurobiol*. 1999 Jun;9(3):343–8.
78. De Simoni A, Griesinger CB, Edwards FA. Development of Rat CA1 Neurones in Acute Versus Organotypic Slices: Role of Experience in Synaptic Morphology and Activity. *J Physiol*. 2003 Jul;550(1):135–47.
79. Peters A, Kaiserman-Abramof IR. The small pyramidal neuron of the rat cerebral cortex. The perikaryon, dendrites and spines. *Am J Anat*. 1970 Apr;127(4):321–55.
80. Fiala JC, Allwardt B, Harris KM. Dendritic spines do not split during hippocampal LTP or maturation. *Nat Neurosci*. 2002 Apr 18;5(4):297–8.
81. Bailey CH, Kandel ER. Structural Changes Accompanying Memory Storage. *Annu Rev Physiol*. 1993 Oct;55(1):397–426.
82. Bourne J, Harris KM. Do thin spines learn to be mushroom spines that remember? *Curr Opin Neurobiol*. 2007;17(3):381–6.
83. Biever A, Glock C, Tushev G, Ciirdaeva E, Dalmay T, Langer JD, et al. Monosomes

- actively translate synaptic mRNAs in neuronal processes. *Science* (80-). 2020 Jan 31;367(6477):eaay4991.
84. Maiti P, Manna J, Ilavazhagan G, Rossignol J, Dunbar GL. Molecular regulation of dendritic spine dynamics and their potential impact on synaptic plasticity and neurological diseases. *Neurosci Biobehav Rev*. 2015;59(101):208–37.
 85. Fischer M, Kaech S, Knutti D, Matus A. Rapid actin-based plasticity in dendritic spines. *Neuron*. 1998;20(5):847–54.
 86. Phillips M, Pozzo-Miller L. Dendritic spine dysgenesis in autism related disorders. *Neurosci Lett*. 2015;1–11.
 87. Berry KP, Nedivi E. Spine Dynamics: Are They All the Same? *Neuron*. 2017;96(1):43–55.
 88. Matsuzaki M, Honkura N, Ellis-Davies GCR, Kasai H. Structural basis of long-term potentiation in single dendritic spines. *Nature*. 2004;429(June):761–6.
 89. Okamoto KI, Nagai T, Miyawaki A, Hayashi Y. Rapid and persistent modulation of actin dynamics regulates postsynaptic reorganization underlying bidirectional plasticity. *Nat Neurosci*. 2004;7(10):1104–12.
 90. Zhou Q, Homma KJ, Poo M. Shrinkage of Dendritic Spines Associated with Long-Term Depression of Hippocampal Synapses. *Neuron*. 2004 Dec;44(5):749–57.
 91. Honkura N, Matsuzaki M, Noguchi J, Ellis-Davies GCR, Kasai H. The Subspine Organization of Actin Fibers Regulates the Structure and Plasticity of Dendritic Spines. *Neuron*. 2008 Mar;57(5):719–29.
 92. Frost NA, Shroff H, Kong H, Betzig E, Blanpied TA. Single-Molecule Discrimination of Discrete Perisynaptic and Distributed Sites of Actin Filament Assembly within Dendritic Spines. *Neuron*. 2010 Jul;67(1):86–99.
 93. Bosch M, Castro J, Saneyoshi T, Matsuno H, Sur M, Hayashi Y. Structural and molecular remodeling of dendritic spine substructures during long-term potentiation. *Neuron*. 2014;82(2):444–59.
 94. Menna E, Zambetti S, Morini R, Donzelli A, Disanza A, Calvigioni D, et al. Eps8 controls dendritic spine density and synaptic plasticity through its actin-capping activity. *EMBO J*. 2013;32(12):1730–44.
 95. De Roo M, Klauser P, Muller D. LTP Promotes a Selective Long-Term Stabilization and Clustering of Dendritic Spines. Sheng M, editor. *PLoS Biol*. 2008 Sep 9;6(9):e219.
 96. Watson DJ, Ostroff L, Cao G, Parker PH, Smith H, Harris KM. LTP enhances synaptogenesis in the developing hippocampus. *Hippocampus*. 2016;26(5):560–76.
 97. Bosch M, Hayashi Y. Structural plasticity of dendritic spines. *Curr Opin Neurobiol*. 2012;22(3):383–8.
 98. Martin SJ, Grimwood PD, Morris RGM. Synaptic Plasticity and Memory: An Evaluation of the Hypothesis. *Annu Rev Neurosci*. 2000;
 99. Trachtenberg JT, Chen BE, Knott GW, Feng G, Sanes JR, Welker E, et al. Long-term in vivo imaging of experience-dependent synaptic plasticity in adult cortex. *Nature*. 2002 Dec;420(6917):788–94.

100. Grutzendler J, Kasthuri N, Gan W-B. Long-term dendritic spine stability in the adult cortex. *Nature*. 2002 Dec;420(6917):812–6.
101. Holtmaat AJGD, Trachtenberg JT, Wilbrecht L, Shepherd GM, Zhang X, Knott GW, et al. Transient and Persistent Dendritic Spines in the Neocortex In Vivo. *Neuron*. 2005 Jan;45(2):279–91.
102. Yang G, Pan F, Gan W-B. Stably maintained dendritic spines are associated with lifelong memories. *Nature*. 2009 Dec 29;462(7275):920–4.
103. Xu T, Yu X, Perlik AJ, Tobin WF, Zweig JA, Tennant K, et al. Rapid formation and selective stabilization of synapses for enduring motor memories. *Nature*. 2009 Dec 29;462(7275):915–9.
104. Hayashi-Takagi A, Yagishita S, Nakamura M, Shirai F, Wu YI, Loshbaugh AL, et al. Labelling and optical erasure of synaptic memory traces in the motor cortex. *Nature*. 2015 Sep 9;525(7569):333–8.
105. Gu L, Kleiber S, Schmid L, Nebeling F, Chamoun M, Steffen J, et al. Long-Term In Vivo Imaging of Dendritic Spines in the Hippocampus Reveals Structural Plasticity. *J Neurosci*. 2014 Oct 15;34(42):13948–53.
106. Attardo A, Fitzgerald JE, Schnitzer MJ. Impermanence of dendritic spines in live adult CA1 hippocampus. *Nature*. 2015;523(7562):592–6.
107. Pfeiffer T, Poll S, Bancelin S, Angibaud J, Inavalli VK, Keppler K, et al. Chronic 2P-STED imaging reveals high turnover of dendritic spines in the hippocampus in vivo. *Elife*. 2018 Jun 22;7.
108. Hasegawa S, Sakuragi S, Tominaga-Yoshino K, Ogura A. Dendritic spine dynamics leading to spine elimination after repeated inductions of LTD. *Sci Rep*. 2015 Jul 9;5(1):7707.
109. Dindot S V., Antalffy BA, Bhattacharjee MB, Beaudet AL. The Angelman syndrome ubiquitin ligase localizes to the synapse and nucleus, and maternal deficiency results in abnormal dendritic spine morphology. *Hum Mol Genet*. 2008;17(1):111–8.
110. Jay V, Becker LE, Chan F-W, Perry TL. Puppet-like syndrome of Angelman: A pathologic and neurochemical study. *Neurology*. 1991 Mar 1;41(3):416–416.
111. Armstrong D, Dunn JK, Antalffy B, Trivedi R. Selective Dendritic Alterations in the Cortex of Rett Syndrome. *J Neuropathol Exp Neurol*. 1995 Mar;54(2):195–201.
112. Chapleau CA, Calfa GD, Lane MC, Albertson AJ, Larimore JL, Kudo S, et al. Dendritic spine pathologies in hippocampal pyramidal neurons from Rett syndrome brain and after expression of Rett-associated MECP2 mutations. *Neurobiol Dis*. 2009 Aug;35(2):219–33.
113. Belichenko P V., Oldfors A, Hagberg B, Dahlström A. Rett syndrome: 3-D confocal microscopy of cortical pyramidal dendrites and afferents. *Neuroreport*. 1994 Jul;5(12):1509–13.
114. Rudelli RD, Brown WT, Wisniewski K, Jenkins EC, Laure-Kamionowska M, Connell F, et al. Adult fragile X syndrome. *Acta Neuropathol*. 1985;67(3–4):289–95.
115. Hinton VJ, Brown WT, Wisniewski K, Rudelli RD. Analysis of neocortex in three males with the fragile X syndrome. *Am J Med Genet*. 1991 Dec 1;41(3):289–94.

116. Irwin SA, Patel B, Idupulapati M, Harris JB, Crisostomo RA, Larsen BP, et al. Abnormal dendritic spine characteristics in the temporal and visual cortices of patients with fragile-X syndrome: A quantitative examination. *Am J Med Genet*. 2001 Jan 15;98(2):161–7.
117. Dorostkar MM, Zou C, Blazquez-Llorca L, Herms J. Analyzing dendritic spine pathology in Alzheimer’s disease: problems and opportunities. *Acta Neuropathol*. 2015 Jul 11;130(1):1–19.
118. Knobloch M, Mansuy IM. Dendritic Spine Loss and Synaptic Alterations in Alzheimer’s Disease. *Mol Neurobiol*. 2008 Feb 26;37(1):73–82.
119. Naslavsky N, Caplan S. The enigmatic endosome – sorting the ins and outs of endocytic trafficking. *J Cell Sci*. 2018;131(13):jcs216499.
120. Hiester BG, Becker MI, Bowen AB, Schwartz SL, Kennedy MJ. Mechanisms and Role of Dendritic Membrane Trafficking for Long-Term Potentiation. *Front Cell Neurosci*. 2018;12(October):1–15.
121. Morgan JR, Comstra HS, Cohen M, Faundez V. Presynaptic Membrane Retrieval and Endosome Biology: Defining Molecularly Heterogeneous Synaptic Vesicles. *Cold Spring Harb Perspect Biol*. 2013 Oct 1;5(10):a016915–a016915.
122. Kiral FR, Kohrs FE, Jin EJ, Hiesinger PR. Rab GTPases and Membrane Trafficking in Neurodegeneration. *Curr Biol*. 2018 Apr;28(8):R471–86.
123. Terenzio M, Schiavo G, Fainzilber M. Compartmentalized Signaling in Neurons: From Cell Biology to Neuroscience. *Neuron*. 2017 Nov;96(3):667–79.
124. Winckler B, Faundez V, Maday S, Cai Q, Guimas Almeida C, Zhang H. The Endolysosomal System and Proteostasis: From Development to Degeneration. *J Neurosci*. 2018;38(44):9364–74.
125. Huotari J, Helenius A. Endosome maturation. *EMBO J*. 2011;30(17):3481–500.
126. Bucci C, Parton RG, Mather IH, Stunnenberg H, Simons K, Hoflack B, et al. The small GTPase rab5 functions as a regulatory factor in the early endocytic pathway. *Cell*. 1992 Sep;70(5):715–28.
127. Vitelli R, Santillo M, Lattero D, Chiariello M, Bifulco M, Bruni CB, et al. Role of the Small GTPase RAB7 in the Late Endocytic Pathway. *J Biol Chem*. 1997 Feb 14;272(7):4391–7.
128. Clairfeuille T, Mas C, Chan ASM, Yang Z, Tello-Lafoz M, Chandra M, et al. A molecular code for endosomal recycling of phosphorylated cargos by the SNX27–retromer complex. *Nat Struct Mol Biol*. 2016 Oct 5;23(10):921–32.
129. Gallon M, Clairfeuille T, Steinberg F, Mas C, Ghai R, Sessions RB, et al. A unique PDZ domain and arrestin-like fold interaction reveals mechanistic details of endocytic recycling by SNX27–retromer. *Proc Natl Acad Sci*. 2014 Sep 2;111(35):E3604–13.
130. McNally KE, Faulkner R, Steinberg F, Gallon M, Ghai R, Pim D, et al. Retriever is a multiprotein complex for retromer-independent endosomal cargo recycling. *Nat Cell Biol*. 2017 Oct 11;19(10):1214–25.
131. Ciechanover A, Iwai K. The Ubiquitin System: From Basic Mechanisms to the Patient Bed. *IUBMB Life (International Union Biochem Mol Biol Life)*. 2004 Apr 1;56(4):193–201.

132. Platt FM, Boland B, van der Spoel AC. Lysosomal storage disorders: The cellular impact of lysosomal dysfunction. *J Cell Biol.* 2012 Nov 26;199(5):723–34.
133. Ferguson SM. Neuronal lysosomes. *Neurosci Lett.* 2018;(April):0–1.
134. Xie Z, Klionsky DJ. Autophagosome formation: core machinery and adaptations. *Nat Cell Biol.* 2007 Oct;9(10):1102–9.
135. Kraft C, Martens S. Mechanisms and regulation of autophagosome formation. *Curr Opin Cell Biol.* 2012 Aug;24(4):496–501.
136. Wang J, Davis S, Zhu M, Miller EA, Ferro-Novick S. Autophagosome formation: Where the secretory and autophagy pathways meet. *Autophagy.* 2017 May 4;13(5):973–4.
137. Christ L, Raiborg C, Wenzel EM, Campsteijn C, Stenmark H. Cellular Functions and Molecular Mechanisms of the ESCRT Membrane-Scission Machinery. *Trends Biochem Sci.* 2017 Jan;42(1):42–56.
138. Kulkarni VV, Maday S. Compartment-specific dynamics and functions of autophagy in neurons. *Dev Neurobiol.* 2018 Mar;78(3):298–310.
139. Dragich JM, Kuwajima T, Hirose-Ikeda M, Yoon MS, Eenjes E, Bosco JR, et al. Autophagy linked FYVE (Alfy/WDFY3) is required for establishing neuronal connectivity in the mammalian brain. *Elife.* 2016 Sep 20;5.
140. Tang G, Gudsnuk K, Kuo S-H, Cotrina ML, Rosoklija G, Sosunov A, et al. Loss of mTOR-Dependent Macroautophagy Causes Autistic-like Synaptic Pruning Deficits. *Neuron.* 2014 Sep;83(5):1131–43.
141. Lieberman OJ, McGuirt AF, Tang G, Sulzer D. Roles for neuronal and glial autophagy in synaptic pruning during development. *Neurobiol Dis.* 2019 Feb;122:49–63.
142. Gowrishankar S, Wu Y, Ferguson SM. Impaired JIP3-dependent axonal lysosome transport promotes amyloid plaque pathology. *J Cell Biol.* 2017 Oct 2;216(10):3291–305.
143. Ascano M, Richmond A, Borden P, Kuruvilla R. Axonal Targeting of Trk Receptors via Transcytosis Regulates Sensitivity to Neurotrophin Responses. *J Neurosci.* 2009 Sep 16;29(37):11674–85.
144. Park M, Salgado JM, Ostroff L, Helton TD, Camenzind G, Harris KM, et al. Plasticity-induced growth of dendritic spines by exocytic trafficking from recycling endosomes. *Neuron.* 2006;52(5):817–30.
145. Prekeris R, Foletti DL, Scheller RH. Dynamics of Tubulovesicular Recycling Endosomes in Hippocampal Neurons. *J Neurosci.* 1999 Dec 1;19(23):10324–37.
146. Cooney JR, Hurlburt JL, Selig DK, Harris KM, Fiala JC. Endosomal Compartments Serve Multiple Hippocampal Dendritic Spines from a Widespread Rather Than a Local Store of Recycling Membrane. *J Neurosci.* 2002 Mar 15;22(6):2215–24.
147. Gordon MK, Bench KG, Deanin GG, Gordon MW. Histochemical and biochemical study of synaptic lysosomes. *Nature.* 1968 Feb;217(5128):523–7.
148. Malenka RC, Nicoll RA. NMDA-receptor-dependent synaptic plasticity: multiple forms and mechanisms. Vol. 16, *Trends in Neurosciences.* 1993. p. 521–7.
149. Huganir RL, Nicoll R a. AMPARs and synaptic plasticity: The last 25 years. *Neuron.*

- 2013;80(3):704–17.
150. Isaac JTR, Nicoll RA, Malenka RC. Evidence for silent synapses: Implications for the expression of LTP. *Neuron*. 1995 Aug;15(2):427–34.
 151. Liao D, Hessler NA, Malinow R. Activation of postsynaptically silent synapses during pairing-induced LTP in CA1 region of hippocampal slice. *Nature*. 1995 Jun;375(6530):400–4.
 152. Roche KW, O'Brien RJ, Mammen AL, Bernhardt J, Huganir RL. Characterization of Multiple Phosphorylation Sites on the AMPA Receptor GluR1 Subunit. *Neuron*. 1996 Jun;16(6):1179–88.
 153. Barria A, Muller D, Derkach V, Griffith LC, Soderling TR. Regulatory phosphorylation of AMPA-type glutamate receptors by CaM-KII during long-term potentiation. *Science* (80-). 1997 Jun 27;276(5321):2042–5.
 154. Benke TA, Lüthi A, Isaac JTR, Collingridge GL. Modulation of AMPA receptor unitary conductance by synaptic activity. *Nature*. 1998 Jun;393(6687):793–7.
 155. Shi SH, Hayashi Y, Petralia RS, Zaman SH, Wenthold RJ, Svoboda K, et al. Rapid spine delivery and redistribution of AMPA receptors after synaptic NMDA receptor activation. *Science*. 1999 Jun 11;284(5421):1811–6.
 156. Diering GH, Huganir RL. The AMPA Receptor Code of Synaptic Plasticity. *Neuron*. 2018;100(2):314–29.
 157. Banke TG, Bowie D, Lee H-K, Huganir RL, Schousboe A, Traynelis SF. Control of GluR1 AMPA Receptor Function by cAMP-Dependent Protein Kinase. *J Neurosci*. 2000 Jan 1;20(1):89–102.
 158. Wenthold R, Petralia R, Blahos J I, Niedzielski A. Evidence for multiple AMPA receptor complexes in hippocampal CA1/CA2 neurons. *J Neurosci*. 1996 Mar 15;16(6):1982–9.
 159. Selcher JC, Xu W, Hanson JE, Malenka RC, Madison D V. Glutamate receptor subunit GluA1 is necessary for long-term potentiation and synapse unsilencing, but not long-term depression in mouse hippocampus. *Brain Res*. 2012;1435:8–14.
 160. Chater TE, Goda Y. The role of AMPA receptors in postsynaptic mechanisms of synaptic plasticity. *Front Cell Neurosci*. 2014;8(November):1–14.
 161. Anggono V, Huganir RL. Regulation of AMPA receptor trafficking and synaptic plasticity. *Curr Opin Neurobiol*. 2012;22(3):461–9.
 162. Heynen AJ, Quinlan EM, Bae DC, Bear MF. Bidirectional, Activity-Dependent Regulation of Glutamate Receptors in the Adult Hippocampus In Vivo. *Neuron*. 2000 Nov;28(2):527–36.
 163. Broutman G, Baudry M. Involvement of the Secretory Pathway for AMPA Receptors in NMDA-Induced Potentiation in Hippocampus. *J Neurosci*. 2001 Jan 1;21(1):27–34.
 164. Lu W-Y, Man H-Y, Ju W, Trimble WS, MacDonald JF, Wang YT. Activation of Synaptic NMDA Receptors Induces Membrane Insertion of New AMPA Receptors and LTP in Cultured Hippocampal Neurons. *Neuron*. 2001 Jan;29(1):243–54.
 165. Lledo PM, Zhang X, Südhof TC, Malenka RC, Nicoll RA. Postsynaptic membrane fusion

- and long-term potentiation. *Science* (80-). 1998 Jan 16;279(5349):399–403.
166. Park M, Penick EC, Edwards JG, Kauer J a, Ehlers MD. Recycling endosomes supply AMPA receptors for LTP. *Science*. 2004;305(5692):1972–5.
 167. Kopec CD, Real E, Kessels HW, Malinow R. GluR1 links structural and functional plasticity at excitatory synapses. *J Neurosci*. 2007;27(50):13706–18.
 168. Yang Y, Wang X -b., Frerking M, Zhou Q. Spine Expansion and Stabilization Associated with Long-Term Potentiation. *J Neurosci*. 2008 May 28;28(22):5740–51.
 169. Kennedy MJ, Davison IG, Robinson CG, Ehlers MD. Syntaxin-4 defines a domain for activity-dependent exocytosis in dendritic spines. *Cell*. 2010;141(3):524–35.
 170. Keith DJ, Sanderson JL, Gibson ES, Woolfrey KM, Robertson HR, Olszewski K, et al. Palmitoylation of A-kinase anchoring protein 79/150 regulates dendritic endosomal targeting and synaptic plasticity mechanisms. *J Neurosci*. 2012;32(21):7119–36.
 171. Roman-Vendrell C, Chevalier M, Acevedo-Canabal AM, Delgado-Peraza F, Flores-Otero J, Yudowski GA. Imaging of kiss-and-run exocytosis of surface receptors in neuronal cultures. *Front Cell Neurosci*. 2014 Nov 3;8.
 172. Hiester BG, Bourke AM, Sinnen BL, Cook SG, Gibson ES, Smith KR, et al. L-Type Voltage-Gated Ca²⁺ Channels Regulate Synaptic-Activity-Triggered Recycling Endosome Fusion in Neuronal Dendrites. *Cell Rep*. 2017;21(8):2134–46.
 173. Woolfrey KM, Sanderson JL, Dell'Acqua ML. The palmitoyl acyltransferase DHHC2 regulates recycling endosome exocytosis and synaptic potentiation through palmitoylation of AKAP79/150. *J Neurosci*. 2015;35(2):442–56.
 174. Patterson MA, Szatmari EM, Yasuda R. AMPA receptors are exocytosed in stimulated spines and adjacent dendrites in a Ras-ERK-dependent manner during long-term potentiation. *Proc Natl Acad Sci U S A*. 2010;107(36):15951–6.
 175. Borgdorff AJ, Choquet D. Regulation of AMPA receptor lateral movements. *Nature*. 2002 Jun;417(6889):649–53.
 176. Ehlers MD, Heine M, Groc L, Lee M-C, Choquet D. Diffusional Trapping of GluR1 AMPA Receptors by Input-Specific Synaptic Activity. *Neuron*. 2007 May;54(3):447–60.
 177. Choquet D, Triller A. The role of receptor diffusion in the organization of the postsynaptic membrane. *Nat Rev Neurosci*. 2003 Apr;4(4):251–65.
 178. Petrini EM, Lu J, Cognet L, Lounis B, Ehlers MD, Choquet D. Endocytic trafficking and recycling maintain a pool of mobile surface AMPA receptors required for synaptic potentiation. *Neuron*. 2009;63(1):92–105.
 179. Makino H, Malinow R. AMPA Receptor Incorporation into Synapses during LTP: The Role of Lateral Movement and Exocytosis. *Neuron*. 2009;64(3):381–90.
 180. Ashby MC, Maier SR, Nishimune A, Henley JM. Lateral Diffusion Drives Constitutive Exchange of AMPA Receptors at Dendritic Spines and Is Regulated by Spine Morphology. *J Neurosci*. 2006 Jun 28;26(26):7046–55.
 181. Penn AC, Zhang CL, Georges F, Royer L, Breillat C, Hosy E, et al. Hippocampal LTP and contextual learning require surface diffusion of AMPA receptors. *Nature*.

- 2017;549(7672):384–8.
182. Choquet D. Linking Nanoscale Dynamics of AMPA Receptor Organization to Plasticity of Excitatory Synapses and Learning. *J Neurosci*. 2018;38(44):9318–29.
 183. Opazo P, Labrecque S, Tigaret CM, Frouin A, Wiseman PW, De Koninck P, et al. CaMKII Triggers the Diffusional Trapping of Surface AMPARs through Phosphorylation of Stargazin. *Neuron*. 2010 Jul;67(2):239–52.
 184. Hayashi Y, Shi SH, Esteban JA, Piccini A, Poncer JC, Malinow R. Driving AMPA receptors into synapses by LTP and CaMKII: requirement for GluR1 and PDZ domain interaction. *Science* (80-). 2000 Mar 24;287(5461):2262–7.
 185. Schnell E, Sizemore M, Karimzadegan S, Chen L, Brecht DS, Nicoll RA. Direct interactions between PSD-95 and stargazin control synaptic AMPA receptor number. *Proc Natl Acad Sci*. 2002 Oct 15;99(21):13902–7.
 186. Bats C, Groc L, Choquet D. The Interaction between Stargazin and PSD-95 Regulates AMPA Receptor Surface Trafficking. *Neuron*. 2007;53(5):719–34.
 187. Kopeck CD, Li B, Wei W, Boehm J, Malinow R. Glutamate receptor exocytosis and spine enlargement during chemically induced long-term potentiation. *J Neurosci*. 2006;26(7):2000–9.
 188. Wang Z, Edwards JG, Riley N, Provance DW, Karcher R, Li X dong, et al. Myosin Vb Mobilizes Recycling Endosomes and AMPA Receptors for Postsynaptic Plasticity. *Cell*. 2008;135(3):535–48.
 189. Esteves da Silva M, Adrian M, Schätzle P, Lipka J, Watanabe T, Cho S, et al. Positioning of AMPA Receptor-Containing Endosomes Regulates Synapse Architecture. *Cell Rep*. 2015;933–43.
 190. Lüscher C, Xia H, Beattie EC, Carroll RC, von Zastrow M, Malenka RC, et al. Role of AMPA Receptor Cycling in Synaptic Transmission and Plasticity. *Neuron*. 1999 Nov;24(3):649–58.
 191. Ehlers MD. Reinsertion or Degradation of AMPA Receptors Determined by Activity-Dependent Endocytic Sorting. *Neuron*. 2000;28(2):511–25.
 192. Lee SH, Simonetta A, Sheng M. Subunit rules governing the sorting of internalized AMPA receptors in hippocampal neurons. *Neuron*. 2004;43(2):221–36.
 193. Lu J, Helton TD, Blanpied TA, Rácz B, Newpher TM, Weinberg RJ, et al. Postsynaptic Positioning of Endocytic Zones and AMPA Receptor Cycling by Physical Coupling of Dynamin-3 to Homer. *Neuron*. 2007 Sep;55(6):874–89.
 194. Carroll RC, Beattie EC, Xia H, Luscher C, Altschuler Y, Nicoll RA, et al. Dynamin-dependent endocytosis of ionotropic glutamate receptors. *Proc Natl Acad Sci*. 1999 Nov 23;96(24):14112–7.
 195. Opazo P, Choquet D. A three-step model for the synaptic recruitment of AMPA receptors. *Mol Cell Neurosci*. 2011 Jan;46(1):1–8.
 196. Roche KW, Standley S, McCallum J, Dune Ly C, Ehlers MD, Wenthold RJ. Molecular determinants of NMDA receptor internalization. *Nat Neurosci*. 2001 Aug;4(8):794–802.

197. Lavezzari G, McCallum J, Lee R, Roche KW. Differential binding of the AP-2 adaptor complex and PSD-95 to the C-terminus of the NMDA receptor subunit NR2B regulates surface expression. *Neuropharmacology*. 2003 Nov;45(6):729–37.
198. Lee SH, Liu L, Wang YT, Sheng M. Clathrin Adaptor AP2 and NSF Interact with Overlapping Sites of GluR2 and Play Distinct Roles in AMPA Receptor Trafficking and Hippocampal LTD. *Neuron*. 2002 Nov;36(4):661–74.
199. Lee H-K, Barbarosie M, Kameyama K, Bear MF, Huganir RL. Regulation of distinct AMPA receptor phosphorylation sites during bidirectional synaptic plasticity. *Nature*. 2000 Jun;405(6789):955–9.
200. Esteban JA, Shi S-H, Wilson C, Nuriya M, Huganir RL, Malinow R. PKA phosphorylation of AMPA receptor subunits controls synaptic trafficking underlying plasticity. *Nat Neurosci*. 2003 Feb 21;6(2):136–43.
201. Hanley JG. The regulation of AMPA receptor endocytosis by dynamic protein-protein interactions. *Front Cell Neurosci*. 2018;12(October):1–10.
202. Sumioka A, Yan D, Tomita S. TARP Phosphorylation Regulates Synaptic AMPA Receptors through Lipid Bilayers. *Neuron*. 2010 Jun;66(5):755–67.
203. Lee H-K, Kameyama K, Huganir RL, Bear MF. NMDA Induces Long-Term Synaptic Depression and Dephosphorylation of the GluR1 Subunit of AMPA Receptors in Hippocampus. *Neuron*. 1998 Nov;21(5):1151–62.
204. Tomita S, Stein V, Stocker TJ, Nicoll RA, Brecht DS. Bidirectional Synaptic Plasticity Regulated by Phosphorylation of Stargazin-like TARPs. *Neuron*. 2005 Jan;45(2):269–77.
205. Goo MS, Sancho L, Slepak N, Boassa D, Deerinck TJ, Ellisman MH, et al. Activity-dependent trafficking of lysosomes in dendrites and dendritic spines. 2017;1–15.
206. Lin A, Hou Q, Jarzylo L, Amato S, Gilbert J, Shang F, et al. Nedd4-mediated AMPA receptor ubiquitination regulates receptor turnover and trafficking. *J Neurochem*. 2011;
207. Schwarz LA, Hall BJ, Patrick GN. Activity-dependent ubiquitination of GluA1 mediates a distinct AMPA receptor endocytosis and sorting pathway. *J Neurosci*. 2010;30(49):16718–29.
208. Widagdo J, Chai Y, Ridder MC, Chau Y, Johnson RC, Sah P, et al. Activity-Dependent ubiquitination of GluA1 and GluA2 regulates AMPA receptor intracellular sorting and degradation. *Cell Rep*. 2015;10(5):783–95.
209. Fritschy JM, Panzanelli P. GABAA receptors and plasticity of inhibitory neurotransmission in the central nervous system. *Eur J Neurosci*. 2014;39(11):1845–65.
210. Jacob TC, Moss SJ, Jurd R. GABA(A) receptor trafficking and its role in the dynamic modulation of neuronal inhibition. *Nat Rev Neurosci*. 2008;9(5):331–43.
211. Luscher B, Fuchs T, Kilpatrick CL. GABAA Receptor Trafficking-Mediated Plasticity of Inhibitory Synapses. *Neuron*. 2011;70(3):385–409.
212. Vithlani M, Moss SJ, Terunuma M. The dynamic modulation of GABAA receptor trafficking and its role in the formation of inhibitory synapses. *Physiol Rev*. 2011;91(3):1009–22.

213. Bogdanov Y, Michels G, Armstrong-Gold C, Haydon PG, Lindstrom J, Pangalos M, et al. Synaptic GABAA receptors are directly recruited from their extrasynaptic counterparts. *EMBO J*. 2006 Sep 20;25(18):4381–9.
214. Bannai H, Lévi S, Schweizer C, Inoue T, Launey T, Racine V, et al. Activity-Dependent Tuning of Inhibitory Neurotransmission Based on GABAAR Diffusion Dynamics. *Neuron*. 2009 Jun;62(5):670–82.
215. Niwa F, Bannai H, Arizono M, Fukatsu K, Triller A, Mikoshiba K. Gephyrin-independent GABAAR mobility and clustering during plasticity. *PLoS One*. 2012;7(4).
216. Shrivastava AN, Triller A, Sieghart W, Sarto-Jackson I. Regulation of GABA A Receptor Dynamics by Interaction with Purinergic P2X 2 Receptors. *J Biol Chem*. 2011 Apr 22;286(16):14455–68.
217. Mukherjee J, Kretschmannova K, Gouzer G, Maric H-M, Ramsden S, Tretter V, et al. The Residence Time of GABAARs at Inhibitory Synapses Is Determined by Direct Binding of the Receptor 1 Subunit to Gephyrin. *J Neurosci*. 2011 Oct 12;31(41):14677–87.
218. Renner M, Schweizer C, Bannai H, Triller A, Lévi S. Diffusion Barriers Constrain Receptors at Synapses. Tell F, editor. *PLoS One*. 2012 Aug 13;7(8):e43032.
219. Petrini EM, Ravasenga T, Hausrat TJ, Iurilli G, Olcese U, Racine V, et al. Synaptic recruitment of gephyrin regulates surface GABAA receptor dynamics for the expression of inhibitory LTP. *Nat Commun*. 2014;5:3921.
220. Hosie AM, Wilkins ME, da Silva HMA, Smart TG. Endogenous neurosteroids regulate GABAA receptors through two discrete transmembrane sites. *Nature*. 2006 Nov 15;444(7118):486–9.
221. Fang C, Deng L, Keller CA, Fukata M, Fukata Y, Chen G, et al. GODZ-Mediated Palmitoylation of GABAA Receptors Is Required for Normal Assembly and Function of GABAergic Inhibitory Synapses. *J Neurosci*. 2006 Dec 6;26(49):12758–68.
222. Tyagarajan SK, Fritschy J-M. Gephyrin: a master regulator of neuronal function? *Nat Rev Neurosci*. 2014;15(3):141–56.
223. Thomas P, Mortensen M, Hosie AM, Smart TG. Dynamic mobility of functional GABAA receptors at inhibitory synapses. *Nat Neurosci*. 2005 Jul 12;8(7):889–97.
224. Kittler JT, Delmas P, Jovanovic JN, Brown DA, Smart TG, Moss SJ. Constitutive Endocytosis of GABA A Receptors by an Association with the Adaptin AP2 Complex Modulates Inhibitory Synaptic Currents in Hippocampal Neurons. *J Neurosci*. 2000 Nov 1;20(21):7972–7.
225. Smith KR, Muir J, Rao Y, Browarski M, Gruenig MC, Sheehan DF, et al. Stabilization of GABAA Receptors at Endocytic Zones Is Mediated by an AP2 Binding Motif within the GABAA Receptor 3 Subunit. *J Neurosci*. 2012 Feb 15;32(7):2485–98.
226. Kittler JT, Chen G, Kukhtina V, Vahedi-Faridi A, Gu Z, Tretter V, et al. Regulation of synaptic inhibition by phospho-dependent binding of the AP2 complex to a YECL motif in the GABAA receptor 2 subunit. *Proc Natl Acad Sci*. 2008 Mar 4;105(9):3616–21.
227. Klauck TM, Faux MC, Labudda K, Langeberg LK, Jaken S, Scott JD. Coordination of

- Three Signaling Enzymes by AKAP79, a Mammalian Scaffold Protein. *Science* (80-). 1996 Mar 15;271(5255):1589–92.
228. Kittler JT, Thomas P, Tretter V, Bogdanov YD, Haucke V, Smart TG, et al. Huntingtin-associated protein 1 regulates inhibitory synaptic transmission by modulating γ -aminobutyric acid type A receptor membrane trafficking. *Proc Natl Acad Sci*. 2004 Aug 24;101(34):12736–41.
 229. Twelvetrees AE, Yuen EY, Arancibia-Carcamo IL, MacAskill AF, Rostaing P, Lumb MJ, et al. Delivery of GABAARs to Synapses Is Mediated by HAP1-KIF5 and Disrupted by Mutant Huntingtin. *Neuron*. 2010 Jan;65(1):53–65.
 230. Blaesse P, Airaksinen MS, Rivera C, Kaila K. Cation-Chloride Cotransporters and Neuronal Function. *Neuron*. 2009 Mar;61(6):820–38.
 231. Ben-Ari Y. Excitatory actions of gaba during development: the nature of the nurture. *Nat Rev Neurosci*. 2002;3(9):728–39.
 232. Braat S, Kooy RF. The GABA A Receptor as a Therapeutic Target for Neurodevelopmental Disorders. *Neuron*. 2015;86(5):1119–30.
 233. Puskarjov M, Seja P, Heron SE, Williams TC, Ahmad F, Iona X, et al. A variant of KCC2 from patients with febrile seizures impairs neuronal Cl⁻ extrusion and dendritic spine formation. *EMBO Rep*. 2014;15(6):723–9.
 234. Campbell SL, Robel S, Cuddapah VA, Robert S, Buckingham SC, Kahle KT, et al. GABAergic disinhibition and impaired KCC2 cotransporter activity underlie tumor-associated epilepsy. *Glia*. 2015 Jan;63(1):23–36.
 235. Boulenguez P, Liabeuf S, Bos R, Bras H, Jean-Xavier C, Brocard C, et al. Down-regulation of the potassium-chloride cotransporter KCC2 contributes to spasticity after spinal cord injury. *Nat Med*. 2010;16(3):302–7.
 236. Banerjee A, Rikhye R V., Breton-Provencher V, Tang X, Li C, Li K, et al. Jointly reduced inhibition and excitation underlies circuit-wide changes in cortical processing in Rett syndrome. *Proc Natl Acad Sci*. 2016 Nov 15;113(46):E7287–96.
 237. Deidda G, Allegra M, Cerri C, Naskar S, Bony G, Zunino G, et al. Early depolarizing GABA controls critical-period plasticity in the rat visual cortex. *Nat Neurosci*. 2015;18(1):87–96.
 238. Tyzio R, Nardou R, Ferrari DC, Tsintsadze T, Shahrokhi A, Eftekhari S, et al. Oxytocin-Mediated GABA Inhibition During Delivery Attenuates Autism Pathogenesis in Rodent Offspring. *Science* (80-). 2014 Feb 7;343(6171):675–9.
 239. Ben-Ari Y, Gaiarsa JL, Tyzio R, Khazipov R. GABA: A pioneer transmitter that excites immature neurons and generates primitive oscillations. *Physiol Rev*. 2007;87(4):1215–84.
 240. Moore YE, Kelley MR, Brandon NJ, Deeb TZ, Moss SJ. Seizing Control of KCC2: A New Therapeutic Target for Epilepsy. *Trends Neurosci*. 2017 Sep;40(9):555–71.
 241. Casey JR, Grinstein S, Orlowski J. Sensors and regulators of intracellular pH. *Nat Rev Mol Cell Biol*. 2010;11(1):50–61.
 242. Van Dyke RW. Acidification of lysosomes and endosomes. *Subcell Biochem*. 1996;27:331–60.

243. Hu YB, Dammer EB, Ren RJ, Wang G. The endosomal-lysosomal system: From acidification and cargo sorting to neurodegeneration. *Transl Neurodegener.* 2015;4(1).
244. Duve C, Gianetto R, Appelmans F, Wattiaux R. Enzymic Content of the Mitochondria Fraction. *Nature.* 1953 Dec;172(4390):1143–4.
245. Gianetto R, De Duve C. Tissue fractionation studies. 4. Comparative study of the binding of acid phosphatase, β -glucuronidase and cathepsin by rat-liver particles. *Biochem J.* 1955 Mar 1;59(3):433–8.
246. Forgac M. Vacuolar ATPases: rotary proton pumps in physiology and pathophysiology. *Nat Rev Mol Cell Biol.* 2007 Nov;8(11):917–29.
247. Cipriano DJ, Wang Y, Bond S, Hinton A, Jefferies KC, Qi J, et al. Structure and regulation of the vacuolar ATPases. *Biochim Biophys Acta - Bioenerg.* 2008 Jul;1777(7–8):599–604.
248. Kane PM. The long physiological reach of the yeast vacuolar H⁺-ATPase. *J Bioenerg Biomembr.* 2007 Dec 15;39(5–6):415–21.
249. Wu MM, Grabe M, Adams S, Tsien RY, Moore H-PH, Machen TE. Mechanisms of pH Regulation in the Regulated Secretory Pathway. *J Biol Chem.* 2001 Aug 31;276(35):33027–35.
250. Steinberg BE, Huynh KK, Brodovitch A, Jabs S, Stauber T, Jentsch TJ, et al. A cation counterflux supports lysosomal acidification. *J Cell Biol.* 2010 Jun 28;189(7):1171–86.
251. Jentsch TJ. CLC Chloride Channels and Transporters: From Genes to Protein Structure, Pathology and Physiology. *Crit Rev Biochem Mol Biol.* 2008 Jan 11;43(1):3–36.
252. Scheel O, Zdebik AA, Lourdel S, Jentsch TJ. Voltage-dependent electrogenic chloride/proton exchange by endosomal CLC proteins. *Nature.* 2005;436(7049):424–7.
253. Syntichaki P, Samara C, Tavernarakis N. The Vacuolar H⁺-ATPase Mediates Intracellular Acidification Required for Neurodegeneration in *C. elegans*. *Curr Biol.* 2005 Jul;15(13):1249–54.
254. Jentsch TJ, Poët M, Fuhrmann JC, Zdebik AA. Physiological functions of CLC Cl⁻ channels gleaned from human genetic disease and mouse models. *Annu Rev Physiol.* 2005 Mar 17;67(1):779–807.
255. Pedersen SF, Counillon L. The SLC9A-C mammalian Na⁺/H⁺ exchanger family: Molecules, mechanisms, and physiology. *Physiol Rev.* 2019;99(4):2015–113.
256. Orłowski J, Grinstein S. Na⁺/H⁺ exchangers. *Compr Physiol.* 2011 Oct;1(4):2083–100.
257. Fuster DG, Alexander RT. Traditional and emerging roles for the SLC9 Na⁺/H⁺ exchangers. *Pflugers Arch.* 2014 Jan;466(1):61–76.
258. Nakamura N, Tanaka S, Teko Y, Mitsui K, Kanazawa H. Four Na⁺/H⁺ exchanger isoforms are distributed to Golgi and post-Golgi compartments and are involved in organelle pH regulation. *J Biol Chem.* 2005 Jan 14;280(2):1561–72.
259. Chintapalli VR, Kato A, Henderson L, Hirata T, Woods DJ, Overend G, et al. Transport proteins NHA1 and NHA2 are essential for survival, but have distinct transport modalities. *Proc Natl Acad Sci.* 2015 Sep 15;112(37):11720–5.
260. Windler F, Bönigk W, Körschen HG, Grahn E, Strücker T, Seifert R, et al. The solute carrier

- SLC9C1 is a Na⁺/H⁺-exchanger gated by an S4-type voltage-sensor and cyclic-nucleotide binding. *Nat Commun.* 2018;9(1):2809.
261. Hisamitsu T, Ben Ammar Y, Nakamura TY, Wakabayashi S. Dimerization is crucial for the function of the Na⁺/H⁺ + exchanger NHE1. *Biochemistry.* 2006;45(44):13346–55.
 262. Hisamitsu T, Pang T, Shigekawa M, Wakabayashi S. Dimeric Interaction between the Cytoplasmic Domains of the Na⁺ /H⁺ + Exchanger NHE1 Revealed by Symmetrical Intermolecular Cross-Linking and Selective Co-immunoprecipitation †. *Biochemistry.* 2004 Aug;43(34):11135–43.
 263. Maes M, Rimon A, Kozachkov-Magrisso L, Friedler A, Padan E. Revealing the Ligand Binding Site of NhaA Na⁺ /H⁺ Antiporter and Its pH Dependence. *J Biol Chem.* 2012 Nov 2;287(45):38150–7.
 264. Călinescu O, Dwivedi M, Patiño-Ruiz M, Padan E, Fendler K. Lysine 300 is essential for stability but not for electrogenic transport of the Escherichia coli NhaA Na⁺ /H⁺ antiporter. *J Biol Chem.* 2017 May 12;292(19):7932–41.
 265. Huang Y, Chen W, Dotson DL, Beckstein O, Shen J. Mechanism of pH-dependent activation of the sodium-proton antiporter NhaA. *Nat Commun.* 2016 Dec 6;7(1):12940.
 266. Wakabayashi S, Hisamitsu T, Pang T, Shigekawa M. Kinetic Dissection of Two Distinct Proton Binding Sites in Na⁺ /H⁺ + Exchangers by Measurement of Reverse Mode Reaction. *J Biol Chem.* 2003 Oct 31;278(44):43580–5.
 267. Wakabayashi S, Hisamitsu T, Pang T, Shigekawa M. Mutations of Arg 440 and Gly 455 /Gly 456 Oppositely Change pH Sensing of Na⁺ /H⁺ + Exchanger 1. *J Biol Chem.* 2003 Apr 4;278(14):11828–35.
 268. Touret N, Poujeol P, Counillon L. Second-Site Revertants of a Low-Sodium-Affinity Mutant of the Na⁺ /H⁺ + Exchanger Reveal the Participation of TM4 into a Highly Constrained Sodium-Binding Site †. *Biochemistry.* 2001 Apr;40(16):5095–101.
 269. Slepko ER, Rainey JK, Sykes BD, Fliegel L. Structural and functional analysis of the Na⁺/H⁺ exchanger. *Biochem J.* 2007 Feb 1;401(3):623–33.
 270. Velisek L. Extracellular acidosis and high levels of carbon dioxide suppress synaptic transmission and prevent the induction of long-term potentiation in the CA1 region of rat hippocampal slices. *Hippocampus.* 1998;8(1):24–32.
 271. Chesler M. Regulation and modulation of pH in the brain. *Physiol Rev.* 2003;83(4):1183–221.
 272. Sinning A, Hübner C a. Minireview: pH and synaptic transmission. *FEBS Lett.* 2013;587(13):1923–8.
 273. Li P-A, Siesjö BK. Role of hyperglycaemia-related acidosis in ischaemic brain damage. *Acta Physiol Scand.* 1997 Nov 2;161(4):567–80.
 274. Chesler M. Regulation and Modulation of pH in the Brain. *Physiol Rev.* 2003 Oct;83(4):1183–221.
 275. Schuchmann S, Schmitz D, Rivera C, Vanhatalo S, Salmen B, Mackie K, et al. Experimental febrile seizures are precipitated by a hyperthermia-induced respiratory alkalosis. *Nat Med.*

- 2006 Jul 2;12(7):817–23.
276. Malo ME, Fliegel L. Physiological role and regulation of the Na⁺/H⁺ exchanger. *Can J Physiol Pharmacol*. 2006;84(11):1081–95.
 277. Fuster D, Moe OW, Hilgemann DW. Steady-state Function of the Ubiquitous Mammalian Na/H Exchanger (NHE1) in Relation to Dimer Coupling Models with 2Na/2H Stoichiometry. *J Gen Physiol*. 2008 Oct 1;132(4):465–80.
 278. Aronson PS. Kinetic Properties of the Plasma Membrane Na⁺ -H⁺ Exchanger. *Annu Rev Physiol*. 1985 Oct;47(1):545–60.
 279. Guissart C, Li X, Leheup B, Drouot N, Montaut-Verient B, Raffo E, et al. Mutation of SLC9A1, encoding the major Na⁺/H⁺ exchanger, causes ataxia-deafness Lichtenstein-Knorr syndrome. *Hum Mol Genet*. 2015;24(2):463–70.
 280. Zhu X, Petrovski S, Xie P, Ruzzo EK, Lu Y-F, McSweeney KM, et al. Whole-exome sequencing in undiagnosed genetic diseases: interpreting 119 trios. *Genet Med*. 2015 Oct 15;17(10):774–81.
 281. Iwama K, Osaka H, Ikeda T, Mitsuhashi S, Miyatake S, Takata A, et al. A novel SLC9A1 mutation causes cerebellar ataxia. *J Hum Genet*. 2018 Oct 17;63(10):1049–54.
 282. Mendoza-Ferreira N, Coutelier M, Janzen E, Hosseinibarkooie S, Löhr H, Schneider S, et al. Biallelic CHP1 mutation causes human autosomal recessive ataxia by impairing NHE1 function. *Neurol Genet*. 2018 Feb;4(1):e209.
 283. Cox GA, Lutz CM, Yang CL, Biemesderfer D, Bronson RT, Fu A, et al. Sodium/hydrogen exchanger gene defect in slow-wave epilepsy mutant mice. *Cell*. 1997;91(1):139–48.
 284. Bell SM, Schreiner CM, Schultheis PJ, Miller ML, Evans RL, Vorhees C V., et al. Targeted disruption of the murine Nhe1 locus induces ataxia, growth retardation, and seizures. *Am J Physiol Physiol*. 1999 Apr 1;276(4):C788–95.
 285. Yao H, Gu X, Haddad GG. Intracellular pH regulation of CA1 neurons in Na⁺ / H⁺ isoform 1 mutant mice Find the latest version : Na⁺ / H⁺ isoform 1 mutant mice. 1999;104(5):637–45.
 286. Gu XQ, Yao H, Haddad GG. Increased neuronal excitability and seizures in the Na⁺/H⁺ exchanger null mutant mouse. *Am J Physiol - Cell Physiol*. 2001;281(2 50-2):496–503.
 287. Xia Y, Zhao P, Xue J, Gu XQ, Sun X, Yao H, et al. Na⁺ channel expression and neuronal function in the Na⁺/H⁺ exchanger 1 null mutant mouse. *J Neurophysiol*. 2003;89(1):229–36.
 288. Jang IS, Brodwick MS, Wang ZM, Jeong HJ, Choi BJ, Akaike N. The Na⁺/H⁺ exchanger is a major pH regulator in GABAergic presynaptic nerve terminals synapsing onto rat CA3 pyramidal neurons. *J Neurochem*. 2006;99(4):1224–36.
 289. Dietrich CJ, Morad M. Synaptic Acidification Enhances GABAA Signaling. *J Neurosci*. 2010 Nov 24;30(47):16044–52.
 290. Trudeau L-E, Parpura V, Haydon PG. Activation of Neurotransmitter Release in Hippocampal Nerve Terminals During Recovery From Intracellular Acidification. *J Neurophysiol*. 1999 Jun 1;81(6):2627–35.

291. Bocker HT, Heinrich T, Liebmann L, Hennings JC, Seemann E, Gerth M, et al. The Na⁺/H⁺ Exchanger Nhe1 Modulates Network Excitability via GABA Release. *Cereb Cortex*. 2019;29(10):4263–76.
292. Ronicke R, Schroder UH, Bohm K, Reymann KG. The Na⁺/H⁺ exchanger modulates long-term potentiation in rat hippocampal slices. *Naunyn Schmiedebergs Arch Pharmacol*. 2009;379(3):233–9.
293. Baird NR, Orlowski J, Szabó EZ, Zaun HC, Schultheis PJ, Menon AG, et al. Molecular Cloning, Genomic Organization, and Functional Expression of Na⁺ /H⁺ Exchanger Isoform 5 (NHE5) from Human Brain. *J Biol Chem*. 1999 Feb 12;274(7):4377–82.
294. Szászi K, Paulsen A, Szabó EZ, Numata M, Grinstein S, Orlowski J. Clathrin-mediated Endocytosis and Recycling of the Neuron-specific Na⁺ /H⁺ Exchanger NHE5 Isoform. *J Biol Chem*. 2002 Nov 8;277(45):42623–32.
295. Lukashova V, Jinadasa T, Ilie A, Verbich D, Cooper E, Orlowski J. The Na⁺/H⁺ exchanger NHE5 is sorted to discrete intracellular vesicles in the central and peripheral nervous systems. In: *Advances in Experimental Medicine and Biology*. 2013. p. 397–410.
296. Jinadasa T, Szabó EZ, Numata M, Orlowski J. Activation of AMP-activated Protein Kinase Regulates Hippocampal Neuronal pH by Recruiting Na⁺ /H⁺ Exchanger NHE5 to the Cell Surface. *J Biol Chem*. 2014;289(30):20879–97.
297. Diering GH, Mills F, Bamji SX, Numata M. Regulation of dendritic spine growth through activity-dependent recruitment of the brain-enriched Na⁺/H⁺ exchanger NHE5. *Mol Biol Cell*. 2011;22(13):2246–57.
298. Chen X, Wang X, Tang L, Wang J, Shen C, Liu J, et al. Nhe5 deficiency enhances learning and memory via upregulating Bdnf/TrkB signaling in mice. *Am J Med Genet Part B Neuropsychiatr Genet*. 2017;174(8):828–38.
299. Lin P, Williams W, Y L, RS M, Orlowski J, Numata M. Secretory carrier membrane proteins interact and regulate trafficking of the organellar (Na⁺,K⁺)/H⁺ exchanger NHE7. *J Cell Sci*. 2005 May 1;118(9):1885–97.
300. Ohgaki R, Van Ijzendoorn SCD, Matsushita M, Hoekstra D, Kanazawa H. Organellar Na⁺/H⁺ exchangers: Novel players in organelle pH regulation and their emerging functions. *Biochemistry*. 2011 Feb 1;50(4):443–50.
301. Khayat W, Hackett A, Shaw M, Ilie A, Dudding-Byth T, Kalscheuer VM, et al. A recurrent missense variant in SLC9A7 causes nonsyndromic X-linked intellectual disability with alteration of Golgi acidification and aberrant glycosylation. *Hum Mol Genet*. 2019;28(4):598–614.
302. Patak J, Faraone S V., Zhang-James Y. Sodium hydrogen exchanger 9 NHE9 (SLC9A9) and its emerging roles in neuropsychiatric comorbidity. *Am J Med Genet Part B Neuropsychiatr Genet*. 2020;(December 2019):289–305.
303. Brett CL, Wei Y, Donowitz M, Rao R. Human Na⁽⁺⁾/H⁽⁺⁾ exchanger isoform 6 is found in recycling endosomes of cells, not in mitochondria. *Am J Physiol Cell Physiol*. 2002 May;282(5):C1031–41.

304. Ullman JC, Yang J, Sullivan M, Bendor J, Levy J, Pham E, et al. A mouse model of autism implicates endosome pH in the regulation of presynaptic calcium entry. 2018;
305. Ilie A, Weinstein E, Boucher A, McKinney RA, Orłowski J. Impaired posttranslational processing and trafficking of an endosomal Na⁺/H⁺ exchanger NHE6 mutant ($\Delta(370)WST(372)$) associated with X-linked intellectual disability and autism. *Neurochem Int.* 2014 Jul;73:192–203.
306. Ohgaki R, Matsushita M, Kanazawa H, Ogihara S, Hoekstra D, van Ijzendoorn SCD. The Na⁺/H⁺ exchanger NHE6 in the endosomal recycling system is involved in the development of apical bile canalicular surface domains in HepG2 cells. *Mol Biol Cell.* 2010 Apr 1;21(7):1293–304.
307. Roxrud I, Raiborg C, Gilfillan GD, Strømme P, Stenmark H. Dual degradation mechanisms ensure disposal of NHE6 mutant protein associated with neurological disease. *Exp Cell Res.* 2009 Oct 15;315(17):3014–27.
308. Xinhan L, Matsushita M, Numaza M, Taguchi A, Mitsui K, Kanazawa H. Na⁺/H⁺ exchanger isoform 6 (NHE6/SLC9A6) is involved in clathrin-dependent endocytosis of transferrin. *Am J Physiol Cell Physiol.* 2011 Dec;301(6):C1431–44.
309. Ouyang Q, Lizarraga SB, Schmidt M, Yang U, Gong J, Ellisor D, et al. Christianson Syndrome Protein NHE6 Modulates TrkB Endosomal Signaling Required for Neuronal Circuit Development. *Neuron.* 2013 Oct 2;80(1):97–112.
310. Mayle KM, Le AM, Kamei DT. The intracellular trafficking pathway of transferrin. *Biochim Biophys Acta - Gen Subj.* 2012 Mar;1820(3):264–81.
311. Numata M, Petrecca K, Lake N, Orłowski J. Identification of a Mitochondrial Na/H Exchanger. *J Biol Chem.* 1998;273(12):6951–9.
312. Morrow EM, Yoo S-Y, Flavell SW, Kim T-K, Lin Y, Hill RS, et al. Identifying autism loci and genes by tracing recent shared ancestry. *Science (80-).* 2008 Jul 11;321(5886):218–23.
313. Prasad H, Rao R. The Na⁺ / H⁺ Exchanger NHE6 Modulates Endosomal pH to Control Processing of Amyloid Precursor Protein in a Cell Culture Model of Alzheimer Disease. *J Biol Chem.* 2015 Feb 27;290(9):5311–27.
314. Martinelli-Boneschi F, Giacalone G, Magnani G, Biella G, Coppi E, Santangelo R, et al. Pharmacogenomics in Alzheimer's disease: a genome-wide association study of response to cholinesterase inhibitors. *Neurobiol Aging.* 2013 Jun;34(6):1711.e7-1711.e13.
315. Pérez-Palma E, Bustos BI, Villamán CF, Alarcón MA, Avila ME, Ugarte GD, et al. Overrepresentation of Glutamate Signaling in Alzheimer's Disease: Network-Based Pathway Enrichment Using Meta-Analysis of Genome-Wide Association Studies. Potash JB, editor. *PLoS One.* 2014 Apr 22;9(4):e95413.
316. Miyazaki E, Sakaguchi M, Wakabayashi S, Shigekawa M, Mihara K. NHE6 protein possesses a signal peptide destined for endoplasmic reticulum membrane and localizes in secretory organelles of the cell. *J Biol Chem.* 2001 Dec 28;276(52):49221–7.
317. Ohgaki R, Fukura N, Matsushita M, Mitsui K, Kanazawa H. Cell surface levels of organellar Na⁺/H⁺ exchanger isoform 6 are regulated by interaction with RACK1. *J Biol Chem.* 2008

- Feb 15;283(7):4417–29.
318. Pulakat L, Cooper S, Knowle D, Mandavia C, Bruhl S, Hetrick M, et al. Ligand-dependent complex formation between the Angiotensin II receptor subtype AT2 and Na⁺/H⁺ exchanger NHE6 in mammalian cells. *Peptides*. 2005 May;26(5):863–73.
 319. Gendron L, Payet M, Gallo-Payet N. The angiotensin type 2 receptor of angiotensin II and neuronal differentiation: from observations to mechanisms. *J Mol Endocrinol*. 2003 Dec 1;31(3):359–72.
 320. Guimond M-O, Gallo-Payet N. How does angiotensin AT2 receptor activation help neuronal differentiation and improve neuronal pathological situations? *Front Endocrinol (Lausanne)*. 2012;3(164).
 321. Gao L, Zucker IH. AT2 receptor signaling and sympathetic regulation. *Curr Opin Pharmacol*. 2011 Apr;11(2):124–30.
 322. Hill JK, Brett CL, Chyou A, Kallay LM, Sakaguchi M, Rao R, et al. Vestibular hair bundles control pH with (Na⁺, K⁺)/H⁺ exchangers NHE6 and NHE9. *J Neurosci*. 2006;26(39):9944–55.
 323. Liu L, Schlesinger PH, Slack NM, Friedman P a., Blair HC. High capacity Na⁺/H⁺ exchange activity in mineralizing osteoblasts. *J Cell Physiol*. 2011;226(September):1702–12.
 324. Kucharava K, Brand Y, Albano G, Sekulic-Jablanovic M, Glutz A, Xian X, et al. Sodium-hydrogen exchanger 6 (NHE6) deficiency leads to hearing loss, via reduced endosomal signalling through the BDNF/Trk pathway. *Sci Rep*. 2020;10(1):1–14.
 325. Lein ES, Hawrylycz MJ, Ao N, Ayres M, Bensinger A, Bernard A, et al. Genome-wide atlas of gene expression in the adult mouse brain. *Nature*. 2007 Jan 6;445(7124):168–76.
 326. Deane EC, Ilie AE, Sizdahkhani S, Das Gupta M, Orlowski J, McKinney RA. Enhanced recruitment of endosomal Na⁺/H⁺ exchanger NHE6 into Dendritic spines of hippocampal pyramidal neurons during NMDA receptor-dependent long-term potentiation. *J Neurosci*. 2013 Jan 9;33(2):595–610.
 327. Chao M V. Neurotrophins and their receptors: A convergence point for many signalling pathways. *Nat Rev Neurosci*. 2003 Apr;4(4):299–309.
 328. Huang EJ, Reichardt LF. Neurotrophins: Roles in Neuronal Development and Function. *Annu Rev Neurosci*. 2001 Mar;24(1):677–736.
 329. Carvalho a L, Caldeira M V, Santos SD, Duarte CB. Role of the brain-derived neurotrophic factor at glutamatergic synapses. *Br J Pharmacol*. 2008;153 Suppl(December 2007):S310–24.
 330. Leal G, Afonso PM, Salazar IL, Duarte CB. Regulation of hippocampal synaptic plasticity by BDNF. *Brain Res*. 2014;1–20.
 331. Rex CS, Lin C-Y, Kramar EA, Chen LY, Gall CM, Lynch G. Brain-Derived Neurotrophic Factor Promotes Long-Term Potentiation-Related Cytoskeletal Changes in Adult Hippocampus. *J Neurosci*. 2007 Mar 14;27(11):3017–29.
 332. Rajagopal R. Transactivation of Trk Neurotrophin Receptors by G-Protein-Coupled

- Receptor Ligands Occurs on Intracellular Membranes. *J Neurosci.* 2004;24(30):6650–8.
333. Xu B, Gottschalk W, Chow a, Wilson RI, Schnell E, Zang K, et al. The role of brain-derived neurotrophic factor receptors in the mature hippocampus: modulation of long-term potentiation through a presynaptic mechanism involving TrkB. *J Neurosci.* 2000;20(18):6888–97.
 334. Koleske AJ. Molecular mechanisms of dendrite stability. *Nat Rev Neurosci.* 2013;14(8):536–50.
 335. Cosker KE, Courchesne SL, Segal R a. Action in the Axon: generation and transport of signaling endosomes. *Curr Opin Neurobiol.* 2008;18(3):270–5.
 336. Walkley SU, Vanier MT. Pathomechanisms in Lysosomal Storage Disorders. *Biochim Biophys Acta - Mol Cell Res.* 2009;1793(4):726–36.
 337. Strømme P, Dobrenis K, Sillitoe R V, Gulinello M, Ali NF, Davidson C, et al. X-linked Angelman-like syndrome caused by Slc9a6 knockout in mice exhibits evidence of endosomal-lysosomal dysfunction. *Brain a J Neurol.* 2011 Nov;134(Pt 11):3369–83.
 338. Walkley SU, Sikora J, Micsenyi M, Davidson C, Dobrenis K. Lysosomal compromise and brain dysfunction: examining the role of neuroaxonal dystrophy. *Biochem Soc Trans.* 2010 Dec 1;38(6):1436–41.
 339. Xu M, Ouyang Q, Gong J, Pescosolido MF, Pruett BS, Mishra S, et al. Mixed Neurodevelopmental and Neurodegenerative Pathology in Nhe6 -Null Mouse Model of Christianson Syndrome. *eNeuro.* 2017 Nov;4(6):ENEURO.0388-17.2017.
 340. Sikora J, Leddy J, Gulinello M, Walkley SU. X-linked Christianson syndrome: heterozygous female Slc9a6 knockout mice develop mosaic neuropathological changes and related behavioral abnormalities. *Dis Model Mech.* 2015;(October).
 341. Kerner-Rossi M, Gulinello M, Walkley S, Dobrenis K. Pathobiology of Christianson syndrome: Linking disrupted endosomal-lysosomal function with intellectual disability and sensory impairments. *Neurobiol Learn Mem.* 2018;(December 2017):0–1.
 342. Petitjean H, Fatima T, Mouchbahani-Constance S, Davidova A, Ferland CE, Orlowski J, et al. Loss of SLC9A6/NHE6 impairs nociception in a mouse model of Christianson Syndrome. *Pain.* 2020.
 343. Horton AC, Ehlers MD. Neuronal polarity and trafficking. *Neuron.* 2003;40(2):277–95.
 344. Kondapalli KC, Hack A, Schushan M, Landau M, Ben-Tal N, Rao R. Functional evaluation of autism-associated mutations in NHE9. *Nat Commun.* 2013;4(SEPTEMBER):2510.
 345. Ilie A, Gao AYL, Reid J, Boucher A, McEwan C, Barrière H, et al. A Christianson syndrome-linked deletion mutation ($\Delta^{287}ES^{288}$) in SLC9A6 disrupts recycling endosomal function and elicits neurodegeneration and cell death. *Mol Neurodegener.* 2016;11(1).
 346. Ilie A, Gao AYL, Boucher A, Park J, Berghuis AM, Hoffer MJV, et al. A potential gain-of-function variant of SLC9A6 leads to endosomal alkalinization and neuronal atrophy associated with Christianson Syndrome. *Neurobiol Dis.* 2019;121.
 347. Ilie A, Boucher A, Park J, Berghuis AM, McKinney RA, Orlowski J. Assorted dysfunctions of endosomal alkali cation/proton exchanger SLC9A6 variants linked to Christianson

- syndrome. *J Biol Chem*. 2020 May 15;295(20):7075–95.
348. Meusser B, Hirsch C, Jarosch E, Sommer T. ERAD: the long road to destruction. *Nat Cell Biol*. 2005 Aug;7(8):766–72.
 349. Viana RJS, Nunes AF, Rodrigues CMP. Endoplasmic Reticulum Enrollment in Alzheimer's Disease. *Mol Neurobiol*. 2012 Oct 20;46(2):522–34.
 350. Lin JH, Walter P, Yen TSB. Endoplasmic Reticulum Stress in Disease Pathogenesis. *Annu Rev Pathol Mech Dis*. 2008;3(1):399–425.
 351. Doyle KM, Kennedy D, Gorman AM, Gupta S, Healy SJM, Samali A. Unfolded proteins and endoplasmic reticulum stress in neurodegenerative disorders. *J Cell Mol Med*. 2011 Oct;15(10):2025–39.
 352. Tabas I, Ron D. Integrating the mechanisms of apoptosis induced by endoplasmic reticulum stress. *Nat Cell Biol*. 2011 Mar 1;13(3):184–90.
 353. Sano R, Reed JC. ER stress-induced cell death mechanisms. *Biochim Biophys Acta - Mol Cell Res*. 2013;1833(12):3460–70.
 354. Urano F, Wang X, Bertolotti A, Zhang Y, Chung P, Harding HP, et al. Coupling of stress in the ER to activation of JNK protein kinases by transmembrane protein kinase IRE1. *Science* (80-). 2000 Jan 28;287(5453):664–6.
 355. Aguilaniu H, Gustafsson L, Rigoulet M, Nyström T. Asymmetric inheritance of oxidatively damaged proteins during cytokinesis. *Science* (80-). 2003 Mar 14;299(5613):1751–3.
 356. Katajisto P, Dohla J, Chaffer CL, Pentimikko N, Marjanovic N, Iqbal S, et al. Asymmetric apportioning of aged mitochondria between daughter cells is required for stemness. *Science* (80-). 2015 Apr 17;348(6232):340–3.
 357. Ouyang Q, Lena J-C, Mishra S, Riaz HA, Schmidt M, Morrow EM. Functional Assessment In Vivo of the Mouse Homologue of the Human Ala-9-Ser NHE6 Variant. *eNeuro*. 2019;6(December):1–15.
 358. Kurosinski P, Guggisberg M, Götz J. Alzheimer's and Parkinson's disease – overlapping or synergistic pathologies? *Trends Mol Med*. 2002 Jan;8(1):3–5.
 359. Jiang T, Yu J-T, Tian Y, Tan L. Epidemiology and etiology of Alzheimer's disease: from genetic to non-genetic factors. *Curr Alzheimer Res*. 2013 Oct;10(8):852–67.
 360. Ross CA, Poirier MA. Protein aggregation and neurodegenerative disease. *Nat Med*. 2004;
 361. Bonifacino JS, Traub LM. Signals for Sorting of Transmembrane Proteins to Endosomes and Lysosomes. *Annu Rev Biochem*. 2003 Jun;72(1):395–447.
 362. De Strooper B. Aph-1, Pen-2, and Nicastrin with Presenilin Generate an Active γ -Secretase Complex. *Neuron*. 2003 Apr;38(1):9–12.
 363. Yu WH, Cuervo AM, Kumar A, Peterhoff CM, Schmidt SD, Lee J-H, et al. Macroautophagy – a novel β -amyloid peptide-generating pathway activated in Alzheimer's disease. *J Cell Biol*. 2005 Oct 10;171(1):87–98.
 364. Sun J, Roy S. The physical approximation of APP and BACE-1: A key event in Alzheimer's disease pathogenesis. *Dev Neurobiol*. 2018 Mar;78(3):340–7.
 365. Das U, Scott DA, Ganguly A, Koo EH, Tang Y, Roy S. Activity-Induced Convergence of

- APP and BACE-1 in Acidic Microdomains via an Endocytosis-Dependent Pathway. *Neuron*. 2013 Aug;79(3):447–60.
366. Sannerud R, Declerck I, Peric A, Raemaekers T, Menendez G, Zhou L, et al. ADP ribosylation factor 6 (ARF6) controls amyloid precursor protein (APP) processing by mediating the endosomal sorting of BACE1. *Proc Natl Acad Sci*. 2011 Aug 23;108(34):E559–68.
 367. Cirrito JR, Kang J-E, Lee J, Stewart FR, Verges DK, Silverio LM, et al. Endocytosis Is Required for Synaptic Activity-Dependent Release of Amyloid- β In Vivo. *Neuron*. 2008 Apr;58(1):42–51.
 368. Prasad H, Rao R. The Amyloid Clearance Defect in ApoE4 Astrocytes is Corrected by Epigenetic Restoration of NHE6. *Proc Natl Acad Sci*. 2018;115(28):243097.
 369. Henley JM, Wilkinson KA. Synaptic AMPA receptor composition in development, plasticity and disease. *Nat Rev Neurosci*. 2016;advance on(6):337–50.
 370. Walkley SU. Pathogenic mechanisms in lysosomal disease: A reappraisal of the role of the lysosome. In: *Acta Paediatrica, International Journal of Paediatrics*. 2007.
 371. Ghosh P, Dahms NM, Kornfeld S. Mannose 6-phosphate receptors: New twists in the tale. *Nature Reviews Molecular Cell Biology*. 2003.
 372. Hyttinen JMT, Niittykoski M, Salminen A, Kaarniranta K. Maturation of autophagosomes and endosomes: A key role for Rab7. *Biochim Biophys Acta - Mol Cell Res*. 2013 Mar;1833(3):503–10.
 373. Razi M, Chan EYW, Tooze SA. Early endosomes and endosomal coatome are required for autophagy. *J Cell Biol*. 2009 Apr 20;185(2):305–21.
 374. Tooze J, Hollinshead M, Ludwig T, Howell K, Hoflack B, Kern H. In exocrine pancreas, the basolateral endocytic pathway converges with the autophagic pathway immediately after the early endosome. *J Cell Biol*. 1990 Aug 1;111(2):329–45.
 375. Feng Z, Tang L, Wu L, Cui S, Hong Q, Cai G, et al. Na⁺/H⁺ exchanger-1 reduces podocyte injury caused by endoplasmic reticulum stress via autophagy activation. *Lab Investig*. 2014;94(4):439–54.
 376. Togashi K, Wakatsuki S, Furuno A, Tokunaga S, Nagai Y, Araki T. Na⁺/H⁺ exchangers induce autophagy in neurons and inhibit polyglutamine-induced aggregate formation. *PLoS One*. 2013;8(11):1–8.
 377. Patak J, Zhang-James Y, Faraone S V. Endosomal system genetics and autism spectrum disorders: A literature review. *Neurosci Biobehav Rev*. 2016;65:95–112.
 378. Kondapalli KC, Llongueras JP, Capilla-González V, Prasad H, Hack A, Smith C, et al. A leak pathway for luminal protons in endosomes drives oncogenic signalling in glioblastoma. *Nat Commun*. 2015;6.
 379. Chen J, Yang H, Wen J, Luo K, Liu Q, Huang Y, et al. NHE9 induces chemoradiotherapy resistance in esophageal squamous cell carcinoma by upregulating the Src/Akt/ β -catenin pathway and Bcl-2 expression. *Oncotarget*. 2015 May 20;6(14):12405–20.
 380. Dunaevsky A, Tashiro A, Majewska A, Mason C, Yuste R. Developmental regulation of

- spine motility in the mammalian central nervous system. *Proc Natl Acad Sci U S A*. 1999;96(23):13438–43.
381. Henley JM, Wilkinson K a. AMPA receptor trafficking and the mechanisms underlying synaptic plasticity and cognitive aging. *Dialogues Clin Neurosci*. 2013;15:11–27.
 382. Spence EF, Soderling SH. Actin out: Regulation of the synaptic cytoskeleton. *J Biol Chem*. 2015;290(48):28613–22.
 383. Gu J, Lee CW, Fan Y, Komlos D, Tang X, Sun C, et al. ADF/cofilin-mediated actin dynamics regulate AMPA receptor trafficking during synaptic plasticity. *Nat Neurosci*. 2010;13(10):1208–15.
 384. Parisiadou L, Yu J, Sgobio C, Xie C, Liu G, Sun L, et al. LRRK2 regulates synaptogenesis and dopamine receptor activation through modulation of PKA activity. *Nat Neurosci*. 2014;17(3):367–76.
 385. Sasahara T, Yayama K, Tahara T, Onoe H, Okamoto H. Na⁺/H⁺ exchanger inhibitor augments hyperosmolarity-induced vasoconstriction by enhancing actin polymerization. *Vascul Pharmacol*. 2013 Nov;59(5–6):120–6.
 386. Fan SH-Y, Numata Y, Numata M. Endosomal Na⁺ /H⁺ exchanger NHE5 influences MET recycling and cell migration. Gruenberg JE, editor. *Mol Biol Cell*. 2016 Feb 15;27(4):702–15.
 387. Alexander RT, Grinstein S. Tethering, recycling and activation of the epithelial sodium-proton exchanger, NHE3. *J Exp Biol*. 2009 Jun 1;212(11):1630–7.
 388. Minichiello L. TrkB signalling pathways in LTP and learning. *Nat Rev Neurosci*. 2009;10(12):850–60.
 389. Panja D, Bramham CR. BDNF mechanisms in late LTP formation: A synthesis and breakdown. *Neuropharmacology*. 2014;76(PART C):664–76.
 390. Korte M, Carroll P, Wolf E, Brem G, Thoenen H, Bonhoeffer T. Hippocampal long-term potentiation is impaired in mice lacking brain-derived neurotrophic factor. *Proc Natl Acad Sci*. 1995 Sep 12;92(19):8856–60.
 391. Messaoudi E, Kanhema T, Soulé J, Tiron A, Dagyte G, da Silva B, et al. Sustained Arc/Arg3.1 synthesis controls long-term potentiation consolidation through regulation of local actin polymerization in the dentate gyrus in vivo. *J Neurosci*. 2007;27(39):10445–55.
 392. Zhao L, Sheng AL, Huang SH, Yin YX, Chen B, Li XZ, et al. Mechanism underlying activity-dependent insertion of TrkB into the neuronal surface. *J Cell Sci*. 2009;
 393. Huang S, Wang J, Sui W-H, Chen B, Zhang X-Y, Yan J, et al. BDNF-Dependent Recycling Facilitates TrkB Translocation to Postsynaptic Density during LTP via a Rab11-Dependent Pathway. *J Neurosci*. 2013 May 22;33(21):9214–30.
 394. Messaoudi E, Ying SW, Kanhema T, Croll SD, Bramham CR. Brain-derived neurotrophic factor triggers transcription-dependent, late phase long-term potentiation in vivo. *J Neurosci*. 2002;22(17):7453–61.
 395. Prasad H, Rao R. Histone deacetylase-mediated regulation of endolysosomal pH. *J Biol Chem*. 2018;293(18):6721–35.

396. Seese RR, Le AA, Wang K, Cox CD, Lynch G, Gall CM. A TrkB agonist and ampakine rescue synaptic plasticity and multiple forms of memory in a mouse model of intellectual disability. *Neurobiol Dis.* 2020;134(July 2019):104604.
397. Ren E, Roncagé V, Trazzi S, Fuchs C, Medici G, Gennaccaro L, et al. Functional and structural impairments in the perirhinal cortex of a mouse model of CDKL5 deficiency disorder are rescued by a TrkB agonist. *Front Cell Neurosci.* 2019;13(April):1–15.
398. Stagni F, Giacomini A, Guidi S, Emili M, Uguagliati B, Salvalai ME, et al. A flavonoid agonist of the TrkB receptor for BDNF improves hippocampal neurogenesis and hippocampus-dependent memory in the Ts65Dn mouse model of DS. *Exp Neurol.* 2017;298(September):79–96.
399. Tian M, Zeng Y, Hu Y, Yuan X, Liu S, Li J, et al. 7, 8-Dihydroxyflavone induces synapse expression of AMPA GluA1 and ameliorates cognitive and spine abnormalities in a mouse model of fragile X syndrome. *Neuropharmacology.* 2015;89:43–53.
400. Gao L, Tian M, Zhao HY, Xu QQ, Huang YM, Si QC, et al. TrkB activation by 7, 8-dihydroxyflavone increases synapse AMPA subunits and ameliorates spatial memory deficits in a mouse model of Alzheimer's disease. *J Neurochem.* 2016;136(3):620–36.
401. Zeng Y, Lv F, Li L, Yu H, Dong M, Fu Q. 7,8-Dihydroxyflavone Rescues Spatial Memory and Synaptic Plasticity in Cognitively Impaired Aged Rats. *J Neurochem.* 2012;122(4):800–11.
402. Castello NA, Nguyen MH, Tran JD, Cheng D, Green KN, LaFerla FM. 7,8-dihydroxyflavone, a small molecule TrkB agonist, improves spatial memory and increases thin spine density in a mouse model of alzheimer disease-like neuronal loss. *PLoS One.* 2014;9(3):17–9.
403. Zhang Z, Liu X, Schroeder JP, Chan CB, Song M, Yu SP, et al. 7,8-dihydroxyflavone prevents synaptic loss and memory deficits in a mouse model of Alzheimer's disease. *Neuropsychopharmacology.* 2014;39(3):638–50.
404. Devi L, Ohno M. 7,8-dihydroxyflavone, a small-molecule TrkB agonist, reverses memory deficits and BACE1 elevation in a mouse model of alzheimer's disease. *Neuropsychopharmacology.* 2012;37(2):434–44.
405. Isackson PJ, Huntsman MM, Murray KD, Gall CM. BDNF mRNA expression is increased in adult rat forebrain after limbic seizures: Temporal patterns of induction distinct from NGF. *Neuron.* 1991 Jun;6(6):937–48.
406. Ampuero E, Dagnino-Subiabre A, Sandoval R, Zepeda-Carreño R, Sandoval S, Viedma A, et al. Status epilepticus induces region-specific changes in dendritic spines, dendritic length and TrkB protein content of rat brain cortex. *Brain Res.* 2007 May;1150:225–38.
407. Danzer SC, He X, McNamara JO. Ontogeny of seizure-induced increases in BDNF immunoreactivity and TrkB receptor activation in rat hippocampus. *Hippocampus.* 2004;14(3):345–55.
408. Mathern GW, Babb TL, Micevych PE, Blanco CE, Pretorius JK. Granule cell mRNA levels for BDNF, NGF, and NT-3 correlate with neuron losses or supragranular mossy fiber

- sprouting in the chronically damaged and epileptic human hippocampus. *Mol Chem Neuropathol*. 1997 Jan;30(1–2):53–76.
409. Takahashi M, Hayashi S, Kakita A, Wakabayashi K, Fukuda M, Kameyama S, et al. Patients with temporal lobe epilepsy show an increase in brain-derived neurotrophic factor protein and its correlation with neuropeptide Y. *Brain Res*. 1999 Feb;818(2):579–82.
 410. Isgor C, Pare C, McDole B, Coombs P, Guthrie K. Expansion of the dentate mossy fiber–CA3 projection in the brain-derived neurotrophic factor-enriched mouse hippocampus. *Neuroscience*. 2015 Mar;288:10–23.
 411. Cunha C, Angelucci A, D’Antoni A, Dobrossy MD, Dunnett SB, Berardi N, et al. Brain-derived neurotrophic factor (BDNF) overexpression in the forebrain results in learning and memory impairments. *Neurobiol Dis*. 2009 Mar;33(3):358–68.
 412. Olofsdotter K, Lindvall O, Asztély F. Increased synaptic inhibition in dentate gyrus of mice with reduced levels of endogenous brain-derived neurotrophic factor. *Neuroscience*. 2000 Nov;101(3):531–9.
 413. Henneberger C, Jüttner R, Rothe T, Grantyn R. Postsynaptic Action of BDNF on GABAergic Synaptic Transmission in the Superficial Layers of the Mouse Superior Colliculus. *J Neurophysiol*. 2002 Aug 1;88(2):595–603.
 414. Henneberger C, Kirischuk S, Grantyn R. Brain-derived neurotrophic factor modulates GABAergic synaptic transmission by enhancing presynaptic glutamic acid decarboxylase 65 levels, promoting asynchronous release and reducing the number of activated postsynaptic receptors. *Neuroscience*. 2005 Jan;135(3):749–63.
 415. Kokaia M, Ernfors P, Kokaia Z, Elmér E, Jaenisch R, Lindvall O. Suppressed Epileptogenesis in BDNF Mutant Mice. *Exp Neurol*. 1995 Jun;133(2):215–24.
 416. He X-P, Kotloski R, Nef S, Luikart BW, Parada LF, McNamara JO. Conditional Deletion of TrkB but Not BDNF Prevents Epileptogenesis in the Kindling Model. *Neuron*. 2004 Jul;43(1):31–42.
 417. McNamara JO, Scharfman HE. Temporal Lobe Epilepsy and the BDNF Receptor, TrkB. *Jasper’s Basic Mechanisms of the Epilepsies*. 2012;1–29.
 418. Wardle RA, Poo M. Brain-Derived Neurotrophic Factor Modulation of GABAergic Synapses by Postsynaptic Regulation of Chloride Transport. *J Neurosci*. 2003 Sep 24;23(25):8722–32.
 419. González MI. Brain-derived neurotrophic factor promotes gephyrin protein expression and GABAA receptor clustering in immature cultured hippocampal cells. *Neurochem Int*. 2014;72(1):14–21.
 420. Vithlani M, Hines RM, Zhong P, Terunuma M, Hines DJ, Revilla-Sanchez R, et al. The Ability of BDNF to Modify Neurogenesis and Depressive-Like Behaviors Is Dependent upon Phosphorylation of Tyrosine Residues 365/367 in the GABA A -Receptor $\gamma 2$ Subunit. *J Neurosci*. 2013 Sep 25;33(39):15567–77.
 421. Bolton MM, Pittman AJ, Lo DC. Brain-Derived Neurotrophic Factor Differentially Regulates Excitatory and Inhibitory Synaptic Transmission in Hippocampal Cultures. *J*

- Neurosci. 2000 May 1;20(9):3221–32.
422. Paul J, Gottmann K, Lessmann V. NT-3 regulates BDNF-induced modulation of synaptic transmission in cultured hippocampal neurons. *Neuroreport*. 2001 Aug;12(12):2635–9.
 423. Baldelli P, Novara M, Carabelli V, Hernández-Guijo JM, Carbone E. BDNF up-regulates evoked GABAergic transmission in developing hippocampus by potentiating presynaptic N- and P/Q-type Ca²⁺ channels signalling. *Eur J Neurosci*. 2002 Dec;16(12):2297–310.
 424. Jovanovic JN, Thomas P, Kittler JT, Smart TG, Moss SJ. Brain-Derived Neurotrophic Factor Modulates Fast Synaptic Inhibition by Regulating GABAA Receptor Phosphorylation, Activity, and Cell-Surface Stability. *J Neurosci*. 2004 Jan 14;24(2):522–30.
 425. Brünig I, Penschuck S, Berninger B, Benson J, Fritschy J-M. BDNF reduces miniature inhibitory postsynaptic currents by rapid downregulation of GABA A receptor surface expression. *Eur J Neurosci*. 2001 Apr;13(7):1320–8.
 426. Tanaka T, Saito H, Matsuki N. Inhibition of GABA A Synaptic Responses by Brain-Derived Neurotrophic Factor (BDNF) in Rat Hippocampus. *J Neurosci*. 1997 May 1;17(9):2959–66.
 427. Frerking M, Malenka RC, Nicoll RA. Brain-Derived Neurotrophic Factor (BDNF) Modulates Inhibitory, But Not Excitatory, Transmission in the CA1 Region of the Hippocampus. *J Neurophysiol*. 1998 Dec 1;80(6):3383–6.
 428. Mizoguchi Y, Ishibashi H, Nabekura J. The action of BDNF on GABAA currents changes from potentiating to suppressing during maturation of rat hippocampal CA1 pyramidal neurons. *J Physiol*. 2003 May 1;548(3):703–9.
 429. Li X, Zhou J, Chen Z, Chen S, Zhu F, Zhou L. Long-term expressional changes of Na⁺-K⁺-Cl⁻ co-transporter 1 (NKCC1) and K⁺-Cl⁻ co-transporter 2 (KCC2) in CA1 region of hippocampus following lithium-pilocarpine induced status epilepticus (PISE). *Brain Res*. 2008;1221:141–6.
 430. Ye H, Kaszuba S. Inhibitory or excitatory? Optogenetic interrogation of the functional roles of GABAergic interneurons in epileptogenesis. *J Biomed Sci*. 2017;24(1):93.
 431. Cohen I, Navarro V, Clemenceau S, Baulac M, Miles R. On the Origin of Interictal Activity in Human Temporal Lobe Epilepsy in Vitro. *Science* (80-). 2002 Nov 15;298(5597):1418–21.
 432. Huberfeld G, Wittner L, Clemenceau S, Baulac M, Kaila K, Miles R, et al. Perturbed chloride homeostasis and GABAergic signaling in human temporal lobe epilepsy. *J Neurosci*. 2007;27(37):9866–73.
 433. Woo N-S, Lu J, England R, McClellan R, Dufour S, Mount DB, et al. Hyperexcitability and epilepsy associated with disruption of the mouse neuronal-specific K-Cl cotransporter gene. *Hippocampus*. 2002;12(2):258–68.
 434. Pathak HR, Weissinger F, Terunuma M, Carlson GC, Hsu F-C, Moss SJ, et al. Disrupted Dentate Granule Cell Chloride Regulation Enhances Synaptic Excitability during Development of Temporal Lobe Epilepsy. *J Neurosci*. 2007 Dec 19;27(51):14012–22.

435. Aguado F, Carmona MA, Pozas E, Aguiló A, Martínez-Guijarro FJ, Alcantara S, et al. BDNF regulates spontaneous correlated activity at early developmental stages by increasing synaptogenesis and expression of the K⁺/Cl⁻ co-transporter KCC2. *Development*. 2003 Apr 1;130(7):1267–80.
436. Rivera C, Voipio J, Thomas-Crusells J, Li H, Emri Z, Sipilä S, et al. Mechanism of activity-dependent downregulation of the neuron-specific K-Cl cotransporter KCC2. *J Neurosci*. 2004;24(19):4683–91.
437. Ludwig A, Uvarov P, Soni S, Thomas-Crusells J, Airaksinen MS, Rivera C. Early Growth Response 4 Mediates BDNF Induction of Potassium Chloride Cotransporter 2 Transcription. *J Neurosci*. 2011 Jan 12;31(2):644–9.
438. Carmona MA, Pozas E, Martínez A, Espinosa-Parrilla JF, Soriano E, Aguado F. Age-dependent Spontaneous Hyperexcitability and Impairment of GABAergic Function in the Hippocampus of Mice Lacking trkB. *Cereb Cortex*. 2006 Jan 1;16(1):47–63.
439. Rivera C, Li H, Thomas-Crusells J, Lahtinen H, Viitanen T, Nanobashvili A, et al. BDNF-induced TrkB activation down-regulates the K⁺-Cl⁻ cotransporter KCC2 and impairs neuronal Cl⁻ extrusion. *J Cell Biol*. 2002;159(5):747–52.
440. Wake H, Watanabe M, Moorhouse AJ, Kanematsu T, Horibe S, Matsukawa N, et al. Early changes in KCC2 phosphorylation in response to neuronal stress result in functional downregulation. *J Neurosci*. 2007;27(7):1642–50.
441. Shulga A, Thomas-Crusells J, Sigl T, Blaesse A, Mestres P, Meyer M, et al. Posttraumatic GABA(A)-mediated [Ca²⁺]_i increase is essential for the induction of brain-derived neurotrophic factor-dependent survival of mature central neurons. *J Neurosci*. 2008 Jul;28(27):6996–7005.
442. Puskarjov M, Ahmad F, Kaila K, Blaesse P. Activity-dependent cleavage of the K-Cl cotransporter KCC2 mediated by calcium-activated protease calpain. *J Neurosci*. 2012;32(33):11356–64.
443. Di Cristo G, Awad PN, Hamidi S, Avoli M. KCC2, epileptiform synchronization, and epileptic disorders. *Prog Neurobiol*. 2018;162:1–16.
444. Porcher C, Medina I, Gaiarsa JL. Mechanism of BDNF modulation in GABAergic synaptic transmission in healthy and disease brains. *Front Cell Neurosci*. 2018;12(August):1–9.
445. Wang W, Gong N, Xu T-L. Downregulation of KCC2 following LTP contributes to EPSP–spike potentiation in rat hippocampus. *Biochem Biophys Res Commun*. 2006 May;343(4):1209–15.
446. Reid KH, Li G-Y, Payne RS, Schurr A, Cooper NGF. The mRNA level of the potassium-chloride cotransporter KCC2 covaries with seizure susceptibility in inferior colliculus of the post-ischemic audiogenic seizure-prone rat. *Neurosci Lett*. 2001 Jul;308(1):29–32.
447. Zhou HY, Chen SR, Byun HS, Chen H, Li L, Han HD, et al. N-methyl-D-aspartate receptor- and calpain-mediated proteolytic cleavage of K⁺-Cl⁻ cotransporter-2 impairs spinal chloride homeostasis in neuropathic pain. *J Biol Chem*. 2012;287(40):33853–64.
448. Lee HHC, Deeb TZ, Walker JA, Davies PA, Moss SJ. NMDA receptor activity

- downregulates KCC2 resulting in depolarizing GABAA receptor-mediated currents. *Nat Neurosci*. 2011 Jun 1;14(6):736–43.
449. Chamma I, Heubl M, Chevy Q, Renner M, Moutkine I, Eugène E, et al. Activity-dependent regulation of the K/Cl transporter KCC2 membrane diffusion, clustering, and function in hippocampal neurons. *J Neurosci*. 2013;33(39):15488–503.
 450. Karlócai MR, Wittner L, Tóth K, Maglóczy Z, Katarova Z, Rásonyi G, et al. Enhanced expression of potassium-chloride cotransporter KCC2 in human temporal lobe epilepsy. *Brain Struct Funct*. 2016;221(7):3601–15.
 451. Kaila K, Lamsa K, Smirnov S, Taira T, Voipio J. Long-lasting GABA-mediated depolarization evoked by high-frequency stimulation in pyramidal neurons of rat hippocampal slice is attributable to a network-driven, bicarbonate-dependent K⁺ transient. *J Neurosci*. 1997 Oct 15;17(20):7662–72.
 452. Viitanen T, Ruusuvuori E, Kaila K, Voipio J. The K⁺-Cl⁻ cotransporter KCC2 promotes GABAergic excitation in the mature rat hippocampus. *J Physiol*. 2010;588(9):1527–40.
 453. Gamba G, Miyanoshita A, Lombardi M, Lytton J, Lee W Sen, Hediger MA, et al. Molecular cloning, primary structure, and characterization of two members of the mammalian electroneutral sodium-(potassium)-chloride cotransporter family expressed in kidney. *J Biol Chem*. 1994 Jul 1;269(26):17713–22.
 454. Flamenbaum W, Friedman R. Pharmacology, Therapeutic Efficacy, and Adverse Effects of Bumetanide, A New “Loop” Diuretic. *Pharmacother J Hum Pharmacol Drug Ther*. 1982 Jul 8;2(4):213–22.
 455. Halstenson CE, Matzke GR. Bumetanide: A New Loop Diuretic (Bumex, Roche Laboratories). *Drug Intell Clin Pharm*. 1983 Nov 4;17(11):786–97.
 456. Ward A, Heel RC. Bumetanide A Review of its Pharmacodynamic and Pharmacokinetic Properties and Therapeutic Use. *Drugs*. 1984 Nov;28(5):426–64.
 457. Walcott BP, Kahle KT, Simard JM. Novel Treatment Targets for Cerebral Edema. *Neurotherapeutics*. 2012 Jan 29;9(1):65–72.
 458. Xu W, Sun X, Song C, Mu X, Ma W, Zhang X, et al. Bumetanide promotes neural precursor cell regeneration and dendritic development in the hippocampal dentate gyrus in the chronic stage of cerebral ischemia. *Neural Regen Res*. 2016;11(5):745.
 459. Yan Y, Dempsey RJ, Sun D. Na⁺ + -K⁺ + -Cl⁻ Cotransporter in Rat Focal Cerebral Ischemia. *J Cereb Blood Flow Metab*. 2001 Jun;21(6):711–21.
 460. Kintner DB, Luo J, Gerdt J, Ballard AJ, Shull GE, Sun D. Role of Na⁺-K⁺-Cl⁻ cotransport and Na⁺/Ca²⁺ exchange in mitochondrial dysfunction in astrocytes following in vitro ischemia. *Am J Physiol Physiol*. 2007 Mar 1;292(3):C1113–22.
 461. Kahle KT, Staley KJ, Nahed B V., Gamba G, Hebert SC, Lifton RP, et al. Roles of the cation - Chloride cotransporters in neurological disease. *Nat Clin Pract Neurol*. 2008;4(9):490–503.
 462. Löscher W, Puskarjov M, Kaila K. Cation-chloride cotransporters NKCC1 and KCC2 as potential targets for novel antiepileptic and antiepileptogenic treatments.

- Neuropharmacology. 2013;69:62–74.
463. Holmes GL, Tian C, Hernan AE, Flynn S, Camp D, Barry J. Alterations in sociability and functional brain connectivity caused by early-life seizures are prevented by bumetanide. *Neurobiol Dis.* 2015;77:204–19.
 464. Cleary RT, Sun H, Huynh T, Manning SM, Li Y, Rotenberg A, et al. Bumetanide Enhances Phenobarbital Efficacy in a Rat Model of Hypoxic Neonatal Seizures. Avoli M, editor. *PLoS One.* 2013 Mar 11;8(3):e57148.
 465. Deidda G, Parrini M, Naskar S, Bozarth IF, Contestabile A, Cancedda L. Reversing excitatory GABA A R signaling restores synaptic plasticity and memory in a mouse model of Down syndrome. *Nat Med.* 2015;21(4):318–26.
 466. Amin H, Marinaro F, Tonelli DDP, Berdondini L. Developmental excitatory-to-inhibitory GABA-polarity switch is disrupted in 22q11.2 deletion syndrome: A potential target for clinical therapeutics. *Sci Rep.* 2017;7(1):1–18.
 467. Pisella LI, Gaiarsa JL, Diabira D, Zhang J, Khalilov I, Duan JJ, et al. Impaired regulation of KCC2 phosphorylation leads to neuronal network dysfunction and neurodevelopmental pathology. *Sci Signal.* 2019;12(603).
 468. Kharod SC, Kang SK, Kadam SD. Off-label use of bumetanide for brain disorders: An overview. *Front Neurosci.* 2019;13(APR).
 469. Lemonnier E, Ben-Ari Y. The diuretic bumetanide decreases autistic behaviour in five infants treated during 3 months with no side effects. *Acta Paediatr.* 2010 Dec;99(12):1885–8.
 470. Lemonnier E, Villeneuve N, Sonie S, Serret S, Rosier A, Roue M, et al. Effects of bumetanide on neurobehavioral function in children and adolescents with autism spectrum disorders. *Transl Psychiatry.* 2017;7(3):e1056-9.
 471. Ben-Ari Y. NKCC1 Chloride Importer Antagonists Attenuate Many Neurological and Psychiatric Disorders. *Trends Neurosci.* 2017;40(9):536–54.
 472. James BJ, Gales MA, Gales BJ. Bumetanide for Autism Spectrum Disorder in Children: A Review of Randomized Controlled Trials. *Ann Pharmacother.* 2019;53(5):537–44.
 473. Lemonnier E, Degrez C, Phelep M, Tyzio R, Josse F, Grandgeorge M, et al. A randomised controlled trial of bumetanide in the treatment of autism in children. *Transl Psychiatry.* 2012 Dec 11;2(12):e202–e202.
 474. Zhang L, Huang C-C, Dai Y, Luo Q, Ji Y, Wang K, et al. Symptom improvement in children with autism spectrum disorder following bumetanide administration is associated with decreased GABA/glutamate ratios. *Transl Psychiatry.* 2020 Jan;10(1):9.
 475. Eftekhari S, Mehvari Habibabadi J, Najafi Ziarani M, Hashemi Fesharaki SS, Gharakhani M, Mostafavi H, et al. Bumetanide reduces seizure frequency in patients with temporal lobe epilepsy. *Epilepsia.* 2013 Jan;54(1):e9–12.
 476. Hasannejad H, Takeda M, Taki K, Shin HJ, Babu E, Jutabha P, et al. Interactions of Human Organic Anion Transporters with Diuretics. *J Pharmacol Exp Ther.* 2004 Mar;308(3):1021–9.

477. Nielsen S, Maunsbach AB, Ecelbarger CA, Knepper MA. Ultrastructural localization of Na-K-2Cl cotransporter in thick ascending limb and macula densa of rat kidney. *Am J Physiol Physiol*. 1998 Dec 1;275(6):F885–93.
478. Puskarjov M, Kahle KT, Ruusuvuori E, Kaila K. Pharmacotherapeutic targeting of cation-chloride cotransporters in neonatal seizures. *Epilepsia*. 2014 Jun;55(6):806–18.
479. Töpfer M, Töllner K, Brandt C, Twele F, Bröer S, Löscher W. Consequences of inhibition of bumetanide metabolism in rodents on brain penetration and effects of bumetanide in chronic models of epilepsy. *Eur J Neurosci*. 2014 Feb;39(4):673–87.
480. Römermann K, Fedrowitz M, Hampel P, Kaczmarek E, Töllner K, Erker T, et al. Multiple blood-brain barrier transport mechanisms limit bumetanide accumulation, and therapeutic potential, in the mammalian brain. *Neuropharmacology*. 2017 May;117:182–94.
481. Payne JA, Rivera C, Voipio J, Kaila K. Cation–chloride co-transporters in neuronal communication, development and trauma. *Trends Neurosci*. 2003 Apr;26(4):199–206.
482. Delpire E, Days E, Lewis LM, Mi D, Kim K, Lindsley CW, et al. Small-molecule screen identifies inhibitors of the neuronal K-Cl cotransporter KCC2. *Proc Natl Acad Sci*. 2009 Mar 31;106(13):5383–8.
483. Auer T, Schreppe P, Erker T, Schwarzer C. Functional characterization of novel bumetanide derivatives for epilepsy treatment. *Neuropharmacology*. 2020;162(August 2019):107754.
484. Zeng L-H, Xu L, Rensing NR, Sinatra PM, Rothman SM, Wong M. Kainate Seizures Cause Acute Dendritic Injury and Actin Depolymerization In Vivo. *J Neurosci*. 2007 Oct 24;27(43):11604–13.
485. Guo D, Arnsperger S, Rensing NR, Wong M. Brief seizures cause dendritic injury. *Neurobiol Dis*. 2012 Jan;45(1):348–55.
486. Isokawa M. Remodeling dendritic spines in the rat pilocarpine model of temporal lobe epilepsy. *Neurosci Lett*. 1998 Dec;258(2):73–6.
487. Kurz JE, Moore BJ, Henderson SC, Campbell JN, Churn SB. A cellular mechanism for dendritic spine loss in the pilocarpine model of status epilepticus. *Epilepsia*. 2008 Oct;49(10):1696–710.
488. Santos VR, de Castro OW, Pun RYK, Hester MS, Murphy BL, Loepke AW, et al. Contributions of mature granule cells to structural plasticity in temporal lobe epilepsy. *Neuroscience*. 2011 Dec;197:348–57.
489. Muller M, Gähwiler BH, Rietschin L, Thompson SM. Reversible loss of dendritic spines and altered excitability after chronic epilepsy in hippocampal slice cultures. *Proc Natl Acad Sci*. 1993 Jan 1;90(1):257–61.
490. Thompson SM, Fortunato C, McKinney RA, Müller M, Gähwiler BH. Mechanisms underlying the neuropathological consequences of epileptic activity in the rat hippocampus in vitro. *J Comp Neurol*. 1996 Sep 2;372(4):515–28.
491. Zha X, Green SH, Dailey ME. Regulation of hippocampal synapse remodeling by epileptiform activity. *Mol Cell Neurosci*. 2005 Aug;29(4):494–506.

492. Wong M, Guo D. Dendritic spine pathology in epilepsy: Cause or consequence? *Neuroscience*. 2013;251:141–50.
493. Holmes GL. Cognitive impairment in epilepsy: the role of network abnormalities. *Epileptic Disord*. 2015 Jun;17(2):101–16.
494. O'Brien RJ, Kamboj S, Ehlers MD, Rosen KR, Fischbach GD, Huganir RL. Activity-Dependent Modulation of Synaptic AMPA Receptor Accumulation. *Neuron*. 1998 Nov;21(5):1067–78.
495. Siddoway B, Hou H, Xia H. Molecular mechanisms of homeostatic synaptic downscaling. *Neuropharmacology*. 2014 Mar;78:38–44.
496. Turrigiano GG, Leslie KR, Desai NS, Rutherford LC, Nelson SB. Activity-dependent scaling of quantal amplitude in neocortical neurons. *Nature*. 1998 Feb;391(6670):892–6.
497. Gulyás AI, Sík A, Payne JA, Kaila K, Freund TF. The KCl cotransporter, KCC2, is highly expressed in the vicinity of excitatory synapses in the rat hippocampus. *Eur J Neurosci*. 2001 Jun;13(12):2205–17.
498. Li H, Khirug S, Cai C, Ludwig A, Blaesse P, Kolikova J, et al. KCC2 Interacts with the Dendritic Cytoskeleton to Promote Spine Development. *Neuron*. 2007;56(6):1019–33.
499. Fiumelli H, Briner A, Puskarjov M, Blaesse P, Belem BJ, Dayer AG, et al. An ion transport-independent role for the cation-chloride cotransporter kcc2 in dendritic spinogenesis in vivo. *Cereb Cortex*. 2013;23(2):378–88.
500. Gauvain G, Chamma I, Chevy Q, Cabezas C, Irinopoulou T, Bodrug N, et al. The neuronal K-Cl cotransporter KCC2 influences postsynaptic AMPA receptor content and lateral diffusion in dendritic spines. *Proc Natl Acad Sci U S A*. 2011;108(37):15474–9.
501. Blaesse P, Schmidt T. K-Cl cotransporter KCC2—a moonlighting protein in excitatory and inhibitory synapse development and function. *Pflugers Arch Eur J Physiol*. 2015;467(4):615–24.
502. Awad PN, Amegandjin CA, Szczurkowska J, Carriço JN, Fernandes Do Nascimento AS, Baho E, et al. KCC2 Regulates Dendritic Spine Formation in a Brain-Region Specific and BDNF Dependent Manner. *Cereb Cortex*. 2018;28(11):4049–62.
503. Salmon CK, Pribiag H, Gizowski C, Farmer WT, Cameron S, Jones E V., et al. Depolarizing GABA Transmission Restrains Activity-Dependent Glutamatergic Synapse Formation in the Developing Hippocampal Circuit. *Front Cell Neurosci*. 2020;14(February):1–16.
504. Schwede M, Garbett K, Mirnics K, Geschwind DH, Morrow EM. Genes for endosomal NHE6 and NHE9 are misregulated in autism brains. *Mol Psychiatry*. 2013 Mar;19(3):1–3.
505. Ko M, Quiñones-Hinojosa A, Rao R. Emerging links between endosomal pH and cancer. *Cancer Metastasis Rev*. 2020 Jun 6;39(2):519–34.
506. Lucien F, Pelletier P-P, Lavoie RR, Lacroix J-M, Roy S, Parent J-L, et al. Hypoxia-induced mobilization of NHE6 to the plasma membrane triggers endosome hyperacidification and chemoresistance. *Nat Commun*. 2017 Aug 21;8(1):15884.
507. Pall AE, Juratli L, Guntur D, Bandyopadhyay K, Kondapalli KC. A gain of function paradox: Targeted therapy for glioblastoma associated with abnormal NHE9 expression. *J*

- Cell Mol Med. 2019 Nov 18;23(11):7859–72.
508. Eltokhi A, Janmaat IE, Genedi M, Haarman BCM, Sommer IEC. Dysregulation of synaptic pruning as a possible link between intestinal microbiota dysbiosis and neuropsychiatric disorders. *J Neurosci Res*. 2020 Jul 2;98(7):1335–69.
 509. Spronck EA, Brouwers CC, Vallès A, de Haan M, Petry H, van Deventer SJ, et al. AAV5-miHTT Gene Therapy Demonstrates Sustained Huntingtin Lowering and Functional Improvement in Huntington Disease Mouse Models. *Mol Ther - Methods Clin Dev*. 2019 Jun;13:334–43.
 510. Du S, Ou H, Cui R, Jiang N, Zhang M, Li X, et al. Delivery of Glucosylceramidase Beta Gene Using AAV9 Vector Therapy as a Treatment Strategy in Mouse Models of Gaucher Disease. *Hum Gene Ther*. 2019 Feb;30(2):155–67.
 511. Roy DS, Kitamura T, Okuyama T, Ogawa SK, Sun C, Obata Y, et al. Distinct Neural Circuits for the Formation and Retrieval of Episodic Memories. *Cell*. 2017;170(5):1000–1012.e19.
 512. Wulff P, Ponomarenko AA, Bartos M, Korotkova TM, Fuchs EC, Bähner F, et al. Hippocampal theta rhythm and its coupling with gamma oscillations require fast inhibition onto parvalbumin-positive interneurons. *Proc Natl Acad Sci U S A*. 2009;106(9):3561–6.
 513. Hijazi S, Heistek TS, Scheltens P, Neumann U, Shimshek DR, Mansvelder HD, et al. Early restoration of parvalbumin interneuron activity prevents memory loss and network hyperexcitability in a mouse model of Alzheimer's disease. *Mol Psychiatry*. 2019;
 514. Gruber R, McKinney A, Orlowski J, Wise MS. 0798 Reported Sleep Disturbances in Individuals with Christianson Syndrome. *Sleep*. 2018 Apr 27;41(suppl_1):A296–A296.
 515. Mathieu M-L, de Bellescize J, Till M, Flurin V, Labalme A, Chatron N, et al. Electrical status epilepticus in sleep, a constitutive feature of Christianson syndrome? *Eur J Paediatr Neurol*. 2018 Nov 1;22(6):1124–32.
 516. Wehr TA, Turner EH, Shimada JM, Lowe CH, Barker C, Leibenluft E. Treatment of a Rapidly Cycling Bipolar Patient by Using Extended Bed Rest and Darkness to Stabilize the Timing and Duration of Sleep. *Biol Psychiatry*. 1998 Jun;43(11):822–8.
 517. Jagannath A, Peirson SN, Foster RG. Sleep and circadian rhythm disruption in neuropsychiatric illness. *Curr Opin Neurobiol*. 2013 Oct;23(5):888–94.
 518. Lamont EW, Coutu DL, Cermakian N, Boivin DB. Circadian rhythms and clock genes in psychotic disorders. *Isr J Psychiatry Relat Sci*. 2010;47(1):27–35.
 519. Van Erum J, Van Dam D, De Deyn PP. PTZ-induced seizures in mice require a revised Racine scale. *Epilepsy Behav*. 2019 Jun;95:51–5.
 520. Kalume F, Westenbroek RE, Cheah CS, Yu FH, Oakley JC, Scheuer T, et al. Sudden unexpected death in a mouse model of Dravet syndrome. *J Clin Invest*. 2013/03/25. 2013 Apr;123(4):1798–808.
 521. Li R, Buchanan GF. Scurrying to Understand Sudden Expected Death in Epilepsy: Insights From Animal Models. *Epilepsy Curr*. 2019 Nov 16;19(6):390–6.

APPENDIX

As indicated in the Preface, this appendix contains the following two manuscripts in their original published forms:


1. Ilie A, **Gao AY**, Reid J, Boucher A, McEwan C, Barrière H, Lukacs GL, McKinney RA, Orłowski J (2016). A Christianson syndrome-linked deletion mutation ($\Delta(287)ES(288)$) in *SLC9A6* disrupts recycling endosomal function and elicits neurodegeneration and cell death. *Mol Neurodegener.* 11(1):63. DOI: [10.1186/s13024-016-0129-9](https://doi.org/10.1186/s13024-016-0129-9)
 - This article is distributed under the terms of the Creative Commons Attribution 4.0 International License (<http://creativecommons.org/licenses/by/4.0/>), which permits unrestricted use, distribution, and reproduction in any medium.
2. Ilie A, **Gao AYL**, Boucher A, Park J, Berghuis AM, Hoffer MJV, Hilhorst-Hofstee Y, McKinney RA, Orłowski J (2019). A potential gain-of-function variant of *SLC9A6* leads to endosomal alkalinization and neuronal atrophy associated with Christianson Syndrome. *Neurobiol Dis.* 121:187-204. DOI: [10.1016/j.nbd.2018.10.002](https://doi.org/10.1016/j.nbd.2018.10.002)

RESEARCH ARTICLE

Open Access



A Christianson syndrome-linked deletion mutation ($\Delta^{287}\text{ES}^{288}$) in SLC9A6 disrupts recycling endosomal function and elicits neurodegeneration and cell death

Alina Ilie¹, Andy Y. L. Gao², Jonathan Reid¹, Annie Boucher¹, Cassandra McEwan¹, Hervé Barrière¹, Gergely L. Lukacs¹, R. Anne McKinney² and John Orlowski^{1*} 

Abstract

Background: Christianson Syndrome, a recently identified X-linked neurodevelopmental disorder, is caused by mutations in the human gene SLC9A6 encoding the recycling endosomal alkali cation/proton exchanger NHE6. The patients have pronounced limitations in cognitive ability, motor skills and adaptive behaviour. However, the mechanistic basis for this disorder is poorly understood as few of the more than 20 mutations identified thus far have been studied in detail.

Methods: Here, we examined the molecular and cellular consequences of a 6 base-pair deletion of amino acids Glu²⁸⁷ and Ser²⁸⁸ (ΔES) in the predicted seventh transmembrane helix of human NHE6 expressed in established cell lines (CHO/AP-1, HeLa and neuroblastoma SH-SY5Y) and primary cultures of mouse hippocampal neurons by measuring levels of protein expression, stability, membrane trafficking, endosomal function and cell viability.

Results: In the cell lines, immunoblot analyses showed that the nascent mutant protein was properly synthesized and assembled as a homodimer, but its oligosaccharide maturation and half-life were markedly reduced compared to wild-type (WT) and correlated with enhanced ubiquitination leading to both proteasomal and lysosomal degradation. Despite this instability, a measurable fraction of the transporter was correctly sorted to the plasma membrane. However, the rates of clathrin-mediated endocytosis of the ΔES mutant as well as uptake of companion vesicular cargo, such as the ligand-bound transferrin receptor, were significantly reduced and correlated with excessive endosomal acidification. Notably, ectopic expression of ΔES but not WT induced apoptosis when examined in AP-1 cells. Similarly, in transfected primary cultures of mouse hippocampal neurons, membrane trafficking of the ΔES mutant was impaired and elicited marked reductions in total dendritic length, area and arborization, and triggered apoptotic cell death.

Conclusions: These results suggest that loss-of-function mutations in NHE6 disrupt recycling endosomal function and trafficking of cargo which ultimately leads to neuronal degeneration and cell death in Christianson Syndrome.

Keywords: NHE6/SLC9A6, Christianson syndrome, X-linked intellectual disability, Protein misfolding, Ubiquitination, Endosomal pH homeostasis, Membrane trafficking, Apoptosis

(Continued on next page)

* Correspondence: john.orkowski@mcgill.ca

¹Department of Physiology, McGill University, Bellini Life Sciences Bldg., Rm, 166, 3649 Promenade Sir-William-Osler, Montreal, QC H3G 0B1, Canada
Full list of author information is available at the end of the article

(Continued from previous page)

Abbreviations: 7-AAD, 7-amino actinomycin D; AMPAR, α -amino-3-hydroxy-5-methyl-4-isoxazolepropionic acid receptor; AP-1, Chinese hamster ovary (CHO) cells deficient in the Na^+/H^+ antiporter 1 isoform; AP2, Adaptor protein 2; Arf6, ADP-ribosylation factor 6; ARNO, ADP-ribosylation factor nucleotide site opener; AS, Angelman syndrome; ASK1, Apoptosis signal-regulating kinase 1; BDNF, Brain-derived neurotrophic factor; cCASP3, Cleaved caspase 3 (Asp175); ChFP, Monomeric Cherry fluorescent protein; CS, Christianson syndrome; DMSO, Dimethylsulfoxide; EEA1, Early endosome antigen 1; EGF, Epidermal growth factor; EGFR, Epidermal growth factor receptor; EndoH, Endoglycosidase H; ER, Endoplasmic reticulum; ERAD, Endoplasmic reticulum-associated degradation; ESCRT, Endosomal sorting complex required for transport; FITC, Fluorescein isothiocyanate; FRIA, Fluorescence ratiometric image analysis; GAPDH, Glyceraldehyde-3-phosphate dehydrogenase; GFP, Green fluorescent protein; HA, Influenza virus hemagglutinin epitope; IRE1, Inositol-requiring kinase 1; JNK, c-Jun N-terminal kinase; Lamp-2, Lysosome-associated membrane protein 2; M.I.F., Median intensity fluorescence; NHE6/SLC9A6, Sodium/proton exchanger isoform 6; NMDAR, *N*-methyl-D-aspartate receptor; NT-4, Neurotrophin-4; p75^{NTR} , p75 neurotrophin receptor; PI, Propidium iodide; PNGaseF, Peptide-N-glycosidase F; SDS-PAGE, Sodium dodecyl sulfate polyacrylamide gel electrophoresis; siRNA, small interfering ribonucleic acids; Tf, Transferrin; Tfr, Transferrin receptor; TrkB, Tropomyosin-related kinase receptor B; Ub, Ubiquitin; UBE3A/E6AP, E3 ubiquitin ligase 3A; UPR, Unfolded protein response; WT, Wild-type; XLID, X-linked intellectual disability; ΔES , Deletion of Glu287-Ser288

Background

Christianson syndrome (CS) is a recently described neurodevelopmental and progressively neurodegenerative disorder characterized by moderate to severe intellectual disability, epilepsy, mutism, truncal ataxia, hyperkinesia, happy demeanor, postnatal microcephaly and is often accompanied by one or more secondary symptoms (e.g., autistic behaviour, eye movement dysfunction, hypotonia, gastroesophageal reflux, low height and/or weight, high pain threshold, motor regression, cerebellar vermis and brain stem atrophy as well as neuronal cell loss) [1–3]; a phenotype that partially mimics Angelman syndrome (AS) [4, 5]. However, the underlying pathogenic gene variants are different. Whereas AS is caused by defects in the E3 ubiquitin ligase UBE3A/E6AP gene located at chromosome 15q11.2 [6, 7], CS was recently found to arise from mutations in the gene encoding the pH-regulating solute carrier (Na^+ , K^+)/ H^+ exchanger NHE6/SLC9A6 located at chromosome Xq26.3 [2, 3, 8, 9]. The frequency of CS amongst X-linked developmental brain disorders has been estimated at approximately 1 to 2 % [3, 10–12], which places NHE6 amongst the more commonly mutated genes associated with X-linked intellectual disability (XLID) [13–17]. The descriptions of autistic behaviour in patients with CS also parallels recent findings of a significant reduction in NHE6 gene expression in postmortem cerebral cortex from patients with idiopathic autism compared to control tissue [18], further implicating an important role for this transporter in disorders of cognitive development. As with most X-linked disorders, mutations in NHE6 profoundly affect males whereas female carriers are either asymptomatic or display a milder phenotype [1, 3, 8].

NHE6 belongs to the endomembrane subclass of mammalian alkali cation/proton exchangers that are sorted differentially to discrete organelles along the secretory and degradative pathways [19, 20]. In the case of NHE6, it is widely expressed but most abundant in excitable tissues such as brain, heart, and skeletal muscle. In non-neuronal cells, the bulk of the transporter accumulates preferentially in a transferrin receptor (Tfr)-enriched recycling endosomal compartment [21–23] where it has been implicated in the regulation of vesicular pH and trafficking [24, 25] and maintenance of epithelial cell polarity [24]. In the central nervous system, NHE6 is expressed in all regions and is particularly high in the hippocampus, cortex, and Purkinje cell layer of the cerebellum [26–28] (also see Allen Brain Atlas; <http://mouse.brain-map.org>; [29]). Within hippocampal neurons, NHE6 is present in both the soma and neurites, where it overlaps with known early and recycling endosomal markers and is especially prevalent in vesicles containing the glutamatergic α -amino-3-hydroxy-5-methyl-4-isoxazolepropionic acid receptor (AMPA) subunit GluA1 [27] and the neurotrophin tropomyosin-related kinase receptor B (TrkB) which preferentially binds brain-derived neurotrophic factor (BDNF) and neurotrophin-4 (NT-4) [28]. Like AMPA [30] and TrkB [31], NHE6 is recruited into dendritic spines (i.e., the postsynaptic compartment of the majority of excitatory synapses) upon induction of *N*-methyl-D-aspartate receptor (NMDAR)-dependent long term potentiation, thereby implicating its involvement in learning and memory processes [27]. In a NHE6 null mouse model, hippocampal neurons showed reduced axonal and dendritic arborization and decreased circuit activity [28] as well as a progressive loss of cerebellar Purkinje cells

[26], further linking its participation in processes underlying neuronal growth, maturation, function and survival.

A variety of inherited and de novo mutations in NHE6 have recently been identified in CS patients, including frameshifts, nonsense, missense and deletions, although their precise consequences on neuronal function have yet to be elucidated [2, 3, 8, 9, 11, 12, 32–41]. The majority of these mutations cause premature translation termination and loss-of-function. However mutations that do not truncate the protein may have different consequences on its membrane targeting and activity which, in conjunction with other genetic factors, may account for the phenotypic diversity of patients with CS [3]. For example, Garbern et al. [9] described an in-frame excision of three amino acids (³⁷⁰Trp-Ser-Thr³⁷², ΔWST) in the predicted ninth transmembrane helix of NHE6 that caused the protein to be largely retained in the endoplasmic reticulum (ER) [42]. While these patients displayed many of the pathophysiological and behavioural features ascribed to CS, they were distinguished by atypical accumulation of the microtubule protein tau in neuronal and glial cells of cortical and sub-cortical regions and widespread neuronal loss, features that are characteristic of adult-onset neurodegenerative disorders such as Alzheimer's disease [9]. Patients with this mutation also exhibited only occasional mild microcephaly, modest gross motor disability and absence of the dysmorphic features attributed to the Christianson and Angelman-like syndromes.

Here, we examine one of the original CS mutations identified by Gilfillan et al. [8] that results in an in-frame deletion of two highly conserved amino acids (p.E255_S256del, ΔES) in the predicted seventh transmembrane helix of a short splice-variant of NHE6 (i.e., NHE6v2). This mutant variant was found to be unstable [43], though the precise mechanism of its pathogenicity remains poorly understood. In our study, we established relevant non-neuronal and neuronal cell model systems to gain greater insight into the molecular and cellular consequences provoked by this mutation, but using the equally abundant longest splice-variant of NHE6 (i.e., p.E287_S288del in NHE6v1) as a template for study. Our results show that though the mutant protein assembles properly as a homodimer and is sorted to the plasma membrane, its oligosaccharide maturation, half-life and steady-state abundance are greatly reduced. In addition, the membrane trafficking of the ΔES mutant and certain other associated cargo are also impaired, ultimately eliciting cell death in both non-neuronal and neuronal cells.

Methods

Antibodies and reagents

Mouse monoclonal anti-hemagglutinin (HA) antibody was purchased from Covance Inc. (Berkeley, CA); rabbit

polyclonal anti-HA, monoclonal anti-glyceraldehyde-3-phosphate dehydrogenase (GAPDH) and monoclonal anti-GFP antibodies were obtained from Abcam Inc. (Cambridge, MA); mouse monoclonal anti-Flag M2 antibody was from Sigma; rabbit polyclonal anti-GFP antibody was from Life Technologies. Mouse monoclonal anti-human transferrin antibody was from Invitrogen. Mouse monoclonal anti-β-tubulin was from Sigma. Mouse monoclonal anti-ubiquitin antibody (P4D1) was from Santa Cruz Biotechnology. Rabbit polyclonal anti-cleaved caspase-3 (Asp175) antibody was purchased from Cell Signaling Technology (kindly provided by Dr. Peter Siegel, McGill University). Horseradish peroxidase-conjugated secondary IgG antibodies, as well as FITC-conjugated goat anti-mouse secondary Fab were purchased from Jackson ImmunoResearch Laboratories (West Grove, PA). All Alexa Fluor® conjugated secondary antibodies were purchased from Molecular Probes (Eugene, OR). Alpha-minimum essential medium (α-MEM), fetal bovine serum, penicillin/streptomycin, and trypsin-EDTA were purchased from Wisent (Saint-Bruno, QC, Canada). The DMEM/F12 medium was from Corning. All other chemical and reagents were obtained from BioShop Canada (Burlington, ON, Canada), Sigma or Fisher Scientific and were of the highest grade available.

Recombinant DNA constructs and mutagenesis

The long transcript splice-variant of human NHE6 (NHE6v1; NCBI refseq NM_001042537) was cloned from a human brain Matchmaker™ cDNA library (Clontech) using PCR methodology and was engineered to contain the influenza virus hemagglutinin (HA) (YPYDVPDYAS) epitope at its extreme C-terminal end. This construct was termed wild-type NHE6_{HA} (NHE6_{HA}-WT) and inserted into the *HindIII* and *XbaI* sites of the mammalian expression vector pcDNA3 (Invitrogen), as described previously [42]. NHE6_{HA} was then used as a template to engineer the following mutations by PCR mutagenesis: double deletion mutation of amino acids E287 and S288 (ΔE287/S288, ΔES), the conservative double substitution E287Q/S288A, and the single mutations E287A, E287Q, and S288A.

The same template (NHE6_{HA}) was also used to introduce a triple Flag epitope (AAADYKDDDDKGDYKDDDDKGDYKDDDDKAAA) in the first extracellular loop immediately after residue Met⁵³. First, PCR was used to engineer an in-frame *NotI* restriction site after M53, followed by the introduction of annealed primers representing the 3xFlag epitope, which generated a construct termed 3FNHE6_{HA}. This construct was further used as a template to introduce the ΔE287/S288, E287Q/S288A, E287Q, and S288A mutations using PCR mutagenesis.

Green fluorescent protein (GFP) C-terminal-tagged forms of NHE6 WT and ΔES mutant were constructed

by insertion between the *XhoI* and *HindIII* restriction sites of the pAcGFP1-N1 vector (BD Biosciences Clontech, Palo Alto, CA). Insertion of the different epitope tags in the various positions did not alter the biochemical properties or cellular distribution of exogenous NHE6 compared to the endogenous protein [42]. All constructs were sequenced to insure that no additional mutations were introduced during PCR.

Cell culture

Chinese hamster ovary AP-1 cells [44], HeLa, and HEK293 cells were cultured in α -MEM supplemented with 10 % fetal bovine serum, penicillin (100 units/mL), streptomycin (100 μ g/mL), and 25 mM NaHCO_3 (pH 7.4). Human neuroblastoma SH-SY5Y cells were cultured in high glucose Dulbecco's Modified Eagle Medium (DMEM)/Ham's F12 medium supplemented with 10 % fetal bovine serum.

Primary cultures of mouse hippocampal neurons were prepared from post-natal day (PD) 0–2 day C57BL/6 and L17 transgenic mice as previously described [27]. The L17 mice line express membrane-targeted enhanced GFP (mGFP) under the control of a Thy1.2 promoter cassette in a subset of hippocampal neurons, allowing the visualization of cell soma and other neuronal structures. To prepare cultures, the pups were decapitated, their brains were removed, and the hippocampi were dissected out. These hippocampi were maintained in chilled HBSS supplemented with 0.1 M HEPES buffer and 0.6 % glucose, then digested with 165 U papain for 20 min at 37 °C. Neurons and glia were dissociated by trituration and suspended in DMEM supplemented with 1 % penicillin-streptomycin, 10 % FBS, and 0.6 % glucose. Cells were then plated onto poly-D-lysine-coated 10 mm coverslips at an approximate density of 12,000 cells/cm² and placed in an incubator at 37 °C. Twenty-four hours later, plating media was then replaced with Neurobasal-A growth media supplemented with 2 % B-27 supplement, 1 % GlutaMAX, and 1 % penicillin-streptomycin. Cultures were then fed every 3–4 days and maintained at 37 °C in a humidified environment of 95 % air, 5 % CO₂.

Western blotting

For western blot analyses, AP-1, HeLa or SH-SY5Y cells were grown in 10-cm dishes and transiently transfected with 5 μ g of plasmid DNA encoding NHE6_{HA} wild-type or mutant constructs using Lipofectamine2000™ (Invitrogen) according to the manufacturer's recommended procedure. Cell lysates were prepared following 6 to 48 h post-transfection (as indicated in the figure legends) by washing cells twice on ice with ice-cold PBS, followed by scraping in 0.5 mL of lysis buffer (0.5 % NP40/0.25 % sodium deoxycholate/PBS supplemented with protease

inhibitor cocktail (Roche Diagnostics). Lysates were incubated for 30 min on a rocker at 4 °C, and then centrifuged for 20 min at 4 °C to pellet the nuclei and cellular debris. Twenty μ g of protein from the resulting supernatants were eluted in sodium dodecyl sulfate (SDS)-sample buffer (50 mM Tris-HCl, pH 6.8, 1 % SDS, 50 mM dithiothreitol, 10 % glycerol, 1 % bromophenol blue), and subjected to 9 % SDS-polyacrylamide gel electrophoresis (SDS-PAGE), then transferred to polyvinylidene fluoride (PVDF) membranes (Millipore, Nepean, Ontario, Canada) for immunoblotting. The membranes were blocked with 5 % non-fat skim milk for 1 h, then incubated with the specified primary antibodies (mouse monoclonal HA 1:5000, anti- β -tubulin 1:10,000, anti-ubiquitin 1:2000, or GAPDH 1:50,000) in PBS containing 0.1 % Tween 20, followed by extensive washes and incubation with goat anti-mouse horseradish peroxidase (HRP)-conjugated secondary antibody for 1 h. Immunoreactive bands were detected using Western Lightning™ Plus-ECL blotting detection reagents (Perkin Elmer Inc., Waltham, MA).

Endoglycosidase treatments

To obtain post-nuclear supernatants of AP-1 cells transiently expressing NHE6_{HA} WT or Δ ES (24-h transfection), cells grown in 10-cm dishes were washed with ice-cold PBS, collected in 1 ml PBS, and then pelleted at 10,000 \times g for 4 min at 4 °C. Pellets were resuspended in 300 μ l sucrose solution (250 mM sucrose, 10 mM HEPES-NaOH, 1 mM EDTA, pH 7.5), and passaged 15 times through a 26.5-gauge needle. The nuclei and insoluble cell debris were sedimented at 700 \times g for 15 min at 4 °C. The resulting post-nuclear supernatants were treated with endoglycosidases, according to the manufacturer's recommendations. First, glycoproteins were denatured in 1x denaturing buffer (0.5 % SDS, 1 % β -mercaptoethanol) at 100 °C for 10 min. Samples were then divided equally and treated with either Peptide N-glycosidase F (PNGase F) (750 units, New England Biolabs, Mississauga, ON, Canada) or Endo- β -N-acetylglucosaminidase H (Endo H) (750 units, New England Biolabs, Mississauga, ON, Canada). The enzymes were added to 30 μ l reactions and incubated overnight at 37 °C. Next day, samples were diluted with two-fold concentrated SDS-PAGE sample buffer, incubated for 30 min at room temperature, briefly centrifuged, and analyzed by SDS-PAGE and western blotting with monoclonal anti-HA antibody.

Cell surface biotinylation

AP-1 cells expressing NHE6_{HA} WT or Δ ES constructs were cultured in 10-cm dishes to sub-confluence, placed on ice and washed three times with ice-cold PBS containing 1 mM MgCl₂ and 0.1 mM CaCl₂, pH 8.0 (PBS-

CM). Next, cells were incubated at 4 °C for 30 min with the membrane-impermeable reagent N-hydroxysulfosuccinimide-SS-biotin (0.5 mg/mL) (ThermoScientific, Rockford, IL). Cells were washed and incubated twice in quenching buffer (50 mM glycine in PBS-CM) for 7 min each on ice to remove unreacted biotin. After two more washes in PBS-CM, the cells were lysed for 30 min on ice, and then centrifuged at $16,000 \times g$ for 20 min at 4 °C to remove insoluble cellular debris. A fraction of the resulting supernatant was removed and this represents the total fraction. The remaining supernatant was incubated with 100 μ L of 50 % NeutrAvidin® Agarose Resin slurry (Fisher Scientific, Whitby, ON, Canada) in lysis buffer overnight at 4 °C to extract biotinylated membrane proteins. The proteins were then resolved by SDS-PAGE and analyzed by western blotting.

Stability of NHE6 WT and Δ ES mutant

To determine the stability of wild-type and mutant NHE6, AP-1 cells were grown in 10-cm dishes and transfected with NHE6_{HA} wild-type or Δ ES mutant constructs. Twenty-four hours post-transfection, the cells were transferred to 6-well plates and further grown for 24 h. To inhibit new protein synthesis, cells were treated with cycloheximide (150 μ g/mL) in α -MEM supplemented with 10 % FBS and penicillin/streptomycin for up to 24 h. At specific time points, cells were lysed, protein concentrations were measured, and equal quantities of protein were subjected to SDS-PAGE and immunoblotting with mouse monoclonal anti-HA and anti-GAPDH antibodies. The intensity of the bands was quantified by densitometry of X-ray films exposed in the linear range and analyzed using ImageJ software.

Ubiquitination and protein degradation

To examine ubiquitination of NHE6 WT and Δ ES, AP-1 cells expressing NHE6_{HA} WT or Δ ES were lysed 24 h after transfection in lysis buffer containing 10 mM N-ethylmaleimide (Sigma). Equal amounts of total protein were pre-cleared for 2 h on Protein G-Sepharose beads™ (GE Healthcare). After removing a small fraction of the pre-cleared cell lysate for immunoblotting, the remaining lysate was divided into two equal fractions: one fraction was used to immunoprecipitate the NHE6 protein overnight at 4 °C with a rabbit polyclonal anti-HA antibody (Abcam); the second fraction was subjected to immunoprecipitation with a nonspecific rabbit IgG antibody (Southern Biotech) as a negative control. Next day, the lysates were incubated with a 50 % slurry of Protein G-Sepharose beads for 3 h at 4 °C. The beads were subsequently washed and the immunoprecipitated proteins were eluted in sodium dodecyl sulfate (SDS)-sample buffer (50 mM

Tris-HCl, pH 6.8, 1 % SDS, 50 mM dithiothreitol, 10 % glycerol, 1 % bromophenol blue). The immunoprecipitated proteins, along with aliquots representing the total lysate were subjected to 9 % SDS-polyacrylamide gel electrophoresis (SDS-PAGE), then transferred to polyvinylidene fluoride (PVDF) membranes (Millipore, Nepean, Ontario, Canada) for immunoblotting with a mouse monoclonal anti-ubiquitin antibody (Santa Cruz Biotechnology). The membranes were then stripped and reblotted with a mouse monoclonal anti-HA antibody (Covance).

AP-1 cells were cultured in 3.5-cm dishes and transfected with NHE6_{HA} WT or Δ ES using Lipofectamine2000™ (Invitrogen). Twenty-four hours after transfection, cells were treated with DMSO as control, the proteasomal inhibitors MG-132 (40 μ M) or lactacystin (30 μ M), the lysosomal inhibitors leupeptin/pepstatin (100 μ g/mL) or chloroquine (500 μ M), all in the presence of cycloheximide (150 μ g/mL) to prevent new protein synthesis. Cellular lysates were obtained after 4 and 8 h of treatment and equal amounts of proteins were subjected to SDS-PAGE and western blotting with a mouse monoclonal anti-HA antibody. The membranes were also immunoblotted with mouse monoclonal anti-GAPDH antibody as a loading control.

Co-immunoprecipitation

To test the hypothesis that WT and Δ ES mutant can heterodimerize, HeLa cells were cultured in 10-cm dishes and transfected with a total of 8 μ g of expression plasmid DNA containing NHE6_{HA} WT, NHE6v1_{GFP} Δ ES or empty vector (pCMV), either singly or in combination (4 μ g each), using FuGene6 (Promega), according to the manufacturer's instructions. Forty hours post-transfection, lysates were prepared by washing the cells twice with ice-cold PBS and scraping them into 500 μ L of cell lysis buffer (0.5 % Nonidet-P40, 0.25 % sodium deoxycholate, and protease inhibitors in PBS, pH 7.4). Cell lysates were rocked at 4 °C for 30 min and centrifuged for 20 min at $16,000 \times g$ to pellet cellular debris. Supernatants were pre-cleared for 2 h on Protein G-Sepharose beads™ (GE Healthcare). The beads were removed by brief centrifugation and a fraction of the cell lysate was removed for immunoblotting. Rabbit polyclonal anti-HA antibody (5 μ g) was added to the remaining cell lysates and incubated with gentle rocking overnight at 4 °C. Subsequently, a 50 % slurry of Protein G-Sepharose beads was added to each tube and incubated with the immunoprecipitates for 2 h at 4 °C. The immunoprecipitated proteins, as well as aliquots of initial lysates were resolved by SDS-PAGE, transferred to polyvinylidene fluoride membranes, and immunoblotted with the indicated mouse monoclonal antibodies.

Fluorescence-based endocytosis assay

AP-1 cells were grown in 10-cm dishes and transiently transfected with 6 μ g of $3F$ NHE6_{HA} WT or Δ ES DNA constructs. Twenty-four h post-transfection, cells were transferred to 12 well-plates and grown for an additional 12 to 24 h. Cells were chilled on ice, washed with ice-cold PBS-CM, pH 7.4, blocked in 10 % goat serum/PBS-CM, and then incubated with a mouse monoclonal anti-Flag antibody (1:3000) (Sigma) on ice. Internalization of the bound antibody was initiated by incubating the cells with warm (37 °C) α -MEM for the indicated time points and terminated by placing the plates on ice. Cells were washed and labeled with goat anti-mouse HRP-conjugated secondary antibody (1:1000) (GE Healthcare). After extensive washes with PBS-CM, cells were treated on ice with Amplex[®] Red reagent (Invitrogen). Aliquots were transferred to 96-well plates and fluorescence readings were taken with a POLARstar OPTIMA (BMG Labtech. Inc, Offenburg, Germany) plate reader using 544-nm excitation and 585-nm emission wavelengths. All experiments were performed in triplicates and repeated at least three times. Results were expressed as a percentage of the fluorescence recorded prior to internalization, after subtraction of the value measured with mock-transfected cells. Results are shown as mean \pm standard error of the mean (S.E.M.).

Measurement of endosomal pH

AP-1 cells were transfected with $3F$ NHE6_{HA} WT or Δ ES and cell surface resident proteins were labeled on ice with mouse monoclonal anti-Flag antibody (1:2000 dilution, Sigma-Aldrich) and FITC-conjugated goat anti-mouse secondary Fab fragment (1:1000 dilution, Jackson ImmunoResearch Laboratories, West Grove, PA). Cells were then washed in PBS-CM and chased for the indicated time points in growth medium at 37 °C. Endosomal pH was measured by single-cell fluorescence ratiometric imaging analysis (FRIA) on an Axiovert 100 inverted fluorescence microscope (Carl Zeiss MicroImaging, Toronto, ON, Canada) at room temperature equipped with a Hamamatsu ORCA-ER 1394 (Hamamatsu, Japan) cooled CCD camera and a Planachromat (63 \times NA 1.4) objective essentially as described previously [45]. Image acquisition and FRIA were performed with MetaFluor software (Molecular Devices, Downingtown, PA). Images were acquired at 490 \pm 5 and 440 \pm 10 nm excitation wavelengths, using a 535 \pm 25-nm emission filter. In each experiment, the pH of 100–1000 vesicles was determined. Mono- or multippeak Gaussian distributions of vesicular pH values were obtained with Origin 7.5 software (OriginLab, Northampton, MA). Calibration curves have been performed as previously described [45]. Briefly, *in situ* calibration was performed by clamping the vesicular pH between 4 and 7.5 in K⁺-rich medium (135 mM KCl,

10 mM NaCl, 20 mM Hepes or 20 mM MES, 1 mM MgCl₂, and 0.1 mM CaCl₂) with 10 μ M nigericin, 10 μ M monensin, 0.4 μ M bafilomycin and 20 μ M carbonyl cyanide m-chlorophenyl hydrazone (CCCP) and recording the fluorescence ratios.

Calcium-phosphate transfection

Primary neurons were transfected by calcium phosphate-mediated transfection [46]. Briefly, at 10–12 DIV, coverslips were transferred into a 35-mm dish filled with warmed preconditioned growth media. For four coverslips, 4 μ g of DNA plasmid was mixed with 50 μ l 250 mM CaCl₂ solution, which was then added to 50 μ l 2x HEPES-buffered phosphate solution, pH 7.05 to form DNA-tagged calcium phosphate precipitate. This was added dropwise to each dish of coverslips, which were then incubated at 37 °C for 90 min. Afterwards, 33 μ l of 0.3 M MES hydrate solution, pH 5.5, was added to each dish, which acidified the media to dissolve any remaining precipitate. The coverslips were returned to their original plates with fresh growth media, and cultures were then maintained at 37 °C for 48 h before being processed and fixed.

Cultures prepared from C57BL/6 mice were transfected with GFP and NHE6_{ChFP} WT and NHE6_{ChFP} Δ ES. The L17 cultures, which already express myristoylated GFP (mGFP), were instead transfected with NHE6_{ChFP} WT and NHE6_{ChFP} Δ ES and incubated with Tf-AF⁶³³ (100 μ g/ml) for 1 h at 37 °C and then fixed.

Immunofluorescence confocal microscopy

To examine the internalization of NHE6 into transferrin-containing endosomes, AP-1 cells were grown in 10-cm dishes and transfected with $3F$ NHE6_{HA} WT or Δ ES mutant. Twenty-four hours post-transfection, the cells were transferred to fibronectin-coated glass coverslips and grown for an additional 12 to 24 h (as specified in text). For the zero time point, cells were serum-depleted for 1 h, incubated with 10 μ g/ml Alexa Fluor[®] 488-conjugated transferrin (Tf-AF⁴⁸⁸) for 45 min in serum-free media at 37 °C, and then placed on ice. Cells were then labelled for 1 h on ice with mouse monoclonal anti-Flag antibody (1:2000) in PBS-CM/10 mM glucose/10 mM HEPES, pH 7.4, washed 3 times with PBS supplemented with 1 mM MgCl₂ and 0.1 mM CaCl₂ (PBS-CM), and then incubated on ice with goat anti-mouse Alexa Fluor[®] 568-conjugated secondary antibody (1:1300). After extensive washes with PBS, cells were fixed in 2 % paraformaldehyde/PBS for 20 min at room temperature and mounted onto glass slides. For the 60 min endocytosis time point, after serum depletion, cells were labeled on ice with the primary anti-Flag and secondary Alexa Fluor[®] 568-conjugated antibodies, and then chased with serum free media at 37 °C for 1 h. For transferrin labeling, the chasing media contained 10 μ g/ml Tf-AF⁴⁸⁸

during the last 45 min of chase. Cells were subsequently fixed and mounted. Cells were examined by laser scanning confocal microscopy using the ZEN software of a Zeiss LSM 710 Meta equipped with a PMT detector, with images acquired using a $63 \times /1.4$ N.A. oil immersion objective lens.

Primary hippocampal neuronal cultures were fixed with 4 % PFA/0.1 M PB, pH 7.4 (Sigma Aldrich) for 15 min at room temperature and washed with 0.1 M PB. C57BL/6 cultures immunoprocessed for cleaved caspase-3 (cCASP3) were first permeabilized for 1 min in 0.2 % Triton X-100/0.1 M PB and blocked for 1 h at room temperature in 0.2 % Triton X-100/1 % HHS/0.1 M PB before being incubated with a primary rabbit polyclonal antibody against cleaved caspase-3 (Asp175) (cCASP3) (Cell Signaling Technology, 1:300) diluted in blocking solution overnight at 4 °C. After subsequent washing, cells were incubated with a secondary goat anti-rabbit DyLight 649-conjugated secondary antibody (Jackson laboratories, 1:1000) diluted in 1 % HHS/0.1 M PB for 45 min at room temperature, washed again, and mounted. All coverslips were mounted onto SuperFrost (Menzel-Glaser) microscope slides using UltraMount fluorescence mounting medium (Dako) and left to dry overnight at room temperature in the dark. The soma of transfected neurons were then examined for cCASP3 staining to assess apoptosis.

Mounted primary hippocampal cultures were imaged using a Leica SP2 confocal microscope. Images were acquired using 40X and 63X HCXPL APO oil-immersion objectives (NAs 1.25 and 1.4, respectively). GFP was imaged using a 488 nm Ar laser line; mCherry was imaged using a 543 nm HeNe laser line, and Alexa Fluor 647, Alexa Fluor 633 and DyLight 649 were imaged using the 633 nm HeNe laser line. Channels were acquired sequentially to prevent spectral overlap of fluorophores. Optical sections of 300–500 nm were taken and frame averaged 3X at low resolution or line-averaged 2X at high resolution to improve the signal-to-noise ratio. Images were first deconvolved using Huygen's Essential software by using a full maximum likelihood extrapolation algorithm (Scientific Volume Imaging), and 3D images were compiled as maximum intensity projections using Imaris software (Bitplane Ag). Colocalization analyses between NHE6 and AF-Tfn were determined using the ImarisColoc algorithm, which generated a new channel (coloc) containing voxels representing pixels of channel overlap. This also automatically calculated Mander's coefficient M1-M2 values between NHE6 and Tf-AF⁶³³ channels from a set threshold. Thresholds were applied relatively consistently between cells in order to remove subjectivity during the analysis.

Topographical order of neuronal morphology was performed on 3D confocal images of primary hippocampal neurons prepared from C57BL/6 mice. Images were analyzed using the FilamentTracer program (Bitplane AG, Zurich, Switzerland), which semi-automatically detects 3D neuronal GFP-labeled filament structures and calculates parameters such as the number of branch points, total dendrite length and area.

Flow cytometry

To measure transferrin and EGF uptake by flow cytometry, HeLa cells were transfected with GFP alone, NHE6_{GFP} WT or Δ ES mutant using FuGene6 (Promega). Forty-eight h after transfection, the cells were serum-depleted for 2 h, and then incubated with Alexa Fluor[®] 633-conjugated transferrin (Tf-Alexa⁶³³, 10 μ g/mL) or Alexa Fluor[®] 647-conjugated EGF (EGF-Alexa⁶⁴⁷, 100 ng/ml) for 5 min at 37 °C, in the absence or presence of 10-fold excess unlabelled transferrin or EGF, respectively, followed by washes to remove unbound transferrin or EGF. Cells were detached from the plates by trypsinization and 5 μ L of the cell viability dye 7-amino-actinomycin D (7-AAD, eBioscience) was added to each cell suspension. Cells were analyzed by flow cytometry using a FACS Aria Sorter (Becton Dickinson, San Jose, CA). A gate was set around the GFP-positive cells and the amount of Tf-Alexa⁶³³ or EGF-Alexa⁶⁴⁷ taken up by 10⁴ GFP-expressing live cells (i.e., 7-AAD negative) was measured using the BD FACS Diva software.

siRNA Knockdown

HeLa cells were cultured in 6-well plates and transfected with 100 nM control siRNA pool #1 (scrambled siRNA) or SMARTpool[®] NHE6 siRNA (Dharmacon, Lafayette, CO) using Dharmafect1 transfection reagent (Dharmacon) according to the manufacturer's recommended protocol. Seventy-two hours post-transfection, the cells were serum-starved for 1.5 h and then incubated with Tf-AF⁶³³ for 20 min at 37 °C. 10⁵ cells were analyzed by flow cytometry per experiment.

Apoptosis assays

Apoptosis was measured using three independent methods: (1) a flow cytometry assay that measures changes in plasma membrane asymmetry (annexin V-allophycocyanin conjugate (Annexin V-APC) binding to phosphatidylserine) and permeability (propidium iodide, PI); (2) a luminescent assay to detect caspase 3/7 activity; and (3) an immunofluorescence-immunocytochemistry assay to detect activated cleaved caspase-3 (Asp175).

For flow cytometry, AP-1 cells were grown in 6-cm dishes and transfected with 4 μ g of GFP, NHE6v1_{GFP} WT or Δ ES using Lipofectamine2000 (Invitrogen). Forty-eight h post-transfection, the cells were washed twice with

warm (37 °C) PBS, detached using Cell Dissociation Buffer (GIBCO), and then collected by centrifugation. The cell pellets were re-suspended in PBS and labeled using the Annexin V-APC Apoptosis Detection Kit (eBioscience) according to the manufacturer's instructions. After labeling, cells were placed on ice, and 1×10^4 GFP-positive cells were examined on a BD™LSR II flow cytometer and the percentage of AnnexinV-positive cells (i.e., early apoptotic), PI-positive (i.e., necrotic), and AnnexinV/PI – double positive cells (i.e., late apoptotic), was determined.

Caspase 3/7 activity was measured using the luminescent Caspase-Glo® 3/7 assay (Promega). AP-1 cells were transfected in 10 cm dishes with 8 µg of GFP vector, NHE6v1_{GFP} wild-type or ΔES using Lipofectamine2000 (Invitrogen). Twenty-four hours after transfection, cells were sorted using a Becton Dickinson FACSaria Sorter and 5×10^4 GFP-positive cells were plated in each well of a 96-well plate. Twenty-four hours later, the assay was performed according to the manufacturer's instructions and luminescence was read in white-walled 96-well luminometer plates.

To measure apoptosis in primary hippocampal neurons, immunocytochemistry was performed on fixed neurons transfected with cytosolic GFP alone or co-transfected with GFP and NHE6v1_{ChFP} WT or ΔES using a primary rabbit polyclonal antibody against cleaved caspase-3 (Asp175) (cCASP3) (Cell Signaling Technology, 1:300) and a secondary goat anti-rabbit DyLight 649-conjugated secondary antibody (1:1000) from Jackson laboratories. The soma of transfected neurons were then examined for cCASP3 staining to assess apoptosis.

Real-time PCR (RT-PCR)

HeLa cells were grown in 6-well plates and transfected with 100 nM siRNA control pool #1 (scrambled siRNA) or SMARTpool® NHE6 siRNA (Dharmacon) using Dharmafect1 transfection reagent (Dharmacon) according to the manufacturer's recommended protocol. Total RNA was extracted with TRIzolreagent (InvitrogenCanada Inc.). Real-time PCRs were performed using IQ SYBR Green Supermix (Bio-Rad Laboratories Inc., ON) and analyzed with Gene Expression Analysis for iCycler iQ® Real-Time PCR Detection System (BioRad).

Statistical analyses

The data represent the mean ± the standard error of the mean (S.E.M.) and statistical analyses were performed by using the Student's *t*-test or a one-way analysis of variance (ANOVA) followed by a Tukey test. A minimum *p*-value of <0.05 was considered significant.

Results

Post-translational processing and stability of NHE6ΔES is impaired

A foundational study by Gilfillan et al. [8] identified four mutations in NHE6 (ΔV176-R201, H203fsX59, ΔE287-S288, R500X in the longest splice-variant of NHE6, NHE6v1, as illustrated in Fig. 1a) in patients affected by a severe form of X-linked intellectual disability originally identified in a multigenerational South African family [1] - since termed Christianson syndrome. The most subtle mutation identified in these patients that would produce a near-intact protein was the two amino acid in-frame deletion ΔE287-S288 (ΔES). These amino acids are highly conserved in all human NHE isoforms (Additional file 1: Figure S1).

To assess the consequences of ΔES deletion on NHE6 biosynthesis, the mutation was engineered into NHE6v1 which contained an HA-epitope at its C-terminus (called NHE6v1_{HA}). This construct was then examined in a subline of Chinese hamster ovary cells (AP-1 cells) that expresses negligible levels of endogenous NHE6 [27]. Previous light microscopy analyses indicated that human NHE6 is properly sorted to the plasma membrane and recycling endosomes in this cell line [42]. We now show by electron microscopy that the transporter further partitions to microvilli and other small plasma membrane projections (Additional file 1: Figure S2) present in Chinese hamster ovary cells [47]; a pattern that mimics the trafficking of NHE6 to dendritic spines of hippocampal pyramidal neurons [27]. Thus, these cells provide an ideal tractable model system to study the wild-type (WT) as well as mutant NHE6 transporters in isolation of each other. In addition to AP-1 cells, some experiments were also performed in human neuroblastoma SH-SY5Y cells which do express NHE6 natively [27]. Since NHEs assemble as homodimers [48–50], this would allow us to examine the impact of the mutation on the biosynthesis and post-translational processing of either a homodimer (ΔES/ΔES) or potentially heterodimer (WT/ΔES) in AP-1 and SH-SY5Y cells, respectively. Indeed, biochemical and cellular analyses showed that the WT and ΔES proteins can form a heterodimer protein complex by co-immunoprecipitation assays and partially colocalize in transfected cells (Additional file 1: Figure S3). As presented in Fig. 1b and c and consistent with earlier findings [21, 42], analyses of total cell lysates from AP-1 and SH-SY5Y cells showed that the WT transporter migrated identically in both preparations as multiple bands that reflect the oligomeric and post-translational oligosaccharide state of the transporter: (1) a slower migrating, high molecular weight band (~200–250 kDa) representing the fully-glycosylated dimeric form of the exchanger that does not fully dissociate under SDS-PAGE conditions; (2) a major diffuse, fully-

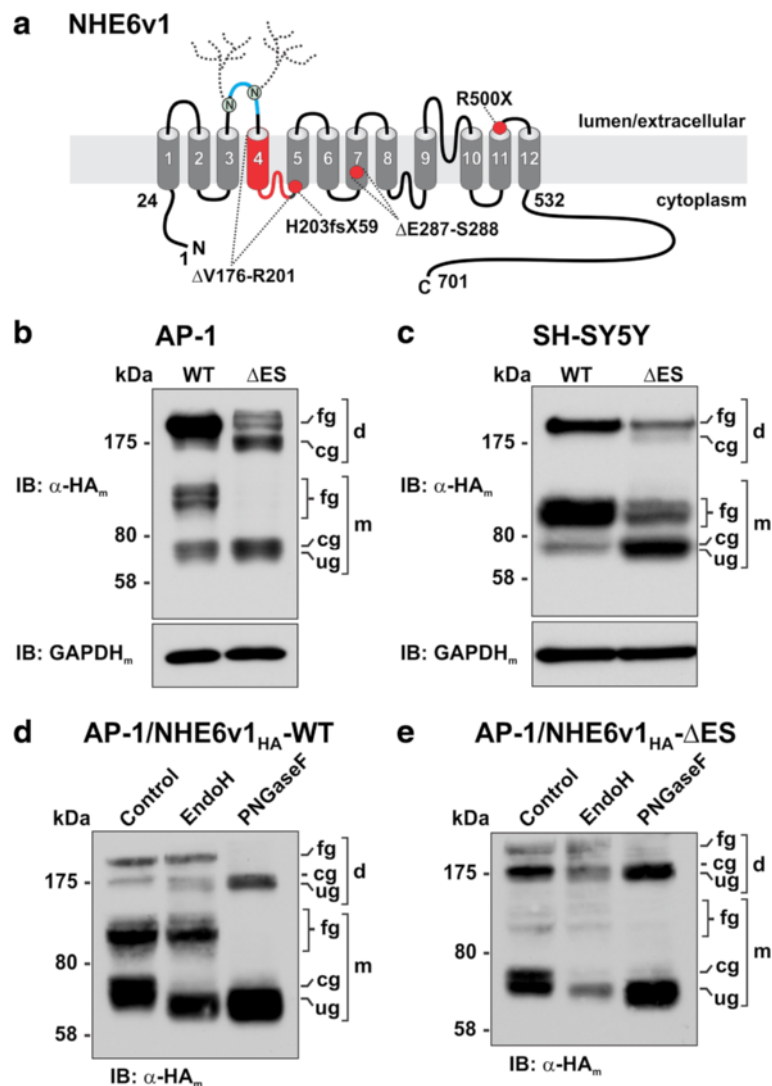


Fig. 1 Expression and post-translational processing of NHE6 ΔES mutant protein is impaired in transfected AP-1 and SH-SY5Y cells. **a** Schematic drawing of the predicted membrane topology of mammalian NHE6v1 (based on sequence alignment and transmembrane organization of NHE1 proposed by Wakabayashi et al. [127] and Nygaard et al. [128]) and locations of mutations (red shading) identified by Gilfillan et al. [8] in patients with Christianson syndrome. The blue shading in the second extracellular loop (EL2) represents the additional 32 amino acids (residues 145–176) present in the NHE6v1 splice-variant. Two predicted N-glycosylation sites within EL2 are also illustrated. **b** AP-1 and **c** SH-SY5Y cells were transiently transfected (24 h) with NHE6_{HA} WT or ΔES mutant. Total cell lysates of WT and ΔES-transfectants were examined by SDS-PAGE. The immunoblots were probed with a mouse monoclonal anti-HA antibody (α-HA_m) to detect NHE6v1. NHE6v1 migrates as multiple bands: slower migrating high molecular weight bands representing the fully-glycosylated (fg) and core-glycosylated (cg) dimeric forms of the exchanger (~200 and 175 kDa, respectively) that do not fully dissociate under SDS-PAGE conditions and faster migrating fully-glycosylated (fg, ~100 kDa) and core-glycosylated (cg, ~70 kDa) and unglycosylated (ug, ~65 kDa) forms of the monomeric protein. To control for protein loading, the blots were reprobed with a mouse monoclonal anti-GAPDH antibody (α-GAPDH_m). **d, e** To confirm the nature of the oligosaccharide modifications of the NHE6 bands, AP-1 cells transiently transfected (24 h) with WT or ΔES constructs were lysed in non-detergent buffers and post-nuclear supernatants were left untreated or incubated with either endoglycosidase H (EndoH), which cleaves only asparagine-linked mannose-rich oligosaccharides (i.e., core-glycosylated) but not more highly processed complex oligosaccharides (i.e., fully-glycosylated), or peptide-N-glycosidase F (PNGaseF) which cleaves between the innermost N-acetylglucosamine and asparagine residues of all oligosaccharide structures (i.e., high mannose, hybrid, and complex). The lysates were then subjected to SDS-PAGE and immunoblotting with an α-HA_m antibody. The data are representative of three independent experiments

glycosylated form(s) of the monomeric protein (~100–120 kDa); and (3) minor faster migrating, lower molecular weight bands characteristic of the newly synthesized core-glycosylated (~70 kDa) or unglycosylated (~65 kDa)

monomers. By contrast, the level of expression of the ΔES mutant was noticeably reduced compared to WT in both cell lines, but especially in AP-1 cells. Densitometric analysis of the immunoblots (using multiple exposures of

the immunoblots to ensure the signal intensities of the bands were within the linear range of the X-ray film) indicated that the levels of expression of the Δ ES mutant in AP-1 and SH-SY5Y cells were 22.1 ± 3.2 ($n = 3$) and 79.8 ± 4.0 ($n = 3$) of WT levels (normalized to GAPDH expression), respectively. Unlike WT, in both cell lines the Δ ES mutant migrated predominantly as a single band at the level of the immature core-glycosylated or unglycosylated monomers. However, fainter diffuse bands corresponding to the predicted fully-glycosylated monomer (~ 100 – 120 kDa) and/or the fully- (~ 250 kDa) and core-glycosylated (~ 175 kDa) dimers were visible, suggesting that a fraction of the mutant protein is capable of undergoing further processing and oligosaccharide maturation. The similar patterns of expression of Δ ES in both cell lines also indicate that though the overall abundance of the Δ ES mutant was greater in the SH-SY5Y cells, possibly due to stabilizing effects mediated by dimerization with endogenous WT NHE6, the relative oligosaccharide processing of the exogenous Δ ES mutant remained compromised.

To confirm the post-translational oligosaccharide state of the proteins, cell lysates of AP-1 cells transiently expressing NHE6v1_{HA} WT or Δ ES constructs were prepared using detergent-free buffers and then subjected to treatment with either endoglycosidase H (EndoH), which cleaves only asparagine-linked mannose-rich oligosaccharides (i.e., core-glycosylated) but not more highly processed complex oligosaccharides (i.e., fully-glycosylated), or peptide-N-glycosidase F (PNGaseF) which cleaves between the innermost N-acetylglucosamine and asparagine residues of all oligosaccharide structures (i.e., high mannose, hybrid, and complex). As shown in the immunoblots presented in Fig. 1d and e for WT and Δ ES, respectively, EndoH treatment decreased the size of only the core-glycosylated dimeric ($\sim 175 \rightarrow \sim 165$ kDa) and monomeric ($\sim 70 \rightarrow \sim 65$ kDa) proteins for both WT and Δ ES, whereas the more diffuse fully-glycosylated dimeric (~ 250 kDa) and monomeric (~ 100 – 120 kDa) bands were unaffected. Conversely, PNGaseF removed essentially all the oligosaccharide moieties for both WT and Δ ES, resulting in smaller dimeric and monomeric bands that migrated at ~ 165 and ~ 65 kDa, respectively.

To assess the relative contribution of Glu²⁸⁷ and Ser²⁸⁸ to the observed processing behaviour, we engineered the following point mutations into NHE6v1: the single conservative (i.e., E287Q) and non-conservative (i.e., E287A or S288A) substitutions as well as the double substitution E287Q/S288A. The electrophoretic profiles of the conservative E287Q as well as the S288A mutants appear similar to WT (Additional file 1: Figure S4). By contrast, mutants containing the double E287Q/S288A and single non-conservative E287A substitutions showed reduced abundance, though not as severe as Δ ES. Collectively, these data suggest both residues work synergistically

to promote the proper maturation of NHE6v1, though Glu²⁸⁷ appears more critical.

The marked reduction in abundance of the Δ ES mutant might be due to impaired biosynthetic maturation, reduced stability, or a combination of the two. To obtain an approximate measure of their biosynthetic maturation, AP-1 cells were transiently transfected with NHE6v1_{HA} WT or Δ ES constructs, and cellular lysates were obtained at periodic intervals over 48 h. Quantitative immunoblot analysis revealed that the WT protein is efficiently processed to the fully-glycosylated mature form (monomer and dimer) within 12 h, such that at 36 h most of the transiently synthesized protein is fully processed (Fig. 2a, c). On the contrary, while protein production and dimer assembly of the Δ ES mutant are similar to WT during the first 6–12 h, the subsequent post-translational maturation of the protein is deficient, as revealed by a marked reduction in the addition of complex sugars at 18 h which is more apparent in the dissociated monomeric form (Fig. 2b, d). Moreover, the abundance of Δ ES is greatly decreased at 36 and 48 h after transfection relative to WT, suggesting that it might be subject to more rapid degradation.

In order to estimate the half-lives of the respective proteins, AP-1 cells were transfected with WT or Δ ES for 24 h and then treated with cycloheximide for an additional 2 to 24 h in order to block de novo protein synthesis while tracking the fate of the previously synthesized transporters. As shown in the immunoblots presented in Fig. 3a and quantified in Fig. 3b, the WT protein was relatively stable even after 24 h of treatment ($t_{1/2} > 24$ h). By contrast, the Δ ES mutant was rapidly degraded with a calculated half-life of ~ 2.5 h. As a loading control, the expression of the glycolytic enzyme glyceraldehyde-3-phosphate dehydrogenase (GAPDH) was measured and found to be invariant over the treatment period. The enhanced degradation of the Δ ES mutant could arise by shuttling the defective protein to proteasomes and/or lysosomes, pathways previously implicated in the proteolysis of the shorter NHE6v2- Δ ES splice variant [43]. Incubating the cells with MG132 or lactacystin, two widely used inhibitors of the proteasomal machinery, concurrently with cycloheximide did not noticeably alter the levels of NHE6 WT over a subsequent 8-h period compared to diluent (dimethylsulfoxide, DMSO) controls (Fig. 3c), whereas they markedly abrogated the decline in the levels of Δ ES (Fig. 3d). Similarly, incubating the transfected cells with lysosomal inhibitors leupeptin/pepstatin or chloroquine did not noticeably affect the abundance of the WT transporter, whereas degradation of the Δ ES mutant was lessened significantly by either treatment regimen. These results reveal that deletion of amino acids Glu²⁸⁷ and Ser²⁸⁸ in NHE6v1_{HA} drastically decreases the stability of the

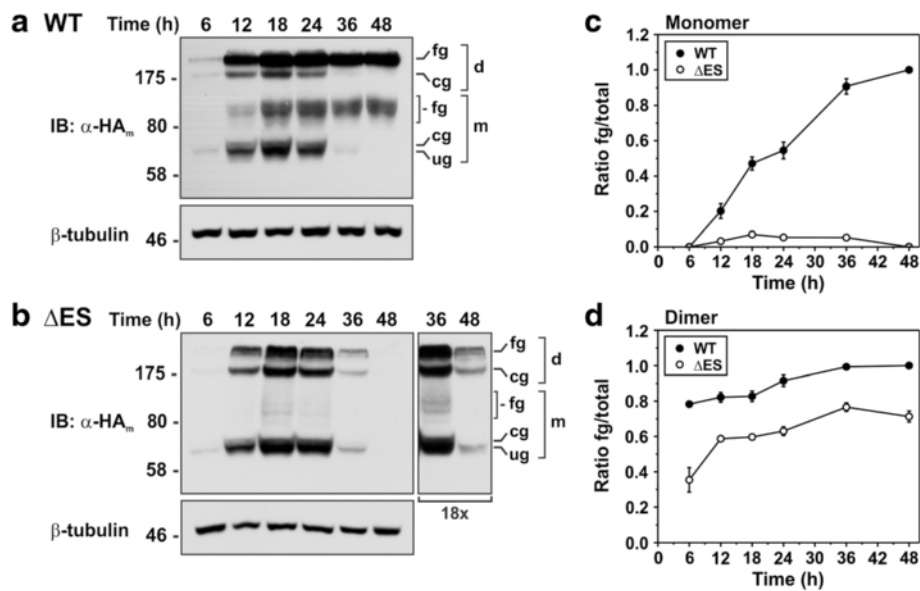


Fig. 2 Biosynthetic maturation of NHE6 is reduced for the Δ ES mutant. AP-1 cells were transiently transfected with **a** NHE6v1_{HA} WT or **b** Δ ES and lysed at the indicated time points over a 48 h period. Equal amounts of proteins were subjected to SDS-PAGE and immunoblotting with a monoclonal anti-HA antibody (α -HA). The identities of the various NHE6 bands are as described in the legend to Fig. 1. For the Δ ES immunoblot in panel **B**, a longer X-ray film exposure (18X) of the 36 h and 48 h time points is also shown. The same immunoblots were also probed with a monoclonal anti- β -tubulin antibody as a loading control. **c-d** Densitometric quantification of the relative abundances of the monomeric and dimeric forms of WT or Δ ES was assessed using ImageJ software and expressed as ratios of fully glycosylated/total protein (fg/total). For quantification, multiple exposures of the immunoblots were taken to ensure the signal intensities of the bands were within the linear range of the X-ray film. Data are shown as mean \pm standard error of the mean (S.E.M.) of four different experiments

protein. Moreover, this degradation appears to be performed by two pathways; initially by the proteasomal machinery indicating that disposal of the mutant protein is mediated by the endoplasmic reticulum-associated degradation (ERAD) pathway [51, 52] and subsequently by the peripheral (i.e., plasma membrane and endosomes) protein quality control machinery that sorts conformationally impaired membrane proteins that escape the ERAD pathway to lysosomes (i.e., endosomal sorting complex required for transport (ESCRT)-dependent lysosomal degradation) [53, 54].

A common molecular signature of misfolded proteins targeted for degradation by the ERAD or peripheral quality control machinery is enhanced multi-monoubiquitination or polyubiquitination [52, 55–57]. To test biochemically for increased levels of ubiquitin, NHE6v1_{HA} WT and Δ ES were transiently expressed (24 h) in AP-1 cells, followed by immunoprecipitation with a rabbit polyclonal antibody against the HA-epitope (α -HA_p) and immunoblotting with a monoclonal anti-ubiquitin antibody (α -Ub_m). As illustrated in Fig. 4a and quantified by densitometry in Fig. 4b, the levels of ubiquitination of Δ ES were markedly increased (~13-fold) relative to WT on a protein mass basis, as revealed by stripping the ubiquitin-probed immunoblot and reblotting with a monoclonal anti-HA antibody (α -HA_m) to detect NHE6v1_{HA}. The visibly diffuse signals for ubiquitin represent various levels of ubiquitination of

NHE6 monomers and dimers that would increase their molecular weight, extending from ~75 to >250 kDa.

Cell surface abundance and internalization kinetics of NHE6 Δ ES are reduced in AP-1 cells

Although NHE6 WT accumulates in a perinuclear recycling endosomal compartment, a minor fraction (i.e., ~5–10 % of total NHE6) resides at the plasma membrane as the transporter transits along the recycling endosomal pathway [22, 42]. To investigate whether the Δ ES mutant can traffic to the cell surface, plasmalemmal localization was measured biochemically in transfected AP-1 cells using a cell surface biotinylation assay [58]. For these experiments, a triple Flag epitope-tag was inserted in the first extracellular loop of WT and Δ ES (3_FNHE6v1_{HA}-WT and 3_FNHE6v1_{HA}- Δ ES) as illustrated Fig. 5a (upper panel). Insertion of epitopes in this position has no discernible effects on the processing, trafficking and function of the transporter [22, 42]. As shown in the immunoblot in Fig. 5a (lower panel), the extracted biotinylated cell surface fraction of the WT protein was markedly higher compared to the Δ ES mutant, and essentially only fully-glycosylated transporters (intact dimer and dissociated monomer) were detected in the cell surface-enriched fraction. The Δ ES mutant protein also reached the cell surface mainly in its dimeric fully-glycosylated form, although a minor

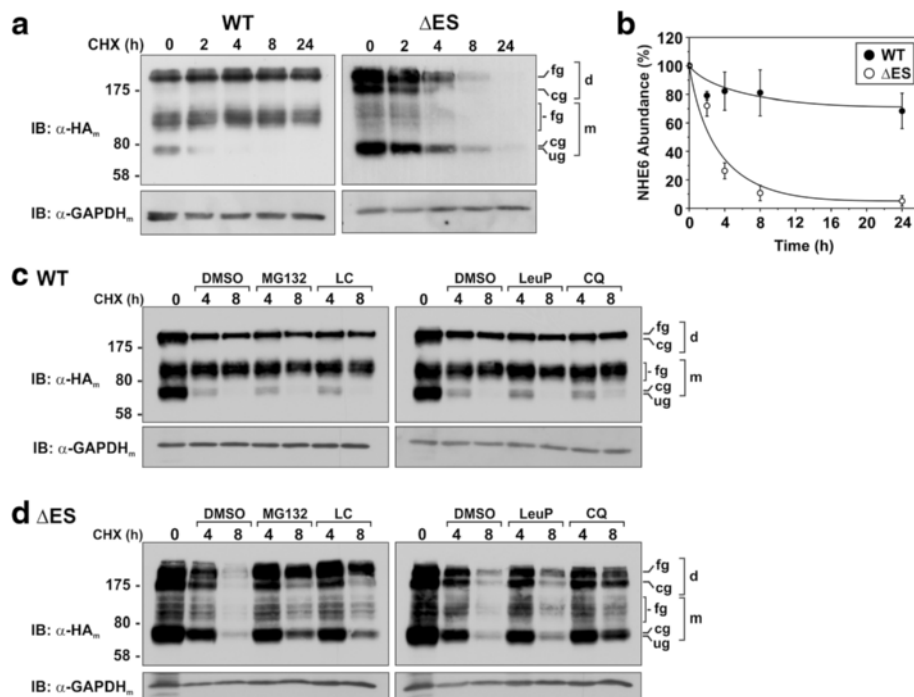
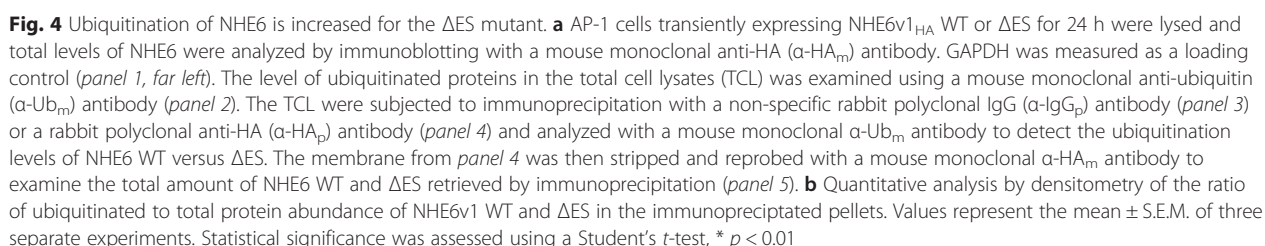


Fig. 3 Stability of NHE6 is diminished for ΔES mutant. **a** AP-1 cells were transiently transfected with NHE6v1_{HA} WT or ΔES mutant for 24 h and then treated with 150 μg/mL cycloheximide for the indicated time points, lysed and analysed by SDS-PAGE and immunoblotting with a mouse monoclonal anti-HA (α-HA_m) antibody. Equal amounts of proteins were loaded, as shown by probing the membranes with a monoclonal anti-GAPDH antibody (α-GAPDH_m). **b** Quantitative analysis by densitometry of NHE6v1 WT and ΔES protein abundance (normalized to GAPDH levels) as a function of time in the presence of cycloheximide. Values represent the mean ± S.E.M. of three separate experiments. **c-d** AP-1 cells were transiently transfected with NHE6v1_{HA} WT (**c**) or ΔES (**d**) for 24 h and then treated with 150 μg/mL cycloheximide for the indicated time points in the presence of DMSO (vehicle), the proteasomal inhibitors MG-132 (40 μM) or lactacystin (LC, 30 μM) (left panels), or the lysosomal inhibitors leupeptin/pepstatin (LeuP, 100 μg/ml) or chloroquine (CQ, 500 μM) (right panels). Cellular lysates were analysed by immunoblotting with a mouse monoclonal α-HA_m antibody. Membranes were also probed with a mouse monoclonal α-GAPDH_m antibody as a loading control

amount of the core-glycosylated protein was also detected. The non-biotinylated fractions of WT and ΔES, representative of their intracellular pools that comprise ~90–95 % of total expression, were comparable to their respective abundances in the total cell lysates, as expected. To ensure that the extracted cell surface biotinylated proteins were not contaminated with intracellular proteins, the immunoblots were probed simultaneously with an antibody to GAPDH. GAPDH was readily detected in the total cell lysates and non-biotinylated fractions, but not in the plasmalemmal fractions; thereby confirming the selective enrichment of cell surface proteins. The presence of NHE6v1 WT and ΔES at the plasma membrane was further confirmed visually by imaging of fixed, non-permeabilized AP-1 cells (Fig. 5b). These analyses also showed that the cell surface distribution of NHE6 was discontinuous or punctate. The basis for this is unclear, but may reflect sites of exocytosis and/or endocytosis though other explanations are also possible.

To further characterize the subcellular distribution of NHE6v1 WT and ΔES, dual immunolabelling experiments

were performed with various organellar markers using detergent permeabilized cells. As expected, the WT transporter highly co-localized with internalized Alexa Fluor® 594-conjugated transferrin (Tf-AF⁵⁹⁴), a marker of recycling endosomes that is internalized in an adaptor protein 2 (AP2)/clathrin-dependent manner. Conversely, the fluorescence signals for the ΔES mutant showed minimal overlap with Tf-AF⁵⁹⁴ and, furthermore, the intracellular accumulation of Tf-AF⁵⁹⁴ in cells expressing ΔES was visibly reduced relative to neighboring untransfected cells (Fig. 5c). More quantitatively, by calculating the Mander's overlap coefficient, a statistical parameter that describes the degree of channel overlap that is not dependent upon correlated intensity, the degree of colocalization was significantly reduced for the ΔES mutant compared to WT (i.e., WT-Tf, 0.80 ± 0.05 , versus ΔES-Tf, 0.36 ± 0.03 , $p < 0.01$). Additional subcellular localization analyses showed that immunostaining of ΔES mutant had minimal overlap with signals for the transfected ER marker KDEL_{GFP} [59] and endogenous early endosomal marker EEA1 [60], whereas it overlapped strongly with the transfected late endosomal/multivesicular body marker



Having established that a fraction of ${}_{3F}NHE6_{HA}$ ΔES can reside at the cell surface and intracellular vesicles, we next assessed whether its rate of internalization was different from that of the WT protein. To this end, ${}_{3F}NHE6v1_{HA}$ WT and ΔES were transiently expressed in AP-1 cells and their internalization was examined both visually by confocal microscopy and quantitatively using a cell-based enzyme-linked immunosorbent assay [62]. For image analysis, the cells were preincubated for 45 min with Alexa Fluor® 488-conjugated transferrin (Tf-AF⁴⁸⁸) to label the recycling endosomal compartment, then placed on ice and incubated with primary mouse monoclonal anti-Flag antibody and Alexa Fluor® 568-conjugated goat anti-mouse secondary antibody to label cell surface ${}_{3F}NHE6v1_{HA}$, followed by internalization of the labelled pool at 37 °C for 60 min. Confocal microscopy analysis of these cells revealed the presence of both WT and ΔES at the cell surface before the initiation of endocytosis (Fig. 6a, *first row of upper and lower*

panels). After 60 min of internalization, WT was highly concentrated in the perinuclear Tf-AF⁴⁸⁸-containing recycling endosomal pool (Fig. 6a, upper panel, second row). By comparison, the punctate signals for ΔES mutant and Tf-AF⁴⁸⁸ were more dispersed throughout the cell after 60 min of internalization rather than coalescing into a more compact perinuclear compartment, but nevertheless were partially overlapping. However, similar to results described in Fig. 5c, the accumulation of Tf-AF⁴⁸⁸ by the ΔES-expressing cells was visibly diminished compared to neighboring non-transfected cells (Fig. 6a, lower panel, second row). Quantitative measurements of NHE6 internalization using a cell-based enzyme-linked immunosorbent assay showed that the WT transporter was endocytosed more rapidly than the ΔES mutant (Fig. 6b). Fitting the data to a first order exponential decay function yielded time constants of 2.76 ± 0.48 and 4.81 ± 2.68 min for WT and ΔES, respectively. Collectively, these results indicate that the sequence ²⁸⁷Glu-Ser²⁸⁸ is important for the efficient biosynthetic maturation and stability of NHE6, which in turn seemingly affects the internalization of NHE6-containing recycling endosomes and associated vesicular cargo.

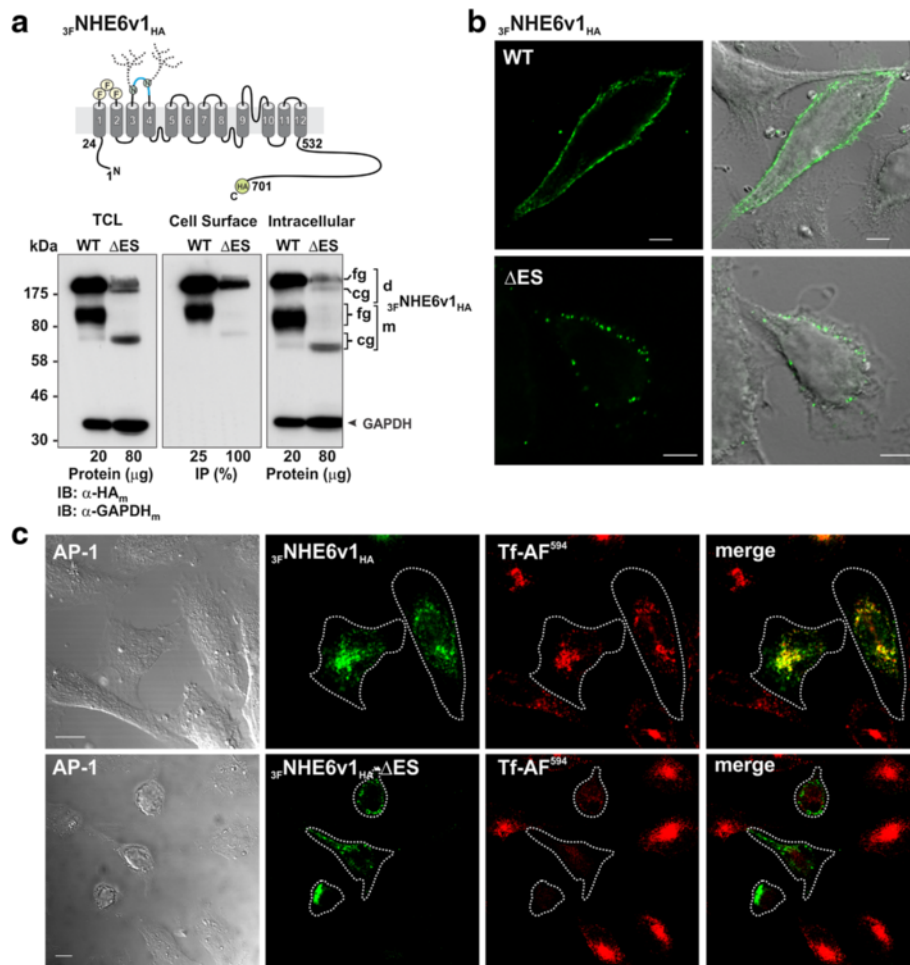
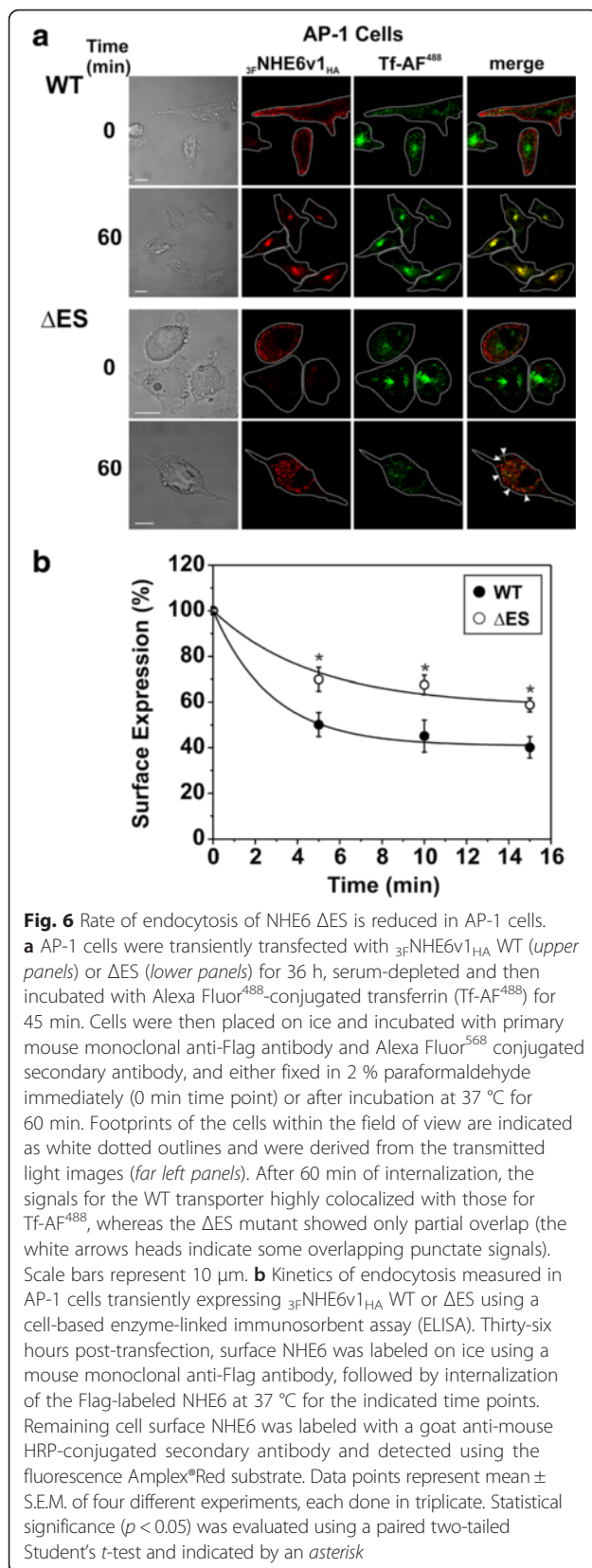


Fig. 5 Subcellular distribution of NHE6 Δ ES is altered in AP-1 cells. **a** Plasma membrane location of NHE6v1 as measured biochemically using a cell-surface biotinylation assay. To detect cell surface expression of NHE6v1, a triple Flag epitope-tag was inserted into the first predicted extracellular loop of NHE6v1_{HA} ($3F$ NHE6v1_{HA}), as illustrated in the upper panel. AP-1 cells were transiently transfected with $3F$ NHE6v1_{HA} WT or Δ ES for 36 h and cell surface proteins were labeled with biotin as described in 'Material and Methods'. Total cell lysates (TCL) were prepared and a small portion representing the total fraction was removed. The remaining supernatants containing equal amounts of total protein for WT and Δ ES were loaded onto NeutrAvidin® Agarose beads to purify the biotinylated cell surface proteins from the non-biotinylated (intracellular) proteins. For the TCL and the remaining non-biotinylated fractions, aliquots containing 20 μ g and 80 μ g protein for WT and Δ ES, respectively, were examined by Western blotting (left and right lower panels, respectively). For the plasma membrane fraction, 25 % and 100 % of the biotinylated proteins extracted from the total cell lysates of WT and Δ ES transfectants, respectively, were subjected to Western blotting (middle lower panel). All immunoblots were probed with mouse monoclonal anti-HA_m antibody to detect NHE6 and anti-GAPDH_m antibody to assess the enrichment of the biotinylated fraction, as GAPDH is a cytosolic protein. **b** Confocal fluorescence microscopy and transmitted light images of fixed non-permeabilized AP-1 cells showing surface expression of $3F$ NHE6v1_{HA} WT or Δ ES. Scale bars represent 5 μ m. **c** AP-1 cells were transiently transfected with $3F$ NHE6v1_{HA} WT (upper panels) or Δ ES (lower panels). Thirty-six h after transfection, cells were loaded with Alexa Fluor⁵⁹⁴-labelled transferrin (Tf-AF⁵⁹⁴, 10 μ g/mL) for 45 min, fixed in 4 % paraformaldehyde, permeabilized, mounted onto glass slides and then examined by confocal microscopy. Footprints of the transfected cells are indicated as white dotted outlines and were derived from the transmitted light images (far left panels). Scale bars represent 10 μ m

NHE6-mediated stimulation of transferrin, but not EGF, uptake is lost in cells expressing the Δ ES mutant

The above imaging results indicated that the uptake of Tf-AF⁴⁸⁸ by Δ ES-expressing cells was impaired relative to untransfected neighbouring cells. This observation is consistent with a previous study [25] which reported that siRNA knockdown of NHE6 expression in HeLa cells also decreased internalization of the transferrin

receptor (TfR). To determine the effect of the Δ ES mutant on internalization of Tf more quantitatively, we developed a flow cytometry-based assay to measure the uptake of red Alexa Fluor® 633-conjugated Tf (Tf-AF⁶³³). For these experiments, HeLa cells were used instead of AP-1 cells because the signal to noise ratio of Tf-AF⁶³³ uptake was much greater (4-fold) in HeLa versus AP-1 cells at the early linear phase of endocytosis (i.e., 5 min



uptake) (Fig. 7a), presumably due to the higher plasma membrane and total cellular abundance (3- to 4-fold) of the TfR in HeLa cells (Fig. 7b). To this end, internalization of Tf-AF⁶³³ was monitored by flow cytometry in live HeLa cells transiently expressing GFP alone or GFP-tagged constructs of NHE6 WT or Δ ES (Fig. 7c). Live cells were distinguished from non-viable cells by their ability to exclude the membrane-impermeant fluorescent dye 7-amino actinomycin D (7-AAD). The median intensity fluorescence (M.I.F.) of internalized Tf-AF⁶³³ was measured in 10⁴ live (i.e., 7-AAD negative) GFP-positive HeLa cells. As illustrated in Fig. 7d, cells expressing WT_{GFP} exhibited a significant increase in Tf-AF⁶³³ uptake compared to GFP-only expressing cells (GFP: 100 \pm 6 %; WT_{GFP}: 145 \pm 5 %; $p < 0.01$, one-way ANOVA followed by a Tukey test). However, this stimulation was not evident in cells expressing Δ ES_{GFP} and, if anything, showed a slight, albeit statistically non-significant, decrease to 85 \pm 7 % ($p = 0.26$) of GFP control levels, suggesting that the mutant is defective in enhancing the uptake of Tf-AF⁶³³ and possibly other cargo internalized via AP2/clathrin-dependent endocytosis. To validate that the measured fluorescent signal was due to receptor-mediated uptake of Tf-AF⁶³³ rather than non-specific bulk endocytosis, parallel competition experiments were performed in the presence of 10-fold excess unlabeled Tf. As shown in Fig. 7e, the fluorescent signal was dramatically reduced to background levels in the presence of competing unlabeled Tf, suggesting that the measurements are indicative of receptor-mediated endocytosis of fluorescently-labelled Tf. Moreover, reducing endogenous NHE6 levels in HeLa cells using siRNA (Fig. 7f) decreased Tf-AF⁶³³ uptake by ~23 % (77 \pm 2; $p < 0.01$, one-sample Student's *t*-test) relative to controls (Fig. 7g). Hence, up- or down-regulation of NHE6 expression reciprocally modulates the endocytosis of the ligand-bound TfR.

Mechanistically, the elevated uptake of Tf-AF⁶³³ in NHE6_{GFP}-WT expressing HeLa cells could arise from an enhanced rate of NHE6-dependent endocytosis due to the elevated abundance of NHE6. However, overexpression of NHE6_{GFP}-WT in HeLa cells may also increase the abundance of the TfR at the cell surface due to enhanced recycling or exocytosis of the receptor and thereby increase net Tf-AF⁶³³ uptake, an effect that is abolished by the Δ ES mutation. To examine this latter hypothesis, TfR cell surface levels were examined using a biotinylation assay in HeLa cells expressing GFP, WT_{GFP} or Δ ES_{GFP}. As shown in Fig. 7h, the levels of TfR at the cell surface were significantly higher (~1.6 fold) in HeLa cells expressing WT_{GFP} as compared to cells expressing GFP alone. By contrast, in cells expressing Δ ES_{GFP} no enhanced recruitment of TfR at the plasma membrane was observed. Thus, NHE6 expression levels appear to

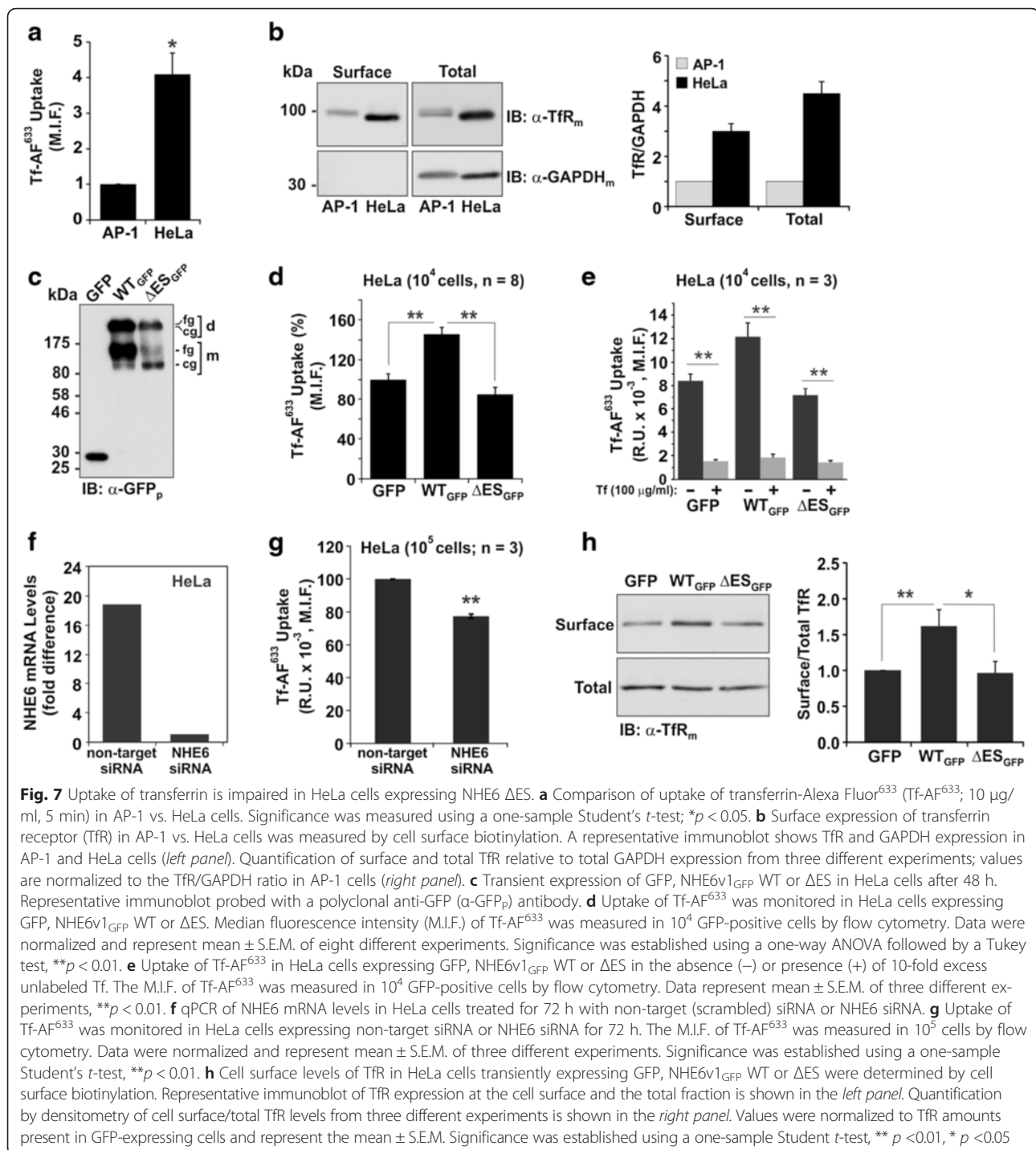


Fig. 7 Uptake of transferrin is impaired in HeLa cells expressing NHE6 ΔES. **a** Comparison of uptake of transferrin-Alexa Fluor⁶³³ (Tf-AF⁶³³, 10 μg/ml, 5 min) in AP-1 vs. HeLa cells. Significance was measured using a one-sample Student's *t*-test; **p* < 0.05. **b** Surface expression of transferrin receptor (TfR) in AP-1 vs. HeLa cells was measured by cell surface biotinylation. A representative immunoblot shows TfR and GAPDH expression in AP-1 and HeLa cells (left panel). Quantification of surface and total TfR relative to total GAPDH expression from three different experiments; values are normalized to the TfR/GAPDH ratio in AP-1 cells (right panel). **c** Transient expression of GFP, NHE6v1_{GFP} WT or ΔES in HeLa cells after 48 h. Representative immunoblot probed with a polyclonal anti-GFP (α-GFP_p) antibody. **d** Uptake of Tf-AF⁶³³ was monitored in HeLa cells expressing GFP, NHE6v1_{GFP} WT or ΔES. Median fluorescence intensity (M.I.F.) of Tf-AF⁶³³ was measured in 10⁴ GFP-positive cells by flow cytometry. Data were normalized and represent mean ± S.E.M. of eight different experiments. Significance was established using a one-way ANOVA followed by a Tukey test, ***p* < 0.01. **e** Uptake of Tf-AF⁶³³ in HeLa cells expressing GFP, NHE6v1_{GFP} WT or ΔES in the absence (-) or presence (+) of 10-fold excess unlabeled Tf. The M.I.F. of Tf-AF⁶³³ was measured in 10⁴ GFP-positive cells by flow cytometry. Data represent mean ± S.E.M. of three different experiments, ***p* < 0.01. **f** qPCR of NHE6 mRNA levels in HeLa cells treated for 72 h with non-target (scrambled) siRNA or NHE6 siRNA. **g** Uptake of Tf-AF⁶³³ was monitored in HeLa cells expressing non-target siRNA or NHE6 siRNA for 72 h. The M.I.F. of Tf-AF⁶³³ was measured in 10⁵ cells by flow cytometry. Data were normalized and represent mean ± S.E.M. of three different experiments. Significance was established using a one-sample Student's *t*-test, ***p* < 0.01. **h** Cell surface levels of TfR in HeLa cells transiently expressing GFP, NHE6v1_{GFP} WT or ΔES were determined by cell surface biotinylation. Representative immunoblot of TfR expression at the cell surface and the total fraction is shown in the left panel. Quantification by densitometry of cell surface/total TfR levels from three different experiments is shown in the right panel. Values were normalized to TfR amounts present in GFP-expressing cells and represent the mean ± S.E.M. Significance was established using a one-sample Student *t*-test, ***p* < 0.01, **p* < 0.05

upregulate the surface abundance and recycling of certain cargo.

While NHE6 is seemingly important for the internalization of Tf-TfR, the study by Xinhan et al. [25] also indicated that this effect was somewhat selective, as uptake of other clathrin-mediated cargo such as the epidermal growth factor (EGF) at a concentration of 1 ng/ml was unaffected. However, an earlier study [63] proposed

that the EGF receptor (EGFR) could follow different internalization pathways depending on the concentration of its ligand EGF. Accordingly, at low concentrations of EGF (1–2 ng/ml), the EGFR was endocytosed via a clathrin-dependent route, whereas at higher ligand concentrations (10–100 ng/ml), the receptor partitioned roughly equally between clathrin-coated pits and caveolae, suggesting that it can be internalized by both

clathrin- and lipid raft-dependent mechanisms [63, 64]. While subsequent studies have disputed these latter findings [65], we nevertheless tested whether NHE6 could internalize the ligand-activated EGFR at higher EGF concentrations that involve not only clathrin mediated endocytosis, but could also potentially favour a caveolae-dependent route, and whether the Δ ES mutant impairs this function. To this end, we measured the uptake of EGF-AF⁶⁴⁷ at the higher concentration of 100 ng/ml in HeLa cells. As shown in Fig. 8a, the signals for neither NHE6 WT_{GFP} nor Δ ES_{GFP} overlapped with those for the EGFR labelled with EGF-AF⁶⁴⁷ by image analysis. Consistent with this observation, overexpressing WT_{GFP} or Δ ES_{GFP} did not alter the uptake of EGF-AF⁶⁴⁷ when compared to control cells expressing GFP alone (Fig. 8b). The specificity of the EGF fluorescent signal was validated by competition experiments in the presence of 10-fold excess unlabeled EGF (Fig. 8c). Thus, even at high concentrations of EGF, NHE6 does not colocalize with the EGF-EGFR complex. These data are

consistent with earlier findings by Xinhan et al. [25] and confirm that NHE6 regulates the internalization of some, but not all, clathrin (or potentially caveolin)-dependent cargo, at least in HeLa cells.

The pH of NHE6 Δ ES-containing endosomes fails to alkalinize

The impaired uptake of Tf-AF⁶³³ in cells expressing NHE6 Δ ES suggested that recycling endosomal function has been compromised. Since proper acidification of organelles is an important determinant of membrane trafficking [66–68] and because NHE6 is believed to operate as an alkalinizing mechanism to counter the acidification generated by the vacuolar H⁺-ATPase [25], we measured the vesicular pH (pH_v) of NHE6 WT- and Δ ES-containing endosomes by fluorescence ratiometric image analysis (FRIA) [69]. To this end, AP-1 cells were transfected with 3F-NHE6v1_{HA} WT or Δ ES. Thirty-six h post-transfection, cell surface NHE6 molecules were labeled on ice with a primary mouse monoclonal anti-

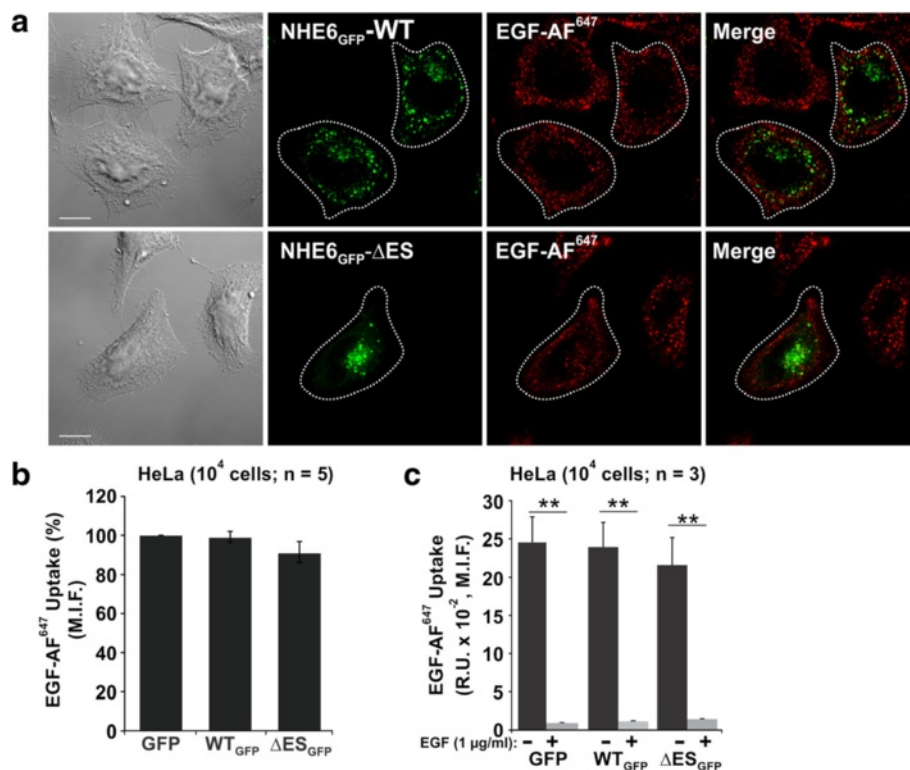


Fig. 8 Expression of NHE6 does not affect trafficking of the EGF receptor in HeLa cells. **a** HeLa cells were transiently transfected with NHE6v1_{GFP} WT (upper panels) or Δ ES (lower panels). Forty-eight h after transfection, cells were loaded with Alexa Fluor⁶⁴⁷-labelled EGF (EGF-AF⁶⁴⁷, 100 ng/ml) for 5 min, fixed in 4 % paraformaldehyde, permeabilized, mounted onto glass slides and then examined by confocal microscopy. Footprints of the transfected cells within the field of view are indicated as white dotted outlines and were derived from the transmitted light images (far left panels). Scale bars represent 10 μ m. **b** Uptake of EGF-AF⁶⁴⁷ (100 ng/ml, 5 min) in 10⁴ GFP-positive HeLa cells expressing GFP, NHE6v1_{GFP} WT or Δ ES measured by flow cytometry. Data were normalized and represent mean \pm S.E.M. of five different experiments. **c** Uptake of EGF-AF⁶⁴⁷ (100 ng/ml, 5 min) in HeLa cells expressing GFP, NHE6v1_{GFP} WT or Δ ES in the absence (-) or presence (+) of 10-fold excess unlabeled EGF (1 μ g/ml). Median fluorescence intensity (M.I.F.) of EGF-AF⁶⁴⁷ was measured in 10⁴ GFP-positive cells by flow cytometry and values represent the mean \pm S.E.M. of three different experiments. Significance was established using a one sample Student t-test, ***p* < 0.001

Flag antibody, followed by incubation with a Fab secondary antibody conjugated to the pH-sensitive ratiometric dye fluorescein isothiocyanate (FITC). Cells were then incubated in cell culture media at 37 °C for 30 min or 60 min and individual vesicles were analyzed by FRIA. The pH calibration curve is shown in Fig. 9a and an example of the pH distribution of newly formed recycling endosomes as a function of time is presented in Fig. 9b, with the median vesicular pH values from multiple experiments summarized in Fig. 9c. After 30 min of internalization, both WT and Δ ES were predominantly targeted to a compartment with median pH_v values of $\sim 6.25 \pm 0.35$ and 5.80 ± 0.39 , respectively, consistent with accumulation in early/sorting endosomes, though in the case of Δ ES-expressing cells a minor fraction of the transporter was also detected in more acidic vesicles ($pH_v \sim 5.0$) (Fig. 9b). At 60 min after internalization, the WT protein was found in a more alkaline vesicular pool (median $pH_v \sim 6.50 \pm 0.09$), corresponding to the recycling endosomal compartment, whereas the bulk of the Δ ES mutant protein accumulated in a very acidic

compartment ($pH_v \sim 5.37 \pm 0.25$) (Fig. 9c) more consistent with late endosomes and lysosomes, suggesting that its' alkalinizing function was compromised. As a control, we also measured the luminal pH of recycling endosomes in untransfected AP-1 cells using FITC-conjugated Tf as a pH-sensitive probe. After 30 min of internalization, the pH_v was 6.26 ± 0.14 (mean \pm S.E.M., $n = 4$) and remained at that level after 60 min (Additional file 1: Figure S6). These values are intermediate between those obtained for the WT- and Δ ES-transfected cells. Collectively, these data further confirm an important role for NHE6 in the late-phase alkalinization of recycling endosomes.

NHE6 Δ ES expression enhances apoptosis in AP-1 cells

During the course of these studies, we noted that the morphology of a significant proportion of AP-1 cells expressing the Δ ES mutant appeared smaller, more rounded, showed surface blebbing and exhibited extensive loss of filamentous actin stress fibers (Fig. 10a, Additional file 1: Figure S5), all features consistent with cells undergoing apoptosis [70–72]. To examine this

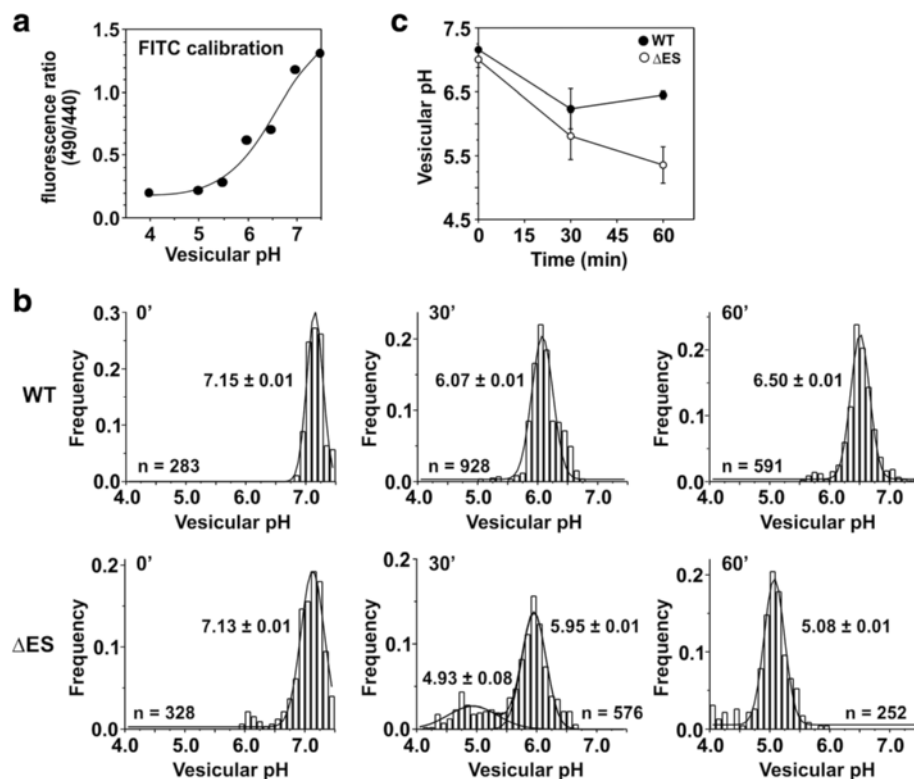


Fig. 9 Over-acidification of endosomes containing NHE6 Δ ES. AP-1 cells were transiently transfected with $3F$ NHE6_{HA} WT and Δ ES and endosomal delivery was assessed 36 h post-transfection. Anti-Flag M2 primary and FITC-conjugated Fab secondary antibodies were bound to live cells for 1 h on ice. The temperature was raised to 37 °C for 30 or 60 min and endosomal pH was measured by fluorescence ratio imaging (FRIA). **a** *In situ* calibration of FITC fluorescence as a function of vesicular pH was performed by clamping the vesicular pH between 4 and 7.5 as described in "Methods". **b** Measurement of vesicular pH as a function of time upon internalization of $3F$ NHE6_{HA} WT and Δ ES. The pH values represent the mean \pm S.E.M. and the number of vesicles (~ 250 to 1000 vesicles) analyzed from a representative experiment are shown. **c** Graphical plot of the median vesicular pH as a function of time derived from four experiments (mean \pm S.E.M.)

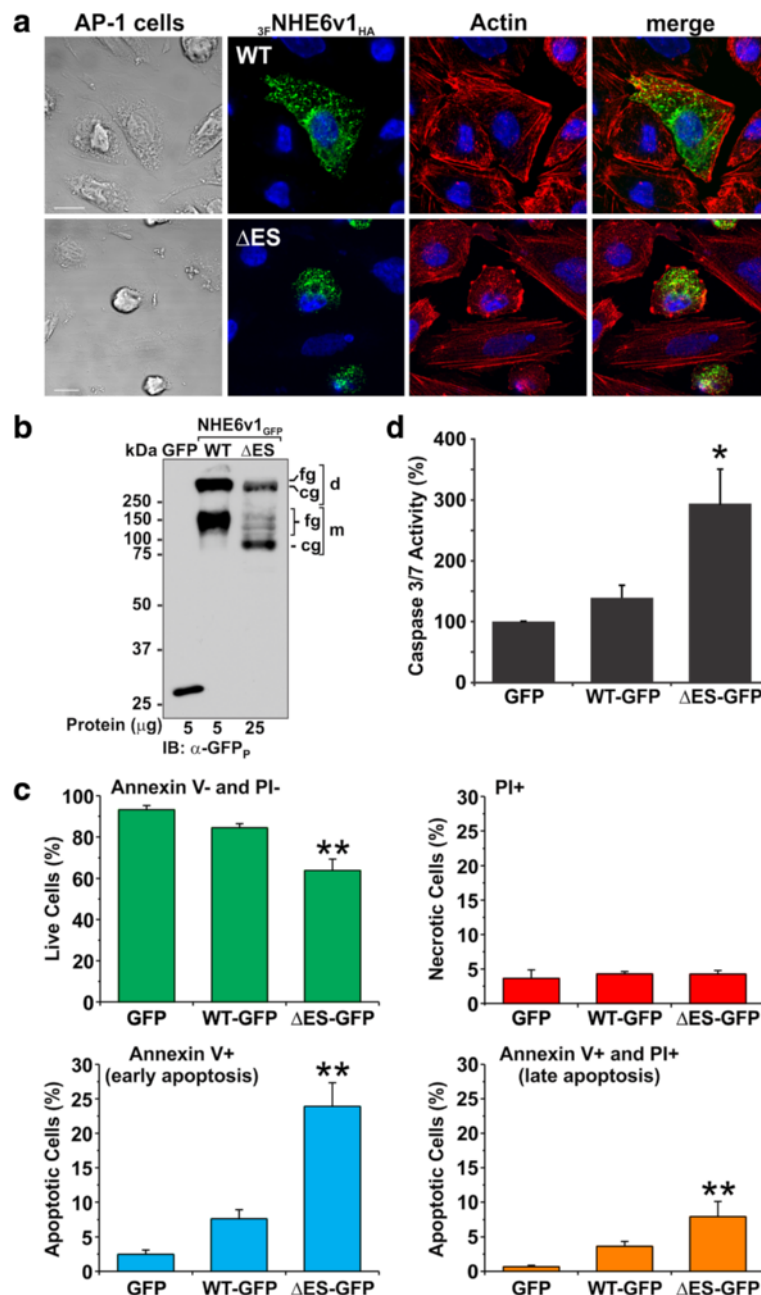


Fig. 10 Expression of NHE6 ΔES enhances apoptosis in AP-1 cells. **a** Confocal microscopy of fixed AP-1 cells expressing 3xNHE6v1_{HA} WT (upper panels) or ΔES (lower panels). NHE6 was labelled with a mouse monoclonal anti-HA_m antibody and an Alexa Fluor⁴⁸⁸-conjugated goat anti-mouse secondary antibody. Actin filaments were labelled with rhodamine-phalloidin and the nuclei were stained with DAPI. **b** Transient expression (48 h) of GFP, NHE6v1_{GFP} WT or ΔES in AP-1 cells. Representative immunoblot probed with a polyclonal anti-GFP antibody (α-GFP_p). **c** Flow cytometry analysis of AP-1 cells transfected with GFP alone, NHE6_{GFP} WT or ΔES. Forty-eight hours after transfection, cells were labeled with Annexin V-APC and propidium iodide (PI) and 10⁴ GFP-positive cells were examined by flow cytometry for each transfectant. Annexin V- and PI- double negative cells represent viable cells. Cells taking up only PI (PI+) are indicative of dead cells; Annexin V+ and PI- double positive cells represent early apoptotic cells whereas Annexin V+ and PI+ double positive cells represent late apoptotic cells. Results are shown as mean ± S.E.M. of eight independent experiments. Significance was determined using a paired two-tailed Student *t*-test, ***p* < 0.01. **d** AP-1 cells transiently expressing GFP alone, NHE6_{GFP} WT or ΔES were isolated by cell sorting and then assayed for caspase 3/7 activity as described in "Materials and Methods". Data were normalized to values for GFP-expressing cells and displayed as mean ± S.E.M. of four independent experiments, each done in triplicate. Significance was determined using a paired two-tailed Student *t*-test, **p* < 0.05

possibility, AP-1 cells were transfected with GFP as a control, GFP-tagged NHE6v1 WT or Δ ES (Fig. 10b). Forty-eight hours post-transfection, the cells were incubated in the presence of the fluorescent annexin V-allophycocyanin conjugate (Annexin V-APC) and propidium iodide (PI) and analyzed by flow cytometry to determine the fraction of apoptotic cells. Annexin V is a Ca^{2+} -dependent phospholipid-binding protein with high affinity for phosphatidylserine which is normally present in the inner leaflet of the plasma membrane [73]. Propidium iodide is a fluorescent molecule whose signal is enhanced 20- to 30-fold upon binding to double-stranded DNA and RNA but generally cannot cross the intact plasma membrane of viable cells. During the early stages of apoptosis, phosphatidylserine is translocated to the outer leaflet of the plasma membrane, where it is now accessible for binding to an Annexin V-APC probe. However, the integrity of the plasma membrane at this stage is maintained, so PI cannot penetrate inside the cells. As such, Annexin V-APC positive and PI negative cells are considered to be early apoptotic. In the later stages of apoptosis, as well as in necrosis (unregulated cell death) or necroptosis (programmed necrosis) [74], the plasma membrane becomes leaky, allowing PI to enter the cells and to bind to nucleic acids, so Annexin V-APC/PI-double positive cells are late apoptotic or necrotic, whereas PI-only positive cells are considered necrotic [75]. GFP-positive cells (10^4 cells per experiment) were analyzed and a significantly higher proportion of early and late apoptotic cells were detected among the Δ ES-expressing cells compared to cells expressing wild-type NHE6_{GFP} (Fig. 10c). To further substantiate the activation of an apoptotic pathway, which is defined as a caspase-dependent form of regulated cell death [76, 77], we measured caspase 3 and 7 activity using the luminescent Caspase-Glo[®] 3/7 assay from Promega. To this end, GFP-positive AP-1 cells transiently expressing GFP, NHE6_{GFP} WT or Δ ES were isolated by fluorescence-activated cell sorting (FACS) 24 h post-transfection and grown for an additional 24 h. As shown in Fig. 10d, the activation of caspase 3 and 7 is significantly higher (~3-fold) in cells expressing the NHE6_{GFP}- Δ ES mutant compared to GFP or NHE6_{GFP}-WT, consistent with the flow cytometry analyses.

The distribution of the NHE6 Δ ES mutant is altered in primary mouse hippocampal neurons

The above results show that NHE6 Δ ES is mislocalized in non-neuronal cells. To investigate whether the subcellular distribution of the mutant protein is similarly altered in neurons, primary cultures of differentiated hippocampal pyramidal neurons (10–12 days in vitro, DIV) prepared from C57BL/6 mice were transfected

with GFP alone or GFP and either fluorescent mCherry (ChFP)-tagged constructs of NHE6 WT or Δ ES (NHE6_{ChFP}-WT and NHE6_{ChFP}- Δ ES, respectively) and visualized by confocal microscopy after 48 h. Following fixation and mounting, multiple z-stack optical sections of 300–500 nm were taken and frame averaged 3X at low resolution or line-averaged 2X at high resolution to improve the signal-to-noise ratio. Images were then deconvolved by using a full maximum likelihood extrapolation algorithm Huygens deconvolution software (SVI), and 3D images were compiled as maximum intensity projections using Imaris software (Bitplane AG). As shown in Fig. 11a, representative neurons expressing control GFP alone or GFP and NHE6_{ChFP}-WT exhibited extensive dendritic arborization, whereas those expressing GFP and NHE6_{ChFP}- Δ ES displayed an apparent reduction in higher-order dendritic branching, though the number of primary dendrites (originating from the soma) was similar to controls (GFP: 5.67 ± 0.95 ; WT: 4.86 ± 0.59 ; Δ ES: 4.14 ± 0.44 ; $p > 0.05$). Using Filament-Tracer Imaris software, there were significant reductions in total dendritic length, surface area and number of branch points of the neurons expressing NHE6_{ChFP}- Δ ES (~50 % for each parameter; $p < 0.01$ one-way ANOVA followed by a Tukey test) compared to control GFP or GFP and NHE6_{ChFP}-WT (Fig. 11b–d).

To investigate the vesicular nature of the NHE6-positive puncta, dual labelling experiments were performed using Tf-AF⁶³³ to mark recycling endosomes. Visual analysis revealed that within the soma, the signals for NHE6 WT closely overlapped with those for Tf-AF⁶³³, though this spatial relationship diminished markedly for the Δ ES mutant (Fig. 12a). Quantitative calculation of the Mander's overlap coefficient M1-M2 indicated that the degree of colocalization was significantly reduced for the Δ ES mutant compared to WT (i.e., M1; WT-Tf, 51.9 % \pm 5.1, versus Δ ES-Tf, 35.0 % \pm 4.4, $p < 0.05$; M2; Tf:WT, 78.7 % \pm 2.7 versus Tf- Δ ES, 44.6 % \pm 1.7, $p < 0.01$) (Fig. 12b). These data suggest that the Δ ES mutant is being partitioned away from the recycling endosomal pool, results consistent with those obtained for AP-1 cells.

Given the above observations, we next investigated the viability of the primary neurons transiently expressing GFP alone, NHE6_{ChFP}-WT or NHE6_{ChFP}- Δ ES by immunolabelling for the activated, cleaved form of caspase-3 (caspase-3 (Asp175); cCASP3) as a convenient indicator of apoptotic cell death. As shown in Fig. 13, the percentage of neurons expressing GFP alone or GFP and NHE6_{ChFP}-WT that co-stained for cCASP3 was low in each case (~ < 20 %), whereas the percentage of transfected cells expressing NHE6_{ChFP}- Δ ES that were positive for cCASP3 increased 3-fold, indicative of pronounced cell death.

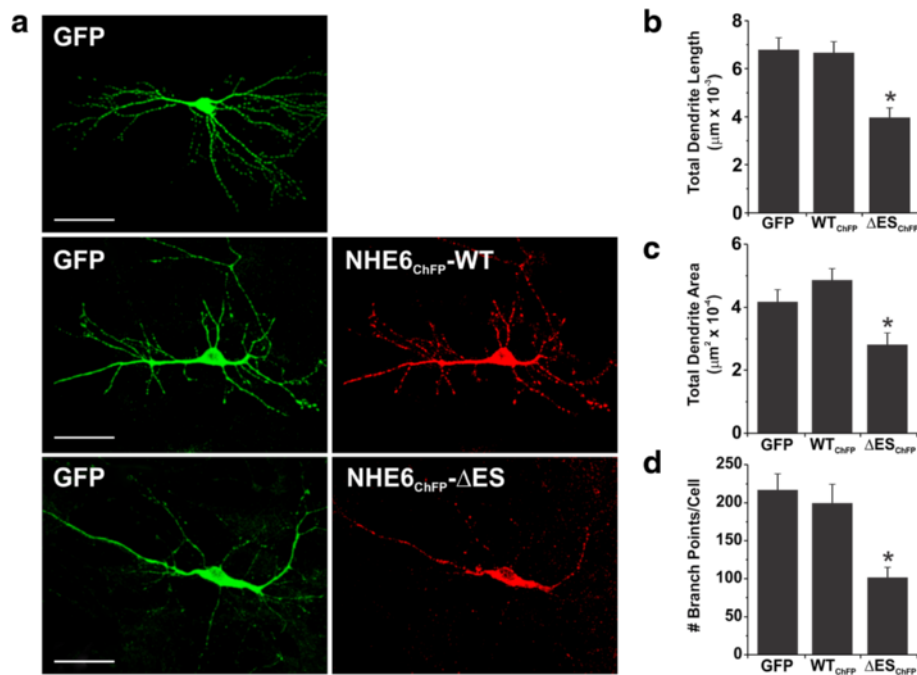


Fig. 11 Expression of NHE6 Δ ES decreases the complexity of dendritic arborisation in primary hippocampal neurons. **a** Confocal images of mouse primary hippocampal neurons transfected with cytosolic GFP alone or co-transfected with GFP and monomeric cherry fluorescent protein-tagged NHE6 (NHE6_{ChFP}) WT or Δ ES. Forty-eight h post-transfection, cells were fixed in 4 % paraformaldehyde, mounted onto glass slides, and examined by confocal microscopy. Images show each channel individually. **b-d** Quantification of parameters related to neuronal branching, including the sums of total dendritic length (**b**) and area (**c**), as well as the total number of branch points per cell (**d**), using the FilamentTracer plug-in module from Imaris Software. Transfection of NHE6_{ChFP}- Δ ES appeared to reduce the extent of neuronal arborisation, as can be discerned from the representative images in **a**. Data from four experiments is represented as mean \pm S.E.M. values. *: $p < 0.01$, one-way ANOVA with Tukey post-hoc test. Scale bar: 60 μ m

Discussion

Patients with CS possess a spectrum of core and secondary clinical symptoms [1, 3, 8, 9], the variability of which may depend on the severity of the mutation in NHE6, functional overlap with other pH-regulating solute carrier proteins, or genetic-modifier effects. In the present study, we examined in detail the molecular and cellular consequences of one of the originally identified CS mutations that causes an in-frame deletion of two highly conserved amino acids in the predicted seventh transmembrane helix of the transporter, using the longest splice-variant as a template (i.e., NHE6v1 Δ ²⁸⁷ES²⁸⁸). Compared to the WT protein, excision of these two residues markedly reduced its rate of post-translational maturation to complex oligosaccharides, as revealed by a greater accumulation of its core-glycosylated form relative to the total Δ ES population in transient transfection assays in both fibroblastic and neuroblastoma cell lines. This correlated with a significant reduction (\sim 10-fold) in its half-life compared to WT, effects that could be partially prevented by inhibitors of both proteasomal- and lysosomal-mediated proteolysis; indicative of processing via the endoplasmic reticulum (i.e., ERAD) and peripheral (i.e., ESCRT) quality control pathways,

respectively. Activation of ERAD indicates that newly synthesized mutant proteins have an increased propensity to misfold and undergo multi-monoubiquitination or polyubiquitination and retrotranslocation from the ER to the cytoplasm for degradation by the proteasome [51, 52]. Consistent with this notion, the overall state of ubiquitination of the Δ ES mutant was significantly elevated (\sim 13-fold) compared to WT. By light microscopy, there was limited accumulation of the mutant protein in the ER, suggesting that the ERAD system was not overly saturated due to ectopic expression under our experimental conditions and could adequately handle the misfolded mutated proteins. The remaining fraction of mutated NHE6, however, was able to undergo post-translational modification and assembly as a fully-glycosylated homodimer and, furthermore, was delivered correctly to the plasma membrane. However, upon internalization, the Δ ES mutant was redirected away from the recycling endosomal compartment as it showed minor overlap with markers of recycling endosomes (transferrin) and early endosomes (i.e., EEA1), and instead accumulated in Rab7-associated late endosomes/multivesicular bodies prior to degradation in lysosomes. Consistent with the microscopic evidence, degradation

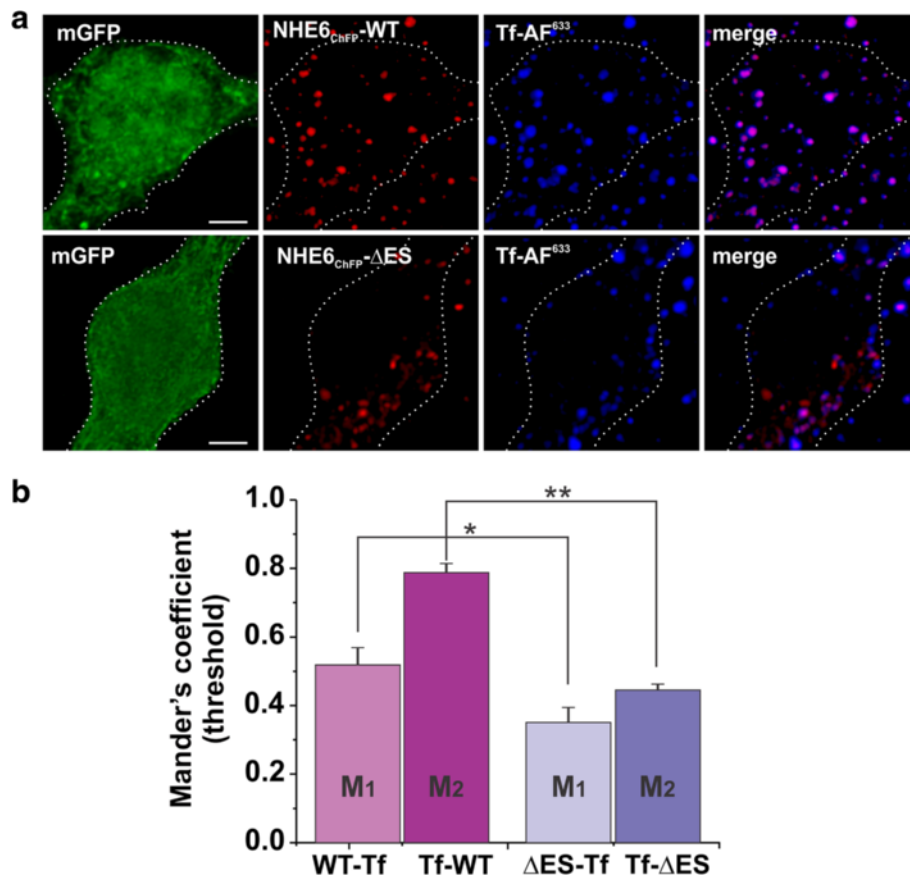


Fig. 12 Expression of NHE6ΔES causes a reduction in transferrin uptake and colocalization in primary hippocampal neurons. **a** Confocal images of the cell bodies of primary hippocampal neurons transfected with GFP (green) and NHE6_{ChFP} WT or ΔES (red) and incubated with Alexa Fluor⁶³³-tagged transferrin (Tf-AF⁶³³) (pseudo-coloured blue) to assess endocytotic transferrin uptake and colocalization. Images show each channel individually, with merged images of the NHE6_{ChFP} and Tf-AF⁶³³ channels. **b** Quantitative summary of mean ± S.E.M. thresholded Mander's coefficients, a measure of colocalization, between Tf-AF⁶³³ and NHE6_{ChFP} from four experiments. By the Mander's coefficient, the majority of Tf-AF⁶³³ was colocalized with NHE6_{ChFP} WT than the inverse. The degree of colocalization was decreased with the NHE6_{ChFP} ΔES mutant. *: $p < 0.0001$; **: $p < 0.05$, independent Student's *t*-test, two-tailed. Scale bar: 10 μm

of this population of transporters could be partly attenuated by lysosomal inhibitors. These findings are comparable to the lysosomal degradation of other misfolded plasma membrane proteins that escape the ERAD pathway, such as certain mutant Cl⁻ channels (i.e., cystic fibrosis transmembrane regulator, CFTR) responsible for cystic fibrosis [78, 79] and defective K⁺ channels (i.e., human ether-a-go-go-related, hERG) that cause long QT syndrome 2 [80], and highlight the importance of a secondary peripheral quality control mechanism to eliminate the accumulation of improperly folded proteins. These findings partially corroborate those of an earlier study that showed that the analogous mutation in the shorter NHE6v2 splice-variant (i.e., Δ²⁵⁵ES²⁵⁶) also caused the protein to be highly unstable and rapidly degraded by the proteasome and lysosome [43]. However, in this latter study, the GFP-tagged WT and Δ²⁵⁵ES²⁵⁶ proteins were detected as single ~70 kDa

bands by Western blotting which is considerably smaller than its predicted molecular mass of ~100 kDa, and unlike the multiple core- and fully-glycosylated monomers and dimers detected in the present study using the longer NHE6v1 variant. Moreover, the GFP-tagged NHE6v2-Δ²⁵⁵ES²⁵⁶ protein accumulated mainly in the endoplasmic reticulum, with only a minor fraction detected in early endosomes but not recycling endosomes. The basis for these differences is unclear, but may relate to technical variances or the biochemical natures of the respective splice-variants.

Aside from the intrinsic instability of the NHE6v1-ΔES protein, its rate of internalization from the cell surface of AP-1 cells was also significantly reduced compared to its WT counterpart. By microscopy, ΔES-expressing AP-1 cells showed visibly reduced uptake and accumulation of fluorescently-labelled Tf compared to neighboring untransfected cells. Comparable results

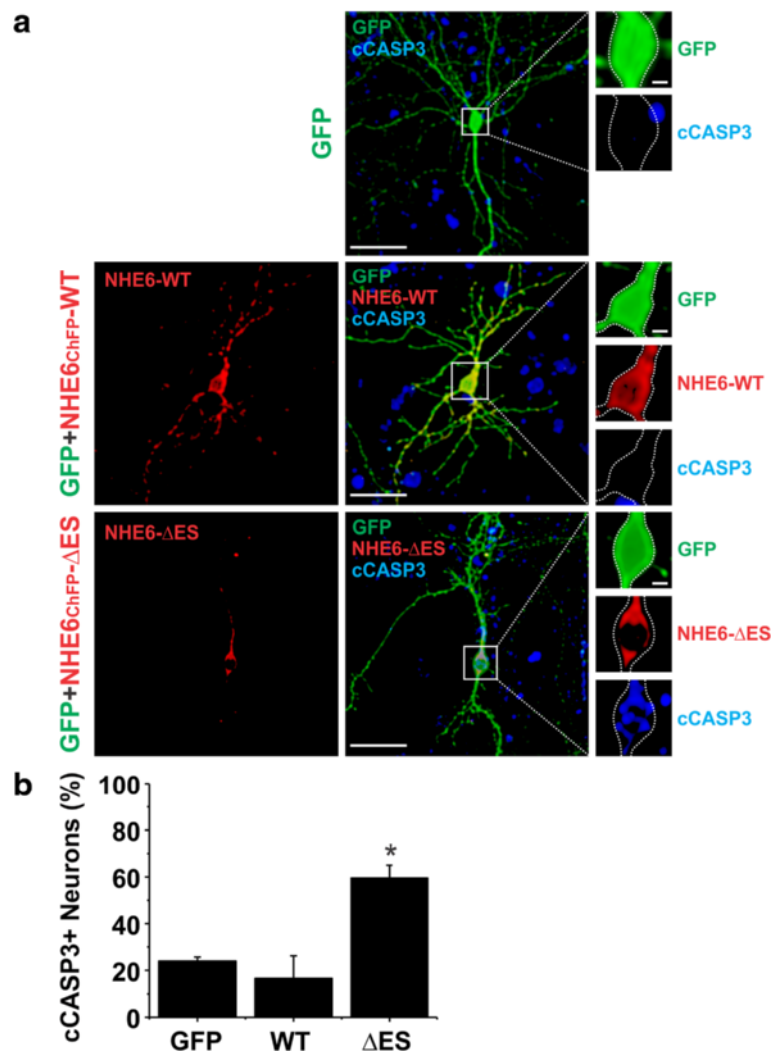


Fig. 13 Expression of NHE6 Δ ES induces apoptotic cell death of primary hippocampal neurons. **a** Representative confocal images of primary hippocampal neurons transfected with cytosolic GFP alone or GFP co-transfected with either NHE6_{ChFP}-WT or NHE6_{ChFP}- Δ ES. Forty-eight h post-transfection, cells were fixed, permeabilized, blocked, and assessed for apoptosis by immunostaining for cleaved caspase-3 (cASP3, blue). For each transfection condition, an overview is presented of the entire transfected neuron with the GFP, ChFP, and cASP3 channels merged (middle panels) with higher magnification cut-away images of the area around the cell soma (indicated by the white square) with each channel displayed separately (right panels). For the co-transfected cells, the signals for the ChFP-tagged NHE6 constructs are also shown separately (left panels). As noted in the images, cASP3 was also detected in nontransfected cells, which could include not only neurons, but also astrocytes and glia. Hence, to estimate the background level of apoptotic cells per field of view, companion cultures in each preparation were fixed, permeabilized and immunolabelled for cASP3 and stained with propidium iodide to mark the nuclei in order to calculate total cell density/field of view. Under each treatment condition, the average number of cells per field of view ranged from 350 to 400 and the percentage of apoptotic cells per field of view for GFP, GFP + NHE6_{ChFP}-WT or GFP + NHE6_{ChFP}- Δ ES was 9.8 % \pm 0.7, 9.7 % \pm 1.0 and 9.1 % \pm 0.8 (mean \pm S.E.M.), respectively. Hence, \sim 10 % of the cells in the background were apoptotic under each condition. **b** Quantitative representation of the percentages of cASP3-positive (cASP3+) neurons of examined GFP or GFP- and NHE6_{ChFP} transfected cells within each condition for four separate experiments. Data are presented as the mean \pm S.E.M. (total transfected cells examined ranged from 21–25 cells per condition). Compared to transfection with GFP alone or GFP + NHE6_{ChFP}-WT, significantly more neurons transfected with GFP + NHE6_{ChFP}- Δ ES were cASP3-positive. *: p < 0.01, one-way ANOVA with Tukey post-hoc test. Scale bar: whole cell images, 60 μ m; high magnification images, 10 μ m

were also obtained in HeLa cells using a flow cytometry-based assay where the net uptake of the labelled Tf-TfR complex was significantly lower in Δ ES compared to WT transfected cells, and slightly lower than values obtained for GFP-transfected control cells, though the

latter difference was not statistically significant. One possibility for the apparent lack of a strong dominant-negative effect of the Δ ES mutant in HeLa cells compared to AP-1 cells is that its level of expression might not be sufficient to completely suppress the

actions of the endogenous NHE6 WT transporter, which is well expressed in HeLa cells [23] but negligible in AP-1 cells. For this reason, we also performed a siRNA knockdown (>95 %) of NHE6 in HeLa cells to validate its involvement in endocytosis of Tf-TfR complexes, and indeed we observed a small, but statistically significant, depressive effect (~23 %, Fig. 7g), consistent with earlier findings [25]. By contrast, other clathrin-mediated cargo such as the EGF-bound EGFR was unaffected. The molecular basis for the differential regulation of clathrin-dependent cargo by NHE6 is unknown, but may relate to the recruitment of different endocytic adaptor proteins and associated accessory proteins. Unlike the activated Tf-TfR which is highly dependent on the AP2 adaptor complex for internalization [81], the EGF-EGFR is less restricted and can bind to AP2 as well as alternate endocytic adaptors such as epsin-1 [82] and Grb2 [83, 84] and then is preferentially sorted to the lysosome for degradation. Hence, NHE6 appears to play a role in the endocytosis of a discrete subpopulation of clathrin-dependent cargo that is preferentially targeted to recycling endosomes in HeLa cells and presumably other cell types as well. In addition, we found that overexpression of NHE6 WT, but not Δ ES, also increased the abundance of TfR at the plasma membrane. Based on these data, we propose that NHE6 elevates the net uptake of Tf not only by enhancing endocytosis but also in part by promoting the exocytosis and steady-state cell surface abundance of the TfR, and that this upregulation is deficient in cells expressing the Δ ES mutant.

The deficit in Tf uptake in Δ ES-expressing cells also correlated with aberrant over-acidification of endosomes relative to those in WT-expressing cells. Using an immunological-based approach that selectively targeted a pH-sensitive fluorescent probe to the lumen of NHE6-containing vesicles in AP-1 cells, we found that WT-containing vesicles initially acidified (i.e., $\text{pH}_v \sim 6.25 \pm 0.35$) followed by a gradual alkalization (i.e., $\text{pH}_v \sim 6.50 \pm 0.09$) over a 60 min period. This biphasic pH fluctuation is consistent with previous reports of pH transients along the recycling endosomal pathway [85–87]. By contrast, the Δ ES-containing vesicles became progressively more acidic throughout the measurement period (i.e., $\text{pH}_v \sim 5.37 \pm 0.25$). This suggests that the catalytic activity of the mutant was compromised and unable to counter the H^+ influx driven by the vacuolar H^+ -ATPase, resulting in a net increase in the luminal H^+ concentration. This loss-of-function is perhaps not unexpected as mutation of the analogous glutamate residue (i.e., E262) in the plasmalemmal-type NHE1 isoform was also found to significantly decrease its total cellular and plasma membrane abundance as well as intrinsic catalytic activity (~20 % of wild-type activity) [88]. Thus, this glutamate residue is critical not only for protein stability, but

also for its catalytic activity. The increased endosomal acidification would also be consistent with the partitioning of Δ ES-containing vesicles and any associated cargo towards the endo-lysosomal degradative pathway.

Acidification has long been recognized as an important determinant of vesicular biogenesis, trafficking and function [67, 86, 87, 89]. While the roles of acidification on enzymatic processing of proteins along the secretory and degradative pathways are well appreciated, the precise mechanisms by which intraorganellar pH is sensed and transmitted to the cytoplasmic molecular machinery that controls vesicular events such as budding, coat formation, sorting and fusion are less well understood. However, emerging evidence indicates that endosomal pH-regulators themselves can serve as both pH-sensors and scaffolds to recruit components of the vesicular trafficking machinery. Recent studies by Marshansky and colleagues [90, 91] have shown that two distinct subunits of the transmembrane V_0 complex of the vacuolar H^+ -ATPase, the c- and $\alpha 2$ -subunits, directly recruit the small GTPase Arf6 (ADP-ribosylation factor 6) and its associated guanine nucleotide exchange factor ARNO (ADP-ribosylation factor nucleotide site opener), respectively, in an intra-endosomal pH-dependent manner; interactions that are critical for endosomal trafficking between the early and late endosomal compartments. This process is seemingly selective, as it does not appear to influence membrane trafficking along the recycling endosomal pathway. This is intriguing, but unexpected, since previous findings had also linked Arf6 to the recycling pathway [92–94]. This suggests that other endosomal pH-regulatory transporters, such as NHE6, may play a more prominent role in directing vesicular trafficking along the recycling endosomal pathway and that this process is impaired in the Δ ES-expressing cells.

In addition to disrupting recycling endosomal pH and trafficking, we found that expression of the NHE6 Δ ES mutant in AP-1 cells elicited morphological and biochemical changes symptomatic of programmed 'apoptotic' cell death [95, 96], as revealed by (1) disassembly of the filamentous actin network accompanied by cell rounding and retraction, (2) plasma membrane blebbing, phospholipid flipping (i.e., external exposure of phosphatidylserine) and permeabilization, and (3) elevated activities of caspases 3 and 7. Similarly, ectopic expression of Δ ES in primary hippocampal neurons showed aberrant subcellular distribution of Δ ES-containing endosomes and pronounced neurodegeneration, as manifested by significantly reduced dendritic length, surface area and number of secondary branch points as well as increased activation of caspase 3; features consistent with regulated cell death [97]. These observations complement earlier *in vitro* studies showing that manipulations that disrupt the molecular machinery involved in recycling

endosomal trafficking at dendritic spines of hippocampal neurons also cause pronounced morphological changes, including decreased dendritic spine size and density and impair long-term potentiation [98, 99]. Indeed, we have recently shown that NHE6 exhibits a high degree of colocalization with vesicles containing the glutamatergic AMPA GluA1-containing receptor in dendrites and dendritic spines of hippocampal neurons, suggestive of a role for NHE6-containing vesicles in synapse formation, maturation, and plasticity [27].

The above findings are also consistent with in vivo observations of progressive neurodegeneration in NHE6 null mice [26, 28] and Christianson syndrome patients [1, 3, 8, 9]. In the null mouse model, both mutant male (*Nhe6*^{-Y}) and homozygous female (*Nhe6*^{-/-}) knockout mice exhibit impaired endo-lysosomal function (i.e., aberrant accumulation of GM2 ganglioside and cholesterol) in subpopulations of neurons within the amygdala, hippocampus, hypothalamus and cerebral cortex as well as pronounced formation of axonal spheroids and degeneration of cerebellar Purkinje cells, features typical of many lysosomal storage diseases [26, 100]. Furthermore, hippocampal and cortical pyramidal neurons of *Nhe6* knockout mice examined in vivo and in vitro displayed morphological and functional abnormalities typified by enhanced endosomal acidification, reduced axonal and dendritic arborization, decreased synapse density and maturation, and impaired circuit activity [28]. These changes correlated with marked decreases in the levels of total and phospho-activated forms of the neurotrophin receptor TrkB, effects that could be largely mitigated by pharmacological inhibitors of lysosomal proteolysis or by chronic incubation with the exogenous TrkB ligand BDNF [28]. Moreover, immunohistochemical staining revealed substantial colocalization of NHE6 and TrkB in endosomes in the perinuclear region and along growing axons and dendrites of hippocampal neurons. Thus, loss of NHE6 was proposed to lead to excess degradation of the TrkB receptor (and possibly neurotransmitter receptors such as AMPAR) and attenuation of downstream signalling due to over-acidification of the endosome compartment and sorting to lysosomes. Impairment in TrkB signaling has also been implicated in the development of Angelman Syndrome [101], a disorder that bears many features in common with Christianson Syndrome [8]. Hence, these findings suggest that disruption of endosomal trafficking that promotes neurotrophin receptor-mediated prosurvival signals (e.g., via TrkB) [31, 102–104] may shift the balance towards neurotrophin receptor-mediated proapoptotic signals (e.g., via p75^{NTR}) [105–108] leading to neuronal cell death. Analogous perturbations of plasma membrane/endomembrane-triggered signaling pathways may also apply in non-neuronal cells expressing the NHE6-ΔES mutant when the equilibrium

between prosurvival growth factor receptors and proapoptotic death- or dependence-receptors is chronically perturbed [109–112].

While loss of NHE6 function may disrupt trophic or activity-dependent survival signals leading to cell deterioration and death, ER stress [113] may also be another important factor that reduces cell function and viability in cells possessing the ΔES mutant. The mutant protein might trigger the unfolded protein response (UPR), an intricate homeostatic process that results in the arrest of general protein translation, while simultaneously permitting enhanced production of molecular chaperones involved in protein folding, and increased protein polyubiquitination and export of misfolded proteins to the cytoplasm for proteasome-mediated degradation [114, 115]. Consistent with this process, the ΔES mutant is highly ubiquitinated and its degradation can be partly blocked by proteasomal inhibitors. However, like many neurodegenerative diseases that arise from prolonged impaired protein folding, such as Alzheimer's, Parkinson's and Huntington's disease, the UPR is not always sufficient to rescue the cell and apoptosis will be induced. Prolonged ER stress is known to activate several kinases, including glycogen synthase kinase-3β [116] and inositol-requiring kinase 1 (IRE1) which activates apoptosis signal-regulating kinase 1 (ASK1) that, in turn, stimulates c-Jun N-terminal kinase (JNK) [113, 117], ultimately leading to caspase activation and cell death. Postmitotic neurons are especially susceptible to ER stress, as they are not protected from the accumulation of misfolded proteins through the dilution of the ER following cell division [118]. This may also account for the higher percentage of cell death observed in ΔES-transfected primary hippocampal neurons (i.e., 60 %) compared to immortalized AP-1 fibroblastic cells (i.e., ~30 %), at least under our experimental conditions.

Conclusions

To conclude, our results provide new insight into the molecular mechanisms by which disruption of NHE6 activity impairs recycling endosomal trafficking and promotes neurodegeneration in the context of CS. These analyses provide a framework for future investigations of other NHE6 mutations and potential avenues for therapeutic interventions aimed at modulating the trafficking of NHE6-dependent recycling endosomal cargo, such as TrkB and AMPAR, thereby mitigating cell dysfunction and damage in CS. These findings may also be relevant to our understanding of other neurodevelopmental or neurodegenerative disorders such as autism [119–123], fragile X syndrome [124, 125] and Alzheimer's disease [126] where aberrations in recycling endosomal-associated cargo and signaling events have been implicated as contributing factors.

Additional file

Additional file 1: Supplementary data. (PDF 915 kb)

Acknowledgements

We are grateful for the services provided by McGill Life Sciences Advanced Biolmaging Facility and the Flow Cytometry Facility, the Electron Microscopy Facility of the Department of Pharmacology and Therapeutics (McGill University), and Genome Québec for DNA sequencing.

Funding

This work was supported by research funds from the Canadian Institutes of Health Research to JO (MOP-111191), RAM (MOP-86724) and GLL (MOP-66996) and a Canada Research Chair to GLL. AYL is the recipient of an Alexander Graham Bell Canada Graduate Scholarship.

Availability of data and materials

All data generated or analysed during this study are included in this published article and its supplementary information file (Additional file 1). Additional file 1: Figure S1. Sequence alignment of the different human NHE isoforms in the region encompassing the E287-S288 mutation. Figure S2. Detection of NHE6 at the plasma membrane and endosomes in transfected AP-1 cells by transmission electron microscopy. Figure S3. NHE6v1 wild-type and ΔES can form a complex in intact cells. Figure S4. Expression of wild-type and mutant NHE6v1 constructs in transfected AP-1 cells. Figure S5. Subcellular localization of NHE6v1 ΔES in transfected AP-1 cells. Figure S6. Measurement of recycling endosomal pH in AP-1 cells.

Authors' contributions

AI, AB, and CM performed molecular, biochemical and data analyses; HB and AI performed the vesicular pH measurements; AI, AYL and JR performed the immunofluorescence imaging studies; AI, RAM, GLL and JO designed, supervised and coordinated different aspects of the experiments and data analyses; AI and JO wrote the manuscript; all authors critically discussed results, revised and approved the manuscript.

Authors' information

Not applicable.

Competing interests

The authors declare that they have no competing interests.

Consent for publication

Not applicable.

Ethics approval and consent to participate

All procedures for animal handling were approved by the McGill University Facility Animal Care Committee (FACC) and carried out in full compliance with the Policies and Guidelines of the Canadian Council on Animal Care (CCAC).

Author details

¹Department of Physiology, McGill University, Bellini Life Sciences Bldg., Rm, 166, 3649 Promenade Sir-William-Osler, Montreal, QC H3G 0B1, Canada.

²Department of Pharmacology and Therapeutics, McGill University, Montreal, Canada.

Received: 24 February 2016 Accepted: 27 August 2016

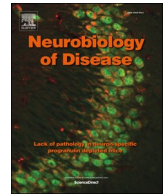
Published online: 02 September 2016

References

- Christianson AL, Stevenson RE, van der Meyden CH, Pelser J, Theron FW, van Rensburg PL, et al. X linked severe mental retardation, craniofacial dysmorphology, epilepsy, ophthalmoplegia, and cerebellar atrophy in a large South African kindred is localised to Xq24-q27. *J Med Genet.* 1999;36:759–66.
- Schroer RJ, Holden KR, Tarpey PS, Matheus MG, Griesemer DA, Friez MJ, et al. Natural history of Christianson syndrome. *Am J Med Genet A.* 2010;152A:2775–83.
- Pescosolido MF, Stein DM, Schmidt M, El Moufawad AC, Sabbagh M, Rogg JM, et al. Genetic and phenotypic diversity of NHE6 mutations in Christianson syndrome. *Ann Neurol.* 2014;76:581–93.
- Angelman H. Syndrome of coloboma with multiple congenital abnormalities in infancy. *Br Med J.* 1961;1:1212–4.
- Williams CA, Angelman H, Clayton-Smith J, Driscoll DJ, Hendrickson JE, Knoll JH, et al. Angelman syndrome: consensus for diagnostic criteria. Angelman syndrome foundation. *Am J Med Genet.* 1995;56:237–8.
- Sutcliffe JS, Jiang YH, Galijaard RJ, Matsuura T, Fang P, Kubota T, et al. The E6-AP ubiquitin-protein ligase (UBE3A) gene is localized within a narrowed Angelman syndrome critical region. *Genome Res.* 1997;7:368–77.
- Kishino T, Lalonde M, Wagstaff J. UBE3A/E6-AP mutations cause Angelman syndrome. *Nat Genet.* 1997;15:70–3.
- Gillfillan GD, Selmer KK, Roxrud I, Smith R, Kyllerman M, Eiklid K, et al. SLC9A6 mutations cause X-linked mental retardation, microcephaly, epilepsy, and ataxia, a phenotype mimicking Angelman syndrome. *Am J Hum Genet.* 2008;82:1003–10.
- Garbern JY, Neumann M, Trojanowski JQ, Lee VM, Feldman G, Norris JW, et al. A mutation affecting the sodium/proton exchanger, SLC9A6, causes mental retardation with tau deposition. *Brain.* 2010;133:1391–402.
- Tarpey PS, Smith R, Pleasance E, Whibley A, Edkins S, Hardy C, et al. A systematic, large-scale resequencing screen of X-chromosome coding exons in mental retardation. *Nat Genet.* 2009;41:535–43.
- Schuurs-Hoeijmakers JH, Vulto-van Silfhout AT, Vissers LE, van de Vondervoort II, van Bon BW, de Ligt J, et al. Identification of pathogenic gene variants in small families with intellectually disabled siblings by exome sequencing. *J Med Genet.* 2013;50:802–11.
- Tzschach A, Grasshoff U, Beck-Woedl S, Dufke C, Bauer C, Kehrer M, et al. Next-generation sequencing in X-linked intellectual disability. *Eur J Hum Genet.* 2015.
- Inlow JK, Restifo LL. Molecular and comparative genetics of mental retardation. *Genetics.* 2004;166:835–81.
- Vaillend C, Poirier R, Laroche S. Genes, plasticity and mental retardation. *Behav Brain Res.* 2008;192:88–105.
- Géczy J, Shoubbridge C, Corbett M. The genetic landscape of intellectual disability arising from chromosome X. *Trends Genet.* 2009;25:308–16.
- Ropers HH. Genetics of early onset cognitive impairment. *Annu Rev Genomics Hum Genet.* 2010;11:161–87.
- Lubs HA, Stevenson RE, Schwartz CE. Fragile X and X-linked intellectual disability: four decades of discovery. *Am J Hum Genet.* 2012;90:579–90.
- Schwede M, Garbett K, Mirnics K, Geschwind DH, Morrow EM. Genes for endosomal NHE6 and NHE9 are misregulated in autism brains. *Mol Psychiatry.* 2013;19:277–9.
- Brett CL, Donowitz M, Rao R. Evolutionary origins of eukaryotic sodium/proton exchangers. *Am J Physiol Cell Physiol.* 2005;288:C223–39.
- Orlowski J, Grinstein S. Na⁺/H⁺ exchangers. *Compr Physiol.* 2011;1:2083–100.
- Miyazaki E, Sakaguchi M, Wakabayashi S, Shigekawa M, Mihara K. NHE6 protein possesses a signal peptide destined for endoplasmic reticulum membrane and localizes in secretory organelles of the cell. *J Biol Chem.* 2001;276:49221–7.
- Brett CL, Wei Y, Donowitz M, Rao R. Human Na⁺/H⁺ exchanger isoform 6 is found in recycling endosomes of cells, not in mitochondria. *Am J Physiol Cell Physiol.* 2002;282:C1031–41.
- Nakamura N, Tanaka S, Teko Y, Mitsui K, Kanazawa H. Four Na⁺/H⁺ exchanger isoforms are distributed to Golgi and post-Golgi compartments and are involved in organelle pH regulation. *J Biol Chem.* 2005;280:1561–72.
- Ohgaki R, Matsushita M, Kanazawa H, Ogihara S, Hoekstra D, Van IJendoorn SC. The Na⁺/H⁺ exchanger NHE6 in the endosomal recycling system is involved in the development of apical bile canalicular surface domains in HepG2 cells. *Mol Biol Cell.* 2010;21:1293–304.
- Xinhan L, Matsushita M, Numaza M, Taguchi A, Mitsui K, Kanazawa H. Na⁺/H⁺ exchanger isoform 6 (NHE6/SLC9A6) is involved in clathrin-dependent endocytosis of transferrin. *Am J Physiol Cell Physiol.* 2011;301:C1431–44.
- Stromme P, Dobrenis K, Sillitoe RV, Gulinello M, Ali NF, Davidson C, et al. X-linked Angelman-like syndrome caused by Slc9a6 knockout in mice exhibits evidence of endosomal-lysosomal dysfunction. *Brain.* 2011;134:3369–83.
- Deane EC, Ilie AE, Sizdahkhani S, Das Gupta M, Orlowski J, McKinney RA. Enhanced recruitment of endosomal Na⁺/H⁺ Exchanger NHE6 into dendritic spines of hippocampal pyramidal neurons during NMDA receptor-dependent long-term potentiation. *J Neurosci.* 2013;33:595–610.

28. Ouyang Q, Lizarraga SB, Schmidt M, Yang U, Gong J, Ellis D, et al. Christianson syndrome protein NHE6 modulates TrkB endosomal signaling required for neuronal circuit development. *Neuron*. 2013;80:97–112.
29. Lein ES, Hawrylycz MJ, Ao N, Ayres M, Bensinger A, Bernard A, et al. Genome-wide atlas of gene expression in the adult mouse brain. *Nature*. 2007;445:168–76.
30. Lu W, Man H, Ju W, Trimble WS, MacDonald JF, Wang YT. Activation of synaptic NMDA receptors induces membrane insertion of new AMPA receptors and LTP in cultured hippocampal neurons. *Neuron*. 2001;29:243–54.
31. Huang SH, Wang J, Sui WH, Chen B, Zhang XY, Yan J, et al. BDNF-dependent recycling facilitates TrkB translocation to postsynaptic density during LTP via a Rab11-dependent pathway. *J Neurosci*. 2013;33:9214–30.
32. Hu H, Wroegemann K, Kalscheuer V, Tzschach A, Richard H, Haas SA, et al. Mutation screening in 86 known X-linked mental retardation genes by droplet-based multiplex PCR and massive parallel sequencing. *Hugo J*. 2009;3:41–9.
33. Madrigal I, Fernandez-Burriel M, Rodriguez-Revela L, Cabrera JC, Marti M, Mur A, Mila M. Xq26.2-q26.3 microduplication in two brothers with intellectual disabilities: clinical and molecular characterization. *J Hum Genet*. 2010;55:822–6.
34. Takahashi Y, Hosoki K, Matsushita M, Funatsuka M, Saito K, Kanazawa H, et al. A loss-of-function mutation in the SLC9A6 gene causes X-linked mental retardation resembling Angelman syndrome. *Am J Med Genet B Neuropsychiatr Genet*. 2011;156B:799–807.
35. Tzschach A, Ullmann R, Ahmed A, Martin T, Weber G, Decker-Schwering O, et al. Christianson syndrome in a patient with an interstitial Xq26.3 deletion. *Am J Med Genet A*. 2011;155A:2771–4.
36. Piton A, Gauthier J, Hamdan FF, Lafreniere RG, Yang Y, Henrion E, et al. Systematic resequencing of X-chromosome synaptic genes in autism spectrum disorder and schizophrenia. *Mol Psychiatry*. 2011;16:867–80.
37. Riess A, Rossier E, Kruger R, Dufke A, Beck-Woedl S, Horber V, et al. Novel SLC9A6 mutations in two families with Christianson syndrome. *Clin Genet*. 2013;83:596–7.
38. Bosemani T, Zanni G, Hartman AL, Cohen R, Huisman TA, Bertini E, Poretti A. Christianson syndrome: spectrum of neuroimaging findings. *Neuropediatrics*. 2014;45:247–51.
39. Mignot C, Heron D, Bursztyn J, Momtchilova M, Mayer M, Whalen S, et al. Novel mutation in SLC9A6 gene in a patient with Christianson syndrome and retinitis pigmentosa. *Brain Dev*. 2013;35:172–6.
40. Zanni G, Barresi S, Cohen R, Specchio N, Basel-Vanagaite L, Valente EM, et al. A novel mutation in the endosomal Na⁺/H⁺ exchanger NHE6 (SLC9A6) causes Christianson syndrome with electrical status epilepticus during slow-wave sleep (ESES). *Epilepsy Res*. 2014;108:811–5.
41. Redin C, Gerard B, Lauer J, Herenger Y, Muller J, Quartier A, et al. Efficient strategy for the molecular diagnosis of intellectual disability using targeted high-throughput sequencing. *J Med Genet*. 2014;51:724–36.
42. Ilie A, Weinstein E, Boucher A, McKinney RA, Orlowski J. Impaired posttranslational processing and trafficking of an endosomal Na⁺/H⁺ exchanger NHE6 mutant (D³⁷⁰W³⁷²) associated with X-linked intellectual disability and autism. *Neurochem Int*. 2014;73:192–203.
43. Roxrud I, Raiborg C, Gilfillan GD, Stromme P, Stenmark H. Dual degradation mechanisms ensure disposal of NHE6 mutant protein associated with neurological disease. *Exp Cell Res*. 2009;315:3014–27.
44. Rotin D, Grinstein S. Impaired cell volume regulation in Na⁺/H⁺ exchange-deficient mutants. *Am J Physiol*. 1989;257:C1158–65.
45. Barriere H, Lukacs GL. Analysis of endocytic trafficking by single-cell fluorescence ratio imaging. *Curr Protoc Cell Biol*. 2008;Chapter 15:1–21.
46. Jiang M, Chen G. High Ca²⁺-phosphate transfection efficiency in low-density neuronal cultures. *Nat Protoc*. 2006;1:695–700.
47. Porter K, Prescott D, Frye J. Changes in surface morphology of Chinese hamster ovary cells during the cell cycle. *J Cell Biol*. 1973;57:815–36.
48. Fafournoux P, Noël J, Pouyssegur J. Evidence that Na⁺/H⁺ exchanger isoforms NHE1 and NHE3 exist as stable dimers in membranes with a high degree of specificity for homodimers. *J Biol Chem*. 1994;269:2589–96.
49. Hisamitsu T, Pang T, Shigekawa M, Wakabayashi S. Dimeric interaction between the cytoplasmic domains of the Na⁺/H⁺ exchanger NHE1 revealed by symmetrical intermolecular cross-linking and selective co-immunoprecipitation. *Biochemistry*. 2004;43:11135–43.
50. Hisamitsu T, Ammar YB, Nakamura TY, Wakabayashi S. Dimerization Is Crucial for the Function of the Na⁺/H⁺ Exchanger NHE1. *Biochemistry*. 2006;45:13346–55.
51. Meusser B, Hirsch C, Jarosch E, Sommer T. ERAD: the long road to destruction. *Nat Cell Biol*. 2005;7:766–72.
52. Raasi S, Wolf DH. Ubiquitin receptors and ERAD: a network of pathways to the proteasome. *Semin Cell Dev Biol*. 2007;18:780–91.
53. Raiborg C, Stenmark H. The ESCRT machinery in endosomal sorting of ubiquitylated membrane proteins. *Nature*. 2009;458:445–52.
54. Apaja PM, Xu H, Lukacs GL. Quality control for unfolded proteins at the plasma membrane. *J Cell Biol*. 2010;191:553–70.
55. Goder V. Roles of ubiquitin in endoplasmic reticulum-associated protein degradation (ERAD). *Curr Protein Pept Sci*. 2012;13:425–35.
56. Barriere H, Nemes C, Du K, Lukacs GL. Plasticity of polyubiquitin recognition as lysosomal targeting signals by the endosomal sorting machinery. *Mol Biol Cell*. 2007;18:3952–65.
57. Piper RC, Dikic I, Lukacs GL. Ubiquitin-dependent sorting in endocytosis. *Cold Spring Harb Perspect Biol*. 2014;6.
58. Le Bivic A, Real FX, Rodriguez-Boulant E. Vectorial targeting of apical and basolateral plasma membrane proteins in a human adenocarcinoma epithelial cell line. *Proc Natl Acad Sci U S A*. 1989;86:9313–7.
59. Dayel MJ, Hom EF, Verkman AS. Diffusion of green fluorescent protein in the aqueous-phase lumen of endoplasmic reticulum. *Biophys J*. 1999;76:2843–51.
60. Wilson JM, de Hoop M, Zorzi N, Toh BH, Dotti CG, Parton RG. EEA1, a tethering protein of the early sorting endosome, shows a polarized distribution in hippocampal neurons, epithelial cells, and fibroblasts. *Mol Biol Cell*. 2000;11:2657–71.
61. Vanlandingham PA, Ceresa BP. Rab7 regulates late endocytic trafficking downstream of multivesicular body biogenesis and cargo sequestration. *J Biol Chem*. 2009;284:12110–24.
62. Glozman R, Okiyoneda T, Mulvihill CM, Rini JM, Barriere H, Lukacs GL. N-glycans are direct determinants of CFTR folding and stability in secretory and endocytic membrane traffic. *J Cell Biol*. 2009;184:847–62.
63. Sigismund S, Woelk T, Puri C, Maspero E, Tacchetti C, Transidico P, et al. Clathrin-independent endocytosis of ubiquitinated cargos. *Proc Natl Acad Sci U S A*. 2005;102:2760–5.
64. Sigismund S, Argenzio E, Tosoni D, Cavallaro E, Polo S, Di Fiore PP. Clathrin-mediated internalization is essential for sustained EGFR signaling but dispensable for degradation. *Dev Cell*. 2008;15:209–19.
65. Kazazic M, Roepstorff K, Johannessen LE, Pedersen NM, van Deurs B, Stang E, Madhus IH. EGF-induced activation of the EGF receptor does not trigger mobilization of caveolae. *Traffic*. 2006;7:1518–27.
66. Johnson LS, Dunn KW, Pytowski B, McGraw TE. Endosome acidification and receptor trafficking: bafilomycin A1 slows receptor externalization by a mechanism involving the receptor's internalization motif. *Mol Biol Cell*. 1993;4:1251–66.
67. Weisz OA. Acidification and protein traffic. *Int Rev Cytol*. 2003;226:259–319.
68. Casey JR, Grinstein S, Orlowski J. Sensors and regulators of intracellular pH. *Nat Rev Mol Cell Biol*. 2010;11:50–61.
69. Barriere H, Apaja P, Okiyoneda T, Lukacs GL. Endocytic sorting of CFTR variants monitored by single-cell fluorescence ratiometric image analysis (FRIA) in living cells. *Methods Mol Biol*. 2011;741:301–17.
70. Hacker G. The morphology of apoptosis. *Cell Tissue Res*. 2000;301:5–17.
71. Maeno E, Ishizaki Y, Kanaseki T, Hazama A, Okada Y. Normotonic cell shrinkage because of disordered volume regulation is an early prerequisite to apoptosis. *Proc Natl Acad Sci U S A*. 2000;97:9487–92.
72. Bortner CD, Cidlowski JA. The role of apoptotic volume decrease and ionic homeostasis in the activation and repression of apoptosis. *Pflugers Arch*. 2004;448:313–8.
73. Andree HA, Reutelingsperger CP, Hauptmann R, Hemker HC, Hermens WT, Willems GM. Binding of vascular anticoagulant alpha (VAC alpha) to planar phospholipid bilayers. *J Biol Chem*. 1990;265:4923–8.
74. Vandenabeele P, Galluzzi L, Vanden Berghe T, Kroemer G. Molecular mechanisms of necroptosis: an ordered cellular explosion. *Nat Rev Mol Cell Biol*. 2010;11:700–14.
75. Vermes I, Haanen C, Steffens-Nakken H, Reutelingsperger C. A novel assay for apoptosis. Flow cytometric detection of phosphatidylserine expression on early apoptotic cells using fluorescein labelled Annexin V. *J Immunol Methods*. 1995;184:39–51.
76. Galluzzi L, Aaronson SA, Abrams J, Alnemri ES, Andrews DW, Baehrecke EH, et al. Guidelines for the use and interpretation of assays for monitoring cell death in higher eukaryotes. *Cell Death Differ*. 2009;16:1093–107.
77. Galluzzi L, Bravo-San Pedro JM, Vitale I, Aaronson SA, Abrams JM, Adam D, et al. Essential versus accessory aspects of cell death: recommendations of the NCCD 2015. *Cell Death Differ*. 2015;22:58–73.

78. Sharma M, Pampinella F, Nemes C, Benharouga M, So J, Du K, et al. Misfolding diverts CFTR from recycling to degradation: quality control at early endosomes. *J Cell Biol.* 2004;164:923–33.
79. Okiyoned T, Barriere H, Bagdany M, Rabeh WM, Du K, Hohfeld J, et al. Peripheral protein quality control removes unfolded CFTR from the plasma membrane. *Science.* 2010;329:805–10.
80. Apaja PM, Foo B, Okiyoned T, Valinsky WC, Barriere H, Atanasiu R, et al. Ubiquitination-dependent quality control of hERG K⁺ channel with acquired and inherited conformational defect at the plasma membrane. *Mol Biol Cell.* 2013;24:3787–804.
81. Motley A, Bright NA, Seaman MN, Robinson MS. Clathrin-mediated endocytosis in AP-2-depleted cells. *J Cell Biol.* 2003;162:909–18.
82. Kazazic M, Bertelsen V, Pedersen KW, Vuong TT, Grandal MV, Rodland MS, et al. Epsin 1 is involved in recruitment of ubiquitinated EGF receptors into clathrin-coated pits. *Traffic.* 2009;10:235–45.
83. Jiang X, Huang F, Marusyk A, Sorkin A. Grb2 regulates internalization of EGF receptors through clathrin-coated pits. *Mol Biol Cell.* 2003;14:858–70.
84. Johannessen LE, Pedersen NM, Pedersen KW, Madhusu IH, Stang E. Activation of the epidermal growth factor (EGF) receptor induces formation of EGF receptor- and Grb2-containing clathrin-coated pits. *Mol Cell Biol.* 2006;26:389–401.
85. Yamashiro DJ, Tycko B, Fluss SR, Maxfield FR. Segregation of transferrin to a mildly acidic (pH 6.5) para-Golgi compartment in the recycling pathway. *Cell.* 1984;37:789–800.
86. Mellman I, Fuchs R, Helenius A. Acidification of the endocytic and exocytic pathways. *Annu Rev Biochem.* 1986;55:663–700.
87. Maxfield FR, McGraw TE. Endocytic recycling. *Nat Rev Mol Cell Biol.* 2004;5:121–32.
88. Ding J, Rainey JK, Xu C, Sykes BD, Fliegel L. Structural and functional characterization of transmembrane segment VII of the Na⁺/H⁺ exchanger isoform 1. *J Biol Chem.* 2006;281:29817–29.
89. van Weert AW, Dunn KW, Gueze HJ, Maxfield FR, Stoorvogel W. Transport from late endosomes to lysosomes, but not sorting of integral membrane proteins in endosomes, depends on the vacuolar proton pump. *J Cell Biol.* 1995;130:821–34.
90. Hurtado-Lorenzo A, Skinner M, El AJ, Futai M, Sun-Wada GH, Bourgoin S, et al. V-ATPase interacts with ARNO and Arf6 in early endosomes and regulates the protein degradative pathway. *Nat Cell Biol.* 2006;8:124–36.
91. Merkulova M, Bakulina A, Thaker YR, Gruber G, Marshansky V. Specific motifs of the V-ATPase a2-subunit isoform interact with catalytic and regulatory domains of ARNO. *Biochim Biophys Acta.* 1797;2010:1398–409.
92. Souza-Schorey C, van Donselaar E, Hsu WW, Yang C, Stahl PD, Peters PJ. ARF6 targets recycling vesicles to the plasma membrane: insights from an ultrastructural investigation. *J Cell Biol.* 1998;140:603–16.
93. Radhakrishna H, Al-Awar O, Khachikian Z, Donaldson JG. ARF6 requirement for Rac ruffling suggests a role for membrane trafficking in cortical actin rearrangements. *J Cell Sci.* 1999;112(Pt 6):855–66.
94. Prigent M, Dubois T, Raposo G, Derrien V, Tenza D, Rosse C, et al. ARF6 controls post-endocytic recycling through its downstream exocyst complex effector. *J Cell Biol.* 2003;163:1111–21.
95. Taylor RC, Cullen SP, Martin SJ. Apoptosis: controlled demolition at the cellular level. *Nat Rev Mol Cell Biol.* 2008;9:231–41.
96. Galluzzi L, Bravo-San Pedro JM, Kroemer G. Organelle-specific initiation of cell death. *Nat Cell Biol.* 2014;16:728–36.
97. Bredesen DE, Rao RV, Mehlen P. Cell death in the nervous system. *Nature.* 2006;443:796–802.
98. Park M, Salgado JM, Ostroff L, Helton TD, Robinson CG, Harris KM, Ehlers MD. Plasticity-induced growth of dendritic spines by exocytic trafficking from recycling endosomes. *Neuron.* 2006;52:817–30.
99. Petrini EM, Lu J, Cognet L, Lounis B, Ehlers MD, Choquet D. Endocytic trafficking and recycling maintain a pool of mobile surface AMPA receptors required for synaptic potentiation. *Neuron.* 2009;63:92–105.
100. Walkley SU, Vanier MT. Secondary lipid accumulation in lysosomal disease. *Biochim Biophys Acta.* 1793;2009:726–36.
101. Cao C, Rioult-Pedotti MS, Migani P, Yu CJ, Tiwari R, Parang K, et al. Impairment of TrkB-PSD-95 Signaling in Angelman Syndrome. *PLoS Biol.* 2013;11, e1001478.
102. Ip NY, Li Y, Yancopoulos GD, Lindsay RM. Cultured hippocampal neurons show responses to BDNF, NT-3, and NT-4, but not NGF. *J Neurosci.* 1993;13:3394–405.
103. Leal G, Afonso PM, Salazar IL, Duarte CB. Regulation of hippocampal synaptic plasticity by BDNF. *Brain Res.* 1621;2015:82–101.
104. Huang EJ, Reichardt LF. Neurotrophins: roles in neuronal development and function. *Annu Rev Neurosci.* 2001;24:677–736.
105. Coulson EJ, Reid K, Bartlett PF. Signaling of neuronal cell death by the p75NTR neurotrophin receptor. *Mol Neurobiol.* 1999;20:29–44.
106. Zagrebelsky M, Holz A, Dechant G, Barde YA, Bonhoeffer T, Korte M. The p75 neurotrophin receptor negatively modulates dendrite complexity and spine density in hippocampal neurons. *J Neurosci.* 2005;25:9989–99.
107. Friedman WJ. Neurotrophins induce death of hippocampal neurons via the p75 receptor. *J Neurosci.* 2000;20:6340–6.
108. Troy CM, Friedman JE, Friedman WJ. Mechanisms of p75-mediated death of hippocampal neurons. Role of caspases. *J Biol Chem.* 2002;277:34295–302.
109. Schenck A, Goto-Silva L, Collinet C, Rhinn M, Giner A, Habermann B, et al. The endosomal protein Appl1 mediates Akt substrate specificity and cell survival in vertebrate development. *Cell.* 2008;133:486–97.
110. Schutze S, Tchikov V, Schneider-Brachert W. Regulation of TNFR1 and CD95 signalling by receptor compartmentalization. *Nat Rev Mol Cell Biol.* 2008;9:655–62.
111. Bredesen DE, Mehlen P, Rabizadeh S. Receptors that mediate cellular dependence. *Cell Death Differ.* 2005;12:1031–43.
112. Thibert C, Fombonne J. Dependence receptors: mechanisms of an announced death. *Cell Cycle.* 2010;9:2085–91.
113. Tabas I, Ron D. Integrating the mechanisms of apoptosis induced by endoplasmic reticulum stress. *Nat Cell Biol.* 2011;13:184–90.
114. Doyle KM, Kennedy D, Gorman AM, Gupta S, Healy SJ, Samali A. Unfolded proteins and endoplasmic reticulum stress in neurodegenerative disorders. *J Cell Mol Med.* 2011;15:2025–39.
115. Viana RJ, Nunes AF, Rodrigues CM. Endoplasmic reticulum enrollment in Alzheimer's disease. *Mol Neurobiol.* 2012;46:522–34.
116. Brewster JL, Linseman DA, Bouchard RJ, Loucks FA, Precht TA, Esch EA, Heidenreich KA. Endoplasmic reticulum stress and trophic factor withdrawal activate distinct signaling cascades that induce glycogen synthase kinase-3 beta and a caspase-9-dependent apoptosis in cerebellar granule neurons. *Mol Cell Neurosci.* 2006;32:242–53.
117. Urano F, Wang X, Bertolotti A, Zhang Y, Chung P, Harding HP, Ron D. Coupling of stress in the ER to activation of JNK protein kinases by transmembrane protein kinase IRE1. *Science.* 2000;287:664–6.
118. Roussel BD, Kruppa AJ, Miranda E, Crowther DC, Lomas DA, Marciniak SJ. Endoplasmic reticulum dysfunction in neurological disease. *Lancet Neurol.* 2013;12:105–18.
119. Correia CT, Coutinho AM, Sequeira AF, Sousa IG, Lourenco VL, Almeida JP, et al. Increased BDNF levels and NTRK2 gene association suggest a disruption of BDNF/TrkB signaling in autism. *Genes Brain Behav.* 2010;9:841–8.
120. Scattoni ML, Martire A, Cartocci G, Ferrante A, Ricceri L. Reduced social interaction, behavioural flexibility and BDNF signalling in the BTBR T+ tf/J strain, a mouse model of autism. *Behav Brain Res.* 2013;251:35–40.
121. Koh JY, Lim JS, Byun HR, Yoo MH. Abnormalities in the zinc-metalloprotease-BDNF axis may contribute to megalencephaly and cortical hyperconnectivity in young autism spectrum disorder patients. *Mol Brain.* 2014;7:64.
122. Purcell AE, Jeon OH, Zimmerman AW, Blue ME, Pevsner J. Postmortem brain abnormalities of the glutamate neurotransmitter system in autism. *Neurology.* 2001;57:1618–28.
123. Carlson GC. Glutamate receptor dysfunction and drug targets across models of autism spectrum disorders. *Pharmacol Biochem Behav.* 2012;100:850–4.
124. Lauterborn JC, Rex CS, Kramar E, Chen LY, Pandeyarajan V, Lynch G, Gall CM. Brain-derived neurotrophic factor rescues synaptic plasticity in a mouse model of fragile X syndrome. *J Neurosci.* 2007;27:10685–94.
125. Louhivuori V, Vicario A, Uutela M, Rantamaki T, Louhivuori LM, Castren E, et al. BDNF and TrkB in neuronal differentiation of Fmr1-knockout mouse. *Neurobiol Dis.* 2011;41:469–80.
126. Gao L, Tian M, Zhao HY, Xu QQ, Huang YM, Si QC, et al. TrkB activation by 7, 8-dihydroxyflavone increases synapse AMPA subunits and ameliorates spatial memory deficits in a mouse model of Alzheimer's disease. *J Neurochem.* 2016;136:620–36.
127. Wakabayashi S, Pang T, Su X, Shigekawa M. A novel topology model of the human Na⁺/H⁺ exchanger isoform 1. *J Biol Chem.* 2000;275:7942–9.
128. Nygaard EB, Lagerstedt JO, Bjerre G, Shi B, Budamagunta M, Poulsen KA, et al. Structural modeling and electron paramagnetic resonance spectroscopy of the human Na⁺/H⁺ exchanger isoform 1, NHE1. *J Biol Chem.* 2011;286: 634–48.



A potential gain-of-function variant of *SLC9A6* leads to endosomal alkalinization and neuronal atrophy associated with Christianson Syndrome

Alina Ilie^a, Andy Y.L. Gao^b, Annie Boucher^a, Jaeok Park^c, Albert M. Berghuis^c,
Mariëtte J.V. Hoffer^d, Yvonne Hilhorst-Hofstee^d, R. Anne McKinney^b, John Orlowski^{a,*}

^a Department of Physiology, McGill University, Montreal, Canada

^b Department of Pharmacology and Therapeutics, McGill University, Montreal, Canada

^c Department of Biochemistry, McGill University, Montreal, Canada

^d Department of Clinical Genetics, Leiden University Medical Center, Leiden, the Netherlands

ARTICLE INFO

Keywords:

Christianson Syndrome
X-linked intellectual disability
Alkali cation/proton exchangers –SLC9A6/
NHE6
Endosomal pH homeostasis
Membrane trafficking
Neurodegeneration

ABSTRACT

Loss-of-function mutations in the recycling endosomal (Na⁺,K⁺)/H⁺ exchanger gene *SLC9A6/NHE6* result in overacidification and dysfunction of endosomal-lysosomal compartments, and cause a neurodevelopmental and degenerative form of X-linked intellectual disability called Christianson Syndrome (CS). However, knowledge of the disease heterogeneity of CS is limited. Here, we describe the clinical features and underlying molecular and cellular mechanisms associated with a CS patient carrying a *de novo* missense variant (p.Gly218Arg; G218R) of a conserved residue in its ion translocation domain that results in a potential gain-of-function. The patient manifested several core symptoms typical of CS, including pronounced cognitive impairment, mutism, epilepsy, ataxia and microcephaly; however, deterioration of motor function often observed after the first decade of life in CS children with total loss of SLC9A6/NHE6 function was not evident. In transfected non-neuronal cells, complex glycosylation and half-life of the G218R were significantly decreased compared to the wild-type transporter. This correlated with elevated ubiquitination and partial proteasomal-mediated proteolysis of G218R. However, a major fraction was delivered to the plasma membrane and endocytic pathways. Compared to wild-type, G218R-containing endosomes were atypically alkaline and showed impaired uptake of recycling endosomal cargo. Moreover, instead of accumulating in recycling endosomes, G218R was redirected to multivesicular bodies/late endosomes and ejected extracellularly in exosomes rather than progressing to lysosomes for degradation. Attenuated acidification and trafficking of G218R-containing endosomes were also observed in transfected hippocampal neurons, and correlated with diminished dendritic branching and density of mature mushroom-shaped spines and increased appearance of filopodia-like protrusions. Collectively, these findings expand our understanding of the genetic diversity of CS and further elucidate a critical role for SLC9A6/NHE6 in fine-tuning recycling endosomal pH and cargo trafficking, processes crucial for the maintenance of neuronal polarity and mature synaptic structures.

Abbreviations: AMPAR, α -amino-3-hydroxy-5-methyl-4-isoxazolepropionic acid receptor; Arf6, ADP-ribosylation factor 6; ARNO, ADP-ribosylation factor nucleotide site opener; AP-1, Chinese hamster ovary (CHO) cells deficient in the Na⁺/H⁺ exchanger 1 isoform; CANX, calnexin; ChFP, monomeric Cherry fluorescent protein; CNS, central nervous system; CS, Christianson syndrome; DMSO, dimethylsulfoxide; EV, extracellular vesicles; ER, endoplasmic reticulum; ERAD, endoplasmic reticulum-associated degradation; ESCRT, endosomal sorting complex required for transport; FRIA, fluorescence ratiometric image analysis; G218R, mutation of amino acid Gly to Arg at position 218 in NHE6v1; GAPDH, glyceraldehyde-3-phosphate dehydrogenase; GFP, green fluorescent protein; HA, influenza virus hemagglutinin epitope; Hsp70, heat shock protein 70; Lamp1, lysosome-associated membrane protein 1; LE, late endosomes; LeuP, leupeptin/pepstatin; M.I.F, median intensity fluorescence; MVB, multivesicular bodies; OMIM, Online Mendelian Inheritance in Man; PCR, polymerase chain reaction; pHv, vesicular pH; PM, plasma membrane; SDS-PAGE, sodium dodecyl sulfate polyacrylamide gel electrophoresis; SLC9A6/NHE6, (sodium, potassium)/proton exchanger isoform 6; TCL, total cell lysate; Tf, transferrin; TfR, transferrin receptor; TGN, trans-Golgi network; TRKB, tropomyosin receptor kinase B; TSG 101, tumor susceptibility gene 101 protein; Ub, ubiquitin; WT, wild-type; XLID, X-linked intellectual disability.

* Corresponding author at: Department of Physiology, McGill University, Bellini Life Sciences Bldg., Rm, 166 3649 Promenade Sir-William-Osler, Montreal H3G 0B1, Canada.

E-mail address: john.orkowski@mcgill.ca (J. Orlowski).

<https://doi.org/10.1016/j.nbd.2018.10.002>

Received 19 July 2018; Received in revised form 18 September 2018; Accepted 3 October 2018

Available online 05 October 2018

0969-9961/ © 2018 Elsevier Inc. All rights reserved.

1. Introduction

Christianson Syndrome (CS; OMIM 300243) is a rare but increasingly diagnosed neurodevelopmental and regressive form of X-linked intellectual disability (XLID) first described in a multigenerational South African family in 1999 (Christianson et al., 1999). The causative gene, *SLC9A6* (solute carrier family 9, member A6), was identified at chromosomal position Xq26.3 in 2008 and encodes the (Na⁺, K⁺)/H⁺ exchanger isoform 6 (also called *NHE6*) (Gilfillan et al., 2008). Since then, over 50 different mutations in *NHE6* have been identified worldwide, many causing premature truncation of the protein in its N-terminal transmembrane domain that likely results in total loss-of-function (Gilfillan et al., 2008; Pescosolido et al., 2014) (also see supplementary data Tables S1 and S2, and databases ClinVar (<https://www.ncbi.nlm.nih.gov/clinvar/>) and DECIPHER (<https://decipher.sanger.ac.uk/>)). The CS population frequency is estimated to range from 1 in 16,000 to 100,000 (Pescosolido et al., 2014), although this may be an underestimate due to incomplete diagnoses. In addition to significant limitations in cognitive abilities and social/behavioral adaptive skills, all affected males lack speech despite noticeable auditory perception, and most have seizures, microcephaly, ataxia, atrophy and neuronal loss in brain regions including the cerebellum and brain stem, and reduced life expectancy. While most female carriers are asymptomatic, they may present with mild learning and behavioral difficulties (Christianson et al., 1999; Masurel-Paulet et al., 2016; Sinajon et al., 2016). Deficits in *NHE6* function may also extend to other neurodevelopmental disorders, as significantly reduced *NHE6* gene expression has been described in postmortem cerebral cortex from patients with idiopathic autism (Schwede et al., 2013); further suggesting a critical role for this transporter in cognitive development. However, the spectrum and frequency of clinical symptoms and genotype-phenotype correlations remain to be documented.

NHE6 is expressed in most tissues (Fagerberg et al., 2014) but is highest in the central nervous system (CNS), consistent with the prominent neuropathologic phenotype of CS. In non-neuronal cells, it is abundant in recycling endosomes together with the transferrin receptor (TfR) (Brett et al., 2002; Nakamura et al., 2005). Loss of *NHE6* function results in excess endosomal acidification, impaired TfR trafficking and dissolution of epithelial apical surface polarity (Ilie et al., 2016; Ohgaki et al., 2010; Xinhan et al., 2011). In the CNS, *NHE6* has been extensively studied in mouse hippocampal neurons and found in vesicles throughout the soma, dendrites and dendritic spines (i.e., the postsynaptic compartment) that also contain glutamatergic α -amino-3-hydroxy-5-methyl-4-isoxazolepropionic acid receptors (AMPA) (Deane et al., 2013) and neurotrophin tropomyosin receptor kinase B (TRKB) (Ouyang et al., 2013). It is also present in ill-defined vesicles along axons and at most presynaptic boutons (Deane et al., 2013; Ouyang et al., 2013) and is linked to neuronal growth, maturation and excitatory synaptic transmission; processes that govern memory and learning. Indeed, loss of *NHE6* function in knockout mice results in a CS-like neuropathologic phenotype with reduced hippocampal and cortical pyramidal neurite branching, synapse density, and circuit function (Ouyang et al., 2013) and patterned degeneration of cerebellar Purkinje cells that correlate with dysfunction of the endolysosomal pathway and deficits in mouse visuospatial memory and motor coordination (Sikora et al., 2016; Stromme et al., 2011). However, the molecular and cellular mechanisms responsible for this disorder have yet to be fully defined. Only a few human variants which leave the transporter intact have been studied at the molecular and cellular levels (Ilie et al., 2016; Ilie et al., 2014; Roxrud et al., 2009). Understanding the underlying pathobiology of CS may suggest novel therapeutic strategies for the disease.

Herein we report on a Dutch family in which a male presented with CS-like symptoms. Exome sequencing of the X chromosome of family members identified a *de novo* variant in *NHE6* (Xq26.3:g.135080689G > A:NM_001042537.1:c.652G > A:p.Gly218

Arg) of the affected male that results in substitution of a highly conserved glycine at position 218 with an arginine in the transmembrane domain of the longest splice-variant of *NHE6* (i.e., *NHE6v1*). We investigate the effects of this mutation on the biosynthetic processing, stability and membrane trafficking of *NHE6* and its impact on endosomal function and neuronal morphology. These results identify a novel molecular pathology for organellar pH-regulating transporters and provides further insight into the pathogenesis of this important neurological syndrome.

2. Materials and methods

2.1. Antibodies and reagents

Mouse monoclonal anti-hemagglutinin (HA) antibody was purchased from Covance Inc. (Berkeley, CA); rabbit polyclonal anti-HA, mouse monoclonal anti-GAPDH, rabbit polyclonal anti-Lamp1, and rabbit monoclonal anti-TSG101 were obtained from Abcam Inc. (Cambridge, MA); mouse monoclonal anti-Flag M2 antibody was from Sigma; rabbit polyclonal anti-GFP antibody was from Life Technologies. Rabbit polyclonal anti-calnexin and mouse monoclonal anti-Hsp70 antibodies were from Enzo Life Sciences, Inc. Mouse monoclonal anti-ubiquitin antibody (P4D1) was obtained from Santa Cruz Biotechnology. Rabbit polyclonal anti-cleaved caspase-3 (Asp175) (cCASP3) antibody was purchased from Cell Signaling Technology. The mEmerald GFP-tagged TGN46 was a gift from Michael Davidson (Addgene, mEmerald-TGNP-N-10 plasmid # 54279). Rab4-GFP, Rab5-GFP, and Rab7-GFP were a kind gift from Dr. Terry Hébert (McGill University). Horseradish peroxidase-conjugated secondary IgG antibodies were purchased from Jackson ImmunoResearch Laboratories (West Grove, PA). All Alexa Fluor® conjugated secondary antibodies were purchased from Molecular Probes (Eugene, OR). Alpha-minimum essential medium (α -MEM), fetal bovine serum, penicillin/streptomycin, and trypsin-EDTA were purchased from Wisent (Saint-Bruno, QC, Canada). The DMEM/F12 medium was from Corning. All other chemical and reagents were obtained from BioShop Canada (Burlington, ON, Canada), Sigma or Fisher Scientific and were of the highest grade available.

2.2. Genetic analyses

Whole-exome sequencing (WES) was performed using a trio diagnostic approach (proband and both parents). Genomic DNA was extracted from blood and fragmented into 200 to 500 bp fragments by means of Adaptive Focused Acoustics (Covaris Inc., Woburn, USA) shearing according to the manufacturer's protocol. Exome capture was performed by means of SureSelectXT Human all Exon v5 kit (Agilent, Santa Clara, USA) accompanied by Illumina paired-end Sequencing library preparation, sequencing on the Illumina HiSeq2500 (Illumina, San Diego, USA), generating 2 × 100 bp paired end reads with at least 70 × median coverage. The in-house sequence analysis pipeline Modular GATK-Based Variant Calling Pipeline (MAGPIE) (LUMC Sequencing Analysis Support Core, LUMC) based on read alignment using Burrows-Wheeler Alignment (BAM-MEM) (<http://arxiv.org/abs/1303.3997>) and variant calling using Genome Analysis Toolkit (GATK) (McKenna et al., 2010) was used to map FASTQ files, generate BAM files, mapping and variant calling. Reads were aligned to human genome build GRCh37/UCSC hg19. Variants were annotated using variant effect predictor (VEP, Ensembl) for calling of variants in coding regions and intron boundaries. Using variant databases (dbSNP132, ExAC and the 1000 Genomes Project database), frequent (> 5%) variants were excluded. LOVDplus (Leiden Genome Technology Center, LUMC, Leiden) was used for further analysis of variants. The data generated were deposited in the DECIPHER database (patient 368,102; <http://decipher.sanger.ac.uk/>) (Firth et al., 2009).

2.3. Animal procedures

All procedures for animal handling were approved by the McGill

University Facility Animal Care Committee (FACC) and carried out in full compliance with the Policies and Guidelines of the Canadian Council on Animal Care (CCAC).

2.4. Recombinant DNA constructs and mutagenesis

The long transcript splice-variant of human NHE6 (NHE6v1; NCBI NM_001042537) was cloned from a human brain Matchmaker™ cDNA library (Clontech) using PCR methodology and was engineered to contain the influenza virus hemagglutinin (HA) (YPYDVPDYAS) epitope at its extreme C-terminal end as described previously (Ilie et al., 2014). NHE6_{HA} was then used as a template to engineer the G218R missense mutation by PCR mutagenesis. The same templates was also used to introduce a triple Flag epitope in the first extracellular loop immediately after residue Met53 (Ilie et al., 2014). Enhanced green fluorescent protein (GFP) and monomeric Cherry fluorescent protein (ChFP) were also fused to the C-terminus NHE6 WT and G218R mutant. Insertion of the different epitope tags in the various positions did not alter the biochemical properties or cellular distribution of exogenous NHE6 compared to the endogenous protein (Ilie et al., 2014). All constructs were sequenced to insure that no additional mutations were introduced during PCR.

2.5. Cell culture

Chinese hamster ovary AP-1 and HeLa cells were cultured in α -MEM supplemented with 10% fetal bovine serum, penicillin (100 units/ml), streptomycin (100 μ g/ml), and 25 mM NaHCO₃ (pH 7.4). Primary cultures of mouse hippocampal neurons were prepared from postnatal day (PD) 0–2 day C57BL/6 mice as described previously (Deane et al., 2013; Ilie et al., 2014).

2.6. Western blotting

For western blot analyses, AP-1 and HeLa cells were grown in 10-cm dishes and transiently transfected with 5 μ g of plasmid DNA encoding NHE6_{HA} wild-type or mutant constructs using Lipofectamine2000™ (Invitrogen), as described previously (Ilie et al., 2016).

2.7. Cell surface biotinylation

Extraction of biotinylated plasma membrane proteins was performed by treating cells with the membrane-impermeable reagent N-hydroxysulfosuccinimide-SS-biotin (0.5 mg/ml) (ThermoScientific, Rockford, IL) as previously described (Ilie et al., 2016).

2.8. Isolation of extracellular membrane vesicles

AP-1 cells were grown in 15-cm dishes (5 for each construct) and transfected with 20 μ g of NHE6_{HA} WT or G218R in serum-free α -MEM using Lipofectamine2000. Twenty-four hours after transfection, the culture medium was collected in 50-ml Falcon tubes and centrifuged at 500 \times g for 5 min, then at 2000 \times g for 10 min, in order to remove any intact cells and cell debris. The supernatant resulting from these two centrifugations was concentrated to 1.5 ml using Amicon® Ultra-15 centrifugal filters with 100,000 NMWL (Nominal Molecular Weight Limit), according to the manufacturer's instructions. This concentrated culture medium was subjected to ultracentrifugation at 100,000 \times g for 2 h at 4 °C to obtain the membrane fraction. The resulting pellet was washed in 1.5 ml PBS and re-centrifuged at 100,000 \times g for 1.5 h at 4 °C. The membrane vesicle-enriched pellet was resuspended in lysis buffer and stored at –80 °C. Total cellular lysates were also obtained by lysing the cells of each dish in 1.5 ml lysis buffer. Protein concentrations were measured and 40 μ g of exosomal protein, along with 10 μ g of total cellular protein, were subjected to SDS-PAGE and immunoblotting with the indicated antibodies. On average, the total protein levels of the

exosomal preparations for WT- and G218R-transfectants represented ~3–4% of the total cell lysate protein content.

For chloroquine treatment, AP-1 cells were transfected with NHE6_{HA} WT or G218R in serum-free α -MEM for 10 h, then the medium was changed to serum-free α -MEM containing no chloroquine (control samples) or 250 μ M chloroquine for 15 h. Extracellular vesicles and total cellular lysates were then obtained as described.

2.9. Neuronal DNA transfection

Primary hippocampal neuronal cultures were prepared from C57BL/6 mice and co-transfected at 10–12 days *in vitro* (DIV) with GFP and mCherry fluorescent protein (ChFP) or NHE6_{ChFP} WT or G218R by calcium phosphate-mediated transfection as previously described (Ilie et al., 2016).

2.10. Immunofluorescence confocal microscopy

AP-1 cells were cultured on fibronectin-coated 18-mm glass coverslips, transfected with 3F-NHE6_{HA} WT or G218R mutant, and fixed 24 h post-transfection with 4% paraformaldehyde for 20 min at room temperature. To label NHE6 present on the plasma membrane, cells were incubated with mouse monoclonal anti-Flag antibody (1:1000) in PBS-CM/10 mM glucose/10 mM HEPES/2% goat serum, pH 7.4 for 1 h at room temperature (wash buffer), washed 4 times, and then incubated with goat anti-mouse Alexa Fluor® 488-conjugated secondary antibody (1:1300) for 1 h at room temperature. After extensive washes with PBS, cells were permeabilized with 0.1% saponin/PBS for 20 min at room temperature and then incubated with rabbit polyclonal anti-HA antibody (1:400) in wash buffer supplemented with 0.01% saponin at 4 °C overnight to label the total cellular pool of NHE6. After washes with PBS, cells were labelled with goat anti-rabbit Alexa Fluor® 568-conjugated secondary antibody (1:1200) for 1 h at room temperature, washed, and mounted onto glass slides.

To examine the subcellular distribution of WT and G218R mutant, AP-1 cells were co-transfected with NHE6_{ChFP} WT or G218R and different GFP-tagged organellar markers (Rab4, Rab5, Rab7, and TGN46), fixed and mounted 24 h post-transfection. To label transferrin-containing recycling endosomes, AP-1 cells transfected with NHE6_{ChFP} WT or G218R for 24 h, were incubated with Alexa Fluor® 488-conjugated transferrin (Tf-AF⁴⁸⁸) for 45 min in serum-free α -MEM, washed, fixed, and mounted. To visualize the ER and lysosomes, AP-1 cells expressing NHE6_{ChFP} WT or G218R were fixed 24 h after transfection and labelled with rabbit polyclonal anti-calnexin or anti-Lamp1 primary antibodies, respectively, followed by goat anti-rabbit Alexa Fluor® 488-conjugated secondary antibodies, washed, and mounted. Cells were examined by laser scanning confocal microscopy using the ZEN software of a Zeiss LSM 780 microscope equipped with a PMT detector, with images acquired using a 63 \times /1.4 NA oil immersion objective lens.

Mounted primary hippocampal cultures were imaged using a Leica SP2 confocal microscope. Images were acquired using 40 \times and 63 \times HCXPL APO oil-immersion objectives (NAs 1.25 and 1.4, respectively). GFP was imaged using a 488 nm Ar laser line; mCherry was imaged using a 543 nm HeNe laser line, and Dylight 649 was imaged using the 633 nm HeNe laser line. Channels were acquired sequentially to prevent spectral overlap of fluorophores. Optical sections of 300–500 nm were taken and frame averaged 3 \times at low resolution or line-averaged 2 \times at high resolution to improve the signal-to-noise ratio. Images were first deconvolved using Huygen's Essential software by using a full maximum likelihood extrapolation algorithm (Scientific Volume Imaging), and 3D images were compiled as maximum intensity projections using Imaris software (Bitplane Ag).

Topographical order of neuronal morphology was performed on 3D confocal images of primary hippocampal neurons prepared from C57BL/6 mice. Images were analyzed using the FilamentTracer program (Bitplane AG, Zurich, Switzerland), which semi-automatically detects 3D

neuronal GFP-labelled filament structures and calculates parameters such as the number of branch points, total dendrite length and area.

2.11. Measurement of endosomal pH

AP-1 cells for grown overnight on FluoroDishes™ (World Precision Instruments, Inc.) coated with fibronectin/PBS (2 µg/ml, for 2–4 h at 37 °C). Cells were transfected with 1 µg/dish of NHE6v1 (WT or G218R) containing pHluorin2 in the first extracellular loop (inserted at amino acid position M53) (pH2NHE6v1) using Lipofectamine2000 reagent according to the manufacturer's instructions. Twenty-four h after transfection, cells were incubated for 5 h with 100 µg/ml cycloheximide in complete medium. Before imaging, cells were switched to CO₂-independent medium. Vesicular pH was measured by single-cell fluorescence ratiometric imaging analysis (FRIA) at 37 °C, using a Zeiss LSM 780 confocal microscope, equipped with a PMT detector. Images were acquired with a 63×/1.4 NA oil immersion objective lens by sequential line scanning at 405 and 488 excitation wavelengths, with emission set at 500–550 for both channels. All cells were imaged in a heated chamber (37 °C) at 3× zoom, while the laser power, resolution, speed of scanning, digital gain and offset, pinhole opening and line averaging were identical for both channels. Average intensities of fluorescent puncta (0.3 to 3 µm in diameter) were obtained for both the 405 and 488 channels using the MetaXpress software (Molecular Devices, Downingtown, PA) and 488/405 ratios were calculated. Calibration curves of fluorescence as a function of vesicular pH were performed *in situ* in AP-1 cells expressing pH2NHE6v1 WT by clamping the vesicular pH between 5 and 7.8 in K⁺-rich medium (135 mM KCl, 10 mM NaCl, 20 mM Hepes or 20 mM MES, 1 mM MgCl₂, and 0.1 mM CaCl₂) with 10 µM nigericin, 10 µM monensin, 0.4 µM bafilomycin and 20 µM carbonyl cyanide *m*-chlorophenyl hydrazone (CCCP) and recording the 488/405 fluorescence ratios, as described above. The calibration curves and Gaussian distributions of vesicular pH values were plotted with OriginPro 8 software (OriginLab, Northampton, MA).

2.12. Flow cytometry

To measure transferrin uptake by flow cytometry, HeLa cells were transfected with GFP alone, NHE6_{GFP} WT or G218R mutant using FuGene6 (Promega). Twenty-four h after transfection, the cells were serum-depleted for 2 h, and then incubated with Alexa Fluor® 633-conjugated transferrin (Tf-AF⁶³³, 10 µg/ml) for 5 min at 37 °C, followed by washes to remove unbound transferrin. Cells were detached from the plates by trypsinization and 5 µl of the cell viability dye 7-amino-actinomycin D (7-AAD, eBioscience) was added to each cell suspension. Cells were analyzed by flow cytometry using a FACS Aria Sorter (Becton Dickinson, San Jose, CA). A gate was set around the GFP-positive cells and the amount of Tf-AF⁶³³ taken up by 10⁴ GFP-expressing live cells (*i.e.*, 7-AAD negative) was measured using the BD FACS Diva software.

2.13. Statistical analyses

The data represent the mean ± the standard error of the mean (S.E.) and statistical analyses were performed by using the Student's *t*-test or a one-way analysis of variance (ANOVA) followed by suitable post-hoc tests as indicated (Tukey, Bonferroni, or Dunns). A minimum *p*-value of < 0.05 was considered significant.

3. Results

3.1. Clinical features

The affected male patient, now 22 years of age, was the second child born to non-consanguineous healthy parents of Dutch origin. He also has a healthy older sister (24 years old). The proband displayed many core symptoms ascribed to CS, including severe intellectual disability,

epilepsy, absence of verbal communication, happy demeanor, microcephaly, slender physique, truncal ataxia and hyperactivity. Several common secondary symptoms were also evident, including autism-like behaviors, ophthalmoplegia, flexed arms, sleep disturbances, low weight, excessive drooling and incontinence; however, motor regression that often manifests after the first decade of life in CS children with complete NHE6 loss-of-function was not apparent. A more complete clinical description and list of symptoms compared to a subset of other CS families (where comparable clinical information was available) is presented in supplementary Table S1.

3.2. Mutation analyses

Extensive genetic analyses were performed, including single nucleotide polymorphism (SNP)-array analysis, methylation analysis of the Angelman/Prader-Willi region, sequencing of the *UBE3A*- and *SLC6A8*-gene, all without abnormalities. Trio-based whole-exome sequencing revealed two hemizygous missense variants, one in *FGD1* (FYVE, RhoGEF and PH domain-containing protein 1) (Xp11.22:g.54492214A > G:NM_004463.2:c.1412 T > C:p.Val471 Ala) and one in *SLC9A6/NHE6* (Xq26.3:g.135080689G > A:NM_001042537.1:c.652G > A:p.Gly218Arg). The *FGD1* variant was present in the mother, while the sister was not tested for this variant. Mutations in *FGD1* are linked to Aarskog-Scott syndrome (OMIM 300546), also known as faciogenital dysplasia, but the proband did not exhibit clinical features characteristic of this disorder, suggesting the variant is benign. By contrast, the *NHE6* variant was not present in the mother or sister, indicating it was unique to the proband and arose by *de novo* mutation (Fig. 1A). This Gly residue is in the predicted 5th membrane-spanning segment (M5) of NHE6 and is conserved in all human NHE paralogs (Fig. 1B) and NHE6 orthologs from mammals to fruit flies (Supplementary Fig. S1), and hence likely essential for function. Human *NHE6* undergoes alternate splicing at its 5' untranslated sequence and coding region to generate at least four distinct cytoplasmic mRNAs (NHE6v1 to v4), of which NHE6v1 (701 amino acids, NCBI NM_001042537.1) encodes the longest transcript. The mutation that would be present in all splice variants. The relative abundances and functional differences, if any, between the splice variants are unknown. A list of other documented NHE6 variants (missense, frameshift, nonsense, in-frame deletions, and splice-site variants) linked to Christianson Syndrome are tabulated in supplementary Table S2.

3.3. Structural homology modelling of NHE6

To gain insight into the possible significance of Gly218 for structure and function, we performed homology modelling of *homo sapiens* NHE6v1 (*HsNHE6v1*) using the high-resolution crystal structures of distantly-related bacterial Na⁺/H⁺ antiporters (15–20% identity; 27–29% similarity), an approach that has been instructive in validating the tertiary conformation of *HsNHE1* (Landau et al., 2007; Nygaard et al., 2011). Swiss-Model software was used to generate a 3D structural model of the N-terminal transmembrane region (encompassing residues 74–540) of *HsNHE6v1*. Its sequence was threaded onto the outward-facing conformation of the *Thermus thermophilus* NapA (*TtNapA*) structure (Protein Data Bank accession code 5bz3.1.A; 2.30 Å, 15% identity, 27% similarity) (Coincon et al., 2016), which provided the broadest coverage, highest resolution, and best spatial fit among crystallized bacterial Na⁺/H⁺ antiporters. An alignment of the two sequences is presented in Supplementary Fig. S2A and the resulting theoretical 3D structure of monomeric *HsNHE6v1* (*N.B.*, mammalian and bacterial Na⁺/H⁺ exchangers/antiporters assemble as homodimers) is shown in Fig. 1C. In this model, the alpha carbon atoms of Gly218 and Arg457 are separated by ~5 Å (Fig. 1D). Conservation of these closely packed residues in all mammalian NHEs (Supplementary Fig. S2B) and bacterial antiporters *TtNapA* (Gly94 and Lys305) and *EcNhaA* (Gly104

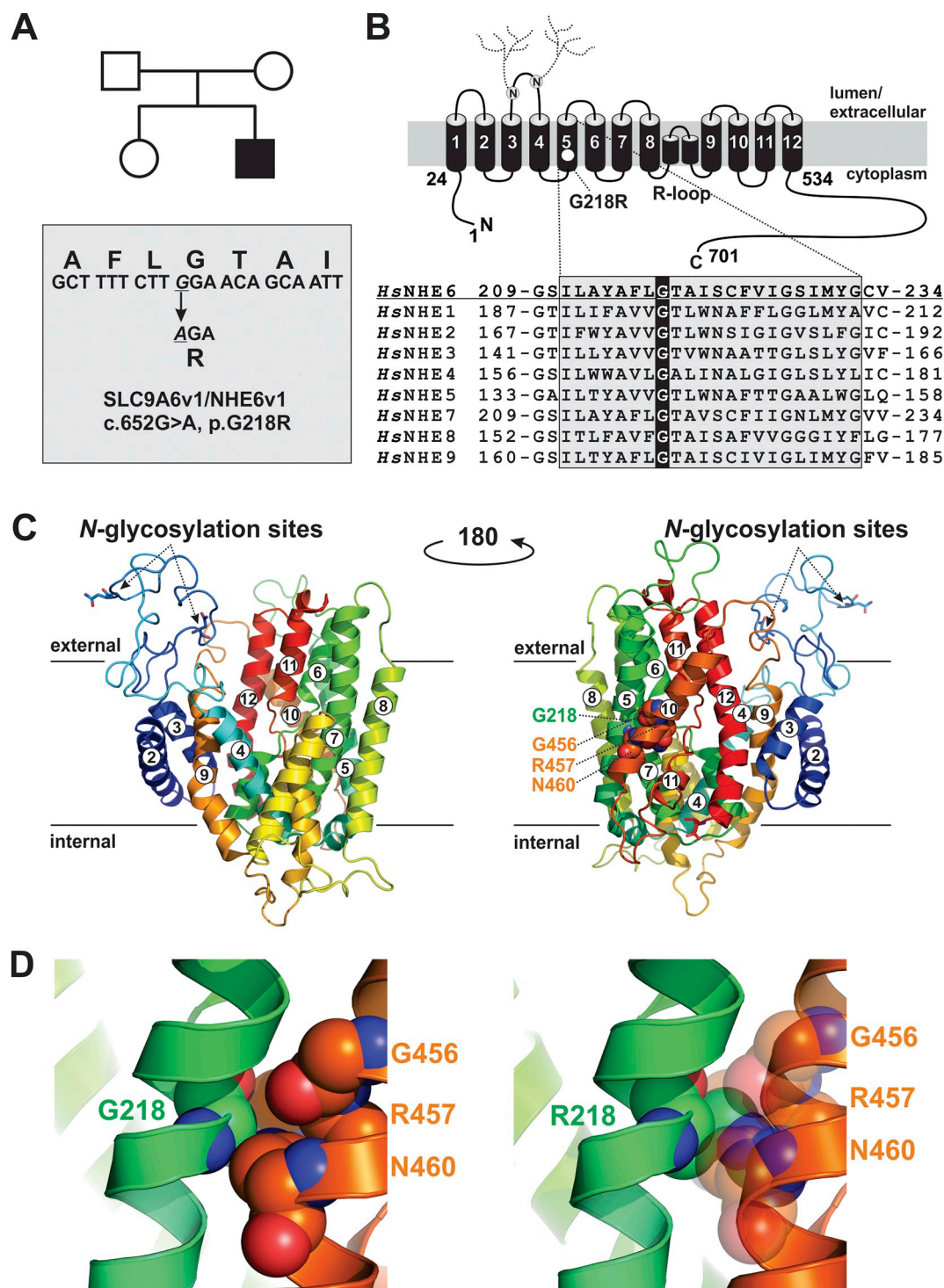


Fig. 1. Identification of a *de novo* missense mutation in SLC9A6/NHE6 in a patient with Christianson Syndrome. **A**, Family pedigree and description of a *de novo* missense mutation (c.652G > A: p.Gly218Arg) (G218R) in the longest splice variant (v1) of SLC9A6/NHE6. **B**, Schematic planar drawing of the predicted membrane topology of mammalian NHE6v1 based on comparisons of the proposed transmembrane topology of NHE1 (Landau et al., 2007; Nygaard et al., 2011) and location of the pG218R mutation (white circle) in the predicted fifth membrane-spanning (M5) helix. Two consensus N-glycosylation sites (N128 and N145) within extracellular loop 2 have been verified experimentally (data not shown) and are illustrated in the drawing. Also presented is the sequence alignment of the M5 helix and conserved Gly residue of all *Homo sapiens* Na⁺/H⁺ exchangers (*HsNHE1*–9). **C**, Side-view (left panel) of a 3D structure homology model of monomeric *HsNHE6v1* (N.B., NHEs normally assemble as homodimers) based on the crystal structure of the smaller bacterial *Thermus thermophilus* Na⁺/H⁺ antiporter NapA (TtNapA) (Protein Data Bank accession code 5bz3.1.A; 2.30 Å, 15% identity, 27% similarity) (Coincon et al., 2016) which provided the broadest coverage, highest resolution, and best spatial fit compared to other crystallized bacterial Na⁺/H⁺ antiporters. The proposed structure includes only the membrane-spanning helices (M2–M12) that aligned with homologous segments of TtNapA as well as the connecting loops and location of the two N-glycosylation sites. The opposite side-view (right panel) is illustrated to expose the Gly218 residue and neighboring amino acids Gly456, Arg457 and Asn460. **D**, Enlargement of the region encompassing Gly218 (left panel) and analogous representation of the same region where Gly218 has been replaced with Arg218.

and Lys300) suggests they have a critical role. Mutating Arg425 of HsNHE1 (equivalent to Arg457 of HsNHE6v1) markedly reduces its glycosylation, stability, plasma membrane targeting and catalytic activity (Li et al., 2014; Nygaard et al., 2011). Likewise, mutations of Lys305 in TtNapA (Lee et al., 2013) and Lys300 in EcNhaA (Kozachkov et al., 2007; Maes et al., 2012) were found to decrease the substrate affinities and structural integrity of those antiporters (Calinescu et al., 2017). Although the significance of the apposed Gly residue has not been examined, based on homology modelling we speculated that replacement of Gly with a large, positively-charged Arg residue (G218R) would cause steric and electrostatic repulsion between Arg218 and Arg457 (Fig. 1D) and alter the structural stability and catalytic activity of the transporter.

3.4. Post-translational processing and stability of NHE6-G218R are impaired

The Chinese hamster ovary-derived AP-1 cell line is a useful expression system for studying and comparing the molecular and cellular properties of NHE6 variants because endogenous NHE6 levels are negligible and its subcellular distribution and behaviour are similar to that in primary and organotypic cultures of hippocampal pyramidal neurons (Deane et al., 2013; Ilie et al., 2016). Immunoblotting for C-terminal HA epitope-tagged NHE6v1 (NHE6v1_{HA}) revealed striking differences between the wild-type (WT) and mutant G218R constructs with respect to their biosynthetic maturation and stability (Fig. 2A). Under SDS-PAGE conditions, NHE6v1_{HA} migrates as multiple bands reflecting different oligomeric and post-translational oligosaccharide states, consistent with earlier findings (Ilie et al., 2014; Miyazaki et al., 2001). The WT migrates as fully-glycosylated dimeric (~200-

250 kDa) and monomeric (100–120 kDa) forms, and newly synthesized core-glycosylated (~70 kDa) monomer was also observed. By contrast, G218R migrated predominantly as immature core-glycosylated monomeric and dimeric forms, although a diffuse band corresponding to the fully-glycosylated dimer was also detected suggestive of limited posttranslational processing. Quantitation of the immunoblot signals revealed that total expression of the G218 was significantly reduced compared WT (Fig. 2B).

To estimate the half-lives of WT and G218R, pulse-chase experiments were performed 24 h after transfection. Cells were treated with cycloheximide for an additional 2–24 h to inhibit *de novo* protein synthesis and the levels of the previously synthesized transporters were monitored by immunoblotting. As shown in Fig. 2C–D, WT was relatively stable with a half-life ($t_{1/2}$) exceeding 24 h whereas the G218R mutant was rapidly removed ($t_{1/2}$ of ~1.5 h).

Rapid clearance of the G218R mutant could occur by multiple mechanisms, including proteasomal degradation via the ERAD (endoplasmic reticulum-associated degradation) pathway (Meusser et al., 2005) or later in lysosomes by the peripheral quality control ESCRT (endosomal sorting complex required for transport)-dependent degradative pathway (Raiborg and Stenmark, 2009). To explore these possibilities, we first examined G218R ubiquitination (i.e., multi-mono- or poly-ubiquitination), a distinguishing feature of both mechanisms. To compare the ubiquitination of WT and G218R transporters (ub-WT and ub-G218R), they were transiently expressed in AP-1 cells for 24 h, immunoprecipitated from cell lysates, and immunoblots were probed with a monoclonal anti-ubiquitin antibody. The signals for ub-WT and ub-G218R ranged from ~150 kDa to > 250 kDa, which presumably represent ubiquitin conjugates of NHE6 monomers and/or undissociated dimers (Fig. 2E). Ubiquitination of G218R was significantly elevated (~5-fold) compared to WT when normalized to total NHE6 levels in their respective immunoprecipitates (Fig. 2E–F). This also revealed that only minor fractions of total WT and G218R were ubiquitinated.

To identify pathways mediating the degradation of G218R, we exposed cycloheximide-treated cells to inhibitors of proteasomal (MG132, lactacystin) or lysosomal (leupeptin plus pepstatin (LeuP), chloroquine)

proteolysis. As expected, the proteasomal and lysosomal inhibitors did not affect WT levels appreciably over 8 h compared to vehicle-treated controls (Fig. 3A). By comparison, inhibiting

the proteasome partially reduced the cellular loss of G218R (Fig. 3B), implicating a limited role for the ERAD pathway. Curiously, the lysosomal protease inhibitors LeuP were ineffective whereas chloroquine was a potent blocker. Unlike LeuP which are direct competitive inhibitors of lysosomal peptidases, chloroquine is a weak base that accumulates in acidic organelles where it becomes protonated (Maxfield, 1982). The resulting alkalization of these compartments impairs the activities of acidic hydrolases (Seglen et al., 1979). However, given the ineffectiveness of LeuP, and the ability of chloroquine to block the rapid disappearance of G218R suggested it acted through a different mechanism. We postulated that one such pathway could involve exosomes, small lipid vesicles formed by the inward budding of late endosomes (LE) (also termed multivesicular bodies, MVB) (Colombo et al., 2014). When MVB/LE fuse with the plasma membrane rather than with lysosomes, they discharge their intraluminal vesicles (comprised of lipids, proteins and ribonucleic acids) into the extracellular milieu. Similar to the sorting of cargo to lysosomes, ubiquitination (Buschow et al., 2005) and the ESCRT machinery (Colombo et al., 2013) are also involved in the biogenesis and secretion of exosomes.

3.5. Extracellular vesicular release of G218R

To assess this possible mechanism, an extracellular vesicular (EV) fraction was prepared using serum-free culture media collected from AP-1 cell cultures transiently expressing either WT or G218R after 24 h using an established differential ultracentrifugation protocol (Greening et al., 2015). High-molecular weight G218R (presumably ub-G218R) was greatly enriched in the EV fraction compared to WT (Fig. 3C). The nature of the EV membrane fraction was confirmed by probing the immunoblots for EV markers, tumor susceptibility gene 101 protein (TSG101, a component of the ESCRT-I complex that recognizes ubiquitinated proteins), and heat shock protein 70 (HSP70, HSPA1A/B, a molecular chaperone that promotes protein folding and also disposal of defective proteins). TSG101 is specific for MVB/LE-derived exosomes whereas HSP70 is in both exosomes and PM-derived microvesicles (also called ectosomes) (Kowal et al., 2016). The levels of both EV markers prepared from WT- and G218R-transfected cells were relatively equivalent, suggesting that expression of G218R did not markedly perturb the net secretion of EVs, but was selectively enriched in them. This was supported by measurements of the absolute protein content of the EV and total cell lysate fractions derived from WT- and G218R-transfected cells. In both cases, the EV fractions were equivalent when expressed as a percentage of the total cell lysates (WT: 3.71% ± 0.19; G218R: 3.70% ± 0.46) (Fig. 3E). As a negative control, immunoblots were also probed for calnexin (CANX), an integral membrane protein involved in endoplasmic reticulum (ER) quality control (Bergeron et al., 1994). As expected, it was virtually absent in the EV fraction (Fig. 3C), which excludes cell lysis as a contributing factor to the extracellular membrane fraction.

Exposure to chloroquine (250 μM, 15 h) blocked secretion of both WT and G218R in EVs and, conversely, increased the total amount of WT and G218R within cells (Fig. 3D). Chloroquine treatment also impaired the oligosaccharide maturation of both constructs, though this was more pronounced for WT. Golgi alkalization is known to reduce glycosylation (Maeda and Kinoshita, 2010). However, this treatment did not affect the relative levels of either TSG101 or HSP70 in EVs or total cell lysates, indicating that the molecular composition and formation of EVs were not adversely affected by chloroquine. Indeed, chloroquine actually increased the net release of EVs per cell by ~3-fold, although there was no difference between WT and G218R-transfected cells (WT: 11.77% ± 0.59; G218R: 10.24% ± 0.74) (Fig. 3E). Thus, chloroquine may disrupt an earlier pH-dependent step in the trafficking and/or fusion of NHE6-containing endosomes to MVB/LE.

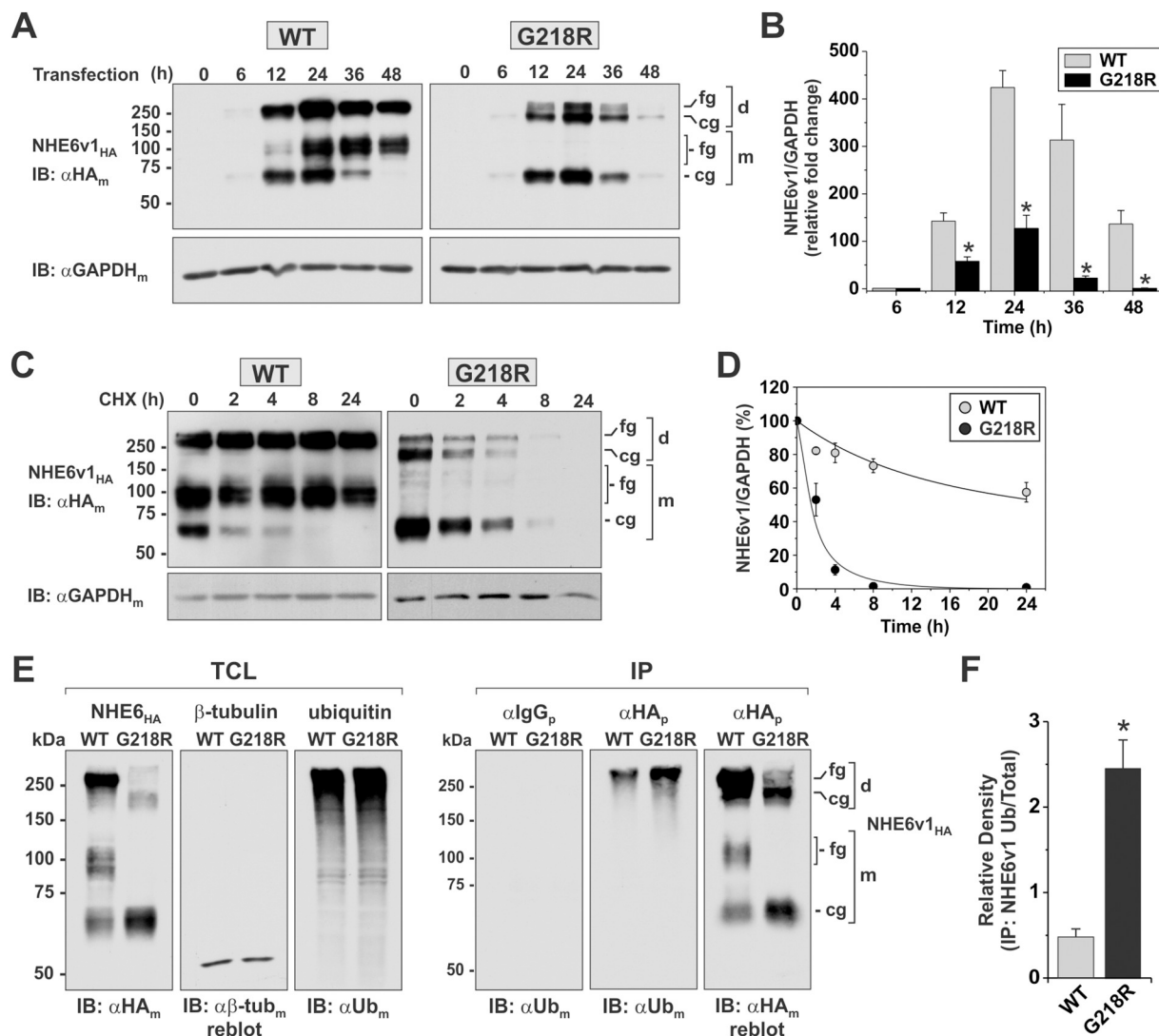


Fig. 2. Biosynthetic maturation and stability of NHE6 is reduced for the G218R mutant. **A**, AP-1 cells were transiently transfected with NHE6v1_{HA} WT or G218R and lysed at the indicated time points over a 48 h period. Equal amounts of proteins (20 µg) were subjected to Western blotting and probed with a monoclonal anti-HA antibody (αHA_m). NHE6v1 migrates as multiple bands: slower migrating high molecular weight bands representing the fully-glycosylated (fg) and core-glycosylated (cg) dimeric forms of the exchanger (~200 and 175 kDa, respectively) that do not fully dissociate under SDS-PAGE conditions and faster migrating fully-glycosylated (fg, ~100 kDa) and core-glycosylated (cg, ~70 kDa) forms of the monomeric protein. To control for protein loading, the blots were reprobed with a mouse monoclonal anti-GAPDH antibody (αGAPDH_m). **B**, Densitometric quantification of the relative total cellular abundances of WT, G218R and GAPDH was expressed as a ratio NHE6v1/GAPDH. Data are shown as mean ± standard error of the mean (S.E.) of three different experiments. Statistical significance was assessed using a paired Student's *t*-test, * *p* < 0.01. **C**, AP-1 cells were transiently transfected with WT or G218R for 24 h and then treated with 150 µg/ml cycloheximide for the indicated time points, lysed and equal amounts of protein (20 µg) were analyzed by Western blotting using a mouse monoclonal anti-HA (αHA_m) antibody. Blots were reprobed with a mouse monoclonal anti-GAPDH antibody (αGAPDH_m) to control for loading. **D**, Densitometric quantification of WT and G218R protein abundance (normalized to GAPDH levels) as a function of time in the presence of cycloheximide. Values represent the mean ± S.E. (*n* = 3). **E**, AP-1 cells were transiently transfected with NHE6v1_{HA} WT or G218R for 24 h, then lysed and their expression in total cell lysates (TCL) was analyzed by Western blotting with a mouse monoclonal anti-HA (αHA_m) antibody (*panel 1*). The blots were stripped and reprobed with a monoclonal antibody to β-tubulin (αβ-tub_m) as a loading control (*panel 2*). The level of ubiquitinated proteins in the TCL was examined using a mouse monoclonal anti-ubiquitin (αUb_m) antibody (*panel 3*). The TCLs were further subjected to immunoprecipitation (IP) with a non-specific rabbit polyclonal IgG (αIgG_p) antibody (*panel 4*) or a rabbit polyclonal anti-HA (αHA_p) antibody (*panel 5*) and analyzed with a mouse monoclonal αUb_m antibody to detect ubiquitination of WT and G218R. The membrane from *panel 5* was then stripped and reprobed with a mouse monoclonal αHA_m antibody to examine the total amount of WT and G218R retrieved by immunoprecipitation (*panel 6*). **F**, Densitometric quantification of the ratio of ubiquitinated to total protein abundance of WT and G218R in the immunoprecipitated pellets. Values represent the mean ± S.E. (*n* = 4). Statistical significance was assessed using a Student's *t*-test, * *p* < 0.01.

ER-resident CANX was not detected in EVs in the absence or presence of chloroquine. However, total cellular levels of CANX were increased upon chloroquine treatment, perhaps due to ER stress (Ruddock and Molinari, 2006).

3.6. G218R causes intracellular mislocalization of NHE6

To gain more insight into the membrane trafficking fate of G218R,

we performed subcellular localization analyses using other biochemical and imaging approaches. Most NHE6 WT normally resides in recycling endosomes, however in some cell types a small fraction (~5%) appears on the cell surface through endosomal recycling (Brett et al., 2002), and this was confirmed for AP-1 cells (Supplementary Fig. S3). To determine if the G218R mutant can also traffic to the cell surface, PM localization was assayed using cell surface biotinylation (Le Bivic et al., 1989). Total cellular expression of G218R was ~22% that of WT

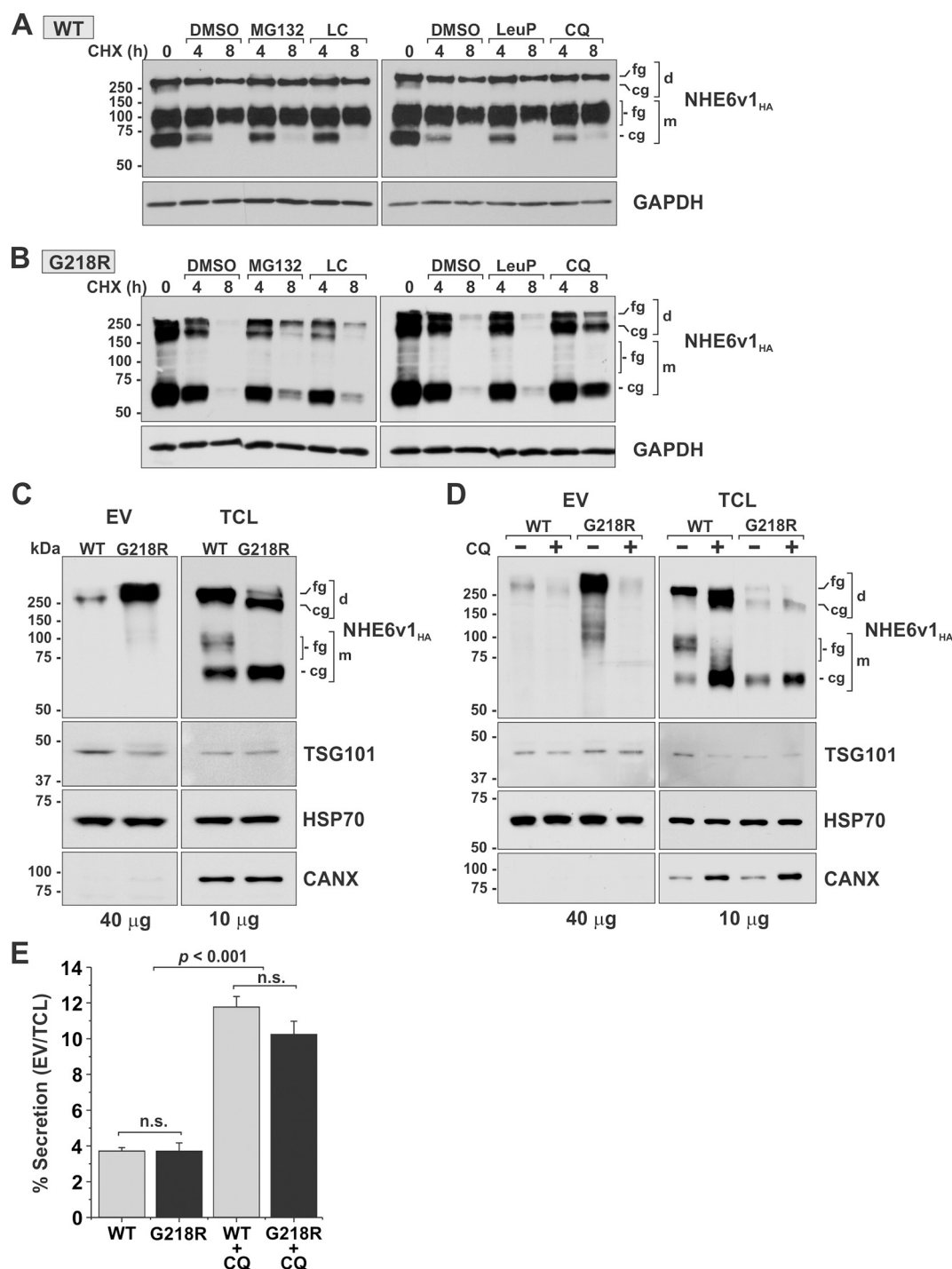


Fig. 3. Effect of proteasomal and lysosomal inhibitor on half-life and cellular clearance of NHE6. AP-1 cells were transiently transfected with (A) WT or (B) G218R for 24 h and then treated with 150 μ g/ml cycloheximide for the indicated time points in the presence of diluent (dimethylsulfoxide, DMSO), the proteasomal inhibitors MG-132 (40 μ M) or lactacystin (LC, 30 μ M) (*left panels*), or the lysosomal inhibitors leupeptin/pepstatin (LeuP, 100 μ g/ml) or chloroquine (CQ, 500 μ M) (*right panels*). Total cell lysates were analyzed by Western blotting with a mouse monoclonal α HA_m antibody. Membranes were also probed for GAPDH expression as a loading control. The immunoblots are representative of two separate experiments. C, AP-1 cells were transiently transfected with NHE6v1_{HA} WT or G218R for 24 h in serum-free culture media. The media was collected and the extracellular vesicular (EV) membrane fractions were isolated by a differential ultracentrifugation protocol (Greening et al., 2015). The EV fractions as well as total cell lysates (TCL) were analyzed by Western blotting for expression of NHE6v1_{HA} detected with a mouse monoclonal anti-HA (α HA_m) antibody. The blots were repeatedly stripped and reprobed for expression of the ESCRT I complex protein TSG101, heat shock protein 70 (HSP70), and calnexin (CANX). D, AP-1 cells transiently expressing WT or G218R at 9 h post-transfection were left untreated (–) or treated (+) with chloroquine (CQ, 250 μ M) for an additional 15 h in serum-free culture media. EV and TCL fractions were isolated 24 h post-transfection and analyzed by Western blotting with the indicated antibodies. The amount of protein loaded per lane is indicated at the bottom of the immunoblots. The immunoblots are representative of three independent experiments. E, Quantitation of the total protein levels of the EV fractions expressed as a percentage of its corresponding TCL fractions in the absence or presence of CQ. Values represent the mean \pm S.E. (n = 3). Statistical significance was determined by performing a one-way ANOVA with a Tukey post-hoc test; n.s., not significant.

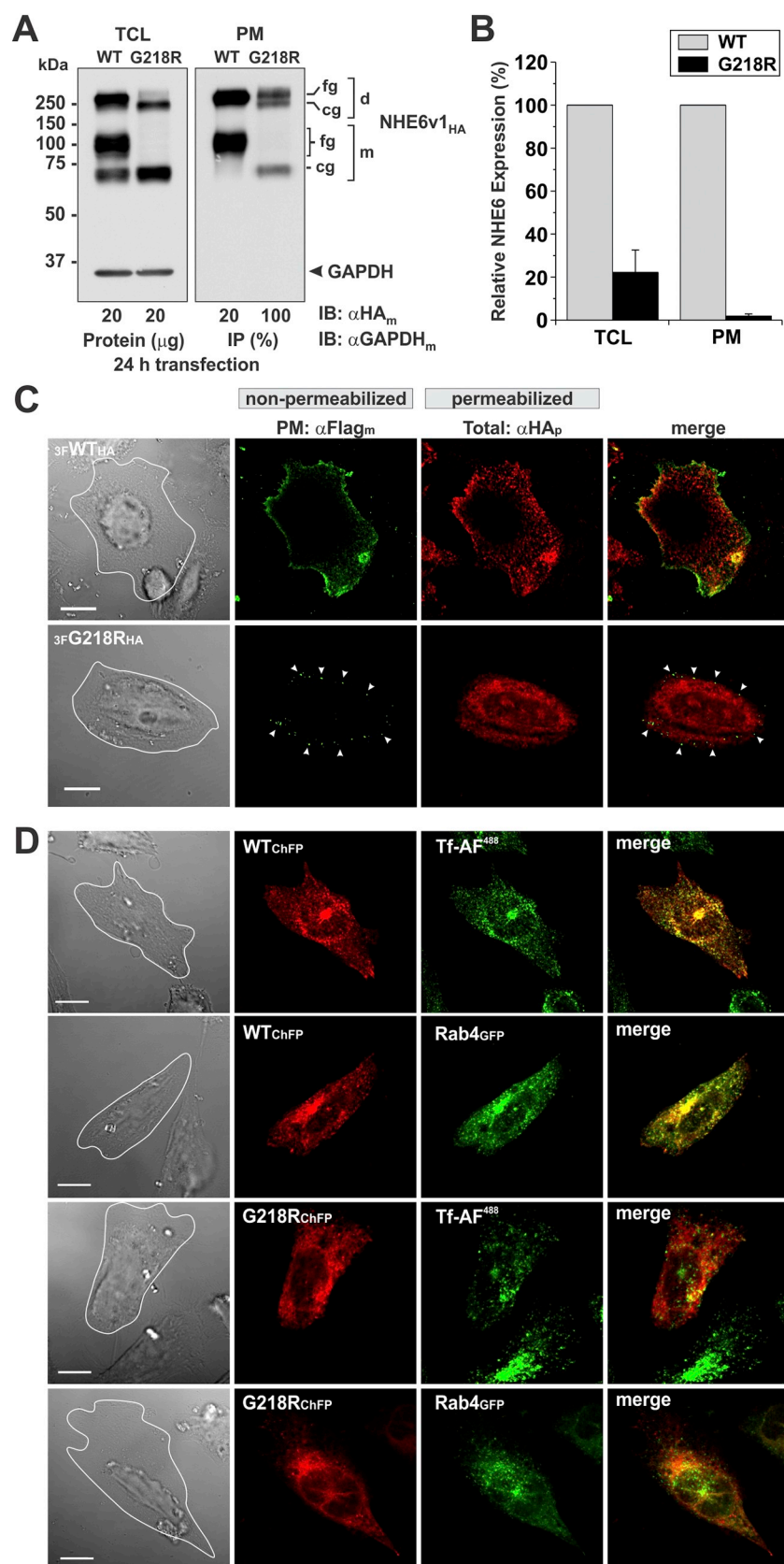


Fig. 4. Membrane trafficking of NHE6 G218R is impaired. **A**, AP-1 cells were transiently transfected with NHE6v1_{HA} WT or G218R for 24 h and cell surface proteins were labelled with biotin as described in 'Materials and Methods'. Total cell lysates (TCL) were prepared and a small portion representing the total fraction was removed. The remaining supernatants containing equal amounts of total protein for WT and G218R were loaded onto NeutrAvidin® Agarose beads to purify the biotinylated plasma membrane (PM) proteins from the non-biotinylated (intracellular) proteins. For the TCL fraction, aliquots containing 20 μ g protein for WT and G218R, were examined by Western blotting (left panel). For the plasma membrane (PM) fraction, 20% and 100% of the biotinylated proteins extracted from the TCL of WT and G218R transfectants, respectively, were subjected to Western blotting (right panel). Both immunoblots were probed with a mouse monoclonal anti-HA_m antibody (α HA_m) to detect NHE6v1_{HA}, and an anti-GAPDH_m antibody to assess the purity of the biotinylated PM fraction. **B**, Densitometric quantification of the relative TCL and PM abundances of WT and G218R. For TCL, the relative protein abundance was expressed as a ratio of NHE6/GAPDH. For the PM level, the relative abundance of the biotinylated G218R was normalized to that of WT, taking into account the differences in protein loading. Values represent the mean \pm S.E. (n = 4). **C**, Cell surface expression of NHE6v1 was also assessed by imaging. To this end, a triple Flag epitope-tag was inserted into the first extracellular loop of NHE6v1_{HA} (3F-NHE6v1_{HA}), as described previously (Ilie et al., 2016). AP-1 cells were transiently transfected (24 h) with WT and G218R, fixed but not permeabilized with detergent to detect only surface expression using a mouse monoclonal anti-Flag antibody (α Flag_m). Cells were then permeabilized with saponin to detect total cellular expression using a rabbit polyclonal anti-HA antibody (α HA_p) and fluorescence and transmitted light images were acquired using confocal microscopy. Footprints of the transfected cells are indicated as white outlines in the transmitted light images (far left panels). **D**, Representative images of AP-1 cells transiently transfected (24 h) with NHE6v1_{ChFP} WT or G218R individually, or in combination with an organellar marker for recycling endosomes (Rab4_{GFP}). Recycling endosomes were also labelled by uptake of Alexa Fluor⁴⁸⁸-conjugated transferrin (Tf-AF⁴⁸⁸, 10 μ g/ml) for 45 min. Scale bars represent 10 μ m.

(Fig. 4A-B), consistent with Fig. 2B, however the fraction of G218R at the PM was < 2% of surface WT levels (note the 5-fold higher protein loading in the G218R lane). This indicates there was not only a reduction in protein half-life and abundance, but also impaired delivery

and/or retention of the mutant at the cell surface. Moreover, while only fully-glycosylated WT protein was detected in the PM-enriched fraction, the G218R mutant reached the cell surface in both its fully- and core-glycosylated forms.

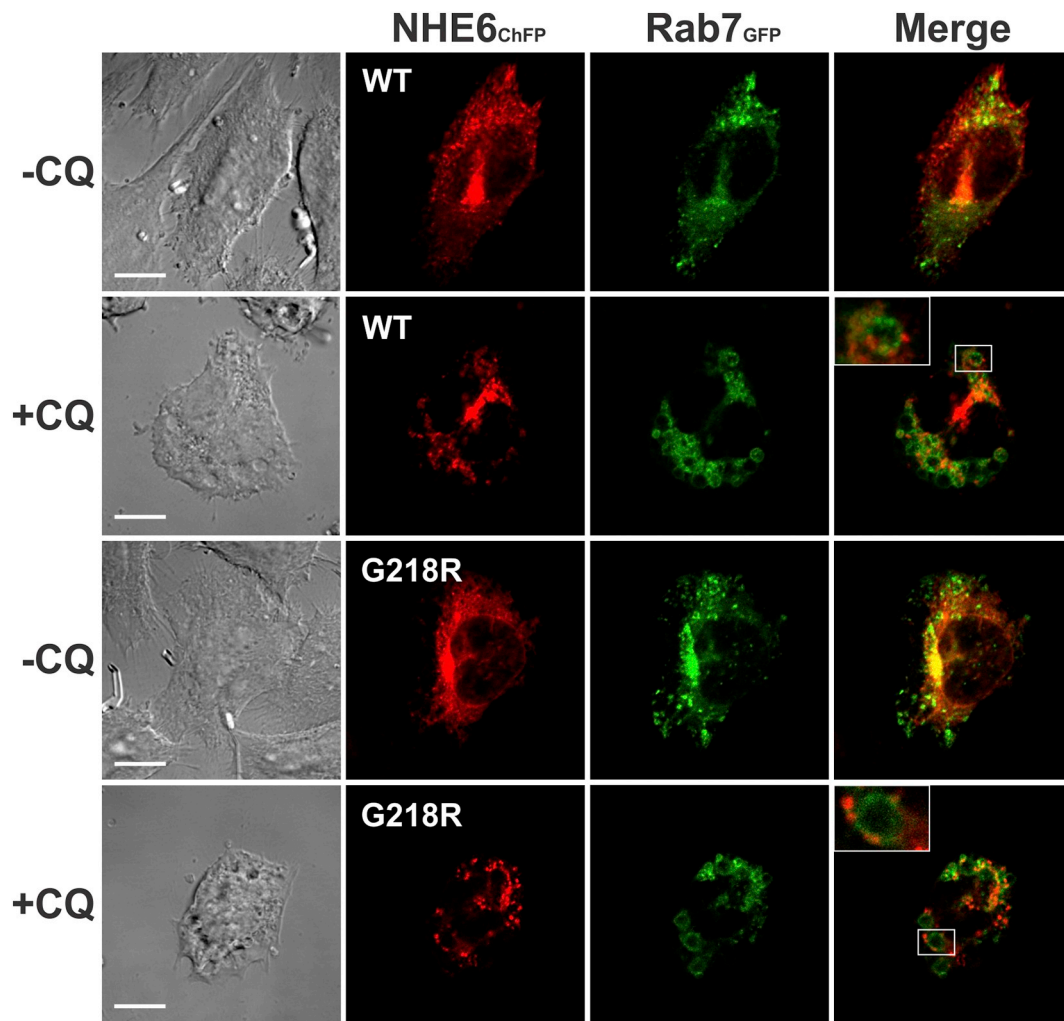


Fig. 5. Chloroquine blocks the fusion of NHE6 G218R-containing vesicles with late endosomes. AP-1 cells were transiently transfected with NHE6v1_{ChFP} WT or G218R in combination with Rab7_{GFP} for 9 h, then left untreated (–) or treated (+) with chloroquine (CQ, 250 μ M) for an additional 15 h in serum-free culture media. Representative images from two independent experiments are shown. Scale bars represent 10 μ M.

The distribution of WT and G218R was also verified by fluorescence imaging. A triple Flag epitope-tag (3F) was inserted in the first extracellular loop of NHE6v1_{HA} (3F-NHE6v1_{HA}) as described previously (Ilie et al., 2014). AP-1 cells were transiently transfected (24 h) and fixed but not permeabilized to immuno-detect only surface transporters. Cells were then permeabilized with saponin for detection of total cellular expression using an anti-HA antibody. The WT transporter was distributed on the cell surface in a relatively continuous pattern whereas the G218R mutant had minor punctate immunostaining (Fig. 4C). Intracellularly, the WT transporter was in discrete round-oval and tubulovesicular vesicles throughout the cell as expected. By contrast, the G218R mutant showed a more diffuse, partially reticular, distribution in addition to punctate signals.

To further compare the subcellular distribution of WT and G218R, dual-labelling experiments were performed with C-terminal monomeric Cherry fluorescent protein (ChFP)-tagged constructs of NHE6v1 (*i.e.*, WT_{ChFP} and G218R_{ChFP}) and organellar markers. The WT_{ChFP} transporter showed a punctate distribution with substantial accumulation in a compact pericentriolar compartment that overlapped extensively with established markers of recycling endosomes (*i.e.*, Alexa Fluor 488-conjugated transferrin, Tf-AF⁴⁸⁸ and Rab4_{GFP}) (Fig. 4D). As expected, WT_{ChFP} also showed partial overlap but distinct distribution with markers of the *trans*-Golgi network (TGN) and associated secretory vesicles (*i.e.*; TGN46_{GFP}), clathrin-coated vesicles/early endosomes (*i.e.*; Rab5_{GFP}), and peripheral recycling endosomes (*i.e.*; Rab11_{myc}), whereas minimal overlap was

observed with markers of the ER (*i.e.*; CANX), MVB/LEs (*i.e.*; Rab7_{GFP}) and lysosomes (*i.e.*, Lamp1) (Supplementary Fig. S4). Conversely, immunofluorescence signals for the G218R_{ChFP} mutant were more dispersed and showed very limited colocalization with Tf-AF⁴⁸⁸ and Rab4_{GFP} (Fig. 4D). Moreover, G218R-expressing cells had visibly reduced uptake and accumulation of Tf-AF⁴⁸⁸ compared to neighboring untransfected cells, suggesting a defect in recycling endosomal trafficking. The G218R_{ChFP} mutant also showed more discernible overlap with markers of the ER, as well as the TGN, early endosomes and MVB/LE, while overlap with peripheral recycling endosomes or lysosomes was less evident (Supplementary Fig. S5). To test whether the negligible detection of G218R at lysosomes was simply a consequence of lysosomal proteolysis of the fluorophore-tagged transporter, cells were treated with cycloheximide and LeuP for 6 h to track the fate of existing protein while inhibiting lysosomal proteolysis. Blocking *de novo* protein synthesis and lysosomal proteolysis resulted in the detection of both WT and G218R in dispersed vesicles, but did not result in their enrichment in Lamp1-labelled lysosomes (Supplementary Fig. S6). These data are consistent with the biochemical data presented in Fig. 3B where inhibition of lysosomal proteases with LeuP did not block the loss of WT or G218R.

We next examined the effects of chloroquine which, unlike LeuP, did lessen the loss of G218R (see Fig. 3B). Exposure to chloroquine (250 μ M, 15 h) induced the formation of abnormally large, membrane-bounded structures that colocalized with Rab7_{GFP}, indicative of malformed MVB/LEs (Fig. 5); results consistent with the vacuologenic

effects of chloroquine (Fedorko, 1967). Notably, it largely prevented the signal overlap between G218R_{ChFP} and Rab7_{GFP} that was observed in untreated cells. However, the G218R_{ChFP}-containing endosomes were positioned immediately adjacent to the Rab7_{GFP}-labelled compartments, as if docked but not fused. Collectively, this subcellular distribution pattern suggests that chloroquine blocks the fusion of G218R-endosomes with MVB/LE.

3.7. G218R-containing endosomes fail to acidify

Acidification of organelles is important for efficient sorting and movement of proteins and lipids along the biosynthetic and endocytic pathways (Casey et al., 2010; Weisz, 2003). To measure intraluminal pH (pH_v) of NHE6-containing vesicles, we inserted pHluorin2, a ratio-metric pH-sensitive green fluorescent protein (Mahon, 2011), into the first exofacial loop of the WT and mutant NHE6 (pH_2 WT and pH_2 G218R) (Fig. 6A). This insertion did not alter biosynthesis and post-translational maturation (Fig. 6B) or the subcellular distribution (Fig. 6C, right panel and data not shown) of the proteins. An *in situ* calibration curve of pHluorin2 fluorescence as a function of pH (using cells transfected with pH_2 WT) is presented in Fig. 6C (left panel).

To compare the pH_v profiles of pH_2 WT and pH_2 G218R-containing vesicles, AP-1 cells were transiently transfected with each construct for 24 h, and then incubated with cycloheximide for an additional 5 h to block new protein synthesis while allowing the existing WT and G218R to mature biosynthetically and accumulate in vesicles prior to imaging (see examples of imaged vesicles in the insets of Fig. 6D). The pH_v spectrum of vesicles from all pH_2 WT or pH_2 G218R transfected cells analyzed ($n = 12$ cells per construct) display a single-peak Gaussian distribution (Fig. 6D). The average steady-state pH_v of pH_2 WT-containing vesicles was 6.59 ± 0.03 (mean \pm S.E., $n = 12$ cells), which is within the range (pH_v 6.4–6.8) of transferrin-enriched recycling endosomes reported earlier using other approaches (Ilie et al., 2016; Teter et al., 1998; Xinhan et al., 2011; Yamashiro et al., 1984). By contrast, the mean pH_v of pH_2 G218R-containing vesicles was shifted significantly to more alkaline levels; i.e., pH_v 7.09 ± 0.04 (mean \pm S.E., $n = 12$ cells; $p < 0.001$, two-sample Student's *t*-test). This result suggests G218R activity is altered, possibly enhanced (i.e., increased influx of cytoplasmic Na^+ or K^+ in exchange for luminal H^+), which may disrupt recycling endosomal trafficking.

Earlier studies have shown that NHE6 overexpression stimulates the uptake of Tf-TfR complexes into recycling endosomes in a manner that is dependent on its ion transport capabilities (Ilie et al., 2016; Xinhan et al., 2011). As mentioned above, microscopy visualization of Tf-AF⁴⁸⁸ uptake in G218R-expressing cells appears decreased (Fig. 4D). To assess this quantitatively, we used a flow cytometry-based assay to measure the uptake of Alexa Fluor 633-conjugated Tf (Tf-AF⁶³³) as a measure of recycling endosomal trafficking. For these experiments, HeLa cells transiently expressing GFP alone or comparable levels of GFP-tagged constructs of WT or G218R (Fig. 6E) were used instead of AP-1 cells because of the significantly higher signal to noise ratio of Tf-AF⁶³³ uptake, as previously described (Ilie et al., 2016). WT_{GFP}-expressing cells exhibited a significant increase in Tf-AF⁶³³ uptake compared to GFP-transfected controls (WT_{GFP}: $171\% \pm 11$, $p < 0.01$, one-sample Student's *t*-test), whereas this stimulation was attenuated in cells expressing G218R_{GFP} cells ($123\% \pm 5$; $p < 0.01$) (Fig. 6F). Collectively, these data indicate that cargo trafficking along the recycling endosomal pathway is compromised in G218R-expressing cells.

3.8. Overexpression of G218R mutant alters dendritic morphology of mouse hippocampal neurons

Previous examination of NHE6 null mice have revealed a crucial role for the transporter in the development and maintenance of axonal and dendritic branching and synapse number of cortical and hippocampal pyramidal neurons (Ouyang et al., 2013). Likewise, analogous

changes in the morphology of cultured mouse hippocampal neurons were also observed upon overexpression of NHE6 deletion mutants (p.W370-T372del and p.E287-S288del) (Ilie et al., 2016; Ilie et al., 2014). To investigate whether overexpression of G218R affects the morphological integrity of mature neurons *in vitro*, primary cultures of differentiated hippocampal pyramidal neurons (10–12 days *in vitro*, DIV) prepared from C57BL/6 mice were cotransfected with GFP and ChFP (controls) or GFP plus ChFP-tagged constructs of WT or G218R (i.e., WT_{ChFP} and G218R_{ChFP}) and visualized by deconvolution confocal microscopy after 48 h. As shown Fig. 7A, WT_{ChFP}-containing vesicles were distributed throughout the soma and neurites in a pattern that mirrors that of endogenous NHE6 (Deane et al., 2013) and the neurons exhibited extensive dendritic arborization comparable to control GFP + ChFP-transfectants. By contrast, in GFP + G218R_{ChFP} co-transfected neurons, the majority of G218R_{ChFP}-containing vesicles were concentrated in the soma and primary dendrites, at least as revealed at this low level of resolution. Furthermore, this was associated with striking reductions in higher-order dendritic branching. Using FilamentTracer Imaris software, total dendritic length, surface area and number of branch points of the neurons expressing GFP + G218R_{ChFP} were significantly decreased (ranging from ~26–36% for each parameter) compared to control GFP + ChFP or GFP + WT_{ChFP} (Fig. 7B–D). These observations are consistent with G218R_{ChFP} acting in a dominant-negative manner to suppress endogenous NHE6 function and to disrupt the gross morphology of differentiated neurons.

We next examined whether these changes also correlated with corresponding changes in the distribution of G218R at dendritic spines as well as in spine density and shape, with the latter parameter thought to be a dynamic structural correlate of the strength and maturity of each spine-synapse (i.e., stubby: ambiguous; thin: weak and plastic; mushroom: strong and stable) (Harris et al., 1992). For these analyses, we used the colocalization tool and spine detection and classification algorithm of Imaris. Puncta localized within spines were then tallied based upon their presence in the base, neck, or head subregions of these spines. As shown visually in Fig. 8A–C, the fraction of spines associated with NHE6v1 declined by ~38% for G218R_{ChFP} compared to WT_{ChFP} (WT_{ChFP}, $79.6\% \pm 2.0$; G218R_{ChFP}, $49.7\% \pm 4.0$; $p < 0.0001$). Moreover, of the NHE6v1-associated spines, there was a significant decrease (~62%) in the accumulation of G218R_{ChFP} in the head (WT_{ChFP}, $42.5\% \pm 2.0$; G218R_{ChFP}, $16.1\% \pm 3.7$; $p < 0.0001$) and a reciprocal increase (~63%) at the base (WT_{ChFP}, $46.1\% \pm 2.4$; G218R_{ChFP}, $75.3\% \pm 5.3$; $p < 0.0001$) of spines compared to WT_{ChFP}, whereas no change was detected in the neck subregion. These changes coincided with a marked reduction in total spine density of G218R_{ChFP}-transfected neurons compared to control GFP + ChFP or GFP + WT_{ChFP} transfectants (25% and 34%, respectively) (# spines/ μ m dendrite: ChFP, 0.91 ± 0.06 ; WT_{ChFP}, 1.02 ± 0.05 ; G218R_{ChFP}, 0.68 ± 0.04 ; $p < 0.0001$) (Fig. 8D). This decrease was attributed solely to the loss of mature mushroom-shaped spines (ChFP, 0.35 ± 0.03 ; WT_{ChFP}, 0.40 ± 0.02 ; G218R_{ChFP}, 0.17 ± 0.01) and coincided with a several-fold increase in the density of immature filopodial-like protrusions (# filopodia/ μ m dendrite: ChFP, 0.012 ± 0.006 ; WT_{ChFP}, 0.005 ± 0.005 ; G218R_{ChFP}, 0.064 ± 0.014 ; $p < 0.01$) (Fig. 8E). Thus, in addition to gross changes in neuronal morphology, expression of G218R selectively impairs the formation of mature synapses.

To compare the steady-state pH_v of WT and G218R-containing vesicles, the neurons were transiently transfected with the pH_2 WT and pH_2 G218R constructs for 24 h, but in this instance were not further treated with cycloheximide as this was not well tolerated by the G218R-expressing cells. To ensure pH measurements were confined to endosomes (and not newly synthesized NHE6v1 in the ER), image analyses were focused primarily on discrete punctate in dendritic shafts and spines (see insets of Fig. 8F). The average steady-state pH_v of pH_2 WT-containing vesicles was 6.79 ± 0.02 , whereas the mean pH_v of pH_2 G218R-containing vesicles was shifted significantly to more alkaline levels; i.e., pH_v 7.14 ± 0.02 ($p < 0.001$) (Fig. 8F). These findings are

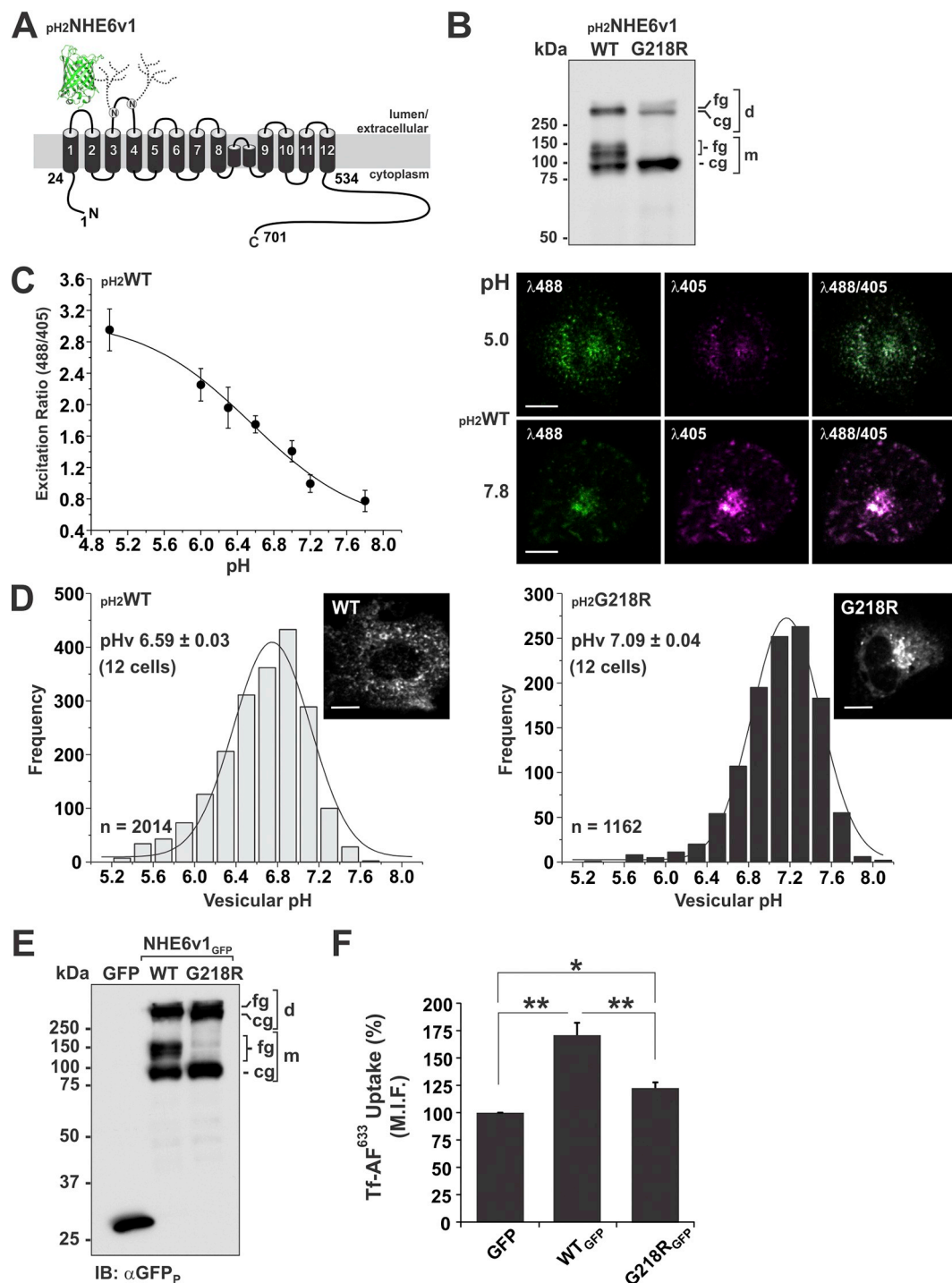


Fig. 6. Acidification and cargo trafficking of NHE6 G218R-containing vesicles are impaired. **A**, Illustration of NHE6v1 containing the pH-sensitive pHluorin2 (pH 2) inserted in its first extracellular loop (pH2NHE6v1). **B**, Representative Western blot of total cell lysates of AP-1 cells transiently expressing (24 h) pH2WT or pH2G218R. The immunoblot was probed with a polyclonal anti-GFP antibody (α GFP_p). **C**, Vesicular pH was measured by single-cell fluorescence ratiometric imaging analysis (FRIA) at 37 °C using a Zeiss LSM 780 confocal microscope as described in ‘Materials and Methods’. The *left panel* shows the *in situ* calibration curve of pH 2 fluorescence (excitation ratio 488/405) as a function of vesicular pH performed by *in situ* clamping of vesicular pH between 5 and 7.8. The *right panel* shows representative fluorescence images of AP-1 cells expressing pH2WT when excited at 488 nm (green) and 405 nm (pseudo-coloured magenta) as well as the merged (488/405) images when clamped at pH 5 and 7.8. **D**, Graphical plot of the intraluminal pH of pH2WT- and pH2G218R-containing vesicles. The experiment was repeated 3 times and the plots show the frequency of vesicles as a function their intraluminal pH analyzed from 12 cells for each construct. The total number of vesicles analyzed (n) and the average vesicular pH (pH_v) (mean \pm S.E.) are indicated in the plots. Insets shows representative images of pH2WT- and pH2G218R-containing vesicles in transfected cells. **E**, HeLa cells were transiently transfected (24 h) with GFP, NHE6v1_{GFP} WT or G218R. Total cell lysates were prepared and analyzed by Western blotting using a polyclonal anti-GFP (α GFP_p) antibody. **F**, Uptake of Tf-AF⁶³³ was monitored in HeLa cells expressing GFP, WT_{GFP} or G218R_{GFP}. Median fluorescence intensity (M.I.F.) of Tf-AF⁶³³ was measured in 10⁴ GFP-positive cells by flow cytometry. Data were normalized and represent mean \pm S.E. (n = 4). Significance was established using a Student’s *t*-test, **p* < 0.05, ***p* < 0.01. (For interpretation of the references to colour in this figure legend, the reader is referred to the web version of this article.) (I’m not sure i understand what is meant by this comment. What is the reader being referred to?)

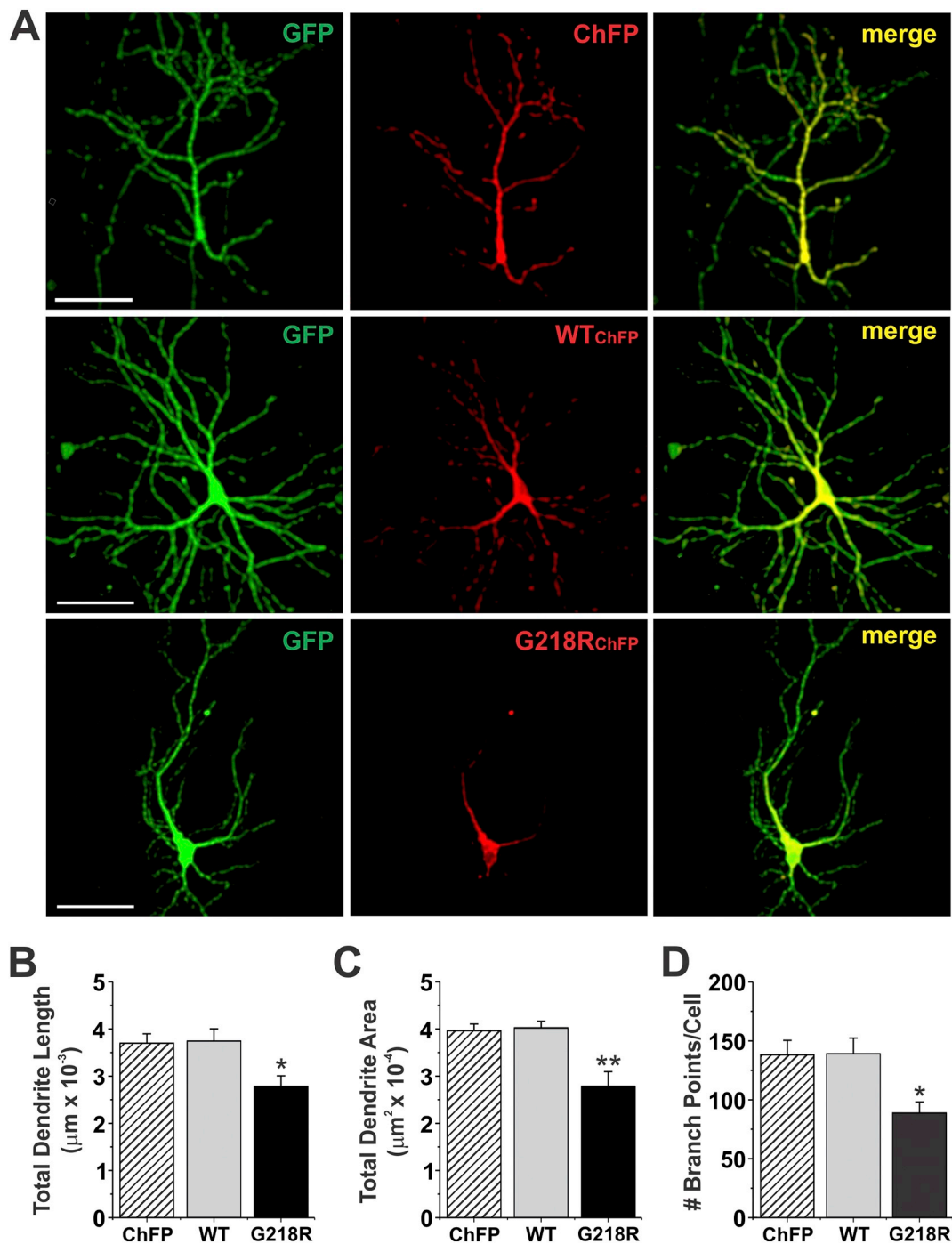


Fig. 7. Heterologous expression of G218R decreases the complexity of dendritic arborisation in mouse hippocampal neurons. **A**, Confocal images of primary hippocampal pyramidal neurons co-transfected with cytosolic enhanced GFP (to visualize cell morphology) and monomeric cherry fluorescent protein (ChFP) (as a transfection control), or with GFP and ChFP-tagged NHE6 WT or G218R (WT_{ChFP} and G218R_{ChFP}, respectively). Forty-eight h post-transfection, cells were fixed in 4% paraformaldehyde, mounted onto glass slides, and examined by confocal microscopy. Images show each channel separately and merged. **B–D**, Quantification of parameters related to neuronal branching, including the sums of total dendritic length (**B**) and area (**C**), as well as the total number of branch points per cell (**D**) using the FilamentTracer plug-in module from Imaris Software. Values represent the mean \pm S.E. of 3 separate experiments ($n = 5$ neurons for each condition/experiment). * $p < 0.05$; ** $p < 0.01$, one-way ANOVA with a Bonferroni post-hoc test. Scale bar: 60 μm .

comparable to results obtained in AP-1 cells.

4. Discussion

In this report, we describe a unique SLC9A6/NHE6 missense variant (p.G218R) associated with Christianson Syndrome that results in an apparent gain-of-function, as manifested by hypoacidification (*i.e.*,

alkalinization) of G218R-endosomes. Despite this ostensible “gain-of-function”, the transporter was nonetheless recognized as defective as evidenced by its elevated state of ubiquitination and rapid expulsion from the cell by exosomal release. A schematic representation depicting these events is illustrated in Fig. 9. This contrasts with other mutations that cause total loss-of-function and correlate with overacidification and premature activation of acid proteases within endosomes and/or

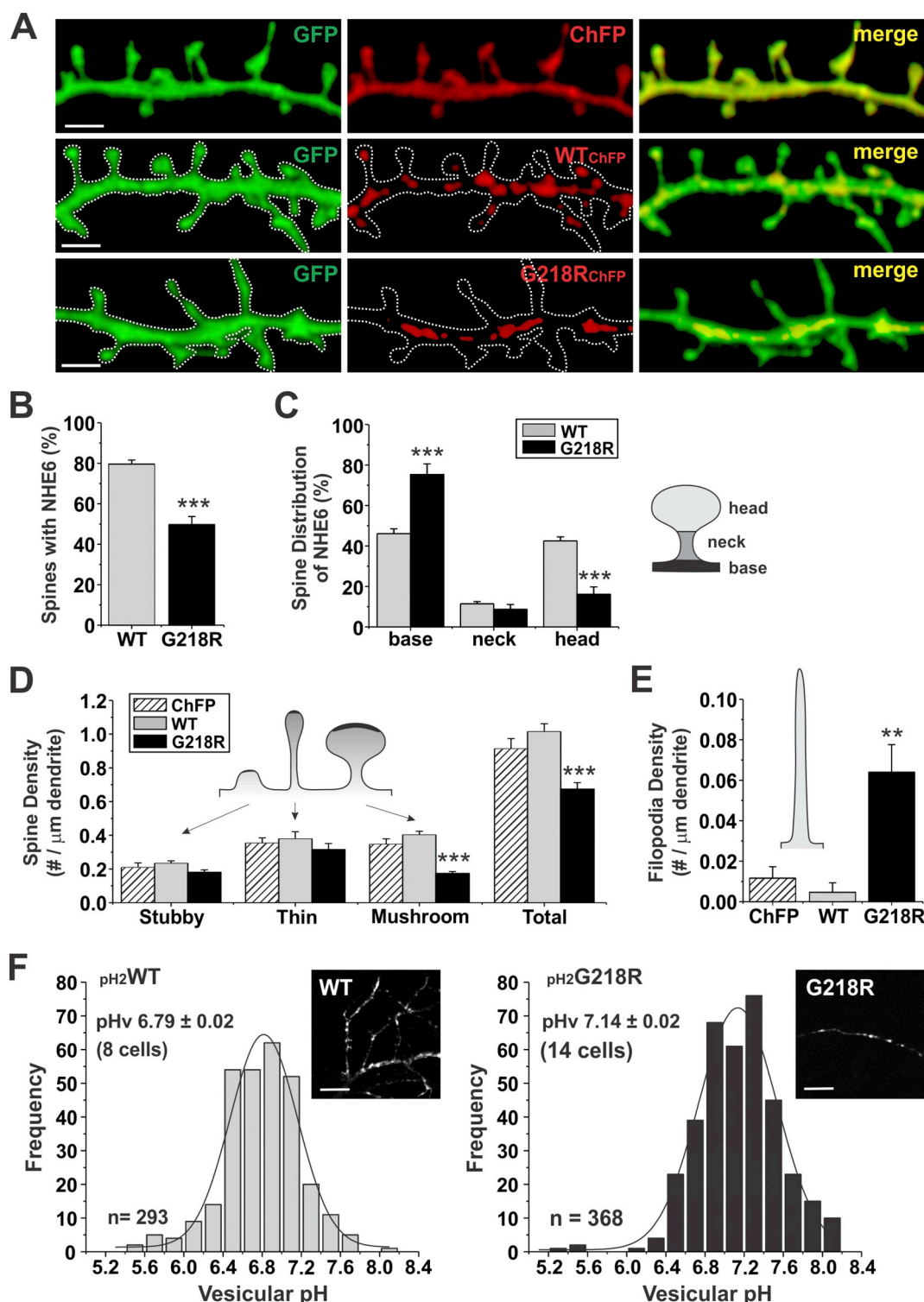


Fig. 8. Heterologous expression of G218R reduces the density of mature dendritic spines and increases appearance of filopodia.

A, Representative confocal images of secondary and tertiary dendrites of 14+ DIV primary hippocampal neurons co-transfected with enhanced GFP and ChFP alone or with GFP and WT_{ChFP} or G218R_{ChFP}. GFP and ChFP channels are shown individually and merged. Scale bar: 2 μ m. B, Quantification of the fraction of spines (mean \pm S.E.) containing puncta of transfected WT_{ChFP} or G218R_{ChFP} of all spines analyzed for each transfection condition. C, Quantification of the proportion (mean \pm S.E.) of spine-localized puncta of overexpressed WT_{ChFP} or G218R_{ChFP} in each major spine subregion. *i.e.* base (black), neck (dark gray), and head (light gray). D-E, Quantification of the density (mean \pm S.E.) of each major spine subtype, *i.e.* stubby, mushroom, and thin (D), as well as immature filopodia-like structures (E). Data were collected from 3 separate experiments: GFP control: $n = 214$ spines and 2 filopodia along 234 μ m of dendrite from 8 cells; WT_{ChFP}: $n = 234$ spines and 1 filopodia along 236 μ m of dendrite from 8 cells; G218R_{ChFP}: $n = 158$ spines and 15 filopodia along 232 μ m of dendrite from 8 cells. **: $p < 0.01$; ***: $p < 0.0001$, one-way ANOVA with Bonferroni post-hoc test for all comparisons except filopodia (Kruskal-Wallis test with Dunn's post-hoc). F, Graphical plot of the intraluminal pH of pH_2 WT- and pH_2 G218R-containing vesicles in transfected primary mouse hippocampal neurons. The experiment was repeated 3 times and the plots show the frequency of vesicles as a function their intraluminal pH (pH_v) analyzed from 8 to 14 cells for each construct. The total number of vesicles analyzed and the average pH values (mean \pm S.E.) are indicated in the plots. Insets shows representative images of pH_2 WT- and pH_2 G218R-containing vesicles in neurites of transfected cells.

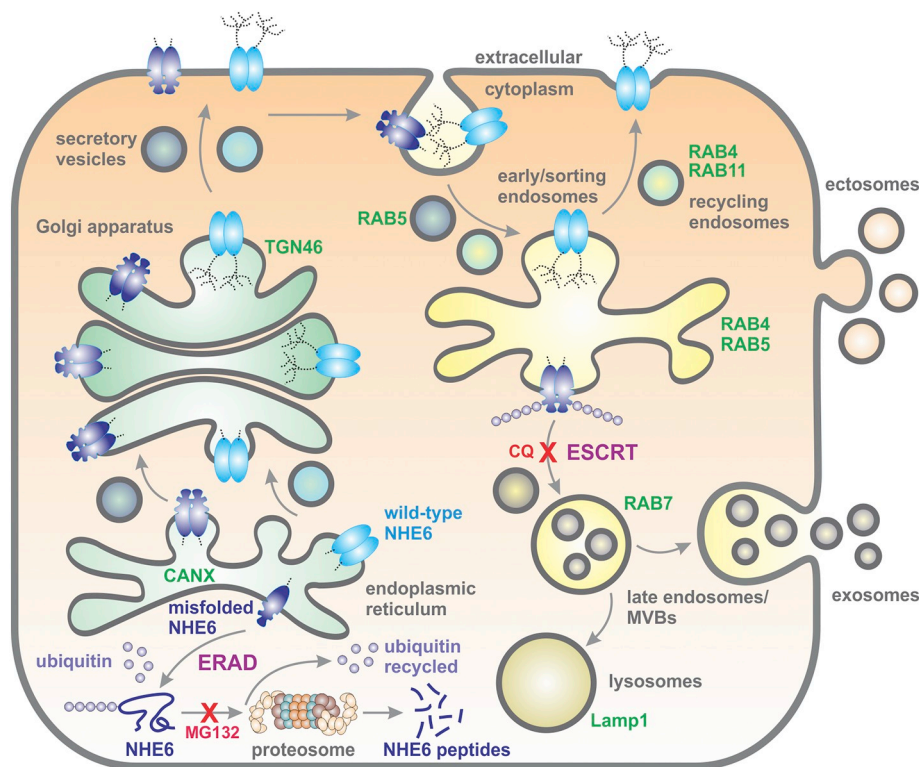


Fig. 9. Cellular processing and membrane trafficking of NHE6. Schematic representation of the cellular processing of NHE6v1 WT and G218R along the exocytic and endocytic pathways. Nascent transporters are cotranslationally inserted into the ER membrane where they undergo N-linked core glycosylation. Upon proper folding and dimer assembly, the WT transporter is exported to the Golgi where it is subject to additional complex glycosylation, prior to export to the plasma membrane (PM). By contrast, the G218R transporter is more prone to misfolding at the ER and is targeted for ubiquitination and proteasomal degradation (i.e., ERAD pathway), effects that are partially blocked by proteasomal inhibitors such as MG132 (and lactacystin, not shown). However, a significant fraction of G218R is able to assemble as a homodimer and traffic through the Golgi to the PM, though complex glycosylation is largely impaired. PM-resident WT is internalized and normally recycled back to the PM. By contrast, G218R is recognized by the peripheral quality control machinery (i.e., ESCRT pathway) and targeted to late endosomes/multivesicular bodies (MVBs) that subsequently fuse with the PM and release their intraluminal vesicles (or exosomes) containing NHE6 into the extracellular milieu. The lysosomotropic agent chloroquine (CQ) blocks the transfer of G218R from early/sorting endosomes to late endosomes/MVBs.

expansion of the lysosomal compartment (Ilie et al., 2016; Ouyang et al., 2013; Roxrud et al., 2009). Despite these differences, in both cases there is a net loss of NHE6 protein which correlated with similar deleterious consequences on endosomal trafficking and neuronal morphology (Ilie et al., 2016; Ouyang et al., 2013; Roxrud et al., 2009). Clinically, the proband exhibited the vast majority of symptoms observed in CS patients devoid of NHE6 expression, with the exception of underdeveloped but stable motor skills. The significance, if any, of this latter feature in relation to the G218R mutation is unclear. It could be due to the variable degree and onset of motor regression in CS patients as well as other genetic modifier effects.

The G218R mutation compromises the structure-function integrity of the transporter. While the mutant transporter was capable of assembling as a homodimer, its level of complex glycosylation was significantly diminished and correlated with enhanced ubiquitination. A fraction of ubiquitinated G218R was subjected to proteasomal proteolysis, but contrary to expectations the bulk of ubiquitinated G218R was secreted in EVs rather than targeted to lysosomes. EVs are generated by virtually all cells and represent a heterogeneous population of vesicles that include nanoscale vesicles or exosomes (~30–100 nm in diameter) spawned by invagination and abscission of the limiting membrane of MVB/LEs and subsequently expelled after fusion with the PM, and larger-sized vesicles (often termed microparticles, microvesicles or ectosomes that range in size from ~100–1000 nm) formed by the outward budding and shedding of discrete subdomains of the PM (Colombo et al., 2014). Cellular discharge of EVs was initially described as a unique non-degradative route for removing unwanted or damaged macromolecules (Johnstone et al., 1987). However, subsequent studies have demonstrated that EVs also serve as a significant mode of intercellular communication under different physiological and pathological conditions due to their ability to fuse with and transfer biologically active molecules to neighboring or more distally located cells (Budnik et al., 2016; Colombo et al., 2014; Simons and Raposo, 2009). While our isolation methods did not distinguish between exosomes and ectosomes, the partial signal overlap of G218R_{ChFP} with Rab7_{GFP}-labelled MVB/LEs suggests that exosomal release is the likely route for

cellular clearance. Thus, CS can be added to a growing list of neurodegenerative diseases, such as Alzheimer's, Parkinson's and amyotrophic lateral sclerosis, associated with exosomal release of defective proteins (Levy, 2017; Rajendran et al., 2014; Vella et al., 2016).

The mechanisms underlying the enhanced accumulation of ubiquitinated G218R in MVB/LEs destined to fuse with the PM rather than merge with lysosomes (i.e., secretory versus degradative MVB/LEs, respectively) is unknown. However, the coexistence of discrete subpopulations of MVB/LEs within cells is supported by biochemical and ultrastructural studies. For instance, intraluminal vesicles of MVB/LEs released as exosomes are highly enriched in cholesterol and the sphingolipids ceramide, sphingomyelin and ganglioside GM3; components associated with lipid raft microdomains in the plasma membrane (Mobius et al., 2003; Trajkovic et al., 2008; Wubbolts et al., 2003). Inhibition of ceramide formation from sphingomyelin by pharmacological antagonists or RNAi depletion of neutral sphingomyelinase 2 (nSMase2), which has an optimum pH of 7.4, reduces release of exosomes without impairing lysosomal function (Trajkovic et al., 2008). By contrast, intraluminal membranes of another subpopulation of MVB/LE that progress to lysosomes are largely devoid of cholesterol but positive for a unique phospholipid, bis(monoacylglycerol)phosphate (BMP) - also known as lysobisphosphatidic acid (LBPA) (Kobayashi et al., 1998; Mobius et al., 2003), that is absent from exosomes (Wubbolts et al., 2003). Interestingly, the intrinsic biophysical properties of BMP/LBPA promote the formation of MVB/LE internal vesicles in a manner that is dependent on acidic pH and Alix, an ESCRT-associated protein (Hayakawa et al., 2007; Matsuo et al., 2004). Thus, these findings provide some evidence for the coexistence of at least two separate subpopulations of MVB/LEs that can be distinguished not only by their lipid composition, but also by their intraluminal pH (i.e., acidic versus alkaline). Based on these observations, we speculate that the more alkaline environment of G218R-containing early endosomes may favour ceramide production and the sequestering of G218R into lipid raft-enriched intraluminal vesicles of MVB/LEs destined for secretion as exosomes.

This raises the question of whether intraluminal pH plays a more

direct role in regulating the trafficking fate of distinct subpopulations of MVB/LE. This possibility is supported by studies showing that pathogen-mediated neutralization of endolysosomal pH in bladder epithelial cells acts as a critical signal that selectively activates the transient receptor potential mucolipin-3 (TRPML3) cation channel to release their luminal stores of Ca^{2+} , triggering cellular expulsion rather than internal degradation of bacteria-containing exosomes by lysosomes (Miao et al., 2015). Conversely, low luminal pH is thought to potentiate Ca^{2+} conductance of the endolysosomal TRPML1 channel and promote lysosomal biogenesis and function (Cheng et al., 2010; Xu et al., 2007). Thus, differential regulation of endolysosomal pH and pH-sensitive Ca^{2+} channels may play important roles in determining whether vesicle-associated cargo is destined for secretion or degradation, though the precise sorting mechanisms remain obscure.

Consistent with the above notion, we found that chloroquine which non-selectively neutralizes acidic endomembrane compartments enhanced the bulk release of EVs from CHO/AP-1 cells. However, while it fostered release of EVs, it also concomitantly blocked the extracellular export of G218R by preventing the fusion of G218R-vesicles with enlarged Rab7_{GFP}-labelled MVB/LEs. This effect agrees with earlier observations that chloroquine causes accumulation of endocytosed macromolecules in early endosomes that otherwise would be transferred to MVB/LEs and lysosomes (Lippincott-Schwartz and Fambrough, 1987; Stenseth and Thyberg, 1989). Other studies have also shown that dissipation of the proton gradient by inhibiting the vacuolar H^+ -ATPase with bafilomycin preferentially abrogated protein trafficking between the early and late endosomal compartments (Baravalle et al., 2005), whereas internalization and recycling of membrane cargo back to the cell surface were slowed but not blocked (Presley et al., 1997). Why this particular step in endomembrane trafficking along the degradative pathway is especially sensitive to agents that disrupt intraluminal acidification is not fully understood. However, emerging evidence has revealed that the vacuolar H^+ -ATPase operates not only as a pH-regulator, but also as a platform to recruit components of the vesicular trafficking machinery (i.e., small GTPase Arf6 and its associated guanine nucleotide exchange factor ARNO) in an intra-endosomal pH-dependent manner (Hurtado-Lorenzo et al., 2006). Notably, these interactions were found to be critical for endosomal trafficking between the early and late endosomal compartments, but not the recycling endosomal pathway. Accordingly, this behaviour could explain how chloroquine preferentially blocked the extracellular release of G218R, but did not impair the secretions of EV-associated TSG101 or HSP70 which may be sorted to MVB/LE independently of early endosomal delivery. Thus, bulk release of EVs at later stages of exocytosis do not appear to be dependent on luminal acidification, but instead may be stimulated by alkalization.

Under steady-state conditions, NHE6 operates as an alkalizing mechanism (i.e., cytoplasmic Na^+ or K^+ influx in exchange for luminal H^+) to counterbalance the acidifying effects of the vacuolar H^+ -ATPase, achieving an intraluminal pH in the range of ~6.4–6.6 in various cell types, including fibroblasts (Ilie et al., 2016; Xinhan et al., 2011), epithelia (Ohgaki et al., 2010) and neurons (Ouyang et al., 2013). Downregulating NHE6 expression or catalytic activity result in overacidification of recycling endosomes which, by an ill-defined mechanism, reduces their shuttling to and from the PM (Ilie et al., 2016; Ohgaki et al., 2010; Ouyang et al., 2013; Xinhan et al., 2011). Significantly, this impaired vesicle trafficking was associated with loss of epithelial apical cell polarity (Ohgaki et al., 2010) and neuronal degeneration and death (Ilie et al., 2016; Ouyang et al., 2013; Stromme et al., 2011). In contrast to loss-of-function mutations, we found that G218R-containing endosomes where considerably more alkaline compared to WT-endosomes in both AP-1 cells and primary cultures of mouse hippocampal neurons. While the precise consequences of this mutation on the kinetic properties of NHE6 will require further study, the elevated pH_v could simply be explained by a gain-of-function, though other mechanisms are possible. For instance, the mutation could

result in uncoupled H^+ efflux in a manner analogous to uncoupled Cl^- conductance for mutated forms of endosomal electrogenic $2\text{Cl}^-/1\text{H}^+$ exchangers of the CLC family (Scheel et al., 2005). Notwithstanding, this mutation still negatively impacted recycling endosomal trafficking in both cell types.

In hippocampal neurons, G218R overexpression resulted in pronounced reductions in dendritic arborization and spine density, with a selective loss of mature mushroom-shaped spines and the emergence of immature filopodial-like protrusions. These morphological alterations closely resemble effects observed when disrupting components of the cytoplasmic molecular machinery (i.e., Rab11, syntaxin13, and EHD1/Rme1) that control the trafficking of recycling endosomes, including rapid declines in dendritic spine size and density and abolition of AMPAR trafficking and long-term potentiation (LTP), a well-established cellular model of learning and memory (Park et al., 2006). The colocalization of NHE6 with AMPAR (Deane et al., 2013) and TRKB (Ouyang et al., 2013) in recycling endosomes suggests that NHE6 may function as a molecular link between the fine control of endosomal pH and trafficking signals that direct cargo needed for neurons to mature, function and survive.

In conclusion, disruption of NHE6 activity through either loss- or gain-of-function impairs optimal recycling endosomal function and thus may explain many of the neurodevelopmental and neurodegenerative symptoms associated with the pathophysiology of CS.

Ethics approval and consent to participate

For all family members, informed consent was obtained for participation in this study according to relevant institutional and national guidelines and regulations. All procedures for animal handling were approved by the McGill University Facility Animal Care Committee (FACC) and carried out in full compliance with the Policies and Guidelines of the Canadian Council on Animal Care (CCAC).

Availability of data and materials

The genetic data were deposited in the DECIPHER database (patient 368,102; <http://decipher.sanger.ac.uk>). All other data generated or analyzed during this study are included in this published article and its supplementary data file.

Competing interests

The authors declare that they have no competing interests.

Funding

This work was supported by research funds from the Canadian Institutes of Health Research (CIHR) (MOP-111191, PJT-155976) and McGill Faculty of Medicine to J.O., and the CIHR (MOP-86724) to R.A.M. A.Y.L.G. is the recipient of an Alexander Graham Bell Canada Graduate Scholarship.

Authors' contributions

Y-H.H. and M.J.V.H. performed the clinical diagnosis and genetic testing of the CS patient. A.I. and A.B. performed molecular, biochemical and data analyses; A.I. and A.Y.L.G. performed the immunofluorescence imaging studies; J.P. and A.M.B. performed the structure homology modelling of NHE6v1; A.I., R.A.M. and J.O. designed, supervised and coordinated different aspects of the experiments and data analyses; A.I. and J.O. wrote the manuscript; all authors critically discussed results, revised and approved the final version of the manuscript.

Acknowledgements

The authors wish to express sincere appreciation to Dr. John Hanrahan (McGill University) for critically reviewing the manuscript. We are grateful for the services provided by McGill Life Sciences Advanced Bioimaging Facility and the Flow Cytometry Facility, and Genome Québec for DNA sequencing; platforms supported by funding from the Canadian Foundation for Innovation.

Appendix A. Supplementary data

Supplementary data to this article can be found online at <https://doi.org/10.1016/j.nbd.2018.10.002>.

References

- Baravalle, G., et al., 2005. Transferrin recycling and dextran transport to lysosomes is differentially affected by bafilomycin, nocodazole, and low temperature. *Cell Tissue Res.* 320, 99–113.
- Bergeron, J.J., et al., 1994. Calnexin: a membrane-bound chaperone of the endoplasmic reticulum. *Trends Biochem. Sci.* 19, 124–128.
- Brett, C.L., et al., 2002. Human Na⁺/H⁺ exchanger isoform 6 is found in recycling endosomes of cells, not in mitochondria. *Am. J. Physiol. Cell Physiol.* 282, C1031–C1041.
- Budnik, V., et al., 2016. Extracellular vesicles round off communication in the nervous system. *Nat. Rev. Neurosci.* 17, 160–172.
- Buschow, S.I., et al., 2005. Exosomes contain ubiquitinated proteins. *Blood Cells Mol. Dis.* 35, 398–403.
- Calinescu, O., et al., 2017. Lysine 300 is essential for stability but not for electrogenic transport of the Escherichia coli NhaA Na⁺/H⁺ antiporter. *J. Biol. Chem.* 292, 7932–7941.
- Casey, J.R., et al., 2010. Sensors and regulators of intracellular pH. *Nat. Rev. Mol. Cell Biol.* 11, 50–61.
- Cheng, X., et al., 2010. Mucolipins: Intracellular TRPML1-3 channels. *FEBS Lett.* 584, 2013–2021.
- Christianson, A.L., et al., 1999. X linked severe mental retardation, craniofacial dysmorphism, epilepsy, ophthalmoplegia, and cerebellar atrophy in a large South African kindred is localised to Xq24-q27. *J. Med. Genet.* 36, 759–766.
- Coincon, M., et al., 2016. Crystal structures reveal the molecular basis of ion translocation in sodium/proton antiporters. *Nat. Struct. Mol. Biol.* 23, 248–255.
- Colombo, M., et al., 2013. Analysis of ESCRT functions in exosome biogenesis, composition and secretion highlights the heterogeneity of extracellular vesicles. *J. Cell Sci.* 126, 5553–5565.
- Colombo, M., et al., 2014. Biogenesis, secretion, and intercellular interactions of exosomes and other extracellular vesicles. *Annu. Rev. Cell Dev. Biol.* 30, 255–289.
- Deane, E.C., et al., 2013. Enhanced recruitment of endosomal Na⁺/H⁺ Exchanger NHE6 into dendritic spines of hippocampal pyramidal neurons during NMDA receptor-dependent long-term potentiation. *J. Neurosci.* 33, 595–610.
- Fagerberg, L., et al., 2014. Analysis of the human tissue-specific expression by genome-wide integration of transcriptomics and antibody-based proteomics. *Mol. Cell. Proteomics* 13, 397–406.
- Fedorok, M., 1967. Effect of chloroquine on morphology of cytoplasmic granules in maturing human leukocytes—an ultrastructural study. *J. Clin. Invest.* 46, 1932–1942.
- Firth, H.V., et al., 2009. DECIPHER: Database of Chromosomal Imbalance and Phenotype in Humans using Ensembl Resources. *Am. J. Hum. Genet.* 84, 524–533.
- Gilfillan, G.D., et al., 2008. SLC9A6 mutations cause X-linked mental retardation, microcephaly, epilepsy, and ataxia, a phenotype mimicking Angelman syndrome. *Am. J. Hum. Genet.* 82, 1003–1010.
- Greening, D.W., et al., 2015. A protocol for exosome isolation and characterization: evaluation of ultracentrifugation, density-gradient separation, and immunoaffinity capture methods. *Methods Mol. Biol.* 1295, 179–209.
- Harris, K.M., et al., 1992. Three-dimensional structure of dendritic spines and synapses in rat hippocampus (CA1) at postnatal day 15 and adult ages: implications for the maturation of synaptic physiology and long-term potentiation. *J. Neurosci.* 12, 2685–2705.
- Hayakawa, T., et al., 2007. pH-dependent formation of membranous cytoplasmic body-like structure of ganglioside GM1/bis(monoacylglycerol)phosphate mixed membranes. *Biophys. J.* 92, L13–L16.
- Hurtado-Lorenzo, A., et al., 2006. V-ATPase interacts with ARNO and Arf6 in early endosomes and regulates the protein degradative pathway. *Nat. Cell Biol.* 8, 124–136.
- Ilie, A., et al., 2014. Impaired posttranslational processing and trafficking of an endosomal Na⁺/H⁺ exchanger NHE6 mutant (D³⁷⁰WST³⁷²) associated with X-linked intellectual disability and autism. *Neurochem. Int.* 73, 192–203.
- Ilie, A., et al., 2016. A Christianson syndrome-linked deletion mutation (D²⁸⁷ES²⁸⁸) in SLC9A6 disrupts recycling endosomal function and elicits neurodegeneration and cell death. *Mol. Neurodegener.* 11.
- Johnstone, R.M., et al., 1987. Vesicle formation during reticulocyte maturation. Association of plasma membrane activities with released vesicles (exosomes). *J. Biol. Chem.* 262, 9412–9420.
- Kobayashi, T., et al., 1998. A lipid associated with the antiphospholipid syndrome regulates endosome structure and function. *Nature* 392, 193–197.
- Kowal, J., et al., 2016. Proteomic comparison defines novel markers to characterize heterogeneous populations of extracellular vesicle subtypes. *Proc. Natl. Acad. Sci. U. S. A.* 113, E968–E977.
- Kozachkov, L., et al., 2007. Functional and structural interactions of the transmembrane domain X of NhaA, Na⁺/H⁺ antiporter of Escherichia coli, at physiological pH. *Biochemistry* 46, 2419–2430.
- Landau, M., et al., 2007. Model structure of the Na⁺/H⁺ exchanger 1 (NHE1): functional and clinical implications. *J. Biol. Chem.* 282, 37854–37863.
- Le Bivic, A., et al., 1989. Vectorial targeting of apical and basolateral plasma membrane proteins in a human adenocarcinoma epithelial cell line. *Proc. Natl. Acad. Sci. U. S. A.* 86, 9313–9317.
- Lee, C., et al., 2013. A two-domain elevator mechanism for sodium/proton antiporter. *Nature* 501, 573–577.
- Levy, E., 2017. Exosomes in the diseased brain: first insights from in vivo Studies. *Front. Neurosci.* 11, 142.
- Li, X., et al., 2014. Functional role of arginine 425 in the mammalian Na⁺/H⁺ exchanger. *Biochem. Cell Biol.* 92, 541–546.
- Lippincott-Schwartz, J., Fambrough, D.M., 1987. Cycling of the integral membrane glycoprotein, LEP100, between plasma membrane and lysosomes: kinetic and morphological analysis. *Cell* 49, 669–677.
- Maeda, Y., Kinoshita, T., 2010. The acidic environment of the Golgi is critical for glycosylation and transport. *Methods Enzymol.* 480, 495–510.
- Maes, M., et al., 2012. Revealing the ligand binding site of NhaA Na⁺/H⁺ antiporter and its pH dependence. *J. Biol. Chem.* 287, 38150–38157.
- Mahon, M.J., 2011. pHluorin2: an enhanced, ratiometric, pH-sensitive green fluorescent protein. *Adv. Biosci. Biotechnol.* 2, 132–137.
- Masurel-Paulet, A., et al., 2016. A new family with an SLC9A6 mutation expanding the phenotypic spectrum of Christianson syndrome. *Am. J. Med. Genet. A* 170, 2103–2110.
- Matsuo, H., et al., 2004. Role of LBPA and Alix in multivesicular liposome formation and endosome organization. *Science* 303, 531–534.
- Maxfield, F.R., 1982. Weak bases and ionophores rapidly and reversibly raise the pH of endocytic vesicles in cultured mouse fibroblasts. *J. Cell Biol.* 95, 676–681.
- McKenna, A., et al., 2010. The Genome Analysis Toolkit: a MapReduce framework for analyzing next-generation DNA sequencing data. *Genome Res.* 20, 1297–1303.
- Meusser, B., et al., 2005. ERAD: the long road to destruction. *Nat. Cell Biol.* 7, 766–772.
- Miao, Y., et al., 2015. A TRP channel senses lysosome neutralization by pathogens to trigger their expulsion. *Cell* 161, 1306–1319.
- Miyazaki, E., et al., 2001. NHE6 protein possesses a signal peptide destined for endoplasmic reticulum membrane and localizes in secretory organelles of the cell. *J. Biol. Chem.* 276, 49221–49227.
- Mobius, W., et al., 2003. Recycling compartments and the internal vesicles of multivesicular bodies harbor most of the cholesterol found in the endocytic pathway. *Traffic* 4, 222–231.
- Nakamura, N., et al., 2005. Four Na⁺/H⁺ exchanger isoforms are distributed to Golgi and post-Golgi compartments and are involved in organelle pH regulation. *J. Biol. Chem.* 280, 1561–1572.
- Nygaard, E.B., et al., 2011. Structural modeling and electron paramagnetic resonance spectroscopy of the human Na⁺/H⁺ exchanger isoform 1, NHE1. *J. Biol. Chem.* 286, 634–648.
- Ohgaki, R., et al., 2010. The Na⁺/H⁺ exchanger NHE6 in the endosomal recycling system is involved in the development of apical bile canalicular surface domains in HepG2 cells. *Mol. Biol. Cell* 21, 1293–1304.
- Ouyang, Q., et al., 2013. Christianson syndrome protein NHE6 modulates TrkB endosomal signaling required for neuronal circuit development. *Neuron* 80, 97–112.
- Park, M., et al., 2006. Plasticity-induced growth of dendritic spines by exocytic trafficking from recycling endosomes. *Neuron* 52, 817–830.
- Pescosolido, M.F., et al., 2014. Genetic and phenotypic diversity of NHE6 mutations in Christianson syndrome. *Ann. Neurol.* 76, 581–593.
- Presley, J.F., et al., 1997. Bafilomycin A1 treatment retards transferrin receptor recycling more than bulk membrane recycling. *J. Biol. Chem.* 272, 13929–13936.
- Raiborg, C., Stenmark, H., 2009. The ESCRT machinery in endosomal sorting of ubiquitinated membrane proteins. *Nature* 458, 445–452.
- Rajendran, L., et al., 2014. Emerging roles of extracellular vesicles in the nervous system. *J. Neurosci.* 34, 15482–15489.
- Roxrud, I., et al., 2009. Dual degradation mechanisms ensure disposal of NHE6 mutant protein associated with neurological disease. *Exp. Cell Res.* 315, 3014–3027.
- Ruddock, L.W., Molinari, M., 2006. N-glycan processing in ER quality control. *J. Cell Sci.* 119, 4373–4380.
- Scheel, O., et al., 2005. Voltage-dependent electrogenic chloride/proton exchange by endosomal CLC proteins. *Nature* 436, 424–427.
- Schwede, M., et al., 2013. Genes for endosomal NHE6 and NHE9 are misregulated in autism brains. *Mol. Psychiatry* 19, 277–279.
- Seglen, P.O., et al., 1979. Inhibition of the lysosomal pathway of protein degradation in isolated rat hepatocytes by ammonia, methylamine, chloroquine and leupeptin. *Eur. J. Biochem.* 95, 215–225.
- Sikora, J., et al., 2016. X-linked Christianson syndrome: heterozygous female SLC9A6 knockout mice develop mosaic neuropathological changes and related behavioral abnormalities. *Dis. Model. Mech.* 9, 13–23.
- Simons, M., Raposo, G., 2009. Exosomes-vesicular carriers for intercellular communication. *Curr. Opin. Cell Biol.* 21, 575–581.
- Sinajon, P., et al., 2016. The expanding phenotypic spectrum of female SLC9A6 mutation carriers: a case series and review of the literature. *Hum. Genet.* 135 (8), 841–850.
- Stensth, K., Thyberg, J., 1989. Monensin and chloroquine inhibit transfer to lysosomes of endocytosed macromolecules in cultured mouse peritoneal macrophages. *Eur. J. Cell Biol.* 49, 326–333.

- Stromme, P., et al., 2011. X-linked Angelman-like syndrome caused by Slc9a6 knockout in mice exhibits evidence of endosomal-lysosomal dysfunction. *Brain* 134, 3369–3383.
- Teter, K., et al., 1998. Cellubrevin-targeted fluorescence uncovers heterogeneity in the recycling endosomes. *J. Biol. Chem.* 273, 19625–19633.
- Trajkovic, K., et al., 2008. Ceramide triggers budding of exosome vesicles into multivesicular endosomes. *Science* 319, 1244–1247.
- Vella, L.J., et al., 2016. Focus on Extracellular Vesicles: Exosomes and their Role in Protein trafficking and Biomarker potential in Alzheimer's and Parkinson's Disease. *Int. J. Mol. Sci.* 17, 173.
- Weisz, O.A., 2003. Acidification and protein traffic. *Int. Rev. Cytol.* 226, 259–319.
- Wubbolts, R., et al., 2003. Proteomic and biochemical analyses of human B cell-derived exosomes Potential implications for their function and multivesicular body formation. *J. Biol. Chem.* 278, 10963–10972.
- Xinhan, L., et al., 2011. Na⁺/H⁺ exchanger isoform 6 (NHE6/SLC9A6) is involved in clathrin-dependent endocytosis of transferrin. *Am. J. Physiol Cell Physiol.* 301, C1431–C1444.
- Xu, H., et al., 2007. Activating mutation in a mucolipin transient receptor potential channel leads to melanocyte loss in varitint-waddler mice. *Proc. Natl. Acad. Sci. U. S. A.* 104, 18321–18326.
- Yamashiro, D.J., et al., 1984. Segregation of transferrin to a mildly acidic (pH 6.5) Para-Golgi compartment in the recycling pathway. *Cell* 37, 789–800.